Detection and Perturbation of MicroRNAs using Synthetic Chemical Probes

by

Nicholas Michael Ankenbruck

B.A. Chemistry, Ball State University, 2011

M.S. Chemistry, Ball State University, 2013

Submitted to the Graduate Faculty of the

Dietrich School of Arts and Sciences in partial fulfillment

of the requirements for the degree of

Doctor of Philosophy

University of Pittsburgh

2019

UNIVERSITY OF PITTSBURGH

DIETRICH SCHOOL OF ARTS AND SCIENCES

This dissertation was presented

by

Nicholas Michael Ankenbruck

It was defended on

April 26, 2019

and approved by

W. Seth Childers, Assistant Professor, Department of Chemistry

Kabirul Islam, Assistant Professor, Department of Chemistry

Subha Das, Assistant Professor, Department of Chemistry, Carnegie Mellon University

Dissertation Director: Alexander Deiters, Professor, Department of Chemistry

Detection and Perturbation of MicroRNAs using Synthetic Chemical Probes

Nicholas Michael Ankenbruck, PhD

University of Pittsburgh, 2019

microRNAs (miRNAs) are small, non-coding RNA molecules capable of regulating protein expression in cells via binding to a complementary sequence within the 3' untranslated region (3' UTR) or coding domain sequence (CDS) of target messenger RNAs (mRNAs), thereby inducing translational repression and ultimately mRNA degradation. As such, its unsurprising that dysregulation of miRNAs has been implicated in a wide range of diseases in humans, including cancer. While regulation of miRNAs has largely been mediated by oligonucleotide reagents, current technologies exhibit limitations in terms of stability and pharmacological properties. In contrast, small molecules possess many advantageous qualities as tools to perturb miRNA function, including fast activity, systematic delivery, and enhanced cell permeability. Two luciferase-based reporters were developed into a cell-based assay employed in separate high-throughput screens of >300,000 compounds to identify selective small molecule modifiers of miR-21 or miR-122 function. The work presented herein discusses validation of oxadiazole, ether-amide, and *N*-acylhydrazone miR-21 inhibitors as well as sulfonamide and methanone inhibitors of miR-122 function identified in their respective high-throughput screens. In addition to secondary assays to confirm function and specificity of the lead molecules, structure-activity relationship (SAR) studies were carried out in order to determine important structural features of each scaffold and to attempt to improve their activity. Moreover, preliminary functional assays were carried out to evaluate therapeutic potential of improved molecules identified through the SAR study. Collaborations with start-up companies to discover small molecule inhibitors of

miRNA processing are also presented. Additionally, delivery of DNA logic devices capable of recognizing miRNAs in cells or releasing a small molecule output in response to miRNA inputs are discussed. Optical regulation of chemical tools using light affords spatial and temporal control over biological processes and as such, a second-generation caged promoter was incorporated into a plasmid to afford optical control of transcription. Finally, methods for delivery of γ-modified peptide nucleic acids (PNAs) and morpholino oligomers into mammalian cells for use as splice-switching oligonucleotides or anti-miRNA agents were explored.

Table of Contents

List of Tables

List of Figures

Preface

I would like to thank my advisor, Dr. Alexander Deiters, for his guidance, support, and for giving me the opportunity to work and learn in his laboratory as well as conduct exciting research. I have appreciated his mentorship as well as his high expectations as they have pushed me to become a better scientist. I also would like to extend a special 'thank you' to my committee, Dr. Kabirul Islam, Dr. Seth Childers, and Dr. Subha Das for their support and guidance.

Thank you to past and present group members including Yuta Naro, Cole Emanuelson, Anirban Bardhan, Kristie Darrah, Taylor Courtney, Alexander Prokup, James Hemphill, and Kalyn Brown for teaching me laboratory techniques (including my brief foray into synthetic chemistry), providing feedback on manuscripts and presentations, and for their kind friendship. I would like to extend a 'thank you' to Rohan Kumbhare for his close collaboration as my dedicated synthetic chemist for the miR-122 project. I am grateful to my many collaborators including Dr. Glenn Randall from the University of Chicago, Marvin Yu from MS^2 Array, and Isaac Kimsey from Nymirum.

Finally, thank you to my family for their loving support as I pursued this seemingly endless endeavor. And last (but not least), I would like to thank my wife, Christina, for her love and patience as well as her motivation and reassurance during difficult times.

List of Abbreviations

2'-*O*-Me	2'-*O*-methyl modification
2DCS	2-dimensional combinatorial screening
2DPBM	2-(diphenylphosphino)benzamide
3' UTR	3' untranslated region
5' UTR	5' untranslated region
γPNA	gamma-modified PNA
ABNI	4-amino-N-butyl-1,8-naphthalimide
ADAR	adenosine deaminase acting on RNA
ADP	adenosine diphosphate
AGO2 (Ago2)	Argonaute2
Ago HITS-CLIP	Ago2 high-throughput sequencing of RNAs isolated by CLIP
AMC	amino-methyl coumarin
AMO	anti-miRNA oligonucleotide
AP-1	activation protein 1
ASO	antisense oligonucleotide
ATP	adenosine triphosphate
BIST	bisstyrylthiophene
bp	base pair
C. elegans	*Caenorhabditis elegans*
ceRNA	competing endogenous RNA
CHR	cascade hybridization reaction
CLIP	crosslinking and immunoprecipitation
CPP	cell penetrating peptide
DAPI	4'6-diamidino-2-phenylindole fluorophore, nuclear stain
DEACM	diethyl amino coumarin
DGCR8	DiGeorge syndrome critical region 8
DMEM	Dulbecco's modified Eagle's medium

DMSO	dimethyl sulfoxide
DMTr	dimethoxytrityl-[bis-(4-methoxyphenyl)phenylmethyl]
DNA	deoxyribonucleic acid
dsDNA	double-stranded DNA
dsRNA	double-stranded RNA
E. coli	*Escherichia coli*
EDTA	ethylenediaminetetraacetic acid
EGFP	enhanced green fluorescent protein
EPEI	ethoxylated polyethylenimine
EXPO5	exportin-5
F-12K	Kaighn's modification of Ham's F-12 medium
Fluc	firefly luciferase
FRET	fluorescence energy transfer
GAPDH	glyceraldehyde 3-phosphate dehydrogenase
H_2O	water
HBV	hepatitis B virus
HCC	hepatocellular carcinoma
HCR	hybridization chain reaction
HCV	hepatitis C virus
HIV	human immunodeficiency virus
HIV Tat	HIV trans-activator of transcription
HNF	hepatocyte nuclear factor
HRP	horseradish peroxidase
IRES	internal ribosome entry site
kb	kilobases
K_d	dissociation constant
LED	light-emitting diode
LETF	liver-enriched transcription factor
LNA	locked nucleic acid
mCherry	*Discosoma sp.* red fluorescent protein
miRNA	microRNA

mRNA	messenger RNA
MO	morpholino oligomer
ncRNA	non-coding RNA
NPOM	6-nitropiperonyloxymethyl caging group
nt	nucleotide
PACT	protein activator of the interferon-induced protein kinase
PAGE	polyacrylamide gel electrophoresis
PBS	phosphate-buffered saline
PCR	polymerase chain reaction
PDCD4	programmed cell death 4
PNA	peptide nucleic acid
pre-miRNA	precursor miRNA
pri-miRNA	primary miRNA
P/S	penicillin-streptomycin
PS	phosphorothioate modification
PTEN	phosphatase and tensin homolog
RISC	RNA-induced silencing complex
RLC	RISC loading complex
Rluc	*Renilla* luciferase
RLU	relative luminescence unit
RNA	Ribonucleic acid
RNAi	RNA interference
RT-qPCR	quantitative real time PCR
SAR	structure-activity relationship
SDM	site-directed mutagenesis
shRNA	short hairpin RNA
siRNA	small interfering RNA
ssDNA	single-stranded DNA
ssRNA	single-stranded RNA
SSO	splice-switching oligonucleotide
TE/Mg^{2+}	tris base, EDTA, magnesium buffer

TAMRA	tetramethylrhodamine
TATA box	Goldberg-Hogness transcription initiator sequence
TBE	Tris base, borate, EDTA buffer
TBP	TATA box binding protein
TCEP	tris(2-carboxyethyl)phosphine
T_m	melting temperature
TFO	triplex-forming oligonucleotide
TRBP	transactivation response element RNA binding protein
UV	ultraviolet light
X-Gal	5-bromo-4-chloro-2-indolyl-D-galactopyranoside
XTT	2,3-Bis-(2-methoxy-4-nitro-5-sulphenyl)-2*H*-tetrazolium-5-carboxanilide

1.0 Introduction to MicroRNAs

It has been estimated that while 80% of the human genome is transcribed,[1,2] only 2% is translated into protein[3] leaving a significant amount of non-coding RNA (ncRNA) untranslated. Originally thought to be 'junk molecules', ncRNAs have gained increasing interest over the last several decades after findings that many exhibit biological function and have implications in initiation and progression of diseases.[4,5] MicroRNAs (miRNAs) are short, single-stranded ncRNAs of ~22 nucleotides that regulate gene expression via binding to the 3' untranslated region (3' UTR) of complementary messenger RNA (mRNA).[6] The first miRNA, lineage defective 4 (*lin-4*), was discovered by Victor Ambros in 1993.[7,8] At the time, *lin-4* was known to temporally regulate events in early development of *Caenorhabditis elegans* (*C. elegans*) larvae, however, the mechanism was not understood. Ambros determined that the *lin-4* gene did encode a protein, but rather transcribed 2 small transcripts (22 and 61 nucleotides in length) that were complementary to a segment in the 3' UTR of the *lin-14* mRNA. Furthermore, they found that the *lin-4* transcripts repressed translation of the LIN-14 protein, and postulated that this occurred via an anti-sense RNA-RNA interaction with the *lin-14* 3' UTR.[7] In 2000, Ruvkun's laboratory discovered the second miRNA, lethal 7 (*let-7*) in *C. elegans*. They found that *let-7* was transcribed into a 21 nucleotide RNA molecule that was complementary to the 3' UTR of *lin-14, lin-28, lin-41, lin-42,* and abnormal dauer formation 12 (*daf-12*) genes. The discovery of *let-7* became a major turning point in the miRNA field because unlike *lin-4,* which was found only in *C. elegans*, *let-7* was conserved across multiple species, including humans.[9] The discovery has sparked increasing interest in performing research to try to better understand miRNA biogenesis, function, and mechanism of regulation,[10] prompting the discovery of 2,654 mature miRNAs in humans currently

reported on the miRNA repository miRBase.[11] Furthermore, miRNAs were demonstrated to regulate 21% of protein-coding genes in humans via photoactivatable ribonucleoside enhanced cross-linking and immunoprecipitation (PAR-CLIP),[12] so its unsurprising that dysregulation of miRNAs plays a major role in many diseases.[13]

1.1 MicroRNA Biogenesis and Function

In the canonical miRNA pathway, miRNA genes are first transcribed by RNA polymerase II or III into primary miRNA (pri-miRNA) of hundreds or thousands of nucleotides in length.[14] The pri-miRNA is then cleaved by a 'Microprocessor' complex comprised of the ribonuclease (RNase) III enzyme Drosha and protein DiGeorge Syndrome Critical Region 8 (DGCR8).[15] DGCR8 recognizes specific motifs such as N6-methyladenylated GGAC at the junction of the stem and single-stranded region of the pri-miRNA[16] followed by recruitment and subsequent cleavage of the pri-miRNA by Drosha at the base of the hairpin. This cleavage event produces a short 60-90 base precursor-miRNA (pre-miRNA) hairpin[17] bearing a 2 nucleotide 3' overhang and phosphate and hydroxyl modifications at the 5' and 3' termini, respectively.[18]

The pre-miRNA is then exported from the nucleus to the cytoplasm by protein Exportin-5 (XPO5) in complex with the small nuclear guanine triphosphatase (GTPase) RanGTP.[19] The XPO5:RanGTP complex interacts with the pre-miRNA via the 2 nucleotide overhang and the double-stranded stem, protecting the RNA from degradation. Following release from the XPO5:RanGTP complex in the cytoplasm, the pre-miRNA is recognized by the RNase III enzyme Dicer in complex with transactivation response element RNA-binding protein (TRBP) or protein activator of the interferon-induced protein kinase (PACT) via the 5' phosphate.[18] Dicer-mediated

cleavage of the loop occurs a defined distance 20 – 22 bases upstream of the 5' terminus of the RNA hairpin, effectively serving as a molecular ruler. TRBP coordinates recognition of pre-miRNAs over structurally similar substrates[20] and aids in recruitment of Argonaute 2 (Ago2) to the Dicer:TRBP complex.[21,22] Furthermore, TRBP has been shown to play a role in guide strand selection and miRNA length determination.[21] Recruitment of Ago2 to the Dicer:TRBP complex forms the RNA-induced Silencing Complex (RISC) Loading Complex (RLC) which processes the pre-miRNA and loads the resulting mature miRNA duplex into Ago2.[23] Some miRNAs have also been shown to be processed directly by Ago2, independently of Dicer.[24] The guide strand of the mature miRNA duplex is bound to Ago2 via two distinct interactions: 1) the 5' phosphate is recognized between the MID and PIWI domains and 2) the 3' terminus is held by the PAZ domain via the phosphate backbone.[25] Following loading of the mature miRNA duplex, Ago2 dissociates from the rest of the RLC and ejects the passenger strand, forming the activated minimal RISC. Most often, the guide strand then directs RISC to the 3' UTR of a target mRNA via partial sequence complementarity mainly through the 6 nucleotide seed region which then modulates gene expression (Figure 1-1).[26] However, recent studies utilizing Ago2 high-throughput sequencing of RNAs isolated by crosslinking immunoprecipitation (Ago HITS-CLIP) suggest that ~15-80% of miRNA-target interactions *in vivo* are mediated by non-seed region sites[27,28] and have been shown to bind to the 5' UTR[29] and coding regions of mRNA,[30] suggesting the underlying mechanism of miRNA-mediated gene regulation is more complex than originally thought.

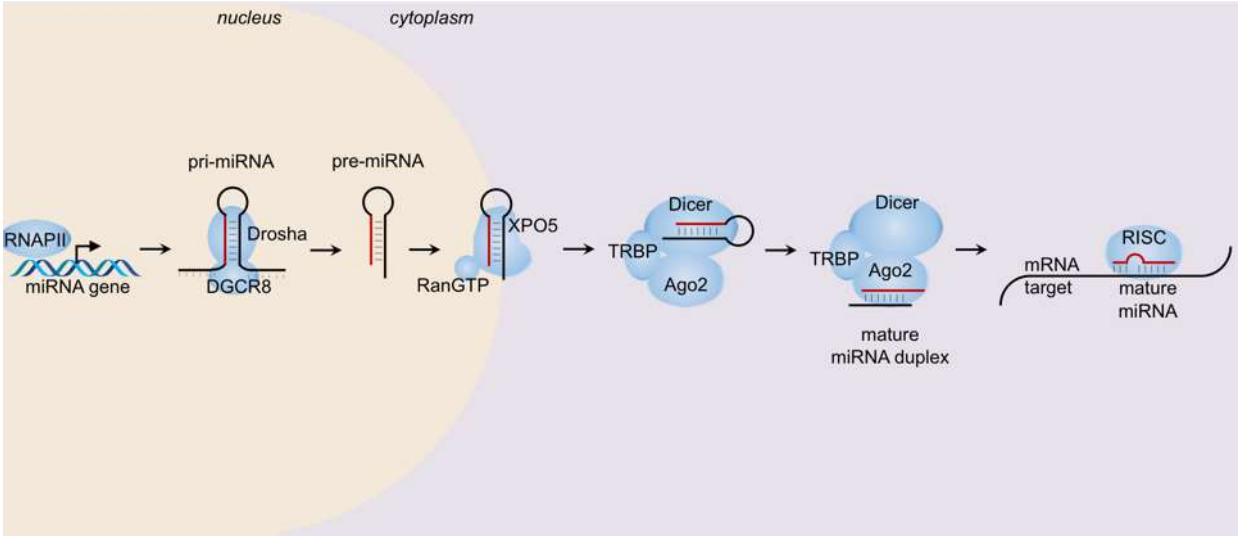

Figure 1-1 MicroRNA biogenesis pathway

MiRNAs are transcribed and processed into precursor miRNA (pre-miRNA), then exported from the nucleus. Once in the cytoplasm, the precursor hairpin is further cleaved into a miRNA duplex which is subsequently loaded into Argonaute2 (Ago2) where the mature miRNA guide strand (red) is retained and the complementary passenger strand (black) is released. Together, Ago2 and the mature miRNA form the active minimal RNA-Induced Silencing Complex (RISC) which targets complementary mRNA and modulates gene expression.

The activated RISC represses gene expression in mammals primarily by blocking translational machinery and recruiting proteins for mRNA degradation.[31-33] As an alternative, Ago2 is capable of endonuclease activity when the miRNA cargo is completely complementary to the mRNA target,[34] however, this process is uncommon for miRNAs in mammalian cells. While initial hypotheses suggested that the pathway for RISC-mediated translational repression was determined by the composition of RISC (i.e. the minimal RISC or a complex formed between RISC and recruited proteins),[35,36] recent models propose that miRNAs likely inhibit translation initiation then undergo degradation via deadenylation and decay in a sequential fashion.[32,37,38]

Ribosome and polysome profiling experiments have provided further evidence to support this model by ruling out post-transcriptional control of mRNAs via translation elongation, protein degradation, and ribosome drop-off.[39]

In contrast to its role in translational repression, the mechanism by which the activated RISC inhibits or promotes gene transcription is less understood. MiRNAs that negatively regulate gene transcription are concomitant with recruitment of argonaute proteins to the gene promoter and recruitment of Polycomb group (PcG) proteins, increases in trimethyl histone H3 lysine 27 (H3K27me3), decreases in H3K4me3, and DNA methylation within the promoter region, however it is unclear how they contribute epigenetic modifications.[40,41] Similarly, miRNAs that enhance gene transcription have been associated with recruitment of Ago2, but also promote RNA polymerase II or III enrichment at the promoter and increase H3K3me3.[42,43] These RISC-associated miRNAs are hypothesized to promote transcription via two mechanisms: (1) cleavage of antisense transcripts followed by subsequent release of chromatin effectors and derepression of sense transcription[44,45] and (2) binding of RISC to the 5' UTR promoter region and recruiting a protein complex comprised of chromatin modifiers that induce chromatin rearrangement and increase transcription.[43] However, additional studies are ongoing to further elucidate these mechanisms.

Taken together, many reports suggest that miRNAs are capable of regulating hundreds of genes through conserved or non-conserved miRNA binding sites with varying degrees of strength because they only require sequence complementarity in the 6 nucleotide seed region to function.[46] Furthermore, the discovery that some miRNAs are capable of regulating activity of other miRNAs[47] provides another layer of complexity to understanding their function. While the evolutionary origin of miRNAs remains unknown, one prominent hypothesis suggests a model by

which *de novo* RNA hairpins providing beneficial regulation were selected for over time and were correlated with timing and location of gene expression during construction of the body plan in embryonic development.[48] However, computational prediction of miRNA targets can often inflate the number of functional interactions a miRNA has with fully or partially complementary sequences and as such, additional studies in biological systems are ongoing in order to further characterize these interactions.

1.2 MicroRNA as a Potential Therapeutic Target

MiRNAs play a regulatory role in a variety of biological processes including development, immune response, apoptosis, and host-viral interactions.[13] Furthermore, miRNAs can exhibit global expression or isolated expression within a specific tissue or organ[49] and miRNA expression patterns can vary at defined timepoints during development.[50-52] As such, dysregulation of miRNAs has been implicated across a wide array of human diseases including cancer, hepatitis, cardiovascular disease, and metabolic disorders.[53,54]

Two years after the discovery of let-7, the first miRNAs with potential a regulatory role in disease were identified. In a study of a deleted region of chromosome 13q14, a deletion found in more than half of B cell chronic lymphocytic leukemias (B-CLLs), the Croce lab identified genes encoding miR-15a and miR-16-1.[55] Furthermore, the two miRNA genes were found to be deleted or downregulated in a majority of CLLs evaluated. Additional studies demonstrated that miR-15a and miR-16-1 regulate expression of B cell lymphoma 2 (Bcl2), an antiapoptotic protein found dysregulated in CLLs, and increased levels of miR-15a and miR-16-1 induced apoptosis in a leukemia cell model, suggesting their role as tumor suppressors.[56] Analogously, the miR-17-92

gene cluster was identified to encode oncogenic miRNAs (oncomiRs) capable of enhancing tumor development in a mouse B cell lymphoma model.[57] Upregulation of miR-17-92 was attributed to overexpression of cellular myelocytomatosis (c-MYC), an oncogene found overexpressed in a majority of all human neoplasms that encodes a transcription factor responsible for regulation of cell proliferation, growth, and apoptosis.[58] A later study found that miRNA genes are often located within fragile sites on chromosomal loci frequently prone to alteration due to chromosomal rearrangement in cancer.[59] In general, tumor suppressor miRNAs target oncogenes and are downregulated in cancer, while oncomiRs inhibit translation of tumor suppressors and exhibit higher expression levels in cancer.

In addition to their expression in cells, miRNAs have been discovered in a variety of bodily fluids including blood serum and plasma,[60-63] saliva,[64] urine,[65] breast milk,[66] and others.[67] Interestingly, these extracellular or circulating miRNAs have been shown to be incredibly stable compared to intracellular miRNAs.[15] The enhanced stability of extracellular miRNAs has been attributed to association with vesicles (e.g. exosomes or apoptotic bodies)[68,69] or proteins (e.g. Ago2),[70,71] however, contrasting data regarding the predominant mode of protection suggest that determination of vesicle or protein association may be dependent on several factors including identity of the miRNA, cell type, or other factors.[15] Additionally, differential expression patterns between intracellular and extracellular exosomal-associated miRNAs have been observed,[72-76] suggesting sorting of mature miRNAs for export occurs, however this mechanism is poorly understood. The current hypothesis is that extracellular miRNAs encapsulated in exosomes or apoptotic bodies may function in cellular communication as evidenced by observations that secreted miRNAs are capable of altering gene expression in recipient cells.[72,73,76] In contrast, protein-bound extracellular miRNAs are proposed to originate from dead or dying cells with no

apparent function.[77] Ongoing studies continue to explore the mechanism by which circulating miRNAs are released in addition to their function, however the discovery of their unique expression signatures in bodily fluids has promoted their use as prognostic and diagnostic markers in a variety of cancer phenotypes.[78]

The majority of studies have focused on the dysregulation of miRNAs in cancer onset and progression, however several miRNAs have been implicated in a variety of other human diseases as well.[13] For example, miR-124a2, -195, -15a/b, -16,[79,80] and -375[81,82] have been shown to mediate pancreatic development and function while miR-130a, -200, and -410 were demonstrated to be involved in insulin secretion,[83] suggesting these miRNAs may play a role in diabetes. MiR-33a/b, -33a/b*, -144, and others regulate networks that control biogenesis and uptake of high-density lipoprotein (HDL)[84] which has been associated with a higher risk for heart disease and cardiac arrest.[85] Additionally, dysregulation of cardiac-specific miR-1, -133, and -208 has been demonstrated to induce ventricular hypertrophy and heart failure.[86] Recent studies have also found that misregulation of miR-29 and -107 regulate amyloid plaque production, while miR-106 has been associated with modulating amyloid-β (Aβ) peptide and Apolipoprotein E (ApoE) production.[87] Similarly, miR-125b, -138, -195, -219-5p and others were linked to Tau phosphorylation and production,[88] a key contributor to Alzheimer's disease.[89]

In addition to their implication in disease initiation, many miRNAs have been identified to elicit immunomodulatory effects by regulating maintenance and development of immune responses as well as function of mature immune cells.[90] Furthermore, several studies have demonstrated that miRNAs can exhibit dual functions as both tumor suppressors or oncomiRs in addition to immune regulators. For example, differential expression of miR-146a/b, miR-147, miR-21, and miR-155 has been found to modulate macrophage activity.[91] Additionally, tumor-

secreted miR-214 was shown to promote tumor growth by targeting phosphatase and tensin homolog (PTEN) protein following delivery into cluster of differentiation 4 $(CD4)^+$ T cells and subsequent induction of regulatory T cell (T_{reg}) expansion,[92] a poor prognostic marker in several cancer phenotypes.[93]

Given their involvement in immune responses, it's unsurprising that miRNAs have also been linked to host-pathogen interactions. Several strains of bacteria have been associated with dysregulated miRNA expression signals in mammalian cells and animals following infection, simultaneously deregulating inflammatory, innate and adaptive immune responses and promoting their own survival by modulating cell penetration and tissue remodeling.[94] Additionally, miRNAs have been demonstrated to mediate viral infection, replication, and survival. A study analyzing human infecting viral genomes found enrichment of human miRNA target sequences, in particular for single-stranded RNA viruses,[95] suggesting these miRNAs may have evolved as a mechanism to eliminate viral infections. MiR-199a-3p, -210, and 125a-5p have been shown to inhibit hepatitis B virus (HBV) replication and expression of the HBV surface antigen (HBsAg),[96,97] a protein responsible for stabilizing viral core assembly and binding receptors during infection to attenuate immune response.[98,99] Additionally, miR-155 modulates macrophage function in response to viral infection and inhibits translation of human immunodeficiency virus (HIV) Dependency Factors (HDFs).[100] Conversely, induction of miR-155 expression in human B lymphocytes infected with Epstein-Barr virus (EBV) has been linked to maintenance of the EBV genome and immortalization of the B lymphocytes via modulation of the nuclear factor kappa B (NF-κB) signaling.[101] Furthermore, interferon (IFN) treatment in humans, the primary endogenous antiviral defense in vertebrates,[102] induced expression of miR-196, -296, -351, -431, and -448 and inhibited replication of hepatitis C virus (HCV) RNA.[103]

Taken together, miRNAs play key roles in a wide array of complex gene regulatory networks and their dysregulation has been attributed to the onset and progression of a variety of diseases. Distinct miRNA expression profiles have been discovered in several cancer phenotypes (Figure 1-2), prompting the use of miRNAs as biomarkers for cancer onset, progression, and metastasis.[104] In addition to their function as oncogenes and tumor suppressors, miRNAs can regulate cell proliferation, cell death pathways, metastasis, and cell migration and invasion.[105] As such, recent efforts have been focused on developing new chemical tools for targeting miRNAs that may provide new therapeutic approaches for treatment of cancer and other diseases.[53,90] Compared to the vast amount of the genes and proteins associated with cancer,[106] 42 miRNAs, including 25 upregulated and 17 downregulated, have been predicted to be consistently dysregulated across nine different cancer phenotypes.[107] Furthermore, some cancers have been shown to exhibit 'oncomiR addiction', whereby inhibition of a single miRNA results in complete abrogation of the malignancy.[108,109] This suggests that altering function of a single miRNAs could reverse or eliminate disease phenotypes via modulation of a variety of gene regulatory networks.

Cancer	miRNA	Selected targets	Presumed target function
Brain	miR-21↑	TPM1, PDCD4	Tumor suppressors
	miR-221↑	$p27^{kip1}$	Tumor suppressor, cell cycle inhibitor
	miR-378↑	Sufu, Fus-1	Tumor suppressors
Thyroid	miR-138↓	hTERT	Oncogenic activity
	miR-221/222↑	$p27^{kip1}$	Tumor suppressor, cell cycle inhibitor
Breast	miR-10b↑	HOXD10	Inhibition of breast cancer metastasis
	miR-21↑	TPM1, PDCD4	Tumor suppressors
	miR-27a↑	ZBTB10, Myt1	Tumor suppressors
	miR-125a/b↓	HER2, HER3	Oncogenes, EGF receptor family members
	miR-206↓	ERα	Promoter of cell proliferation
Lung	let-7/miR-98↓	HMGA2, RAS, c-Myc	Oncogene, related to metastasis, promoter of carcinogenesis
	miR-29↓	DNMT3A/B	Oncogenic activity, DNA methyltransferase
	miR-34↑	Bcl2	Anti-apoptotic factor, promoter of proliferation
	miR-221/222↑	$p27^{kip1}$	Cell cycle inhibitor, cell growth inhibitor
Liver	miR-21↑	PTEN	Tumor suppressor, negative regulation of PI3k
	miR-122↓	Cyclin G, Bcl-w	Anti-apoptotic factor
Biliary	miR-21↑	PTEN	Tumor suppressor, negative regulation of PI3k
	miR-29↓	Mcl-1	Oncogene, anti-apoptotic factor
Pancreas	miR-155↑	TP53INP1	Induction of growth arrest, apoptosis
Colon/rectum	miR-143↓	ERK5	Promoter of cell growth and proliferation
	miR-145↓	IRS1	Oncogene, strong mitogenic activity
Prostate	miR-20a↓	E2F1, E2F3, E2F3	Pro-apoptotic factors, regulation of cell cycle
	miR-125b↓	Bak1	Pro-apoptotic factors, induction of apoptosis
	miR-126↓	SLC45A3	Oncogene
	miR-221/222↑	$p27^{Kip1}$	Tumor suppressor, cell cycle inhibitor
Bladder	miR-127↓	BCL6	Proto-oncogene, suppression of p53
Testis	miR-372/373↑	LATS2	Tumor suppressor
Ovarian	let-7/miR-98↓	HMGA2, RAS, c-Myc	Oncogene, related to metastasis, promoter of carcinogenesis
	miR-210↓	E2F3	Pro-apoptotic factor, regulation of cell cycle
	miR-214↑	PTEN	Tumor suppressor, negative regulation of PI3k
Cervix	miR-218↓	LAMB3	Promoter of cell migration and tumorigenicity
Lymphoma	miR-143↓	ERK5	Promoter of cell proliferation and cell growth
Leukemia	miR-15/16↓	Bcl2	Anti-apoptotic factor, promoter of cell growth
	miR-29/181↓	Tcl1	Oncogene, co-activator of the Akt oncoprotein
	miR-221/222↑	Kit	Proto-oncogene, tyrosine-protein kinase

Figure 1-2 Selected expression patterns of miRNAs misregulated in different cancer phenotypes

Reprinted by permission from: *AAPS* 2010*, 12,* 51, Copyright 2010.

1.2.1 Endogenous Regulation of MicroRNAs

Because miRNAs play a critical role in regulation of nearly all biological processes and are commonly misregulated in disease, living organisms have evolved several mechanisms to control their biogenesis and function.[110,111] At the transcriptional level, miRNA expression is likely mediated by several epigenetic factors including DNA methylation, DNA hydroxymethylation,

and post-translational modification of histones.[112] For example, downregulation of tumor suppressor miRNAs has been attributed to hypermethylated CpG islands near their promoter sequence, while hypomethylation often leads to increased expression of oncogenic miRNAs.[113,114] The promoter region of miR-365-3p was recently found to acquire 5-hydroxymethylcytosines (5hmCs) in response to formalin-induced inflammation in mice, resulting in induction of miR-365-3p expression.[115] While a similar relationship has not yet been identified in humans, recent studies have shown that 5hmCs are reduced by 50% in solid tumors[116,117] suggesting they could correlate to miRNA expression in human malignancies. Changes in chromatin states mediating miRNA expression are primarily due to histone acetylation or methylation.[112] For example, overexpression of a histone 3 lysine 27 (H3K27) methyltransferase was found to repress expression of miR-34a, a tumor suppressor miRNA, via trimethylation of its promoter in pancreatic ductal adenocarcinoma.[118] In addition to epigenetic regulation, transcription of miRNAs is mediated by a variety of transcription factors, including some with aberrant expression in cancer. For example, while c-MYC was found to activate the miR-17-92 cluster,[58] it represses transcription of several tumor suppressor miRNAs including miR-15a, -26, -29, -30, and let-7.[119] Similarly, tumor protein p53 (p53), a tumor suppressor and one of the most commonly mutated genes in cancer,[120] was found to increase expression of miR-34a via binding to its promoter sequence and subsequently induce apoptosis.[121,122] Interestingly, miR-34a was also demonstrated to repress expression of SIRT1, a negative regulator of p53, thereby mediating its own expression.[123]

The Microprocessor complex, comprised primarily of Drosha and DGCR8 in addition to other RNA-associated proteins, plays a pivotal role in regulating miRNA function by determining sequence features through processing of the pri-miRNA. Drosha itself is comprised of an intramolecular dimer of RNase III domains for cleaving the pri-miRNA, a central domain

containing a Piwi/Argonaute/Zwille (PAZ)-like domain hypothesized to aid in recognition of the pri-miRNA, a double-stranded RNA binding domain (dsRBD) at the C-terminus, and nuclear localization signal at the N-terminus.[124] Though Drosha alone appears to possess structural features capable of recognizing the pri-miRNA, several studies have shown that the Drosha dsRBD has weak affinity for RNA,[125-127] highlighting the importance of DGCR8 in the Microprocessor complex. DGCR8 stabilizes Drosha through protein-protein interactions[128] and contains two dsRBDs, as well as a RNA-binding heme domain (Rhed) and C-terminal tail region suggested to be responsible for maintaining Drosha function[129] and ensuring efficient Drosha binding,[130] respectively. Interestingly, Drosha has also been shown to regulate DGCR8 by cleaving a hairpin within the DGCR8 transcript thereby destabilizing its mRNA and repressing translation, suggesting a potential role in maintaining homeostatic control of miRNA biogenesis.[128] A recent study found that single-nucleotide substitutions or deletions within the DGCR8 and Drosha genes have been observed in 15% of 534 evaluated Wilms' tumors, the most common renal tumor in children,[131] leading to inhibition of let-7 and miR-200 families.[132] While accessory proteins to Drosha and DGCR8 have been observed as part of the Microprocessor, studies to determine the identity and role of these proteins in pri-miRNA processing are ongoing. Recent studies have found that heterochromatin protein 1 binding protein 3 (HP1B3) mediates recruitment and retention of Drosha at the active site of miRNA transcription[133] in addition to DNA superenhancers and H3K4me3 marks,[134] suggesting the vast majority of pri-miRNAs are likely processed co-transcriptionally. Furthermore, it was also determined that pri-miRNAs that were retained instead of cleaved and released were more efficiently processed into pre-miRNAs,[135] providing additional evidence for this hypothesis. It is estimated that 50-80% of mature miRNAs originated from intronic regions of mammalian transcripts[136] and some studies have suggested that splicing factors

responsible for processing the transcript may aid in recruitment of Drosha. For example, deletion of a 5' splice site within pri-miR-21 reduced processing of the RNA, suggesting small nuclear binding proteins associated with the spliceosome could interact with the Microprocessor and alter its function.[137] In addition to accessory proteins within the Microprocessor complex, other RNA binding proteins are capable of binding the pri-miRNA and inhibiting processing. A complex formed between interleukin-2 dependent transcription factors nuclear factor 90 and 45 (NF90 and NF45) has been shown to bind pri-miR-30a, -15a/16-1, -21, and pri-let-7a-1 with enhanced binding affinity relative to DGCR8 leading to a reduction in corresponding pre-miRNA levels.[138] Additionally, heterogeneous nuclear ribonucleoprotein A1 (hnRNPA-1) recognizes a consensus sequence within the apical loop of pri-miR-18a, inducing relaxation of the stem and promoting Drosha cleavage.[139]

While the Drosha processing step of miRNA biogenesis is considered the prominent mechanism for determining miRNA sequence and dysregulation,[140] Dicer also plays a role. The Dicer enzyme contains helicase domains presumably for binding the pre-miRNA[141-143] as well as a PAZ domain containing a phosphate-binding pocket for recognition of the 5' phosphate of the pre-miRNA, two RNase III domains, and a dsRBD.[144] TRBP and PACT bind to the conserved interface on the surface of Dicer and, each containing three dsRBDs, are hypothesized to be functionally redundant however their roles in pre-miRNA have not been fully characterized.[21] Furthermore, TRBP was demonstrated to enhance stability of Dicer and is mediated by phosphorylation by extracellular-signal regulated kinase (Erk).[145] Several studies have found that Dicer expression is regulated by multiple miRNAs binding to the 3' UTR or coding region of Dicer mRNA including let-7 and miR-103/107.[146,147] Interestingly, aberrant Dicer expression has been associated with various cancer phenotypes. For example, reduced expression of Dicer has been

observed in lung,[148] breast,[149] skin,[150] and ovarian cancers.[151,152] Additionally, Dicer was found to be overexpressed in prostate cancer[153] and Burkitt's lymphoma.[154] Furthermore, mutations within the Dicer gene impacts embryogenesis, differentiation, and homeostasis and can lead to DICER1 syndrome, a hereditary condition concomitant with benign and malignant tumors.[155] Other RBDs can also impact Dicer-mediated processing of pre-miRNAs. The stem cell factor, LIN28, binds the loop of pre-let-7 and inhibits cleavage.[156] Conversely, TAR DNA-binding protein-43 (TDP-43) was shown to specifically bind to the loop of pre-miR-143 and -547 as well as associate with the Dicer:TRBP complex in order to promote processing of these two miRNAs.[157] Furthermore, a recent study utilizing 72 pre-miRNAs in a proteomics-based pull-down experiment identified ~180 RBPs that interact specifically with a pre-miRNA, suggesting there may be additional proteins capable of regulating miRNA processing.[158]

Other proteins involved in key steps of the miRNA biogenesis pathway are tightly regulated and are also prone to modifications that can lead to aberrant miRNA expression. A frameshift mutation in XPO5 results in a truncated protein that fails to form the ternary complex with RanGTP and the pre-miRNA resulting in nuclear retention of the pre-miRNA and reduced expression of the mature miRNA.[159] Alterations in expression of XPO5 have been observed in various cancer phenotypes including increased expression in ovarian serous cystadenocarcinoma[160] and glioblastoma,[161] increased expression and genetic mutations in breast, prostate, and colon cancers,[162] as well as frame shift mutations in human primary colorectal tumors.[159] However, upstream signaling regulators of XPO5 and RanGTP have yet to be identified.[163] Ago2 is also subject to a wide array of modifications. For example, type I collagen prolyl-4-hydroxylase [C-P4H(I)] has been shown to stabilize Ago2 via hydroxylation of proline 700,[164] particularly during hypoxia, leading to accumulation of Ago2 and subsequent increase in

miRNA levels.[165] In one study, Ago2 was found to be polyubiquinated by E3 ligase mouse homolog of Lin-41 (mLin-41), a target of let-7 in differentiated cells, in embryonic stem cells (ESCs) and embryocarcinoma cell lines resulting in proteasomal degradation.[166] However, more recent studies showed no change in Ago2 protein levels following depletion of mLin-41 in ESCs suggesting the E3 ligase may not play a critical role in regulating Ago2.[167,168] Under stress conditions, Ago2 is subject to poly-ADP-ribosylation leading to a reduction in miRNA function.[169] Additionally, Ago2 activity can be regulated via phosphorylation of tryrosine-529 which reduces binding to small RNAs and relieves translational repression[170] or tyrosine-393 which is mediated by EGFR and results in reduced binding of Dicer and subsequent processing of pre-miRNAs.[171] Similarly to XPO5, expression of the Ago2 gene is frequently found to be elevated in a variety of cancer phenotypes including breast invasive carcinoma, prostate adenocarcinoma, and colon and rectal adenocarcinoma.[172]

In addition to miRNA biogenesis machinery, several other factors can act on the miRNA during processing leading to alterations in sequence identity, activity, and turnover. For example, adenosine deaminase acting on RNA (ADAR) converts adenosine to inosine (A-to-I) in a subset of pri-miRNAs, suppressing Drosha-mediated cleavage by reducing stability of the pri-miRNA.[173] A-to-I editing has also been shown to inhibit Dicer-mediated processing of the pre-miRNA,[174] loading into Ago2,[175] and editing within the seed sequence of a miRNA can redirect the mature miRNA to a different set of mRNA target sequences.[176,177] Posttranscriptional non-templated 3' monoadenylation of miR-122 mediated by the poly(A) RNA polymerase germ line development-2 (GLD2) stabilizes the miRNA in human hepatocytes[178] as well as mouse livers and embryonic fibroblasts.[179] In contrast, 3' adenylation of miR-21 by poly(A) polymerase PAP-associated domain-containing protein 5 (PAPD5) leads to degradation of the miRNA. Furthermore, the effect

of non-templated nucleotide additions at the 3' termini of miRNAs has been shown to be miRNA-specific across tissue types, developmental stages, diseases, and species.[180] While some turnover rates are tissue dependent—for example faster turnover for neuronal miRNAs compared to other tissues[181]—posttranscriptional modifications can also alter stability. For example, 'tailing' of the 3' terminus of Ago2-loaded miRNAs (i.e. extending the length of a miRNA via non-templated nucleotide addition) followed by 'trimming' can increase sequence complementarity between the miRNA and mRNA leading to nuclease degradation.[110] Several other pathways that mediate miRNA turnover have been investigated,[182] but studies to fully understand these mechanisms are ongoing.

Taken together, miRNA function and biogenesis are mediated by a variety of tightly regulated pathways, many of which are still poorly understood. In addition to the implication of misregulated miRNAs in cancer and other diseases, this has prompted the development of new chemical tools for further investigation of their modes of action as well as the potential to perturb their function as new therapeutic approaches.

1.2.2 Oligonucleotide-mediated Regulation of MicroRNA Function

The discovery that miRNAs may play a central role in numerous disease states has prompted the development of several tools to modulate miRNA function. Furthermore, the potential to alter expression of multiple proteins in various pathways by targeting a single miRNA holds promise as a new therapeutic strategy. Current oligonucleotide-based approaches include: 1) relief of oncomiR-mediated translation repression of tumor suppressor genes via anti-miRNA oligonucleotides (AMOs); or 2) translational inhibition of oncogenes using miRNA mimics.[183] AMOs are a class of antisense oligonucleotides (ASOs) that function by hybridizing with full

complementarity to their target, thus inhibiting miRNA function.[184] Undesirable properties of unmodified oligonucleotides in biological systems such as susceptibility to nuclease degradation, poor cellular uptake, limited bioavailability and pharmacokinetic properties, and poor binding affinity to target sequences has led to the development of chemically-modified AMOs in order to improve their therapeutic potential (Figure 1-3).[185]

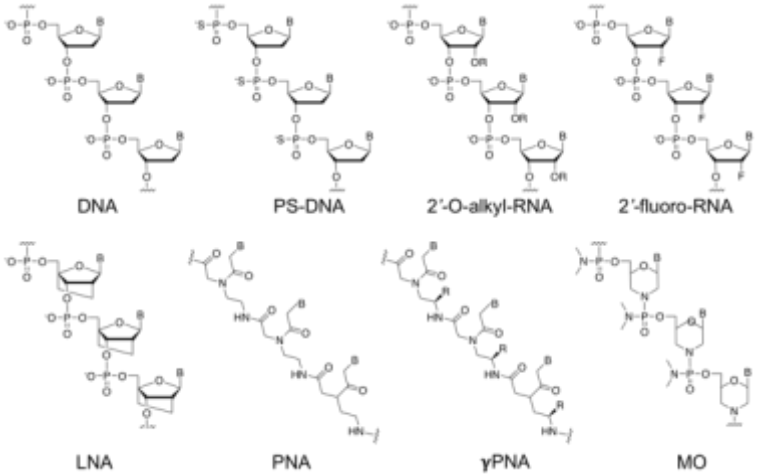

Figure 1-3 Structures of chemical modifications for AMOs

non-modified deoxyribonucleic acid (DNA); phosphorothioate (PS)-modified DNA; 2'-*O*-alkyl-ribonucleic acid (R = methyl, methoxyethyl); 2'-fluoro-modified RNA; locked nucleic acid (LNA); peptide nucleic acid (PNA); gamma-modified PNA (γPNA; R = miniPEG); morpholino oligomer (MO)

The first chemically-modified AMO to successfully inhibit miRNA function was a 2'-*O*-methylated RNA oligonucleotide complementary to let-7 which led to a loss of let-7 phenotype in *c. elegans* larvae.[186] Modification of the 2' hydroxyl moiety inhibits nuclease degradation and enhances thermal stability of complementary hybridization.[185] In a subsequent study, Krützfeldt

and co-workers developed new class of AMOs capable of modulating miRNA function in mice.[187] The new AMOs—termed 'antagomirs'—bore the 2'-*O*-methyl modification in addition to phosphorothioate (PS) linkages in the backbone and a cholesterol moiety at the 3' terminus. Cholesterol was incorporated to improve cellular uptake of the antagomirs[188] while the PS-linkage (replacing a non-bridging oxygen with sulfur in the phosphodiester backbone) increases nuclease resistance as well as binding affinity to serum proteins, lengthening the time available for cellular uptake.[185] While capable of increasing stability on their own, PS-linkages are often used in conjunction with nucleobase modifications, such as 2'-*O*-methyl, because they significantly reduce binding affinity to complementary oligonucleotide targets.[189] Interestingly, while standard synthesis of PS-modified ASOs leads to a mixture of diastereomers, a recent study found that some stereopure PS-modified ASOs displayed improved pharmacological properties and efficacy in mice, suggesting PS stereochemistry may affect their utility in a clinical setting.[190] Additional modifications have also been applied to the 2' hydroxyl group including 2'-fluoro and 2'-*O*-methoxyethyl (MOE),[185] both of which have shown improved inhibition compared to the 2'-*O*-methyl moiety.[191] The 2' oxygen can also be tethered to the 4' oxygen via a methylene bridge generating a locked nucleic acid (LNA).[185] The methylene bridge locks the ribose sugar in an ideal confirmation for Watson-Crick base-pairing and a single LNA substitution can increase the melting temperature of an oligonucleotide by up to 5-10 °C, enabling high binding affinity with shorter sequences. For example, treatment of Huh7 liver carcinoma cells with a 2'-*O*-methyl/LNA mixmer targeting miR-122 led to a dramatic reduction in miR-122 levels compared to the corresponding 2'-*O*-methyl AMO.[192] Furthermore, 8-mer oligonucleotides comprised entirely of LNAs and a PS-backbone complementary to the seed regions of miR-21, miR-122, and let-7 were capable of inhibiting miRNA function in mice.[193]

While AMOs remain the predominant method for inhibiting miRNA function, similar oligonucleotide tools have also been developed. For example, 'miRNA sponges' are RNA transcripts bearing multiple complementary binding sites for a target miRNA that are transiently transfected and expressed in cells in order to sequester the miRNA of interest.[194] The miRNA binding site on the miRNA sponge contains a single base mismatch such that a bulge forms at the Ago2 cleavage, inhibiting degradation of the transcript. Interestingly, recent studies have discovered competing endogenous RNAs (ceRNAs) proposed to have evolved to act as natural miRNA sponges to regulate miRNA function, however, the level of impact the ceRNA transcripts is still being investigated.[195] In contrast to AMOs and miRNA sponges, miRNA-masking ASOs ('miR-masks') have been developed to bind the miRNA binding site of a target mRNA in order to inhibit function.[196] miR-masks are ~22 nucleotide long, chemically-modified oligonucleotides that are fully complementary to a region within the 3' UTR of a target mRNA containing: 1) part of the miRNA-binding site; and 2) a sequence unique to the gene of interest. This enables the miR-mask to inhibit translational repression of a specific miRNA on a single gene of interest in contrast to AMOs and miRNA sponges which alter expression of all gene targets of a single miRNA.

In order to restore function of tumor suppressor miRNAs, miRNA mimetic agents ('miR-mimics') were developed.[183] miR-mimics are chemically-modified RNA duplexes that can be loaded into RISC similar to endogenous miRNAs and subsequently bind target mRNAs to induce translational repression. The efficacy of miR-mimics has been demonstrated in *in vitro* and *in vivo* models,[197-199] suggesting they may hold promise in novel therapeutic approaches. Additionally, miRNA overexpression vectors have been explored as an approach for miRNA replacement therapy, however, several shortcomings have prevented more widespread adoption of plasmid-based tools as therapeutics.

While chemical modifications have improved binding affinity and nuclease resistance of oligonucleotides utilized in these approaches, they are still limited by poor bioavailability and cellular uptake. Furthermore, plasmid-based approaches including non-viral vectors exhibit poor delivery and viral vectors elicit induce immune responses.[200] Modification of oligonucleotides at the 2' hydroxyl position enables broad biodistribution, however, these nucleic acids tend to accumulate in the kidney and liver and most ASOs are not capable of crossing the blood-brain barrier.[201] To improve cellular uptake, several delivery systems have been explored such as poly(lactide-co-glycolide) particles (PLGA),[202] lipid emulsions,[203] polyethylenimine,[204] and dendrimerss[205] Because the negatively-charged backbone renders naked oligonucleotides unable to cross the cell membrane[206] the majority of these approaches incorporate a positively-charged component,[207] however, the cationic charge can often lead to toxicity especially at the high concentrations required for AMOs to be efficacious.[208,209]

As an alternative approach, neutral-charged oligonucleotides have been developed in order to improve cell uptake and bioavailability. For example, peptide nucleic acids (PNAs) are oligonucleotide analogs wherein the sugar-phosphate backbone has been replaced with an achiral backbone comprised of N-(2-aminoethyl)-glycine units, rendering it uncharged.[210] PNAs display enhanced binding affinity for their target sequence compared to DNA and RNA and are resistant to nucleases, however, they possess low water solubility and exhibit only modest improvements in cellular uptake compared to negatively-charged oligonucleotides.[211] Nevertheless, inhibition of miR-155 function in mice following injection with an anti-miR-155 PNA was shown to modulate expression of miR-155 target genes[212] and led to a reduction in lymphoid tumors.[213] More recently, PNA analogs substituted at the γ-position to adopt a pre-organized right-handed motif (γPNAs) have been demonstrated to inhibit miR-210 in a mouse HeLa xenograft model.[214] The pre-ordered

helical structure of γPNAs increases its binding affinity for a complementary sequence, however they still suffer from poor cellular uptake. Similarly, morpholino oligomers (MOs) bearing a phosphorodiamidate backbone and six-membered morpholine ring in place of the sugar ring[215] have been used to inhibit miRNAs in zebrafish and *Xenopus laevis* .[216-218] The modified backbone confers MOs with resistance to nuclease degradation and these oligomers display modest increases in binding affinity compared to DNA and RNA.[219] Furthermore, delivery of MOs into mammalian cells remains difficult[220] and clinical applications of both PNAs and MOs have been limited by rapid clearance from the blood stream via metabolism or excretion in urine.[201]

1.2.2.1 Clinical Development of Oligonucleotide Therapeutics Against MicroRNAs

In spite of the difficulties inherent to use of oligonucleotide therapeutics to treat disease discussed above, the development of new miRNA-targeted drugs has increased over the past decade. The potential to alter expression of multiple genes by manipulating the function of a single miRNA has prompted many pharmaceutical companies to develop miRNA-focused therapeutic strategies toward the treatment of several diseases. In fact, multiple oligonucleotide-based miRNA drugs are currently in pre-clinical or clinical trials (Figure 1-4).[53,221]

Name (company)	Therapeutic agent	Delivery system	Target diseases	Trial details	ClinicalTrials.gov identifier
miRNA-based therapeutics					
Mirvirasen (Santaris Pharma A/S and Hoffmann-La Roche)	AntimiR-122	LNA-modified antisense inhibitor	Hepatitis C (chronic infections included)	Single-centre phase I, completed	NCT01646489
				Multicentre phase II, completed	NCT01200420
				Multicentre phase II, ongoing	NCT01872936
				Single-centre phase II, ongoing	NCT02031133
				Single-centre phase II, ongoing	NCT02508090
RG-101 (Regulus Therapeutics)	AntimiR-122	GalNAc-conjugated antimiR	Chronic hepatitis C	Phase I, completed	–
				Multiple phase II, ongoing	–
RG-125/ AZD4076 (Regulus Therapeutics)	AntimiR-103/107	GalNAc-conjugated antimiR	Patients with type 2 diabetes and non-alcoholic fatty liver diseases	Single-centre phase I, ongoing	NCT02612662
				Single-centre phase I/IIa, ongoing	NCT02826525
MRG-106 (miRagen Therapeutics)	AntimiR-155	LNA-modified antisense inhibitor	Cutaneous T cell lymphoma and mycosis fungoides	Multicentre phase I, ongoing	NCT02580552
MRG-201 (miRagen Therapeutics)	miR-29 mimic	Cholesterol-conjugated miRNA duplex	Scleroderma	Single-centre phase I, ongoing	NCT02603224
MesomiR-1 (EnGeneIC)	miR-16 mimic	EnGeneIC delivery vehicle	Mesothelioma, non-small cell lung cancer	Multi-centre Phase I, ongoing	NCT02369198
MRX34 (Mirna Therapeutics)	miR-34 mimic	LNPs (Smarticles)	Multiple solid tumours	Multicentre phase I, terminated	NCT01829971

Figure 1-4 miRNA-targeted oligonucleotide therapies currently in development

Adapted with permission from *Nat. Rev. Drug Discov.* 2017, 16(3) 203. Copyright 2017 Nature Publishing Group.

Santaris Pharma-sponsored miravirsen, a 15 nucleotide phosphorothioate-modified LNA/DNA mixmer targeting miR-122, was the first miRNA-targeted drug to enter clinical trials as a therapy for treatment of HCV.[222,223] miR-122 has been shown to stabilize HCV RNA via two binding sites within the 5' untranslated region (5' UTR).[224] Preclinical studies in mice and African green monkeys demonstrated that miravirsen was capable of reducing serum cholesterol levels and reducing viral titers of HCV.[222,223] In phase I clinical trials, miravirsen elicited dose-dependent pharmacological responses and did not induce any dose limiting toxicity. Encouraged by these

results, miravirsen was advanced into phase II clinical trials.[225] In phase IIa trials, treatment with miravirsen led to a dose-dependent reduction in HCV load and four out of nine patients who received the highest dose tested had undetectable levels of serum HCV RNA. Furthermore, no mutations were observed within the miR-122 target sites suggesting the virus did not develop resistance to the drug over the five-week trial. The success of both phase I and IIa trials has prompted additional phase II trials to evaluate long-term effects of treatment with miravirsen as well as combination therapy.[221] For example, studies have shown that chronic inhibition of miR-122 function in mice led to an increase in steatohepatitis and hepatocellular carcinoma with age,[226,227] suggesting there may be adverse long-term side effects with miravirsen treatment. Similarly, Regulus Therapeutics developed a *N*-acetyl-D-galactosamine (GalNAc)-conjugated oligonucleotide inhibitor of miR-122 for treatment of HCV infection and evaluated its efficacy in phase I and II clinical trials.[228] GalNAc is a carbohydrate structure reported to enhance uptake of oligonucleotides in liver cells via binding to a hepatocyte-specific asialoglycoprotein receptor.[229] While RG-101 treatment reduced HCV viral load in phase I trials and showed promise as a combination therapy with direct-acting antivirals in phase II trials, the US FDA put trials on hold in 2016 due to multiple cases of jaundice in response to treatment.[53]Since then, Regulus has halted clinical development of RG-101 in addition to two other AMOs: 1) a similar GalNAc2-conjugated oligonucleotide targeting miR-103/107, RG-125, for the treatment of non-alcoholic steatohepatitis (NASH); and 2) a non-conjugated oligonucleotide targeting miR-27, RGLS5040, for treatment of cholestatic disease.[230]

In an analogous fashion, miRagen Therapeutics has developed several miRNA-based therapies which are currently in various stages of preclinical and clinical trials.[221] For example, MRG-106 (cobomarsen) is an LNA anti-miR targeting miR-155 in recently initiated phase II

clinical trials for the treatment of cutaneous T-cell lymphoma (CTCL).[231,232] Phase I clinical trial showed that MRG-106 was well tolerated in human patients with minimal side effects and reduced the size of cutaneous lesions associated with the disease.[232] Similarly, the miR-92 inhibitor MRG-110 was demonstrated to promote angiogenesis and wound healing in diabetic and non-diabetic mouse models[233] and is currently being evaluated in phase I clinical trials for treatment of cardiovascular disease.[234]

MRX34, developed by Mirna Therapeutics, was designed as a miR-34 mimic formulated within a NOV340 lipid nanoparticle carrier to serve as a replacement therapy in a variety of cancer phenotypes.[235] The NOV340 nanoparticles become cationic within low pH environments, such as those in the tumor microenvironment, enabling them to adhere to tumor cells.[236] Promising results in preclinical studies wherein treatment of mice with MRX34 accumulated in tumors and induced a reduction in tumor size prompted the investigation of the drug in phase I clinical trials for treatment of patients with liver cancer, lung cancer, lymphoma, melanoma, multiple myeloma, or renal carcinoma.[237] Unfortunately, although initial phase I trial data was promising,[238 239] immune-related adverse events including three patient deaths prompted termination of clinical trials in 2016.[240]

Using a related approach, EnGeneIC and the Asbestos Diseases Research institute developed a miR-16 mimic encapsulated in EGFR-targeted nanocells for the treatment of malignant pleural mesothelioma, an asbestos-related cancer.[241] An initial phase I study suggested the miR-16 formulation demonstrated an acceptable safety profile, however, administration of the mimic alone was not adequate for abrogation of the disease and future studies will focus on its efficacy in combination therapies.[242] Similarly, Miragen recently advanced a miR-29 mimic (remlarsen) into phase II clinical trials for treatment of scleroderma[243] after promising phase I and

pre-clinical data showed it was well-tolerated in human patients and capable of reducing expression of various proteins involved in fibrous scar formation.[244,245]

1.2.3 Discovery of Small Molecule Modulators of microRNA Function

While recent successes of oligonucleotide approaches for miRNA therapeutics have shown some promise, several inherent limitations imposed on nucleic acid therapies may restrict their efficacy in the clinic. For example, limited stability *in vivo* has necessitated the use of chemically-modified AMOs which are prone to promiscuous inhibition of other family members outside of the target miRNA via enhanced binding affinity for the seed region.[246] These modifications have also been shown to elicit toxicity *in vivo* via induction of immunostimulatory responses and inhibition of coagulation.[247] Additionally, while several strategies have been developed in order to improve delivery of oligonucleotide therapies, high doses are still required in order to ensure sufficient levels of the miRNA drugs reach the target tissue at an effective concentration.[207] Furthermore, antisense oligonucleotides and miRNA sponges are only capable of directly blocking their nucleic acid target.

RNA is involved in many essential cellular functions, thus making it an attractive therapeutic target for modulation by small molecules.[248,249] Despite being considered largely 'undruggable', recent studies have identified small molecules targeting RNAs that adopt specific conformations, contain repeat sequences, or display three-way junctions.[248-259] Limitations imposed by oligonucleotide-based therapies, together with recent success in targeting RNA and RNA-processing proteins with small molecules, has prompted the investigation and discovery of compounds that modulate nearly all stages of miRNA biogenesis (Figure 1-5). Small molecule

modulators of miRNA function display several advantages over oligonucleotides including: 1) improved cell permeability; 2) reversible regulation; 3) capability to induce dose-dependent phenotypic responses.[260] Furthermore, small molecules generally have a low molecular weight (>800 Da) and possess ideal drug properties such as good solubility and bioavailability as well as desirable pharmacokinetic and pharmacodynamic properties.[261] However, it is also important to note there are a few limitations associated with the development of small molecules capable of regulating miRNA function. Discovery of small molecule modulators of miRNA function requires high-throughput screening or rational design approaches to identify a hit compound, followed by confirmatory assays and structure-activity relationship (SAR) studies in order to optimize their activity. For example, while *in vitro* screening platforms and computational prediction approaches offer high-throughput capabilities and yield small molecules with high binding affinity for a target RNA, the hit compounds may not elicit biological activity in a cellular environment. Cell-based assays overcome this limitation to a certain extent, however, secondary assays are required to identify false positive hits and evaluate specificity and the protein targets of small molecules identified in these assays is often unknown. Taken together, small molecule modulators of miRNA function may serve as more promising drug candidates than oligonucleotide approaches because they are easier to deliver, cheaper to manufacture, and display an improved pharmacological profile.

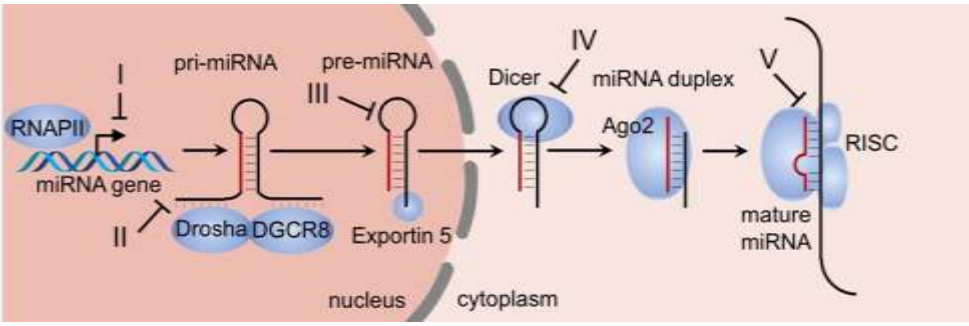

Figure 1-5 Different modes of action of small molecule modifiers of miRNA function

I) Inhibition of transcription. II) Inhibition of pri-miRNA processing. III) Direct binding to pre-miRNA, blocking further processing. IV) Inhibition of Dicer processing. V) Modulation of mature miRNA function via unknown mechanisms.

1.2.3.1 MiRNA Inhibitors Discovered through Biochemical Assays

The development of *in vitro* assays to monitor miRNA maturation has proven instrumental in the discovery of novel inhibitors of miRNA function (for an overview see Figure 1-6). Advantages of biochemical assays are a robust read-out, scalability for use in high-throughput screens, and the limited number of components that obviates target identification for hit compounds, as is frequently the case in cell-based phenotypic screens. Many *in vitro* assays that have been reported were designed to probe direct binding of small molecules to primary and precursor miRNAs or other protein machinery involved in miRNA biogenesis. A second group of assays has been constructed around monitoring the enzymatic function of the machinery involved in miRNA biogenesis. Taken together, these pursuits have led to the development of microarray platform assays, fluorescence-based assays, and more recently, catalytic chemiluminescence-based assays.

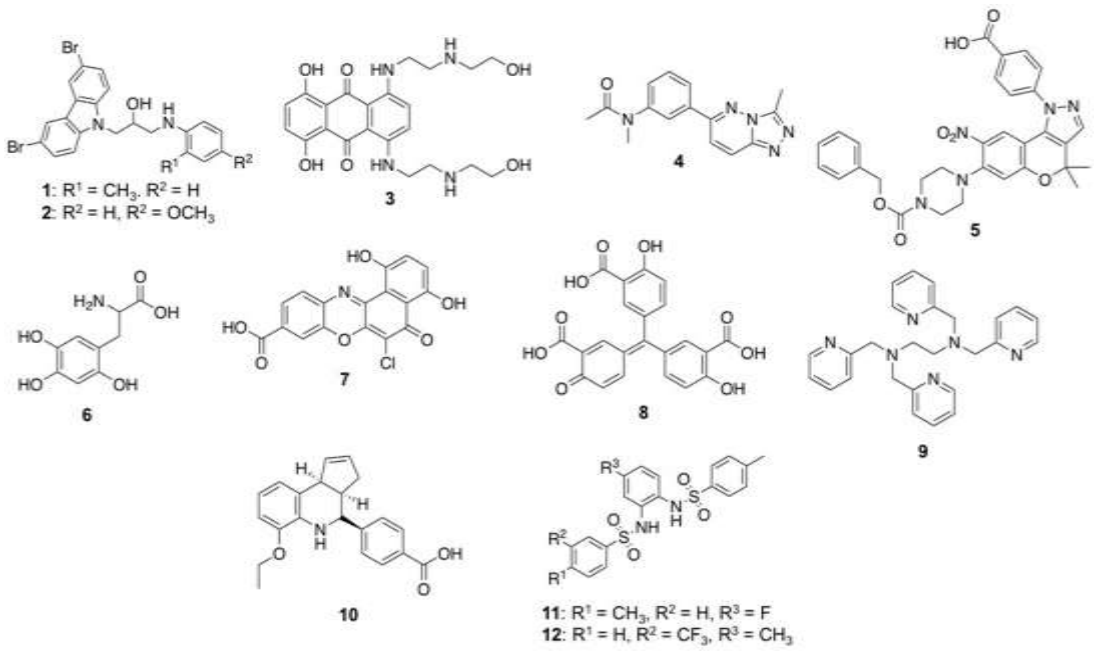

Figure 1-6 Structures of small molecule miRNA inhibitors identified through *in vitro* assays

Microarray technology has provided an efficient approach to screen for specific ligand-RNA interactions in a high-throughput fashion.[262] A typical microarray involves the covalent immobilization of a ligand library onto a glass slide, which is then incubated with a fluorescently labeled RNA molecule. Following washing steps, the molecules that bind and immobilize the labeled RNA can be identified using fluorescence imaging. Conveniently, the slides can also be re-probed with control oligonucleotides to identify interactions that provide specificity for the RNA of interest. As such, the high-throughput capability, design specificity, and robust fluorescence read-out renders microarrays a valuable approach for the identification of ligand-miRNA interactions. The first successful applications of microarray assays for the identification of miRNA inhibitors was the screening of peptoids[263] and

peptides.[264] Both peptoids and peptides are ideal for use in a microarray format because large, diverse libraries can be synthesized rapidly via automated systems and the ligands can be readily immobilized onto slides via the N- or C-termini. A recent approach described by the Schneekloth lab utilized a small molecule microarray to identify low molecular weight compounds capable of directly binding to the precursor miR-21 (pre-miR-21) hairpin.[265] A Cy5-labeled pre-miR-21 hairpin was incubated with a printed array of 20 000 small molecules, while a negative control, a Cy5-labeled HIV TAR hairpin, was employed to reveal non-specific interactions. The screen produced 19 hits, of which 11 were selected for additional binding assays. Initially, differential scanning fluorimetry was used as a qualitative approach to monitor the binding interaction between compound and RNA by measuring the melting temperature (T_m) of the pre-miR-21 hairpin in the presence and absence of compound, where changes in T_m indicate a direct interaction between the small molecule and the RNA. Of the 11 selected compounds, **1** and **2** (Figure 1-6) led to reductions in T_m indicating that small molecule binding to the RNA had a destabilizing effect on the hairpin structure. This mechanism is in contrast to many previously reported small molecule-RNA binding interactions, such as aminoglycosides,[266] which typically stabilize the hairpin structure resulting in an increased T_m. To quantify these interactions and to provide equilibrium dissociation constants (K_d) for the two compounds, two orthogonal fluorescence titration assays were employed. A 1-aminopurine fluorescence titration assay resulted in K_d values of 2.3 μM and 800 nM for compounds **1** and **2**, respectively, while a fluorescence intensity assay produced similar results, with K_d values of 3.2 μM and 700 nM, respectively. Furthermore, both compounds demonstrated specificity for the pre-miR-21 hairpin and showed no binding to the negative control HIV TAR hairpin, however no negative control pre-miRNA hairpins, e.g., of similar sequence, were tested offering limited insight into miRNA specificity of compounds **1** and **2**. Compound **1** was also investigated for its ability to inhibit Dicer processing *in vitro* and was found to abrogate Dicer-mediated

cleavage of fluorophore labeled pre-miR-21 in a dose-dependent manner with an IC_{50} of <1 μM. The effect of **1** on other unrelated precursor miRNAs was not explored and the biological activity of either compound has not been confirmed in cells.

To design a unique platform for probing RNA-motifs and chemical interactions simultaneously, the Disney lab developed a microarray-based two-dimensional combinatorial screening (2DCS) approach.[267,268] Using 2DCS, both RNA motifs and ligands are varied and analyzed simultaneously to identify selective interactions between small molecules and specific RNA motifs. First, a collection of azide-bearing small molecules is immobilized onto an alkyne-modified agarose microarray slide. The immobilized library is then probed for binding to a ^{32}P-labeled RNA library displaying a random 3×3 nucleotide internal loop pattern. Competitor RNA oligonucleotides are included to ensure that RNA-ligand interactions are confined to the random region, while competitor DNA oligonucleotides are added to ensure that the interactions are RNA-specific. After incubation and washing, the microarray slide is imaged using a phosphorimager and bound RNAs are excised from the agarose. The excised RNAs are then amplified and sequenced to determine the identity of the bound RNAs. In the original report, this approach was applied to determine RNA-binding preferences for four aminoglycosides, kanamycin A, tobramycin, neamine, and neomycin B. Disney's results demonstrated that specific RNA motifs have discreet binding preferences between the aminoglycosides screened. Neomycin preferentially interacted with GA pairs, tobramycin preferred internal loops with GG pairs, kanamycin A preferred internal loops containing pyrimidine-pyrimidine pairs, and neamine preferred various internal loops, especially GA pairs. As a proof-of-concept, this innovative study demonstrated the robust and high-throughput capabilities of 2DCS. A large amount of RNA-ligand interaction data was produced using this two-dimensional approach, prompting the development of additional bioinformatics and statistical

analysis tools for larger screens. To meet this need and expand upon this technology, the Disney lab generated a more comprehensive discovery platform, which combines the screening approach of 2DCS with a method to statistically analyze selection data to identify and score RNA motif-small molecule interactions. This approach, termed 'Informa', was successfully applied to identify several small molecule miRNA inhibitors and is described in more detail below (Chapter 1.2.3.3).

A critical limitation of the previously described small molecule microarray technologies is the requirement that the compounds be immobilized onto slides via a covalent tag. This requirement significantly restricts library diversity and accessibility, while also running the risk that covalent modification of the small molecule may render it inactive towards potential targets. To overcome this challenge, the Disney lab developed an approach termed 'AbsorbArray', which allows unmodified compound libraries to be non-covalently adhered onto the surface of microarray plates and probed for binding to RNA libraries in 2DCS fashion, as was described above with Informa.[269] They found that small molecules could be successfully absorbed onto hydrated agarose-coated surfaces and demonstrated that the molecules were retained following washing steps. To validate the platform, an Informa screen was carried out using a library of 727 pharmacologically active compounds that have been used in human clinical trials to identify small molecules that can bind to the pre-miR-21 hairpin. Three topoisomerase inhibitors were identified to bind the adenosine bulge (A-bulge) in the Dicer site of pre-miR-21 with K_d values between 24-58 nM, while the most potent hit, compound **3** (Figure 1-6), also bound the uracil bulge (U-bulge) adjacent to the Dicer site with a K_d of 46 nM. Compound **3** inhibited biogenesis of mature miR-21 in MDA-MB-231 breast cancer cells with an IC_{50} value of 1 μM, as revealed by quantitative reverse transcription polymerase chain reaction (RT-qPCR). As expected, inhibition of mature miR-21 was accompanied by an increase in pre-miR-21 levels, supporting a mechanism in which the compound inhibits Dicer processing of pre-miR-21. To determine the

selectivity of **3**, nine additional miRNAs were quantified using RT-qPCR with only miR-21 showing a significant decrease in mature miRNA levels. Compound **3** was further shown to rescue expression of a miR-21 target, tumor suppressor phosphatase and tensin homolog (PTEN). Using a Boyden chamber assay, inhibition of miR-21 by **3** inhibited the invasive phenotype of MDA-MB-231 cells in a dose-dependent fashion. To confirm that **3** binds pre-miR-21 in cells, a small molecule-RNA profiling approach called 'Chem-CLIP' was employed. The Chem-CLIP probe consists of the parent compound **3** modified with a biotin and a chlorambucil crosslinking moiety capable of covalently modifying its cellular RNA targets.[270] Cells were treated with the probe and the resulting conjugates were isolated by biotin capture followed by analysis by RT-qPCR. Indeed, the Chem-CLIP probe successfully enriched pre-miR-21 by >10-fold, confirming that **3** directly interacts with miR-21 in cells. Furthermore, Chem-CLIP experiments using excess parent compound **3** demonstrated competitive inhibition of labeling in a dose-dependent manner. Lastly, to further probe the selectivity of **3**, the Chem-CLIP approach was expanded to the nine additional miRNAs, which contain the same A-bulge RNA motif found in miR-21 and targeted by **3**. Only two miRNAs, *let-7e* and miR-25, exhibited binding, however, these interactions were not sufficient to reduce mature miRNA levels in cells. The authors believe the selectivity of **3** for miR-21 over the other miRNAs containing the same A-bulge may be due to the existence of the adjacent U-bulge, which is also capable of binding **3** and is only present in pre-miR-21. These results exemplify the promising potential that microarray-based screens have for identifying novel small molecule modulators of miRNA function and the development of AbsorbArray represents a significant solution to a well-known limitation of microarray technology.

While these applications demonstrate advantages of microarray-based screens, they also highlight key limitations. For instance, the assay formats only monitor ligand-RNA interactions and do not assess the ability of compounds to inhibit miRNA maturation or function. In the approaches

highlighted above, many ligands were identified that were capable of binding to the RNA with high affinity, however, were unable to inhibit their function. The development of multiplexed microarray approaches that simultaneously monitor both ligand binding and perturbation of function may further facilitate identification of high-quality inhibitors.

With the goal of identifying inhibitors capable of perturbing miRNA biogenesis, fluorescence resonance energy transfer (FRET) assays have been developed to identify small molecule inhibitors of miRNA maturation. The Arenz lab was the first to develop FRET assays using fluorophore labeled precursor miRNAs, similar to molecular beacons.[271,272] Installation of a 5' fluorophore and a 3' fluorescence quencher at the termini of a pre-miRNA hairpin enabled efficient FRET monitoring of Dicer-mediated cleavage. Importantly, this approach identifies compounds capable of inhibiting miRNA processing rather than identifying compounds that may merely bind the miRNA of interest. This technology has been extensively applied to identify and develop aminoglycoside derivatives as miRNA maturation inhibitors,[273-276] however the broad RNA-binding ability of many aminoglycosides[277] has hampered their ability to distinguish between different miRNA sequences, defining most aminoglycosides as non-specific inhibitors of miRNA biogenesis.[276,278] Tailored FRET assays have also been developed for targeting specific miRNA-protein interactions, such as the approach developed by Hall *et al*. to identify inhibitors of the abnormal cell lineage protein 28 (LIN28)-pre-*let-7* interaction.[279] The LIN28 protein inhibits *let-7* maturation via binding to pri- or pre-*let-7* RNA, resulting in significant inhibition of Drosha- or Dicer-mediated processing.[280] Utilizing a green fluorescent protein (GFP)-LIN28 fusion donor and a black-hole quencher (BHQ)-labeled pre-*let-7* acceptor, Hall was able to detect inhibition of the LIN28-pre-*let-7* interaction.[279] Screening of 16,000 drug-like molecules led to the identification of 14 initial hits, which were subsequently subjected to a secondary luciferase reporter assay in

cells to confirm their activity. Indeed, 7 of the hit compounds demonstrated an increase in mature *let-7*, which corresponds to inhibition of the LIN28-pre-*let-7* interaction. The small molecule **4** was shown to directly bind LIN28 protein as its principal mechanism of action. Treatment of HeLa cells with **4** led to increased levels of *let-7a*, *let-7g*, and *let-7f*, while having no effect on a control miRNA, miR-15; however, additional miRNAs were not evaluated and thus the extent of selectivity is not yet known. Lastly, **4** inhibited proliferation and stem-like properties in several human cancer cell lines with IC_{50} values between 20 and 42 μM.

In an alternative FRET approach, Park *et al*. employed unnatural amino acid mutagenesis to site-specifically fluorescently label the LIN28 protein.[281] Compared to the approach by Hall, this design significantly improved FRET efficiency, imparted by placement of the donor and acceptor in optimal proximity to each other to obtain maximal overlap of the emission spectra of the donor and the absorption spectra of the acceptor. Indeed, FRET quenching efficiencies as high as 85% were obtained, marking a significant improvement over previous assays. Using this assay, the authors screened 4,500 drug-like compounds and identified the benzopyranylpyrazole **5** as a hit compound (Figure 1-6). Compound **5** elicited a dose-dependent increase in fluorescence in the FRET assay yielding an IC_{50} of 4 μM. Mechanism of action studies indicated that **5** directly binds LIN28 and inhibits the LIN28-*let-7* interaction in JAR cells leading to increased levels of all *let-7* family miRNAs without affecting two control miRNAs, miR-20b and miR-214, as revealed by RT-qPCR. This increase in *let-7* miRNA also decreased the endogenous levels of oncogenic target genes of *let-7*, including cellular myelocytomatosis (c-MYC), high mobility group AT-hook 2 (HMGA2), and rat sarcoma viral oncogene homolog (RAS).

As an alternative to FRET-based approaches, the Balasubramanian lab developed a high-throughput fluorescence polarization (FP) assay to identify inhibitors of the LIN28-pre-*let-7*

interaction.[282] Fluorophore-labeled pre-*let-7* was titrated with varying concentrations of recombinant LIN28 in the presence of small molecules and FP was measured. After removing false positives and confirming activity through secondary assays, five of the confirmed hits were identified and subjected to an *in vitro* Dicer processing assay which revealed two compounds **6** and **7** (Figure 1-6) that were capable of rescuing pre-*let-7* processing, demonstrating the ability to inhibit the LIN28-pre-*let-7* interaction in a productive fashion. Compound **6** was capable of fully rescuing Dicer processing of pre-*let-7* at a concentration of 20 μM, however these results were only demonstrated *in vitro* and the selectivity of the compound was not investigated. Also employing an FP-based approach, Kiriakidou *et al*. developed a screen to identify small molecule inhibitors of miRNA-RISC loading using tetramethylrhodamine (TAMRA)-labeled RNAs and recombinant human Ago2.[283] Screening of small molecule collections identified aurintricarboxylic acid **8** (Figure 1-6) as an inhibitor of Ago2 loading with an IC_{50} of 470 nM. Furthermore, **8** inhibited siRNA function in cells and thus likely represents a general inhibitor of Ago2 loading. The ability of **8** to inhibit protein-nucleic acid interactions non-discriminately has previously been established and explains its lack of selectivity.[284] In a similar design, Sliz *et al*. used FAM-labeled pre-*let-7* and recombinantly-expressed LIN28 protein to carry out a FP-based high-throughput screen of 101 017 compounds. Of the compounds screened, six were found to inhibit LIN28-*let-7* binding and impair LIN28-mediated *let-7* oligouridylation. Inhibitors **9** and **10** (Figure 1-6) blocked the LIN28-*let-7* interaction with an IC_{50} of 2.5 μM and 7 μM, respectively. Using a heteronuclear single-quantum coherence (HSQC) approach, the authors identified that **9** interacted with the zinc-knuckle domain of LIN28, inducing significant perturbations and destabilizing its structure. Additionally, HSQC analysis and saturation transfer different spectroscopy revealed that **10** binds to the cold shock domain of LIN28, inhibiting oligouridylation activity of LIN28 with an IC_{50} of 27 μM. To test whether **10** was capable of inhibiting LIN28 function in cells, a dual luciferase reporter

assay containing eight tandem *let-7* recognition sites in the 3' UTR of *Renilla* luciferase was constructed and stably transduced into HeLa cells ectopically expressing LIN28A and LIN28B, two paralogs of LIN28 expressed in mammals. Indeed, compound **10** was capable of significantly reducing *Renilla* luciferase expression, demonstrating inhibition of LIN28 and activation of *let-7* in cells. Supporting this finding, RT-qPCR analysis of *let-7* family miRNAs in cells treated with **10** showed significant enhancement of all *let-7* miRNA levels, while a control miRNA, miR16, showed little change in expression. The overall success of these approaches may point to the benefit of designing highly customized approaches to identifying inhibitors for a specific protein-RNA interaction, however the limited potential for translating these assays to additional protein-RNA targets should not be ignored and may require significant modification and optimization.

As a unique approach to identify inhibitors of pre-miRNA processing, the Garner lab has developed an assay technology termed 'cat-ELCCA' (catalytic enzyme-linked click chemistry assay).[285] In this assay, biotin-labeled pre-miRNAs containing a click chemistry handle (e.g., *trans*-cyclooctene) within the loop-region are immobilized onto streptavidin-coated microtiter plates. Treatment of the wells with Dicer in the absence of inhibitor results in Dicer-mediated cleavage of the loop-region, and loss of the click handle. However, in the presence of an inhibitor, Dicer function is blocked, and the click handle remains intact. Subsequent treatment with horseradish peroxidase (HRP) containing a complementary click chemistry reaction partner (e.g., tetrazine) results in efficient covalent labeling of the intact pre-miRNA and enables robust detection via catalytic HRP-based chemiluminescence signal amplification. To identify inhibitors with high substrate specificity, wells containing additional alternative pre-miRNAs can be analyzed in parallel to allow discrimination between general inhibitors and substrate-specific inhibitors. This assay design offers: (1) increased sensitivity and improved signal-to-noise ratios

due to signal amplification, (2) negligible compound fluorescence interference due to a luminescence read-out, and (3) a functional read-out identifying only ligands capable of inhibiting Dicer processing of the pre-miRNAs. As an implementation of this assay format, the Garner lab applied this approach to a two-dimensional screen identifying inhibitors of pre-miR-21 and pre-*let-7d* Dicer processing.[286] In total, 50,000 small molecules and 33,000 natural product extracts (NPE) were tested, with the small molecules producing 170 confirmed hits and the NPEs producing 47 confirmed hits. Comparing the hit lists from both pre-miR-21 and pre-*let-7d* against each another, the selectivity of the identified hits was examined. While most of the small molecule hits exhibited little to no selectivity for pre-miR-21 over pre-*let-7d*, several NPEs exhibited significant selectivity ratios skewed towards pre-miR-21. The authors are still following up on these NPEs, but they may contain promising candidates for selective inhibition of pre-miR-21 processing. More recently, the Garner lab has also described an adaptation of the cat-ELCCA approach toward identification of small molecule inhibitors of the LIN28-pre-*let-7d* RNA protein interaction.[287] In this assay, biotin-labeled LIN28 was immobilized on streptavidin-coated microtiter plates and bound with pre-*let-7d* bearing a *trans*-cyclooctene, which in turn was reacted with a tetrazine-modified HRP. This led to efficient and robust detection of the RNA-protein complex via a catalytic HRP-based chemiluminescence signal. However, in the presence of a small molecule inhibitor, protein-RNA complex formation is inhibited and no chemiluminescence signal is generated. Using this assay, a high-throughput screen was carried out with a total of 127,007 small molecules screened at a concentration of 25 μM. Initially, 1,468 hits were identified and after follow-up confirmation screens including dose-response assays and Pan Assay Interference Compounds (PAINS) filtering to remove false positives attributed to chemical motifs that are notorious to be identified in screens without a defined and target-specific mode of action,[288] 20

hits were selected for further investigation. From these hits, two structurally similar compounds **11** and **12** were identified that displayed dose-dependent activity in both the cat-ELCCA assay and an electrophoretic mobility shift assay. Furthermore, both compounds did not inhibit Dicer-mediated processing of pre-*let-7* nor an additional unrelated cat-ELCCA-based protein-protein interaction assay indicating that the compounds are specific for the LIN28-pre-*let-7d* interaction. While a brief structure-activity relationship (SAR) study was conducted in hopes of improving their potency, the use of these compounds in cells and the selectivity against other precursor miRNAs was not investigated. Thus, their potential use as chemical probes is still unknown. The application of cat-ELCCA for the identification of novel inhibitors of miRNAs appears promising and, as mentioned above, comes with several advantages over existing assay technologies.

The use of *in vitro* assays to identify inhibitors of miRNA has proven successful via several approaches. While direct binding assays may benefit from high-throughput capabilities, they can often result in the identification of ligands that bind, but do not inhibit miRNA activity or miRNA maturation. On the other hand, while assays that directly monitor function tend to produce active inhibitors, obtaining high substrate specificity remains challenging. Future *in vitro* screening platforms should combine aspects of both direct binding assays and functional inhibition assays to identify more robust hits that have both strong efficacy and substrate specificity. Lastly, but importantly, inhibitors identified through *in vitro* assays run the risk of not eliciting biological activity in a cellular environment due to several factors, including cell permeability, stability, toxicity, as well as other biophysical and pharmacological determinants – which need to be evaluated separately.

1.2.3.2 MiRNA Inhibitors Discovered through Cell-Based Assays

Cellular assays for the discovery of small molecule modulators of miRNA function and biogenesis have distinct advantages over biochemical screening approaches. For example, biochemical assays do not account for factors that may impact the efficacy of a potential hit compound in cells, such as toxicity, cell permeability, and stability. Furthermore, cell-based assays are not limited to known targets, but can be conducted in an unbiased way, thereby enabling the discovery of novel biological interactions and pathways. This section discusses the implementation of cell-based reporter assays for the discovery of small molecule modulators of miRNA function (Figure 1-7).

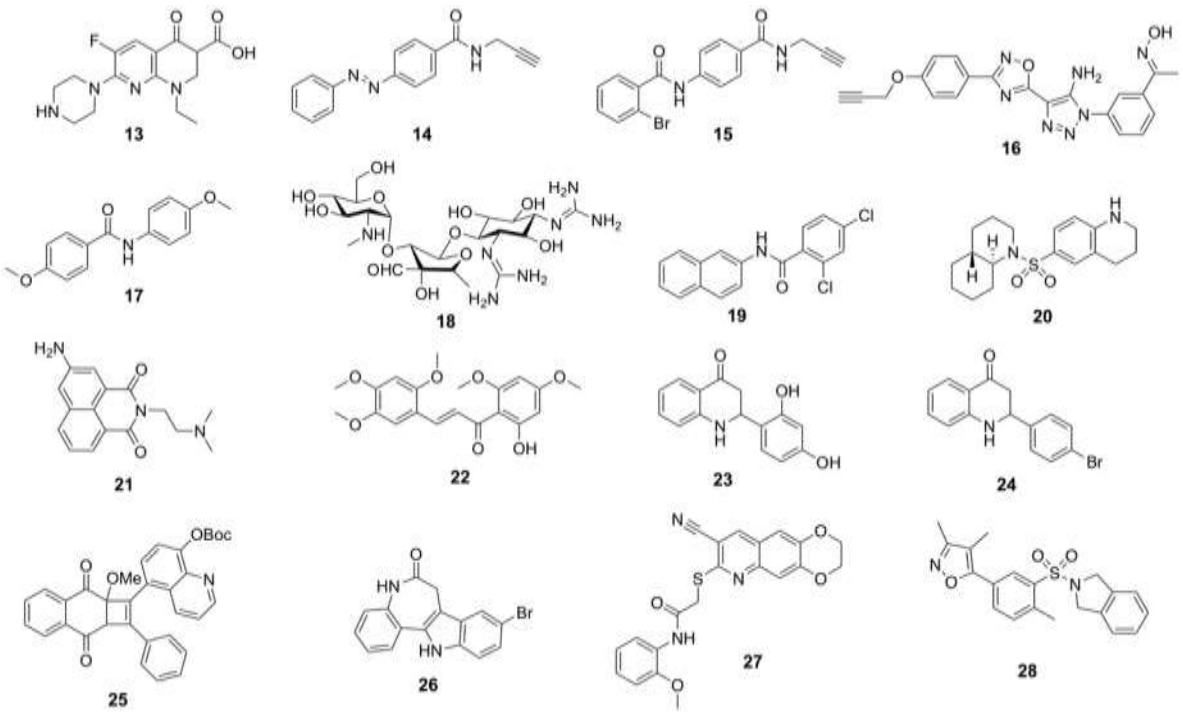

Figure 1-7 Structures of small molecule modifiers of miRNA function identified in cell-based assays

In a typical cell-based assay approach, the miRNA target sequence (either a natural sequence or a full complement) is cloned downstream of a reporter gene, such as luciferase or GFP, thus placing expression of the reporter gene under repression by the endogenous miRNA (Figure 1-8A). Selection of appropriate secondary assays for validation of potential hit compounds is important to rule out false-positives, as can be the case with luciferase-based reporter systems,[289-291] and to assist in determination of mechanisms of action. Additionally, because cell-based assays only indirectly measure alterations in miRNA function or biogenesis, minor changes in activity may be muted resulting in potential hit compounds being overlooked. This is especially problematic in high-throughput screens where small molecules are commonly tested only at a single concentration. Cell-based reporter assays that result in an increase in signal, rather than a decrease, are more robust since the latter can possibly stem from compound-induced changes in cell health unrelated to reporter gene expression.

Figure 1-8 Cell-based reporter assay design

A miRNA target sequence is cloned in the 3' UTR of a luciferase or EGFP reporter gene. A) Binding of a complementary miRNA to the target site results in repression of the reporter. B) Treatment with a small molecule inhibitor of miRNA function leads to an increase in reporter expression. C) Induction of miRNA expression or stabilization of miRNA function elicits further reduction in reporter expression.

Jin and co-workers utilized a HEK293 cell line expressing an enhanced green fluorescent protein (EGFP) reporter together with a stably expressed short hairpin RNA (shRNA) targeting the EGFP mRNA in order to identify small molecule modifiers of the RNA interference (RNAi) pathway (which shares many components with the miRNA pathway).[292] Stable clones expressing low levels of EGFP, a consequence of efficient shRNA repression, were isolated to serve as a platform for the identification of small molecule modifiers of RNAi (Figure 1-8C). Following a screen of 2,000 compounds from the US Food and Drug Administration-approved compounds and natural products collection, **13** (Figure 1-7) was found to reduce EGFP expression, indicative of an enhancement in shRNA repression, with an EC_{50} of 30 μM. Additionally, treatment with **13** improved RNAi-mediated inhibition of several additional genes in multiple cell lines suggesting it is a general enhancer of the RNAi pathway. A 2-fold increase in Ago2-associated siRNAs was observed following treatment with **13**, suggesting a mechanism by which **13** enhances siRNA loading into RISC. Compound **13** also induced a 2-fold increase in the mature forms of 13 selected miRNAs, while decreasing their corresponding precursor and primary miRNAs, as shown by northern blot analysis. Further investigations into a potential mechanism of action including immunoprecipitation and siRNA knockdown experiments suggest that **13**-mediated enhancement of RNAi is dependent on modulation of trans-activation-responsive region RNA-binding protein 2 (TRBP), a critical component required for the formation of the RISC.[293]

A follow-up study confirmed the binding interaction between **13** and TRBP and drew a correlation between the proposed interaction and the enhancement of tumor suppressor miRNAs.[294] To expand upon these initial findings, the Jerónimo lab performed a comprehensive expression profiling study covering 742 miRNAs in prostate cancer cell lines following treatment with **13**.[295] They discovered that while >50% of miRNAs were upregulated in both LNCaP and

DU145 prostate cancer cells, decreased levels of several oncogenic miRNAs was also observed suggesting additional mechanisms of action to the **13**-TRBP interaction. This discovery highlights the importance of evaluating a potential hit compound's activity in the context of multiple miRNAs to develop a more complete picture of its mode of action. To assist in identifying additional cellular targets of **13**, an affinity-based probe was developed.[296] MCF-7 breast cancer cells were treated with the alkyne-modified probe**,** followed by pull-down with biotin-azide and streptavidin beads. Mass spectrometry analysis of the isolated proteins identified P-element induced wimpy testis (Piwi)-like RNA-mediated gene silencing 3 (PIWIL3), an AGO2 protein, to be the most abundant protein and likely target of **13**. This was further supported when siRNA-mediated knockdown of PIWIL3 led to similar changes in both miRNA levels and cell proliferation as that of **13**-treated cells.

Maiti and co-workers developed a similar luciferase-based reporter plasmid by cloning the 3' UTR of programmed cell death protein 4 (PDCD4), a known target of miR-21,[297] downstream of a luciferase gene to screen aminoglycosides as potential inhibitors of miR-21 (Figure 1-8B).[298] After transfection of the reporter into MCF-7 cells, **18** (Figure 1-7) was identified as the most potent miR-21 inhibitor among the 15 aminoglycosides screened eliciting a 1.4-fold increase in luminescence. Confirmatory transfection of a miR-21 antagomir may shed more light on how meaningful this increase is and provide much needed validation for the assay. Additionally, limited compound numbers and confining the screen to a single compound class limited diversity in this study and reduced chances of identifying inhibitors with desired characteristics. While the small increase in luminescence signal suggests that **18** is not a potent miRNA inhibitor, treatment with **18** (5 μM) led to a ~90% reduction in miR-21 levels as observed by RT-qPCR. In addition to miR-21, expression of nine other miRNAs was evaluated and while most of the miRNAs remained

unaffected, miR-27a was downregulated by ~60%. Western blot analysis showed that **18** led to a minor dose-dependent increase in PDCD4 expression while a structurally similar analog elicited no change. Binding of **18** to pre-miR-21 was confirmed through melting experiments and a docking study showed a consensus structure in which **18** forms several hydrogen bonds with residues between G28 and G44 in pre-miR-21. Because **18** is also known to bind the phosphate backbone of 16S ribosomal RNA (rRNA) in the 30S ribosomal subunit via hydrogen bonds with four nucleotides,[299] it may be prone to promiscuous binding to other RNAs with similar sequence motifs limiting its potential as a biochemical probe or therapeutic. Incubation with **18** led to ~0.5-fold reduced Dicer processing of pre-miR-21, while no effect on the processing of pre-miR-103 or -95 was observed, suggesting that the compound is not a general pre-miRNA inhibitor.

The Chen lab developed a reporter plasmid to identify small molecule modifiers of miR-34a function in HCC.[300] miR-34a is a known tumor suppressor miRNA and has been implicated in cell-cycle regulation, differentiation, migration, invasion, and senescence.[301] After confirming activity in HepG2 and Huh7 cells via co-transfection of a miR-34a mimic or antagomir, the miR-34a reporter was utilized in a small molecule screen of 640 compounds from a natural product collection.[300] Among the molecules screened, **22** (Figure 1-7), a plant chalcone derivative,[302] inhibited luciferase activity in a dose-dependent fashion with an IC_{50} of 4 μM. Furthermore, mature miR-34a levels increased by ~3- and ~2-fold in Huh7 and HepG2 cells, respectively, in the presence of **22** (10 μM). Under the same conditions, pri-miR-34a levels increased by ~4- and ~10-fold. Conversely, mature and pri-miR-34a levels remained unchanged in Hep3B cells. A global analysis of miRNA expression showed that the small molecule affects numerous other miRNAs as well, suggesting the compound is not specific to miR-34a activation. The pre-therapeutic potential of **22** was evaluated in five hepatocyte cell lines and growth inhibition was observed in

HepG2, Bel-7404, Huh7, and PLC HCC cell lines, while the compound had no effect on cell growth of non-carcinogenic MIHA cells. In HepG2 xenografted mice, tumor growth was inhibited by up to 90% following treatment and **22** induced apoptosis and inhibited proliferation, further validating the therapeutic potential of small molecule modifiers of miRNA function.

An analogous luciferase reporter assay for small molecule modulators of miR-4644 function stably expressed in MCF-7 cells was employed in a screen of nine aza-flavanones. As mentioned above, utilizing a small compound library severely limits chemical diversity and may impede identification of lead compounds since hit rates from small molecule screens are typically low.[303] Two compounds, **23** and **24** (Figure 1-7), elicited a 4-fold increase in luminescence at 4 μM. Both compounds reduced mature and pri-miR-4644 levels by 20-25% but had no effect on miR-30a levels suggesting that the compounds were likely not general miRNA pathway inhibitors; however additional miRNAs would need to be screened to further elucidate specificity. The aza-flavanones **23** and **24** reduced cell viability by 40% and were found to elicit G1 phase arrest. To evaluate the efficacy of the two hit compounds *in vivo*, a transgenic fly strain expressing a reporter construct with two copies of the miR-14 (a miR-4644 homolog) binding sequence in the 3' UTR of an EGFP gene downstream under control of a tubulin promoter was developed. The reporter is primarily expressed in the wings and endogenous miR-14 suppresses expression of EGFP leading to reduced fluorescence. Treatment with **23** and **24** at 50 μM led to an increase in EGFP fluorescence due to miR-14 inhibition. Furthermore, western blot analysis demonstrated that EGFP expression was upregulated by ~2.5-fold and ~3-fold in the presence of **23** and **24**, respectively. Because of the homology between the two miRNAs, **23** and **24** could be used to elucidate novel miR-4644 or miR-14 regulatory mechanisms in human cells or *Drosophila melanogaster*, while also shedding light on potential evolutionary links.

Following the identification of a universal miRNA activator from the photoreaction products of naphthalene-1,4-dione and acetylenes,[304] Zhang and co-workers sought to employ a similar strategy towards discovery of selective miRNA-targeting small molecules.[305] A series of photocycloaddition reactions between 2-methoxy-1,4-naphthalenequinone and substituted aryl acetylenes led to the generation of 10 analogs that were subsequently screened in parallel cell-based assays utilizing luciferase reporters against miR-1, miR-214, miR-25, and miR-150, miRNAs that have been implicated in the development and proliferation of various diseases.[306-309] The small molecule **25** (10 μM; Figure 1-7) selectively inhibited miR-1, a myogenic miRNA (myomiR) that is enriched in cardiac and skeletal muscle and is implicated in muscle and heart development,[310] leading to a ~7-fold increase in luminescence in C2C12 cells.[305] RT-qPCR analysis showed that intracellular levels of miR-1 were reduced ~4-fold following treatment with **25**. A small SAR study of 15 analogs was performed, however, most analogs showed similar activity to **25** providing no further insight into important structural features required for miRNA inhibition.

In a subsequent report, compound **25** was used to investigate cell signaling pathways downstream of miR-1 to better understand its role in myogenesis.[311] After discovering that compound **25** inhibited differentiation and proliferation of C2C12 cells, expression of myoblast differentiation markers muscle creatine kinase (MCK), myosin heavy chain (MHC), and myoGenin were evaluated. All three transcripts were downregulated (up to 90%), while a proliferation marker, proliferating cell nuclear antigen (PCNA), showed no reduction. While **25** was initially hypothesized to be selective for miR-1,[305] it was found to inhibit myomiRs miR-133a and -206 eliciting 10-fold and 6-fold increases in luminescence in C2C12 cells transfected with their respective reporter plasmids – a similar response to the miR-1 reporter assay. Furthermore,

pri-miRNA levels of miR-1, miR-133a, and miR-206 were found to be downregulated by 60-90% indicating that the compound acts at the transcriptional or pre-transcriptional level and suggesting it may be a general regulator of myomiRs. To determine if **25** regulates myomiRs via myoblast determination protein (myoD), a major transcriptional regulator of myomiRs[312] and regulator of cell differentiation,[313] myoD expression levels were evaluated following compound treatment. Interestingly, while mRNA levels remained unchanged, myoD protein expression was found to be reduced suggesting that **25** inhibits myoD translation. The miRNAs miR-221 and miR-222 have been identified as inhibitors of myoD translation and treatment of C2C12 cells with compound **25** led to 3-fold increases in miR-221/222 expression. Taken together, these results suggest an interesting mechanism of action by which compound **25** inhibits a regulatory pathway by inducing miR-221/222 expression, leading to repression of the transcription factor myoD, and subsequent downregulation of myomiRs.

Similar to the reporter assay developed by the Maiti lab discussed above,[298] Gorospe and co-workers developed a luciferase-based reporter assay system bearing the 3' UTR of KRAS or HMGA2, oncoprotein targets of *let-7*,[314,315] in order to further probe the mechanisms underlying *let-7* biogenesis.[316] An additional luciferase reporter containing two copies of *let-7f* complementary sequences was also constructed. Following co-transfection of the reporters with pre-*let-7f* or control miRNA into BG-1 or UCI-101 ovarian cancers cells for evaluation of activity, the plasmids containing KRAS or HMGA2 3' UTRs elicited only limited reductions in luminescence, while the construct bearing complementary *let-7* sequences showed almost complete loss of luminescence and thus was used for all subsequent assays. This suggests that in this case a fully complementary binding sequence is necessary in cell-based reporter assays to reach an optimal dynamic range. A luciferase assay performed after co-transfection of the

luciferase reporter and precursors of nine *let-7* miRNAs confirmed the plasmid was sufficient for examining overall *let-7* expression levels in cells. A screen of the Screen-Well™ Kinase Inhibitor Library led to the identification of 10 compounds (2 activators and 8 inhibitors) that affected *let-7* function. The compounds elicited no activity in the presence of reporter constructs bearing target sites for five other miRNAs, indicating that the compounds were not general pathway inhibitors. However, a more comprehensive analysis of miRNA expression levels in response to treatment with the compounds should be employed to confirm specificity for *let-7*. Among the 10 hit compounds, **26** (Figure 1-7), a glycogen synthase kinase 3ß (GSK3ß) inhibitor, was found to induce *let-7* expression, eliciting a 49% reduction in luminescence and was selected for follow-up experiments. Because p53 is known to be a downstream target of GSK3ß signaling,[317] as well as a key transcription factor in *let-7* biogenesis,[318] Gorospe and co-workers hypothesized that **26** induced *let-7* levels in a p53-dependent mechanism. siRNA-mediated silencing of GSK3ß in p53 null HCT-116 cells led to only a <20% reduction in luciferase activity of the *let-7* reporter while silencing in wild type colon cancer cells led to a 40% reduction, suggesting that GSK3ß inhibits *let-7* production by repressing p53. Because **26** inhibits several other kinases, its therapeutic potential may be limited, however, it holds promise as a chemical probe to better understand the interaction between GSK3ß and p53 as well as signaling networks upstream of *let-7*.

While the majority of the reported cell-based reporter constructs utilize a single complementary miRNA sequence for activity, Lowry inserted 8 repeats of the *let-7* target site in the 3' UTR of a *Renilla* luciferase gene in a psiCHECK plasmid, hypothesizing that it would lead to a higher rate of mRNA degradation.[319] Following stable expression of the construct in a Huh7.5.1 cell line, a high-throughput screen of 36,480 small molecules from commercial collections yielded 60 potential hit compounds. As an additional control to rule out potential

luciferase inhibitors, the parent psiCHECK plasmid bearing no miRNA target sequence was used. After confirming activity of 29 of the 60 potential hit compounds in the stable Huh7.5.1 cell line and ruling out false positive hits, several remaining compounds demonstrated variable effects on downstream targets. The 60 initial hit compounds were retested in a RT-qPCR experiment monitoring their effect on expression of HMGA2 mRNA in order to identify molecules that specifically and robustly inhibit the repressive function of *let-7* on downstream targets. Treatment with compound **27** (Figure 1-7) elicited a reduction in HMGA2 levels by ~60%, and led to suppression of *let-7* targets v-myc (myelocytomatosis viral related oncogene), neuroblastoma derived (NMYC) and insulin-like growth factor 2 mRNA-binding protein 2 (IMP2). Upon evaluation of the small molecule using SEA viewer structure-target prediction software,[320] phosphodiesterase 10A (PDE10) was identified as a potential target. Because PDE10 is known to regulate cyclic-AMP (cAMP), expression of the downstream target cAMP Responsive Element Binding protein (CREB) was monitored. Consistent with inhibition of PDE10 and a subsequent increase in cAMP signaling, compound **27** induced activation of phosphorylated CREB. In Huh7 and TSU, 686, and UM-SSC-22B squamous cell carcinomas, treatment with **27** (1 μM) led to growth inhibition. Furthermore, compound **27** inhibited cell viability in several lung, liver, and AML cancer cell lines with a low IC_{50} of 0.1 μM.

In contrast to the approaches described above, Min and co-workers developed a reporter assay system in which the miR-21, miR-31, miR-92a-1-3p, or miR-223-3p binding sequences were cloned into the 3' UTR of a secreted alkaline phosphatase (SEAP) gene.[321] Secreted reporter assays can be advantageous over other approaches as they enable monitoring of gene expression without the need for cell lysis, allowing for time-resolved studies and additional secondary assays to be performed on the same cells, such as RT-qPCR; however, secondary assays to account for small

molecules that may inhibit secretion of the reporter should also be included. Initial screening performed by co-transfecting a miRNA expression plasmid and a reporter plasmid for the miRNA of interest into HEK293T cells followed by treatment with compounds from an in-house library led to the identification of an active compound with an aminosulfonylarylisoxazole scaffold. Ectopic expression of miRNAs may lead to exclusion of proteins or other targets present in the normal regulatory pathway of the miRNA thereby potentially lowering the hit rate of a small molecule screen. Additionally, this system could lead to an increase in false positive hits because the mechanisms governing artificial upregulation of the miRNAs differs from the endogenous mechanisms. Inhibition of endogenous miR-31 as well as six other miRNAs by compound **28** (Figure 1-7) was evaluated via RT-qPCR in A549 lung adenocarcinoma cells. Compound **28** was found to selectively inhibit miR-31 expression by ~50%. Treatment with **28** was also found to increase expression of downstream miR-31 targets serine/threonine kinase 40 (STK40) and early region 2 promoter binding factor (E2F) transcription factor 2 (E2F2) but had no effect on protein phosphatase 2 regulatory subunit B alpha (PPP2R2A) expression.

Rather than relying on a reporter system to monitor changes in miRNA function, the Hwang lab directly measured miRNA expression levels via RT-qPCR following treatment with small molecules.[322] After an initial screening of 8 miRNAs that target B-cell lymphoma 2 (BCL2)/adenovirus E1B 19 kDa protein-interacting protein 3 (BNIP3), a regulator of cardiac cell death,[323] in hypoxic cardiomyocytes, it was determined that miR-182 was most effective at reducing expression of the protein following treatment with a miRNA mimic. In an effort to identify potential small molecules capable of inducing miR-182 expression to further investigate this interaction, compounds from an in-house library, including receptor agonists and antagonists, kinase inhibitors, and ion channel inhibitors and activators, were screened in hypoxic

cardiomyocytes followed by RT-qPCR analysis for changes in miR-182 levels. Among the small molecules screened, the GSK3ß inhibitor **26** (Figure 1-7) induced miR-182 expression by two-fold and inhibited expression of BNIP3 in hypoxic cardiomyocytes. Furthermore, treatment with **26** reduced apoptosis by ~25% relative to a DMSO control and led to a decrease in the production of hypoxia-induced reactive oxygen species. The discovery that **26** induces expression of miR-182 and *let-7*, as discussed above,[316] may indicate that it is a non-specific enhancer of miRNAs or may reveal potential biological networks or gene regulatory pathways that link miR-182 and *let-7*. An SAR study of 9 derivatives to identify modifications that would enhance the ability of **26** to induce miR-182 expression led to the identification of an analog bearing a nitro substituent, which elicited a ~1.5-fold improvement in activity relative to the parent compound and was also shown to inhibit BNIP3 expression. To determine if miR-182 levels were increased via a ß-catenin-dependent pathway as a result of GSK3ß inhibition,[324] miR-182 expression was examined in the presence of a ß-catenin inhibitor. Subsequent treatment with compound **26** led to an induction of miR-182 suggesting that the GSK3ß/ß-catenin pathway is not an underlying mechanism of miR-182 expression. Despite the lack of a clear correlation between GSK3ß and miR-182, the therapeutic potential of the analog **26** was evaluated in a rat ischemia-reperfusion (I/R) injury model. Delivery of a miR-182 mimic or compound **26** immediately after I/R injury led to a reduction in cardiac fibrosis,[325] suggesting induction of miR-182 via small molecule treatment may hold therapeutic potential in the treatment of cardiovascular disease.

Cell-based approaches have afforded the discovery of small molecule modulators of miRNAs from a variety of compound classes that may not have been identified through biochemical methods, since the presence of the entire miRNA biogenesis pathway, including upstream regulatory mechanisms, was required. The insertion of a miRNA target sequence in the

3’ UTR of a luciferase gene remains the most common reporter design as it provides high sensitivity and a positive readout (luminescence increase), which reduces false positive hits. Installation of a fully complementary binding sequence has been demonstrated to deliver improved dynamic range compared to the use of the 3’ UTR of a target gene, which may contain mismatches in the target site and increases background reporter activity. A key consideration in the use of luciferase as a reporter gene in cell-based assays is the necessity of employing secondary assays to rule out false positives, such as luciferase stabilizing molecules. Most of the compounds discovered act at the transcriptional level, pre-transcriptional level, or have no known mode of action. In order to better utilize these molecules as biological probes and potential therapeutics, future efforts should focus on identifying their protein targets.

1.2.3.3 Computational and Rational Design Approaches to MiRNA Small Molecule Inhibitors

Rational design of miRNA-targeting small molecules relies on structural information of both the target and the potential small molecule candidates.[326] This is in stark contrast to traditional phenotypic screening assays where the mode of action of potential hit compounds is unknown, necessitating additional assays for target identification. The ability to computationally predict RNA secondary and tertiary motifs accurately from sequences affords an accelerated approach to small molecule drug design.[327,328] However, the requirement for detailed structural information of a potential target can also be a limitation to rational drug design because structures of many disease-relevant RNAs still remain to be elucidated. Additionally, small molecule inhibitors that bind secondary RNA sequence motifs often display low micromolar binding affinity at best, rendering them less appealing as potential drug candidates. Here, reports involving clever rational

design and computational approaches to targeting miRNAs with small molecules (Figure 1-9) are being summarized.[326]

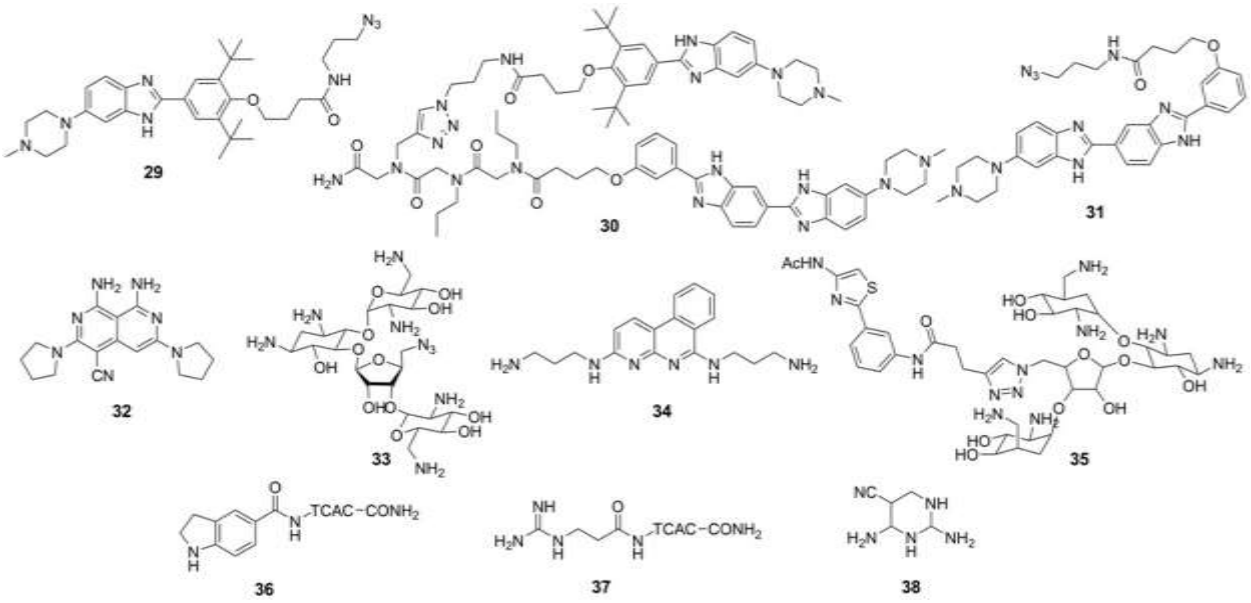

Figure 1-9 Structures of small molecules identified through rational design and computational approaches

The Disney lab developed a new approach for small molecule lead identification, termed Inforna, that integrates experimentally-determined RNA motif-small molecule interactions with an algorithm for scoring such interactions based on statistical analysis.[249] The initial identification of RNA motif-small molecule interactions is carried out by 2DCS, as described above (Chapter 1.2.3.1).[267] Following selection of RNA motifs, these sequences are analyzed by SAR studies through sequencing (StARTS). StARTS is a statistical approach that enables identification of specific features in RNAs by comparing their rate of occurrence in a specific RNA to the rate of occurrence in the entire RNA library.[329,330] Combination of 2DCS data and StARTS analysis

within the Informa platform serves as a database that facilitates the identification of specific small molecule-miRNA pairs based upon tight binding interactions.

The Informa approach was utilized in the discovery of small molecules that bind the Dicer and Drosha sites in disease-relevant pre-miRNAs and pri-miRNAs, respectively.[249] A compound set of 11 benzimidazoles and aminoglycosides, previously identified to bind RNAs,[331,332] were screened against 794 RNA motifs. Compound **29** (Figure 1-9) targeted the Drosha cleavage site of pre-miR-96 and was predicted to have the highest affinity among the 29 small molecule-pre-miRNA binding interactions identified through 2DCS and StARTS analysis, and thus was selected for further evaluation. In MCF-7 cells, compound **29** (40 μM) reduced the levels of mature miR-96 by 90% and pre-miR-96 levels by 50% while eliciting a 2.5-fold increase in pri-miR-96 expression, consistent with compound **29**-mediated inhibition observed in an *in vitro* Drosha processing assay. pre-miR-96, pre-miR-182, and pre-miR-183 belong to a polycistronic miRNA cluster, and thus are transcriptionally co-regulated.[333] Interestingly, **29** was found to specifically downregulate only miR-96 expression, while having no effect on mature miR-182 and miR-183 levels, in good agreement with the hypothesis that **29** inhibits miR-96 by direct RNA binding and not by targeting of an upstream regulatory protein. Furthermore, RT-qPCR profiling of 149 additional miRNAs following treatment with **29** revealed miR-96 to be the only downregulated target, however, transfection with a miR-96 antagomir led to more than 2.5-fold variations in the expression levels of 11 other miRNAs along with miR-96, suggesting **29** shows higher specificity towards miR-96 biogenesis. miR-96 is upregulated in cancer cells and is known to repress the pro-apoptotic transcription factor Forkhead box protein O1 (FOXO1).[334-336] Endogenous expression of FOXO1 increased 2.5-fold upon treatment with **29** (40 μM) in MCF-7 cells consistent with an increase in apoptosis detected via a TUNEL assay.

An additional bis-benzimidazole identified via Inforna to target a 1×1 nucleotide internal loop close to the Drosha site on pri-miR-96[337] was conjugated to **29** by a peptoid backbone yielding the dimeric compound **30** (Figure 1-9), in an attempt to generate a more potent inhibitor. After optimizing the length of the peptoid backbone, compound **30** (with a spacer of 2 glycine units) was found to increase pri-miR-96 levels by ~2-fold while reducing pre- and miR-96 levels by almost 50% at a concentration of 50 nM, indicating that **30** maintains a high affinity for pri-miR-96. Compound **30** binds pri-miR-96 with a K_d of 85 nM, a ~40-fold increase compared to **29**, and elicited a reduction in mature miR-96 levels with an IC_{50} of 50 nM. FOXO1 levels increased 2-fold, consistent with an 80% induction of apoptosis following treatment of MDA-MB-231 cells with **30** (50 nM). Furthermore, **30** (10 mg/kg) inhibited tumor growth in immunodeficient mice injected with MDA-MB-231 cells concurrent with changes in miR-96, pri-miR-96, and FOXO1 levels.

In contrast to **29** and **30**[338] binding the Drosha processing site of pre-miR-96, compound **31** (Figure 1-9) was identified via Inforna to bind the Dicer cleavage site on pre-miR-210 with a K_d of 200 nM. Inforna analysis identified 15 other miRNAs that contain motifs which can also bind to **31** with varying affinities, however, in a RT-qPCR analysis in MDA-MB-231 cells only miR-210 maturation was affected, as indicated by a ~50% reduction in mature miR-210 levels. miR-210 acts as a central regulator of hypoxic response in solid tumors[339] by inhibiting the expression of glycerol-3-phosphate dehydrogenase 1-like enzyme (GPD1L) and subsequent repression of prolyl hydroxylase (PHD). Under normoxic conditions, PHD hydroxylates prolines on hypoxia-inducible factor 1-alpha (HIF-1α) leading to proteolytic degradation of HIF-1α.[340] However under hypoxic conditions, miR-210 is upregulated, inhibiting expression of GPD1L.[339] In MDA-MB-231 cells cultured under hypoxic conditions, miR-210 and HIF-1α protein levels

were upregulated by 15-fold and 10-fold, respectively, while GPD1L protein levels were decreased by 10-fold compared to cells cultured under normoxic conditions. Following treatment with **31** (200 nM), HIF-1α expression levels were reduced by ~75% and GPD1L levels were increased 4-fold. Immunodeficient mice injected with MDA-MB-231 cells displayed reduced tumor sizes upon treatment with **31** relative to untreated control, suggesting **31** may hold some therapeutic potential. As expected, RT-qPCR analysis of the resected tumor masses showed mature miR-210 and HIF-1α levels decreased to ~10% and ~25% of levels in untreated controls, while GPD1L expression was doubled in **31**-treated mice compared to untreated mice.

Haga et al. employed Inforna to identify small molecule binders of a 1×1 nucleotide UU internal loop in pre-miR-544 and discovered **32** (Figure 1-9) to interact with the Dicer cleavage site.[341] miR-544 was previously found to induce expression of Ataxia telangiectasia mutated (ATM) protein.[342] Under hypoxic conditions, induction of ATM protein leads to reduced expression of mammalian target of rapamycin complex 1 (mTORC1), thereby restricting cell growth.[343] Additionally, two potential miR-544 binding sites within the 3'-UTR of mTOR have been identified by a bioinformatics analysis.[341] RT-qPCR analysis confirmed ATM and miR-544 were upregulated while mTOR was downregulated under hypoxic conditions in MDA-MB-231 and MCF-7 cells. Upon treatment with **32** (20 nM), miR-544 levels were reduced by 80%, with a corresponding reduction in ATM levels, while mTOR expression was increased 10-fold. Annexin V staining revealed that apoptosis (~70% of cells) in hypoxic MDA-MB-231 cells was more pronounced upon exposure to **32** compared to transfection of a miR-544 antagomir (~60% apoptotic cells). Furthermore, drug resistant MDA-MB-231 and MCF-7 cells were found to be sensitized to the chemotherapeutic agent 5-fluorouracil upon co-treatment with **32**. Similar to **31** discussed above, treatment of an immunodeficient mouse model with **32** (40 μM) led to decreases

in tumor size concurrent with reductions in expression levels of hypoxia-associated factors ATM and HIF-1α isolated from the excised tumors.

Inforna was also utilized in the identification of a potential interaction between azido-neomycin B **33** (Figure 1-9) and miR-525.[344] Treatment with **33** (25 μM) decreased both mature and pre-miR-525 levels by 40% in HepG2, while pri-miR-525 levels were increased 2-fold, suggesting that **33** binds the Drosha site on pri-miR-525. The invasive and migratory properties of HCC cells is, in part, the result of zinc finger protein 395 (ZNF395) repression by miR-525.[345] Western blotting analysis showed a 2-fold increase in ZNF395 expression in HepG2 cells exposed to **33**.[344] Expression levels of 19 other miRNAs predicted to bind the ZNF395 3' UTR were unaffected following treatment with **33**;[344] however, a previous study showed decreased levels of miR-517c, miR-518e, miR-519d, and miR-525 in response to **33**,[249] suggesting that while **33** is likely not a general miRNA pathway inhibitor it is not specific for miR-525.

Targeting bulges with small molecules is advantageous compared to double-stranded base-paired RNA due to a larger binding pocket and exposed unpaired nucleobase(s).[251] Small molecules such as 2-acylamino-1,8-naphthyridine[346] and *N*,*N*-bis(3-aminopropyl)-2,7-diamino-1,8-naphthyridine (DANP)[347,348] have been reported to bind a single purine or pyrimidine bulge via hydrogen bonding, mimicking natural base pairing interactions. Furthermore, molecular modeling of the RNA-DANP complex suggested π-π stacking interactions of DANP with the neighboring base pairs to be a stabilizing interaction in the B-form RNA duplex, but may be insufficient to promote binding to the A-form RNA duplex.[349] The Nakatani lab developed the benzo-DANP **34** (Figure 1-9) to bind a single cytosine bulge near the Dicer cleavage site in pre-miR-29a with the hypothesis that expansion to a three-ring system would enable formation of π-π stacking interactions and a similar hydrogen bond network as DANP but with improved binding

affinity. miR-29a is known to enhance invasion and cell migration in nasopharyngeal carcinoma.[350] *In vitro* processing of pre-miR-29a by recombinant Dicer was reduced to ~50% in the presence of **34** (200 μM), with an IC_{50} of 70 μM. As expected, **34** (200 μM) did not significantly affect the Dicer processing of pre-miR-29a without the C-bulge. However, Hela cells exposed to **34** (100 μM) elicited a 2-fold increase in miR-29a levels, in stark contrast to previous examples of direct binding between small molecules and pre-miRNA.[338,341] Additionally, expression levels of five other miRNAs (miR-21, miR-92a-1, miR-16-1, miR-15a and miR-34a) exhibited increased expression following treatment with **34**. The authors rationalized that the high concentration of **34** elicited off target effects contributing to this unexpected result, but this was not experimentally confirmed.[349]

miR-372 and miR-373, which share the same seed sequence, act as oncomiRs and are upregulated in gastric cancer, as well as testicular germ cell tumors, esophageal tumors, and thyroid adenomas.[351-354] The Duca lab developed multimodal ligands which bind to the stem-loop region of pre-miR-372 and pre-miR-373 and inhibit Dicer processing.[273] The ligands were based on two RNA-binding motifs: (1) an aminoglycoside that exhibits general high-affinity binding to the stem-loop region of RNAs[355-358] and (2) an artificial nucleobase capable of forming specific Hoogsteen bond interactions, enabling formation of triplex structures with the double-stranded region of the pre-miRNA.[359,360] In an analogous approach to that employed by other labs discussed above (Chapter 1.2.3.1), a FRET-based assay with a fluorophore (fluorescein) and quencher (dabcyl) on the 3' and 5' termini of pre-miR-372 was used to assess Dicer activity. Upon screening of just aminoglycosides, neomycin was found to completely inhibit Dicer cleavage at 250 μM and thus was selected for stem-loop binding. The multimodal ligands were synthesized by conjugating several artificial and natural nucleobases bearing alkynes to an azide-modified analog of

neomycin. After screening the ligands in the FRET assay, **35** (Figure 1-9) was identified as the best inhibitor with an IC_{50} of 2 μM and a K_d of 16 nM. The artificial nucleobase in **35** is known to form three hydrogen bonds with the A-T base pair.[361,362] Importantly, neomycin alone showed a dramatically higher IC_{50} of 125 μM and a K_d of 7.4 μM, highlighting the synergistic effect of both motifs on RNA binding.[273] Both miR-372 and miR-373 are most highly upregulated in gastric cancers, while virtually undetectable in normal gastric epithelial cells. Additionally, these miRNAs repress the translation of large tumor suppressor 2 (LATS2), a serine-threonine kinase involved in cell cycle regulation.[363] To evaluate the pre-therapeutic potential of **35**, AGS gastric cancer cells overexpressing miR-372 and miR-373 were treated with the ligand at 100 μM. After 5 days, the cells exhibited dose-dependent growth inhibition, whereas no significant inhibition was observed in a neomycin control, suggesting cytostatic rather than cytotoxic effects. Immunolabeling of LATS2 protein in AGS cells after exposure to **35** (50 μM) for 5 days revealed LATS2 protein to be upregulated and localized in the nuclei and cytoplasm, due to reduction of miR-372 and miR-373 levels. Furthermore, pri-miR-372 and pri-miR-373 levels remained almost unchanged in **35**-treated AGS cells suggesting the mode of action of **35** to be post-transcriptional. However, this result was not confirmed as mature miR-372 and miR-373 levels were not quantified in these cells. Additionally, treatment with the ligand led to down-regulation of miR-17-5p, miR-21, and miR-200b, indicating the binding interaction between **35** and pre-miR-372/373 to be not specific.

In addition to targeting the Dicer cleavage site, efforts have also been made towards identifying small molecule inhibitors of Ago2. The binding of the Ago2-mature miRNA complex to the 3'-UTR of a target mRNA proceeds with the solvent-exposed seed region (an 8-nucleotide region from the miRNA 5' end) interacting with the mRNA as a rate-dependent step.[364] The Schmidt lab reported a class of multimodal inhibitors consisting of a short peptide nucleic acid

(PNA) sequence complementary to the bases in the miR-122 seed region covalently attached to an AGO2 active site inhibitor.[365] An *in silico* approach was adopted to identify a small molecule ligand for AGO2 by screening the ZINC fragment subset[366] of 627,000 compounds against the AGO2 active site using genetic optimization for ligand docking (GOLD) software.[367] GOLD predicts binding modes between ligands in various conformations and a target protein. The Chemscore piecewise linear potential (ChemPLP) function, an empirical fitness function that scores interactions between ligands and proteins by modeling steric complementarity between structures,[368] was utilized to rank the interactions revealing 1-(4-phenoxybenzyl)guanidine as the most promising candidate. The GOLD program was also used to identify a tetrameric PNA sequence (TCAC) by superimposing the PNA onto the Ago2-miRNA bound structure.[365,369] The N-acetylated-PNA sequence exhibited an IC_{50} of 1 μM, indicating that the tetrameric PNA alone was not sufficient for inhibition. However, when the identified Ago2 inhibitor and the PNA were combined, docking studies were unable to predict a plausible binding conformation, prompting evaluation of different linkers and heterocyclic motifs commonly found in medicinal chemistry.[370] The selected analogs were then synthesized and evaluated in an activity assay where the Ago2 protein was incubated with the compounds, mature miR-122, and a fluorescently labeled anti-miR-122 substrate. Cleavage products were then visualized by denaturing polyacrylamide gel electrophoresis (PAGE). Two inhibitors, **36** and **37** (Figure 1-9)**,** exhibited an IC_{50} of 100 nM. The tetrameric PNA sequence was proposed to confer specificity to these inhibitors towards miR-122, however, their effect on other miRNAs was not investigated. Additionally, no cell-based assays were reported, which may be attributed to poor cellular uptake of PNAs.

The Zhang group developed an *in silico* screening method based on the tertiary structure of the Dicer binding site of pre-miR-21.[371] The authors constructed a 3D model of the pre-miR-21 by utilizing the MC-Fold/MC-Sym pipeline, a web-hosted service for prediction of RNA secondary and tertiary structures.[372] The pipeline consists of two programs, MC-Fold and MC-Sym, working in tandem. The RNA sequence is uploaded to MC-Fold, yielding a secondary structure that is directly fed into MC-Sym to generate the tertiary structure. Energy optimization was carried out on the RNA tertiary structure with TINKER molecular modeling software.[373] The optimized RNA structure was then utilized in a molecular docking study using Autodock.[371] A library of 1,990 structures from the NCI diversity database was virtually screened to reveal 48 compounds with high binding affinity towards the Dicer binding site on pre-miR-21. Without performing *in vitro* Dicer processing or RNA binding assays, miR-21 inhibition in response to treatment with the top 5 compounds was directly evaluated in four human epithelial cancer cell lines (U87, LN229, SGC7901, and MCF-7). It is important to note that *in silico* predictive approaches are limited by the quality and amount of data provided to them, thus *in vitro* assays should be employed to confirm activity. Despite further validation beyond the virtual screen, compound **38** (30 μM; Figure 1-9) was identified as the most potent with ~50% inhibition of miR-21 as determined by RT-qPCR. Levels of 11 other miRNAs remained unchanged following treatment with **38**, suggesting that **38** has specificity toward miR-21. To confirm that **38** inhibits pre-miR-21 processing, Dicer expression was inhibited in U87 and MCF-7 cells by siRNA treatment. Following siRNA knockdown of Dicer, miR-21 levels were decreased to ~50% and subsequent treatment with **38** did not affect miR-21 levels further, supporting that **38** binds to the Dicer cleavage site of pre-miR-21.[371] Additionally, exposure to **38** (30 μM) led to increased expression levels of miR-21 targets, including phosphatase and tensin homolog (PTEN), PDCD4

and reversion-inducing-cysteine-rich protein with kazal motifs (RECK), however, no further pre-therapeutic evaluation of **38** was performed.

Taken together, rational design approaches have mainly targeted primary and precursor miRNAs, presumably due to the availability of more complex secondary structures for small molecule targeting. Although the approaches vary broadly, Drosha and Dicer cleavage sites in pri- and pre-miRNAs are attractive features for small molecule targeting due to the ease of high-throughput screening and computational prediction of secondary motifs. However, rigorous biochemical and cell-based secondary assays need to be performed on potential hits to confirm predicted target specificity.

2.0 MicroRNA-122

2.1 Introduction to MicroRNA-122

MicroRNA-122 (miR-122), a liver-specific miRNA, comprises ~70% of the miRNAs in the liver[374-376] with an estimated 120,000 copies per hepatocyte.[377] The mature miR-122 sequence is highly conserved among vertebrates, highlighting its critical role in the liver.[378] As such, its unsurprising that miR-122 is a key regulator in liver development, differentiation, homeostasis and function.[379] Furthermore, miR-122 has been shown to regulate cholesterol and fatty acid metabolism in the adult liver and maintain systemic iron homeostasis.

Expression of miR-122 is primarily driven by several liver-enriched transcription factors (LETFs) including hepatocyte nuclear factor 1c (HNF1α), HNF3β, HNF4α, HNF6, and CCAAT/enhancer-binding protein α (C/EBPα).[380-382] LETF-mediated miR-122 expression is tightly regulated to maintain a balance between differentiation and proliferation of hepatocytes.[381,382] Additionally, HNF6 and miR-122 were identified to form a positive feedback loop to stimulate hepatocyte differentiation.[382] Circadian rhythms have also been shown to regulate expression of miR-122 via the transcriptional repressor, reverse erythroblastosis virus (REV-ERB)α.[383] Interestingly, while pri- and pre-miR-122 levels fluctuate during the day, mature miR-122 levels remain constant. Germline development 2 (GLD2), a cytoplasmic poly(A) polymerase, has been shown to add a non-templated adenosine to the 3' terminus of mature miR-122, enhancing its stability and contributing to its long half-life of >24 h. Furthermore, expression levels of some miR-122 targets including receptor expressed in lymphoid tissues (RELT)-like protein 1 (Rell1), switch/sucrose non-fermentable (SWI/SNF)-related matrix associated actin-dependent regulator

of chromatin subfamily D member 1 (Smarcd1), and peroxisome proliferator-activated receptor (Ppar)β/δ have been shown to oscillate throughout the day, suggesting miR-122 displays circadian function.

In the first indication that miR-122 plays a role in regulation of cholesterol metabolism, Krützfeldt and co-workers found that treatment of mice with a 2'-*O*-Me-, PS-, and cholesterol-modified antagomir targeting miR-122 led to a 40% reduction in serum cholesterol levels concomitant with a decrease in expression of several genes associated with cholesterol synthesis and transport including 3-hydroxy-3-methylglutaryl-coenzyme A reductase (HMGCR), 7-dehydrocholesterol reductase (DHCR7), mevalonate kinase (MVK), 3-hydroxy-3-methylglutaryl-coenzyme A synthase 1 (HMGCS1), and farnesyl diphosphate synthetase (FDPS).[187] Analogously, using a 2'-*O*-MOE- and PS-modified AMO, Esau and co-workers observed a reduction in fatty acid and cholesterol synthesis rates and an increase in 5' adenosine monophosphate-activated protein kinase (AMPK), suggesting anti-miR-122 directed therapeutics may be effective in treatment of fatty liver disease.[384] Similar results have been demonstrated using LNA-modified AMOs targeting miR-122 in non-human primates.[223]

Given its critical roles in maintenance of liver homeostasis and differentiation, it's unsurprising that dysregulation of miR-122 has be implicated in the progression and onset of several liver-associated diseases. For example, reduced expression of miR-122 has been found in human patients with non-alcoholic steatohepatitis (NASH),[385] a fatty liver disease associated with accumulation of intracytoplasmic lipids as triglycerides, inflammation, hepatocellular ballooning, and fibrosis.[386] Interestingly, increases in expression of miR-122 targets associated with triglyceride biosynthesis (e.g. 1-acylglycerol-3-phosphate O-acyltransferases [AGPATs]1 and 3/9),[227] inflammatory cell recruitment (e.g., C-C motif chemokine ligand 2 [CCL2]),[387] and

profibrogenic transcription factors (e.g., krueppel-like factor 6 [KLF6] and transforming growth factor beta [TGFβ])[226] are concomitant with depletion of miR-122 levels, suggesting miR-122 maintains an environment that prevents NASH development. Furthermore, NASH has been shown to progress to cirrhosis and hepatocellular carcinoma (HCC).[386] Reduced miR-122 expression is often associated with poor prognosis and metastasis of HCC and several miR-122 targets implicated in tumorigenesis including cyclin G1, a disintegrin and metalloprotease (ADAM)10, insulin-like growth factor-1 receptor (IGF1R), serum response factor (SRF), and wingless/integrated (Wnt)1 have been demonstrated to play a role in hepatocarcinogenesis,[388] suggesting miR-122 is a tumor suppressor. Germline knockout (KO) or liver-specific knockout (LKO) of miR-122 in mice exhibited normal development compared to wildtype mice, but developed HCC with age with an incidence of 89% or 23% in male and female KO mice, respectively, and 50% or 10% in male and female LKO mice, respectively.[226,227] Treatment of a MYC-driven mouse model of HCC with a miR-122 mimic led to a reduction in tumor size further supporting its role as a tumor suppressor miRNA.[227]

Importantly, miR-122 is an essential component for the replication of the hepatitis C virus (HCV) in human liver cells.[389-394] Long-term HCV infection accounts for ~30% of liver transplants annually in the U.S. and can lead to development of hepatocellular carcinoma.[395] Furthermore, the CDC found that new cases of HCV infection have tripled in the U.S. over the last five years[396] and the World Health Organization estimates a global incidence rate of 23.7 per 100,000 people as of 2015.[397] HCV is a single-stranded RNA virus in which the genome encoding the viral polyprotein is flanked by 5' and 3' UTRs.[398] The 5' UTR is conserved across viral genotypes and contains essential structures for genome replication and translation.[399,400] Furthermore, the 5' UTR harbors two complementary miR-122 binding sites, and miR-122 has been shown to be required for HCV

replication.[389] In addition to protecting HCV RNA from degradation, miR-122 has been proposed to induce internal ribosomal entry site (IRES) translation,[401] stabilize the viral genome,[402] and stimulate translation,[403] suggesting that miR-122 is a promising target for the treatment of HCV. Current antiviral therapies target viral proteins required for various steps throughout the HCV life cycle including: I) viral entry;[404] II) protease-mediated polyprotein processing;[405] III) RNA replication;[406-408] and IV) virion assembly (Figure 2-1).[408] However, HCV often becomes resistant to treatment with a single direct-acting antiviral agent, prompting the use of co-therapeutic regimens prone to increased toxicity and reduced efficacy due to drug-drug interactions.[409] As such, targeting miR-122 for antiviral treatment represents an attractive therapeutic approach, in particular since function of a host component is removed and no direct selection pressure is placed on the virus.

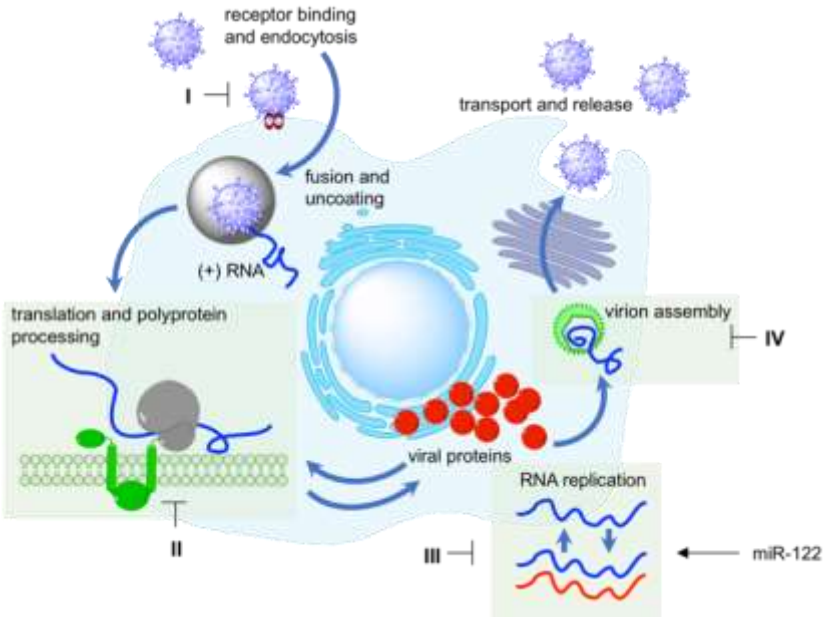

Figure 2-1 HCV life cycle

Current direct-active antiviral agents for treatment of HCV infection target proteins involved in (I) viral entry; (II) polyprotein processing; (III) RNA replication; and (IV) virion assembly. Here, we are reporting small molecule-mediated inhibition of miR-122 impairing HCV RNA replication.

2.2 Discovery of Small Molecule Regulators of miR-122 Function

A cell-based luciferase reporter plasmid was developed by the Deiters lab in order to identify small molecule modifiers of miR-122 function.[410] In contrast to the miR-21 reporter cell line (described in Chapter 3.2 below),[411] the miR-122 reporter bears a second luciferase gene not under control of any miRNA. Use of a constitutively active internal control in cell-based reporter assays accounts for experimental variations including cell number, transfection efficiency, and cell viability. Transfection of the reporter plasmid into Huh7 hepatocellular carcinoma (HCC) cells,

which overexpress miR-122,[384] led to a >90% reduction in luciferase activity compared to miR-122 deficient HeLa cells.[412] Furthermore, co-transfection with a miR-122 antagomir led to an increase in luciferase signal indicating the reporter was amenable for discovery of miR-122 inhibitors. A pilot screen of 1,364 small molecules from the National Cancer Institute (NCI) Diversity Set II[410] yielded compounds **19** and **20** (Figure 1-7) which induced a 7.7- and 12.5-fold increase in luminescence, respectively (similar to the response observed through antagomir transfection). Additionally, amonafide (**21**) (Figure 1-7) was found to be a miR-122 activator, eliciting a 7-fold reduction in luminescence. After verifying that the compounds did not inhibit miR-21 in HeLa-miR21 cells,[411] SAR studies were performed for **19**, **20**, and **21**. Unfortunately, none of the structural modifications led to an improvement in activity relative to the parent molecules. EC_{50} values of 3 μM and 0.6 μM were observed for compounds **19** and **20**, respectively, while **21** elicited an IC_{50} of 3 μM. Treatment with compounds **19** and **20** led to 45% and 72% reductions in mature miR-122 levels and 78% and 97% reductions in pri-miR-122 levels, respectively, while treatment with **41** induced a 4-fold increase of both mature and pri-miR-122 levels. Taken together, these results suggest that all three compounds perturb miR-122 function by acting at the transcriptional or pre-transcriptional level. The psiCHECK-miR122 reporter was also converted into a stable cell line that is amenable to high-throughput screening.[413] miR-122 has been implicated in the hepatitis C virus (HCV) replication cycle[414] and long-term HCV infection may contribute to development of HCC.[395] To this end, compounds **19** and **20** were evaluated for their ability to inhibit HCV replication in Huh7 cells and both were found to reduce HCV RNA levels by almost 50%. In HCC, miR-122 is frequently down-regulated and has been found to inactivate caspase-3.[415] Treatment of HepG2 liver cancer cells with **21** led to an 80% reduction in cell viability coinciding with a 20-fold increase in caspase-3/7 in contrast to Huh7 cells in which

more modest responses were observed, suggesting the activator may have therapeutic potential towards selective treatment of HCC via induction of miR-122. Amonafide is a topoisomerase II inhibitor[416] currently in Phase III clinical trials as a combination therapy towards the treatment of acute myeloid leukemia (AML).[417] Interestingly, several other known chemotherapeutics have also been shown to elicit changes in miRNA expression patterns including cisplatin,[418] 5-fluorouracil, rituximab,[419] bortezomib, perifosine, retinoic acid,[420] and decitabine.[421,422] Furthermore, the Disney lab recently demonstrated that several topoisomerase inhibitors were capable of binding pre-miR-21 as described above.[269] Taken together, these reports suggest that regulation of miRNA expression may be a secondary mode of action for these drugs and could also play a role in their therapeutic effects.

In an approach to continue exploring the therapeutic potential of **20**, the Yao lab generated mesoporous silica nanoparticles coated in a peptide for simultaneous cellular uptake of the small molecule and a miR-122 antagomir.[423] Treatment of Huh7 cells with the nanoparticles led to a ~20% greater reduction in miR-122 levels relative to **20** or miR-122 antagomir alone, confirming the system could be used for controlled release of oligonucleotides and small molecules.

2.3 Sulfonamide Inhibitors of miR-122

Following the identification of the parent compound **39**, a structure-activity relationship study was initiated to improve the potency of **39** and to better understand the chemical functionalities required for its activity. For preparing the analogs, a modular synthetic approach was adopted and **39** was altered on two parts: the benzenesulfonyl and the imidazole. Substituting the 4-methylimidazole with a dimethylamine (**40**) or an ethylamine group (**41**) resulted in a

significant loss in activity. Drastic reductions in activity were also observed when replacing the 4-methylimidazole with a structurally similar pyrrole (**42**), 3-methylpyrrole (**43**), 4-methylpyrazole (**44**), or 3-methylpyrazole (**45**), indicating the importance of the imidazole motif.

We next studied the requirement of the methyl group itself through substitution of 4-methylimidazole with an imidazole (**46**), 4-phenylimidazole (**47**), or 4-nitroimidazole (**48**). Removal of the methyl group or replacement with the phenyl group resulted in a large decrease in activity while the nitro group elicited a more modest reduction. Virtually complete loss of activity was also observed for 2-ethyl- (**49**) or 4,5-dichloro-imidazole (**50**) modifications. Further substitutions of the imidazole by more sterically demanding benzimidazole (**51**) and indole (**52**) motifs also led to a decrease in activity compared to **39**, again indicating the importance of a small 4-methylimidazole (Table 1).

Table 1 Structures and activity of derivatives **39**-**52**

[a]RLU values represent *Renilla* luciferase luminescence signal in the Huh7-miR122 stable cell line and are first normalized to firefly luciferase (dual reporter system) and then normalized to the activity of the original hit compound **39**. Synthesis was performed by Rohan Kumbhare.

[b]*In vitro Renilla* luciferase data are normalized to DMSO.

[c]psiCHECK-empty assay data are normalized to DMSO. Data for all assays represents the average ± standard deviation from at least three independent experiments.

compound	chemical structure	primary screen (RLU)[a]	*Renilla* luciferase assay[b]	psiCHECK-empty assay[c]
39	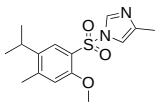	100 ± 3%	80%	127%

Table 1 (continued)

compound	chemical structure	primary screen (RLU)[a]	*Renilla* luciferase assay[b]	psiCHECK-empty assay[c]
40	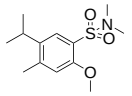	42 ± 3%	--	--
41	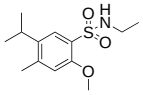	42 ± 3%	--	--
42	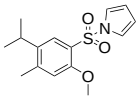	29 ± 1%	--	--
43	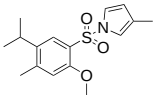	57 ± 4%	87%	--
44	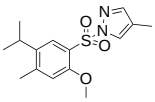	32 ± 1%	--	--
45	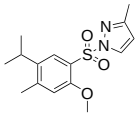	44 ± 1%	--	--
46	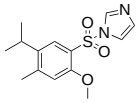	33 ± 4%	--	--
47	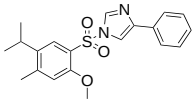	35 ± 1%	--	--
48	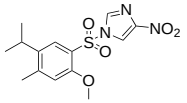	61.1 ± 0.4%	67%	--
49	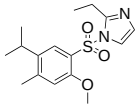	40 ± 1%	--	--
50	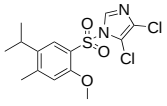	4 ± 1%	--	--
51	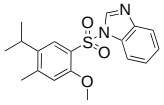	75 ± 3%	45%	--
52	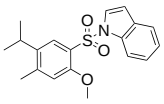	55 ± 1%	94%	--

Focusing our attention on the benzenesulfonyl moiety, a series of analogs were synthesized keeping the 4-methylimidazole constant. Replacing the isopropyl group with a hydrogen (**53**) or a methyl (**54**) abrogated activity. The rotationally-restricted 1,2,3,4-tetrahydronaphthamidyl analog (**55**) also showed a significant loss in activity**.** Furthermore, *O*-ethyl (**56**) and *O*-propargyl (**57**) analogs elicited reduced activity (Table 2).

Table 2 Structures and activity of derivatives **53**-**57**

[a]RLU values represent *Renilla* luciferase luminescence signal in the Huh7-miR122 stable cell line and are first normalized to firefly luciferase (dual reporter system) and then normalized to the activity of the original hit compound **39**. Synthesis was performed by Rohan Kumbhare.

[b]*In vitro Renilla* luciferase data are normalized to DMSO.

[c]psiCHECK-empty assay data are normalized to DMSO. Data for all assays represents the average ± standard deviation from at least three independent experiments.

compound	chemical structure	primary screen (RLU)[a]	*Renilla* luciferase assay[b]	psiCHECK-empty assay[c]
53	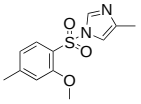	24 ± 3%	80%	--
54	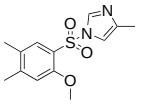	32 ± 5%	--	--
55	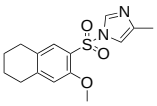	33.3 ± 0.5%	--	--
56	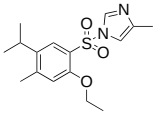	74 ± 10%	70%	--
57	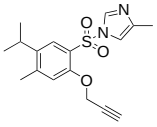	50 ± 3%	97%	--

It was recently reported that sulfonamide derivatives and many other small molecule inhibitors may be prone to increasing the *Renilla* luciferase concentration in cells via ligand-based stabilization, and possibly creating false-positive hits in high-throughput screens.[424] Conversely, biochemical evaluation of the same inhibitors causes a significant decrease in luciferase signal. Thus, the analogues that elicited ≥50% activity of the parent compound **39** in the initial screen were tested in a biochemical *Renilla* luciferase (Rluc) assay. Here, **48**, **51**, and **56** induced ≥30% decrease in *Renilla* luminescence, while analogs **39**, **52**, and **57** only showed modest enzyme inhibition. To further validate the specificity of these inhibitors for acting through the miRNA pathway, Huh7 cells were transfected with the psiCHECK-empty reporter (where the miR-122 binding site was replaced with a linker not targeted by any known miRNAs) and exposed to each analog at 10 μM for 48 h. The parent compound **39** induced a 27% increase in the psiCHECK-empty assay, consistent with Rluc inhibition observed in the *in vitro* assay (Table 1).

A complete scaffold change of the imidazole motif was also investigated. A series of analogs with pyridin-2-amines and anilines were synthesized. Both the unsubstituted pyridine ring (**58**) and methylation at the 2-position (**59**) showed 89% activity relative to the parent compound, while 3-methyl-pyridin-2-amine (**60**) elicited a significant increase in activity. Aniline (**61**) and 2-methylaniline (**62**) analogs showed a reduction in activity. Unfortunately, when assessed in the *in vitro* Rluc assay, **58**-**60** induced significant reductions in luminescence signal indicating they did not display enhanced miRNA-122 inhibition activity (Table 3).

Table 3 Structures and activity of derivatives **58**-**62**

[a]RLU values represent *Renilla* luciferase luminescence signal in the Huh7-miR122 stable cell line and are first normalized to firefly luciferase (dual reporter system) and then normalized to the activity of the original hit compound **39**. Synthesis was performed by Rohan Kumbhare.

[b]*In vitro Renilla* luciferase data are normalized to DMSO.

[c]psiCHECK-empty assay data are normalized to DMSO. Data for all assays represents the average ± standard deviation from at least three independent experiments.

compound	chemical structure	primary screen (RLU)[a]	*Renilla* luciferase assay[b]	psiCHECK-empty assay[c]
58	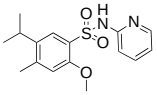	88 ± 1%	8%	--
59	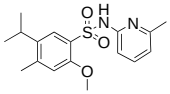	89 ± 11%	2%	--
60	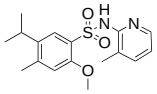	135 ± 4%	17%	--
61	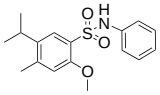	47 ± 3%	--	--
62	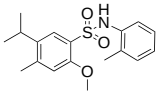	32 ± 3%	--	--

The next modification made was methylation of the secondary amine in the sulfonamide. On inspecting *in vitro Renilla* luciferase assay data and analogs bearing imidazole and pyrazole motifs, we hypothesized that a tertiary sulfonamide would be important for minimizing Rluc inhibition, because secondary sulfonamides form a subset of Rluc inhibitors.[425] In order to convert **58**-**60** to the tertiary sulfonamides **63**-**65**, these analogs were *N*-methylated to minimize further steric perturbation that might have had a negative impact on miR-122 inhibition. Compound **63**

showed a modest reduction in activity, while **64** elicited a 7% increase compared to the parent compound. Unfortunately, **65** induced a disappointing 64% activity relative to **1**, but all three compounds showed no Rluc inhibition supporting our hypothesis (Table 4). Gratifyingly, replacement of the pyridine moiety in **64** and **65** with a benzene ring in compounds **66** and **67** yielded 104% and 122% activity, respectively. Compound **66** showed no Rluc inhibition, while 20% inhibition was observed with **67**. Methylation of the aniline ring at the *para* position (**68**) yielded a modest decrease in activity compared to **39**, while 2,3-dimethyl- (**69**) and 2,5-dimethyl- (**70**) aniline derivatives showed 80% activity relative to the parent compound. Unfortunately, while **68-70** showed no inhibition in the *in vitro* assay, all three compounds displayed >200% activity in the psiCHECK-empty assay, indicating that they increase luciferase activity by non-miRNA dependent mechanisms in cells. Furthermore, compounds **64** and **66** showed little to no inhibition in the psiCHECK-empty assay, consistent with Rluc inhibition observed in the *in vitro* assay (Table 4).

Table 4 Structures and activity of derivatives **63-71**

[a]RLU values represent *Renilla* luciferase luminescence signal in the Huh7-miR122 stable cell line and are first normalized to firefly luciferase (dual reporter system) and then normalized to the activity of the original hit compound **39**. Synthesis was performed by Rohan Kumbhare.

[b]*In vitro Renilla* luciferase data are normalized to DMSO.

[c]psiCHECK-empty assay data are normalized to DMSO. Data for all assays represents the average ± standard deviation from at least three independent experiments.

compound	chemical structure	primary screen (RLU)[a]	*Renilla* luciferase assay[b]	psiCHECK-empty assay[c]
63	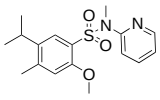	89 ± 4%	100%	88%

Table 4 (continued)

compound	chemical structure	primary screen (RLU)[a]	*Renilla* luciferase assay[b]	psiCHECK-empty assay[c]
64	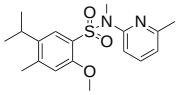	107 ± 1%	100%	117%
65	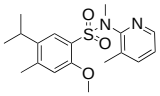	64 ± 12%	100%	87%
66	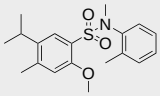	104 ± 7%	100%	90%
67	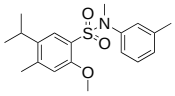	122 ± 1%	78%	103%
68	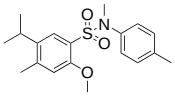	82 ± 1%	100%	218%
69	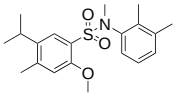	80 ± 4%	93%	225%
70	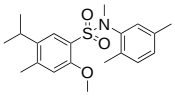	77 ± 1%	100%	245%
71	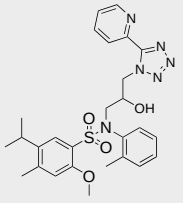	580 ± 25%	102%	178%

While **64** and **66** exhibited an excellent activity profile, poor solubility of the inhibitors presented a limitation of potential applications in animal studies. Because compound **66** elicited less of a response in the psiCHECK-empty assay, analog **71** (Table 4), bearing a 5-phenyl-1*H*-tetrazol moiety, was investigated. Installation of a carboxylic acid or corresponding bioisostere, such as tetrazol, has been shown to enhance the water solubility of small molecules.[426]

Unfortunately, water solubility of compound **71** did not improve. This is somewhat unsurprising, because structural analysis of **66** and **71** using ChemDraw Professional software (PerkinElmer) predicted CLogP values of 2.81 and 4.07, respectively, suggesting installation of the tetrazol moiety may not yield a dramatic increase in water solubility. Interestingly, the analog induced an unexpected increase in luciferase signal compared to compound **39** and **66** and elicited no inhibition in the *in vitro* Rluc assay. However, **71** induced an 80% increase in luminescence in the psiCHECK-empty assay compared to DMSO suggesting it is capable of activating luciferase in cells through an unknown mechanism (Table 4).

The best analogs identified through structural modifications of **39**, were tested in dose-response in Huh7-miR122 cells. The inhibitor **66** elicited an EC_{50} of ~11 µM (Figure 2-2A) while analog **71** showed an improved EC_{50} value of ~4 µM (Figure 2-2B). The inhibitors **66** and **71** were further investigated in RT-qPCR experiments measuring mature miRNA levels. Huh7 cells were exposed to a DMSO control (0.1%) or to the inhibitors at 25 µM for 48 h, total RNA was isolated using the miRNeasy kit (Qiagen), and RT-qPCR was performed in triplicate using TaqMan probes for miR-122 and RNU19 (control). The data were then normalized to the DMSO and RNU19 controls using the $2^{-\Delta\Delta Ct}$ method.[427] Compound **66** exhibited a 38% decrease in miR-122 levels while analog **71** elicited an 87% reduction in miR-122 expression, concomitant with their relative activity in the primary screen (Figure 2-3A).

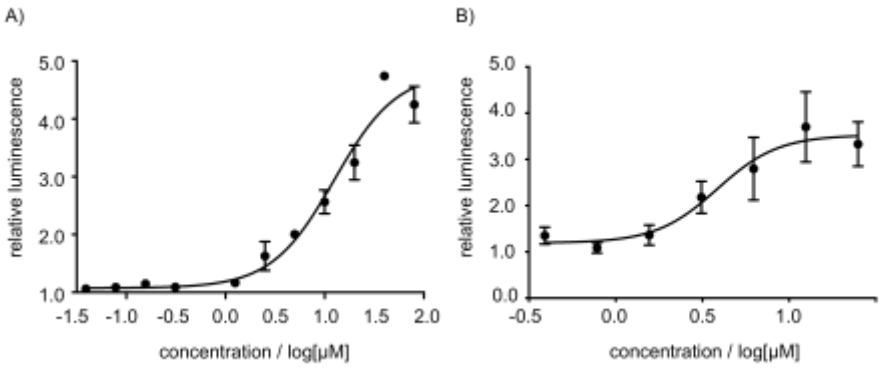

Figure 2-2 Further evaluation of miR-122 inhibition by lead molecules **66** and **71**

A) An EC_{50} of ~12.5 μM was observed for inhibitor 66. B) Compound 71 elicited an EC_{50} of ~3.8 μM. All data is normalized to DMSO and error represents standard deviations of three independent experiments.

In order to begin elucidating the mode of action of inhibitors **66** and **71**, several preliminary experiments were performed. A HeLa cell line that stably expresses a miR-21 reporter[428] was used to further confirm that the compounds are not general inhibitors of the miRNA pathway, since no increase in luciferase signal was observed (Figure 2-3B). To investigate downstream effects of these inhibitors, expression of E-cadherin, a downstream effector of known target miR-122 target Wnt1,[429] was monitored in Huh7 cells following treatment with the **66** and **71.** Endogenous E-cadherin levels are high in Huh7 cells due to Wnt1 repression by miR-122. Thus, treatment with a small molecule inhibitor was expected to show a decrease in E-cadherin expression as a result of its effect on direct targets of miR-122. Treatment with DMSO alone elicited no inhibition of E-cadherin expression as expected, whereas modest reductions in E-cadherin expression were observed upon treatment with **66** and **71**, indicating suppression of the protein via miR-122-mediated induction of Wnt1 (Figure 2-3C). Pri-miR-122 expression was assessed by RT-qPCR to

determine if these compounds inhibited miR-122 transcription. The miR-122 inhibitor **28** (25 µM) elicited up to a 35% decrease in pri-miR-122 expression (Figure 2-3D) while **33** induced a more potent 67% reduction, suggesting that both small molecules affect transcriptional or pre-transcriptional regulation, rather than downstream steps of the miRNA pathway.

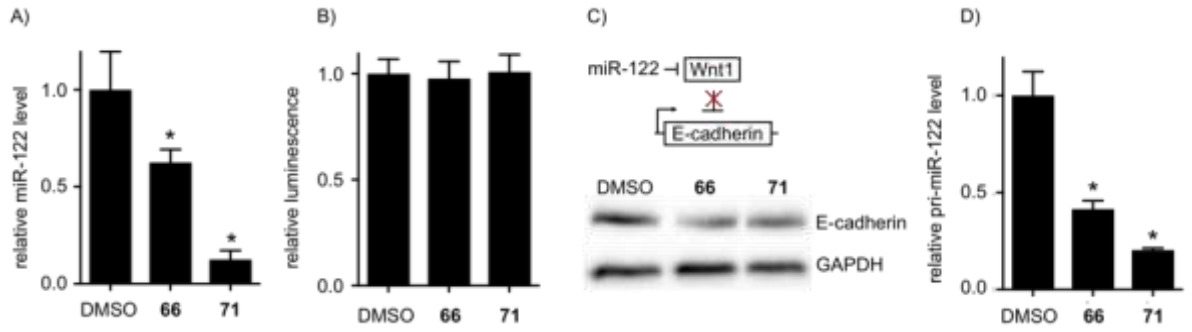

Figure 2-3 Evalution of specificity of **66** and **71**

A) Mature miR-122 levels in Huh7 cells were evaluated via RT-qPCR following 48 h treatment with compounds **66** and **71** (25 µM). Expression of miR-122 was normalized to a DMSO control. RNU19 expression was used as an internal control. B) Bright-Glo assay performed on HeLa-miR21 reporter cells after 48 h treatment with **66** and **71** (10 µM). Luminescence was normalized to DMSO (control). C) miR-122 inhibits Wnt1, thereby releaving its repression of E-cadherin. E-cadherin expression was assessed in Huh7 cells via western blot following treatment with **66** (25 µM) or **71** (10 µM) for 48 h. GAPDH expression was monitored as control. D) Primary miR-122 levels were evaluated via RT-qPCR in Huh7 cells following 48 h treatment with compounds **66** and **71** (25 µM). Expression of pri-miR-122 was normalized to a DMSO control. GAPDH expression was used an interal control. Data represent the averages ± standard deviations from three independent experiments.

To investigate the possibility of targeting miR-122 transcription and related proteins, a reporter plasmid in which a firefly luciferase gene was placed under the control of the miR-122 promoter was developed (Figure 2-4A).[430] Briefly, the miR-122 promoter sequence was PCR amplified from Huh7 genomic DNA and ligated into a multi-cloning site upstream of the firefly luciferase gene in the pGL3-basic plasmid. As expected, almost no luminescence was observed for the control pGL3-basic reporter, while a significant level of luciferase expression was detected in Huh7 cells transfected with pGL3-miR122promoter (Figure 2-4C). Treatment with the small molecule inhibitors **66** and **71** led to a reduction in miR-122 promoter activity (Figure 2-4B), consistent with the also observed decrease in pri-miR-122 levels.

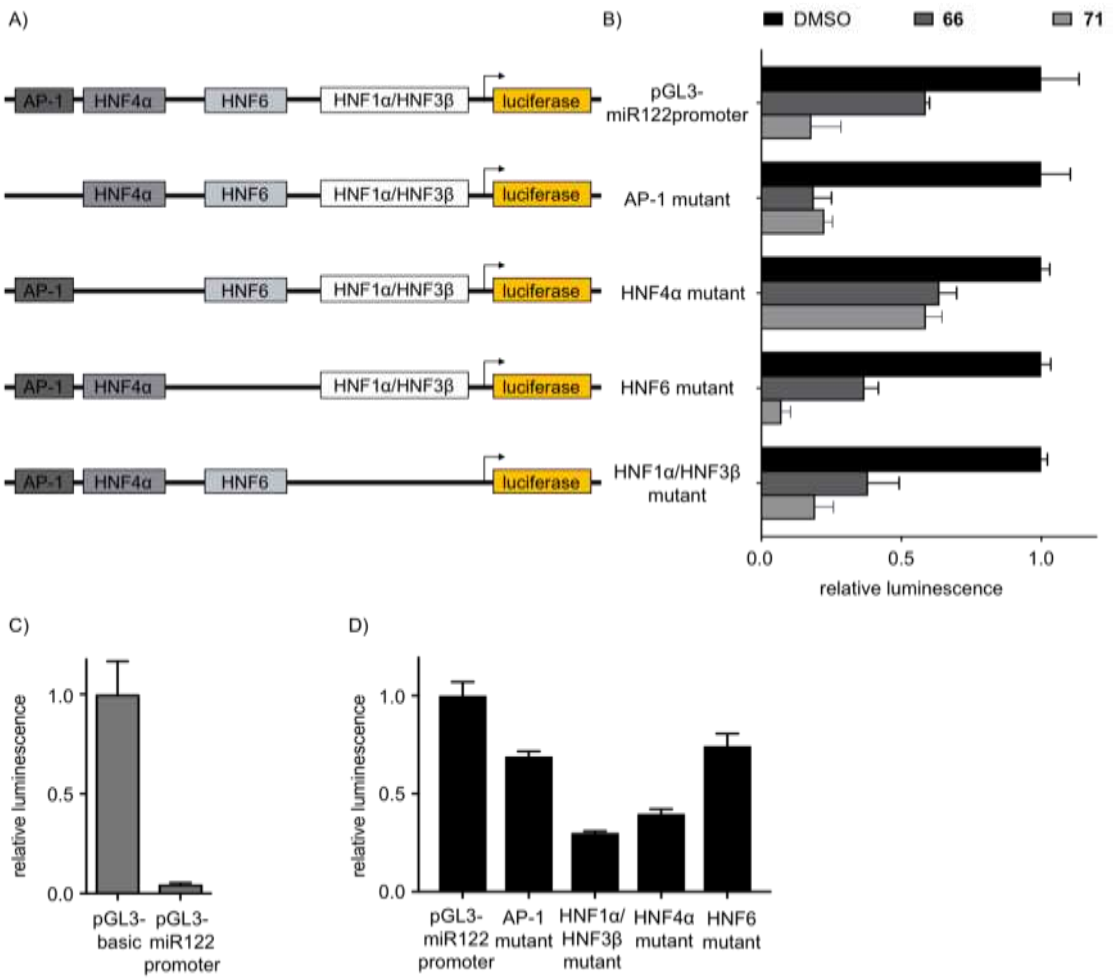

Figure 2-4 miR-122 promoter assay

A) Individual transcription factor binding sites within the miR-122 promoter sequence were mutated or deleted to attempt to identify the potential transcription factor target **66** and **71**. of Huh7 cells were treated with **66** and **71** at 25 µM following transfection with the pGL3-miR122 promoter plasmid. B) Huh7 cells were transfected with the parent reporter plasmid or reporter plasmids in which transcription factor binding sites were mutated/deleted, then treated with compounds **66** and **71** at 25 µM. C) Huh7 cells were transfected with pGL3-basic or pGL3-miR122 promoter plasmid. D) Transcription factor binding sites were deleted within the miR-122 promoter sequence. The resulting reporter plasmids were transfected into Huh7 cells. Luciferase activity was evaluated in all assays after 48 h using a Bright-Glo Assay. All data are normalized to DMSO and represent the averages ± standard deviations from three independent experiments.

After confirming that **66** and **71** inhibited the activity of the miR-122 promoter, a more detailed study was performed to possibly identify the primary transcription factor target. Liver-enriched transcription factors, HNF1α, HNF3β, HNF4α, and HNF6 have been reported to regulate miR-122 transcription.[381,382,430] Additionally, the AP-1 transcription factor was predicted to bind to the miR-122 promoter.[431,432] In order to study the effect of **66** and **71** on each individual transcription factor, reporter plasmids was developed in which a single transcription factor binding site in the miR-122 promoter sequence was mutated or deleted while the remaining binding sites were maintained. Because there is overlap between the HNF1α and HNF3β binding sequences,[381] only a single mutant plasmid was generated for both. The mutated miR-122 promoter constructs were individually tested in Huh7 cells. All mutated constructs showed significant reductions in luciferase activity compared to the parent reporter (Figure 2-4D), suggesting that the interactions between the transcription factors and their corresponding promoters were abrogated by the introduction of mutations. As expected, mutation of the HNF1α/HNF3β and HNF4α binding sites led to a 70% and 60% decrease in promoter activity respectively, indicating these transcription factors significantly contribute to miR-122 expression.[381] AP-1 and HNF6 mutants elicited only 30% reductions in activity. While the modest impact of HNF6 on miR-122 promoter activity reflects previous results,[382] we have found no reports demonstrating the effect of AP-1 on miR-122. Following transfection of HNF1α/HNF3β, HNF6, and AP-1 mutants and subsequent treatment with **66** and **71**, up to 20% further reduction in luciferase activity was observed, indicating that the compounds are still able to inhibit transcription (Figure 2-4B). However, in combination with the HNF4α, mutant, **66** and **71** showed 20% and 32% less inhibition, respectively, compared with the parent construct, indicating that they may have an effect on the function of this transcription factor (Figure 2-4B). Furthermore, small molecules bearing a similar

sulfonamide scaffold have been reported to bind HNF4α and inhibit its function, providing further support for this hypothesis.[433,434]

Antisense oligonucleotide-mediated knockdown of miR-122 has previously been shown to inhibit HCV replication.[435,436] Additionally, combination treatment of human liver cells stably expressing HCV replicons with an anti-miR-122 oligonucleotide and interferon-α2b resulted in additive antiviral activity.[437] Binding of miR-122 to the 5' terminus protects the HCV viral genome from degradation by the exonuclease Xrn1, thereby stabilizing HCV RNA (Figure 2-5A).[438,439] Several additional mechanisms for miR-122-mediated promotion of HCV replication have also been proposed. For example, the 48S ribosomal complex association is enhanced in the presence of miR-122 in rabbit reticulocyte lysate suggesting a potential mechanism for miR-122-mediated regulation of translation;[401] however, conflicting results support an alternative mechanism whereby miR-122 promotes translation independently of ribosome binding by binding downstream of the IRES and altering its structure.[440] A recent study also found that mutations within the IRES led to reductions in RNA core protein expression and viral RNA accumulation.[441] Furthermore, it has been hypothesized that miR-122 displaces cellular factors essential for viral translation, such as poly(rC) binding protein 2 (PCBP2), thereby shifting viral RNA from a translating pool to a replicating pool and enhancing viral replication.[403] This also suggests miR-122 may promote or inhibit interactions with additional RNA-binding proteins. Additionally, miR-122 was proposed to augment positive-strand RNA synthesis by displacing the positive strand from the 3' terminus of the negative strand to be used as a template.[399] Finally, miR-122 been shown to stabilize HCV RNA and enhance RNA synthesis in association with Ago2,[442] potentially through recruitment of viral RNA to replication complexes,[443] however, the latter mechanism is not completely understood. Because compounds **66** and **71** were able to inhibit miR-122 function,

both compounds were investigated for their effect on HCV replication. Huh7.5 cells were pre-treated with **66** and **71** (10 µM) or DMSO (negative control) for one hour, then infected with HCV. After 48 h, total RNA was extracted, and HCV RNA was analyzed via RT-qPCR. Inhibitors **66** and **71** elicited an 88% and 90% reduction in viral RNA expression, respectively (Figure 2-5B), suggesting they may be promising candidates for HCV therapies. Furthermore, Huh7 cells treated with **66** or **71** for 48 h showed no reduction in cell viability at 10 or 25 µM, indicating it is capable of inhibiting miR-122 without toxicity (Figure 2-5C).

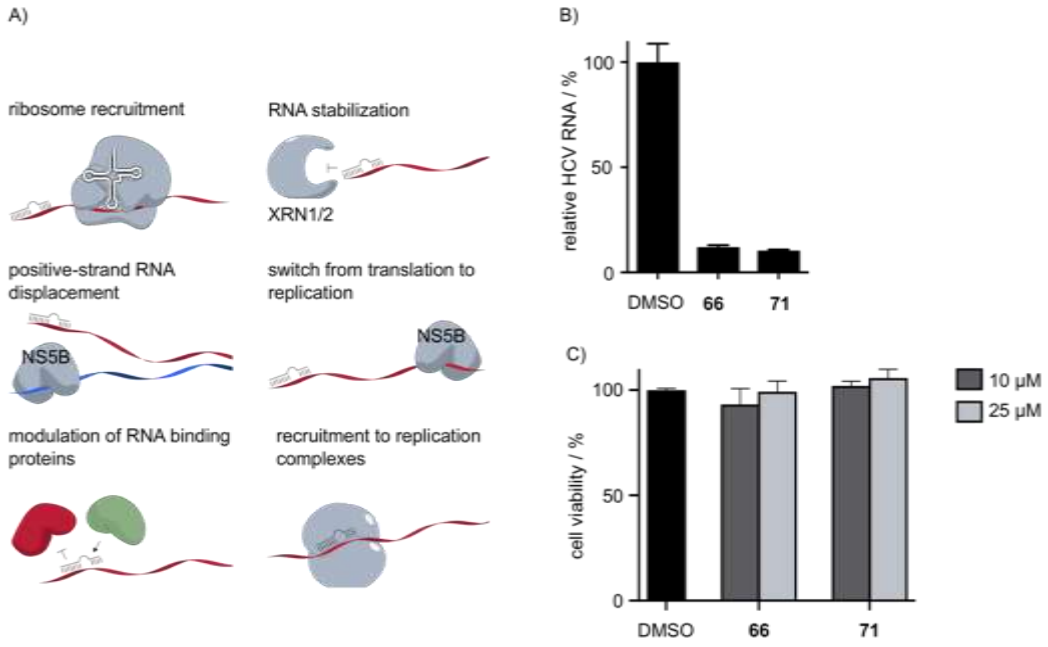

Figure 2-5 Therapeutic potential of **66** and **71**

A) Proposed mechanisms of miR-122-mediated regulation of HCV. B) Huh7.5 cells were pre-treated with **66** and **71** at 10 µM, then infected with HCV. After 48 h, RT-qPCR was performed to evaluate HCV replication. Relative expression of HCV RNA for small molecule treated cells was normalized to a DMSO control and 18S ribosomal RNA expression. C) Huh7 cells were treated with **66** or **71** for 48 h, then an XTT assay was performed to evaluate cell

viability. All data is normalized to DMSO and data represent the averages ± standard deviations from three independent experiments. Data were generated by Yasmine Baktash at University of Chicago.

2.3.1 Summary and Outlook

In summary, a new bis-arylsulfonamide class of small molecule miR-122 inhibitors was identified from a high-throughput screen of >300,000 compounds. Several analogs were evaluated in comprehensive structure-activity relationship studies, demonstrating that 5-isopropyl, 2-methoxy, and 4-methyl groups on the central benzene ring were important for miR-122 inhibitory activity. Replacement of the imidazole moiety led to the identification of several pyridine and aniline derivatives with excellent activity. Unfortunately, many of these compounds were also identified as false-positives due to direct inhibition of the *Renilla* luciferase enzyme and thus its stabilization in cells through small molecule binding. By implementing a series of secondary assays to evaluate *Renilla* luciferase activity in the presence of potential hit compounds, we established that a tertiary sulfonamide moiety was required to prevent luciferase inhibition – a concept that may be generally applicable to other sulfonamides identified in screens using *Renilla* luciferase reporters. The miRNA inhibitor **66** was found to selectively induce downregulation of miR-122 in the Huh7-miR122 reporter cell line, while having no effect on *Renilla* luciferase activity in either biochemical or cell-based control experiment. Furthermore, **66** did not inhibit miR-21 in the HeLa-miR21 reporter cell line, indicating that it is not a general inhibitor of the miRNA pathway. In an attempt to improve aqueous solubility of **66**, we synthesized the analog **71**. Unfortunately, **66**, and several other analogs that we synthesized (not shown), did not improve water solubility; however, the inhibitor displayed further increased activity. Western blot analysis

confirmed that the inhibitors were capable of reducing expression of E-cadherin by relieving translational repression of Wnt1 via miR-122 inhibition. Compounds **66** and **71** were shown to reduce cellular miR-122 levels to 62% and 13% at 25 μM as a result of inhibiting pri-miR-122 transcription, since pri-miR-122 levels were reduced as well. This is further supported by the observed inhibitory effects of the two compounds in a miR-122 native promoter assay. Moreover, deletion of individual transcription factor recognition sites within the miR-122 gene promoter sequence led to the discovery that compounds **66** and **71** decrease miR-122 expression presumably by inhibiting HNF4α-driven promoter activity. Since these small molecule inhibitors act at the transcriptional level, they may be useful probes for the regulation of miR-122 expression. Most importantly, both miR-122 inhibitors **66** and **71** blocked viral HCV RNA replication in human liver cells by ~90%, indicating they may have therapeutic potential in the treatment of HCV infection.

Future work should focus on further evaluating HNF4α as a potential target of **66** and **71**. Specifically, known small molecule inhibitors of HNF4α should be investigated in the miR-122 reporter assay as well as the miR-122 promoter assay. Additionally, experiments such as electrophoretic mobility shift assay (EMSA) or fluorescence polarization should be performed with inhibitors **66** and **71** in combination with the recombinant protein to investigate whether a direct binding interaction occurs.

2.3.2 Materials and Methods

Cell culture. Experiments were performed using Huh7 and HeLa-miR21^{410} cell lines cultured in Dulbecco's Modified Eagle Medium (DMEM; Hyclone) supplemented with 10% (v/v) Fetal Bovine Serum (FBS; Sigma Aldrich) and 1% (v/v) P/S and maintained at 37 °C in a 5% CO_2

atmosphere. Huh7-miR122 cells[444] were cultured in DMEM (Hyclone) supplemented with 10% (v/v) FBS (Sigma Aldrich) and 500 µg/ml of G418 (Sigma Aldrich) and maintained at 37 °C in a 5% CO_2 atmosphere. Experiments were performed in the absence of penicillin-streptomycin.

Compound handling. Compound stocks were prepared by dissolving solid compound (4-5 mg) in an appropriate volume of syringe filtered (0.2 µm filter) DMSO. Initial stocks were typically diluted to 50 – 100 mM depending on the solubility limit, then further diluted as needed. Stock solutions were distributed in 10 – 20 µl aliquots and stored at -20 °C until use. Freeze/thaw cycles were limited to no more than 15 per aliquot.[445] Concentrated stocks were monitored for precipitation following long term storage and were redissolved by briefly heating on a 95 °C heat block when necessary. All compounds were characterized by ^{1}H NMR and HRMS prior to evaluation in biological assays. Purity of compounds was periodically evaluated (once every 6-12 months) via LC-MS. If compounds were redissolved by heating, LC-MS was performed on the sample to ensure integrity of the stock prior to use in biological assays.

For treatment of cells in a 96-well plate format, 2 µl of a DMSO stock (1000x[final]) was diluted in 48 µl of growth media (penicillin/streptomycin-free) in a 96-well plate and mixed by pipetting up and down. Then 5 µl of the diluted compound was added to cells in 195 µl of growth media. For treatment of cells in a 384-well format, 6 µl of the DMSO stock (1000x[final]) was diluted in 69 µl of growth media (penicillin/streptomycin-free) in a 384-well plate and mixed by pipetting up and down with a multichannel pipette. Subsequently, 10 µl of the initial dilution was mixed with 70 µl of growth media in a separate well for each condition. Lastly, 5 µl of the second media dilution was added directly to cells in 45 µl of growth media.

Assay for small-molecule inhibitors of miR-122. Small molecule screens were carried out using our previously described Huh7-miR122 reporter cell line (a stably transfected cell line expressing a miR-122 binding sequence in the 3' UTR of a *Renilla* luciferase gene).[444] Cells were seeded at 15,000 cells per well in white, clear-bottom, 96-well plates (VWR). Following overnight incubation, cells were treated with compound at the desired concentration in 0.1% (v/v) DMSO or DMSO control (0.1% final DMSO concentration) in triplicate. The cells were incubated for 48 h, then analyzed for *Renilla* and firefly luciferase expression with a Dual Luciferase Assay Kit (Promega, see protocol 6.2.13 Luminescence was measured on a microplate reader (Tecan M1000) with an integration time of 1 s and delay time of 5 s.

Assessment of the selectivity of small-molecule inhibitors of miR-122. Selectivity of the small molecules for miR-122 was validated using our previously described HeLa-miR21 reporter cell line (a stably transfected cell line expressing a miR-21 binding sequence in the 3' UTR of a firefly luciferase gene).[411] Cells were seeded at 10,000 cells per well in two white, clear-bottom, 96-well plates (VWR). Following overnight incubation, cells were treated with compound at the desired concentration in 0.1% (v/v) DMSO or DMSO control (0.1% final DMSO concentration) in triplicate. The cells were incubated for 48 h, then one plate of cells was analyzed for firefly luciferase expression with a Bright-Glo Luciferase Reporter Assay Kit (Promega, see protocol 6.2.14 Luminescence was measured on a microplate reader (Tecan M1000) with an integration time of 1 s. The other plate of cells was analyzed for cell viability using an XTT assay. For the XTT assay, XTT reagent (Roche, see protocol 6.2.16 was activated with 8 µl of menadione per 1 ml of XTT solution. Absorbance was measured immediately after addition of reagent and again after 4 h using a microplate reader (Tecan M1000) at 450 nm and 630 nm (control). Cell viability

was determined using this equation: cell viability = $(Absorbance_{450\ nm} - Absorbance_{630\ nm})_{4\ h}$ - $(Absorbance_{450\ nm} - Absorbance_{630\ nm})_{initial}$. Cell viability was averaged and then used to calculate relative luminescence for each well using the equation: relative luminescence = luminescence/cell viability.

To assess inhibition of *Renilla* luciferase in cells, Huh7 cells were seeded at a density of 15,000 per well in white, clear-bottom, 96-well plates (VWR). Following overnight incubation, cells were transfected with 50 ng of psiCHECK-empty using Lipofectamine 2000 (Thermo-Fisher Scientific). After 2 h incubation at 37 °C, media was replaced with DMEM supplemented with the compounds at 10 μM or DMSO (0.1% final DMSO concentration) in triplicate. The cells were incubated for 48 h followed by analysis with a Dual Luciferase Reporter Assay Kit (Promega, see protocol 6.2.13 The luminescence was measured on a microplate reader (Tecan M1000) with an integration time of 1 s and a delay time of 5 s.

Biochemical Rluc inhibition assay. The protocol was adapted from previous reports.[446] The experiment was performed in black, clear-bottom, 384-well plates (VWR) in triplicate. The compounds were diluted to a final concentration of 10 μM (0.1% final DMSO concentration) in PBS and recombinant *Renilla* luciferase enzyme (RayBiotech, 0.108 mg/L final *Renilla* luciferase enzyme concentration) was added to each well. Then, 15 μl of *Renilla*-Glo buffer (Promega) supplemented with the coelenterazine substrate (10 μl of substrate per 1 ml of buffer) was added to each well. The plate was incubated in the dark for 10 min, then luminescence was measured on a microplate reader (Tecan M1000) with an integration time of 1 s.

Quantitative real time PCR (RT-qPCR). Huh7 cells were seeded at 125,000 cells per well in 6-well plates (VWR). Following overnight incubation, cells were treated with compound at 10 or 50 μM or DMSO (0.1% final DMSO concentration). The cells were incubated at 37 °C for 48 h (DMEM, 5% CO_2). Following removal of media, cells were washed with PBS buffer (1 ml; pH 7.4) followed by RNA isolation using the miRNeasy mini kit (Qiagen; see protocol 6.2.6 Total RNA was quantified using a Nanodrop ND-1000 spectrophotometer. Each RNA sample (15 ng) was reverse transcribed using the TaqMan microRNA Reverse Transcription Kit (Thermo-Fisher Scientific) in conjunction with either the miR-122 (Thermo-Fisher Scientific; Assay ID: 002245) or RNU19 control (Thermo-Fisher Scientific; Assay ID: 001003) TaqMan reverse transcription (RT) primer (16 °C, 30 min; 42 °C, 30 min; 85 °C, 5 min) as described below (general protocol 6.2.7). Quantitative real time PCR was conducted with a TaqMan 2x Universal PCR Master Mix (Thermo-Fisher Scientific) and the appropriate TaqMan miRNA assay (Thermo-Fisher Scientific) on a Bio-Rad CFX96 RT-PCR thermal cycler (1.3 μl of RT product; 95 °C, 10 min; followed by 40 cycles of 95 °C, 15 s; 60 °C, 60 s). The triplicate threshold cycles (Ct) obtained for each small molecule treatment were used to determine the relative levels of miR-122 in small molecule treated cells relative to the DMSO control using the $2^{-\Delta\Delta Ct}$ method.[447] The samples were also analyzed by RT-qPCR to measure the expression levels of pri-miR-122.[448] After RNA isolation, 50 ng of each RNA sample were reverse transcribed using the iScript cDNA synthesis kit (Bio-Rad) (25 °C, 5 min; 42 °C, 30 min; 85 °C, 5 min) as described in protocol 6.2.8 Quantitative real time PCR was conducted with a TaqMan 2x Universal PCR Master Mix and the appropriate TaqMan primers for hsa-pri-miR-122 (Thermo-Fisher Scientific; Assay ID: Hs03303072_pri) and GAPDH (Thermo-Fisher Scientific; Assay ID: Hs02758991_g1) on a Bio-Rad CFX96 RT-PCR thermal cycler (2 μl RT product) following the protocol described above. The triplicate threshold cycles (Ct) obtained

for each small molecule treatment were used to determine the relative levels of pri-miR-122 in small molecule treated cells relative to the DMSO control and were normalized to the GAPDH control using the $2^{-\Delta\Delta Ct}$ method.[447]

Western blot for E-cadherin. Huh7 cells were seeded at 125,000 cells per well in 6-well plates (VWR). Following overnight incubation, cells were treated with compound at 10 µM or DMSO (0.1% final DMSO concentration). The cells were incubated at 37 °C for 48 h (DMEM, 5% CO_2). Following removal of media, cells were washed with PBS buffer (1 ml; pH 7.4) followed by lysis (for detailed protocol see 6.2.11 The samples were then boiled at 95 °C and analyzed on a 10% (v/v) SDS-PAGE gel (60 V for 20 min, followed by 150 V for 70 min, see protocol 6.2.12.1). The proteins were transferred to a PVDF membrane (80 V for 1.5 h in transfer buffer, see protocol 6.2.12.3). The membrane was then washed twice with ice-cold TBST and incubated with blocking buffer (5% [w/v] BSA in TBST) for 1 h at room temperature. Next, the membrane was washed twice with ice-cold TBST. The membrane was incubated with polyclonal anti-E-cadherin antibody (1:1,000 dilution; Cell Signaling Technology; catalog# 3195S) or anti-GAPDH polyclonal antibody (1:1,000 dilution; Cell Signaling Technology; catalog# 2118S) at 4 °C overnight. The membranes were washed twice with TBST and incubated with a goat-anti-rabbit-IgG-HRP (1:2,500 dilution; Cell Signaling Technology; catalog# 7074S) secondary antibody at room temperature for 1 h. The membranes were washed 3 times with TBST and then developed by HRP colorimetric staining using SuperSignal West Pico Chemiluminescent Substrate (Thermo-Fisher Scientific). The membranes were incubated with the development reagents for 5 min at RT and imaged on a ChemiDoc XRS+ system (Bio-Rad).

miR-122 promoter activity assay. The miR-122 promoter region was PCR amplified using Phusion polymerase by Meryl Thomas and Colleen Connelly, former members of the Deiters Laboratory, from Huh7 genomic DNA using primers containing the restriction sites for KpnI (forward primer, 5' AAGGGGTACCGAATGCATGGTTAACTACGTCAG 3'; IDT DNA) and XhoI (reverse primer, 5' AACCCCTCGAGCCTCCCGTCATTTCTCGGTC 3'; IDT DNA).[430] Briefly, Huh7 genomic DNA was isolated using the Trizol Reagent (Life Technologies) according to the manufacturer's protocol. A PCR reaction mix was prepared by combining 20 µl of Phusion HF buffer (5x; Thermo-Fisher Scientific), 5.8 µl of genomic DNA (86.6 ng/µl), 5 µl of forward primer (10 µM), 5 µl of reverse primer (10 µM), 2 µl of dNTPs (10 mM), 1 µl of Phusion polymerase, and 61.2 µl of nuclease-free water. The reaction was separated into two aliquots of 50 µl and PCR amplification was performed on a thermal cycler (Bio-Rad; 98 °C, 30 s; followed by 35 cycles of 98 °C, 10 s; 65 °C, 30 s; 72 °C, 30 s; followed by 72 °C, 10 min and hold at 12 °C). The insert was then separated on 0.8% (w/v) agarose gel and purified using the E.Z.N.A. Gel Extraction kit (Omega Bio-tek; see below for detailed protocol 6.1.8 After digesting the insert and pGL3-basic plasmid (Promega) with KpnI and XhoI, followed by purification using the E.Z.N.A. Cycle Pure kit (Omega Bio-tek), the insert was ligated into the linear backbone in front of the firefly luciferase gene using T4 DNA ligase overnight at 4 °C (see protocol 6.1.4 to generate the pGL3-miR122promoter construct. Subsequently, the ligation was digested with NheI to remove any re-circularized plasmid without the insert, and transformed into chemically competent Top10 cells (see protocol 6.1.5 Colonies were then inoculated in 5 ml of LB broth containing ampicillin (100 µg/ml) overnight and plasmid was isolated using the Plasmid Mini kit (Omega Bio-tek; see protocol 6.1.6 The plasmid sequence was confirmed by Sanger sequencing before use. Huh7 cells were seeded at 15,000 cells per well in two white, clear-bottom, 96-well plates (VWR). Following

overnight incubation, cells were transfected with the pGL3-mir122promoter construct using Lipofectamine 2000 (Thermo-Fisher Scientific) for 3 h (for more detail see general protocol 6.2.3.1). After transfection, media was replaced with DMEM and treated with compound at the desired concentration in 0.1% (v/v) DMSO or DMSO control (0.1% final DMSO concentration) in triplicate. The cells were incubated for 48 h, then one plate was analyzed for firefly luciferase expression with a Bright-Glo Luciferase Reporter Assay Kit (see protocol 6.2.14 Luminescence was measured on a microplate reader (Tecan M1000) with an integration time of 1 s. The other plate of cells was analyzed for cell viability using an XTT assay. For the XTT assay, XTT reagent was activated with 8 µl of menadione per 1 ml of XTT solution (for more detail, see general protocol 6.2.16 Absorbance was measured immediately after addition of reagent and again after 4 h on a microplate reader (Tecan M1000) at 450 nm and 630 nm (control) and data were analyzed as described above.

The mutated miR-122 promoter constructs were obtained via site-directed mutagenesis[449] of the pGL3-basic-miR-122promoter using the corresponding primers (Table 5). PCR reactions for each transcription factor contained pGL3-miR122promoter (5 ng), 2.5 µl each of forward and reverse primers (10 µM [stock]; 1 µM [final]), 0.5 µl of dNTPs (10 µM [stock]; 200 nM [final]), 5 µl of Phusion polymerase buffer (5x; Thermo-Fisher Scientific), 1 µl of Phusion DNA polymerase (Thermo-Fisher Scientific), and nuclease-free water up to 25 µl. The PCR amplifications were performed on a T100 thermal cycler (Bio-Rad) using the following program: 95 °C, 5 min; followed by 12 cycles of 95 °C, 1 min; 44 - 60 °C, 1 min; 72 °C, 10 min; then 72 °C, 30 min. Following site-directed mutagenesis, products were digested with the *DpnI* restriction enzyme (NEB) and further incubated at 37 °C for 1 h. The *DpnI* digested products (2 µl) were then transformed into Mach 1 competent cells (see general protocol 6.1.5 Following confirmation of

the mutant promoter plasmids by DNA sequencing (IDT DNA; forward sequencing primer: 5' CTAGCAAAATAGGCTGTCCC 3'), the effect of miR-122 inhibitor treatment on promoter activity was assessed as described above.

Table 5 Sequences of primers for mutant miR-122 promoter plasmids.

Primers were used to introduce mutations into transcription factor binding sites within the miR-122 promoter. Sites of the mutations are underlined.

gene		sequence 5' -> 3'
HNF4α[381]	fwd.	AGTGGCTCGGAGTCGTGCCCTCCCTCCCCCACTGAATCG
	rev.	CACGACTCCGAGCCACTAAGTCAGCACCACCTTTGGTCAAACACACT
HNF1α and HNF3β[381]	fwd.	AAGAATTCAATACTTTTAAACCCTGGATCCCAT
	rev.	AAAAGTATTGAATTCTTTCTCTTTCTGATAAGTCGC
AP-1	fwd.	GGTGCTTTATTAGTGGCCTAAGGTCGTGC
	rev.	CACTAATAAAGCACCACCTTTGGTCAAACACAC
HNF6[382]	fwd.	CCACTGAGACGGGAAATAATGCGACTTATCAGAAAGAGAAAGAAT TGTTTACTTTTAAACCCTGGAT
	rev.	ATTATTTCCCGTCTCAGTGGGGGAGGGAGGGCACGACC

2.4 Methanone Inhibitors of miR-122

While the sulfonamide scaffold was observed in the majority of active compounds identified in the HTS, many of them were found to be potent *Renilla* luciferase inhibitors. As such, we decided to re-evaluate the top 34 hit compounds provided by the Broad Institute. Of the initial hits, only 18 compounds were found to be as active or more active than the previously reported lead compound[410] upon re-testing by Meryl Thomas. Because it was one of two active compounds not bearing a sulfonamide scaffold, we selected **72** for further evaluation (Table 6). Compound **72**

induced a 423% increase in luminescence relative to DMSO in the Huh7-miR122 stable cell line, but unfortunately also showed a ~2-fold increase in luciferase signal in the psiCHECK-empty assay suggesting the activity in the primary screen was non-specific. Similarly, the lead compound elicited a 31% reduction in luminescence in the biochemical *Renilla* luciferase assay. Interestingly, though it had a modest effect on *Renilla* luciferase in the both control assays, **72** also reduced miR-122 levels by ~15% in a RT-qPCR experiment suggesting it may still hold promise as a miR-122 inhibitor. As such, we decided to carry out a SAR study in order to better understand important structural features of **72**, to attempt to discover a more potent lead compound, and to try to eliminate *Renilla* luciferase inhibition due to treatment with the molecule.

Table 6 Structures and activity of derivatives **72**-**79**

RLU values represent *Renilla* luciferase luminescence signal in the Huh7-psiCHECK-miR122 stable cell line normalized to firefly luciferase and relative to **72**. *In vitro Renilla* luciferase and psiCHECK-empty assay data are normalized to DMSO. Data represents the average ± standard deviation from at least three independent experiments. Synthesis was performed by Rohan Kumbhare.

compound	chemical structure	primary screen (RLU)	*Renilla* luciferase assay	psiCHECK-empty assay
72	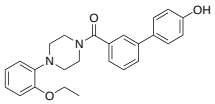	100 ± 9%	69%	1.8-fold
73	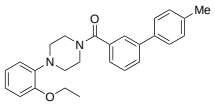	59 ± 12%	--	--
74	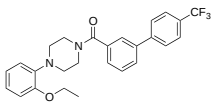	29 ± 4%	--	--
75	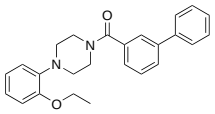	80 ± 7%	--	--

Table 6 (continued)

compound	chemical structure	primary screen (RLU)	*Renilla* luciferase assay	psiCHECK-empty assay
76	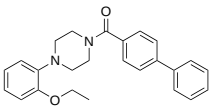	20.4 ± 0.9%	--	--
78	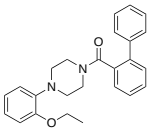	18 ± 1%	--	--
79	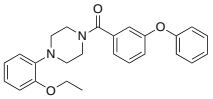	72 ± 8%	--	--

All analogs including the parent compound were synthesized by Rohan Kumbhare in the Deiters laboratory, then evaluated in the Huh7-miR122 stable reporter cell line. Modification of the hydroxy moiety in **72** to a methyl (**73**) or trifluoro methyl (**74**) induced 31% and 71% reductions in activity, respectively, while complete removal of the hydroxy group (**75**) inhibited luciferase signal by 20%, relative to the parent compound (Table 6). Moving the phenyl ring in **75** from the *meta*- position to the *para*- (**76**) or *ortho*- (**77**) relative to the amide moiety also led to dramatic reductions in activity, suggesting they may be important for maintaining inhibitory function. Similarly, replacement of the phenyl group in **75** with a phenoxy functionality (**78**) showed a 28% reduction in activity relative to the parent molecule.

Continuing with **75**, we turned our attention to the phenyl ring on the opposite side of the molecule. Removal of the ethoxy group (**80**) or replacement with a methyl (**81**) or cyano (**82**) moiety led to 55%, 45%, and ~39% reductions in activity, respectively, relative to the parent compound (Table 7). Similarly, replacement of the ethoxy moiety with a nitro group (**83**) or extension of the alkyl chain to a hexyloxy functionality (**84**) led to reductions in activity. Reducing

the length of the alkyl chain to a methoxy group (**85**) or moving the methoxy moiety to the *meta*- (**86**) or *para*- (**87**) position relative to the piperazine functionality led to dramatic reductions in activity, suggesting these positions may be important for inhibitory function.

Table 7 Structures and activity of derivatives **80**-**86**

RLU values represent *Renilla* luciferase luminescence signal in the Huh7-psiCHECK-miR122 stable cell line normalized to firefly luciferase and relative to **72**. *In vitro Renilla* luciferase and psiCHECK-empty assay data are normalized to DMSO. Data represents the average ± standard deviation from at least three independent experiments. Synthesis was performed by Rohan Kumbhare.

compound	chemical structure	primary screen (RLU)
80	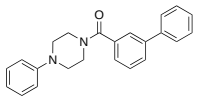	45 ± 3%
81	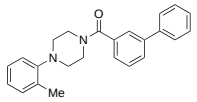	55 ± 4%
82	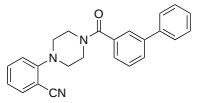	61.1 ± 0.5%
83	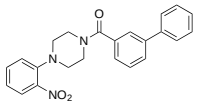	48 ± 2%
84	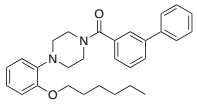	21 ± 1%
85	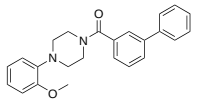	50 ± 2%
86	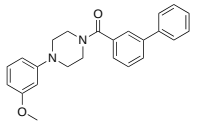	26 ± 2%
87	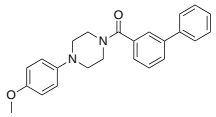	36.0 ± 0.3%

Next, the phenyl group in **75** was replaced with a bromo (**88**) or hydroxy (**89**) moiety, however, this led to 69% and 71% inhibition of luciferase activity relative to the parent compound (Table 8). Complete removal of the phenyl ring (**90**) led to a 72% inhibition of luciferase activity while conversion of the remaining phenyl ring in **90** to a naphthalene (**91**) led to 26% activity relative to the parent compound. Interestingly, removal of the ethoxy moiety in **90** to generate **92** did not lead to further reduction in activity. Similarly to **91**, the central phenyl ring was replaced with an indol (**93**) or benzofuran (**94**) functionality, however, these modifications led to ~85% and 68% reductions in luminescence, respectively, relative to the parent compound. Moreover, replacement of the central phenyl ring with a phenoxy group (**95**) also inhibited activity.

Table 8 Structures and activity of derivatives **88**-**95**

RLU values represent *Renilla* luciferase luminescence signal in the Huh7-psiCHECK-miR122 stable cell line normalized to firefly luciferase and relative to **72**. *In vitro Renilla* luciferase and psiCHECK-empty assay data are normalized to DMSO. Data represents the average ± standard deviation from at least three independent experiments. Synthesis was performed by Rohan Kumbhare.

compound	chemical structure	primary screen (RLU)
88	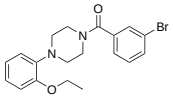	31 ± 5%
89	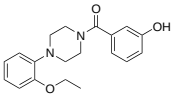	29 ± 2%
90	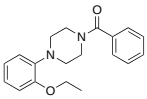	28 ± 5%
91	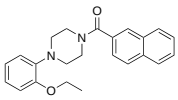	26 ± 2%
92	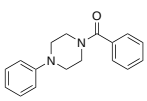	26 ± 2%

Table 8 (continued)

compound	chemical structure	primary screen (RLU)
93	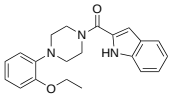	14.6 ± 0.8%
94	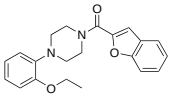	32 ± 4%
95	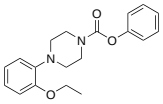	25.0 ± 0.3%

Finally, when the amide group in **75** was replaced with an amine (**96**), luciferase signal was reduced to 36% relative to the parent compound (Table 9). Removal of the phenyl ring in **96** to yield **97** had minimal effect on activity. Moreover, conversion of the amine to a sulfonamide (**98**) led to a modest ~13% reduction in activity relative to **97**.

Table 9 Structures and activity of derivatives **96**-**98**

RLU values represent *Renilla* luciferase luminescence signal in the Huh7-psiCHECK-miR122 stable cell line normalized to firefly luciferase and relative to **72**. *In vitro Renilla* luciferase and psiCHECK-empty assay data are normalized to DMSO. Data represents the average ± standard deviation from at least three independent experiments. Synthesis was performed by Rohan Kumbhare.

compound	chemical structure	primary screen (RLU)
96	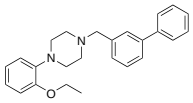	36 ± 3%
97	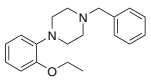	32 ± 3%

Table 9 (continued)

compound	chemical structure	primary screen (RLU)
98	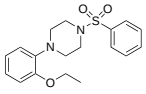	25 ± 2%

2.4.1 Summary and Outlook

In conclusion, we selected an active compound **72** without a sulfonamide scaffold from the original HTS in hopes we could improve its activity and eliminate *Renilla* luciferase inhibition. Based on preliminary SAR studies, the biphenyl ring system is hypothesized to be important for maintaining inhibitory function of the lead compound. More specifically, movement of the phenyl ring from the *meta*-position relative to the central amide leads to dramatic reductions in activity. Similarly, modifications to the ethoxy moiety on the opposite side of the structure are not well tolerated. Unfortunately, none of the analogs displayed improved activity or retained activity relative to the parent compound.

As such, future work should focus on additional SAR studies to better understand important functionalities in this molecule. For example, while the ethoxyphenyl moiety and biphenyl ring system have been explored, however, modification of the piperazine group could also provide valuable insight into the inhibitory activity of the lead compound. Moreover, investigation into potential mechanisms of action for **72** could also hold promise.

2.4.2 Materials and Methods

Detailed protocols for all experiments conducted in this section are described in Materials and Methods section **2.3.2**

3.0 MicroRNA-21

3.1 Introduction to MicroRNA-21

MicroRNA-21 (miR-21) was among the first miRNAs to be discovered in the human genome.[450] A study of miR-21 expression in glioblastoma cells was the first to identify a possible link between aberrant expression of miR-21 and cancer. In addition to its role as an anti-apoptotic and pro-survival factor,[451,452] high expression levels of miR-21 have been identified as a common feature of pathological cell growth or cell stress. For example, miR-21 has been shown to be upregulated in a mouse model of cardiac hypertrophy and vascular lesion formation.[453,454] Furthermore, induction of miR-21 has been associated with cellular de-differentiation.[376] MiR-21 represents an attractive therapeutic target, in part, due to its oncogenic expression in nearly every cancer phenotype. For example, miR-21 was among 3 miRNAs found to be overexpressed in almost all cancer tumor types evaluated in a large scale study of multiple cancer tissues.[455] Additional studies have also shown miR-21 to be overexpressed in hepatocellular carcinomas,[456] gastric cancer,[457] ovarian cancer,[458] cervical carcinoma,[459] head and neck cancers,[460] and papillary thyroid carcinoma.[461]

The miR-21 gene is located on chromosome 17q23.2 in an intron of the protein-coding gene Vacuole Membrane Protein 1 (VMP-1 or TMEM49).[450,462] MiR-21 and TMEM49 are regulated independently of each other. Activation protein 1 (AP-1) has been shown to initiate miR-21 transcription by binding to multiple binding sites in the miR-21 promoter region.[462] One of the main targets of miR-21 is programmed cell death protein 4 (PDCD4), which contains a miR-21 target site within the 3' UTR. Furthermore, miR-21-mediated regulation of PDCD4 has been

associated with breast cancer,[463] colorectal cancer,[464] and glioma.[465] PDCD4 is a tumor suppressor that acts by inhibiting promoter-induced neoplastic transformation,[466] tumorigenesis,[467] and invasion.[468] Additionally, it has been shown that AP-1 activation of miR-21 decreases the expression of PDCD4.[469] Interestingly, PDCD4 is a negative regulator of AP-1[470] suggesting that miR-21 is capable of regulating its own expression, in part, by repressing PDCD4, thereby increasing AP-1 activity. MiR-21 has been also been shown to target reversion-inducing cysteine rich protein with Kazal motifs (RECK). RECK is a tumor and metastasis gene responsible for regulation of matrix metalloproteinases (MMPs) that has been identified as a prognostic marker in various cancer types.[471] Regulation of RECK expression by miR-21 has been observed in glioma and osteoblastoma cells[465] as well as gastric cancers.[457] Additionally, miR-21 is capable of inhibiting the translation of the tumor suppressor protein, phosphatase and tensin homolog (PTEN). PTEN is responsible for regulating the phosphoinositide 3-kinase (PI3K)-AKT-mammalian target or rapamycin (mTOR) pathway, an important factor for cell survival, proliferation, metabolism and structure.[472] PTEN suppression by miR-21 has been observed in colon cancer cells[464] and vascular smooth muscle cells (VSMCs);[453] however it has not been seen in breast cancer,[463] non-small cell lung cancer,[473] or glioma cells[465] which makes it difficult to assess whether miR-21 interacts with PTEN directly, especially since there is no miR-21 target site present in the 3' UTR of PTEN mRNA.

In addition to its role as an oncogene, miR-21 has been associated with mediating chemoresistance in a variety of cancers.[474] For example, knockdown of miR-21 by transfection of an anti-miR-21 oligonucleotide into A172, U87, U373, LN229, LN428, and LN308 glioblastoma cells led to activation of caspase-3 and -7 and ultimately triggered apoptosis.[475] Downregulation of PDCD4 has been linked to upregulation of HER2 via the MAPK and AKT signaling pathways

concomitant with increased levels of miR-21 in estrogen-positive and aromatase inhibitor-resistant breast cancers.[476] MiR-21 has also been correlated with gemcitabine resistance via upregulation of BCL-2 expression in pancreatic cancer.[477] Moreover, tumor cell chemoresistance mediated by repression of PTEN has been linked to miR-21 overexpression in HCC and gastric cancer.[478,479] Interestingly, miR-21 has also been shown to regulate resistance to radiotherapy. For example, anti-miRNA oligonucleotide-mediated knockdown of miR-21 in esophageal squamous cell carcinoma induced cell cycle arrest and sensitized cells to gamma irradiation.[480] Additionally, miR-21 was shown to contribute to radioresistance in non-small cell lung cancers via upregulation of the PI3K/Akt signaling pathway.[481] Furthermore, overexpression of miR-21 has been associated with radioresistance in high-risk human papilloma virus cervical cancer via binding to the 3' UTR of large tumor suppressor kinase 1.[482]

Taken together, miR-21 plays an important regulatory role in cell survival processes and its overexpression is observed in a variety of diseases including most cancers. Furthermore, anti-miRNA oligonucleotide-mediated inhibition of miR-21 has been shown to induce apoptosis in carcinogenic cells and alters chemoresistance of several cancer types. As such, miR-21 has been identified as a prognostic marker for various diseases as well as a novel therapeutic target.

3.2 Discovery of Small Molecule Inhibitors of miR-21

Our lab, in collaboration with the Huang group, were the first to develop a cell-based reporter assay to identify small molecule inhibitors of miRNA function, specifically miR-21.[411] miR-21 is upregulated in numerous cancers and has been implicated in carcinogenesis and drug resistance,[483] highlighting its importance as a therapeutic target. To this end, a reporter in which

the miR-21 binding sequence was cloned downstream of the luciferase gene was stably expressed in HeLa cervical cancer cells (HeLa-miR-21).[411] High endogenous miR-21 levels in HeLa cells[484] resulted in suppression of luciferase expression and decreased luminescence signal; however, in the presence of a miR-21 inhibitor, rescue of luciferase expression results in an increase in luminescence signal. While the authors demonstrated that the reporter construct containing the miR-21 target site exhibited reduced luciferase expression in HeLa cells, to further validate that the reporter system would respond to miRNA inhibition, an antagomir specific to miR-21 could have been delivered. The HeLa-miR-21 cell line was employed in a pilot screen of >1,000 small molecules from an in-house compound collection and the Library of Pharmacologically Active Compounds.[411] An initial hit from the pilot screen was optimized through SAR studies leading to the discovery of **14** (Figure 1-7), which elicited 2-fold higher potency than the initial hit and an EC_{50} of 2 μM. Both mature and primary miR-21 levels were found to be reduced by 78% and 87%, respectively, indicating that **14** likely acts at the transcriptional or pre-transcriptional level. Treatment with **14** in a control HeLa cell line stably expressing a miR-30 reporter showed no reduction in luminescence signal suggesting the small molecule is not a general inhibitor of the miRNA pathway; however, testing the compound against a more comprehensive list of miRNAs was not completed and may reveal additional targets. Despite the absence of a clear biological target, the Yao lab formulated cell-penetrating poly(disulfide)-coated mesoporous silica nanoparticles containing both **14** and a miR-21 antagomir and delivered them into HeLa cells.[485] Upon treatment with the nanoparticles, pronounced reduction of miR-21 levels coinciding with inhibition of cell migration and invasion was observed.

Lu and co-workers performed further SAR studies of **14**, synthesizing a set of 4-benzoylamino-*N*-(prop-2-yn-1-yl)benzamide derivatives,[486] and compound **15** (Figure 1-7) was

identified as the most potent inhibitor, eliciting a ~90% reduction in mature miR-21 levels at 10 μM, a modest, but significant improvement over the parent compound. In addition, **15** did not inhibit levels of *let-7a*, miR-25, miR-26, miR-126, miR-133, miR-143, miR-145, miR-146, miR-148, miR-152, or miR-195 providing further support for the initial claim that this compound class is not a general miRNA pathway inhibitor but instead shows some specificity for miR-21.

Similarly, SAR optimization of an aryl amide inhibitor identified in the high-throughput screen led to the discovery of **17** (Figure 1-7).[487] The inhibitor was subjected to numerous secondary assays analogous to those described above. Treatment of HeLa cells with **17** following transfection with a reporter plasmid in which the luciferase gene was placed under the control of the miR-21 promoter sequence had no effect on luminescence signal. This is in good agreement with a RT-qPCR assay in which the compound showed no effect on pri-miR-21 levels suggesting that it also acts downstream of transcription.

3.3 Oxadiazole Inhibitors of miR-21

This material was reprinted in its entirety with permission from Naro, Y.; Ankenbruck, N.; Thomas, M.; Connelly, C.; Tivon, Y.; Deiters, A., *J. Med. Chem.* 2018, *61*, 5900.

From the initial HTS, 58 small molecules were confirmed as potential inhibitors of miR-21. Of these 58 small molecules, two structurally similar small molecules **99** and **100** were selected for further investigation. These two hits were chosen due to their structural similarities and their promising efficacy in the HeLa-miR21-Luc stable cell line assay relative to other hit compounds. Furthermore, secondary confirmation screens also provided evidence that these two compounds

demonstrated selectivity for miR-21 (PubChem AID 2507) and were not firefly luciferase inhibitors (PubChem AID 493175). Synthesis of hit compounds **99** and **100** and analogs **101**-**118** was accomplished via a convergent synthesis by coupling azidobenzenes with cyanomethylene-functionalized oxadiazole derivatives (Figure 3-1). Azidobenzenes were obtained in good yield through the conversion of commercially available anilines to their diazonium salts using sodium nitrite in concentrated sulfuric acid, followed by treatment with sodium azide. Synthesis of the cyanomethylene-functionalized thiophene-oxadiazole was achieved by conversion of the carbonitrile to the carboximidamide using hydroxylamine. Cyclization to form the oxadiazole ring was accomplished through heating with 1-cyanoacetyl-3,5-dimethyl-1H-pyrazole. Finally, triazole ring formation was completed using sodium methoxide to provide the final compounds (Table 10).

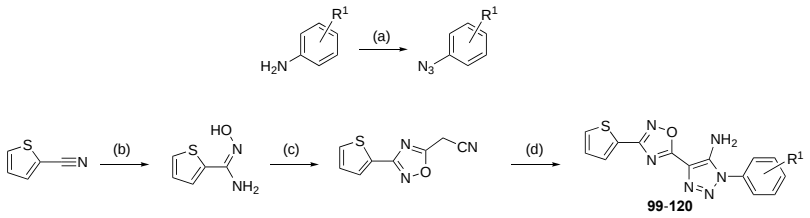

Figure 3-1 Synthesis of derivatives **99**-**120**

Reagents and conditions: a) $NaNO_2$, H_2SO_4, NaN_3, H_2O; b) hydroxylamine HCl, DIPEA, EtOH; c) 1-cyanoacetyl-3,5 dimethyl-1H-pyrazole, dioxane; d) azide, sodium methoxide, methanol. Synthesis performed by Yaniv Tivon, Yuta Naro, Meryl Thomas, Laura Gardner, and Matthew Stephens.

Table 10 Structures and activity of derivatives **99**-**120**

RLU values represent fold-changes in luminescence signal in the HeLa-miR21-Luc stable cell line normalized to cell viability and relative to a DMSO control. Data represents the mean ± standard deviation from at least three independent experiments. Synthesis performed by Yaniv Tivon, Yuta Naro, Meryl Thomas, Laura Gardner, and Matthew Stephens. Luciferase data generated by Yuta Naro.

compound	R^1	RLU (fold-change)	compound	R^1	RLU (fold-change)
99		2.84 ± 0.18	**110**	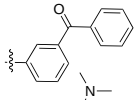	1.82 ± 0.09
100		1.89 ± 0.05	**111**		2.56 ± 0.11
101		2.19 ± 0.04	**112**		2.02 ± 0.20
102		1.93 ± 0.11	**113**		2.30 ± 0.22
103		1.08 ± 0.14	**114**	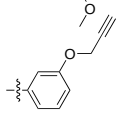	1.61 ± 0.09
104	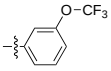	1.40 ± 0.09	**115**	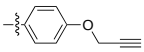	1.47 ± 0.09
105		1.01 ± 0.07	**116**	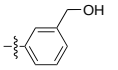	1.67 ± 0.16
106		1.63 ± 0.01	**117**		2.23 ± 0.07
107		1.82 ± 0.14	**118**	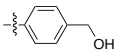	2.14 ± 0.09
108	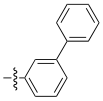	1.06 ± 0.14	**119**	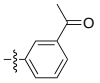	2.46 ± 0.13
109	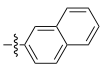	1.39 ± 0.10	**120**	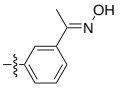	4.54 ± 0.67

Activity of **99** and **100** was confirmed in the HeLa-miR21-Luc cell-based assay. Compound **99** exhibited a 2.84-fold increase in luminescence signal, indicative of a reduction in miR-21 suppression of firefly luciferase expression. Compound **100** exhibited a 1.89-fold increase

in signal, slightly lower than the initial HTS results that were obtained. To generate an activity profile for a better understanding of the essential structural motifs and to improve the potency of compound **99**,[488] we first introduced modifications to the benzene ring. Demethylation (**101**) or halogenations (**102**, **103**, and **104**) at the *meta* position resulted in modest losses in activity, while removal of the methoxy group altogether (**105**) exhibited a complete loss in activity. Aliphatic (**106** and **107**) and aromatic substitutions (**108**, **109**, and **110**) were not well tolerated and resulted in significant losses in activity (>36%), while introduction of a *meta*-dimethylamine (**111**) retained 90% activity compared to **99**. Movement of the *meta*-methoxy group to the *ortho* position (**112**) or incorporation of a *meta*-dimethoxy (**113**) elicited only modest losses in activity, and replacement of the methoxy group with propargyloxy (**114** and **115**) or *meta*-benzylalcohol (**116**) also lead to decreased activity. Incorporation of *ortho*- and *para*-benzylalcohol (**117** and **118)** rescued some activity, while incorporation of a *meta*-methylketone (**119**) exhibited similar activity relative to **99**. However, conversion of the methylketone to an oxime (1**20**) displayed a 60% improvement in activity relative to **99**. Based on these results, we hypothesized that functionalization of the *meta* position is most tolerated.

The importance of the amino substituent on the triazole was investigated through the synthesis of several analogs lacking the amino group (Figure 3-2). Azidobenzenes were cyclized with propargyl alcohol via a [3+2] cycloaddition, followed by oxidation of the alcohol to a carboxylic acid using Jones reagent. Finally, oxadiazole ring formation was completed by reaction with hydroxythiophene-2-carboximidamide and EDC to generate the final products (Table 11).

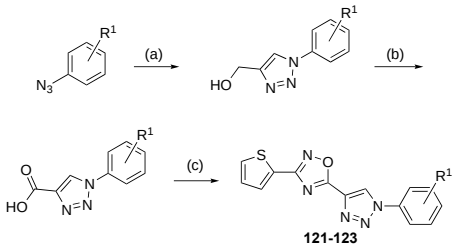

Figure 3-2 Synthesis of **121** – **123**

Reagents and conditions: a) propargyl alcohol, sodium ascorbate, copper (II) sulfate pentahydrate, t-butanol/H2O; b) Jones reagent, acetone; c) hydroxythiophene-2-carboximidamide, EDC, acetonitrile. Synthesis performed by Yaniv Tivon, Yuta Naro, Meryl Thomas, Laura Gardner, and Matthew Stephens.

Table 11 Structures and activity of derivatives **121**-**123**

RLU values represent fold-changes in luminescence signal in the HeLa-miR21-Luc stable cell line normalized to cell viability and relative to a DMSO control. Data represents the mean ± standard deviation from at least three independent experiments. Synthesis performed by Yaniv Tivon, Yuta Naro, Meryl Thomas, Laura Gardner, and Matthew Stephens. Luciferase data generated by Yuta Naro.

compound	R^1	RLU (fold-change)
121		2.20 ± 0.07
122		1.41 ± 0.15
123		1.70 ± 0.07

Compound **121**, lacking the amino group, displayed 77% activity relative to **99**. Removal of the methoxy group (**122**) or replacement with a fluorine (**123**) on the benzene ring resulted in derivatives with similar activity to their counterparts containing the amine. These results suggest that the amine has only a modest effect on activity and thus no further modifications to the triazole ring were pursued.

To determine the importance of the 1,2,4-oxadiazole configuration, several 1,3,4-oxadiazole derivatives were synthesized (Figure 3-3). To generate the cyano-functionalized thiophene-1,3,4-oxadiazole, cyanoacetic acid was converted to the corresponding chloride via oxalyl chloride with a catalytic amount of DMF. Reaction of the resulting acyl chloride with thiophene-2-carbohydrazide, followed by cyclization using neat phosphoryl chloride yielded the corresponding cyano-functionalized thiophene-1,2,4-oxadiazole, which was subjected to the same cyclization conditions as previously described to provide the final 1,3,4-oxadiazole products (Table 12).

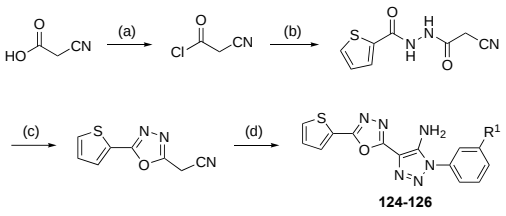

Figure 3-3 Synthesis of **124** – **126**

Reagents and conditions: a) oxalyl chloride, cat. DMF, CH2Cl2; b) thiophene-2-carbohydrazide, TEA, CH2Cl2; c) POCl3; d) azide, sodium methoxide, methanol. Synthesis performed by Yaniv Tivon, Yuta Naro, Meryl Thomas, Laura Gardner, and Matthew Stephens.

Table 12 Structures and activity of derivatives **124** – **126**

RLU values represent fold-changes in luminescence signal in the HeLa-miR21-Luc stable cell line normalized to cell viability and relative to a DMSO control. Data represents the mean ± standard deviation from at least three independent experiments. Synthesis performed by Yaniv Tivon, Yuta Naro, Meryl Thomas, Laura Gardner, and Matthew Stephens. Luciferase data generated by Yuta Naro.

compound	R^1	RLU (fold-change)
124		2.68 ± 0.46
125		1.60 ± 0.14
126		1.72 ± 0.16

The 1,3,4-oxadiazole derivative (**124**) displayed similar activity as its parent 1,2,4-oxadiazole **1**. Additional analogs containing *meta*-fluorine (**125**), and *meta*-isopropyl (**126**) also displayed similar activity to their 1,2,4,-oxadiazole counterparts, thus it was determined that the exact configuration of the oxadiazole ring was not critical for activity.

Lastly, modifications to the thiophene were explored (Table 13). To this end, the synthesis of the cyano-functionalized oxadiazoles (Figure 3-4) was adopted, however alternative aryl groups were introduced in place of the thiophene. Introduction of a furan (**127**), benzene (**128**), or 2-pyridine (**129**), all resulted in slight decreases in activity. Due to the significant activity improvement observed with the introduction of the *meta*-oxime in analog **120**, several analogs were synthesized containing additional benzene modifications in conjunction with the previously described *meta*-oxime moiety. Introduction of a *para*-phenol (**130**) or *para*-methoxy (**131**) group resulted in reduced activity, while introduction of a *para*-ethoxy (**132**) rescued activity to 111%

relative to **99**. However, further increased steric bulk as in a *para*-isopropoxy substituent (**133**) abolished activity, while introduction of a *para*-allyloxy group (**134**) retained activity. Lastly, oxidation of the allyl group to a propargyl group (**135**) resulted in a significant improvement in activity, yielding a 448% increase in activity relative to **99**. Based on these SAR results, it appears that modification of the distal ring systems elicits the largest changes in activity, while the core oxadiazole and triazole rings have limited effect on the miR-21 inhibitory activity of this scaffold.

Table 13 Structures and activity of derivatives **127** – **135**

RLU values represent fold-changes in luminescence signal in the HeLa-miR21-Luc stable cell line normalized to cell viability and relative to a DMSO control. Data represents the mean ± standard deviation from at least three independent experiments. Synthesis performed by Yaniv Tivon, Yuta Naro, Meryl Thomas, Laura Gardner, and Matthew Stephens. Luciferase data generated by Yuta Naro.

compound	R^1	R^2	RLU (fold-change)
127			2.19 ± 0.08
128			2.19 ± 0.07
129			2.23 ± 0.02
130	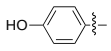	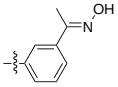	1.98 ± 0.27
131	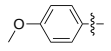	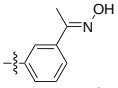	1.51 ± 0.12
132	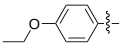	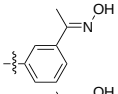	3.14 ± 0.16
133	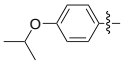	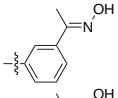	1.19 ± 0.09
134	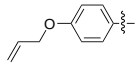	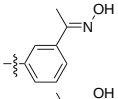	2.96 ± 0.06
135	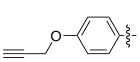	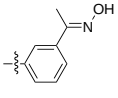	12.19 ± 0.64

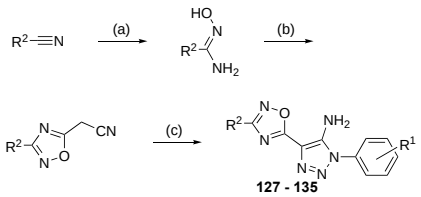

Figure 3-4 Synthesis of derivatives **127** – **135**

Reagents and conditions: a) hydroxylamine HCl, DIPEA, ethanol; b) 1-cyanoacetyl-3,5 dimethyl-1H-pyrazole, dioxane; c) sodium methoxide, methanol. Synthesis performed by Yaniv Tivon, Yuta Naro, Meryl Thomas, Laura Gardner, and Matthew Stephens.

The significantly improved inhibitor **135** was tested in a dilution series in the HeLa-miR21-Luc assay revealing an EC_{50} of 5.3 μM (Figure 3-5A). Recent concerns with the identification of firefly luciferase inhibitors and the appearance of false positive hits in firefly luciferase assays as the result of protein stabilization in cells[289] urged us to test the effect of **37** on luciferase activity in a biochemical assay. Importantly, we did not observe any inhibition of firefly luciferase activity at concentrations up to 50 μM (Figure 3-5B).

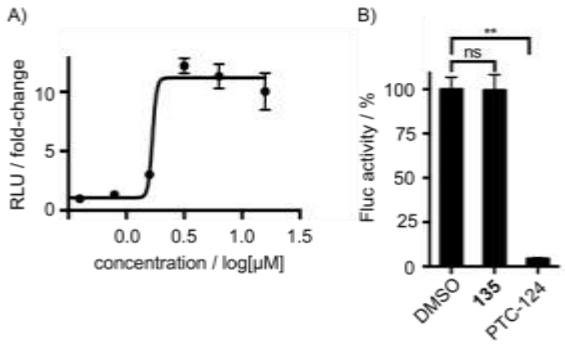

Figure 3-5 Dose-dependent inhibition of miR-21 and *in vitro* firefly luciferase assay

A) Dose-response assay of 135 using the HeLa-miR21-Luc reporter cell line revealed an EC_{50} of 5.3 uM. B) In vitro firefly luciferase activity assay for 1,2,4-oxadiazole miR-21 inhibitor **135**. All data were normalized to DMSO treatment (negative control) and errors bars represent standard deviations from three independent experiments. Statistical significance was determined using an unpaired t-test, ** $P < 0.005$, ns $P > 0.05$. Data generated by Yuta Naro.

A previously described Huh7-psiCHECK-miR122 reporter cell line that expresses *Renilla* luciferase under the control of miR-122 activity[410] was used to determine the selectivity of **135** for miR-21. Following treatment of the reporter cell line with compound **135** at 10 μM for 48 hours, no inhibition of miR-122 was observed (Figure 3-6A). Additional psiCHECK reporters monitoring miR-125b, miR-182, and miR-221 were constructed and their function and dynamic range was confirmed using antagomir treatment as a positive control. These miRNAs were selected due to their established classification as oncomiRs and their up-regulation in several different types of cancers.[489-492] Following transfection of the psiCHECK plasmids, cells were treated with **135** at 10 μM for 48 hours. All reporters showed no inhibition of miRNA function under these conditions since no increase in luminescence was observed following treatments (Figure 3-6B). Taken

together, these results provide evidence that **135** shows some level of selectivity for miR-21 and is not a general miRNA pathway inhibitor.

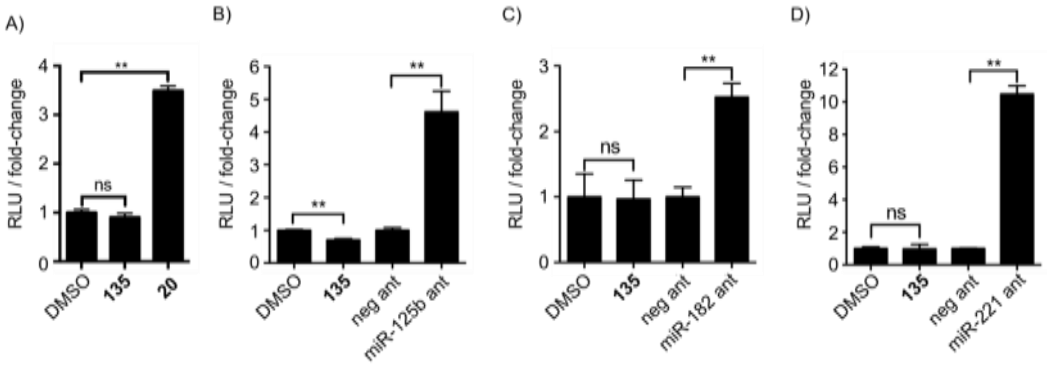

Figure 3-6 psiCHECK miRNA assays with 1,2,4-oxadiazole **135**

A) Huh7-psiCHECK-miR122 treated with 1,2,4-oxadiazole **135**. B) miR-125b in PC-3 cells C) miR-182 in HeLa cells D) miR-221 in PC-3 cells. Data for treatment with **135** was normalized to DMSO treatment (negative control) and data for treatment with antagomir (ant) was normalized to negative, scrambled control antagomir (neg ant). Errors bars represent standard deviations from three independent experiments. Statistical significance was determined using an unpaired t-test, ** $P < 0.005$, ns $P > 0.05$.

The mechanism of action of **135** was investigated via quantitative reverse transcription PCR (RT-qPCR) of both mature and primary miR-21 levels in HeLa cells following treatment with DMSO or **135** (10 μM) for 48 hours. We observed that **135** has no effect on neither mature nor primary miR-21 levels (Figure 3-7A). Compound **135** also elicited no reduction of mature miR-21 levels in three other cancer cell lines (Figure 3-7B). To further confirm that compound **135** has no effect on miR-21 transcription, a previously described luciferase reporter construct pGL4-miR21P[493] which monitors miR-21 promoter activity was transfected into HeLa cells

followed by treatment with DMSO or 10 μM **135** for 48 hours. As expected, no changes in reporter gene expression were observed (Figure 3-7C). These results indicate that **135** may act by inhibiting the function of mature miR-21, without affecting primary or mature miR-21 levels in cells.

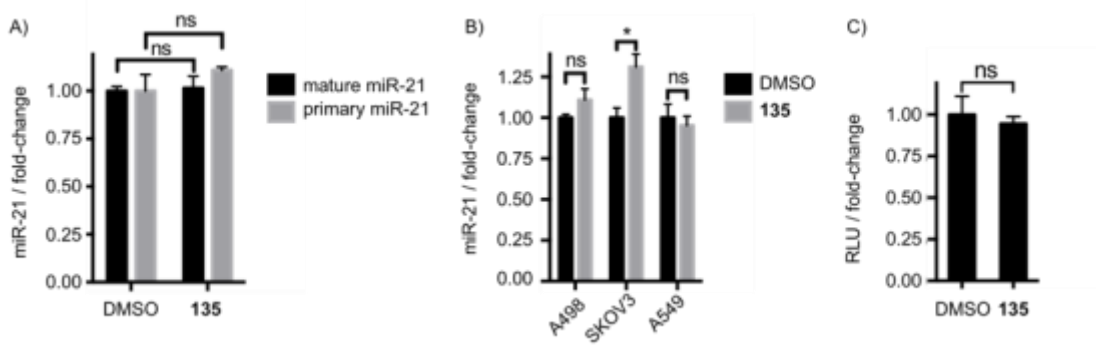

Figure 3-7 RT-qPCR analysis of **135**

A) Treatment of HeLa cells with **135** for 48 h, followed by qPCR analysis of mature miR-21 and primary miR-21 RNA levels showed no decrease. B) Treatment of A498 (RCC), SKOV3 (ovarian carcinoma), or A549 (NSCLC) with DMSO or 10 μM 135, followed by qPCR analysis of mature miR-21 RNA levels showed no decrease. All data were normalized to DMSO treatment (negative control) and errors bars represent standard deviations from three independent experiments. Statistical significance was determined using an unpaired t-test, ns $P > 0.05$.C) Transfection of HeLa cells with a miR-21 promoter gene expression reporter, followed by treatment with 135 also showed no decrease in activity, supporting a mode of action different than inhibition of miR-21 transcription. Data represents the mean ± standard deviation from at least three independent experiments. Statistical significance was determined using an unpaired t-test, ns $P > 0.05$. Data generated by Yuta Naro.

Small molecules that inhibit miRNA function through direct binding to nucleic acids have been previously reported,[494-496] and thus we decided to explore whether **135** may interact directly with RNA, and more specifically miR-21. To this end, melting curve analyses using precursor

miR-21 RNA were carried out in the presence of DMSO, **135**, and tobramycin. Tobramycin was employed as a positive control as it has been previously reported to bind and stabilize RNA, leading to an increased melting temperature.[497] As expected, in the presence of 10 μM tobramycin the melting temperature of pre-miR-21 increased by 19 °C relative to DMSO (Figure 3-8A). However, in the presence of 10 μM **135** no change in melting temperature was observed (Figure 3-8B), suggesting that **135** does not directly interact with RNA. Overall, this demonstrates that **135** does not affect the maturation of miR-21, while also excluding the possibility of destabilization or degradation of mature miR-21 being the mechanism of action. Continuing work is focused on investigating the potential of **135** to perturb functional aspects of mature miR-21 such as RISC regulation, miR-21 subcellular localization, and miR-21 interactions with RNA binding proteins. Regulation of RISC function relies on numerous accessory proteins, some of which have been identified as capable of modulating miRNA activity of only select miRNAs.[498] For example, several TRIM-NHL E3 ubiquitin ligases have been shown to selectively regulate miRNA activity downstream of biogenesis leading to either enhancement or repression of miRNA activity.[499,500] The mechanism by which regulation takes place is not completely understood and it is likely that additional proteins with the ability to modulate RISC function are yet to be discovered. Alternatively, while a majority of miR-21 exists in the cytoplasm, the primary location of its activity, it has been shown that up to 20% of mature miR-21 can exist in the nucleus.[501,502] Therefore, it could be possible that changes in nucleo-cytoplasmic partitioning of miR-21 could elicit diminished translational repression.[498] Lastly, it was recently shown that the RNA-binding protein HuR is capable of sequestering miR-21 by binding to the UUAU sequence within the seed region and in turn diminishing miR-21 function.[503] We are currently investigating whether **135** could be eliciting an effect on the function and/or expression of HuR and other RNA binding

proteins. Consequently, elucidation of the mechanism of action of **135** may provide new insight into how miR-21 activity is regulated, making **37** an encouraging chemical tool for the study of miRNA function.

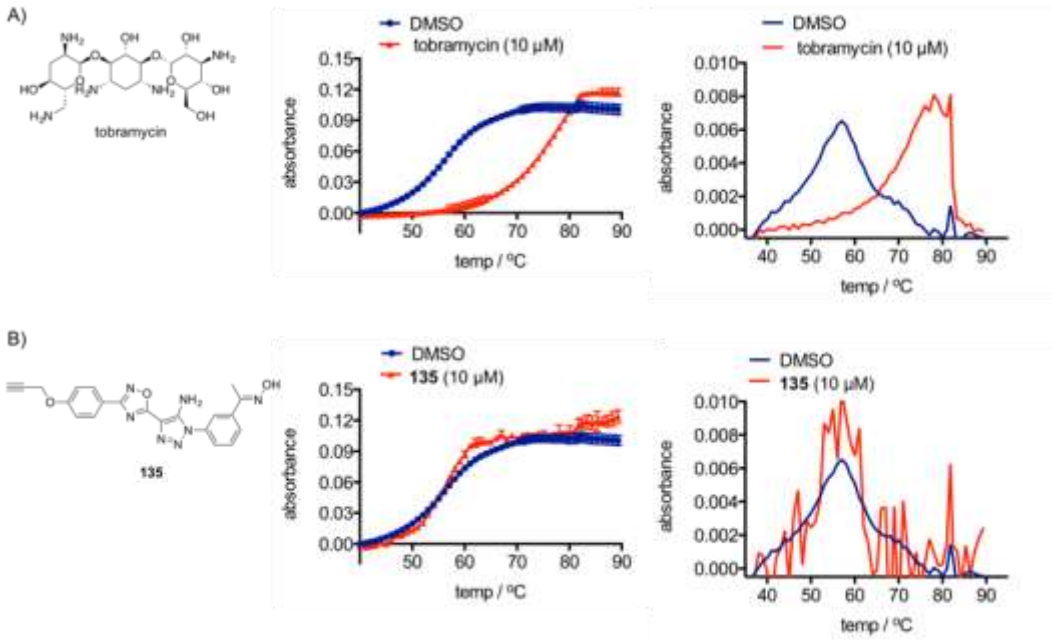

Figure 3-8 Melting temperature evaluation of **135**

A) Melting curves for pre-miR-21 in the absence and presence of tobramycin (left). Differentiation of the melting curves (right) reveals the expected RNA-small molecule interaction leading to stabilization in the presence (T_m from 75.1 °C) of tobramycin compared to its absence (T_m = 56.0 °C). B) Melting curves for pre-miR-21 in the absence and presence of **135** (left). Differentiation of the melting curves (right) reveals no change in melting temperatures in the presence (T_m = 56.1 °C) or absence (T_m = 56.0 °C) of 37. Errors bars represent standard deviations from three independent experiments. Data generated by Yuta Naro.

We next investigated whether inhibition of miR-21 via **135** could elicit a therapeutic effect in cancers which overexpress miR-21. A panel of several different established cancer cell models were subjected to cell viability studies using XTT assays (Figure 3-9A-E). Treatment of cancer cells with increasing concentrations of compound **135** for 72 h exhibited low micromolar potency (IC_{50}) in nearly all the cell lines tested (Table 14). NIH 3T3 mouse fibroblasts were also treated with **135** in a dilution series to demonstrate that this effect was not due to potential general toxicity.[504] As expected, **135** displayed no toxicity to 3T3 cells at concentrations up to 100 μM (Figure 3-9F).

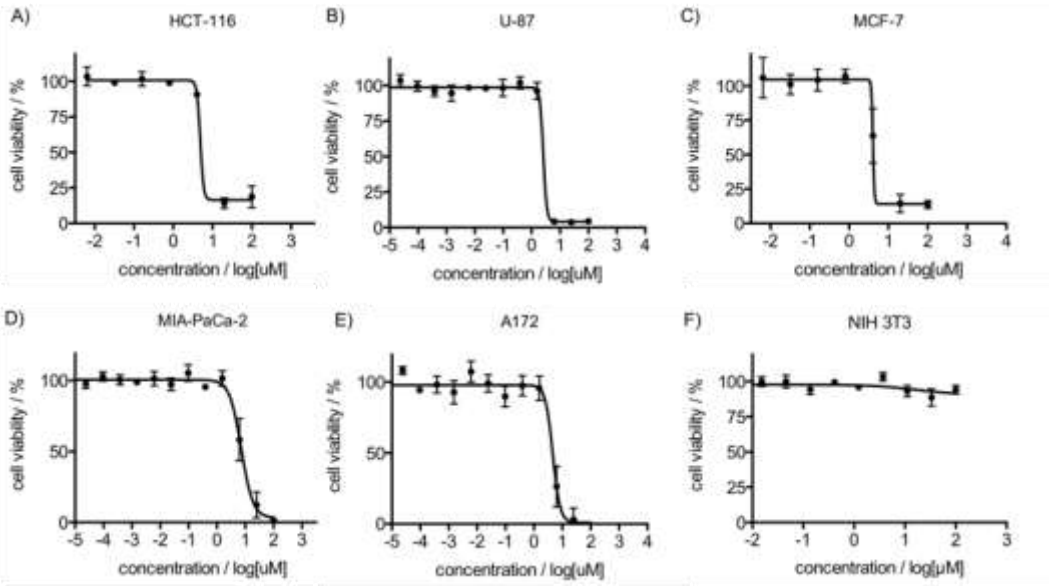

Figure 3-9 Treatment of different cell lines with **135** for 72 h, followed by XTT assay

A) glioblastoma U-87 cells B) colorectal carcinoma HCT-116 cells C) breast carcinoma MCF-7 cells D) pancreatic carcinoma MIA-PaCa-2 cells E) glioblastoma A172 cells and F) mouse fibroblast NIH 3T3 cells. Treatment of non-cancerous NIH 3T3 cells shows no toxicity from 135 at any of the concentrations tested. Errors bars represent standard deviations from three independent experiments.

Table 14 Pre-therapeutic evaluation of miR-21 inhibitors in various cancer cell models

XTT assays were performed to assess cell viability. Data represents the mean ± standard deviation from at least three independent experiments.

cell type	cell line	IC_{50} (μM)
pancreatic carcinoma	MIA PaCa-2	6.7 ± 1.0
glioblastoma	A172	4.6 ± 1.2
glioblastoma	U-87	3.3 ± 1.5
renal cell carcinoma	A498	>100
breast cancer	MCF-7	4.5 ± 0.8
colorectal carcinoma	HCT-116	5.9 ± 2.2

Interestingly, the RCC cell line A498 also displayed very low sensitivity to **135,** with an IC_{50} of >100 μM in the XTT assays. This was not completely unexpected due to reports of miR-21 inhibition via antagomir treatment in RCC leading to modulation of chemoresistance rather than significant induction of apoptosis.[505] Since silencing of miR-21 has been previously shown to enhance chemosensitivity in a variety of human cancer cells,[506-509] including RCC,[505] we hypothesized that inhibition of miR-21 via **135** at concentrations well below its IC_{50} may not directly impact cell viability, but may sensitize A498 cells to treatment with established chemotherapeutics. To this end, we screened chemotherapeutic agents that cover different modes of action in combination with **135**, including 5-fluorouracil (thymidylate synthase inhibitor), docetaxel (microtubule stabilizer), and topotecan (topoisomerase inhibitor). While treatment with 5-fluorouracil or docetaxel in combination with **135** showed little to no enhancement in their activities, combination treatment of **135** with topotecan revealed encouraging results. Topotecan, an FDA-approved chemotherapeutic, has demonstrated success in the treatment of ovarian,[510] cervical,[511] and small cell lung carcinoma,[512] however it has been found ineffective in the treatment

of RCC,[513] possibly due to reduced topoisomerase I expression in RCC.[514] While exposure of A498 cells to topotecan alone exhibited a dissatisfactory IC_{50} of 1 μM, combination of topotecan with **37** produced a dose-dependent sensitization resulting in an IC_{50} of 90 nM – a greater than 11-fold increase in potency compared to topotecan treatment alone (Figure 3-10A). NIH 3T3 cells were also treated with increasing concentrations of topotecan in the presence of **135**, however no sensitization was observed, supporting the specificity of **135**-induced chemosensitization of cancer cells (Figure 3-10B).

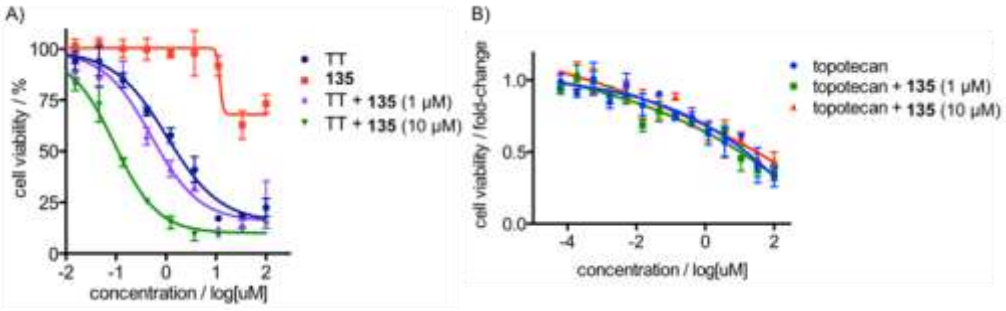

Figure 3-10 Pre-therapeutic evaluation of miR-21 inhibitors in A498 RCC cells

A) Combination treatment of A498 cells with topotecan (TT) and **135** in a dose-response cell viability assay. B) Treatment of mouse fibroblast NIH 3T3 cells with varying concentrations of topotecan with and without the addition of 37 for 72 h, followed by XTT assay. No changes in topotecan efficacy were observed upon the addition of **135**. Data represents the mean ± standard deviation from at least three independent experiments.

Additionally, we investigated the effect that topotecan may have on miR-21 function using the HeLa-miR21-Luc stable cell line. Following treatment of HeLa-miR21-Luc cells with increasing concentrations of topotecan for 48 h we observed no significant changes in miR-21 activity (Figure 3-11).

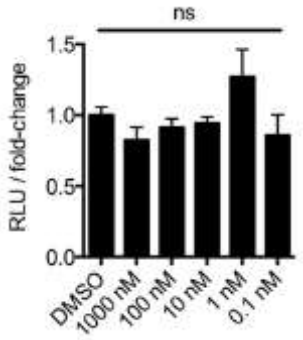

Figure 3-11 Treatment of HeLa-miR21-Luc cells with topotecan for 48 h

Luminescence signal was normalized to XTT assay cell viability and data were set relative to DMSO control. No inhibition of miR-21 was observed any of the concentrations tested. Errors bars represent standard deviations from three independent experiments. Statistical significance was determined using an unpaired t-test, ns $P > 0.05$. Data generated by Yuta Naro.

The long-term cytostatic effects of co-treatment and the ability to inhibit microtumor formation were evaluated using a clonogenic assay. A498 cells were plated in an agar suspension along with compound combinations and incubated for 2-weeks at 37 ºC prior to imaging (Figure 3-12A). Treatment with **135** up to 10 μM elicited no inhibition of colony formation, while topotecan alone exhibited an IC_{50} of 2 μM. Importantly, combination of **135 (**10 μM) with topotecan resulted in sensitization of A498 cells and an IC_{50} of 74 nM, representing a 27-fold

enhancement in activity compared to topotecan alone (Figure 3-12B). These results indicate that co-treatment of A498 cells is capable of inhibiting microtumor formation in a long-term clonogenic assay.

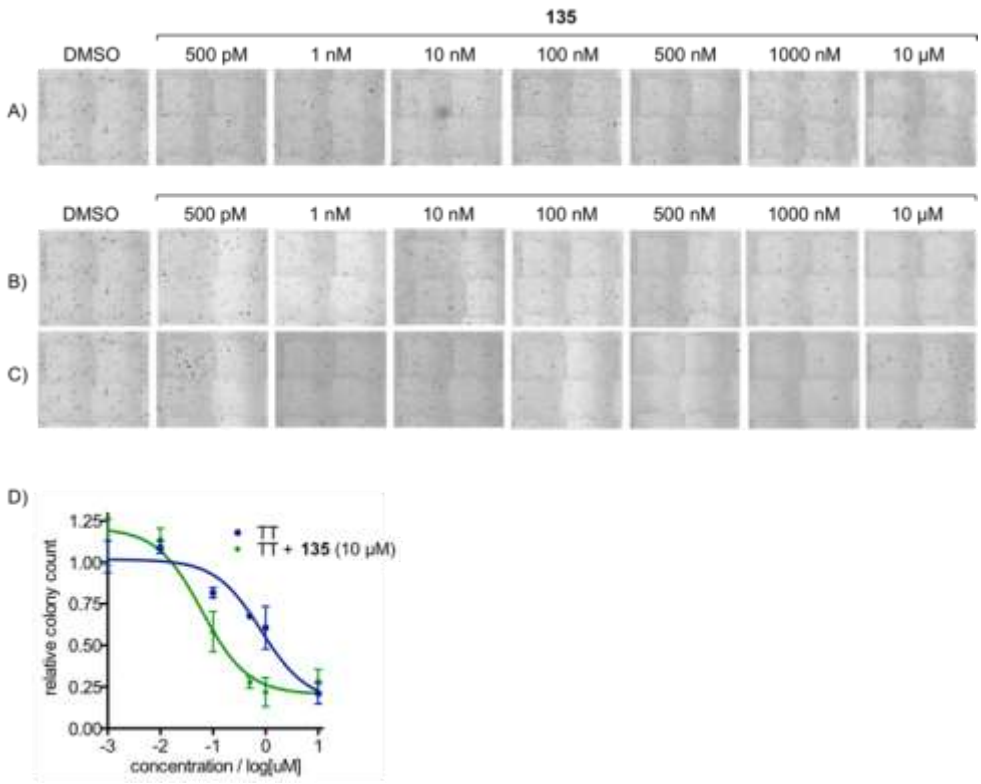

Figure 3-12 Clonogenic Assay

Representative images from clonogenic assays: A) Treatment with **135** in dose response. B) Treatment with topotecan in dose response. Images were cropped to 4 tiles each in the center of the well from the extended depth of focus image. C) Treatment with topotecan in dose response in combination with 10 µM of **135**. D) Combination treatment of A498 cells with topotecan (TT) and **135** in a two-week clonogenic assay. Data represents the mean ± standard deviation from at least three independent experiments.

Next, the mechanism of cell death and potential mode of action for the enhanced chemosensitivity were investigated. We first examined caspase-3/7 activation as an indicator of apoptosis in A498 cells. Treatment of A498 cells with **135 (**10 μM) for 24 h elicited a modest 20% increase in caspase-3/7 activity, while treatment with 1 μM of topotecan alone resulted in a 3-fold increase in caspase-3/7 activity compared to DMSO. However, co-treatment with **135 (**10 μM) and topotecan (1 μM) resulted in a 512% increase in caspase activity, representing a 1.6-fold increase over topotecan treatment alone (Figure 3-13A). These results support our hypothesis that inhibition of miR-21 via small molecule treatment can sensitize A498 cells to topotecan-induced apoptosis. To confirm that the induction of apoptosis as a result of combination treatment acts via a miR-21-dependent pathway, immunoblot detections of PDCD4 and PTEN protein levels were carried out. A498 cells were treated with DMSO or **135 (**10 μM) for 48 hours, followed by protein isolation and quantification. As expected, **135** showed significant rescue of both PDCD4 (9.5-fold increase) and PTEN (1.5-fold increase) tumor suppressor protein levels in A498 cells (Figure 3-13B). These results propose a possible mechanism behind the chemosensitization effect observed following treatment with miR-21 inhibitor **135** and provide additional evidence that while compound **135** does not affect mature miR-21 levels or directly bind miR-21, it is capable of rescuing expression of tumor suppressor proteins, resulting in a pro-apoptotic response in A498 cells. This proposed mechanism of chemosensitization is in good agreement with published evidence that suppression of PDCD4 and PTEN by miR-21 is capable of mediating chemoresistance in RCC,[505,515,516] as we all as other cancers.[506,517-519] Taken together, our results support a mechanism in which **135**-mediated inhibition of miR-21 rescues PDCD4 and PTEN protein levels and improves chemosensitivity and therapeutic response.

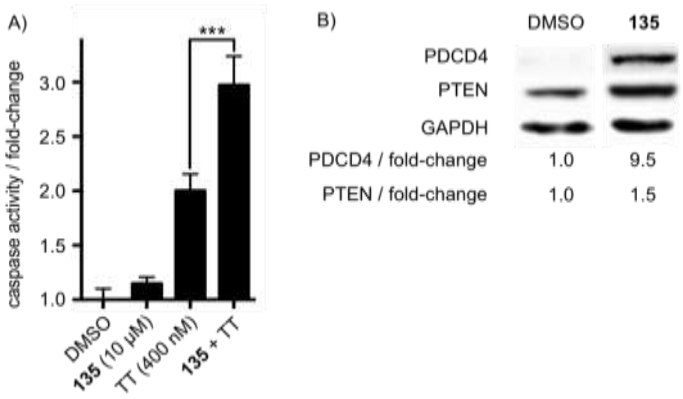

Figure 3-13 Mechanism of therapeutic response to miR-21 inhibition

A) Combination treatment of A498 cells with topotecan (TT) and **135** shows a significant increase in caspase-3/7 activity. B) Treatment of A498 cells with DMSO or **135** for 48 h, followed by Western blot detection of PDCD4, PTEN, and GAPDH (loading control) exhibits rescued expression of anti-apoptotic protein targets of miR-21, relative to a DMSO control. Data represents the mean ± standard deviation from at least three independent experiments. Statistical significance was determined using an unpaired t-test, ** $P < 0.001$, ns $P > 0.05$. Data generated by Yuta Naro.

3.3.1 Summary and Outlook

In summary, oxadiazole inhibitors of miR-21 were identified via a high-throughput screen and subsequent structure-activity relationship studies identified the small molecule **135** as a potent inhibitor of miR-21 function. In contrast to earlier discovered miR-21 inhibitors,[520] preliminary mechanistic studies suggest a mode of action independent of the regulation of miR-21 expression levels. To evaluate therapeutic efficacy, a panel of several cancer cell lines were treated with **37** demonstrating cancer specific inhibition of cell viability at low micromolar concentrations. While the RCC cell line A498 appeared resistant to the effects of **37**, further investigation revealed that

37 was capable of sensitizing A498 cells to the known chemotherapeutic topotecan by significantly increasing the expression of the tumor suppressors PDCD4 and PTEN, targets of miR-21-induced silencing. Therapeutic effects were confirmed through studies of cell viability and clonogenicity, as well as caspase activation. These results suggest that restoration of tumor suppressor function, while challenging to achieve through existing small molecule therapeutics, could play a crucial role in mitigating chemoresistance in RCC. Overall, these discoveries support the development of small molecule miR-21 inhibitors as potential agents to sensitize cancer cells for chemotherapeutic treatment. Small molecule inhibition of a particular miRNA may provide a new approach to enhancing the selectivity and precision of chemotherapy specifically for cancers derived from oncomiR overexpression.

Given the therapeutic potential of **135**-mediated inhibition of miR-21 in sensitization of RCC to topotecan, future work should focus on further elucidating its mechanism of action. Photocrosslinking or pull-down probes should be developed in order to try to isolate potential protein targets of **135**. Alternatively, dedicated assays for proposed modes of action such as interaction with RNA binding proteins or accessory proteins that can alter miRNA function should be explored.

3.3.2 Materials and Methods

Cell culture. Experiments were performed using HeLa-miR-21-Luc, HeLa (ATCC), NIH/3T3 (ATCC), A498 (ATCC), MIA PaCa-2 (ATCC), A172 (ATCC), and HCT-116 (ATCC) cell lines cultured in Dulbecco's Modified Eagle Medium (DMEM; Gibco). U-87 (ATCC) cells were cultured in Eagle's Minimum Essential Medium (EMEM, Gibco), MCF-7 (ATCC) cells were cultured in EMEM supplemented with insulin (0.01 mg/ml), and PC-3 (ATCC) cells were cultured

in F-12K medium (Sigma). All media was supplemented with 10% (v/v) Fetal Bovine Serum (FBS; Sigma-Aldrich) and 5% (v/v) penicillin/streptomycin (VWR) and maintained at 37 °C in a 5% CO_2 atmosphere. Huh7-psiCHECK-miR122 cells were cultured in Dulbecco's Modified Eagle Medium (DMEM; Hyclone) supplemented with 10% (v/v) fetal bovine serum (FBS; VWR), G418 (500 µg/ml; Sigma Aldrich), and 5% (v/v) penicillin/streptomycin (VWR) and maintained at 37 °C in a 5% CO_2 atmosphere. Penicillin/streptomycin was omitted from all media used in experiments. Cell lines were used within passages 1-35 and all cell lines are tested for mycoplasma contamination using the MycoScope PCR Detection kit (Genlantis) every three months.

Compound handling. Compound stocks were prepared by dissolving solid compound (4-5 mg) in an appropriate volume of syringe filtered (0.2 µm filter) DMSO. Initial stocks were typically diluted to 50 – 100 mM depending on the solubility limit, then further diluted as needed. Stock solutions were distributed in 10 – 20 µl aliquots and stored at -20 °C until use. Freeze/thaw cycles were limited to no more than 15 per aliquot.[445] Concentrated stocks were monitored for precipitation following long term storage and were redissolved by briefly heating on a 95 °C heat block when necessary. All compounds were characterized by ^{1}H NMR and HRMS prior to evaluation in biological assays. Purity of compounds was periodically evaluated (once every 6-12 months) via LC-MS. If compounds were redissolved by heating, LC-MS was performed on the sample to ensure integrity of the stock prior to use in biological assays.

For treatment of cells in a 96-well plate format, 2 µl of a DMSO stock (1000x[final]) was diluted in 48 µl of growth media (penicillin/streptomycin-free) in a 96-well plate and mixed by pipetting up and down. Then 5 µl of the diluted compound was added to cells in 195 µl of growth media. For treatment of cells in a 384-well format, 6 µl of the DMSO stock (1000x[final]) was diluted in

69 µl of growth media (penicillin/streptomycin-free) in a 384-well plate and mixed by pipetting up and down with a multichannel pipette. Subsequently, 10 µl of the initial dilution was mixed with 70 µl of growth media in a separate well for each condition. Lastly, 5 µl of the second media dilution was added directly to cells in 45 µl of growth media.

For dilution series, the compounds were diluted by 4-fold five times (for a 96-well plate) or 13 times (for a 384 well plate) in 100% (v/v) DMSO. Then, the DMSO dilutions were mixed with growth media as described above.

Assay for small molecule inhibitors of miR-21. Using our previously described HeLa-miR21-Luc cell line (a stably transfected line harboring a miR-21 binding sequence in the 3' UTR of a firefly luciferase gene).[520] Cells were seeded at a density of 1,000 cells/well (45 µl/well) in two white, clear-bottom, 384-well plates (Greiner). After overnight incubation, cells were treated with compound (5 µl/well) in DMSO (0.1% [v/v]) at the desired concentration or a DMSO control (0.1% [v/v]) in triplicate. The cells were incubated for 48 h and one plate was analyzed with a Bright-Glo luciferase Reporter Assay Kit (Promega, see protocol 6.2.14 while the other was analyzed with an XTT cell viability assay (see protocol 6.2.16). The resulting luminescence for the Bright-Glo assay was measured on a microplate reader (Tecan M1000) with a measurement time of 1 s. For the XTT assay, the absorbance was measured on a microplate reader (Tecan M1000) at 450 nm. The luminescence signal was normalized to cell viability and data were set relative to DMSO control.

Biochemical firefly luciferase inhibition assay. Recombinant firefly luciferase (Promega) was diluted (0.24 fmol/µl) in 1x PBS buffer (50 µl) containing DMSO (0.1% [v/v]), 50 µM of **74** (0.1%

[v/v] DMSO), or 50 μM of PCT-124 (0.1% [v/v] DMSO) in a 384-well plate (Greiner). PTC-124 represents a known firefly luciferase inhibitor,[289,424] and thus was used as a positive control. The plate was incubated at room temperature for 30 min before adding 25 μl of Bright-Glo reagent (Promega, see Bright-Glo luciferase assay protocol 6.2.14 The plate was then incubated on a shaker for 10 min at room temperature before analysis for luminescence, which was measured on a microplate reader (Tecan M1000) with a measurement time of 1 s. Data were normalized to a DMSO control.

Assessment of the selectivity of the small molecule miR-21 inhibitors in the Huh7-psiCHECK-miR122 stable cell line. The previously described Huh7-psiCHECK-miR122 cell line (a stably transfected line harboring a miR-122 binding sequence in the 3' UTR of a *Renilla* luciferase gene) was used to assess the selectivity of compounds.[410] Huh7-psiCHECK-miR122 cells were seeded at a density of 10,000 cells/well (90 μl/well) in white, clear-bottom, 96-well plates (Greiner). After an overnight incubation in media (complete DMEM, free of G418 and penicillin/streptomycin), the cells were treated with 10 μM of compounds (10 μl/well; 0.1% [v/v] DMSO) or a DMSO control (0.1% [v/v]) in triplicate. A previously reported small molecule inhibitor of miR-122, 41D6,[410] was included as a positive control. The cells were incubated for 48 h followed by analysis with a Dual Luciferase Reporter Assay Kit (Promega, see dual-luciferase assay protocol 6.2.13 The luminescence was measured on a microplate reader (Tecan M1000) with a measurement time of 1 s and a delay time of 5 s. *Renilla* luciferase signal was normalized to the firefly luciferase control signal and data were set relative to a DMSO control (RLU).

Quantitative real time PCR analysis. HeLa cells were seeded at a density of 150,000 cells/well in 6-well plates (2 ml/well), grown overnight, and treated with 10 μM of compounds or with DMSO (0.1% [v/v]) in DMEM (2 ml/well). The cells were then incubated at 37 °C for 48 h. The media was removed, and cells were washed with PBS buffer (1 ml; pH 7.4) followed by RNA isolation with the miRNeasy mini kit (Qiagen). The RNA was quantified using a Nanodrop ND-1000 spectrophotometer, and 40 ng of each RNA sample were reverse transcribed using a TaqMan microRNA Reverse Transcription Kit (Applied Biosystems) as described in detail below (see general protocol 6.2.7 in conjunction with either the miR-21 (Thermo-Fisher Scientific; assay ID: 000397) or RNU19 (control; Thermo-Fisher Scientific; assay ID: 001003) TaqMan RT primer (Applied Biosystems; 16 °C, 30 min; 42 °C, 30 min; 85 °C, 5 min). Quantitative Real Time PCR was conducted with a TaqMan 2x Universal PCR Master Mix and the appropriate TaqMan miRNA assay probes on a Bio-Rad CFX96 RT-PCR thermocycler (1.3 μl of the RT product; 95 °C, 10 min; followed by 40 cycles of 95 °C, 15 s; 60 °C, 60 s). The triplicate (3 qPCR reactions) threshold cycles (Ct) were determined using the regression analysis included in the Bio-Rad software and represent the number of cycles required for the fluorescence signal to accumulate exponentially and exceed background levels. Ct values obtained for each small molecule treatment were used to determine the relative levels of miR-21 in small molecule treated cells relative to the DMSO control using the $2^{-\Delta\Delta Ct}$ method.[427] The $2^{-\Delta\Delta Ct}$ method compares the Ct values between target genes using an internal control reference gene to enable direct analysis of relative changes in gene levels. The samples were also analyzed by RT-qPCR to measure the expression levels of pri-miR-21[521] as described in detail in general protocol 6.2.8 After RNA isolation, 50 ng of each RNA sample were reverse transcribed using the iScript cDNA synthesis kit (Bio-Rad) (25 °C, 5 min; 42 °C, 30 min; 85 °C, 5 min). Quantitative Real Time PCR was conducted with a TaqMan 2x Universal PCR

Master Mix and TaqMan primers for hsa-pri-miR-21 (Thermo-Fisher Scientific; assay ID: Hs03302625_pri) and GAPDH (control; Thermo-Fisher Scientific; assay ID: Hs0275991_g1) on a Bio-Rad CFX96 RT-qPCR thermocycler (2 µl of the RT PCR product; 95 °C, 10 min; followed by 40 cycles of 95 °C, 15 s; 60 °C, 60 s). The triplicate threshold cycles (Ct) obtained for each small molecule treatment were used to determine the relative levels of pri-miR-21 in small molecule treated cells relative to the DMSO control and normalized to the GAPDH endogenous control using the $2^{-\Delta\Delta Ct}$ method.

Melting curve analysis of precursor miR-21 RNA. The thermal stability of the stem loop precursor miRNA, pre-miR-21 (IDT; Table 15) was investigated in the presence and absence of compound **135** using temperature-controlled UV spectroscopy. The aminoglycoside tobramycin was used as a positive control for RNA binding.[497] All experiments were conducted on a Cary 3 UV-spectrophotometer. The pre-miR-21 RNA was diluted in 20 mM of sodium phosphate buffer (pH = 7.0) to a final concentration of 1 µM in the presence of 10 µM of **135** (0.1% [v/v] DMSO), 10 µM of tobramycin (0.1% [v/v] DMSO), or DMSO (0.1% [v/v]). The absorbance versus temperature profiles were measured at 260 nm with temperatures ranging from 35 to 90 °C at a ramp rate of 1 °C/min. Absorbance measurements were recorded at 1 °C increments. All measurements were conducted as three independent heating cycles (no absorbance was recorded during cooling). The values at each temperature increment were normalized to the initial absorbance reading at the starting temperature, 35 °C. The three data sets were then averaged, and standard deviations were calculated and presented as errors bars. To determine the melting temperature, the data were used to fit a nonlinear regression curve in GraphPad (Prism) software, with the point at which the RNA is half single stranded and half double stranded (inflection point)

representing the melting temperature (T_m) and the thermal stability of the RNA duplex. In the presence of tobramycin, the melting profile of pre-miR-21 is significantly altered. The T_m of the stem loop pre-miR-21 was increased by 19.1 °C from 56.0 ± 1.2 °C in the absence of tobramycin to 75.1 ± 1.8 °C in the presence of 10 μM of tobramycin. The increased T_m indicates that tobramycin directly binds the double stranded stem loop of pre-miR-21, stabilizing its structure. The observed melting temperature increase is in agreement with previous literature reports, and furthermore tobramycin has been identified as non-sequence specific RNA binder.[497] When treated with the small molecule **135**, no increase in the melting temperature of pre-miR-21 was observed relative to DMSO control. Treatment with DMSO resulted in a T_m of 56.0 ± 1.2 °C, while treatment with **135** exhibited a T_m of 56.1 ± 1.7 °C. In conclusion, the unperturbed thermal stability upon treatment with **135** indicates that the small molecule inhibitor does not directly bind to miR-21.

Table 15 Sequence of pre-miR-21

name	**sequence (5' -> 3')**
pre-miR-21	UAGCUUAUCAGACUGAUGUUGACUGUUGAAUCUCAUGGCAACACC AGUCGAUGGGCUGUC

Assay for the effect of topotecan on miR-21 activity. Using our previously described HeLa-miR21-Luc cell line (a stably transfected line harboring a miR-21 binding sequence in the 3 UTR of a firefly luciferase gene).[520] Cells were seeded at a density of 1,000 cells/well (45 μl/well) in two white, clear-bottom, 384-well plates (Greiner). After overnight incubation, cells were treated (5 μl/well) with topotecan to the desired concentration or a DMSO control (0.1% [v/v] DMSO) in triplicate. The cells were incubated for 48 h and one plate was analyzed with a Bright-Glo

luciferase Reporter Assay Kit (Promega; see Bright-Glo luciferase assay protocol 6.2.14 The luminescence was measured on a microplate reader (Tecan M1000) with a measurement time of 1 s. The other plate was analyzed via XTT cell viability assay (see XTT cell viability assay protocol 6.2.16 Absorbance was measured on a microplate reader (Tecan M1000) at 450 nm. Luminescence signal was normalized to cell viability and data were set relative to DMSO control.

Cell viability assays. A498, U-87, MCF-7, HCT-116, MIA-PaCa-2, A172, or NIH 3T3 cells were seeded at 500 cells/well (total media volume of 45 μl/well) in white, clear-bottom, 384-well plates (Greiner). Following an overnight incubation, cells were treated (5 μl/well) with increasing concentrations of compounds (0.1% [v/v] DMSO) or a DMSO control (0.1% [v/v]) in triplicate. For combination treatment of the compounds and chemotherapeutic agents, cells were treated with increasing concentrations of the chemotherapeutic agent while the miR-21 inhibitor concentration remained constant. DMSO was maintained at 0.1% (v/v) in combination treatment experiments. The cells were incubated for 72 h followed by analysis with an XTT assay (GoldBio or Roche; see XTT assay protocol 6.2.16 .[522,523] Briefly, activated XTT reagent was added to each well. Absorbance was measured at 450 nm and 630 nm (background) after initial addition (Abs-t_{inital}) of the reagent, then incubated at 37 °C in a 5% CO_2 atmosphere for 4 hours, followed by measurement of end-point absorbance (Abs-t_{final}) on a Tecan M1000 plate reader. Following background subtraction of the absorbance measurements at 630 nm, the difference in the Abs-t_{inital} and Abs-t_{final} 450 nm absorbance measurements was calculated. The difference in absorbance for each well was normalized to the DMSO control, then averaged and multiplied by 100 to determine the percent cell viability relative to DMSO. Error bars represent the standard deviation of three

independent replicate wells. IC_{50} values were calculated by fitting the data with a variable slope sigmoidal dose response curve using GraphPad (Prism) software.

Caspase-Glo 3/7 assays. A498 cells were seeded into white, clear-bottomed, 96-well plates (Greiner) at a density of 10,000 cells/well (90 µl). Following overnight incubation, cells were treated (10 µl/well) with either DMSO (0.1% [v/v]), 400 nM of topotecan, 10 µM of **135**, or a combination of 400 nM of topotecan and 10 µM of **135** for 24 h. Following incubation, caspase 3/7 activity was measured (Promega) following the manufacturers protocol. Data were normalized to the DMSO control and represents the mean ± standard deviation from at least three replicate wells. Statistical significance calculated in GraphPad Prism and was determined using an unpaired t-test, ** $P < 0.01$.

Clonogenic assay. The clonogenic assay[524] was performed as described previously and described in detail below (protocol 6.2.18 Briefly, a base layer consisting of 0.7% (w/v) agarose in DMEM growth medium was added to 12-well plates (Greiner) and allowed to solidify. Cells were then seeded at a density of 10,000 cells per well in 0.45% (w/v) low melt agarose in DMEM growth medium supplemented with increasing concentrations of compound in DMSO (0.1% [v/v]) or a DMSO control (0.1% DMSO final concentration) in triplicate. After two weeks, cells were stained with 0.1% (w/v) crystal violet. Images of each well were captured using an MRm camera (Axiocam) and N-Achroplan 5x/0.13 M27 objective on an Axio Observer Z1 microscope (Zeiss). In order to capture images of the whole well, a z-stack of 17 slices over 800 µm of the well was obtained. Each slice contained 114 tiles which were stitched together immediately following image capture using Zen 2012 software. Z-stacks were exported as .tif files and focus stacking was used

to convert the individual slices to generate an extended depth of field image using Helicon Focus software. Extended depth of field images were analyzed using ImageJ.[525] Briefly, identical contrast settings were applied to each image by adjusting the maximum and minimum pixel values to match the histogram. The threshold for each image was then set to 1.03%. Colonies were counted using the "Colony Counter" plugin using a particle size of 500-infinity. Total colonies per well were averaged and normalized to DMSO control. Error bars represent standard deviation of three independent measurements. IC_{50} values were calculated by fitting the data with a variable slope sigmoidal dose response curve using GraphPad (Prism) software.

PTEN and PDCD4 western blot. A498 cells were seeded into a 6-well plate at a density of 250,000 cells/well (2 ml/well). Following overnight incubation, cells were treated with either DMSO (0.1% [v/v]) or 10 μM of **135** for 48 h. Cell lysis and protein extraction was carried out using RIPA lysis buffer (Tris-HCl [50 mM; pH 8.0], NaCl [150 mM], 0.5% [w/v] sodium deoxycholate, 1% [v/v] Triton X-100) supplemented with Halt Protease Inhibitor Cocktail (Thermo-Fisher) (see mammalian protein isolation protocol 6.2.11 Whole cell lysates were boiled in Laemmli sample buffer and separated on a 10% (v/v) SDS-PAGE gel (see SDS-PAGE protocol 6.2.12.1). Following separation, proteins were transferred to a PVDF membrane (GE Healthcare) and the membrane was blocked in TBS with 0.1% (v/v) Tween 20 containing 5% (w/v) BSA for 1 h at room temperature (for more details, see western blot protocol 6.2.12.3). The blots were probed with primary antibodies rabbit mAb anti-PTEN (Cell Signaling, 1:1,000 dilution; catalog#: 9559S), rabbit pAb anti-PDCD4 (Rockland, 1:1,000 dilution; catalog# 600-401-965S), and rabbit mAb anti-GAPDH (Cell Signaling, 1:2,500 dilution; catalog# 2118S) in blocking buffer (5 ml) at 4 °C rocking overnight, followed by secondary antibody detection using an anti-rabbit IgG HRP-

linked antibody (Cell Signaling, 1:1,000 dilution; catalog# 7074S) in TBS with 0.1% (v/v) Tween 20 (5 mL) for 1 h at room temperature. Chemiluminescence was developed using SuperSignal West Pico Chemiluminescent Substrate (Thermo-Fisher Scientific, 5 ml, 5 min) and imaged on a ChemiDoc XRS+ (Bio-Rad) using the chemiluminescence filter and automated exposure settings. Densitometry analysis was carried out using Image Lab software (Bio-Rad), where PTEN and PDCD4 protein bands were normalized to GAPDH, followed by normalization to DMSO control.

3.4 Ether-Amide Inhibitors of miR-21

In addition to the oxadiazole scaffold identified above, an ether-amide inhibitor was also further evaluated from the 58 small molecules identified in the HTS. Analogs of the initial hit **136** were synthesized using a robust synthetic route that allowed for facile functionalization of numerous positions across the structure (Figure 3-14). Commercially available *ortho*-substituted anilines **137** were readily reacted with **138** via a condensation reaction in polyphosphoric acid to obtain the resulting benzoimidazoles, benzothiazoles, and benzoxazoles **139**. Subsequent reaction with acetyl chloride provided the linker region in **140** which readily underwent nucleophilic substitution with phenols, thiols and anilines in the presence of cesium carbonate to yield the final products.

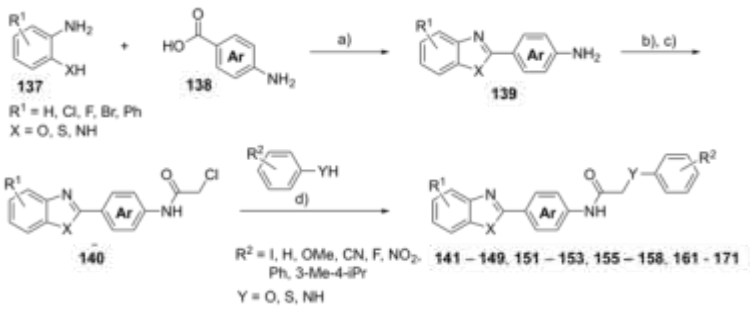

Figure 3-14 Synthetic route to ether-amide miR-21 inhibitors

a) polyphosphoric acid, 170 °C; b) chloroacetyl chloride, toluene, 90 °C; c) sat. $NaHCO_3$, rt; d) Cs_2CO_3, CH_3CN, rt; Ar = phenyl, naphthyl, benzothiazolyl. Synthesis performed by Rohan Kumbhare.

Using this synthetic route, a small panel of analogs was generated, and their biological activity was evaluated using the HeLa-miR21-Luc cell line (Figure 3-15). The initial hit **136** demonstrated modest activity, inducing a 1.55-fold increase in luciferase signal following treatment at 10 μM for 48 h. Removal of the iodide to yield **141** resulted in only a very minor improvement in activity, while loss of the iodide along with introduction of a *para*-methoxy group in **142** also had little to no effect on activity. Turning towards modifying the benzothiazole ring, the benzoxazole derivative of **136** yielded **143**, which maintained the same activity as the parent compound. Keeping the benzoxazole and removal of the iodide resulted in **144**, which showed no change in activity, while introduction of a *para*-methoxy to yield **145** abolished all activity. Expanding upon **144**, addition of a 5-chloro modification to the benzoxazole resulted in **146**, which demonstrated an 85% enhancement in activity compared to the initial hit **136**. Furthermore, addition of a *para*-methoxy substitution to **146** to yield **147** further enhanced activity, eliciting a 314% improvement compared to **136**. Continuing from the promising results obtained from **146**

and **147**, analogs containing benzimidazoles (**148** and **149**) were synthesized, however, only a loss in activity was observed.

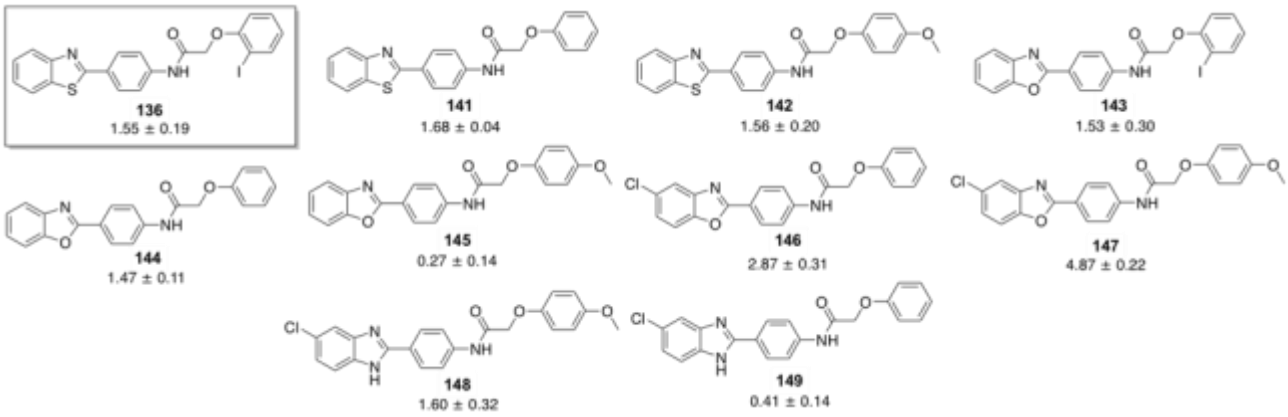

Figure 3-15 Activity of compounds **136** and **141** – **149** in the HeLa-miR21-Luc assay

Values represent fold-changes in luminescence signal in the HeLa-miR21-Luc stable cell line normalized to cell viability and relative to a DMSO control. Data represents the average ± standard deviation from at least three independent experiments. Synthesis performed by Rohan Kumbhare. Luciferase data generated by Yuta Naro.

To build upon the improvement in activity seen in **146** and **147**, an additional round of analogs was synthesized containing further modification to each respective compound. For **146**, moving the 5-chloride to the 6-position yielded **151**, which had only minor impact on activity. Changing the ether-amide linker from the *para*- to the *meta*-position yielded analogs **152** and **153**, which only resulted in losses in activity. The importance of the ether-amide linker was investigated by synthesizing **154** bearing a shorter carbamate linker (Figure 3-16). Compound **154** elicited a 35% increase in activity relative to **146** and a 249% increase relative to the initial hit **136**.

Analogous modifications were also made to **147** to produce **155**, **156**, **157**, and **158**, however only reduced activity was observed in this set of analogs (Figure 3-17).

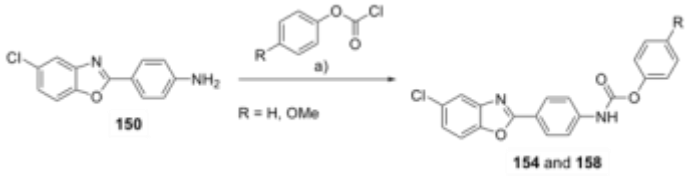

Figure 3-16 Synthetic route to ether-amide miR-21 inhibitors **154** and **158**

a) Et_3N, DCM, 0 °C – rt. Synthesis performed by Rohan Kumbhare.

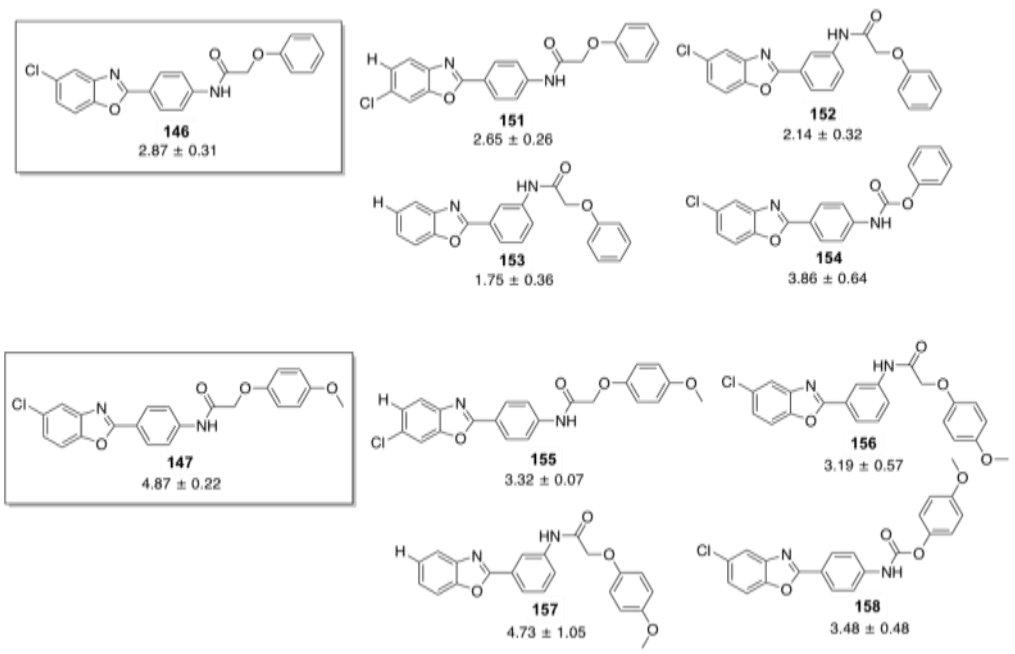

Figure 3-17 Activity of compounds **151** – **158** in the HeLa-miR21-Luc assay

Values represent fold-changes in luminescence signal in the HeLa-miR21-Luc stable cell line normalized to cell viability and relative to a DMSO control. Data represents the average ± standard deviation from at least three independent experiments. Synthesis performed by Rohan Kumbhare. Luciferase data generated by Yuta Naro.

With **147** remaining the most potent inhibitor identified thus far, we decided to investigate further modifications to its structure. To this end, analogs containing modifications to the ether-amide linker and the central aniline ring were synthesized and their activity was tested in the HeLa-miR21-Luc stable cell line (Figure 3-18). Replacement of the ether-amide linker with a thioether amide linker produced analog **159** which exhibited a 54% decrease in activity relative to **147**. Furthermore, incorporation of an amino-amide linker in place of the ether-amide linker resulted in **160** and completely abolished activity. Replacement of the central aniline ring with a naphthalene (**161**) or benzothiazole (**162**) was also detrimental to activity. Lastly, alkylation of the amide

nitrogen in **147** with a methyl or propargyl group, **163** and **164** respectively (Figure 3-19), abolished activity compared to the parent compound **147**. Taken together, these results confirmed the importance of the ether-amide linker to activity and thus we decided to maintain this moiety moving forward with additional analogs.

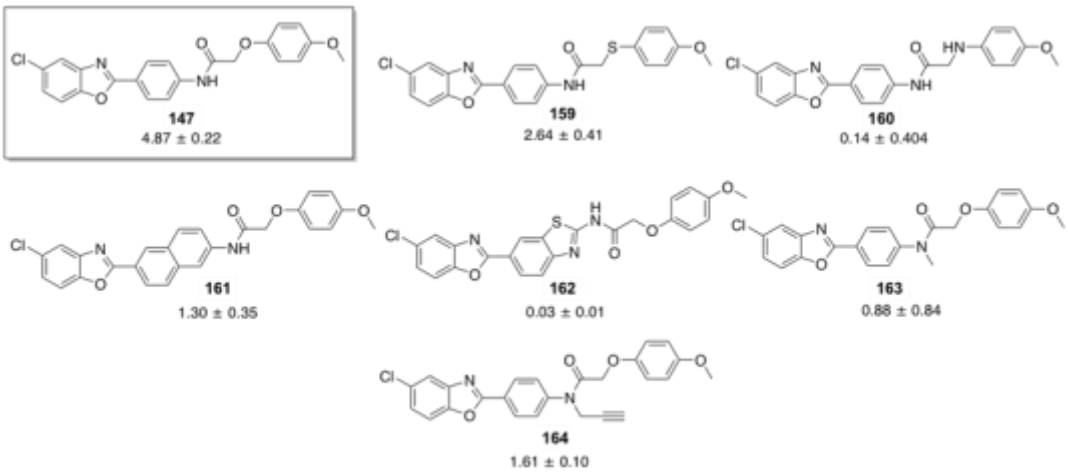

Figure 3-18 Activity of compounds **159** – **164** in the HeLa-miR21-Luc assay

Values represent fold-changes in luminescence signal in the HeLa-miR21-Luc stable cell line normalized to cell viability and relative to a DMSO control. Data represents the average ± standard deviation from at least three independent experiments. Synthesis performed by Rohan Kumbhare. Luciferase data generated by Yuta Naro.

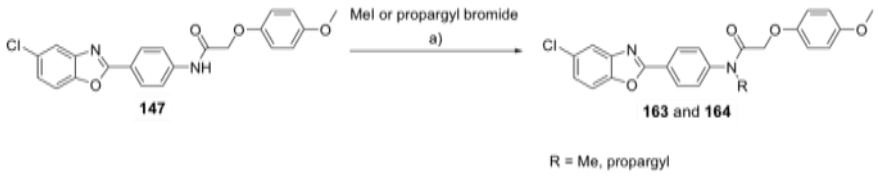

Figure 3-19 Synthetic route to ether-amide miR-21 inhibitors **163** and **164**

a) LiHMDS, MeI, THF, 0 °C – rt (for R = Me); NaH, propargyl bromide, DMF, 0 °C – rt (for R = propargyl). Synthesis performed by Rohan Kumbhare.

Building upon the generated structure-activity information, we decided to synthesize an additional set of analogs based on **147** but containing more diverse changes to two distal ring systems while maintaining the structures of the central region of the scaffold. To this end, additional analogs were synthesized and tested in the miR-21 luciferase reporter (Figure 3-20). Moving the *para*-methoxy to the *meta*-position resulted in **165**, which displayed similar activity to **12**. Replacement of the *para*-methoxy with a nitrile (**166**), fluorine (**167**), nitro (**168**), or phenyl (**169**) group all resulted in losses in activity. Similarly, introduction of a *para*-isopropyl in conjunction with a *meta*-methyl group (**170**) led to a 46% decrease in activity. Interestingly, replacement of the 5-chloro with a 5-fluoro in conjunction with (**171**) or without (**172**) the *para*-methoxy group also reduced activity, providing evidence that the 5-position may be highly sensitive to modifications. To further support this, introduction of a bromine at the 5-position (**173**) resulted in a 27% increase in activity compared to the parent compound **147.** Surprisingly, introduction of a phenyl group at the 5-position (**174**) had an even greater impact on activity, demonstrating a 62% improvement in activity compared to **147**, and a 508% increase in activity relative to the initial hit **136**. Conversion of the benzoxazole to a pyridinyloxazole (**175**) led to a

loss in activity compared to **136** and further supports the critical nature of the 5-position on the benzoxazole.

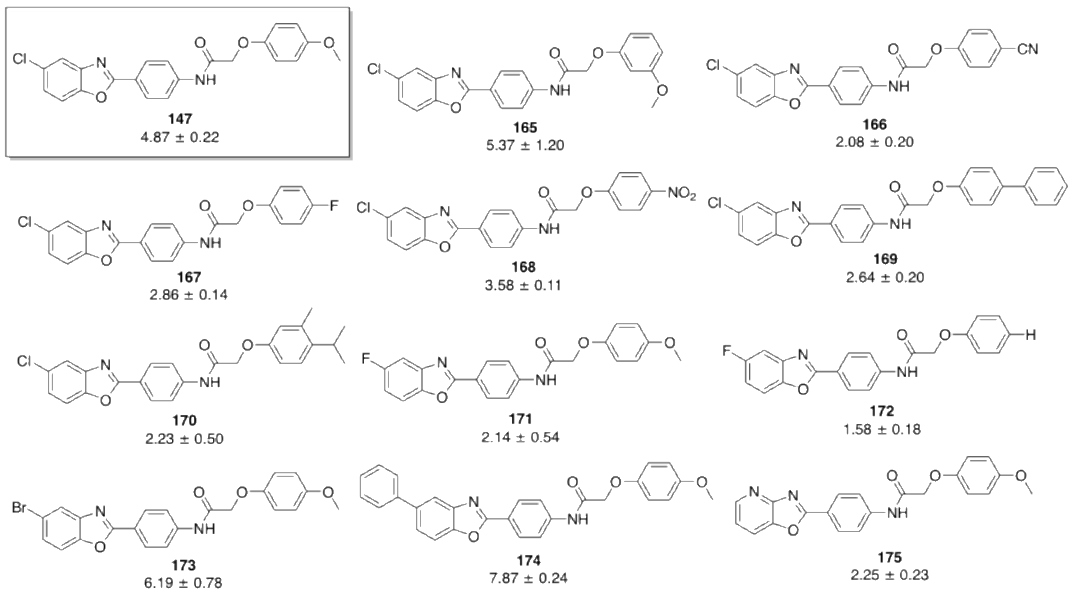

Figure 3-20 Activity of compounds **165** – **175** in the HeLa-miR21-Luc assay

Values represent fold-changes in luminescence signal in the HeLa-miR21-Luc stable cell line normalized to cell viability and relative to a DMSO control. Data represents the average ± standard deviation from at least three independent experiments. Synthesis performed by Rohan Kumbhare. Luciferase data generated by Yuta Naro.

Overall, the SAR studies suggest several key positions on the inhibitor that appear sensitive to modification, including the ether-amide linker core and the 5-position on the benzoxazole ring system. With the promising and improved candidates **147**, **165**, **173**, and **174** in hand, we next evaluated their biological activity and confirmed their function as miR-21 inhibitors.

Firstly, the HeLa-miR21-Luc reporter cell line was treated in dose-response with the most promising analogs, and **147**, **165**, **173**, and **174** all demonstrated reporter activation in a dose-

dependent fashion with EC_{50} values of 6.7 µM, 4.7 µM, 6.4 µM, and 3.5 µM, respectively (Figure 3-21).

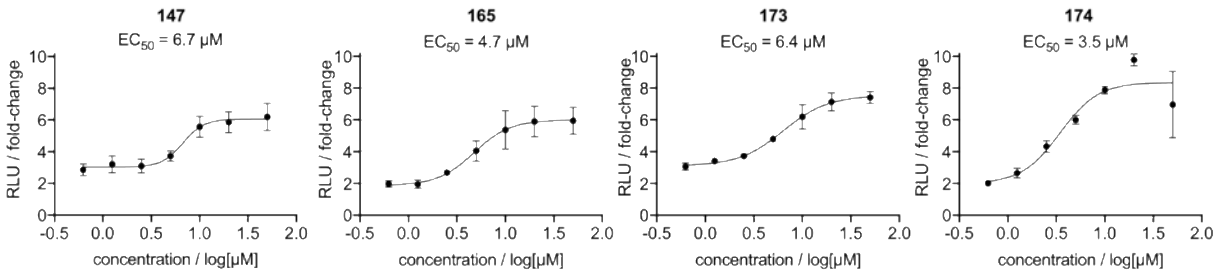

Figure 3-21 HeLa-miR21-Luc stable reporter cells treated with dilution series of inhibitor **147**, **165**, **173**, or **174** Luciferase signal was first normalized to cell viability and then to a DMSO control. Error bars represent standard deviations from three independent experiments. EC_{50} values were determined by fitting data to a nonlinear regression analysis in GraphPad Prism software. Luciferase data generated by Yuta Naro.

Firefly luciferase inhibitors have been previously identified as false positive hits in high-throughput screens due to luciferase enzyme stabilization in cells.[289] Because this is a documented concern when using luciferase reporter assays,[526] we decided to evaluate the effect of **147**, **165**, **173**, and **174** on luciferase activity in a biochemical assay. Treatment with the positive control firefly luciferase inhibitor PTC-124[19] led to a 94% reduction in enzyme activity. While treatment with **147** elicited no significant reduction in luciferase activity, treatment with **165**, **173**, and **174** all led to 44, 38, and 27% reductions in luminescence signal, respectively (Figure 3-22A). To further validate whether these inhibitors act on the miRNA pathway, we transfected HeLa cells with a psiCHECK-empty reporter (containing a sequence not targeted by any known miRNA) followed by treatment with the compounds at 10 µM for 48 h. The positive control PTC-124 and

compounds **165**, **173**, and **174** induced an increase in luminescence signal ranging from 1.5 to 1.8-fold, while compound **147** only showed a minor increase in luciferase activity (Figure 3-22B). These biochemical and cell-based results indicate that **165**, **173**, and **174** may have inflated activity profiles in the HeLa-miR21-Luc assay due to off-target binding of the firefly luciferase enzyme. Taking both the dose-response and *in vitro* firefly luciferase data into account, we decided to carry **147** forward as the primary candidate for further biological testing.

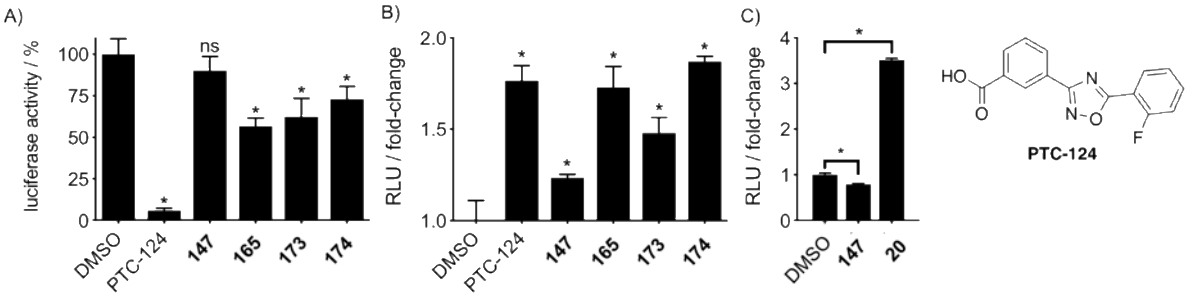

Figure 3-22 Evaluation of selectivity of lead compounds

A) Treatment with inhibitor **147** has no effect on luciferase activity, while **165**, **173**, and **174** all inhibit firefly luciferase *in vitro*. PTC-124, a known firefly luciferase inhibitor, was included as a positive control. B) Hit compound **147** has a minor impact on firefly luciferase activity in HeLa cells transfected with the psiCHECK-empty plasmid. Analogs **165**, **173**, and **174** as well as the positive control induce increases in luminescence. C) Inhibitor **147** does not inhibit miR-122 in the Huh7-miR122 stable cell line. Compound **40** was used as a positive control. RLU values represent *Renilla* luciferase luminescence signal normalized to firefly luciferase luminescence signal. All data were normalized to DMSO treatment (negative control) and error bars represent standard deviations from three independent experiments. Statistical significance was determined using an unpaired t-test, * $P < 0.05$, ns $P \geq 0.05$. Luciferase data in A and C generated by Yuta Naro.

Next, we tested if **147** is a general miRNA pathway inhibitor or if it has selectivity for miR-21. To this end, we employed an additional stable reporter cell line, Huh7-miR122, which places *Renilla* luciferase expression under the control of miR-122 activity.[410] Treatment with **147** (10 μM) elicited only a minor 0.2-fold reduction in *Renilla* luciferase signal, demonstrating that **147** does not inhibit miR-122 activity (Figure 3-22C). As a positive control, cells were also treated with **20**, a known miR-122 inhibitor,[410] which induced a >3.5-fold increase in luminescence, confirming functionality of the assay. Taken together, these results indicate that **147** shows some level of selectivity for miR-21 and is not a general miRNA pathway inhibitor.

To explore the mechanism by which **147** inhibits miR-21 function, levels of mature miR-21 were measured via reverse transcription quantitative PCR (RT-qPCR) after treatment with **147**. To ensure that the effects were not cell line dependent, three different cancer cell lines were tested. These cell lines included the parental cell line of the HeLa-miR21-Luc stable reporter cell line, HeLa cervical carcinoma cells, along with A549 non-small cell lung carcinoma cells, and SKOV3 ovarian cancer cells. Each cell line was treated with **147** (10 μM) or DMSO (0.1%) for 48 h, followed by miRNA isolation and quantification using RT-qPCR. In HeLa cells, a 57% reduction was observed (Figure 3-23A), while in A549 and SKOV3 cells, 33% and 31% reductions were detected, respectively (Figure 3-23B). These results support a mechanism by which treatment with **147** results in depletion of mature miR-21 and subsequent reduction of miR-21 regulatory functions. To determine if **147** inhibits miR-21 maturation via binding directly to pre-miR-21, melting curve analyses were carried out in the presence of DMSO or **147**. The melting temperature of pre-miR-21 in the presence of DMSO control was measured to be 56.0 °C. The presence of **147** (10 μM) had no effect on melting temperature yielding a T_m of 56.2 °C (Figure 3-24). These results

indicate that **147** does not directly interact with miR-21 RNA and that miR-21 levels are likely impacted via an alternative mechanism.

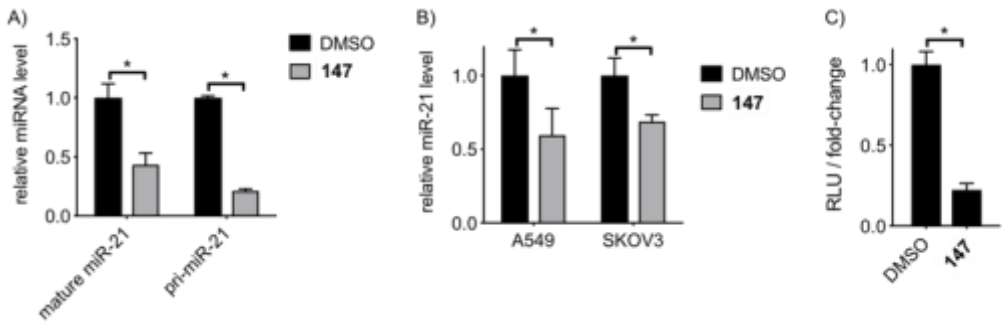

Figure 3-23 RT-qPCR analysis of compound **147** and promoter assay

A) Treatment of HeLa cells with **147** for 48 h, followed by RT-qPCR analysis of mature miR-21 or primary miR-21 (pri-miR-21). B) Treatment of A549 (NSCLC) or SKOV3 (ovarian carcinoma) with DMSO or **147** (10 μM), followed by qPCR analysis of mature miR-21 RNA levels elicited a 33 and 31% decrease, respectively. C) Transfection of HeLa cells with a miR-21 promoter gene expression reporter following treatment with **147**. Data were normalized to DMSO treatment (negative control) and error bars represent standard deviations from three independent experiments. Statistical significance was determined using an unpaired t-test, * $P < 0.05$. Data in B and C generated by Yuta Naro.

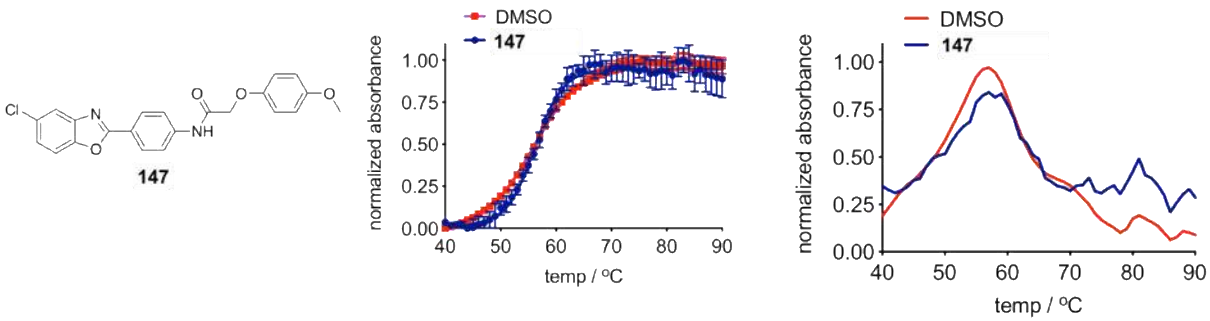

Figure 3-24 Melting temperature analysis of pre-miR-21

Melting curves for pre-miR-21 in the absence and presence of **147** (left). Differentiation of the melting curves (right) reveals no change in melting temperatures in the presence (T_m = 56.2 °C) or absence (T_m = 56.0 °C) of **147**. Error bars represent standard deviations from three independent experiments. Data generated by Yuta Naro.

To further investigate what step of the miR-21 biogenesis pathway **147** may be targeting, primary miR-21 levels were analyzed via RT-qPCR in HeLa cells after treatment with **147** (10 µM) for 48 h. Interestingly, a marked 79% decrease in primary miR-21 levels was observed following treatment (Figure 3-23A). This result supports a mechanism by which **147** is inhibiting transcription of the miR-21 gene, resulting in depletion of primary miR-21 levels. To confirm that compound **147** inhibits miR-21 transcription, HeLa cells were transfected with a previously described luciferase reporter construct that monitors miR-21 promoter activity, pGL4-miR21P,[487] and were treated with DMSO or **147** (10 µM) for 48 h. As expected, treatment with **147** resulted in a 78% decrease in miR-21 promoter activity compared to DMSO control (Figure 3-23C). This result directly supports the drastic reduction in primary miR-21 levels observed via RT-qPCR and further suggests a mechanism of action by which **147** inhibits transcription of the miR-21 gene.

Next, we evaluated whether **147**-mediated inhibition of miR-21 could elicit a therapeutic response in HeLa cells by subjecting them to a cell viability study using an XTT assay.[522] Following treatment with the compound for 72 h, **147** demonstrated a disappointing $IC_{50} > 50$ μM (Figure 3-25A). To further explore this response and determine if **147**-induced limited cell death was due to induction of apoptosis, we examined caspase-3/7 activation in HeLa cells. Antisense oligonucleotide-mediated Inhibition of miR-21 has been previously shown to inhibit cell proliferation and increase apoptosis of HeLa cells.[527] Treatment of HeLa cells with **147** (10 μM) for 24 h elicited a modest 50% increase in caspase-3/7 activity, a 2-fold increase was observed at an increased concentration of 50 μM (Figure 3-25B). This suggests that knockdown of miR-21 by **147** leads to a reduction in cell viability by inducing apoptosis, consistent with previous reports.[527-530]

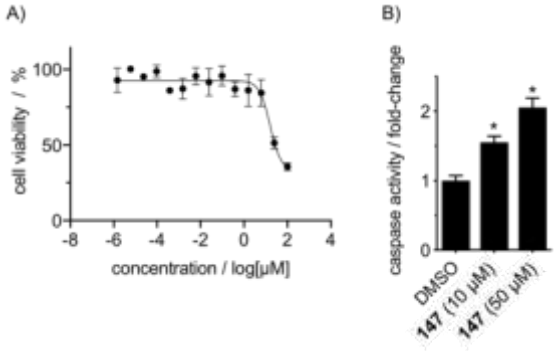

Figure 3-25 Pre-therapeutic evaluation of **147** in HeLa cells

A) Treatment of HeLa cells with **147** for 72 h, followed by a cell viability assay. B) Caspase-3/7 activity was measured in HeLa cells following treatment with **147** for 24 h. Data were normalized to DMSO treatment (negative control) and error bars represent standard deviations from three independent experiments. Data in B generated by Cole Emanuelson.

We further explored the therapeutic potential of **147** by investigating the ability of the small molecule to elicit long-term effects in reducing microtumor formation in a clonogenic assay. Oligonucleotide silencing of miR-21 has been shown to inhibit clonogenicity in several cancer cell models[531-533] including cervical cancer.[527,534] Briefly, HeLa cells were suspended in low melt agarose and exposed to a dilution series of **147** for two weeks at 37 ºC prior to imaging (Figure 3-26A). Treatment with **147** reduced colony formation with an EC_{50} of 7.3 µM (Figure 3-26B), indicating that the compound was capable of inhibiting microtumor formation of HeLa cells.

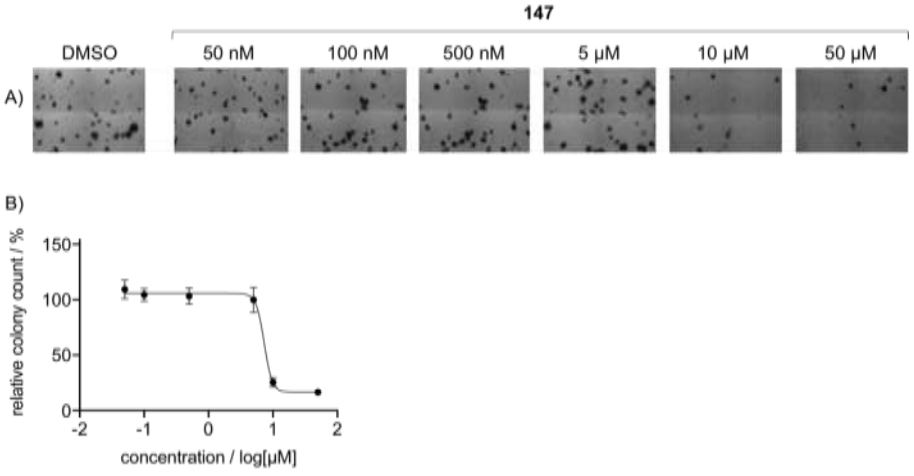

Figure 3-26 Clonogenic assay in HeLa cells treated with compound **147**

A) Representative images from clonogenic assays following 2-week treatment of HeLa cells with a dilution series of **147**. Images were cropped to 4 tiles each in the center of the well from the extended depth of focus image. B) Treatment of HeLa cells with **147** in a two-week clonogenic assay.

3.4.1 Summary and Outlook

In summary, a high-throughput screen for small molecule modulators of miR-21 function led to the identification of a new ether-amide scaffold and a subsequent structure-activity relationship study of the initial hit compound **136** resulted in the identification of the improved miR-21 inhibitor **147**. Through a biochemical and cell-based firefly luciferase assays as well as a miR-122 reporter cell line, we determined that compound **147** was selective for miR-21. Furthermore, **147** was found to inhibit transcription of the miR-21 gene resulting in significant reductions in primary and mature miR-21 levels. This mechanism of action is in contrast to previously reported miR-21 inhibitors which appear to inhibit maturation of pre-miR-21[265,487,535,536] as well as oxadiazole inhibitors which appear to inhibit the function of mature miR-21 without affecting miR-21 levels.[537] However, the ether-amide class does appear to follow a similar mechanism to the previously reported diazobenzene.[538] Pre-therapeutic evaluation of the lead compound using XTT and caspase activation assays demonstrated that miR-21 inhibition mediated by **147** reduces cell viability in HeLa cells by inducing apoptosis. Furthermore, treatment of HeLa cells with **147** in a long-term clonogenic assay inhibited microtumor formation, suggesting inhibitor **147** may have potential as a therapeutic for treating miR-21-related diseases.

Future work should focus on further evaluation of the biological relevance of **147**-mediated inhibition of miR-21. Functional assays that monitor cell viability, caspase activity, clonogenicity, and cell migration should be employed in a variety of cancer cell lines in order to evaluate the therapeutic potential of **147**. Moreover, additional experiments should be performed to try to further elucidate the mechanism by which **147** inhibits miR-21 transcription. The use of photocrosslinking or pull-down probes may enable enrichment of the target protein, while

mutational studies of transcription factor binding sites within the miR-21 promoter may provide valuable insight into the potential mode of action of **147**.

3.4.2 Materials and Methods

Detailed protocols for all experiments conducted in this section are described in Materials and Methods section **3.3.2**

3.5 *N*-Acylhydrazone Inhibitors of miR-21

From the initial HTS, two structurally similar *N*-acylhydrazones, **176** and **177**, were also identified (Figure 3-27A). Subsequently, Meryl Thomas resynthesized the potential hit compounds to verify their activity in the miR-21 assay. Upon testing the newly synthesized compound **177**, a reduction in activity was observed. However, compound **176** elicited a modest 43% increase in luminescence. Unfortunately, activity of **176** was inconsistent in subsequent assays and we hypothesized that variation between assays could be the result of hydrolytic instability in cells.[539-541] To this end, a structure-activity relationship investigation was undertaken in hopes of learning more about the chemical properties surrounding their activity, as well as identifying more potent analogs. The first round of modifications involved replacing the hydrazide moiety with an amide to improve stability, while also modifying the peripheral ring structures. As such, a general approach for synthesis of bis-amide analogs was developed and is readily accessible via commercial building blocks (Figure 3-27B). Beginning with *N*-Boc-p-phenylenediamine, an amide bond is first formed via nucleophilic acyl substitution of acyl

chlorides or functionalization of the carboxylic acid in the presence of *N*-(3-dimethylaminopropyl)-*N'*-ethylcarbodiimide (EDC). Subsequently, Boc deprotection mediated by treatment with 50% (v/v) trifluoroacetic acid (TFA) in dichloromethane (DCM) yields the free aniline which undergoes an amidation step with an acyl chloride or carboxylic acid, generating the final product.

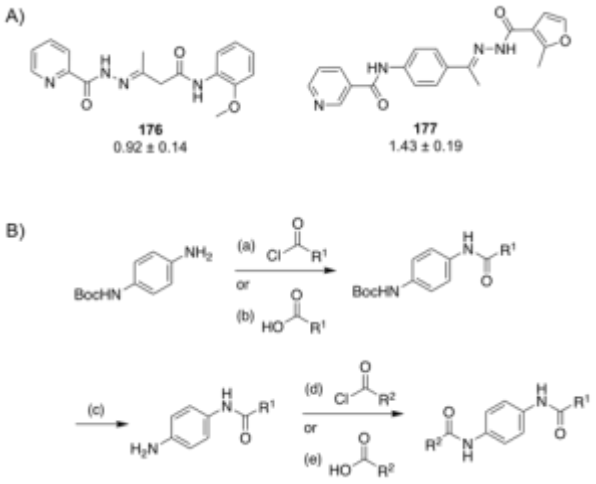

Figure 3-27 Lead molecules from the HTS and general sythetic route to bis-amide analogs

A) Structures of initial hits **176** and **177** identified in the high-throughput screen. Values represent fold-changes in luminescence normalized to cell viability and relative to a DMSO control. Data represents the average ± standard deviation from at least three independent experiments. Compounds were synthesized by Meryl Thomas. Luciferase data were generated by Yuta Naro. B) General sythetic scheme for analogs of **176** and **177**. Reagents and conditions: a) DIPEA, CH_2Cl_2; b) EDC, DIPEA, CH_2Cl_2; c) 50% (v/v) TFA/DCM; d) DIPEA, CH_2Cl_2; e) EDC, DIPEA, CH_2Cl_2.

Analogs of the initial hit compounds were synthesized by Subhas Samantha and evaluated in the HeLa-miR21 reporter cell line by Yuta Naro. Replacement of the methylfuran with a pyridine (**178**) or benzofuran (**179**) completely abrogated activity (Figure 3-28). Interestingly, exchanging the pyridine ring for an additional methylfuran (**180**) led to a ~51% increase in activity relative to the parent compound, suggesting the hydrazide moiety was unnecessary for activity. As such, we next sought to expand upon the newly identified bisamide scaffold. Alternative furan rings (**181** and **182**) were also explored, but only led to diminished activity. Moreover, replacement of the pyridine ring with an *ortho*-anisole (**183**) or *ortho*-cresol (**184**) moiety exhibited similar activity to the parent compound, while methylation of the amide nitrogens yielding (**185**) led to complete abrogation of activity. Finally, modification of the central benzene ring to a cyclohexane (**186**) resulted in a ~20% reduction in activity, relative to the parent molecule.

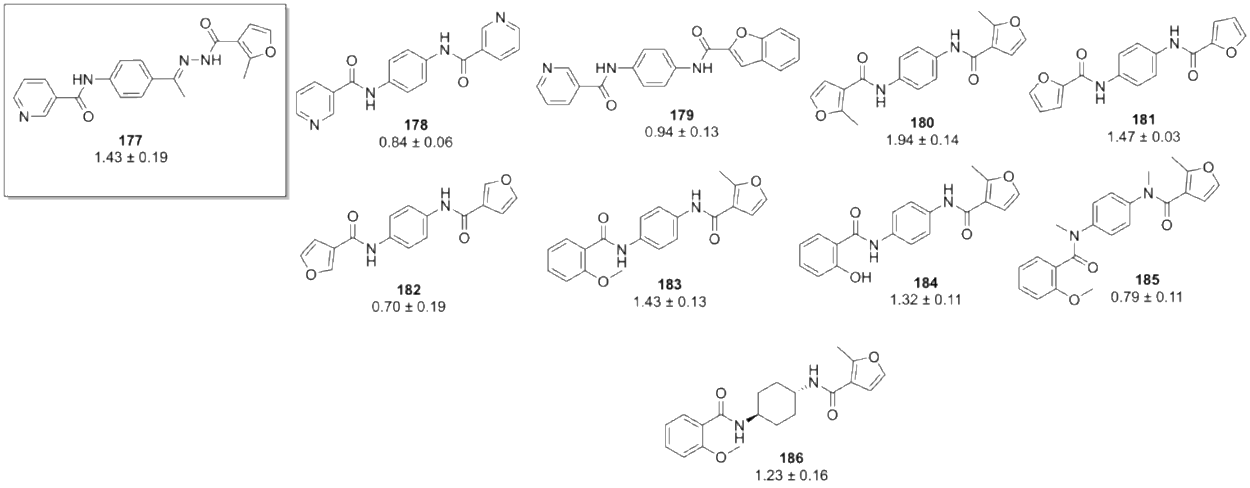

Figure 3-28 Structures and activities of analogs **177** – **186**

Values represent fold-changes in luminescence normalized to cell viability and relative to a DMSO control. Data represents the average ± standard deviation from at least three independent experiments. Compounds were synthesized by Meryl Thomas. Luciferase data were generated by Yuta Naro.

Because compound **180** exhibited the most promising improvement in activity thus far, an additional series of modifications were made to the central benzene ring structure. Alteration of the *para*-bisamide to a *meta*-bisamide (**187**) elicited a slight loss in activity, but when the methylfuran rings were replaced with *ortho*-anisole (**188**) a modest 16% increase in activity was observed, relative to **180** (Figure 3-29). Furthermore, removal of the methyl groups (**189**) showed little change in activity, but extension or replacement of the methyl esters to ethyl esters (**190**) or chlorines (**191**), respectively, led to a dramatic loss in activity. Additionally, movement of the methoxy groups to the *meta*- positions (**192**) induced a minor loss in activity, relative to **180**. Replacement of one of the methylfuran rings with an *ortho*-anisole ring (**193**) resulted in a promising 60% increase in activity relative to **180**, and a 111% increase relative to the parent compound, **177**. Moreover, altering the central benzene ring to a pyridine (**194**), reversing the configuration of one of the amides (**195**), or modifying the *meta*-bisamide to an *ortho*-bisamide configuration (**196**), while maintaining the peripheral rings, all resulted in significant losses in activity.

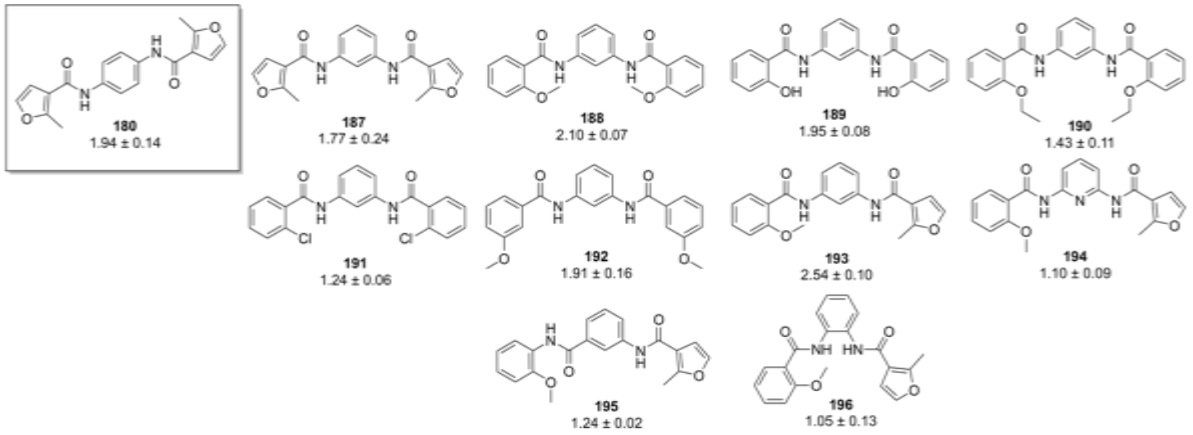

Figure 3-29 Structures and activities of analogs **187** – **196** derived from analog **180**

Values represent fold-changes in luminescence normalized to cell viability and relative to a DMSO control. Data represents the average ± standard deviation from at least three independent experiments. Compounds were synthesized by Meryl Thomas. Luciferase data were generated by Yuta Naro.

Lastly, modifications were also made to the amide linkers. Locking one of the amides into a six-membered ring (**197** and **198**) or extending the linker via a phenol ether functionality (**199** and **200**) induced losses in activity (Figure 3-30). Finally, the amide linker was extended via insertion of a single methylene unit. While this modification was not well tolerated in analogs containing the *ortho*-anisole amide (**201** and **202**), an analog bearing a benzofuran (**203**) displayed a ~14% increase in activity relative to **193**. Moreover, removal of the methoxy group from **203** yielded **204**, which elicited a gratifying 116% increase in activity relative to **193**, and a 227% increase in activity relative to the parent compound, **177**.

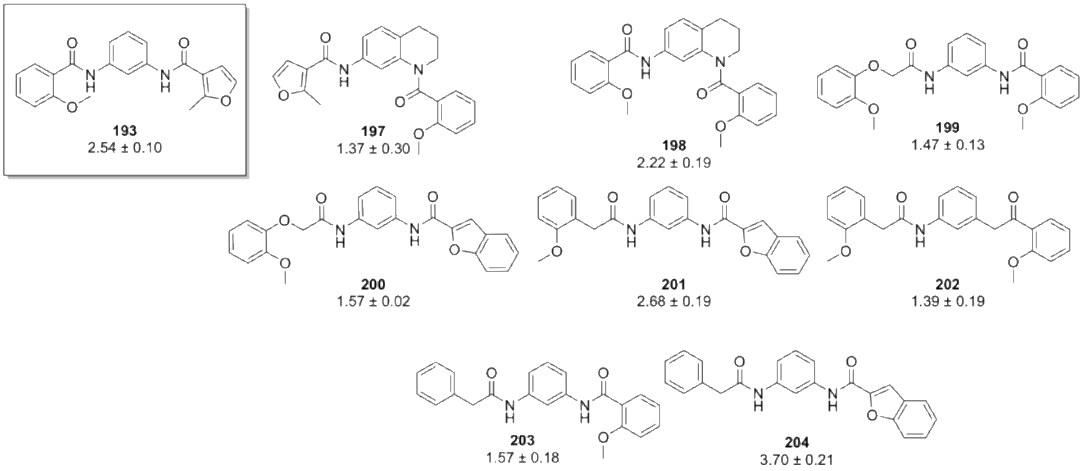

Figure 3-30 Structures and activities of analogs **197** – **204** derived from analog **193**

Values represent fold-changes in luminescence normalized to cell viability and relative to a DMSO control. Data represents the average ± standard deviation from at least three independent experiments. Compounds were synthesized by Meryl Thomas. Luciferase data were generated by Yuta Naro.

The two significantly improved analogs, **193** and **204**, were then evaluated in dose-response in the HeLa-miR21 stable cell line. Treatment with a dilution series of **193** and **204** for 48 h elicited EC_{50} values of 7.9 µM and 4.7 µM, respectively. Subsequently, a biochemical firefly luciferase assay was performed to confirm the activity observed for **193** and **204** was not due to firefly luciferase inhibition. Briefly firefly luciferase enzyme was incubated with **193** or **204** (10 µM) or DMSO (control; 0.1%; [v/v]) for 30 min, followed by addition of Bright-Glo reagent (Promega) and luminescence signal read-out (see Bright-Glo assay protocol 6.2.14 As expected, treatment with the positive control firefly luciferase inhibitor, PTC-124,[542] elicited a 90% reduction in firefly luciferase activity in the *in vitro* assay. However, incubation of the enzyme

with **193** or **204** did not induce any significant reduction in luciferase activity (Figure 3-31), suggesting that neither analog is a firefly luciferase inhibitor.

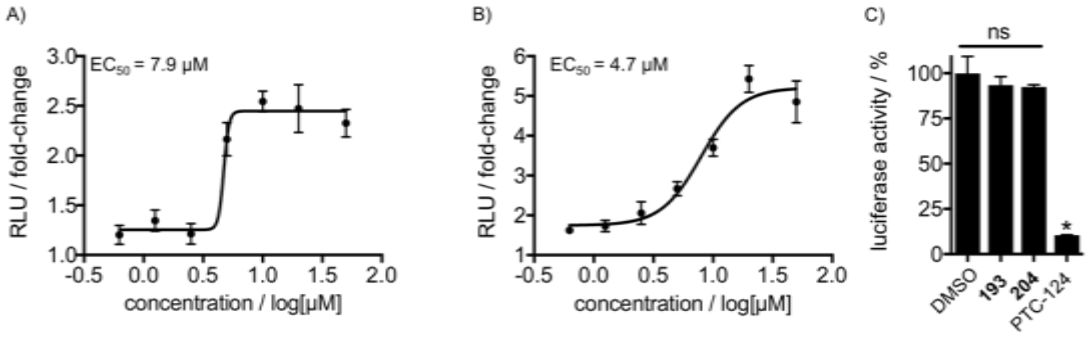

Figure 3-31 Dose-response in the HeLa-miR-21 assay and biochemical Fluc inhibition assay for analogs **193** and **204** HeLa-miR-21 cells were treated with a dilution series of A) analog **193** or B) **204** for 48 h, then a Bright-Glo assay and XTT cell viability assay were performed. Luciferase signal was normalized to cell viability and set relative to a DMSO control (RLU). C) *In vitro* firefly luciferase activity assay for miR-21 inhibitors **193** and **204**. PTC-124 was included as a positive control. All data are normalized to DMSO (negative control) and errors bars represent standard deviations from three independent experiments. Statistical significance was determined using an unpaired t-test, * $P < 0.05$, ns $P \geq 0.05$. Luciferase data were generated by Yuta Naro.

Next, we sought to determine the selectivity of **193** for miR-21 was evaluated by monitoring miR-122 function in the Huh7-miR122 reporter cell line. In contrast to the positive control, **20** (a known miR-122 inhibitor)[410] which induced a 3.5-fold increase in luminescence, treatment with **193** (10 µM) for 48 h had no effect on *Renilla* luciferase signal, demonstrating that **193** does not inhibit miR-122 activity and suggesting it may not be a general miRNA pathway

inhibitor (Figure 3-32). While analog **204** has not been tested in the miR-122 assay, we hypothesize based on the consistent results from **193**, that **204** should not inhibit miR-122 either.

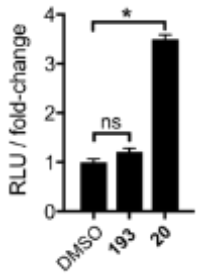

Figure 3-32 Evaluation of **193** in the Huh7-miR122 reporter cell line

Huh7-miR122 cells were treated with 10 µM of **193** for 48 h, then luciferase activity was monitored using a dual luciferase assay. Relative luciferase units (RLU) represents *Renilla* luciferase signal normalized to firefly luciferase control signal (RLU). Errors bars represent standard deviations from three independent experiments. Statistical significance was determined using an unpaired t-test, * $P < 0.05$, ns $P \geq 0.05$. Luciferase data were generated by Yuta Naro.

In order to begin exploring the mechanism by which these analogs inhibit miR-21 function, we utilized RT-qPCR to monitor mature miR-21 levels in response to treatment with **193** and **204**. Briefly, HeLa cells were treated with **193** or **204** at 10 µM or DMSO (0.1% [v/v]) for 48 h, followed by RNA isolation and quantification (see RT-qPCR protocol in section 3.3.2 Interestingly, no reduction in mature miR-21 was observed following treatment with either compound, suggesting a mechanism of action independent of miR-21 levels, similar to the oxadiazole analogs discussed above (Chapter 3.3). To further support this hypothesis, the previously described miR-21 promoter assay was employed to evaluate if analogs **193** and **204**

had any effect on transcription of the miR-21 gene. Transfection of the reporter into HeLa cells, followed by treatment with **193** or **204** (10 µM) or DMSO (0.1% [v/v]) for 48 h led to no changes in luciferase signal demonstrating no effect on miR-21 promoter activity and supporting the RT-qPCR data (Figure 3-33).

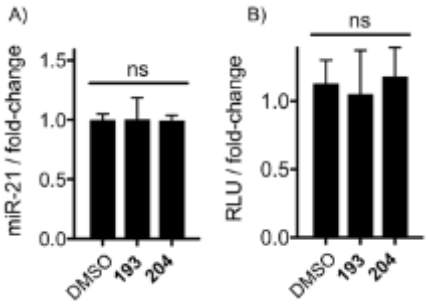

Figure 3-33 Effect of analogs **193** and **204** on mature miR-21 levels and miR-21 promoter activity

A) Treatment of HeLa cells with **193** or **204** (10 µM) for 48 h, followed by RT-qPCR analysis of mature miR-21 levels. RT-qPCR analysis was conducted using RNU19 as an internal standard. B) HeLa cells were transfected with the miR-21 promoter construct, followed by treatment with **193** and **204** (10 µM) for 48 h. Relative luciferase units (RLU) represents *Renilla* luciferase signal normalized to firefly luciferase control signal (RLU). All data were normalized to DMSO (negative control) and errors bars represent standard deviations from three independent experiments. Statistical significance was determined using an unpaired t-test, ns $P \geq 0.05$. Data were generated by Yuta Naro.

In order to further validate their activity, the improved inhibitors **193** and **204** were resynthesized and analyzed again for their miR-21 inhibitory activity. Because miR-21 is an oncomiR, we simultaneously analyzed the compounds for their effect on cell viability. Surprisingly, the resynthesized compounds no longer had any effect on miR-21 activity.

Interestingly, while **193** induced low micromolar efficacy in the majority of cancer cell lines evaluated (Table 16), a potent 145 nM IC_{50} was observed following treatment of SKOV3 ovarian cancer cells with the inhibitor, suggesting it may display cell type-specific toxicity. In contrast, while **204** was screened for its effect on cell viability in fewer cell lines (Table 17), it was only capable of eliciting micromolar IC_{50} values—including in SKOV3 cells—suggesting it is less potent than **193**.

Table 16 Cell viability assays following treatment with serial dilution of **193** for 72 h

cell line	phenotype	IC_{50}
MCF-7	breast cancer	>100 µM
HCT-116	colorectal cancer	2.8 µM
A498	renal cell carcinoma	>100 µM
SKOV3	ovarian cancer	145 nM
A549	lung adenocarcinoma	>100 µM
LN229	glioblastoma	5.6 µM

Table 17 Cell viability assays following treatment with serial dilution of **204** for 72 h

cell line	phenotype	IC_{50}
A498	renal cell carcinoma	>100 µM
SKOV3	ovarian cancer	32 µM
LN229	glioblastoma	10 µM

To determine if **193** might also inhibit tumorigenicity, we performed a two-week clonogenic assay in which SKOV3 cells were treated with a dilution series of the inhibitor or DMSO. Subsequently, each well was imaged on an Axio Observer Z1 microscope (Zeiss) using the tiling feature in Zen 2.0 software in addition to 800 µm thick z-stacks (Figure 3-34A). Contrast of all images was adjusted to be identical and colonies were quantified using ImageJ software. Gratifyingly, compound **193** inhibited colony formation with an EC_{50} of ~5 µM (Figure 3-34B), suggesting it may have therapeutic potential as a selective cytotoxic agent for treatment of ovarian cancer.

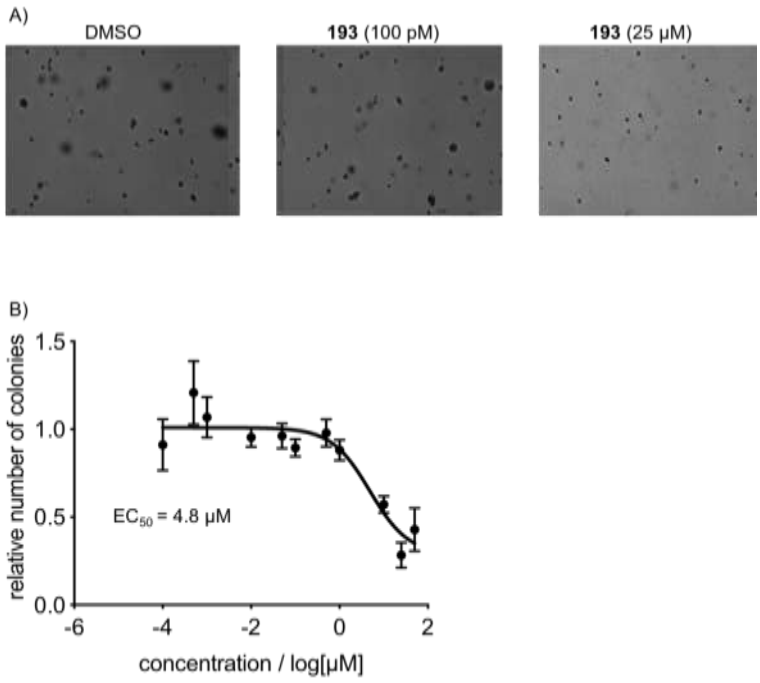

Figure 3-34 Treatment of SKOV3 cells in a two-week clonogenic assay

A) Representative images of a compressed z-stack of a single tile following treatment of SKOV3 cells with DMSO (0.1% [v/v]) or **193** at 100 pM or 25 µM. B) Dose response curve of number of colonies following treatment with **193**.

All data were normalized to DMSO (negative control) and errors bars represent standard deviations from three independent experiments.

3.5.1 Summary and Outlook

In conclusion, a class of selective miR-21 inhibitors was identified through the HTS. Due to potential instability of the hydrazone moiety in cells, the initial hit **177** was converted into a bis-amide scaffold generating several analogs with significantly improved activity over the initial hit. Initial mechanism of action studies support a mechanism by which **193** and **204** inhibit miR-21 independently of miR21 expression or levels of mature miR-21, similar to that of the oxadiazole class of miR-21 inhibitors (see section 3.3). Preliminary functional assays suggest that compound **193** may selectively inhibit cell viability in SKOV3 ovarian cancer cells. Moreover, treatment with **193** in a long-term clonogenic assay demonstrated the compound was capable of inhibiting colony formation in SKOV3 cells, suggesting it may have potential as a novel therapy for ovarian cancer.

That said, future work should focus on additional experiments to elucidate the mechanism of action in order to determine other potential applications of these compounds. Of note, this compound class has drawn concerns over reproducibility and inconsistency between experiments. Furthermore, it has been realized that compound **193** in particular shows a significant amount of toxicity in the HeLa-miR21 reporter cell line and thus its effect on miR-21 should be further explored.

3.5.2 Materials and Methods

Detailed protocols for all experiments conducted in this section are described in Materials and Methods section **3.3.2**

3.6 Nuclear Magnetic Resonance-guided Discovery of miR-21 Inhibitors

It has been estimated that only 1.5% of the human genome encodes proteins[543,544] and only 10 – 15% of these proteins are thought to be disease-related.[545-547] Moreover, current drugs targeting proteins interact with ~0.05% of the human genome.[548] In contrast, it is estimated that ~70% of the human genome is transcribed into non-coding RNAs,[2] and recently several classes of non-coding RNAs—most notably miRNAs—have been implicated in disease.[549,550] As such, there has been increasing interest in development of techniques towards the discovery of small molecules capable of binding directly to RNA with high affinity and specificity. Several methods to discover small molecule inhibitors of miRNAs that interact with the precursor hairpin are described in detail in Chapter 1.2.3 however, these approaches often result in compounds that are not selective or exhibit poor efficacy in cells. In order to overcome these limitations, Nymirum (a biotechnology start-up company in Ann Arbor, MI) is developing a platform for drug discovery based on small molecule-RNA binding interactions.

The platform was designed based on an approach developed by Hashim Al-Hashimi (a co-founder of Nymirum) and co-workers that combined molecular dynamics simulations with nuclear magnetic resonance (NMR) spectroscopy data.[551] Traditional docking approaches are more suitable for simulating protein-ligand binding interactions, but are often inadequate at addressing

the flexibility of RNA molecules. As an alternative, molecular dynamics simulations can be designed to treat the 'receptor' as an ensemble of conformations instead of a rigid conformation, however, these approaches are often prone to identification of false positives in virtual screening for RNA-binding ligands due to the higher flexibility of RNA molecules.[552,553] In order to overcome these limitations, Al-Hashimi developed an ensemble-based virtual screening approach that was informed by NMR residual dipolar coupling (RDC) data for transactivation response element (TAR) RNA.[551] RDCs are dependent on orientation of bond vectors within a biomolecule and can provide information about molecular dynamics on ps to ms time scales.[554,555] Briefly, >100,000 drug-like molecules augmented with 170 known TAR binding small molecules from the literature were screened experimentally for binding to the TAR RNA using a TAR-Tat displacement assay.[551] Subsequently, 17 small molecule hits identified following dose response assays were evaluated for TAR binding by NMR chemical shift titration. The experimental data were then used to generate sub-libraries utilized for evaluating enrichment of the virtual screening algorithm. Enrichment factors define the success of a virtual screening algorithm at suggesting compounds to screen experimentally by ordering the library with most active compounds first.[556] Interestingly, enrichment significantly increased for ensembles generated from molecular dynamics simulations performed with NMR data compared to those without. [551] Moreover, enrichment was highly dependent on ensemble size and accuracy. Taken together, this study suggested that conformational NMR data for RNAs could be combined with virtual screening approaches to identify RNA-binding small molecules.

In order to extend this work towards discovery of small molecule inhibitors of miRNAs, we initiated a collaboration with Nymirum in which we would apply our suite of cell-based screening assays and secondary assays described above to validate predicted hit molecules. All

compounds are commercially available, but the structures were not disclosed. Following receipt of compounds, we evaluated their activity and specificity according to a standard protocol (Figure 3-35). Briefly, a dilution series of each compound was generated, then HeLa-miR21 stable cells were treated with compound. Subsequently, luciferase activity was evaluated via a Bright-Glo assay. Compounds that elicited an increase in luciferase signal in the primary screen were then assessed through biochemical and cell-based firefly luciferase assays to determine if they non-specifically increased luminescence through direct binding to the enzyme or otherwise improving its stability. Potential lead molecules that had no effect in the luciferase control assays were treated in combination with the psiCHECK-miR122 reporter construct in Huh7 cells to identify general miRNA pathway inhibitors. Remaining small molecules that showed specificity for miR-21 over miR-122 were then evaluated via RT-qPCR.

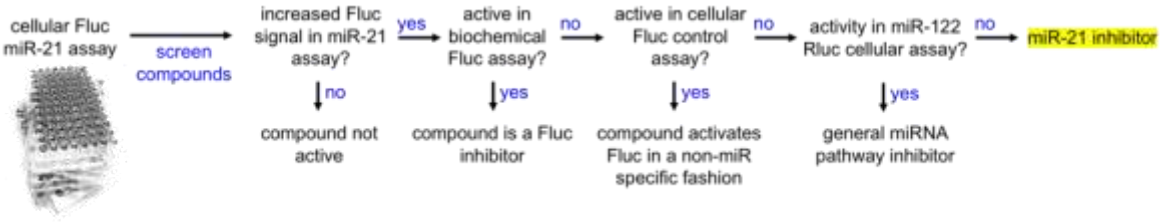

Figure 3-35 Pipeline for identification of miR-21 inhibitors

From the initial batch of six compounds, we identified compound 2 and 6 from the primary screen as potential lead molecules, eliciting an EC_{50} of 0.8 and 4.8 µM, respectively (Figure 3-36A). Compound 2 showed ~30% reduction in cell viability at 12.5 µM, while compound 6 did not induce toxicity at any concentration (Figure 3-36B). In the *in vitro* Fluc assay, the known

luciferase inhibitor PTC-124 displayed almost 80% inhibition of luminescence at 12.5 μM while compound 2 induced up to a ~20% reduction in luciferase signal and compound 6 did not lead to inhibition (Figure 3-36C). Moreover, 2 elicited a ~3.5-fold increase in luminescence in the psiCHECK-empty assay, indicating it inhibits Fluc, while compound 6 had no effect (Figure 3-36D). Finally, while the positive control **20** (10 μM) displayed an 8-fold increase in the miR-122 assay, as expected, compound 6 had no effect at the same concentration, suggesting it is not a general miRNA pathway inhibitor (Figure 3-36E). Similarly, compound 2 did not inhibit miR-122.

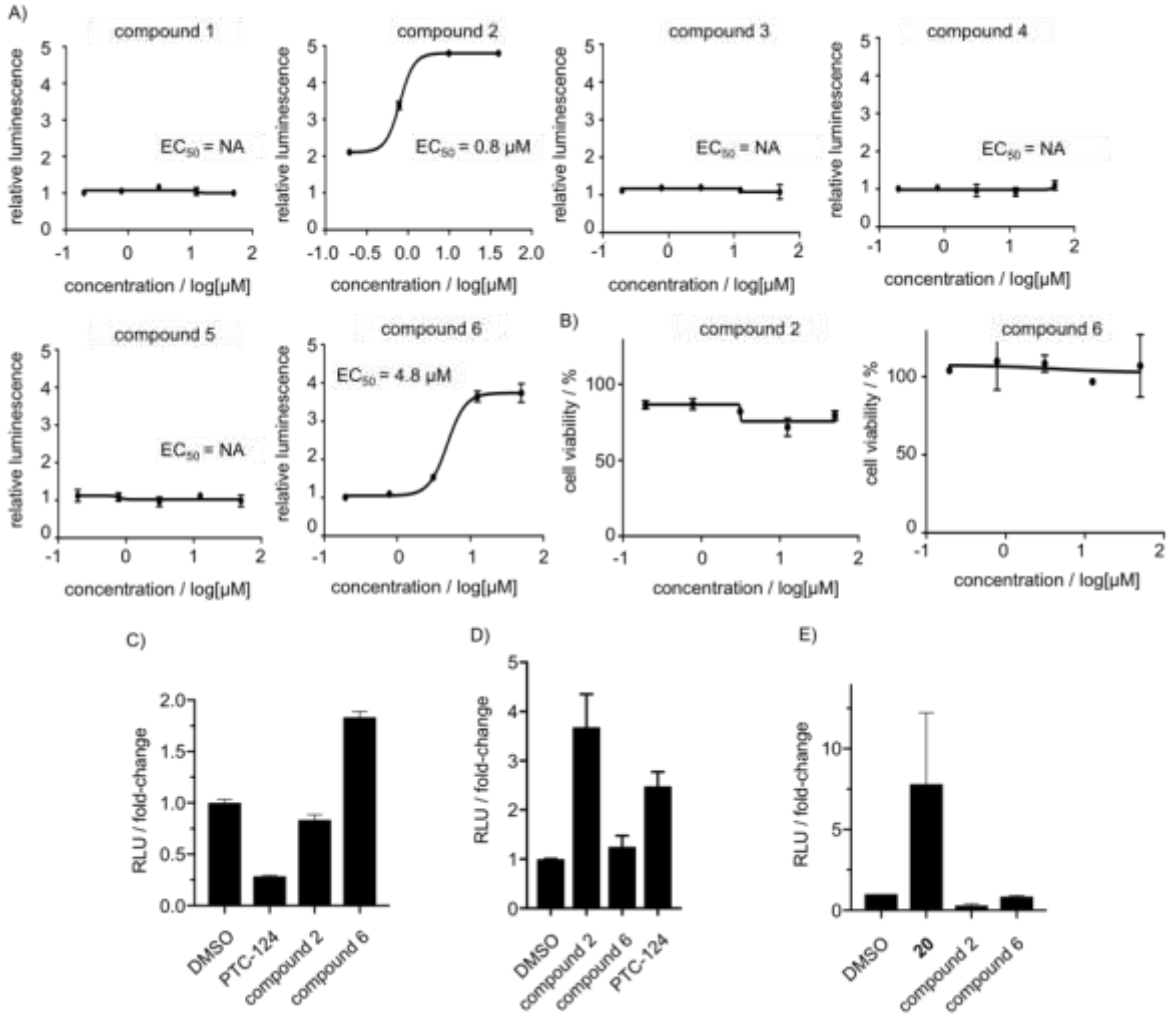

Figure 3-36 Evaluation of Nymirum compounds 1 – 6

A) HeLa-miR21 stable cells treated with a dilution series of each compound or 0.5% (v/v) DMSO (control) for 48 h, followed by BrightGlo luciferase assay and XTT cell viability assay. Luciferase data are normalized to cell viability data for each compound, then set relative to DMSO. B) XTT cell viability assay was performed after treatment with compounds 2 and 6 in HeLa cells for 48 h. C) Recombinant firefly luciferase was incubated with compounds 2, 6, or PTC-124 at 12.5 µM, followed by a BrightGlo luciferase assay. D) HeLa cells were transfected with the psiCHECK-empty plasmid, then treated with compounds 2, 6, or PTC-124 (10 µM) for 48 h, followed by a dual luciferase assay. Firefly luciferase data were normalized to *Renilla* luciferase data. D) Huh7-miR122 cells were treated with compounds 2, 6, or 20 (10) µM for 48 h, then dual luciferase assay was performed. *Renilla* luciferase data were normalized to

firefly luciferase data. All treatment data were normalized to DMSO control. Errors bars represent standard deviations from three independent experiments.

The majority of the molecules from the second set received from Nymirum were inactive in the primary assay (Figure 3-37), however, compound 13 displayed an EC_{50} of 167 nM—an improvement over the previous lead molecule 6.

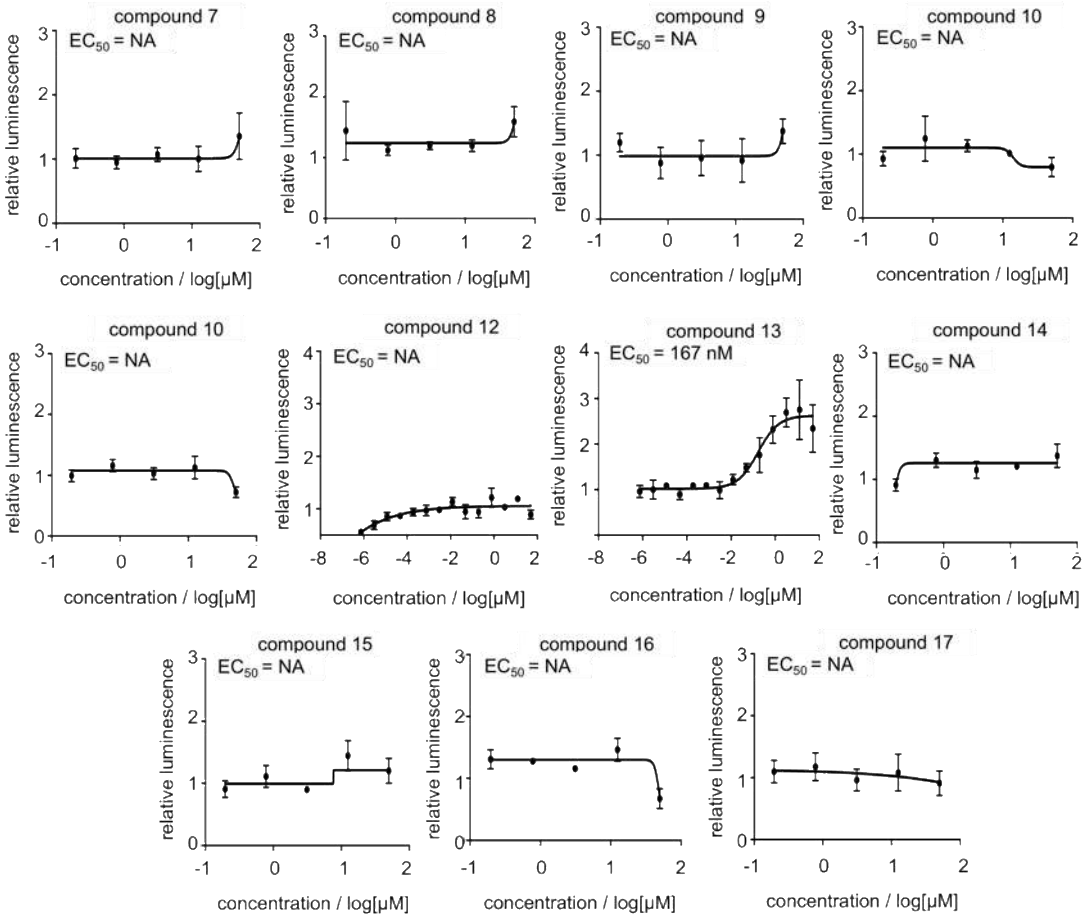

Figure 3-37 Evaluation of Nymirum compounds 7 – 17 in the HeLa-miR21 reporter cell line

HeLa-miR21 stable cells were treated with a dilution series of each compound in 0.5% (v/v) DMSO or 0.5% (v/v) DMSO (control) for 48 h, then BrightGlo luciferase assay and XTT cell viability assay were performed. Luciferase data are normalized to cell viability data for each compound, then set relative to DMSO.

While compound 13 exhibited toxicity at higher concentrations (Figure 3-38B), it had no effect on luciferase expression in the psiCHECK-empty assay (Figure 3-38C). Furthermore, compound 13 does not inhibit miR-122 in the reporter assay, suggesting it is not a general miRNA pathway inhibitor (Figure 3-38D). In a RT-qPCR assay, our previously reported miR-21 inhibitor

14, inhibits both mature and pre-miR-21 levels (Figure 3-38E). Interestingly, compounds 6 and 13 both reduce mature miR-21 expression levels as expected, however, while compound 13 has no effect on pre-miR-21 levels, compound 6 is still capable of inhibiting expression of the precursor miRNA. Taken together, this suggests that compound 6 may not inhibit miR-21 through binding to the hairpin, but inhibitor 13 may stabilize pre-miR-21 thus preventing its processing.

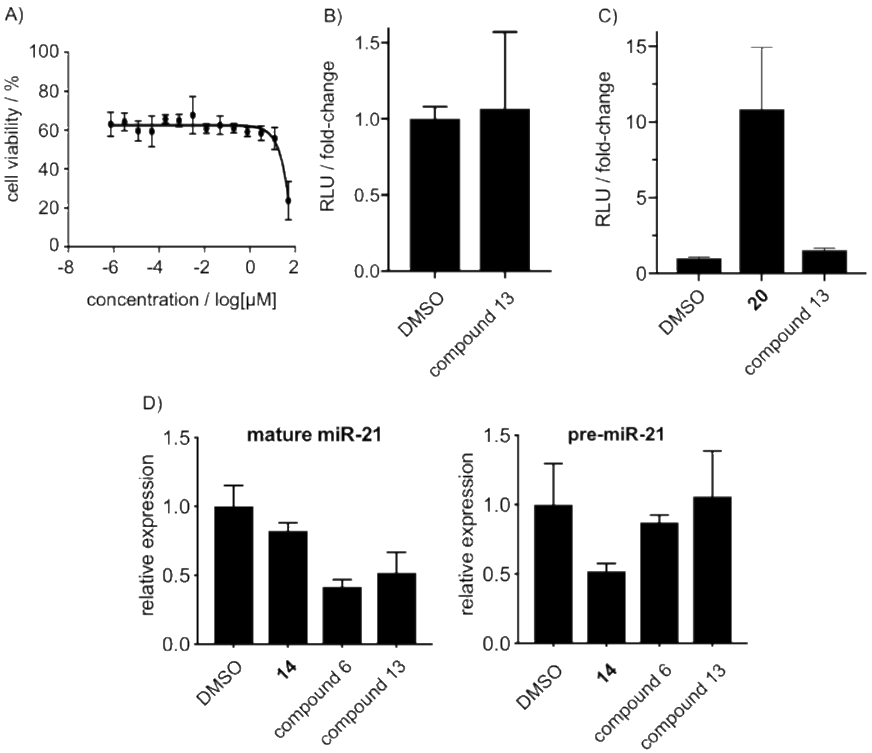

Figure 3-38 Evaluation of specificity of compounds 6 and 13

A) XTT cell viability assay was performed after treatment with compound 13 in HeLa cells for 48 h. Data are normalized to DMSO control. C) HeLa cells were transfected with the psiCHECK-empty plasmid, then treated with compound 13 (10 µM) for 48 h, then dual luciferase assay was performed. Firefly luciferase data were normalized to *Renilla* luciferase data, then all treatment data were normalized to DMSO control. D) Huh7-miR122 cells were treated with compound 13 or 20 for 48 h, then dual luciferase assay was performed. Firefly luciferase data were normalized to *Renilla* luciferase data, then all treatment data were normalized to DMSO control. E) HeLa cells were treated with

14, compound 6, or compound 13 in 0.1% (v/v) DMSO or DMSO control for 48 h, then RT-qPCR was performed using commercial Taqman probes (mature miR-21 and RNU19 [control]) or synthetic DNA probes (pre-miR-21 and GAPDH [control]). Errors bars represent standard deviations from three independent experiments.

Several additional compounds were also evaluated, and while some were active in the primary screen (Figure 3-39), none showed an improvement over the previous compound 13.

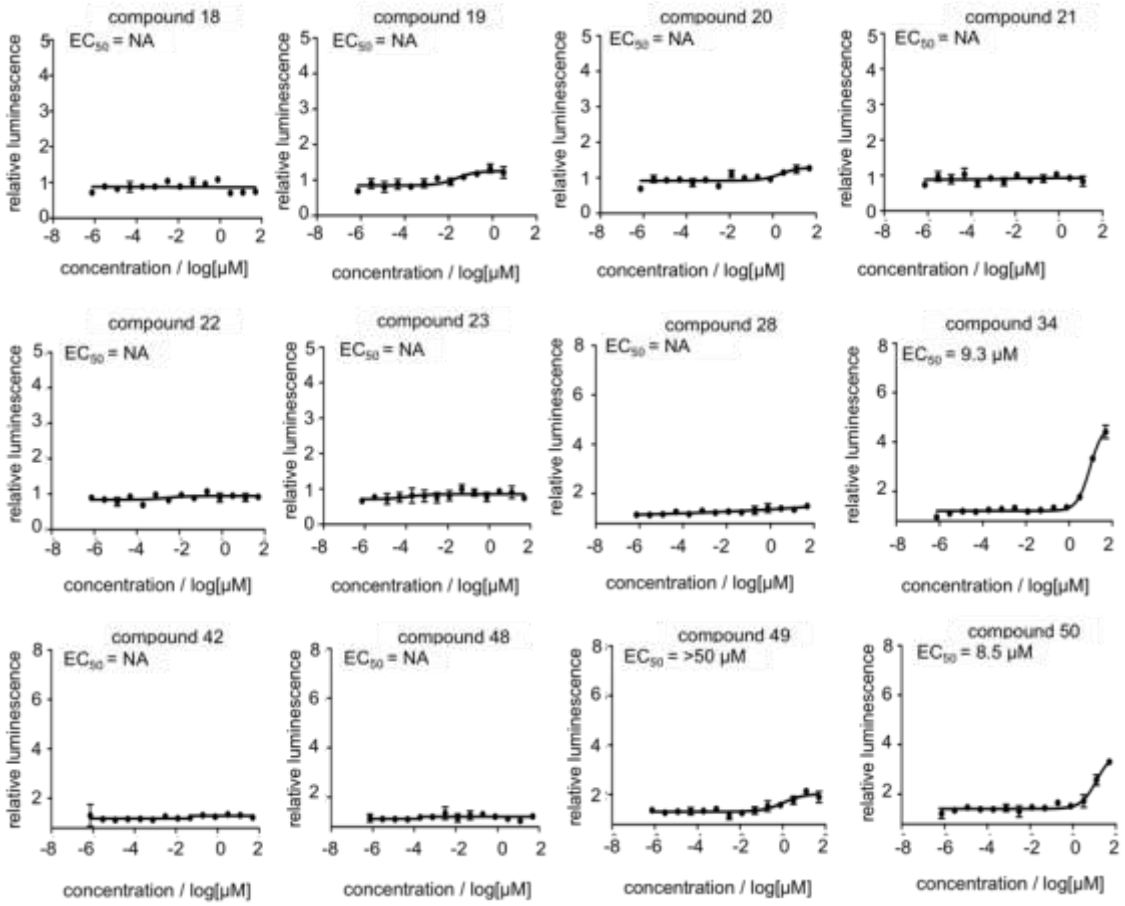

Figure 3-39 Evaluation of Nymirum compounds 18 – 23, 28, 34, 42, and 48-50 in HeLa-miR21 reporter cells. HeLa-miR21 stable cells were treated with a dilution series of each compound in 0.5% (v/v) DMSO or 0.5% (v/v) DMSO (control) for 48 h, then BrightGlo luciferase assay and XTT cell viability assay were performed. Luciferase data are normalized to cell viability data for each compound, then set relative to DMSO. Errors bars represent standard deviations from three independent experiments

As such, we proceeded to explore six analogs of compound 13 in a small SAR study. Unfortunately, none of the analogs displayed increased activity relative to parent compound 13 in the primary screen, however, analogs 13.2 and 13.6 retained activity, eliciting 96 nM and 87.9 nM

EC_{50} values, respectively (Figure 3-40A). Additionally, 13.3, while showing a modest reduction in efficacy relative to the parent compound (1.0 µM), retained a 3-fold increase in luciferase activity at higher concentrations suggesting it was still a potential lead molecule. Moreover, while 13.2 had a modest effect on cell viability at 50 µM, 13.3 and 13.6 were non-toxic at concentrations up to 50 µM (Figure 3-40B).

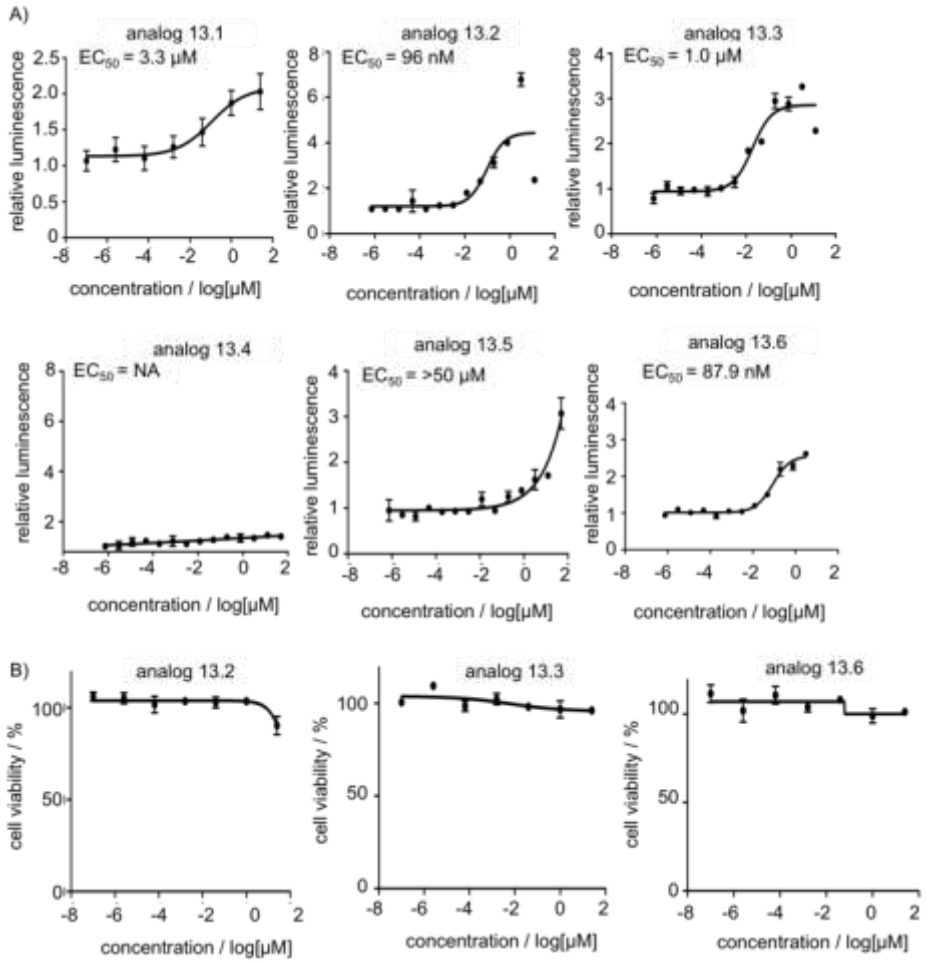

Figure 3-40 Evaluation of Nymirum analogs of compound 13

A) HeLa-miR21 stable cells were treated with a dilution series of each compound in 0.5% (v/v) DMSO or 0.5% (v/v) DMSO (control) for 48 h, then BrightGlo luciferase assay and XTT cell viability assay were performed. Luciferase

data are normalized to cell viability data for each compound, then set relative to DMSO. B) XTT cell viability assay was performed after treatment with analog 13.2, 13.3, and 13.6 in HeLa cells for 48 h. Data are normalized to DMSO control.

Unfortunately, in the psiCHECK-empty assay, 13.2 induced a ~2.5-fold increase in luminescence at 1 μM suggesting it was a false-positive, however, analogs 13.3 and 13.6 had no effect (Figure 3-41C). Additionally, 13.3 and 13.6 were also not identified as general miRNA pathway inhibitors as they had no effect on miR-122 function in the reporter assay (Figure 3-41D). In contrast, 13.2 elicited a similar increase in luminescence to the positive control, **20**. Finally, analogs 13.5 and 13.6 elicited similar reductions in miR-21 levels to the parent compound 13 in RT-qPCR experiments (Figure 3-41E). However, while treatment with 13.5 also led to reduced pre-miR-21 levels, analog 13.6 induced a modest increase in the precursor miRNA, suggesting it stabilizes the hairpin, in contrast to the parent compound.

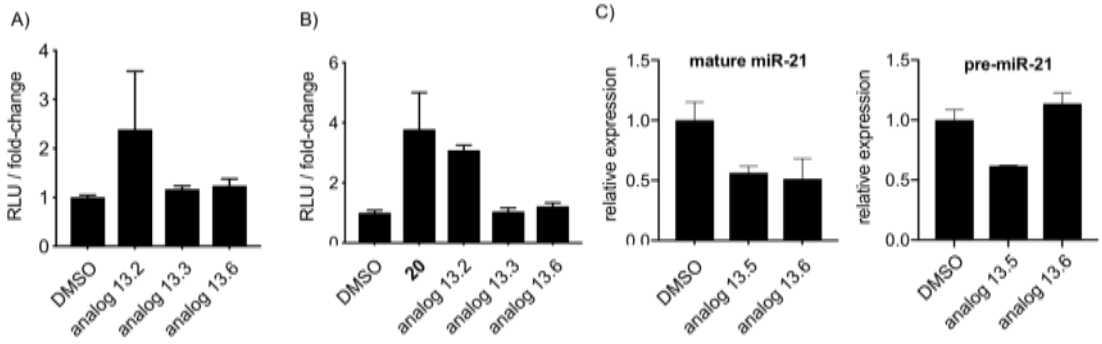

Figure 3-41 Evaluation of specificity of compound 13 analogs

A) HeLa cells were transfected with the psiCHECK-empty plasmid, then treated with 13.2, 13.3, and 13.6 (10 μM) for 48 h, then dual luciferase assay was performed. Firefly luciferase data were normalized to *Renilla* luciferase data. B) Huh7-miR122 cells were treated with 13.2, 13.3, and 13.6 (10 μM) for 48 h, then dual luciferase assay was

performed. Firefly luciferase data were normalized to *Renilla* luciferase data. C) HeLa cells were treated with 13.5 and 13.6 (10 μM) or DMSO control for 48 h, then RT-qPCR was performed using commercial Taqman probes (mature miR-21 and RNU19 [control]) or synthetic DNA probes (pre-miR-21 and GAPDH [control]). All data were normalized to the DMSO control. Errors bars represent standard deviations from three independent experiments.

3.6.1 Summary and Outlook

Taken together, we experimentally evaluated 36 small molecules predicted to bind pre-miR-21 using a computational platform driven by NMR data, as well as six analogs of a lead compound. While several of the molecules were inactive in the stable HeLa-miR21 cell line, we identified multiple potential hit compounds and subjected them to a series of secondary assays. The top molecule from the initial screen, compound 13, displayed an EC_{50} of ~167 nM, similar to our previously reported miR-21 inhibitors, and was capable of reducing mature miR-21 levels by ~50% while maintaining pre-miR-21 levels. Moreover, while the analogs 13.5 and 13.6 showed similar activity to the parent compound in the primary screen as well as in RT-qPCR assessment of mature miR-21 levels, 13.6 was capable of inducing a modest increase in pre-miR-21 levels suggesting it stabilized the hairpin, in good agreement with previously reported precursor miR-21-binding small molecules.

Future studies should focus on developing additional analogs of the lead compound 13 to better determine the structural requirements for its activity and potentially identify a more potent inhibitor. Additionally, small molecules identified as hit compounds should be evaluated against multiple other miRNAs to further validate their specificity. Finally, additional compounds should be screened in order to better inform the virtual screening algorithm in order to potentially identify

a relationship between parameters such as binding affinity or RNA structural features and inhibitory function of the small molecules.

3.6.2 Materials and Methods

Detailed protocols for all experiments conducted in this section are described in Materials and Methods section **3.3.2**

3.7 A HT-MS Method for Discovery of miR-21 Inhibitors

High-throughput screening (HTS) assays are routinely employed toward the discovery of novel drug candidates. The length, complexity, and cost of drug discovery and development are recognized as leading factors in declining productivity within Pharma and Biotech. The process can take 10-15 years with recent cost estimates of $2.9 billion/drug approval.[557] One particular area that is hampered by lengthy drug development timelines is the study of oligonucleotide-mediated processes, such as gene regulation by DNA methylation or non-coding RNAs, which are rapidly gaining attention for their therapeutic and diagnostic potential.[558-563] Utilization of methods such as high-throughput mass spectrometry (HT-MS) have been routinely applied to proteins and peptides,[564-567] however, they have not been extended to nucleic acids due to desalting and analyte enrichment procedures required for handling oligonucleotide samples. As such, and in collaboration with MS^2 Array (a biotechnology start-up company in Pittsburgh, PA), we sought to develop a novel, commercially accessible HT-MS assay platform for analysis of nucleic acids that combines selective analyte enrichment, simple sample preparation, and biological compatibility.

The keystone of this assay is fluorous partitioning-based analyte capture and enrichment. Perfluroalkyl-modified molecules have been previously shown to selectively partition into perfluoroalkyl phases by what is now termed, 'fluorous chemistry'.[568,569] Since its discovery, fluorous partitioning has been employed for separations in the synthesis and purification of various molecules[570-572] including nucleic acids.[573,574] Furthermore, the hydrophobicity and lipophobicity of fluorous partitioning have been exploited in proteomics[575,576] and microarrays[577-579] where its high selectivity, chemical inertness, and bio-orthogonality has been advantageous. In light of these advantages, we attempted to develop a fluorous HT-MS (F-HT-MS) assay platform for miRNA processes that could demonstrate the utility of the platform and provide proof-of-concept data for Phase II studies.

As the primary analytical method for our platform, we chose to employ matrix-assisted laser desorption (MALDI)-mass spectrometry (MS). MALDI-MS makes use of an energy-absorbent, organic matrix to promote soft ionization of an analyte and results in the formation of single ions with minimal fragmentation and excellent sensitivity.[580] Recently, MALDI-MS has emerged as a gold standard for HT-MS, particularly in the analysis of biological samples.[581-583] In contrast, HT-MS of nucleic acids has been challenging primarily due to the susceptibility of the negatively charged phosphodiester backbone to salt adducts and fragmentation.[584] Several desalting protocols[585-588] and matrix formulations[589-593] have been developed, however, their limited robustness and lack of automation are limitations for high-throughput and diagnostic applications.

In a related approach, self-assembled monolayer/MALDI-MS (SAMDI-MS) has been utilized for RNA and DNA HT-MS through the use of biotinylated nucleic acids on a gold-biotin-streptavidin (SAMDI-SA) surface.[594,595] However, SAMDI-MS has several inherent limitations

including surface stability,[596,597] cost,[598] and bio-compatibility.[599-602] To overcome these limitations, MS^2 Array developed the first commercially viable fluorous MS target surface. Fluorous modification of metal oxide coated glass slides forms a fluorous conductive surface necessary for laser ionization of fluorous-tagged analytes.[603,604] Compared to standard MALDI surfaces the fluorous coated plates are amenable to on-surface washing to remove salts, detergents, and other ion suppressive components while retaining the analyte for MS analysis. MS^2 Array has previously demonstrated that fluorous-modified peptides are effectively captured on the fluorous surface and are readily ionized after washing and addition of the matrix. Using this approach, they observed a dramatic improvement in signal to noise (S/N) compared to standard MALDI-MS, enabling detection of peptide concentrations as low as 1 nM or 400 amol. The fluorous surface exhibits enhanced stability (>2-year shelf life), low cost, facile manufacturing, and bio-orthogonality. Furthermore, the fluorous surface has a loading capacity of 5.0×10^{-9} mol/cm^2, a 1000-fold increase compared to SAMDI-SA which only provides a density of 7.9×10^{-12} mol/cm^2,[272] suggesting that the fluorous surface may provide greater sensitivity and dynamic range. It was hypothesized that this improvement in detection of an analyte from a complex biological mixture was achieved via the removal of cellular and buffer components resulting in enhanced matrix crystallization and reduced ion suppression.

With the fluorous-coated plates in hand, we sought to optimize a general protocol for spotting, on-surface desalting and enrichment, matrix addition, and MALDI-MS detection of fluorous-modified nucleic acids. As a proof-of-concept, we decided to apply the methodology towards detection of pre-miRNA cleavage by Dicer which is known to produce different miRNA isoforms (isomiRs),[605,606] as described in detail above. We hypothesized that MS detection would provide a methodology to readily differentiate between various isomiRs. Furthermore, this

approach is proposed to address previous shortcomings in analysis of endogenous nucleic acids from biological samples such as cell lysate usually attributed to poor analyte enrichment, difficulty in sample preparation, and bio-compatibility.

In order to evaluate our approach, we selected pre-miR-21 because of its well-established biological relevance (Chapter 3.1). The full length pre-miR-21 (72 nt), Dicer cleavage fragment (7 nt), and dummy DNA internal control (22 nt) were purchased from Dharmacon and a fluorous-tagged phosphoramidite (**205**) was incorporated after an 18 carbon spacer at the 5' terminus during RNA synthesis (Figure 3-42A). The pre-miR-21 sequence was selected from miRbase, an online miRNA repository, and has been reported to be a suitable substrate for Dicer.[607] Initially, we utilized a recombinant Dicer enzyme kit (Genlantis) to attempt to digest the fluorous-tagged pre-miR-21. In order to determine if the bulky fluorous tag would inhibit Dicer processing, a pre-miR-21 oligonucleotide bearing a less sterically demanding amine modification was employed as a control. Briefly, 1 µg of RNA was combined with assay buffer containing ATP (1 mM) and $MgCl_2$ (2.5 mM), then 1 U of recombinant Dicer was added. The reaction was incubated overnight at 37 °C. The following day, a stop solution (supplied with the kit) was added and the reaction mixture was separated on a 16% native PAGE gel. Subsequently, the gel was stained with SYBR Gold (Invitrogen) and imaged on a ChemiDoc XRS+ (Bio-Rad). Unfortunately, the recombinant Dicer failed to cleave either of the RNAs (Figure 3-42B). Furthermore, the enzyme failed to cleave a green fluorescent protein (GFP) control mRNA utilized by Genlantis to validate activity of their enzymes. After observing no Dicer-mediated cleavage of the GFP control or pre-miR-21 oligonucleotides in two separate experiments, we obtained a second stock of the Dicer enzyme from Genlantis and attempted to perform the Dicer processing assay again following the Genlantis protocol. Unfortunately, even with the new stock of enzyme we did not observe cleavage of the

pre-miRNA hairpin or the control RNA. As such, we hypothesized that cleavage conditions (e.g., buffer content, enzyme concentration, and RNA concentration) would need to be optimized and thus pursued alternative methods based on previous literature reports.

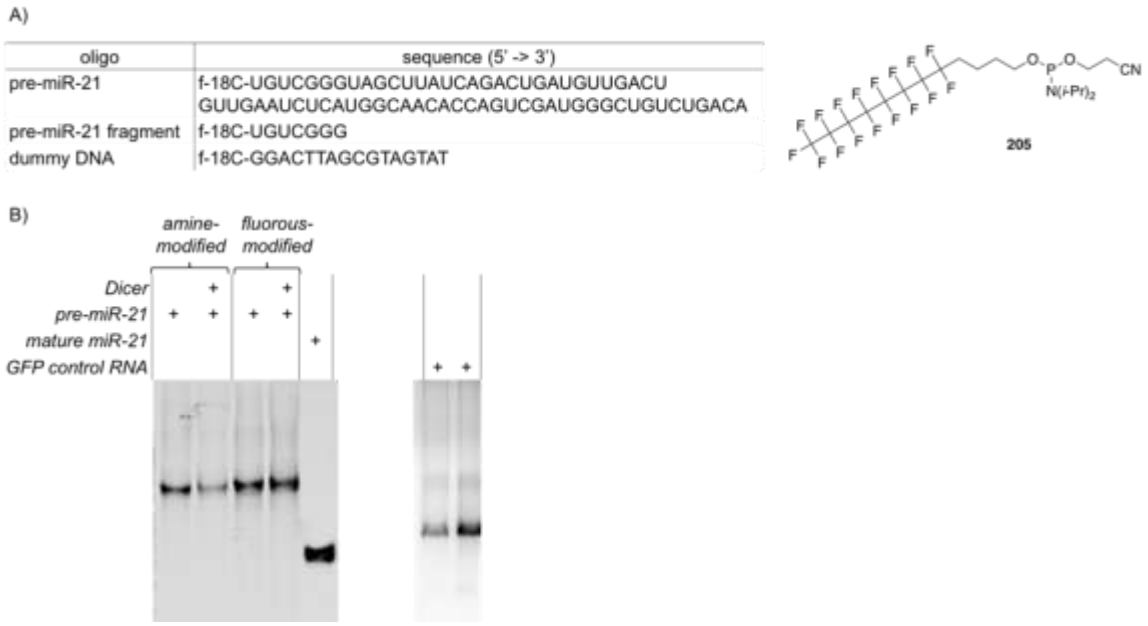

Figure 3-42 Evaluation of a commercial recombinant Dicer enzyme kit

A) Synthetic nucleic acid sequences for pre-miR-21 (72 nt), pre-miR-21 fragment (7 nt), and dummy DNA (22 nt) and structure of the fluorous-tagged phosphoramidite. f = fluorous tag; 18C = 18 carbon spacer. Fluorous tag was added via incorporation of **205** during RNA synthesis by Dharmacon. B) pre-miR-21 (amine- or fluorous-modified) was incubated with recombinant Dicer (Genlantis) following the manufacturer's protocol, then analyzed via native PAGE. GFP mRNA (control) was digested following the same protocol and analyzed via agarose gel electrophoresis.

First, we attempted to use the approach developed by Garner and co-workers in their cat-ELCCA assays.[285] The notable differences in this assay was the lack of ATP as well as alterations to the amount of enzyme, concentration of RNA, and reaction time. Briefly, RNAs were diluted to

500 nM in the assay buffer and combined with 0.25 U of recombinant Dicer (Genlantis). The reaction was incubated at 37 °C for 1 h, followed by native PAGE and visualization on the ChemiDoc XRS+ after SYBR Gold staining. Unfortunately, we did not observe a band corresponding to the mature miR-21 duplex (Figure 3-43A), suggesting this protocol was also not sufficient for achieving Dicer cleavage. Adapting a similar protocol from the Schneekloth laboratory[265] also yielded disappointing results. Concentrations of both the fluorous-modified pre-miR-21 (Figure 3-43B) and Dicer (Figure 3-43C) were varied, however, the mature miR-21 duplex was still not observed. Furthermore, utilizing the same protocol with the non-modified pre-miR-21 hairpin failed to deliver the cleavage product (Figure 3-43D).

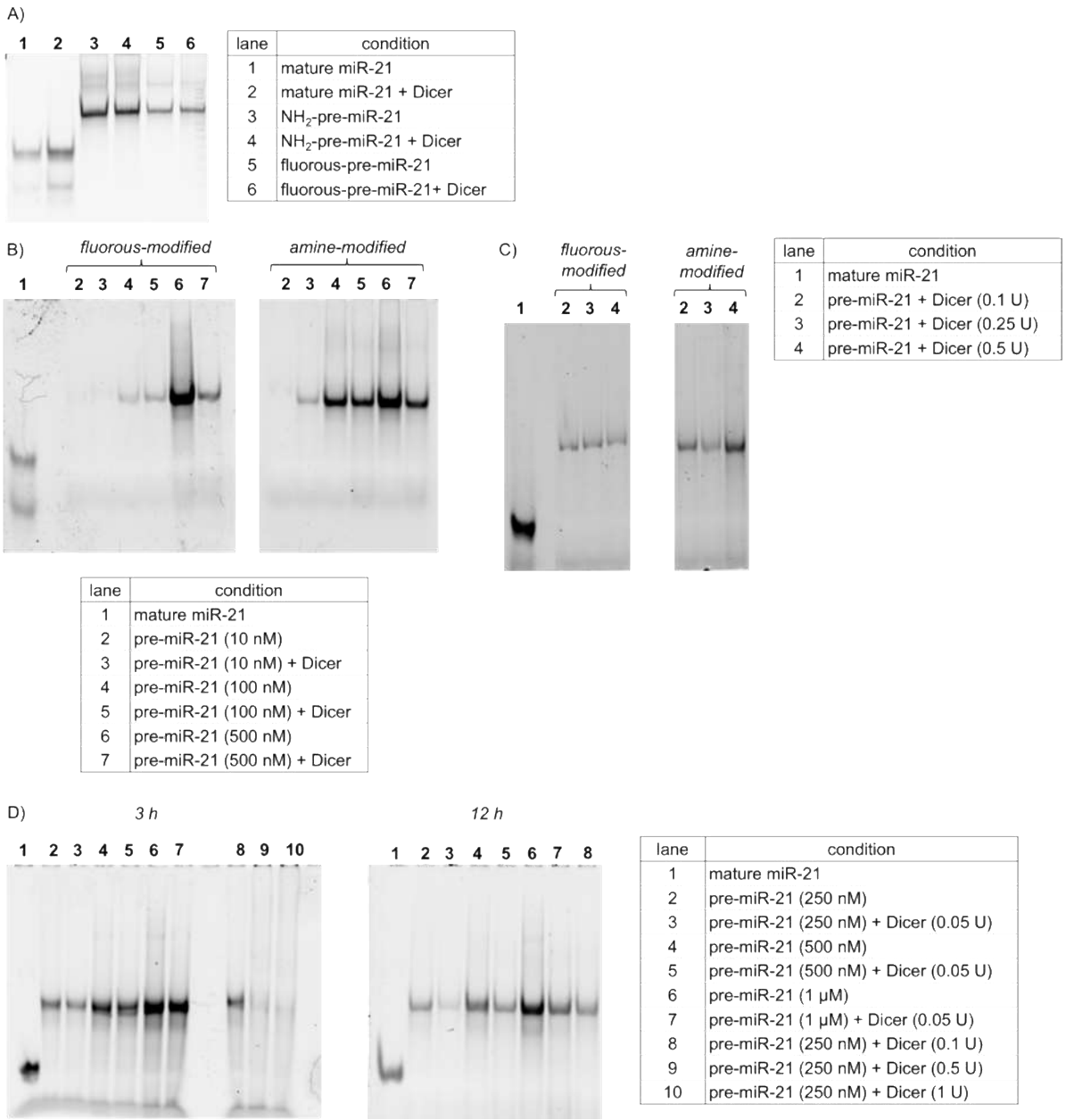

Figure 3-43 *In vitro* pre-miR-21 processing using Genlantis recombinant Dicer

A) Dicer processing assay was performed with 500 nM RNA for 1 h at 37 °C with enzyme (Genlantis; 0.25 U) following Amanda Garner's protocol. B) pre-miR-21 was incubated at different concentrations with Dicer (0.05 U) following Jay Schneekloth's Dicer protocol. C) Dicer concentrations were varied in the presence of pre-miR-21 (10 nM) following Jay Schneekloth's protocol. D) The Dicer processing assay was performed following the Schneekloth

protocol using non-modified pre-miR-21 with variations in RNA concentration, Dicer concentration, and reaction time. Reactions were analyzed via native PAGE followed by SYBR Gold staining.

We hypothesized that the Dicer enzyme obtained from Genlantis exhibited poor activity. To evaluate if the source of the enzyme was causing the lack of activity, we purchased recombinant Dicer from Origene. Unlike the Genlantis Dicer, the enzyme from Origene was not part of a kit, so buffers had to be prepared separately. As such, we adopted a general dicing buffer reported by the MacRae laboratory[608] and successfully employed by our collaborators at Nymirum (see chapter 3.6) to achieve processing of the pre-miRNA with Dicer from Origene (data not shown). Briefly, the amine-, fluorous-, or non-modified pre-miR-21 was pre-incubated at 500 nM in assay buffer (HEPES [40 mM; pH 7.4], NaCl [100 mM], $MgCl_2$ [3 mM], DTT [1 mM]) for 30 min at room temperature. Subsequently, recombinant Dicer (Origene) was added to a final concentration of 61.8 nM and the reaction was incubated at 37 °C for 1 h or overnight. At the completion of the reaction, a stop solution (urea [6 M], EDTA [250 mM], glycerol [10% (v/v)], bromophenol blue [0.1% (w/v)]) was added and the samples were analyzed via native PAGE followed by staining with SYBR Gold and imaging on the ChemiDoc XRS+. Similar to the Dicer obtained from Genlantis, the recombinant Dicer from Origene was not capable of cleaving the pre-miR-21, regardless of modifications or lack thereof (Figure 3-44). This suggests that commercial sources of Dicer may not be optimal for these assays.

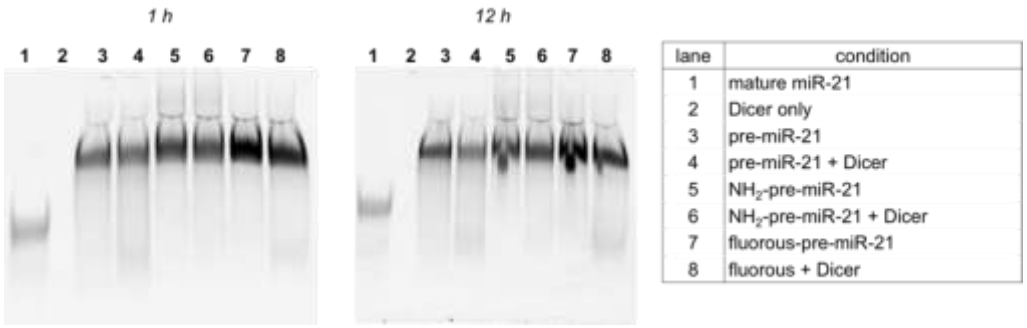

lane	condition
1	mature miR-21
2	Dicer only
3	pre-miR-21
4	pre-miR-21 + Dicer
5	NH_2-pre-miR-21
6	NH_2-pre-miR-21 + Dicer
7	fluorous-pre-miR-21
8	fluorous + Dicer

Figure 3-44 *In vitro* pre-miR-21 processing assay with Origene Dicer

Processing assay was carried out following Ian MacRae's protocol with pre-miR-21 (500 nM) and Dicer (Origene; 61.5 nM). Reacrtions were analyzed after 1 or 12 h via native PAGE followed by SYBR Gold stain.

Several reports have utilized Dicer protein expressed in mammalian cells (as opposed to purchasing the recombinant protein from commercial vendors) to investigate activity of the enzyme.[18,20,609,610] Moreover, binding of TRBP with Dicer has been shown to enhance cleavage of precursor miRNAs.[22,293] As such—and to reduce the cost of the assay—we attempted to perform Dicer cleavage assays utilizing the endogenous enzyme in cell lysate. Initially, we attempted to follow an approach reported by the Arenz lab.[271] Briefly, HEK293T cells were grown to ~95% confluence in a 10 cm tissue culture treated plate, then trypsinized and lysed via vortexing in assay buffer (Tris-HCl [20 mM; pH 7.5], NaCl [12.5 mM], $MgCl_2$ [2.5 mM], and DTT[1 mM]) supplemented with glycerol (10% [w/v]) and 1x protease inhibitor cocktail. Subsequently, the lysate was centrifuged, and the supernatant was retained. For the Dicer cleavage assays, amine-modified pre-miR-21 was diluted in assay buffer and supplemented with 10% (v/v) of lysate. The reaction was incubated at 37 °C for 3 h, then separated via denaturing PAGE and analyzed following SYBR Gold staining on the ChemiDoc XRS+. Unfortunately, the lysate was also not

sufficient for achieving Dicer cleavage (Figure 3-45). Moreover, supplementing recombinant Dicer (Genlantis; 0.25 U) did not yield the expected mature miR-21 duplex.

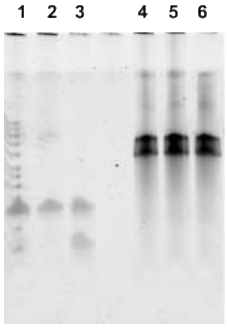

lane	condition
1	mature miR-21 + lysate
2	mature miR-21 + lysate + Dicer
3	mature miR-21
4	NH_2-pre-miR-21 + lysate
5	NH_2-pre-miR-21 + lysate + Dicer
6	NH_2-pre-miR-21

Figure 3-45 Dicer cleavage assay following the Arenz protocol

Dicer processing assay was performed in HEK293T cell lysate with pre-miR-21 (500 nM) and additional recombinant Dicer (Genlantis; 0.25 U) included.

The Garner, Schneekloth, and Arenz methods omitted ATP, however, several reports have suggested that ATP binding to the helicase domain of Dicer is required for its function.[143,144] To determine if the lack of ATP was inhibiting Dicer function, we explored additional protocols. For example, Siomi and co-workers employed an ATP replenishment system in cell lysate wherein creatine phosphokinase generates free ATP by acting on its substrate, creatine phosphate.[611] Disappointingly, after a 3 h incubation of the amine-modified pre-miR-21 with the ATP replenishment system and 10% (v/v) HEK293T lysate, the mature miR-21 duplex was not observed. (Figure 3-46A) We also attempted a similar approach by the Tuschl laboratory,[612] but even after increasing the incubation time from 1 to 12 h, we did not observe cleavage of the

fluorous- or amine-modified pre-miR-21 hairpin (Figure 3-46B,C). Pre-annealing the RNA hairpin also had no effect on Dicer activity.

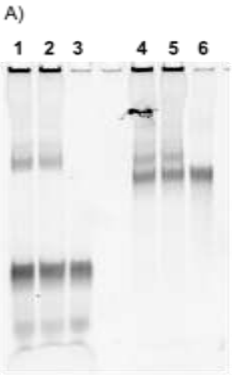

lane	condition
1	mature miR-21 + lysate
2	mature miR-21 + lysate + Dicer
3	mature miR-21
4	NH_2-pre-miR-21 + lysate
5	NH_2-pre-miR-21 + lysate + Dicer
6	NH_2-pre-miR-21

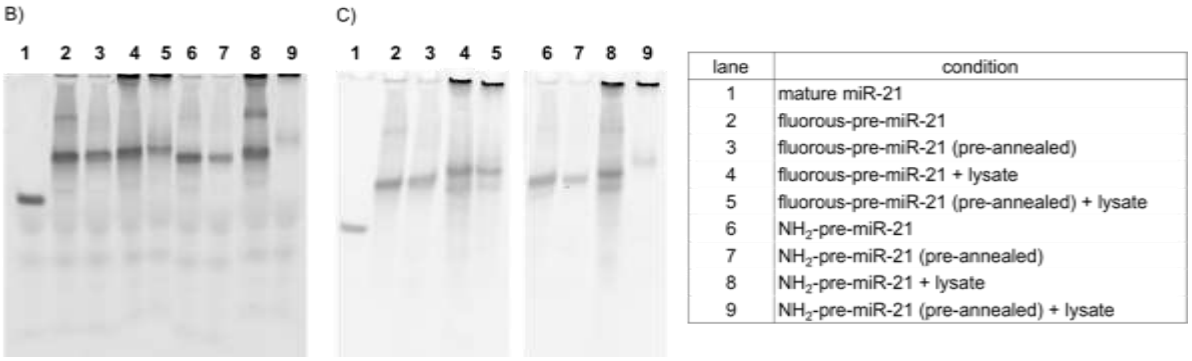

lane	condition
1	mature miR-21
2	fluorous-pre-miR-21
3	fluorous-pre-miR-21 (pre-annealed)
4	fluorous-pre-miR-21 + lysate
5	fluorous-pre-miR-21 (pre-annealed) + lysate
6	NH_2-pre-miR-21
7	NH_2-pre-miR-21 (pre-annealed)
8	NH_2-pre-miR-21 + lysate
9	NH_2-pre-miR-21 (pre-annealed) + lysate

Figure 3-46 Dicer cleavage assay in cell lysate

A) Processing assay was performed in HEK293T lysate with an ATP generation system following Mikiko Siomi's protocol with pre-miR-21 (500 nM). The Dicer processing assay was also attempted with Thomas Tuschl's protocol utilizing HEK293T cell lysate and an ATP generation system as well as pre-annealed or non-pre-annealed pre-miR-21 (500 nM). In the case of the Tuschl protcol, the reaction was incubated for B) 1 h or C) 12 h before analyzing the samples via native PAGE followed by SYBR Gold stain.

We next hypothesized that Dicer expression was not at a sufficient level to achieve pre-miRNA cleavage *in vitro* and thus attempted to overexpress the enzyme prior to lysis using plasmid DNA. Briefly, HEK293T cells were plated in a 10 cm plate at ~80% confluence. The following

day, cells were transfected with 10 μg of a pFRT/TO/FLAG/HA-DEST DICER plasmid (Addgene; plasmid# 19881) using linear polyethylenimine (LPEI) transfection reagent. After 48 h, cells were lysed, and the Dicer processing assay was performed following Tuschl's protocol as described above. Western blot analysis utilizing both anti-HA and anti-FLAG antibodies confirmed expression of the tagged enzyme (Figure 3-47A). Disappointingly, Dicer overexpression did not result in processing of the fluorous- or amine-modified pre-miR-21 regardless of incubation time (Figure 3-47B,C). We also attempted to achieve Dicer cleavage by pre-treating the lysate with proteinase K prior to incubation with the RNA following a protocol by the Filipowicz laboratory which demonstrated the pre-incubation stimulated Dicer function.[613] Unfortunately, regardless of how much proteinase K was incubated with the lysate prior to addition of the amine- or fluorous-tagged pre-miRNA (26 or 250 ng), the mature miR-21 duplex was not observed (Figure 3-47D).

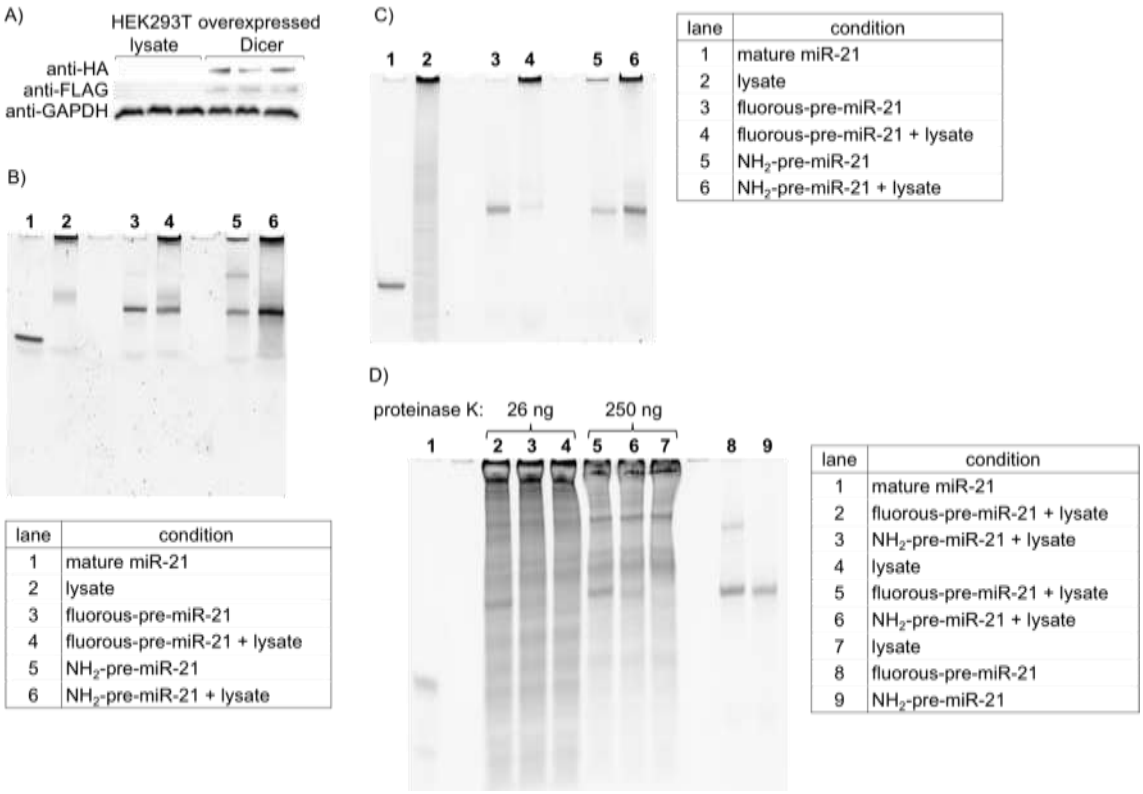

lane	condition
1	mature miR-21
2	lysate
3	fluorous-pre-miR-21
4	fluorous-pre-miR-21 + lysate
5	NH_2-pre-miR-21
6	NH_2-pre-miR-21 + lysate

lane	condition
1	mature miR-21
2	fluorous-pre-miR-21 + lysate
3	NH_2-pre-miR-21 + lysate
4	lysate
5	fluorous-pre-miR-21 + lysate
6	NH_2-pre-miR-21 + lysate
7	lysate
8	fluorous-pre-miR-21
9	NH_2-pre-miR-21

Figure 3-47 Dicer cleavage assays in cell lysate

A) Dicer was overexpressed in HEK293T cells using pFRT/TO/FLAG/HA-DEST DICER. Expression was confirmed via western blot analysis with anti-HA and anti-FLAG antibodies. Using the lysate containing overexpressed Dicer, the processing assay was performed for B) 2 h or C) 12 h at room temperature. The reactions were analyzed via native PAGE followed by SYBR Gold stain. D) To 'activate' Dicer, the lysate was pre-treated with proteinase K (26 or 250 ng) then used to attempt to digest pre-miR-21 (500 nM).

Having exhausted both commercial sources of recombinant Dicer and attempting to utilize Dicer expressed endogenously, we turned our attention back to the pre-miRNA sequence as a potential source of inhibition in our assay. After further investigation, we determined that the pre-miR-21 substrate we had employed in the assays described above was longer than the native Dicer

substrate. Because Dicer is known to recognize the 5' phosphate and 3' hydroxyl as well as a 2-nucleotide overhang on the 3' terminus,[18] we hypothesized that additional bases within the stem region of our pre-miRNA hairpin were inhibiting Dicer recognition of the substrate thereby inhibiting activity. In order to test this hypothesis, we obtained the synthetic non-modified pre-miR-21 (60 nt) from IDT (Figure 3-48A) and subjected it to multiple different Dicer cleavage assay conditions. Unsurprisingly, based on the lack of activity against the GFP control RNA, the recombinant Dicer sourced from Genlantis failed to process the new substrate into the corresponding mature miR-21 duplex and streptomycin (30 μM), a pre-miR-21-binding small molecule,[535] had no effect on activity (Figure 3-48B). Serendipitously, after screening multiple concentrations of recombinant Dicer (Origene) in combination with pre-miR-21 (60 nt; 50 nM), we observed near complete processing of the hairpin into the corresponding mature miRNA duplex after 12 h incubation under the Schneekloth assay conditions when the enzyme and RNA were at a 1:1 molar ratio in the reaction (Figure 3-48C). Furthermore, pre-incubation with **2** (30 μM; Figure 1-6), a compound previously reported by Schneekloth and co-workers to inhibit processing of pre-miR-21,[265] led to ~50% inhibition of Dicer cleavage (Figure 3-48D), suggesting these assay conditions would be optimal for our assay.

A)

oligo	sequence (5' -> 3')
pre-miR-21	UAGCUUAUCAGACUGAUGUUGACUGUUGAAUCUCAUGGCAACACCAGUCGAUGGGCUGUC

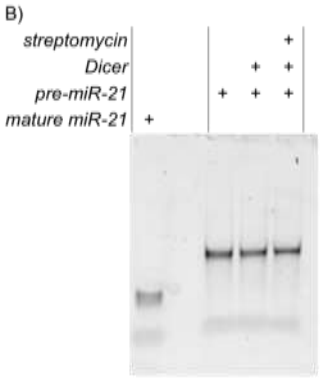

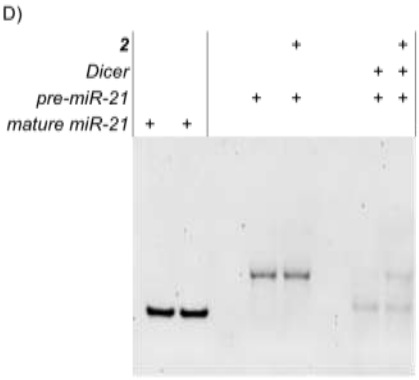

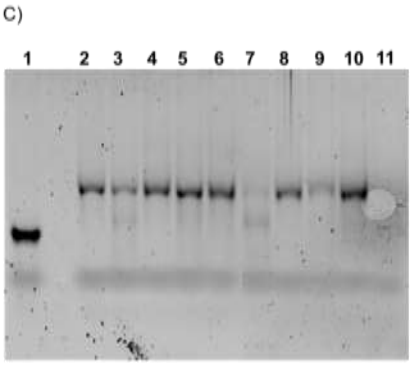

lane	condition
1	mature miR-21
2	pre-miR-21
3	pre-miR-21 + Dicer (6 nM)
4	pre-miR-21
5	pre-miR-21 + Dicer (25 nM)
6	pre-miR-21
7	pre-miR-21 + Dicer (50 nM)
8	pre-miR-21
9	pre-miR-21 + Dicer (100 nM)
10	pre-miR-21
11	pre-miR-21 + Dicer (400 nM)

Figure 3-48 Evaluation of Dicer processing with the 60 nucleotide pre-miR-21 hairpin

A) Sequence of the synthetic pre-miR-21 hairpin (60 nt). B) The Dicer processing assay was performed using recombinant Dicer from Genlantis and 100 nM non-modified pre-miR-21 (60 nt) pre-incubated with streptomycin (30 µM) for 30 min before cleavage with Dicer following the manufacturer's protocol. C) Various concentrations of recombinant Dicer (Origene) were incubated with pre-miR-21 (60 nt; 10 nM) for 12 h at 37 °C. D) Recombinant Dicer (Origene) and pre-miR-21 (60 nt) were incubated at a 1:1 molar ratio for 12 h in the presence of DMSO or compound **2** (30 µM). Reactions were analyzed via native PAGE followed by SYBR Gold stain.

Because the new pre-miR-21 substrate no longer bore the 7-nucleotide fragment on the 5' terminus that we previously tagged with the perfluorous moiety, we needed to re-design our substrate for MALDI-MS experiments. Garner and co-workers had previously demonstrated that an alkyne modification within the loop of pre-miR-21 did not inhibit Dicer cleavage of the hairpin.[285] Thus, we hypothesized that the fluorous tag could be installed at this position without altering Dicer activity. The fluorous-modified pre-miR-21 was generated in two steps. First, esterification of 2H, 2H, 3H, 3H-perfluoroundecanoic acid (**206**) was performed using EDCI and NHS delivering the corresponding NHS ester (**207**) in 54% yield (Figure 3-49). Subsequently, we purchased the synthetic pre-miR-21 (60 nt) or pre-miR-21 loop (16 nt) bearing an internal 5-aminohexylacrylamino-uridine from Dharmacon (Figure 3-50A) and attempted to couple the perfluorous NHS ester to the RNA (Figure 3-50B). A 5'-amino C6 linker-modified dummy DNA (22 nt) was ordered as an internal control for MALDI-MS analysis. Briefly, amine-modified RNA or DNA was added to sodium tetraborate buffer (50 mM; pH 8.3) and 50% (v/v) dry DMSO. The perfluorous NHS ester was then added at 10-fold molar excess once an hour for up to five additions. Subsequently, the fluorous-tagged pre-miR-21 was isolated via high performance liquid chromatography (HPLC) and desalted using a 10 kDa molecular weight cutoff column. After purification, the final fluorous-modified oligonucleotides were obtained in 20-30% yield. Purity was confirmed via HPLC prior to biological assays (Figure 3-50C). Dicer-mediated cleavage of the 60 nucleotide pre-miR-21 hairpin releases the 16-nucleotide loop region from the stem-loop in addition to the mature miR-21 duplex. As a control, we ordered the corresponding amine-modified RNA (16 nt) and coupled it to the perfluorous NHS ester as describe above (Figure 3-50B).

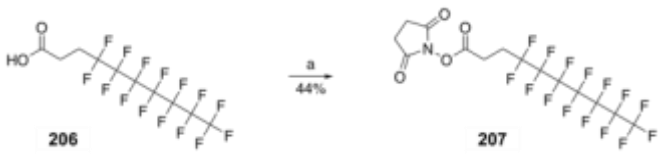

Figure 3-49 Synthetic route to perflurous NHS ester **207**

Reagents and conditions: a) EDCI, NHS, DCM, RT OVN.

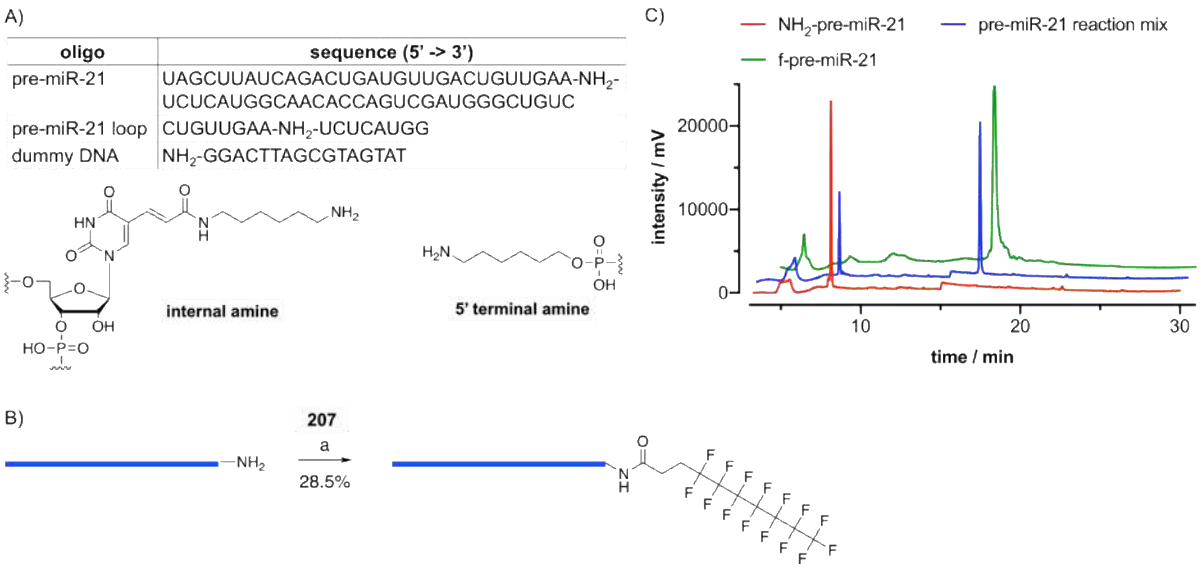

Figure 3-50 Conjugation of the perfluorous NHS ester to amine-modified oligonucleotides

A) Sequences of synthetic amine-modified pre-miR-21 (60 nt), loop (16 nt), and dummy DNA (22 nt) and chemical structures of internal or terminal amine modifications. B) Synthetic route for conjugation of perfluorous NHS ester **207** to amine modified oligonucleotides. Reagents and conditions: a) sodium bicarbonate (100 mM; pH 8.3), 55% (v/v) of DMSO, 10 eq of **207** added every 1 h for up to five additions at room temperature. C) HPLC analysis of amine-modified pre-miR-21 (red), pre-miR-21 reaction mix (blue), and fluorous-tagged pre-miR-21 after purification (green).

We next attempted to compare Dicer-mediated cleavage of the amine-modified pre-miR-21 to the non-modified hairpin following the Schneekloth protocol. Additionally, we had to purchase a new lot of recombinant Dicer from Origene because we expended the previous stock. Unfortunately, after an 8 h or overnight incubation, the new Dicer stock failed to cleave either of the RNAs at a 1:1 molar ratio (Figure 3-51A). Moreover, increasing the Dicer concentration only had a modest effect on the amount of mature miR-21 produced (Figure 3-51B), suggesting this lot of Dicer was less active than the previous stock. Subsequently, a third lot of Dicer was obtained from Origene, but this stock was completely inactive (Figure 3-51C), indicating activity of the enzyme was highly variable between batches.

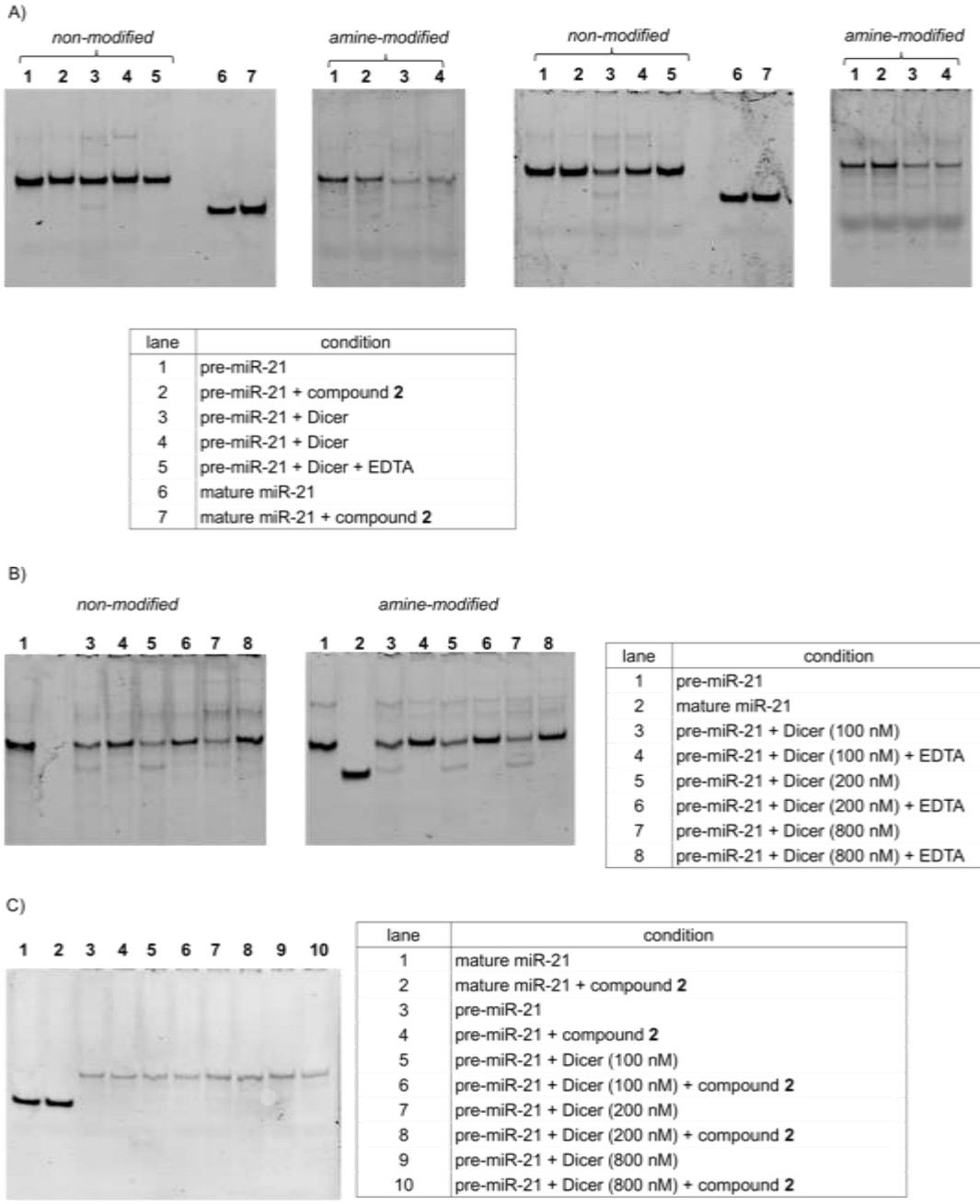

lane	condition
1	pre-miR-21
2	pre-miR-21 + compound **2**
3	pre-miR-21 + Dicer
4	pre-miR-21 + Dicer
5	pre-miR-21 + Dicer + EDTA
6	mature miR-21
7	mature miR-21 + compound **2**

lane	condition
1	pre-miR-21
2	mature miR-21
3	pre-miR-21 + Dicer (100 nM)
4	pre-miR-21 + Dicer (100 nM) + EDTA
5	pre-miR-21 + Dicer (200 nM)
6	pre-miR-21 + Dicer (200 nM) + EDTA
7	pre-miR-21 + Dicer (800 nM)
8	pre-miR-21 + Dicer (800 nM) + EDTA

lane	condition
1	mature miR-21
2	mature miR-21 + compound **2**
3	pre-miR-21
4	pre-miR-21 + compound **2**
5	pre-miR-21 + Dicer (100 nM)
6	pre-miR-21 + Dicer (100 nM) + compound **2**
7	pre-miR-21 + Dicer (200 nM)
8	pre-miR-21 + Dicer (200 nM) + compound **2**
9	pre-miR-21 + Dicer (800 nM)
10	pre-miR-21 + Dicer (800 nM) + compound **2**

Figure 3-51 Origene Dicer displays inconsistent activity between different lots

A) Dicer cleavage assays with the second lot of enzyme from Origene using 1:1 molar ratio of Dicer:pre-miR-21 following Schneekloth's protocol. Inhibitor **2** (30 μM) was included to block Dicer cleavage of the pre-miR-21 hairpin. B) Attempted re-optimization of the Dicer processing assay using increasing concentrations of the enzyme and following the protocol from Jay Schneekloth. EDTA (250 mM) was added to inhibit Dicer cleavage. C) Dicer cleavage

assay with the third lot of Dicer from Origene using increasing concentrations of enzyme. Compound **2** (30 μM) was included to inhibit Dicer processing.

Because the commercially available recombinant Dicer displayed batch-to-batch variability even with the new 60 nt pre-miR-21, we turned our attention back toward using endogenous or overexpressed Dicer in cell lysate. To this end, HEK293T cells were grown to ~95% confluence, followed by lysis and Dicer processing according to Tuschl's protocol as described above. Additionally, we attempted to overexpress Dicer in HEK293T cells and utilize the lysate to digest the pre-miR-21 hairpin. After incubating the RNA (100 nM) with 10% (v/v) of the HEK293T lysate with or without overexpressed Dicer for 2 or 4 h, no processing of pre-miR-21 was observed (Figure 3-52). However, when the reaction was allowed to proceed overnight (12 h), a faint band corresponding to the mature miR-21 duplex was observed on the gel, suggesting Dicer in the lysate was capable of digesting the pre-miRNA hairpin. Unfortunately, treatment with streptomycin (30 μM) did not inhibit Dicer processing during the overnight incubation.

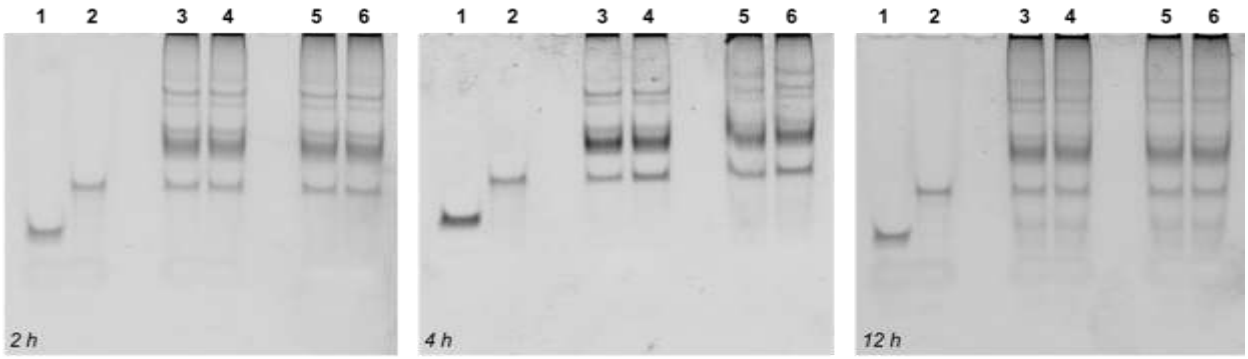

lane	condition	Dicer expression
1.	mature miR-21	--
2.	pre-miR-21	--
3.	pre-miR-21 + lysate	overexpressed
4.	pre-miR-21 + lysate + streptomycin (30 μM)	overexpressed
5.	pre-miR-21 + lysate	endogenous
6.	pre-miR-21 + lysate + streptomycin (30 μM)	endogenous

Figure 3-52 Evaluation of Dicer processing using the 60 nt pre-miR-21 and HEK293T cell lysate

Pre-miR-21 (100 nM) was incubated with HEK293T cell lysate with or without overexpressed Dicer for 2, 4, or 12 h following Tuschl's protocol. Streptomycin (30 μM) was included to inhibit Dicer processing.

A recent report by the Liang laboratory demonstrated the use of recombinant Dicer immobilized on anti-Flag resin to digest pre-miR-21.[614] In an effort to improve the amount of product produced in the Dicer processing assay, we adapted a similar protocol in combination with the Dicer overexpression plasmid described above. Briefly, HEK293T cells were transfected with the expression construct for 72 h, then lysed. The lysate was incubated with anti-Flag antibody overnight, then incubated with protein A/G beads. After overnight incubation, the resin was washed and stored in 50% [w/v] of glycerol at -20 °C until use. For the Dicer cleavage assay, non-modified, amine-modified, or fluorous-modified pre-miR-21 were incubated at 100 nM in assay buffer (Tris-HCl [10 mM; pH 7.5], $MgCl_2$ [5 mM], ATP [1 mM], DTT [1 mM], RNasin RNase

inhibitor [0.4 U/µl]) with 50% [v/v] of immobilized Dicer. The reaction was incubated at 37 °C for 24 h then stopped with the addition of the EDTA stop solution described above. Subsequently, up to ~50% Dicer cleavage was observed with all of the substrates (Figure 3-53A), suggesting not only was the immobilized Dicer active, but also that the amine and fluorous modifications did not inhibit function of the enzyme. Furthermore, addition of the stop solution at the start of the assay did not lead to generation of the mature miR-21 duplex providing further support that the pre-miR-21 hairpin is digested in a Dicer-dependent mechanism. In a subsequent experiment, increasing the amount of immobilized Dicer from 50% [v/v] to 70% [v/v] only had a minor impact on the amount of mature miR-21 duplex produced (Figure 3-53B). Concentrating the Dicer resin slurry stock by 2-fold led to complete disappearance of both the pre-miR-21 *and* the mature miR-21 duplex in a native PAGE gel experiment (Figure 3-53C), suggesting Dicer exhibits non-specific nuclease activity at high concentrations. Furthermore, subsequent expression and immunoprecipitation of Dicer also led to active immobilized enzyme (data not shown). With a more robust assay in hand, we proceeded with development of the MALDI-MS protocol.

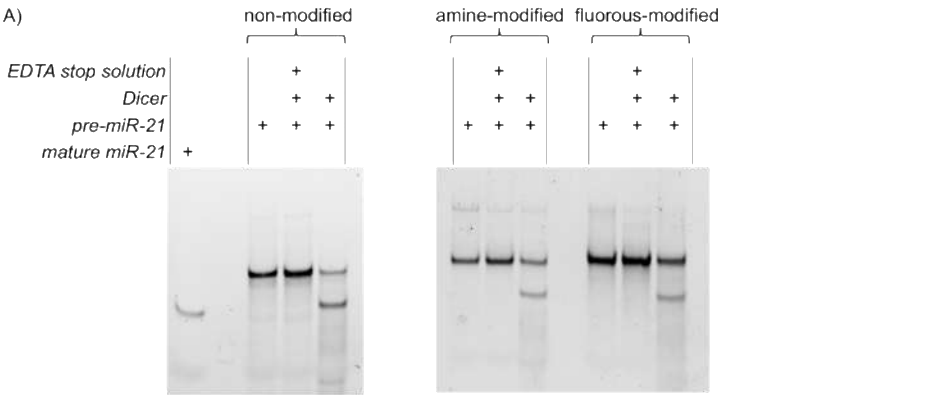

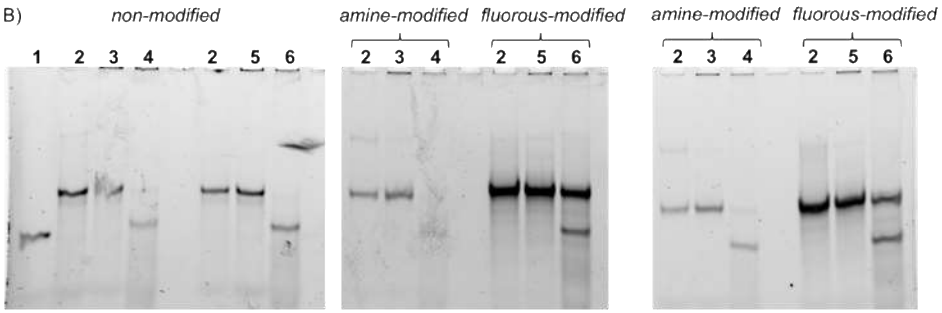

lane	condition	ratio of resin volume to final volume
1.	mature miR-21	--
2.	pre-miR-21	--
3.	pre-miR-21 + immobilized Dicer + EDTA stop solution	0.5
4.	pre-miR-21 + immobilized Dicer	0.5
5.	pre-miR-21 + immobilized Dicer + EDTA stop solution	0.7
6.	pre-miR-21 + immobilized Dicer	0.7

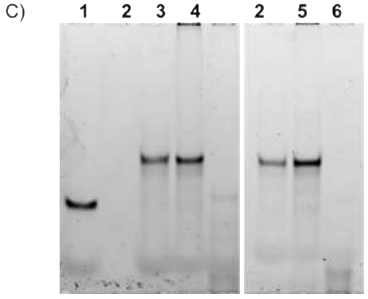

lane	condition	relative resin concentration
1.	mature miR-21	--
2.	pre-miR-21	--
3.	pre-miR-21 + immobilized Dicer + EDTA stop solution	1x
4.	pre-miR-21 + immobilized Dicer	1x
5.	pre-miR-21 + immobilized Dicer + EDTA stop solution	2x
6.	pre-miR-21 + immobilized Dicer	2x

Figure 3-53 Dicer processing assay with immobilized enzyme

A) Dicer was overexpressed in HEK293T cells using pFRT/TO/FLAG/HA-DEST DICER. Flag-Dicer was then immobilized using anti-Flag antibody and protein A/G resin and used directly for Dicer cleavage assays following the

Liang protocol. B) The resin volume in the reaction was increased from 50% to 70% (v/v). C) 50 µl of reaction buffer was added to the resin (instead of 100 µl) and the concentrated immobilized Dicer was used in a cleavage assay.

Optimization of the MALDI-MS protocol was performed utilizing the fluorous-modified loop RNA (16 nt) and dummy DNA (22 nt). To evaluate the protocol, we selected four metrics of success: 1) low ion adduct peaks (<10% by area); 2) high sensitivity (single digit pM); 3) high reproducibility (<15% inter- and intra-spot coefficient of variation [CV]); and 4) low fragmentation (<20% total peak area). In order to achieve these benchmarks we focused on the two important factors in determining MS signal sensitivity and reproducibility: 1) the matrix and 2) the on-surface wash.[615-617] Preliminary studies determined that while identity of the matrix is important (e.g., sinipinic acid was sub-optimal for nucleic acids), choice of matrix solvent is equally vital. For example, studies with sinipinic acid in acetonitrile led to poor ionization, but addition of trifluoroethylene (TFE) dramatically improved the signal. Previously, 5-methoxysalicylic acid (MSA) was demonstrated to reduce fragmentation of oligonucleotides compared to other commonly employed matrices for MALDI-MS analysis of oligonucleotides, 3-hydroxypicolinic acid (HPA) and 6-aza-2-thiothymine (ATT).[618] Moreover, the use of ammonium salts such as diammonium hydrogen citrate have been utilized as matrix additives because they reduce formation of ion adducts. As such, we selected these components for analysis of the fluorous-modified oligonucleotides and, after preliminary evaluation, the optimal matrix composition was determined to be 17.8 mg/ml of 5-MSA and 11.25 mg/ml of diammonium hydrogen citrate. We next altered the composition of the co-solvent. Briefly, 5-MSA and diammonium hydrogen citrate were prepared in various solvents with differing ratios of isopropanol, TFE, and acetonitrile. Subsequently, a solution of fluorous-modified loop RNA at

varying concentrations and the fluorous-modified DNA (100 nM) was spotted on the fluorous coated plate and allowed to evaporate to dryness. Then, the spots were washed by adding a drop of distilled water which was removed after 30 s. Finally, the matrix was added, and the spots were again allowed to proceed to dryness before analyzing the samples via MALDI-MS. Each condition was spotted in triplicate and after calculating the CV for each condition, we found that higher volumes of TFE greatly improved the reproducibility of the assay (Figure 3-54A). Furthermore, we observed a linear response in the ratio of fluorous-modified RNA to DNA to concentrations as low as 50 nM (Figure 3-54B), the detection limit of our assay.

A)

matrix:		M19 = IPA:TFE (80:20)	M21 = IPA:TFE (20:80)	M25 = CH_3CN:IPA:TFE (20:40:40)	M15 = CH_3CN:IPA:TFE (20:20:60)
500 nM f-RNA	average	3.42	3.34	2.79	3.83
	st. dev.	0.48	0.65	1.02	0.57
	CV	0.14	0.19	0.37	0.15
250 nM f-RNA	average	1.93	2.00	1.32	2.11
	st. dev.	0.59	0.12	0.15	0.09
	CV	0.31	0.06	0.11	0.04
100 nM f-RNA	average	1.12	1.26	0.76	1.31
	st. dev.	0.41	0.13	0.10	0.46
	CV	0.37	0.10	0.14	0.35
50 nM f-RNA	average	0.54	0.85	0.60	1.01
	st. dev.	0.01	0.05	0.08	0.13
	CV	0.01	0.06	0.14	0.13
average CV:		0.21	0.10	0.19	0.17

B)

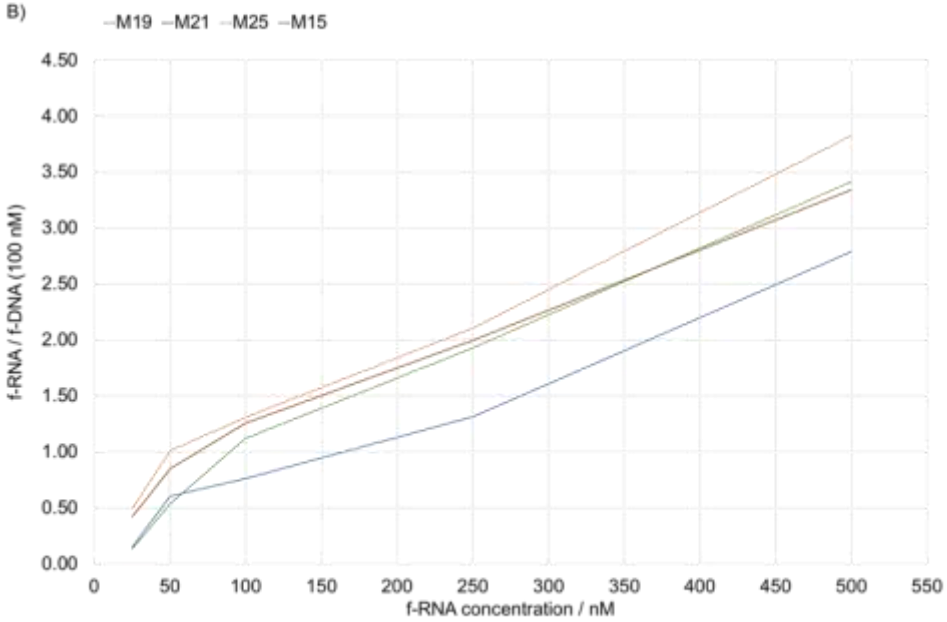

Figure 3-54 Evaluation of matrix formulations for MALDI-MS analysis of pre-miR-21

A) Ratios of trifluoroethanol (TFE), isopropyl alcohol (IPA), and acetonitrile (CH_3CN) in the matrix were varied, then used to spot various concentrations of fluorous-modified pre-miR-21 loop RNA. B) Ratios of fluorous-modified RNA at different concentrations to fluorous-modified DNA (100 nM) were compared with each matrix formulation. Coefficient of variation (CV) was calculated for 3 to 6 replicates. Sample preparation, spotting, and data analysis was performed by Marvin Yu.

Next, we sought to optimize the on-surface wash. While preliminary experiments in which the nucleic acids were diluted in water suggested a wash with distilled water was sufficient for observing a significant signal, dilution of the oligonucleotides in the Dicer assay buffer diminished the MALDI-MS signal as well as the detection limit (Figure 3-55A). In order to overcome this limitation, we evaluated several parameters with a wash solvent composed of n-propanol (3.5% [v/v]) and diammonium hydrogen citrate (0.1 M) including: 1) wash additives; 2) time of wash; 3) number of washes; and 4) type of wash. Inclusion of wash additives such as glycerol, ethylene glycol, or diethylene glycol did not improve the sensitivity of the assay and in some cases inhibited crystallization of the matrix and sample. Additionally, whereas a single wash was sufficient for reducing background signal, a second wash resulted in diminished sample signal. Finally, longer washes (up to 4 min) contributed to improved S/N and it was determined that allowing the wash to completely evaporate (as opposed to aspirating it for removal) was optimal. However, after washing the spots for 8 min, reproducibility started to diminish compared to a 4 min wash (Figure 3-55B). Moreover, spotting the sample and removing it after 4 or 8 min instead of washing the spots hampered reproducibility compared to the washed samples, especially at low concentrations of RNA (Figure 3-55C).

A)

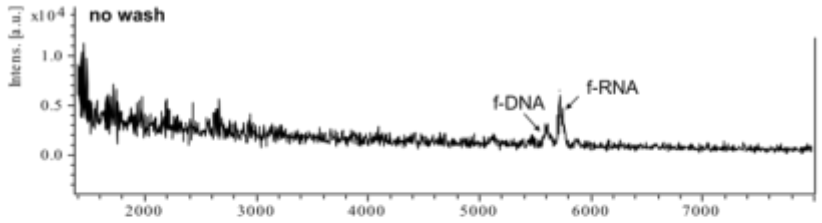

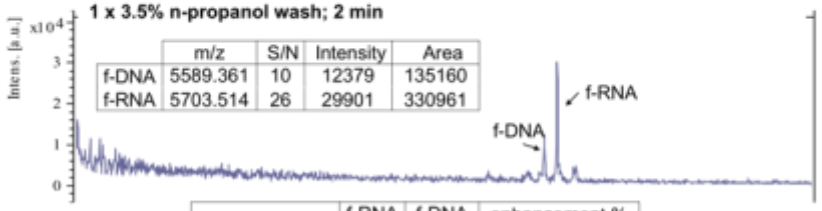

	m/z	S/N	Intensity	Area
f-DNA	5589.361	10	12379	135160
f-RNA	5703.514	26	29901	330961

	f-RNA	f-DNA	enhancement %	
no wash average	5,365	~2000		
3.5% nPrOH wash average	27,147	9,183	506.0%	459.2%

B)

RNA concentration / nM	wash	time / min	average RNA signal	average DNA signal	ratio	CV
500	3.5% n-propanol	4	40,868	21,330	1.92	0.01
		8	64,633	66,847	0.97	0.05
250	3.5% n-propanol	4	22,828	25,290	0.89	0.04
		8	49,401	69,531	0.69	0.19
100	3.5% n-propanol	4	9,590	21,140	0.45	0.13
		8	12,923	35,076	0.37	0.12
50	3.5% n-propanol	4	5,706	30,079	0.19	0.09
		8	5,455	12,825	0.41	0.15

C)

RNA concentration / nM	wash	time / min	average RNA signal	average DNA signal	ratio	CV
500	stand and remove	4	48,158	59,690	0.80	0.01
		8	63,530	60,633	1.05	0.01
250	stand and remove	4	17,569	47,906	0.37	0.23
		8	37,142	57,046	0.60	0.28
100	stand and remove	4	7,902	25,595	0.32	0.13
		8	12,970	37,488	0.34	0.21
50	stand and remove	4	3,697	12,825	0.41	0.15
		8	4,327	22,539	0.36	0.04

Figure 3-55 Evaluation of wash conditions for MALDI-MS analysis of fluorous-modified pre-miR-21

A) Example spectra comparing a sample that was spotted without a wash and a sample that was spotted followed by a wash. Comparison of variation in wash conditions including wash time and 3.5% n-propanol wash vs. no wash for various concentrations of fluorous-modified RNA. Coefficient of variation (CV) was calculated for 3 to 6 replicates. Sample preparation, spotting, and data analysis was performed by Marvin Yu.

3.7.1 Summary and Outlook

In summary, we developed a HT-MS assay for analysis of perfluorous-modified oligonucleotides utilizing MALDI-MS. As a proof-of-concept model, we attempted to develop a prototype assay suitable for HT-MS screening for inhibitors of pre-miR-21 processing. Several screening methods to identify small molecule inhibitors of miRNAs have been previously developed as described in detail above (Chapter 1.2.3), however, they often suffer from the requirement of multiple secondary assays to confirm function of the small molecules. As such, we hypothesized that more direct screening methods would accelerate the process of identifying small molecule inhibitors of miRNA maturation. Toward this goal, we evaluated a variety of methods for performing Dicer-mediated cleavage of pre-miR-21 *in vitro*. While use of commercial sources of Dicer is highly precedented in the literature, we experienced difficulty in obtaining the level of activity required for our assays. As such, artificial overexpression of Dicer from a plasmid in mammalian cells followed by immobilization of the enzyme on resin was determined to be optimal. Moreover, we have determined MALDI-MS conditions that enable us to meet three out of four benchmarks, with the exception of high enough sensitivity to detect nucleic acids at single digit pM concentrations.

Future work will focus on combining the *in vitro* Dicer reaction with MALDI-MS analysis to detect the fluorous-modified loop RNA after Dicer processing. The coupling reaction between the perfluorous NHS ester (**207**) and internal amine-modified pre-miR-21 should be further optimized to maximize fluorous-tagged RNA product. Due to the presence of glycerol in the stop solution, alternative methods to halt the cleavage reaction (e.g., removal of the supernatant from the resin or addition of a high concentration of EDTA without diluting the sample) should be evaluated. Additionally, inhibition of Dicer processing of pre-miR-21 by a small molecule such as

streptomycin,[535] AC1MMYR2,[371] or mitoxantrone[269] should be demonstrated. Finally, the capability of the assay to be multiplexed should be evaluated with additional miRNA targets. Furthermore, this work could be expanded to include a full screen for small molecule inhibitors of miRNA maturation, detection of circulating miRNA, and MS/MS or fragmentation-based methods for RNA modification detection such as methylation, with an emphasis on commercialization.

3.7.2 Materials and Methods

Cell culture. Experiments performed using HEK293T (ATCC) cell line cultured in Dulbecco's Modified Eagle Medium (DMEM; Gibco). Media was supplemented with 10% (v/v) Fetal Bovine Serum (FBS; Sigma-Aldrich) and 1% (v/v) penicillin/streptomycin (VWR) and maintained at 37 °C in a 5% CO_2 atmosphere. Penicillin/streptomycin-free media was used for experiments. Cell line was used within passages 1-35 and was tested for mycoplasma contamination every three months.

RNA annealing protocol. Prior to use in Dicer reactions (where indicated), pre-miR-21 was desalted using a 10 kDa molecular weight cutoff column (Amicon). Briefly, RNA in water (typically ~50 µl) was added to the column and the total volume was increased to 500 µl with nuclease-free water. The column was centrifuged at 14,000 g for 10 min and the flow-through was discarded. Three wash steps consisting of addition of 450 µl and centrifugation at 14,000 g for 10 min were performed. After the third wash, the column was inverted in a clean tube and centrifuged at 1,000 g for 2 min. The recovered eluate contained the RNA which was subsequently quantified by measured absorbance at 260 nm on a Nanodrop ND-1000 spectrophotometer and calculating the concentration (µM) using the molar extinction coefficient. Desalted RNA was diluted to the

desired concentration (100 nM or 1 µM) in 1x PBS and annealed by heating to 95 °C in a thermal cycler (Bio-Rad) and cooled to 12 °C over 10 min.

Dicer processing assays.

Genlantis Recombinant Dicer Enzyme Kit

The Recombinant Dicer Enzyme Kit (Genlantis; T510002) was used to digest RNA following the manufacturer's protocol. Briefly, 116 ng or 1 µg of RNA was added to assay buffer. The 116 ng of RNA corresponds to a final RNA concentration of 500 nM as described by Amanda Garner's protocol discussed below. The assay buffer was prepared by mixing 1 µl of ATP (10 mM), 0.5 µl of $MgCl_2$ (50 mM), 4 µl of Dicer reaction buffer (supplied with the kit), and nuclease-free water up to 8 µl. Then, 2 µl of recombinant Dicer enzyme (1 U) was added. The reaction was incubated overnight in a 37 °C incubator. To stop the reaction, 2 µl of the proprietary Dicer stop solution (supplied with the kit) was added to each reaction. Subsequently, 2 µl of gel loading dye (NEB; 6x) was added to samples (12 µl), and the entire volume (14 µl) was separated on a 16% (v/v) native PAGE gel (see protocol 6.1.9 and electrophoresis was performed at 140 V for 40 min. Following PAGE separation, the gel was stained with SYBR Gold (Invitrogen). Briefly, 5 µl of SYBR Gold stain (10,000x) was diluted in 50 ml of TBE buffer. The gel was rinsed with ~25 ml of TBE, then placed in a gel box with a lid. The 1x SYBR Gold stain was then added directly to the gel and was incubated with rocking at room temperature for 30 min. The gel was imaged on a ChemiDoc XRS+ (Bio-Rad) using the 'SYBR Gold' method.

Amanda Garner's protocol

This protocol was adapted from a method previously reported by Amanda Garner (University of Michigan)[285] using recombinant Dicer from the Recombinant Dicer Enzyme Kit (Genlantis; T510002). RNA was diluted to 500 nM in 10 µl of assay buffer consisting of Tris-HCl (20 mM; pH 7.4), dithiothreitol (DTT; 1 mM), $MgCl_2$ (2.5 mM), NaCl (12 mM), and RNasin RNase inhibitor (Promega; 40 U/ml). Then, recombinant Dicer enzyme (0.25 U) was added. The reaction was incubated for 1 h in a 37 °C incubator. Subsequently, 2 µl of gel loading dye (NEB; 6x) was added to samples (10 µl), and the entire volume (12 µl) was separated on a 16% (v/v) native PAGE gel (see protocol 6.1.9 via electrophoresis performed at 140 V for 40 min. Following PAGE separation, the gel was stained with SYBR Gold (Invitrogen) as described above. The gel was imaged on a ChemiDoc XRS+ (Bio-Rad) using the 'SYBR Gold' method.

Jay Schneekloth's protocol

This protocol was adapted from a method previously reported by Jay Schneekloth (National Institutes of Health)[265] using recombinant Dicer from the Recombinant Dicer Enzyme Kit (Genlantis; T510002) or Origene (catalog#: TP319214). Following desalting and annealing of the pre-miR-21 at 100 nM as described above, the annealed RNA was diluted to 10 nM in assay buffer consisting of Tris-HCl (20 mM; pH 7.4), dithiothreitol (DTT; 1 mM), $MgCl_2$ (2.5 mM), NaCl (12 mM), and RNasin RNase inhibitor (Promega; 40 U/mL) to a final volume of 10 µl. Then, recombinant Dicer enzyme (0.5 U or as defined by the experiment) was added. If the pre-miR-21 inhibitor **2** was included in the experiment, 1 µl of the compound ([stock] = 300 µM; [final] = 30 µM) or DMSO (5% [v/v]) was incubated with the RNA hairpin for 30 min at room temperature prior to addition of the enzyme. The initial reaction was incubated for 2 h in a 37 °C incubator,

however, reaction time was also varied as defined by the experiment. Reactions were stopped by boiling the sample at 95 °C for 10 min in a heat block, followed by cooling to room temperature on a benchtop. Subsequently, 2 µl of gel loading dye (NEB; 6x) was added to samples (10 µl), and the entire volume (12 µl) was separated on a 16% (v/v) native PAGE gel (see protocol 6.1.9 via electrophoresis performed at 140 V for 40 min. Following PAGE separation, the gel was stained with SYBR Gold (Invitrogen) as described above. The gel was imaged on a ChemiDoc XRS+ (Bio-Rad) using the 'SYBR Gold' method.

Ian MacRae's protocol

This protocol was adapted from a method previously reported by Ian MacRae (The Scripps Research Institute)[608] using recombinant Dicer from Origene (catalog#: TP319214). Prior to use in the Dicer reaction, pre-miR-21 was desalted using a 10 kDa molecular weight cutoff column (Amicon) as described above. Desalted RNA was diluted to 500 nM in assay buffer consisting of 4-(2-hydroxyethyl)-1-piperazineethanesulfonic acid (HEPES; 40 mM; pH 7.4), 1 mM dithiothreitol (DTT; 1 mM), $MgCl_2$ (3 mM), and NaCl (100 mM) to a final volume of 9 µl. Then, 1 µl of ATP (10 mM) was added to a final concentration of 1 mM followed by Recombinant Dicer Enzyme at a final concentration of 61.8 nM (or as defined by the experiment). The initial reaction was incubated for 1 h in a 37 °C incubator, however, reaction time was also varied as defined by the experiment. Reactions were stopped by addition of 5 µl of 'quenching buffer' (urea (6 M), EDTA (250 mM), glycerol [10% (w/v)], bromophenol blue [0.1% (w/v)]). Subsequently, samples (15 µl) were separated on a 15% (v/v) native PAGE gel (see protocol 6.1.9 and electrophoresis was performed at 140 V for 40 min. Following PAGE separation, the gel was stained with SYBR

Gold (Invitrogen) as described above. The gel was imaged on a ChemiDoc XRS+ (Bio-Rad) using the 'SYBR Gold' method.

Thomas Tuschl's protocol

This protocol was adapted from a method previously reported by Thomas Tuschl (Rockefeller University)[612] using endogenous or overexpressed Dicer in cell lysate. HEK293T cells were seeded at 125,000 cells per well in a 6-well plate (Corning) treated with poly-D lysine (see protocol 6.2.2 In an alternative adaptation of this protocol, Dicer was also overexpressed using a plasmid as described below. When cells reached ~95% confluence, they were trypsinized, taken up in 10 mL of 1x PBS, and centrifuged at 1000 g and 4 °C for 10 min. The supernatant was discarded and the cell pellet was resuspended in an appropriate volume of lysis buffer (HEPES [30 mM; pH 7.4], potassium acetate [100 mM], magnesium acetate [1 mM], DTT [5 mM], and 1x protease inhibitor cocktail [Thermo-Fisher Scientific]) such that the cell stock was concentrated to ~$1x10^7$ cells per mL. Cells were incubated on ice for 20 min for lysis. The lysate was centrifuged at 16,110 g and 4 °C for 10 min. The supernatant was collected in a new 1.7 ml Eppendorf tube and stored at -20 °C until use. When proteinase K treatment was included for Dicer activation,[613] recombinant proteinase K (Thermo-Fisher Scientific; 26 ng or 250 ng) was added directly to cell lysate and incubated at room temperature for 30 min. Subsequently, RNA was diluted to 500 nM in 10% (v/v) assay buffer consisting of lysis buffer supplemented with ATP (0.5 mM), 0.1 mM each of GTP, UTP, and CTP, creatine phosphate (10 mM), and creatine phosphokinase (10 µg/ml) to a final volume of 5 µl. Then, 50% (v/v) of HEK293T lysate was added and the reaction was incubated for 1 or 12 h at room temperature. Subsequently, 2 µl of gel loading dye (NEB; 6x) was added to samples (10 µl), and the entire volume (12 µl) was separated on a 16% (v/v) native PAGE

gel (see protocol 6.1.9 via electrophoresis performed at 140 V for 40 min. Following PAGE separation, the gel was stained with SYBR Gold (Invitrogen) as described above. The gel was imaged on a ChemiDoc XRS+ (Bio-Rad) using the 'SYBR Gold' method.

Mikiko Siomi's protocol

This protocol was adapted from a method previously reported by Mikiko Siomi (University of Tokushima)[611] using endogenous or overexpressed Dicer in cell lysate. HEK293T cells were seeded at 125,000 cells per well in a 6-well plate (Corning) treated with poly-D lysine (see protocol 6.2.2 In an alternative adaptation of this protocol, Dicer was also overexpressed using a plasmid as described below. When cells reached ~95% confluence, they were trypsinized, taken up in 10 ml of 1x PBS, and centrifuged at 1000 g and 4 °C for 10 min. The supernatant was discarded and the cell pellet was resuspended in an appropriate volume of lysis buffer (HEPES [30 mM; pH 7.4], potassium acetate [100 mM], magnesium acetate [2 mM], DTT [5 mM], glycerol [10% (w/v)] and 1x protease inhibitor cocktail [Thermo-Fisher Scientific]) such that the cell stock was concentrated to ~$1x10^7$ cells per ml. Cells were lysed on ice with vortexing every 5 min for 15 min. The lysate was centrifuged at 16,110 g and 4 °C for 10 min. The supernatant was collected in a new 1.7 ml Eppendorf tube and stored at -20 °C until use. RNA was diluted to 500 nM in assay buffer consisting of lysis buffer without glycerol supplemented with ATP (0.5 mM), creatine phosphate (10 mM), and creatine phosphokinase (30 µg/ml) to a final volume of 9 µl. Then, 10% (v/v) HEK293T lysate was added and the reaction was incubated for 3 h at room temperature. Reactions were stopped by boiling at 95 °C for 10 min in a heat block, then allowing the samples to return to room temperature on the bench top. Subsequently, 2 µl of gel loading dye (NEB; 6x) was added to samples (10 µl), and the entire volume (12 µl) was separated on a 15% native PAGE gel (see

protocol 6.1.9 via electrophoresis performed at 140 V for 40 min. Following PAGE separation, the gel was stained with SYBR Gold (Invitrogen) as described above. The gel was imaged on a ChemiDoc XRS+ (Bio-Rad) using the 'SYBR Gold' method.

Christoph Arenz' protocol

This protocol was adapted from a method previously reported by Christoph Arenz (Humboldt Universität Berlin)[271] using endogenous Dicer in cell lysate. HEK293T cells were seeded at 125,000 cells per well in a 6-well plate (Corning) treated with poly-D lysine (see protocol 6.2.2 When cells reached ~95% confluence, they were trypsinized, taken up in 10 ml of 1x phosphate-buffered saline, and centrifuged at 1000 g and 4 °C for 10 min. The supernatant was discarded and the cell pellet was resuspended in an appropriate volume of assay buffer (Tris-HCl [20 mM; pH 7.4], NaCl [12 mM], $MgCl_2$ [2.5 mM], DTT [1 mM], glycerol [10% (w/v)] and 1x protease inhibitor cocktail [Thermo-Fisher Scientific]) such that the cell stock was concentrated to ~$1x10^7$ cells per mL. Cells were lysed on ice with vortexing every 5 min for 15 min. The lysate was centrifuged at 16,110 g and 4 °C for 10 min. The supernatant was collected in a new 1.7 mL Eppendorf tube and stored at -20 °C until use. RNA was diluted to 500 nM in assay buffer to a final volume of 9 µl. Then, 10% (v/v) of HEK293T lysate was added and the reaction was incubated for 3 h at 37 °C. In one condition, Dicer (Genlantis; 0.25 U) was included in addition to the lysate. Subsequently, samples were stained with 5 µl of RNA loading dye (2x; NEB) and 15 µl of the sample was separated on a 4% (v/v) stacking gel and 16% denaturing PAGE gel. Briefly, 16% (v/v) denaturing gel was generated by mixing 3.2 mL of acrylamide (40% [v/v]) with 4.8 ml of 1x TBE containing urea (7 M) as well as 100 µl of APS (10% [w/v]) and 15 µl of TEMED. The resultant mixture was poured into a 1.5 mm casting apparatus. Saturated 1-butanol in water (500

µl) was added on top of the denaturing gel to ensure flatness. After the denaturing gel solidified, the 1-butanol was poured off and the gel was rinsed three times with distilled water. Subsequently, a 4% (v/v) stacking gel was prepared by mixing 0.5 ml of acrylamide (40% [v/v]) with 4.5 ml of 1x TBE containing 7 M urea in addition to 50 µl of APS and 7.5 µl of TEMED. The gel was pre-run at 140 V for 30 min, then samples were loaded, and electrophoresis was performed at 140 V for 40 min. Following PAGE separation, the gel was stained with SYBR Gold (Invitrogen) as described above. The gel was imaged on a ChemiDoc XRS+ (Bio-Rad) using the 'SYBR Gold' method.

Dicer overexpression. For lysate experiments with overexpressed Dicer, HEK293T cells seeded into 6-well plates (Corning) as described above were transfected with pFRT/TO/FLAG/HA-DEST DICER (Addgene; 19881; 2 µg) using Lipofectamine 2000 (see protocol 6.2.3.1). After 48 h, cells were trypsinized and lysed as described in the above protocols.

For immunoprecipitation experiments,[614] Dicer expression was performed on a larger scale. Briefly, ~2.6 x 10^6 HEK293T cells were plated in a 10 cm plate pre-treated with poly-D lysine (see protocol 6.2.2 The following day, 8 µg of the Dicer expression plasmid was transfected into the cells for 5 h using Lipofectamine 2000. Transfection media was replaced with DMEM growth media (with no antibiotic) and cells were grown to confluence over 72 h. Cells were then washed with PBS, trypsinized, and pelleted by centrifugation. The cell pellet was taken up in 1 ml of lysis buffer (Tris-Cl [50 mM; pH 7.5], NaCl [150 mM], Triton X-100 [1% (v/v)], SDS [0.1% (w/v)]) and incubated on ice for 15 min with vortexing intermittently every 5 min. Next, the lysate was centrifuged at 16,110 g and 4 °C for 10 min. Supernatant was removed and incubated with 25 µl of anti-Flag antibody (Proteintech; catalog# 20543-1-AP; 6 µg) overnight with rocking in a 4

°C cold room. The next day, protein A/G resin (Pierce; catalog# 20421; 100 µl) was washed three times with 500 µl of immunoprecipitation (IP) buffer (Tris-HCl [25 mM; pH 7.2], NaCl [150 mM]) with centrifugation at 600 g for 30 s at room temperature. After the final wash, supernatant was removed and replaced with the lysate previously incubated with the anti-Flag antibody and rocking was continued overnight at 4 °C. The following day, the resin was washed three times with IP buffer followed by centrifugation at 600 g for 30 s. After the final wash, supernatant was removed, and resin was resuspended in 100 µl of glycerol (50% [v/v] in water) and stored at -20 °C until use.

Optimized Dicer processing assay with immobilized enzyme. For the optimized Dicer processing assay, Dicer was overexpressed in HEK293T cells and immobilized on protein A/G beads as described above. Pre-miR-21 (desalted and annealed at 1 µM as described above) was diluted to 200 nM (1 µl) in 4 µl of assay buffer. A basic assay buffer consisting of Tris (10 mM; pH 7.5) and $MgCl_2$ (5 mM) was prepared in a 50 ml conical tube and stored on the bench top at room temperature until use. To prepare the complete assay buffer, 10 µl of ATP (Thermo-Fisher Scientific; [stock] = 100 mM; [final] = 1 mM, 10 µl of freshly prepared DTT ([stock] = 100 mM; [final] = 1 mM, and 0.3 µl of RNasin RNase inhibitor (Promega; 0.4 U/µl) was mixed with 980 µl of the basic assay buffer and used immediately for Dicer processing experiments. Subsequently, resin immobilized Dicer was washed three times in assay buffer. After the last wash, resin was resuspended in 100 µl of assay buffer. For Dicer processing assay, 5 µl of immobilized Dicer slurry was added directly to 5 µl of RNA in assay buffer, such that the final concentration of pre-miR-21 was 100 nM. When the final concentration of RNA in Dicer processing assays was 200 nM, the stock pre-miR-21 was annealed at 2 µM and the remaining volumes were kept the same as

described above. To inhibit Dicer cleavage, EDTA (250 mM) was added in one condition. The reactions were incubated for 24 h at 37 °C. Quenching of the reactions was performed by addition of 5 µl of a stop solution consisting of urea (6 M), EDTA (250 mM), glycerol (10% [w/v]), and bromophenol blue (0.1% [w/v]). The entire 15 µl sample volume was separated on a 15% native PAGE gel (see protocol 6.1.9 stained with 1.5x SYBR gold (Invitrogen) in 1x TBE for 15 min at room temperature with rocking, followed by destaining in 1x TBE for 15 min at room temperature with rocking. The gel was then imaged on a ChemiDoc XRS+ (Bio-Rad) using the 'SYBR Gold' method.

General chemical methods. All reagents were purchased form commercial suppliers and used without further purification. Flash chromatography was performed on a CombiFlash RF (ISCO) with normal-phase silica gel cartridges. NMR spectra were recorded on Bruker spectrometers with assistance from Yuta Naro and Kristie Darrah. The purity of final compound was determined ≥95% via HPLC analysis on a Shimadzu LC-20AD monitored at 280 nm.

2, 5-dioxopyrrolidin-1-yl 4, 4, 5, 5, 6, 6, 7, 7, 8, 8, 9, 9, 10, 10, 10-pentadecafluorodecanoate (207). Commercially available 2H, 2H, 3H, 3H-perfluoroundecanoic acid (**206**; 50 mg, 113.1 µmol) and *N*-hydroxysuccinimide (NHS; 15.6 mg, 135.7 µmol) were dissolved in dry THF (1 ml) in a flame dried glass vial. The vial was capped with a rubber septum and purged with nitrogen. Subsequently, the solution was cooled to 0 °C on ice (~10 min). Finally, EDCI (26.0 mg, 135.7 µmol) was added, and the vial was removed from the ice bath and allowed to warm to room temperature, and the reaction mixture stirred overnight at room temperature. The solvent was evaporated, and the residue was directly purified via silica gel flash chromatography (30% EtOAc

in hexanes) to yield the product as a white solid (21.9 mg, 44% yield). ^{1}H NMR (400 MHz, $CDCl_3$) δ 2.97 (m, 2H), 2.86 (s, 4H), 2.57 (m, 2H). ^{13}C NMR (400 MHz, $CDCl_3$) δ 168.8, 166.8, 26.4, 25.7, 23.0.

Perfluorous-NHS ester coupling to amine modified pre-miR-21 (16 or 60 nt). Custom pre-miR-21 RNA (16 or 60 nt) was synthesized by Dharmacon with an internal 5-aminoallyl-uridine incorporation and was received as a lyophilized solid. The solids were dissolved in nuclease-free water to 1 mM and concentrations and were verified by measuring UV absorbance at 260 nm on a Nanodrop ND-1000 spectrophotometer then calculating the concentration (mM) using the extinction coefficient. Prior to coupling, the full-length pre-miR-21 hairpin was annealed by heating to 95 °C and cooling to 12 °C over 10 min in a thermal cycler (Bio-Rad). For coupling reactions, 10 µl of RNA (1 mM stock) was diluted in 35 µl of sodium bicarbonate buffer (100 mM; pH 8.0) in a 1.7 ml Eppendorf tube. Subsequently, 45 µl of DMSO was added to the solution and mixed by pipetting. Then, 10 µl of perfluorous-NHS ester (10 mM) was added directly to solution and the reaction was incubated at room temperature on a bench top. The perfluorous-NHS ester (10 mM) was added in 10 µl aliquots in five more additions once every 30 – 60 min. After the last addition, the reaction was incubated on the bench top overnight at room temperature. The following day, ethanol precipitation was performed by adding (in order) 2 µl of glycogen (20 mg/mL), 10 µl of sodium acetate (3 M), 10 µl of lithium chloride (8 M), 10 µl of magnesium chloride (100 mM), and 300 µl of ethanol (pre-cooled to -80 °C). The mixture was then incubate at -80 °C for 1 h, then centrifuged at 16,110 g and 4 °C for 30 min. The supernatant was removed, and the pellet was washed with 500 µl of ethanol (70% [v/v] in water). The solution was then

centrifuged a second time at 16,110 g and 4 °C for 30 min. Lastly, 470 µl of the supernatant was removed and the remaining 30 µl was injected on the HPLC to isolate the product.

Product isolation was performed on an Agilent 1200 series HPLC system using an ACE Equivalence C18 column (part# EQV-3C18-1046). Samples were injected at a flow rate of 0.75 ml/ min using a gradient of 5 – 95% acetonitrile/0.1M TEAA over 30 min. Fluorous-modified pre-miR-21 (60 nt) was recovered with a retention time of ~17 min, while the fluorous-modified loop fragment (16 nt) was recovered with a retention time of ~15 min. After isolation from the HPLC, samples were concentrated to ~50 µl on a rotary evaporator (rotovap), then desalted on a 10 kDa molecular weight cut-off (MWCO) column (Amicon). Briefly, 200 µl of nuclease free water was added to the remaining RNA eluate from the HPLC, mixed, then pipetted into the MWCO column. Then, 250 µl of water was used to wash the collection vial a second time, then combined with the previous 250 µl of solution. Next, the column was centrifuged at 14,000 g for 10 min. The flow-through was discarded and 450 µl of nuclease-free water was added to the column to wash the sample. The wash step was repeated two more times. Following the last wash, the column was inverted in a new collection tube and centrifuged at 1,000 g for 2 min. The recovered RNA (usually ~50 µl) was then determined by measuring UV absorbance at 260 nm on a Nanodrop ND-1000 spectrophotometer and calculating concentration (µM) using the extinction coefficient.

4.0 DNA Logic Gates

4.1 Introduction to DNA Computation

Adleman's work solving the Hamiltonian path problem using DNA hybridization, demonstrating that nucleic acid algorithms can be utilized to perform computational operations, is widely regarded as the inception of DNA computation.[619] Since then, the field of DNA computation has expanded to a variety of different devices for numerous applications.[620] In general, DNA-based computation circuits utilize nucleic acids for both structure and function, enabling the design of highly-programmable biological tools capable of precise activation. Watson-Crick base-pairing rules govern duplex formation within DNA computation circuits in a sequence-selective fashion. Various DNA computation devices have been explored including aptamers,[621] deoxyribozymes,[622] G-quadruplexes,[623] and molecular beacons.[624] Among the more recent advances in DNA computation has been the implementation of logic gates for detection of biomolecules.

In traditional silicon-based electronic devices, logic gates serve as electronic switches that process one or more electrical inputs into an electrical output signal according to a defined logic.[625] ON and OFF states of the logic gate are represented by the binary code of 1 (YES or 'true') and 0 (NO or 'false'), respectively. Output signals are true only when the correct combination of inputs is present, according to Boolean logic functions and the corresponding truth tables. For example, in an AND gate, an output is only generated when both inputs are present, otherwise the output is 0 (or false) (Figure 4-1A). Alternatively in the OR gate (Figure 4-1B), an output signal is produced when one or both of the inputs are present. Logic gates can also be designed to detect the absence

of inputs. In the NOT or invertor gate, an output will only be true when the input is false (Figure 4-1C). The exclusive OR (XOR) gate does not produce an output signal unless only one input is present (Figure 4-1D). If both inputs are true, the output will be false.

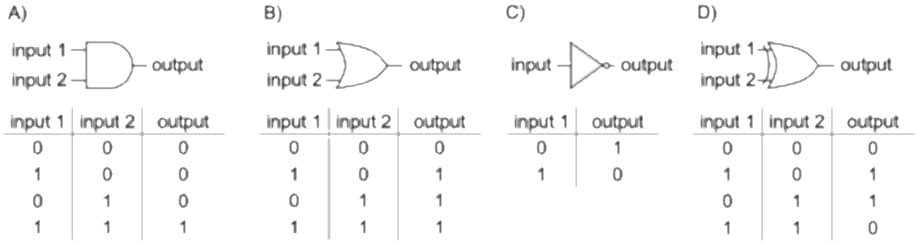

input 1	input 2	output
0	0	0
1	0	0
0	1	0
1	1	1

input 1	input 2	output
0	0	0
1	0	1
0	1	1
1	1	1

input 1	output
0	1
1	0

input 1	input 2	output
0	0	0
1	0	1
0	1	1
1	1	0

Figure 4-1 Logic gate symbols and corresponding truth tables

A) The AND gate will generate an output only in the presence of input 1 and 2. B) The OR gate will generate an output in the presence of input 1 or 2 or both. C) The NOT gate will only generate an output when no input is present. D) The XOR gate will only generate an output in the presence of input 1 or 2 but not both.

DNA logic gates incorporate nucleic acids in place of electrical voltages for inputs and outputs and are capable of converting multiple oligonucleotide inputs (e.g., DNA or RNA) into a single digital output signal while employing Watson-Crick base-pairing for both structure and function. Although there are several limitations to utilizing DNA to mimic silicon-based computation devices including cost of DNA synthesis, slower rate of data readout, lack of rewriting capabilities,[626] and scalability concerns,[627] the development of biologically relevant computation systems offers distinct advantages. For example, DNA computation modules can be readily interfaced with biological and chemical environments. Furthermore, it has been predicted

that 455 exabytes of data can be stored in one gram of DNA[628] and DNA computation devices are hypothesized to be capable of operating at over 100 teraflops.[627]

The key element to DNA logic operations is toehold-mediated strand exchange (Figure 4-2).[629] A toehold is a short region (typically six nucleotides in length) of single-stranded DNA extending from a duplex, which facilitates hybridization, strand displacement, and branch migration. The toehold is designed to anneal to single-stranded nucleic acid inputs in a sequence-selective manner, allowing them to displace bound oligonucleotides from DNA duplexes. When no toehold is available, the reaction is kinetically slow (Figure 4-2A); however, in the presence of an exposed toehold, a complementary single-stranded nucleic acid can hybridize, bringing the two strands within close proximity and initiating a strand displacement reaction (Figure 4-2B). Moreover, the presence of a single toehold (i.e., a toehold only exists for the invading strand) facilitates a kinetically fast strand displacement reaction in one direction, and is thus considered essentially irreversible. In contrast, if there is sequence overlap between the incoming strand and the outgoing strand (i.e., a toehold exists for both sequences), the reaction is kinetically fast and considered reversible (Figure 4-2C). The first step of the toehold-mediated strand displacement reaction—hybridization of the invading strand with the toehold sequence—occurs rapidly ($k_1 = 10^6\ M^{-1}s^{-1}$) and is reversible. In contrast, the second step—branch migration—involves removal of the bound DNA strand from the duplex, is much slower ($k_2 = 1\ s^{-1}$), and generally proceeds in the forward direction.[630] DNA concentration, sequence identity, and length of the toehold contribute to the rate of both steps. For instance, reducing length of the toehold (e.g., from six to five bases) can reduce the reaction rate by a factor of 10.[629] Furthermore, the toehold domain can be rendered essentially unreactive via toehold sequestration (e.g., hybridization between the toehold and a

complementary sequence),[631-633] enabling precise control over timing and order of strand displacement reactions.

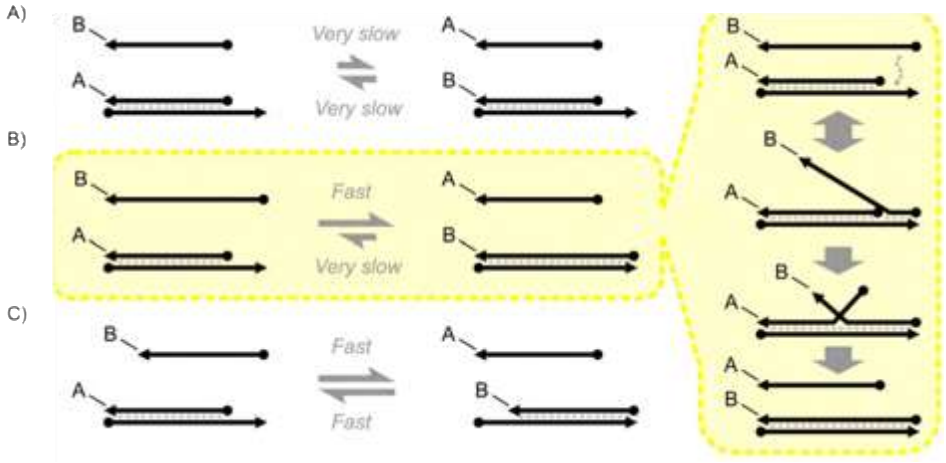

Figure 4-2 Toehold-mediated strand displacement reaction

Toeholds are shown as single-stranded overhangs connected to the DNA duplexes. A) If strand B can't bind to the gate toehold, the displacement of A is unfavorable. B) If a toehold on the gate duplex is available for strand B, but not A, the displacement of strand A is quick and essentially irreversible. The strand exchange reaction outlined in yellow shows the intermediate steps of B binding and removing strand A. C) When toeholds are present in the gate duplex for strands B and A, the displacement reaction is reversible. Adapted with permission from *Curr. Opin. Biotechnol.* **2010**, 21(4), 392-400.

DNA logic gates are modular devices capable of being incorporated into complex circuits of nucleic acids wherein the output of one gate may be used as an input for a downstream gate, effectively generating a signaling cascade.[633,634] Furthermore, they are highly programmable such that their sequences can be designed to recognize a variety of biologically relevant oligonucleotide inputs. For example, Seelig and co-workers designed a series of AND and OR gate circuits to

detect expression patterns of up to six synthetic miRNA inputs.[632] The inputs displaced an output strand from a translator gate that hybridized to a downstream AND gate (Figure 4-3A). miRNA sequences were paired such that two inputs would specifically interact with their respective translator gates and release an output bearing an identical recognition domain, effectively serving as an OR logic gate. The output strands were utilized as inputs for a subsequent AND gate. Upon recognition of the correct combination of inputs, the output of the AND gate interfaced with a threshold gate in order to minimize background activity. The threshold gate is a three-input AND gate in which the output strand will not be released in the presence of substoichiometric amounts of input. However, input concentrations at least two-fold higher than the threshold gate were able to trigger release of an output sequence that interfaced with a downstream fluorophore/quencher-modified gate to monitor the readout. In total, the circuit was comprised of 11 DNA logic gates. Notably, increasing the size of the circuit also reduced the reaction kinetics (i.e., increasing time to completion from 6 to 12 h). However, ON and OFF states were still easily distinguishable, suggesting the circuit was capable of responding to distinct miRNA patterns (Figure 4-3B).

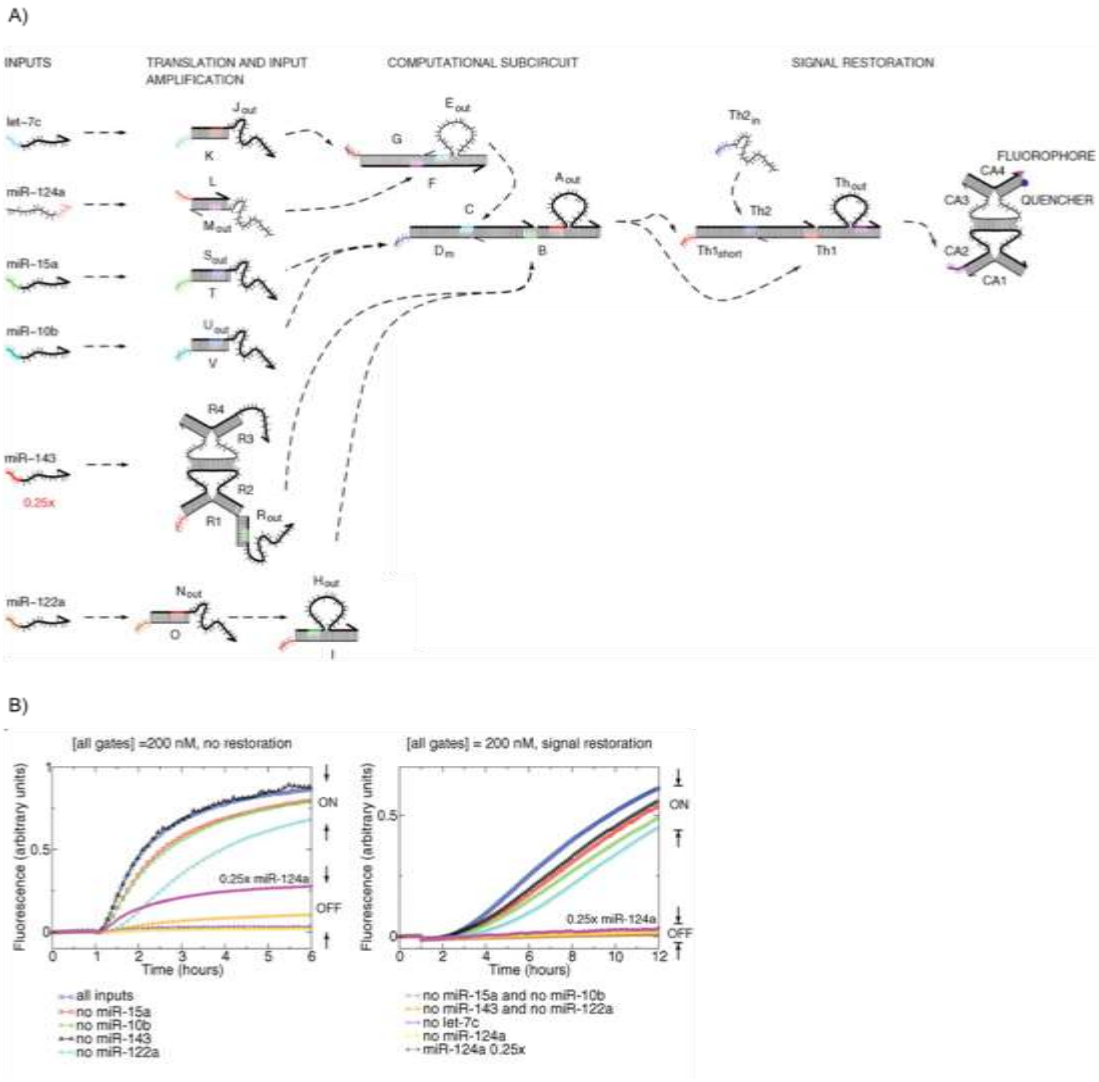

Figure 4-3 Signal propagation through a complex DNA logic gate circuit

A) The five-layer circuit is comprised of 11 gates including AND, OR, sequence translation, input amplification, and signal restoration and accepts six miRNA inputs. B) Fluorescence intesnsity measurements without (left) and with (right) the signal restoration component (threshold plus amplifier). Adapted with permission from *Science*. **2006**, 314, 1585-1588.

Additional logic gate circuits have been developed which are capable of performing a variety of other applications *in vitro* including mathematical operations,[634-636] serving as neural networks and memory systems,[637] and disease diagnosis.[638] For example, Winfree and co-workers developed a 'seesaw' gate design in order to enable large scale DNA logic gate circuits to compute a square root function.[634] In the seesaw gate, a 'fuel' strand displaces an incumbent strand from a gate duplex in a catalytic cycle via exchange of exposed toeholds. By combining seesaw gates with thresholding, Winfree was able to construct a large scale circuit comprised of 130 DNA strands, demonstrating a feasible solution to the common scalability problem associated with DNA computation devices. Because of their ability to hybridize to nucleic acid inputs in a sequence-specific fashion via strand displacement interactions and release an oligonucleotide output capable of interacting with biological systems, development of DNA computation devices that interface with cellular environments has recently gained increasing interest. Nucleic acid-based computation devices have been employed in biological systems for cellular delivery,[639] targeted therapy,[640] and miRNA or mRNA detection.[641-644]

The Deiters laboratory was the first to utilize DNA-based gates to perform logic operations on endogenous miRNA inputs to produce a DNA output in mammalian cells.[645] A logic gate circuit was designed wherein miR-21 and -122 displaced single-stranded outputs from translator gates that subsequently initiated a strand displacement reaction in a downstream AND gate (Figure 4-4A) leading to release of a fluorophore-modified oligonucleotide in Huh7 cells. The use of translator gates enabled a modular circuit design which could be adapted to recognize alternative miRNAs. The AND gate consisted of a DNA duplex with an exposed toehold complementary to the first input, as well as a tetramethylrhodamine (TAMRA) fluorophore functionalized on the 5'-terminus of the output strand and a Black Hole Quencher (BHQ) on the 3'-terminus of the

complementary strand. BHQ is capable of absorbing energy emitted by TAMRA in its excited state in a FRET-like manner, thus inhibiting a fluorescent output signal. In order to validate that the gate only activated in the presence of input 1 and 2, the circuit was first evaluated *in vitro* utilizing synthetic DNA inputs. After 4 h incubation at room temperature, a 2.5-fold increase in fluorescence in the presence of both inputs was detected relative to background (Figure 4-4B). Moreover, minimal gate activation was observed when one or neither of the inputs was added. After confirming the AND gate performed logic operations as predicted, the logic gate circuit was transfected into Huh7 cells—shown to up-regulate both miR-21[646] and miR-122[647]—and activation was evaluated by fluorescence microscopy. After delivery of the gates and 48 h incubation, fluorescence was only observed in cells transfected with the complete circuit (Figure 4-4C).

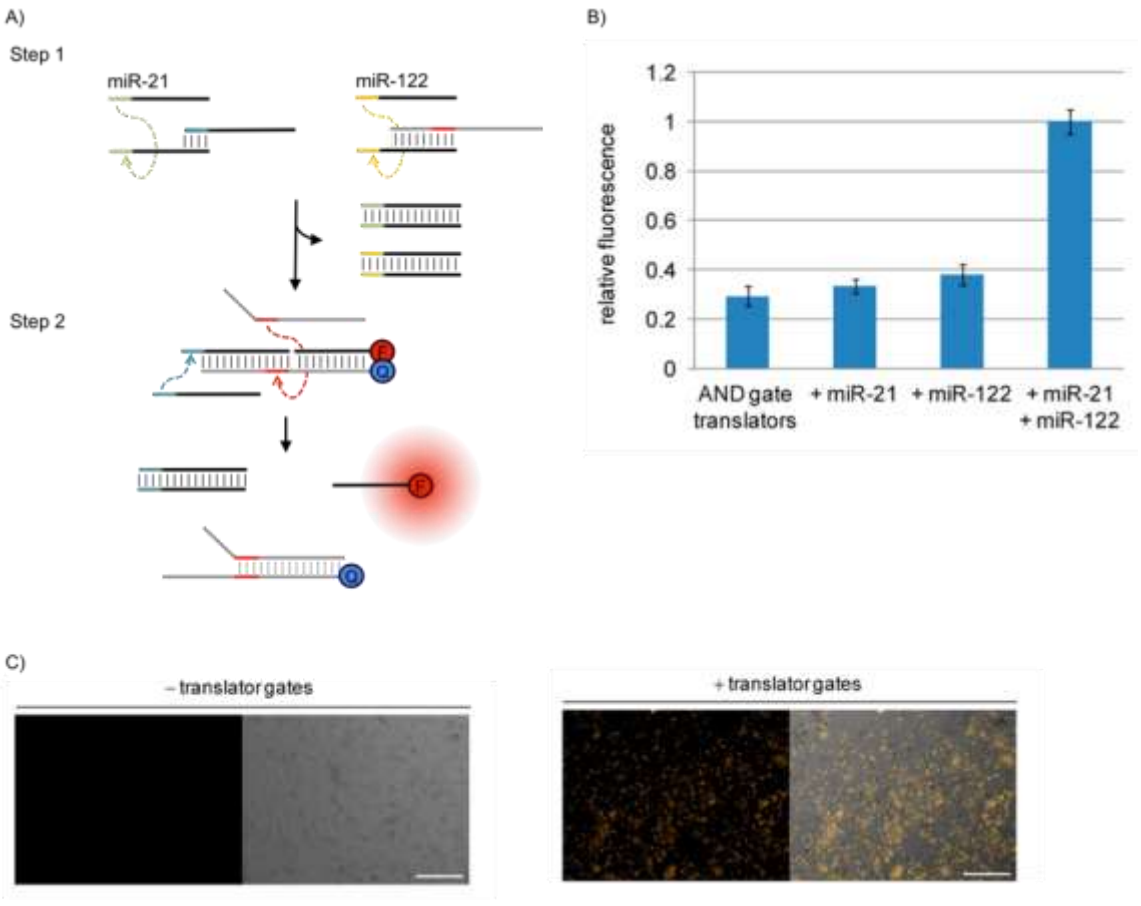

Figure 4-4. AND gate activation *in vitro* and *in cellulo*

A) Schematic of an AND gate targeting miR-21 and miR-122 with corresponding translator gates. In Step 1, miR-21 and miR-122 interact with respective translator gates via toehold mediated strand displacement reaction to generate output strand which serve as new inputs for the AND gate. In Step 2, the new inputs interact with the AND gate in a similar manner to generate a fluorescently labeled output strand. B) The AND gate was activated *in vitro* with both translator gates in the presence of synthetic inputs. C) Transfection of the AND gate in Huh7 cells expressing endogenous miR-21 and miR-122 only yields a fluorescent output with the addition of both translator gates. Adapted with permission from *J. Am. Chem Soc.* **2013**, 135, 10512-10518. Copyright 2013 American Chemical Society.

Recently, Seelig and co-workers employed a logic gate circuit capable of a 4-way strand exchange reaction in order to characterize parameters that affect gate activation in mammalian cells (Figure 4-5A).[648] It was hypothesized that the 4-way strand exchange reaction would enable logic gate activation in a cellular environment with minimal crosstalk with other nucleic acids. After optimizing the gate structure *in vitro* utilizing a reporter gate with a 6-nucleotide toehold domain and 16- or 22-nucleotide branch migration domains, the logic gate circuits were delivered into cells and gate activation was monitored by fluorescence microscopy. Of the chemical modifications evaluated, 2'-*O*-methyl-modified gates led to a ~7-fold activation while the combination of 2'-*O*-methyl and PS modifications led to only a ~3-fold increase in fluorescence in CHO K1 cells. This discrepancy was attributed to reduced thermodynamic stability conferred by the PS modifications. The transfection reagent Lipofectamine 2000 was found to be sufficient for preventing interaction between the reporter gate and input in pre-packaged complexes prior to transfection. Interestingly, sequential transfection of the gate and inputs led to only ~5% co-localization of the two complexes in cells—a dramatic reduction compared to ~40% co-localization observed when the complexes were co-transfected—highlighting an important consideration for delivery of DNA computation circuits bearing multiple components into cells. Finally, the optimized conditions determined from preliminary reporter gate experiments were applied to more complex AND and OR gates utilizing flow cytometry to monitor gate activation (Figure 4-5B). Initially, the OR gate only bore the 2'-*O*-methyl modifications, however while input A induced the expected increase in fluorescence, low fluorescence intensity was observed upon addition of the second input in cells. It was hypothesized that the single-stranded domains of the duplex produced by input B was susceptible to nuclease degradation. To overcome this limitation, PS modifications were incorporated into the OR gate, inputs, and subsequent AND gate designs.

Notably, incubation of the 2'-*O*-methyl- and PS-modified OR gate with non-modified inputs led to a reduction in activation efficiency, similar to the reporter gates described above, highlighting the importance of balancing stability and activity in the design of logic gates for biological systems. The 2'-*O*-methyl- and PS-modified logic gates activated as predicted in cells with the OR gate eliciting a 2.5-3-fold increase in fluorescence following addition of one or both inputs and the AND gate responding to addition of both inputs with a >3.5-fold fluorescence increase (Figure 4-5C).

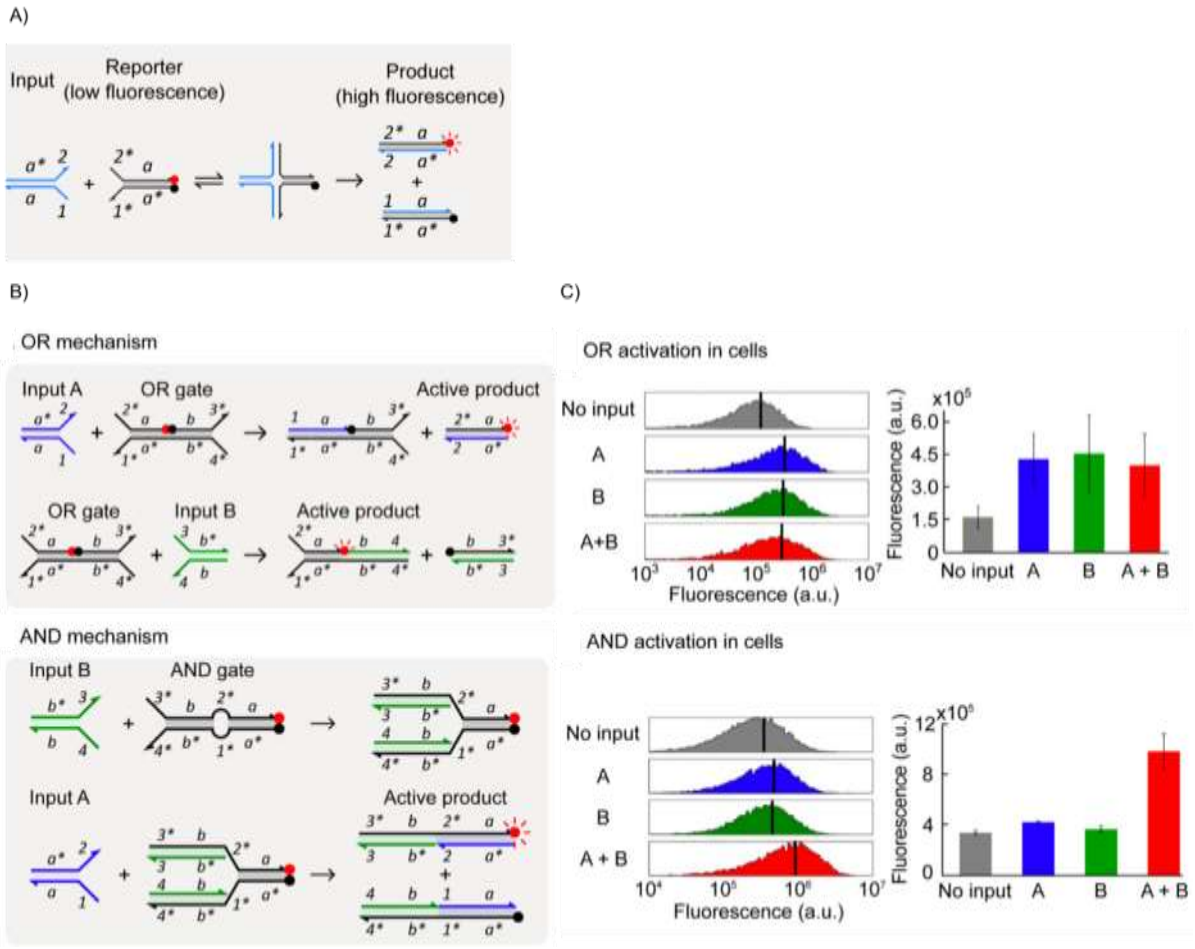

Figure 4-5 DNA logic gate activation in mammalian cells

A) 4-way strand exchange reaction mechanism. Toehold regions are numbered while double-stranded domains are marked with letters. Red circle = TYE665 fluorophore. Black circle = BHQ2 quencher. B) OR and AND logic gate design and mechanism. C) Corresponding flow cytometry data following delivery and activation of OR and AND logic gates in CHO K1 cells. Adapted from *Nat. Nanotechnol*. 2016, 11, 287-294.

In an alternative approach, the Weizmann lab utilized fluorophore-modified DNA hairpins in order to detect endogenous miR-21 in mammalian cells.[649] The hairpins were synthesized using 2'-*O*-methyl-modified nucleobases and PS backbone modifications to improve their stability in a

cellular environment. Using this method, miR-21 hybridizes to first hairpin (HP_1), opening it up and exposing a single-stranded stem region (Figure 4-6A). This stem region then anneals to a second hairpin (HP_2) and opens it to expose another single-stranded stem region capable of interacting with HP_1 and continuing the cascade hybridization reaction (CHR). In the resultant concatemers, the fluorophores at the termini of both hairpins are in close proximity to each other such that the reaction can be visualized using FRET. After delivery into HeLa cells for 4 h, fluorescent puncta were observed via microscopy (Figure 4-6B). Furthermore, low or no fluorescence was observed in HEK293T and MRC-5 cells lines which express little to no miR-21, respectively, compared to HeLa cells, suggesting the CHR system could be capable of differentiating between different cell types based on miRNA expression levels.

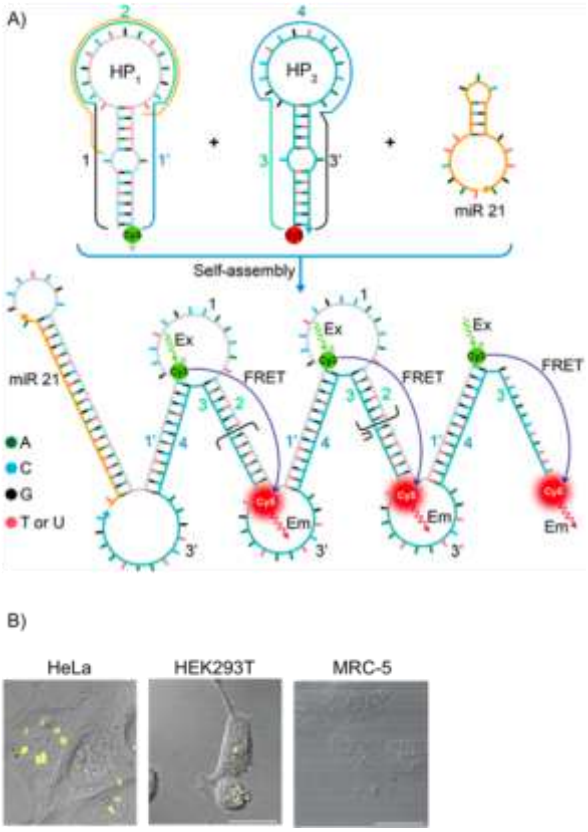

Figure 4-6 Cascade Hybridization Reaction for Detection of miR-21

A) Schematic of cascade hybridization reaction (CHR) mechanism. B) Live-cell FRET analysis of CHR in HeLa, HEK293T, or MRC-5 cells. Adapted with permission from *J. Am. Chem. Soc.* 2015, 137, 6116-6119. Copyright 2015 American Chemical Society.

Several other nucleic acid devices for oligonucleotide detection in cells have also been developed.[650,651] For example, Seelig and co-workers utilized a 2'-*O*-methyl- and fluorophore/quencher-modified DNA duplex to visualize GFP mRNA in HT1080-96X cells.[643] Upon recognition of one of 96 tandem repeat sequences within the 3' UTR of the GFP transcript, the fluorophore-labeled strand was displaced from the gate duplex enabling observation of the

mRNA via fluorescence microscopy. While this study demonstrated that it was possible to initiate a strand displacement reaction by targeting mRNA in cells, the mRNA transcript was stably expressed from an exogenous construct and bore tandem repeats, so it may not be broadly applicable to other mRNA transcripts. In an alternative approach, non-modified DNA hairpins were assembled along a long single-stranded DNA sequence (DNA nanowire) forming a DNA nanostructure capable of responding to a target mRNA sequence in cells with the initiation of a DNA cascade reaction (DCR) observable by fluorescence microscopy.[652] Folic-acid mediated delivery of the so-called 'DNA nanostring light' (DNSL) and subsequent hybridization to survivin mRNA in HeLa cells led to unquenching of the DNA hairpins within the nanostructure and a corresponding increase in fluorescence. Additional methods for detection of nucleic acid logic operations have also been explored. For example, gold nanoparticles and quantum dots have been utilized for the detection of miRNAs and mRNAs in live cells.[644,653-655] Another recent advancement has been the incorporation of nanopores for monitoring logic gate activation.[656,657] In the nanopore system, DNA logic gates and inputs are incapsulated in lipid-coated droplets. When the droplets are brought in close proximity to each other, a bilayer lipid membrane forms. Subsequently, an α-hemolysin (αHL) nanopore forms within the bilayer lipid membrane and application of a positive voltage gradient drives the DNA through the nanopore enabling detection of DNA hybridization via a change in current.

Taken together, DNA computation devices are unique chemical tools capable of interacting with biological systems and providing a binary readout. While the majority of systems rely on FRET-based designs wherein fluorophore-modified oligonucleotides are displaced from complementary quencher-modified strands, several recent advancements have sought to explore alternative detection methods in order to expand the utility of these devices. Furthermore, the

application of DNA computation technologies has been demonstrated in cells, highlighting their utility in biological systems.

4.2 Second Generation Logic Gates for Detection of miRNAs in Cells

While activation of numerous DNA computation devices has been demonstrated in cells and animals,[658-661] the ability to interface with endogenous nucleic acids remains a challenge. Given the importance of miRNAs in various diseases as highlighted above and in light of our previous success in detecting endogenous miRNAs in cells,[645] we sought to design multilayer DNA logic gate circuits capable of recognizing more complex miRNA expression patterns in mammalian cells. Unique miRNA expression signatures have been discovered in various tissues and in serum associated with several cancers,[49,662-664] thus we hypothesized that DNA computation devices could be utilized to differentiate between cancer cell phenotypes.

In order to expand the previous miRNA-targeted DNA logic gate to target additional miRNAs, we designed a miR-21 OR miR-122 AND miR-125b circuit (Figure 4-7). The use of translator gates enables a modular design strategy whereby additional miRNA sequences can be targeted by generating a complementary gate duplex. Furthermore, the use of an arbitrary first input sequence would enable the first input to originate from a more complex circuit upstream of the AND gate if desired. In the presence of miR-21 and/or miR-122, an identical output strand is released from the corresponding translator gate serving as the first input for the downstream AND gate. This reveals a second toehold complementary to miR-125b which can then displace the fluorophore-modified strand from the gate duplex resulting in unquenching of the fluorophore.

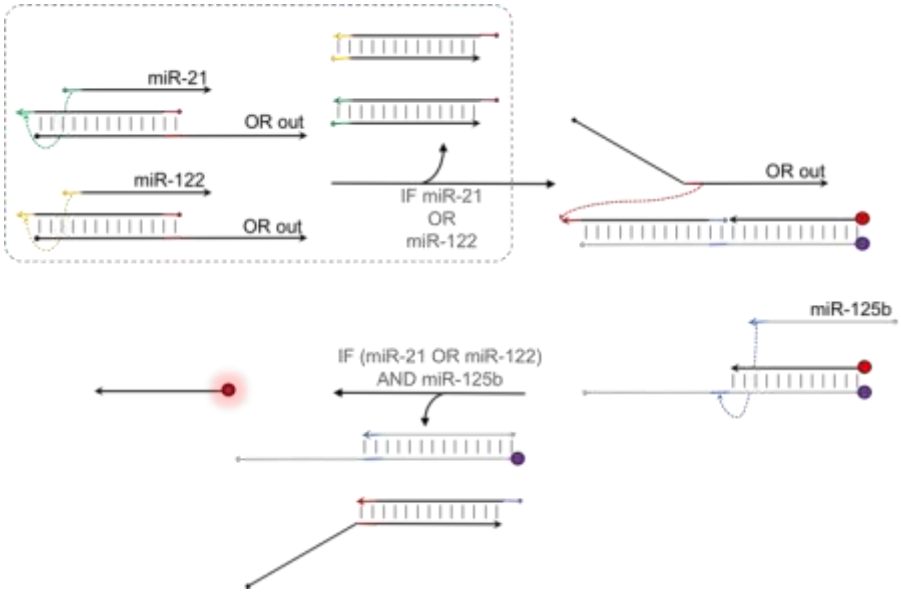

Figure 4-7 Schematic of (miR-21 OR miR-122) AND miR-125b DNA logic gate

Toehold regions are marked in green (miR-21), yellow (miR-122), red (OR out), or blue (miR-125b). Red circle = tetramethylrhodamine (TAMRA). Purple circle = Iowa Black RQ quencher.

Before evaluating the multilayer circuit in cells, a control experiment was performed *in vitro* utilizing synthetic DNA as inputs for the logic gates. Briefly, purified gate duplexes were combined with various combinations of inputs at a 4-fold excess in Tris-EDTA/$MgCl_2$ (TE/Mg^{2+}) buffer, then incubated at 37 °C for 4 h. After completion of the gate reaction, fluorescence was measured on a plate reader. A threshold was calculated for the fluorescence intensity data by multiplying the standard deviation of the dataset by three.[665] Gratifyingly, minimal fluorescence increase was observed when the AND gate was incubated with the OR-21 or -122 gates alone or with their respective miRNA inputs (Figure 4-8). Unfortunately, addition of miR-125b in the absence of the other two inputs led to a modest increase in fluorescence relative to the AND gate alone, suggesting the input was able to non-specifically activate the AND gate. Moreover,

combination of miR-21 or miR-122 and their respective translator gates with miR-125b led to a moderate increase in fluorescence relative to conditions with miR-125b and the AND gate, however, they still fell below the threshold. Gratifyingly, addition of both miR-21 and miR-122 in addition to miR-125b led to an increase in fluorescence intensity above the threshold, suggesting it may be possible to utilize a multilayer logic gate to detect specific miRNA patterns.

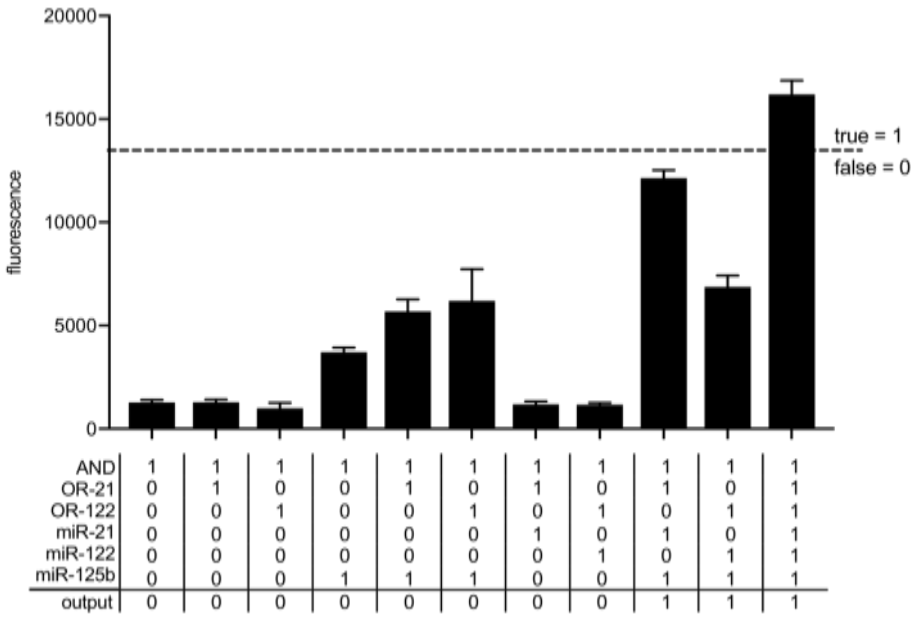

Figure 4-8 *In vitro* evaluation of the (miR-21 OR miR-122) AND miR-125b DNA logic gate

Activation of the logic gate circuit was evaluated with synthetic DNA mimics of miRNA inputs. TAMRA fluorescence was measured after 4 h incubation at 37 °C. Data represents the average of three independent experiments and the error bars indicate standard deviations. Threshold (dashed line) was calculated by multiplying the standard deviation of all data points by three.

Based on promising results *in vitro* we next sought to evaluate the second generation logic gate circuits in mammalian cells. In order to demonstrate selective gate activation, we delivered the gates into cell lines with differential expression levels of miR-21, miR-122, and miR-125b: HEK293T (human embryonic kidney) cells are predicted to express low levels of miR-125b,[666] but do not express miR-21 or miR-122[379,667] and thus should not be able to activate the logic gate circuit. In contrast, HeLa (cervical carcinoma) and PC3 (prostate adenocarcinoma) cells both express miR-21[534,668] and miR-125b,[489] but not miR-122[379] and should elicit an increase in fluorescence. Analogously, the hepatocellular carcinoma cell lines HepG2 and Huh7 express miR-21[503,669] but not miR-125b.[670] Furthermore, while Huh7 cells express high levels of miR-122,[671] HepG2 cells do not.[672] The AND gate, OR-21, and OR-122 gate duplexes were transfected into each cell line for 4 h at which point, the transfection mix was replaced with normal growth media. Because maximal logic gate activation was observed with our previous gate circuit in cells after 24 h,[645] we monitored fluorescence via widefield fluorescence microscopy the following day. James Hemphill, a former member of our laboratory, observed an increase in fluorescence in HeLa and PC3 cells as expected, with minimal background fluorescence in HEK293T, HepG2, and Huh7 cells (negative controls), suggesting the multilayer circuits were capable of activating in response to endogenous miRNAs in mammalian cells (Figure 4-9A). Unfortunately, reproducibility of these data were poor as evidenced by an unexpected increase in fluorescence observed in HEK293T and Huh7 cells in subsequent experiments. (Figure 4-9B).

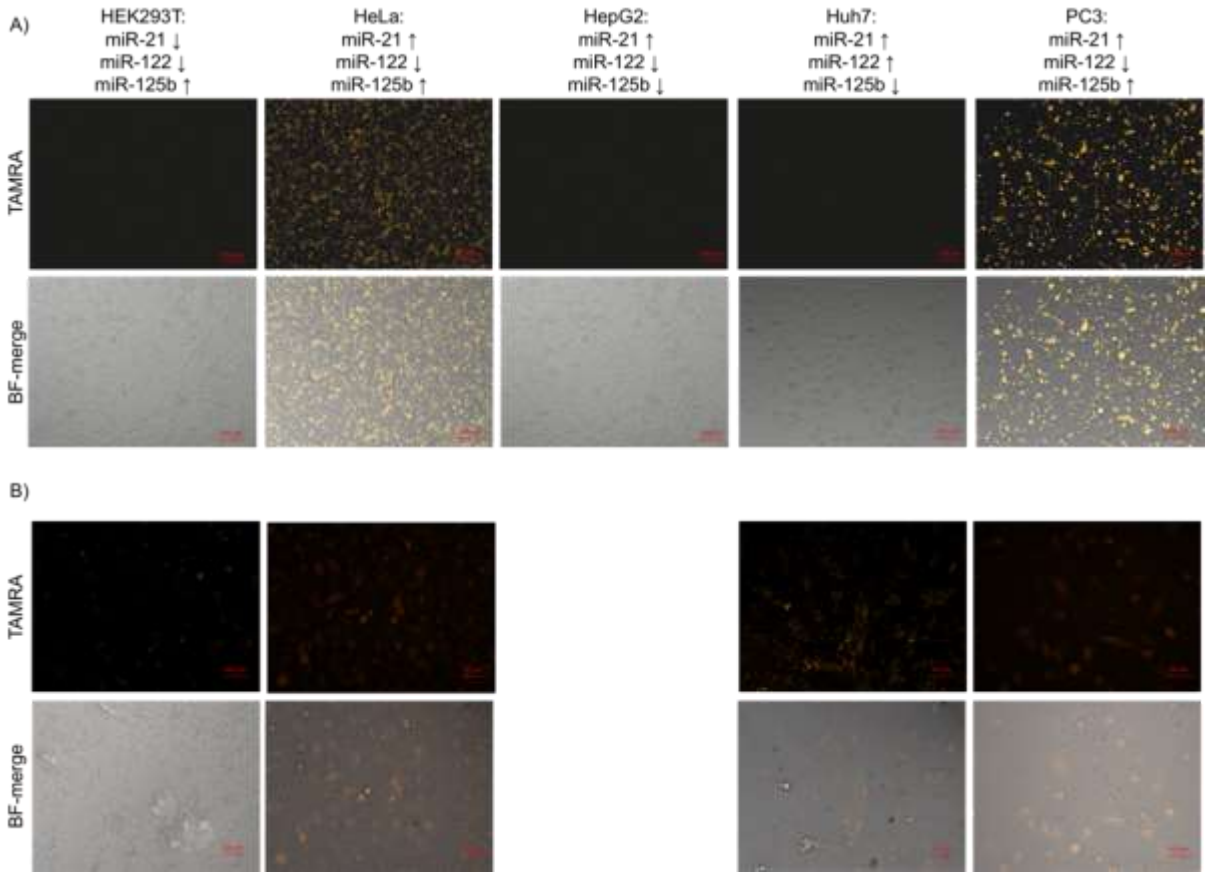

Figure 4-9 Second generation logic gate activation in mammalian cells

A) HEK293T, HeLa, HepG2, Huh7, and PC3 cells were transfected with the AND gate (50 nM) and reporter gates (50 nM) then imaged at 24 h-post gate transfection. Data generated by James Hemphill. B) HEK293T, HeLa, HepG2, Huh7, and PC3 cells were transfected with the AND gate (50 nM) and reporter gates (50 nM) then imaged at 24 h post transfection. 20x magnification. TAMRA (43HE filter; ex/em. = 550/605 nm) and brightfield-merged images are shown. Scale bars indicate 200 µm.

Due to the high background fluorescence observed *in vitro* in the presence of miR-125b but absence of the other two inputs, we hypothesized that non-specific gate activation may have occurred, in part, due to the low miR-125b levels in HEK293T cells. Because miR-125b interacts

directly with the AND gate as the second input, partial dissociation (or 'fraying') of the fluorophore and quencher duplex leading to toehold-less strand displacement reactions. Furthermore, we hypothesized that AT-rich regions within the second toehold of the AND gate may exacerbate fraying, contributing to background activation.[630] In an attempt to circumvent these limitations, we completely redesigned the DNA logic gate circuit (Figure 4-10A). For the miR-21 AND (miR-122 OR miR-125b) gate, miR-21 serves as the first input and interacts directly with the AND gate. In contrast, miR-125b interacts with a translator gate upstream as part of an OR gate with miR-122. Similar to the previous design, an output is only predicted if miR-21 and miR-122 and/or miR-125b participate in the strand displacement reaction. Gratifyingly, when the new gate design was incubated with synthetic DNA inputs *in vitro*, we observed near complete abrogation of background activation in the presence of the second input (Figure 4-10B). A modest additive response was observed with addition of both miR-21 and miR-122 relative to each individual input. Unfortunately, when we attempted to deliver the logic gate circuit into HeLa or Huh7 cells, we observed non-specific gate activation—most concerningly in the absence of any translator gate (Figure 4-10C). Furthermore, while transfection into HEK293T cells yielded a reduction in fluorescence compared to the previous gate design, non-specific background activation was still observed. We hypothesized that the background activation and poor reproducibility may be attributed to nuclease degradation of the gate duplexes upon delivery into cells. In order to circumvent these concerns, we next evaluated methods to protect the logic gate duplexes from degradation such as protecting the termini with hairpins or incorporating 2'-*O*-methyl-modified nucleobases and phosphorothioate backbone linkages.

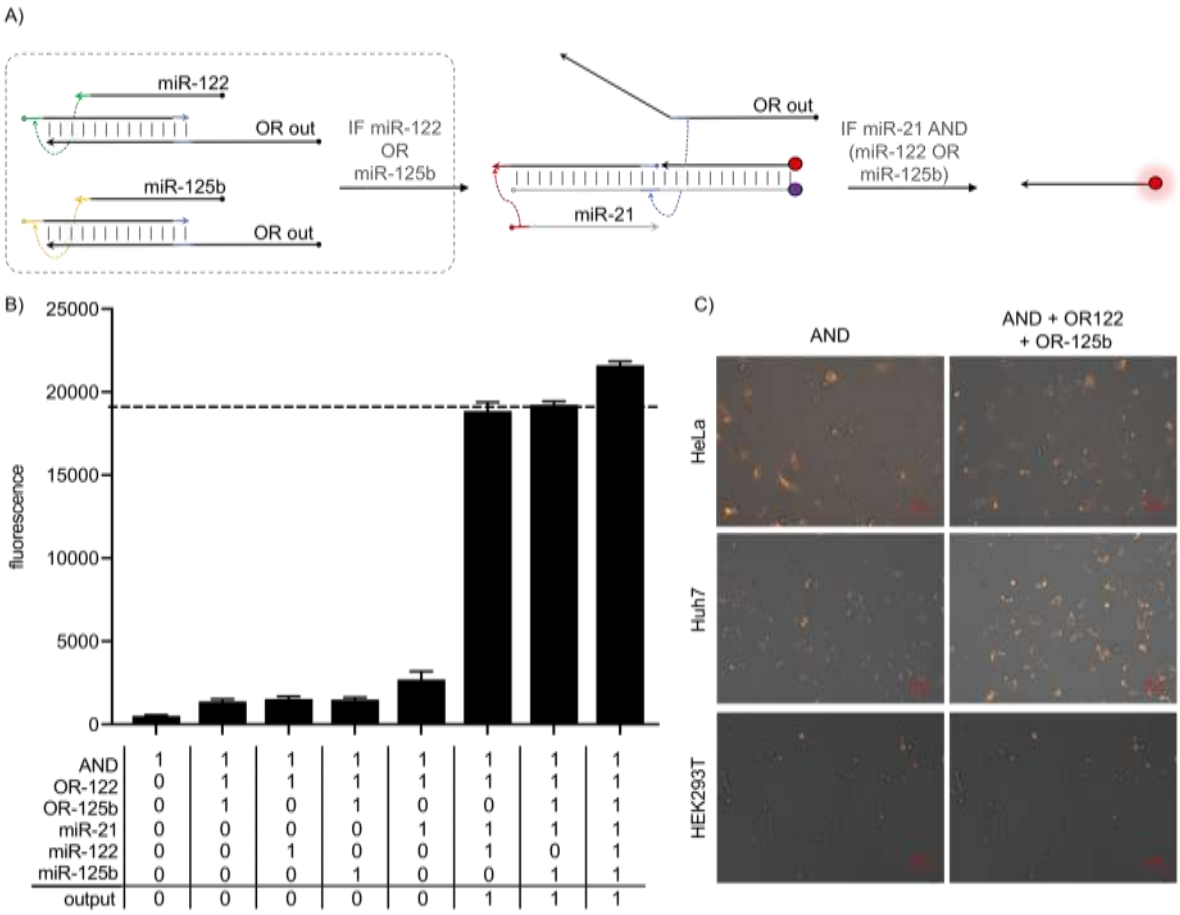

Figure 4-10 Evaluation of the redesigned second generation DNA logic gate

A) Simplified schematic of the miR-21 AND (miR-122 OR miR-125b) logic gate circuit. B) Activation of the logic gate circuit was evaluated with synthetic DNA mimics of miRNA inputs. TAMRA fluorescence (ex/em = 545/585 nm) was measured after 4 h incubation at 37 °C. Data represents the average of three independent experiments ± standard deviation. Threshold (dashed line) was calculated by multiplying the standard deviation of all data points by three. C) HEK293T, HeLa, and Huh7 cells were transfected with the AND gates and reporter gates then imaged at 24 h post transfection. 20x magnification. TAMRA (43HE filter; ex/em. = 550/605 nm) and brightfield-merged images are shown. Scale bars indicate 200 µm.

Single- and double-stranded oligonucleotides are prone to endo- and exonuclease degradation, respectively, in cells and serum.[673,674] One study found that backbone modification of fluorescently-labeled DNA from phosphodiester to phosphorothioate linkages improved the half-life from 15-20 minutes to more than 24 hours.[674] In an analogous report, it was shown that as few as three phosphodiester bonds in a 17-nucleotide oligomer in which the remaining linkages were phosphorothioate was sufficient for compromising nuclease resistance.[675] As discussed above (Chapter 1.2.2 several backbone and nucleobase modifications have been employed in order to improve nuclease resistance of oligonucleotides. Additionally, several reports have shown that short hairpins at the termini of a nucleic acid were sufficient for inhibiting nuclease degradation.[676-679] To attempt to circumvent the cost and difficulty of synthesizing sugar- and phosphodiester-modified oligonucleotides, we hypothesized that modification of our logic gate duplexes with small hairpin structures would be sufficient for inhibiting nuclease degradation. As a proof of concept, we utilized the previously reported AND gate sequence[645] designed to recognize miR-21 and an arbitrary sequence as inputs. Hairpin structures consisting of a GC-rich 7-mer stem and an 'AAA' loop region were incorporated at the termini of the gate strands (Figure 4-11A). To evaluate activity of the hairpin-modified gate, the DNA duplex was incubated with synthetic DNA inputs at a 4-fold excess for 4 h at 37 °C, then subsequently analyzed via native PAGE. The fluorophore- and quencher-modified version of the AND gate without hairpins was utilized as a positive control. As expected, an increase in fluorescence was observed for the non-hairpin-modified AND gate only in the presence of both inputs in a plate reader assay, consistent with the native PAGE gel (Figure 4-11B). Unfortunately, presence of a band corresponding to the gate output was observed when the hairpin-modified gate was incubated with input 2 alone, suggesting non-specific activation of the DNA duplex (Figure 4-11C).

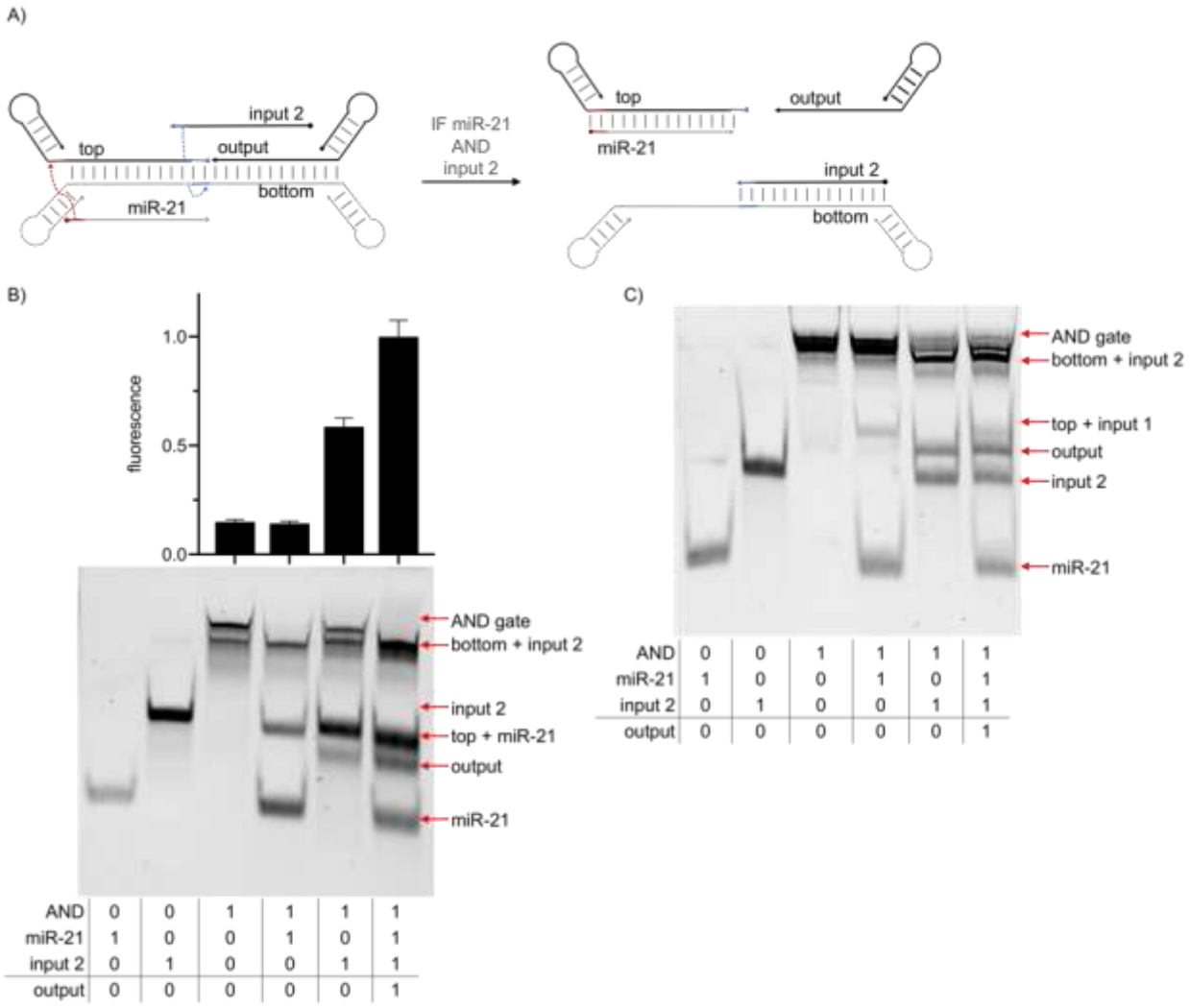

Figure 4-11 Evaluation of hairpin-modified logic gates *in vitro*

A) Simplified schematic of the hairpin-modified AND logic gate. B) The fluorophore- and quencher-modified AND gate was evaluated in a plate reader assay as well as on a native PAGE gel. Data from the plate reader assay represents the average of three independent experiments ± standard deviation. C) Activation of the hairpin-modified AND logic gate was investigated via native PAGE.

To attempt determine the source of background activation with the addition of the hairpins, we analyzed the DNA duplex using The Nucleic Acid Package (NUPACK) software[680] which enabled us to predict its thermodynamic stability. At 37 °C, the probability that base pairs will form near the termini of the non-hairpin-modified gate duplex is ~80% (Figure 4-12A). However, when hairpins are incorporated at the termini the probability of base pair formation at the termini becomes ~60-65%. Taken together, this suggests that fraying can occur at the termini leading to strand displacement in the absence of both inputs. To test this hypothesis, we generated a series of hairpin-modified gate duplexes wherein one or two of the terminal hairpins were removed and evaluated the response in a native PAGE gel-based SAR study (Figure 4-12B). Unfortunately, none of the structural modifications led to a significant reduction in background activation.

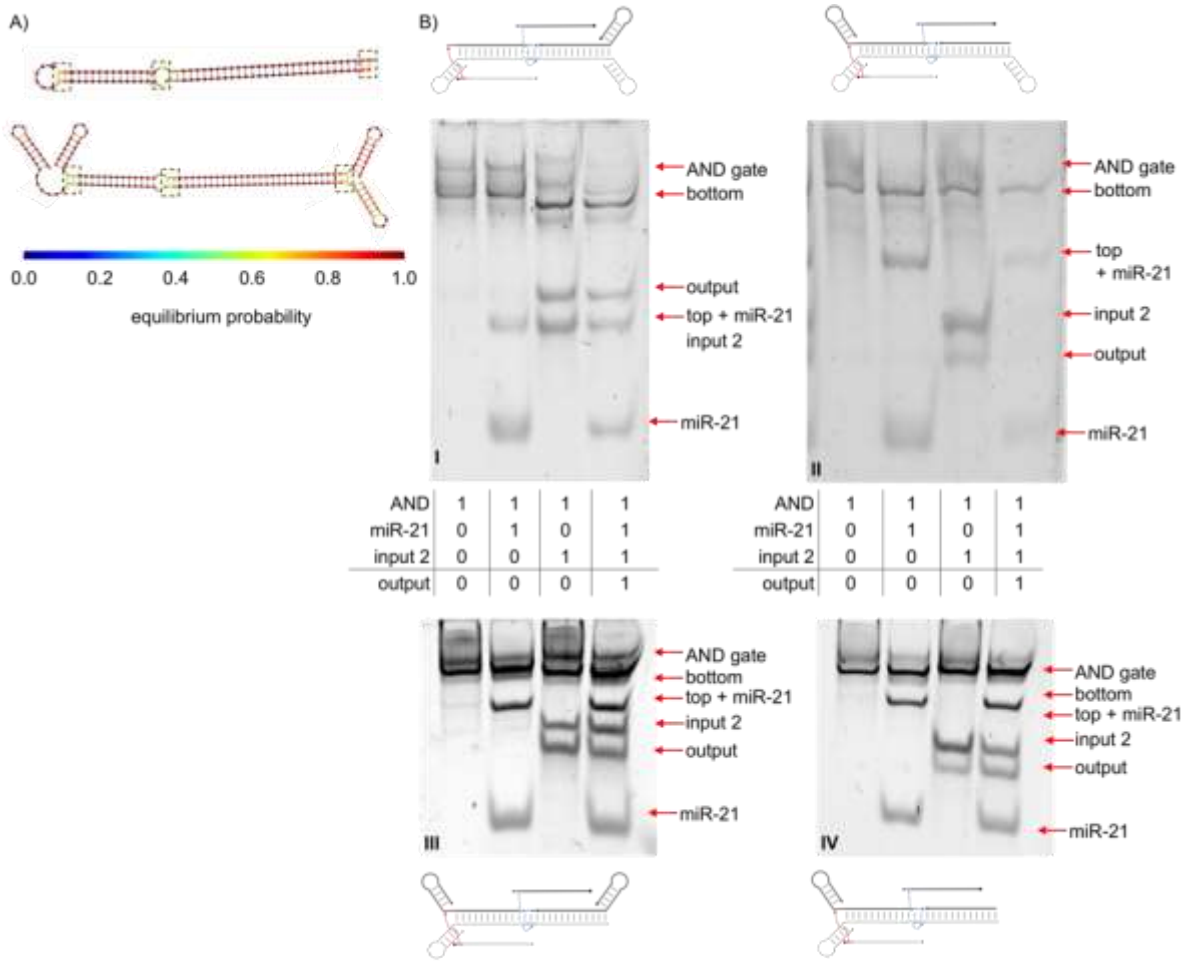

Figure 4-12 Native PAGE evaluation of hairpin-modified AND gate activation

A) NUPACK prediction of duplex stability. Highlighted boxes denote regions where probability of base-pairing is <100%. B) Hairpins were strategically removed from I the top strand; II the 'fluorophore' strand; III the 'quencher' strand; or **I**V the 'fluorophore' and 'quencher' strands of the AND gate duplex to attempt to determine if they contribute to background activation.

In light of the fact that the hairpin modifications induced non-specific gate activation, we decided to investigate whether the hairpins were capable of inhibiting nuclease degradation before moving forward with further optimization of the logic gate design. Utilizing a DNase I digestion

assay,[681] we incubated the hairpin- or non-hairpin-protected DNA logic gate (1 μg) with increasing concentrations of recombinant enzyme for 5 min at 37 °C followed by analysis via 4% agarose gel electrophoresis. A dumbbell DNA decoy was employed as a negative control for nuclease degradation.[682] The DNA decoy was only partially digested with recombinant DNase I activity as high as 0.025 U. However the AND gates were completely digested at the same enzyme concentration (Figure 4-13A). Additionally, we attempted to incubate the AND gates or dumbbell DNA decoy in HeLa cell lysate[683] isolated using two commercially available kits and observed complete loss of the hairpin-modified gate after 6 h incubation at 37 °C. (Figure 4-13B) Furthermore, performing the digest in water or phosphate-buffered saline (PBS) had no effect on enzyme activity. Because neither the non-modified AND gate nor dumbbell decoy were digested at this time point, we hypothesized that destabilization of the hairpin-modified gate may have increased its susceptibility to nuclease degradation. Taken together, this suggests that the hairpins were not sufficient for inhibiting nuclease cleavage and prompted us to pursue alternative strategies for improving stability of the DNA duplexes.

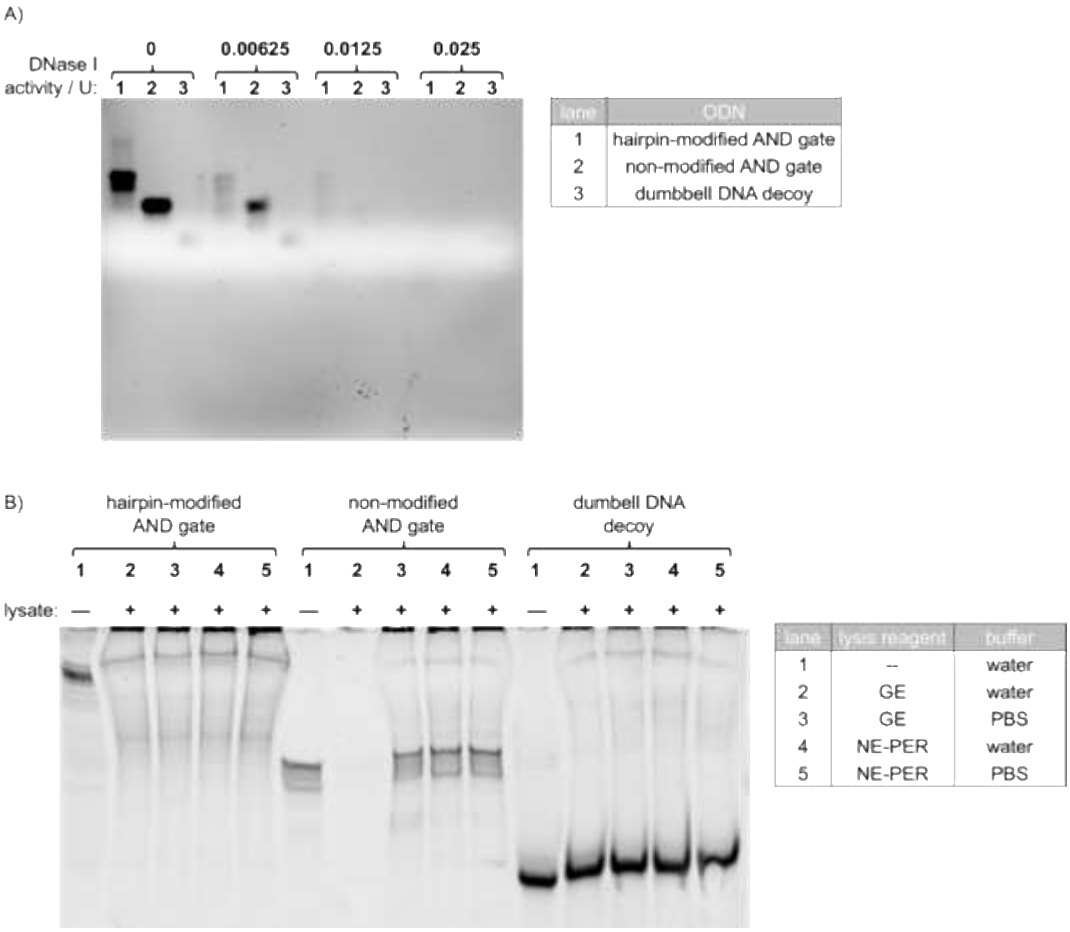

Figure 4-13 Nuclease-mediated degradation of double-stranded DNA oligonucleotides

A) 1 µg of either hairpin-modified AND gate, non-modified AND gate or dumbbell DNA decoy were incubated with recombinant DNase I for 5 min at 37 °C, then evaluated via agarose gel electrophoresis. B) Oligonucleotide duplexes (50 nM) were incubated with HeLa cell lysate generated from commercially available GE or NE-PER kits and evaluated via native PAGE.

Because the hairpin-modified gates were not resistant to nuclease degradation, we decided to incorporate chemical modifications into the DNA logic gates to improve stability. In order to evaluate the effect of phosphorothioate and 2'-*O*-methyl modifications into our circuit, we first

employed a simple reporter gate duplex capable of recognizing miR-21 (Figure 4-14A). A 'full complement' DNA duplex bearing no toehold sequence was designed as a control. Upon incubation of the non-modified reporter gate with a synthetic DNA mimic of miR-21, a ~47-fold increase in fluorescence signal was observed relative to the gate alone, while minimal fluorescence was observed for the full complement gate in the presence of the input (Figure 4-14B). When the reporter gate was synthesized with phosphorothioate linkages or 2'-*O*-methyl-modified nucleobases, a dramatic reduction in fluorescence was observed relative to the non-modified reporter gate; both the PS and 2'-*O*-Me reporters responded to miR-21, eliciting ~7- and ~3-fold increases in fluorescence, respectively (Figure 4-14C). Interestingly, addition of the miR-21 input to fully complementary PS- or 2'-*O*-Me-modified reporters led to ~2.4-fold and ~1.5-fold increases in fluorescence, respectively (Figure 4-14D). This is consistent with previous reports that phosphorothioate linkages decrease thermal stability of DNA duplexes potentially contributing to background activation.[684,685]

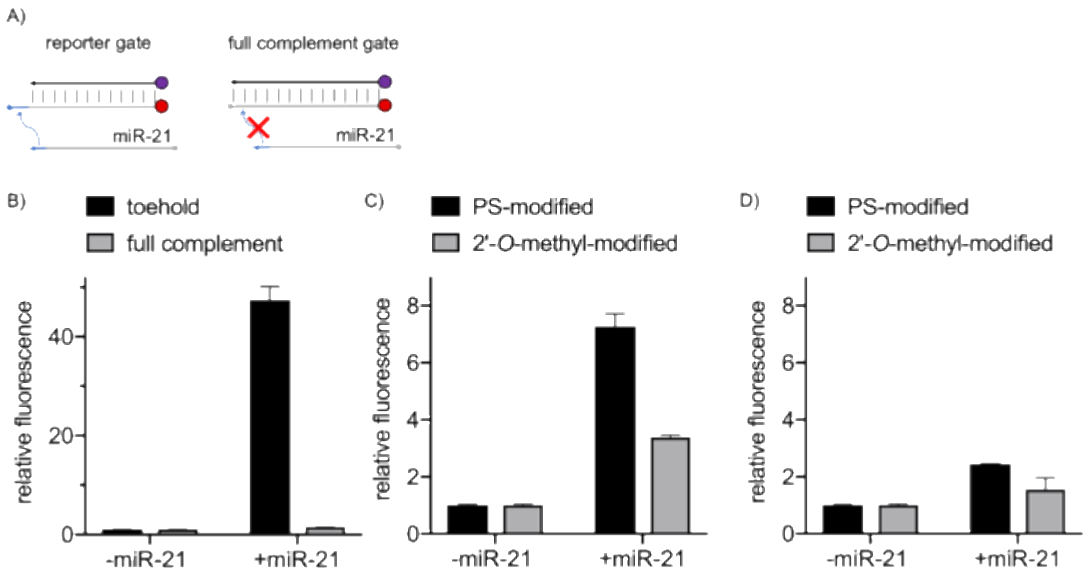

Figure 4-14 Evaluation of chemically modified reporter gates *in vitro*

A) Simplified schematic of the miR-21 reporter gate and full complement gate. B) The non-modified reporter or full complement gate was incubated with a 4-fold excess of synthetic miR-21 DNA mimic for 1 h at 37 °C, then fluorescence was measured on a plate reader. C) Fluorescence intensity of phosphorothioate (PS)- or 2'-*O*-methyl-modified reporter gates incubated with synthetic miR-21 DNA mimic for 1 h at 37 °C. D) The full complement PS- or 2'-*O*-methyl-modified duplexes were incubated with miR-21 DNA mimic in a plate reader assay. Data represents the average of three independent experiments ± standard deviation.

Next, we evaluated the ability of the chemically-modified reporter gates to recognize endogenous miR-21 in cells. Gates were transfected into HeLa, Huh7, or HEK293T cells for 4 h, then transfection media was replaced with normal growth media. Fluorophore and quencher-modified full complement DNA duplexes were transfected as a negative control. After 24 h, gate activation was assessed via fluorescence microscopy. Transfection of the PS-modified reporter gate in HeLa and Huh7 cells led to an increase in fluorescence compared to the full complement

gate, suggesting the duplex was capable of recognizing endogenous miR-21 (Figure 4-15A,B). Moreover, transfection of the gates into HEK293T cells led to minimal gate activation (Figure 4-15C), providing further support that the reporter gate activates in a miR-21-specific manner and the phosphorothioate modifications are sufficient for inhibiting nuclease degradation. Similar results were observed when the 2'-*O*-methyl-modified reporter gate was transfected into PC3, HeLa, or HEK293T cells (Figure 4-15D). The observation of comparable fluorescence levels in HeLa cells for both the PS- and 2'-*O*-methyl-modified reporter gates is somewhat inconsistent with the *in vitro* assay data wherein a greater increase in fluorescence was measured for 2'*O*-Me gates. However, we hypothesized that while the inputs were added in 4-fold excess relative to the gate in the *in vitro* assay, intracellular miR-21 is likely expressed at levels below the concentration of the gate, suggesting maximum activation is reached before the reporter is completely unquenched.

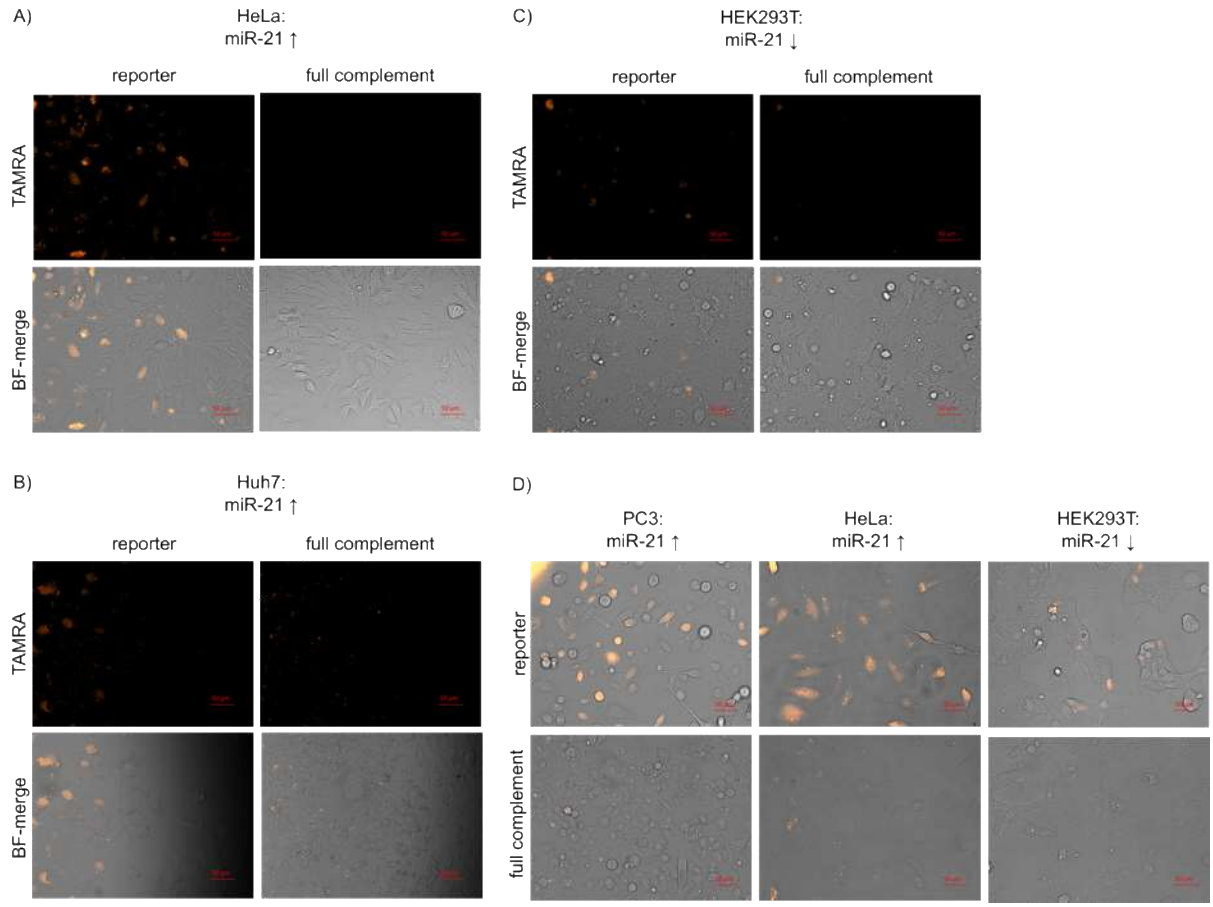

Figure 4-15 Evaluation of chemically-modified miR-21 reporter gates in cells

The phosphorothioate (PS)-modified miR-21 reporter gate or 'full complement' duplex were transfected into: A) HeLa; B) Huh7; and C) HEK293T cells. D) 2'-*O*-methyl-modified reporter or full complement gates were delivered into PC3, HeLa, and HEK293T cells. TAMRA fluorescence was observed via microscopy at 24 h post-transfection. 20x magnification. TAMRA (43HE filter; ex/em. = 550/605 nm) and brightfield-merged images are shown. Scale bars indicate 200 µm.

4.2.1 Summary and Outlook

In conclusion, we developed a multilayer DNA logic gate circuit capable of recognizing up to three miRNA inputs *in vitro*. The initial gate design was optimized to reduce background levels by incorporating an OR gate that generates the second input of a downstream fluorophore- and quencher-modified AND gate. Preliminary gate activation experiments in cells demonstrated that non-modified DNA gate duplexes were susceptible to nuclease degradation in cells, consistent with previous literature reports. Efforts to employ a simple hairpin modification strategy in order to confer nuclease resistance were largely unsuccessful because they reduced stability of the gate duplex leading to higher background activation and failed to inhibit nuclease activity in a biochemical assay and cell lysate experiments. Finally, incorporation of phosphorothioate linkages or 2'-*O*-methyl-modified nucleobases into a reporter gate duplex greatly enhanced nuclease stability in multiple cell lines and reduced background fluorescence.

Future work should focus on installation of these chemical modifications into the multilayer gate circuit followed by evaluation of logic gate activity in cells. While incorporation of PS linkages or 2'-*O*-Me nucleobases led to comparable activation in cells for the miR-21 reporter gate, a combination of the two chemical modifications may need to be utilized in order to balance gate stability and minimization of background activation. Specifically, because background activation can increase with complexity of a DNA logic gate circuit,[686] PS-modifications may reduce thermal stability and exacerbate non-specific strand displacement reactions. In contrast, 2'-*O*-Me-modified gates requiring multiple inputs may be too thermally stable to promote strand displacement reactions in the presence of endogenous non-modified miRNAs. Taken together, this may require incorporation of both PS and 2'-*O*-Me modifications in order to achieve optimal stability and gate activation. In addition, future experiments should

evaluate signal amplification strategies to overcome variable, often low, miRNA expression levels across different cell lines.[376] For example, incorporation of a see-saw reporter gate[634] downstream of the AND gate or modification of the translator gates into see-saw gates would enable recycling of the output or inputs, respectively, thereby amplifying the fluorescence output signal. Alternatively, the AND gate could be interfaced with hybridization chain reaction (HCR) probes with the output serving as an initiator sequence for concatemerization of the hairpins.

4.2.2 Materials and Methods

Cell culture. HeLa (ATCC), HEK293T (ATCC), and Huh7 (ATCC) cell lines were cultured in Dulbecco's Modified Eagle Medium (DMEM; Gibco). PC-3 (ATCC) cells were cultured in F-12K medium (Sigma). All media was supplemented with 10% (v/v) Fetal Bovine Serum (FBS; Sigma-Aldrich) and 1% (v/v) penicillin/streptomycin (VWR) and maintained at 37 °C in a 5% CO_2 atmosphere. Experiments were carried out in penicillin/streptomycin-free growth media supplemented with 10% (v/v) FBS. Cell lines were used within passages 1-35 and all cell lines are tested for mycoplasma contamination every three months using the MycoScope PCR Mycoplasma Detection kit (Genlantis).

Logic gate duplex purification. Oligonucleotides (Table 18, Table 19, Table 20, Table 21) were ordered from IDT (5′ TAMRA, 3′ BHQ2, phosphorothioate, and 2'-*O*-methyl modifications) and Sigma-Aldrich (nonmodified). Gate complexes were generated and purified as described in protocol 6.3.1 Briefly, gate duplexes were assembled at 20 μM in 200 μl of TE/Mg^{2+} buffer (Tris-HCl [0.01 M; pH 8.0], EDTA [100 mM], and $MgCl_2$ [12.5 mM]) and annealed by cooling the solution from 95 to 12 °C over 10 min in a thermal cycler (Bio-Rad).[634] The gates were then

purified on 1.5 mm 16% native TBE-PAGE gels (200 V, 60 min). The full-size duplex bands were identified using a handheld UV lamp via UV shadowing on a TLC plate, excised, cut into small pieces of ~1 mm^3, and eluted by shaking overnight in 500 µl TE/Mg^{2+} buffer.[634] All elutions were subsequently centrifuged at 3,000 g for 5 min to remove any contaminating debris. Gate concentrations (typically 5 – 10 µM) were determined by UV absorption at 260 nm (Nanodrop ND-1000) and calculated with the duplex extinction coefficient (IDT OligoAnalyzer 3.1).

Table 18 DNA sequences for miR-21 and miR-122 translator gates and downstream AND gate

Toeholds are bolded and underlined or italicized.

name	**sequence (5' -> 3')**
21-Comp	***AGTAGT***TCAACATCAGTCTGAT**AAGCTA**
122-Comp	***AGTAGT***TCAAACACCATTGTCAC**ACTCCA**
21-Act	ATCAGACTGATGTTGA***ACTACT***CGTAGGTGTAGGAAAGTCACAA
122-Act	GTGACAATGGTGTTTG***ACTACT***CGTAGGTGTAGGAAAGTCACAA
Toehold	**TTGTGA**CTTTCCTACACCTACG***AGTAGT***
F-OR/AND	TAMRA-TCCCTGAGACCCTAAC
Q-OR/AND	CGTAGGTGTAGGAAAG**TCACAA**GTTAGGGTCTCAGGGA-BHQ2

Table 19 DNA sequences for miR-122 and miR-125b translator gates and downstream AND gate

Toeholds are bolded and underlined or italicized.

name	**sequence (5' -> 3')**
125b-Comp	***ATCATTCAA***TCACAAGTT**AGGGTCTCAGGGA**
122-Comp	***ATCATTCAA***ACACCATTGTC**ACACTCCA**
125b-Act	AACTTGTGA***TTGAATGAT***AAGACGATGTTAGTTTCACG
122-Act	GACAATGGTGT***TTGAATGAT***AAGACGATGTTAGTTTCACG
Toehold	**TCAACATCAGTC**TGATAAGCTA***TTGAATGAT***
F-OR/AND	AAGACGATGTTAGTTTCACG-TAMRA
Q-OR/AND	BHQ2-CGTGAAACTAACATCGTCTT**ATCATTCAA**TAGCTTATCA

Table 20 DNA sequences for hairpin-modified miR-21 and miR-122 AND gate

Toeholds are bolded and underlined. Hairpin sequences are italicized.

name	sequence (5' -> 3')
HP-AND-21-122 Q	*CGCGCGCAAAGCGCGCG*ATCAGACTGATGTTGAATCATTGTCT TCGTGAAACTAACA**<u>TCTAAC</u>***CGCGCGCAAAGCGCGCG*
HP-AND-21-122 F	*GCGCGCGAAACGCGCGC*GTTAGATGTTAGTTTCACGAAGACA ATGAT
HP-AND-21-122 T	TCAACATCAGTCTGAT**<u>AAGCTA</u>***GCGCGCGAAACGCGCGC*

Table 21 DNA sequences for miR-21 reporter gates

Underlined bases were replaced with 2'OMe modified bases or phosphorothioate linkages were inserted between each of the underlined bases.

name	sequence (5' -> 3')
RG-21-Q-full-2	<u>TAGCTT</u>ATCAGACTGA<u>TGTTGA</u>
RG-21-Q-part-2	<u>ATCAGA</u>CTGATG<u>TTGA</u>
RG-21-F-full-2	<u>TCAACA</u>TCAGTCTGAT<u>AAGCTA</u>

Evaluation of gate fluorescence *in vitro*. Synthetic DNA mimics of miRNA sequences were ordered from Sigma-Aldrich (Table 22). Gate reactions were performed as described in detail below (protocol 6.3.2 Briefly, each reaction was set up in 50 μl of TE/Mg^{2+} buffer in triplicate wells and incubated at 37 °C for 4 h. The (miR-21 OR miR-122) AND miR-125b gate circuit and miR-21 AND (miR-122 OR miR-125b) circuit were used at 200 nM with 200 nM translator gates and 800 nM input strands. TAMRA fluorescence was measured on an M1000 plate reader (Tecan)

(ex/em. 545/565 nm; reading from bottom) in black 96-well plates (Greiner) after 4 h at room temperature and normalized to the highest fluorescence signal for the activated logic gate.

Table 22 Synthetic DNA mimics of miRNA inputs

name	**sequence (5' -> 3')**
miR-21 DNA	TAGCTTATCAGACTGATGTTGA
miR-122 DNA	TGGAGTGTGACAATGGTGTTTG
miR-125b DNA	TCCCTGAGACCCTAACTTGTGA

Logic gate transfections. Cells were seeded in a black 96-well plate (Greiner) as described in detail below (see protocol 6.3.3 PC3 and Huh7 cells were seeded at 15,000 cells per well. HeLa cells were plated at 10,000 cells per well. HEK293T cells were seeded at 20,000 cells per well. The following day, cells were transfected with gate duplexes as described in detail below (protocol 6.2.3.2). Briefly, transfections were performed using 0.8 µl of XtremeGENE siRNA transfection reagent (Roche) per well in 100 µl of Opti-MEM. The (miR-21 OR miR-122) AND miR-125b gate or miR-21 AND (miR-122 OR miR-125b) gate were diluted to a final concentration of 50 nM with 200 nM translator gates. The miR-21 reporter gates were transfected at a final concentration of 200 nM. After 4 h at 37 °C, the Opti-MEM transfection mixtures were removed from the cells and replaced with 200 µl of phenol-red free DMEM media supplemented with 10% (v/v) FBS for Huh7, HeLa, HEK293T or 1x PBS for PC3 cells for imaging (described in detail in protocol 6.2.5 In brief, images were captured on a Zeiss Axio Observer Z1 microscope using an Axiocam MRm camera and Zen 2.0 software. Cells were imaged using the mCherry filter cube and brightfield. The TAMRA signal was normalized to a standard setting for fluorescence intensity in Zen 2.0. Fluorescence merged with brightfield images are shown.

Nuclease-resistance analysis of hairpin-modified logic gates. Recombinant DNase I (Roche) was suspended in buffer (Tris-HCl [20 mM; pH 7.4], $MgCl_2$ [1 mM], glycerol [50% (w/v)]) to a final activity of 50 U/µl. Logic gate duplexes were added at 1 µg to DNase reaction buffer (Tris-HCl [10 mM], $MgCl_2$ [2.5 mM], $CaCl_2$ [0.5 mM]). Recombinant DNase I was added as indicated above and reactions were incubated at 37 °C for 5 min. Following incubation, reactions were run on 4% (w/v) agarose gels stained with ethidium bromide or 16% (v/v) native TBE-PAGE gels as indicated above. 4% (w/v) agarose gels were imaged directly on the Chemi-Doc gel imaging system (Bio-Rad).

For cell lysate experiments, HeLa cells were grown to 95% confluence, then trypsinized and counted. Cells were centrifuged at 1000 g for 10 min. Following centrifugation, cells were suspended at ~15,000 cells/ml in phosphate-buffered saline, aliquoted at 1 ml into 1.5 ml Eppendorf tubes, and pelleted at 1000 g for 10 min. The supernatant was removed and replaced with lysis buffer from the Mammalian Protein Extraction Buffer kit (GE) or NE-PER Nuclear and Cytoplasmic Extraction Reagents kit (Thermo-Fisher Scientific). HeLa cells were lysed according to the manufacturer's protocol. Lysates were stored for up to 6 months at -20 °C. DNA logic gates or dumbbell DNA decoy were added directly to 18 µl of lysate and supplemented with water or phosphate-buffered saline to a final concentration of 50 nM and final volume of 50 µl. After 6 h, reactions were loaded directly onto a 20% native TBE-PAGE gel. Following electrophoresis, native PAGE gels were stained with 1x SYBR Gold (Thermo-Fisher Scientific) for 30 min, then imaged on the Chemi-Doc gel imaging system (Bio-Rad).

4.3 Introduction to Nucleic-Acid Templated Reactions

Small molecules are low molecular weight organic compounds that have been widely used as drugs,[687] dyes,[688] and research tools.[689] Their broad applicability makes them excellent candidates for investigating or perturbing biological systems, however given that most small molecule probes interact with a protein, their potential to interact with more than target leading to undesirable side effects presents an inherent limitation to their use. As such, conjugation of small molecules to larger molecules (e.g., oligonucleotides) has been employed in order to enhance their specificity.[690] To this end, a variety of chemoselective biocompatible chemistries have been developed to facilitate site-specific modification of nucleic acids.[691]

The Taylor lab was the first to utilize a templated reaction for oligonucleotide-mediated drug release.[692] As a proof-of-concept, they employed imidazole- and *p*-nitrophenol-modified nucleic acids (15 and 8 nt, respectively) to catalyze the hydrolysis and release of *p*-nitrophenol—a key step in activation of the chemotherapeutic drugs, daunorubicin and fluorouracil—when both oligonucleotides were hybridized to a 23 nt target DNA oligomer. Importantly, catalytic release of the *p*-nitrophenol was observed at a rate of 0.057 μM/min in the presence of all three oligonucleotides, but only 0.002 μM/min in the absence of the target strand. Moreover, introduction of a mismatch in the template DNA reduced the rate of *p*-nitrophenol production by ~7.5-fold, suggesting the design could be used to tune selectivity of drug release.

Since this initial demonstration, several other biorthogonal chemistries have been applied to nucleic acids such as native chemical ligation (NCL), nucleophilic/aromatic substitution (S_N2/S_NAr), carbon-carbon bond formations and various others.[693-698] For example, Grossman and Seitz were the first to develop a system in which interaction with a DNA target catalyzed NCL-mediated transfer of a small molecule (Figure 4-16A).[699] Briefly, donating and accepting PNA

probes 1 and 2, respectively, were designed to hybridize to a complementary DNA template (RasT). Probe 1 (orange) bore a 6-carboxyfluorescein (FAM) moiety (orange circle) initially quenched by Dabcyl (dark red) bound to the PNA as a thioester, while probe 2 (blue) was modified with 5-carboxytetramethylrhodamine (TAMRA; blue) and an N-terminal *iso*-cysteine (*i*Cys) such that hybridization of both probes to the DNA template triggered transthioesterification followed by S→N acyl migration. The product probes 3 and 4 were then displaced by unreacted probes 1 and 2, continuing the catalytic cycle. The corresponding transfer of the Dabcyl moiety was then observed by monitoring changes in fluorescence intensities of FAM and TAMRA (Figure 4-16B). Importantly, the system was also capable of amplifying the signal of the DNA template at concentrations as low as 0.1 nM with a 2-fold enhancement over background after >2 h (Figure 4-16C).

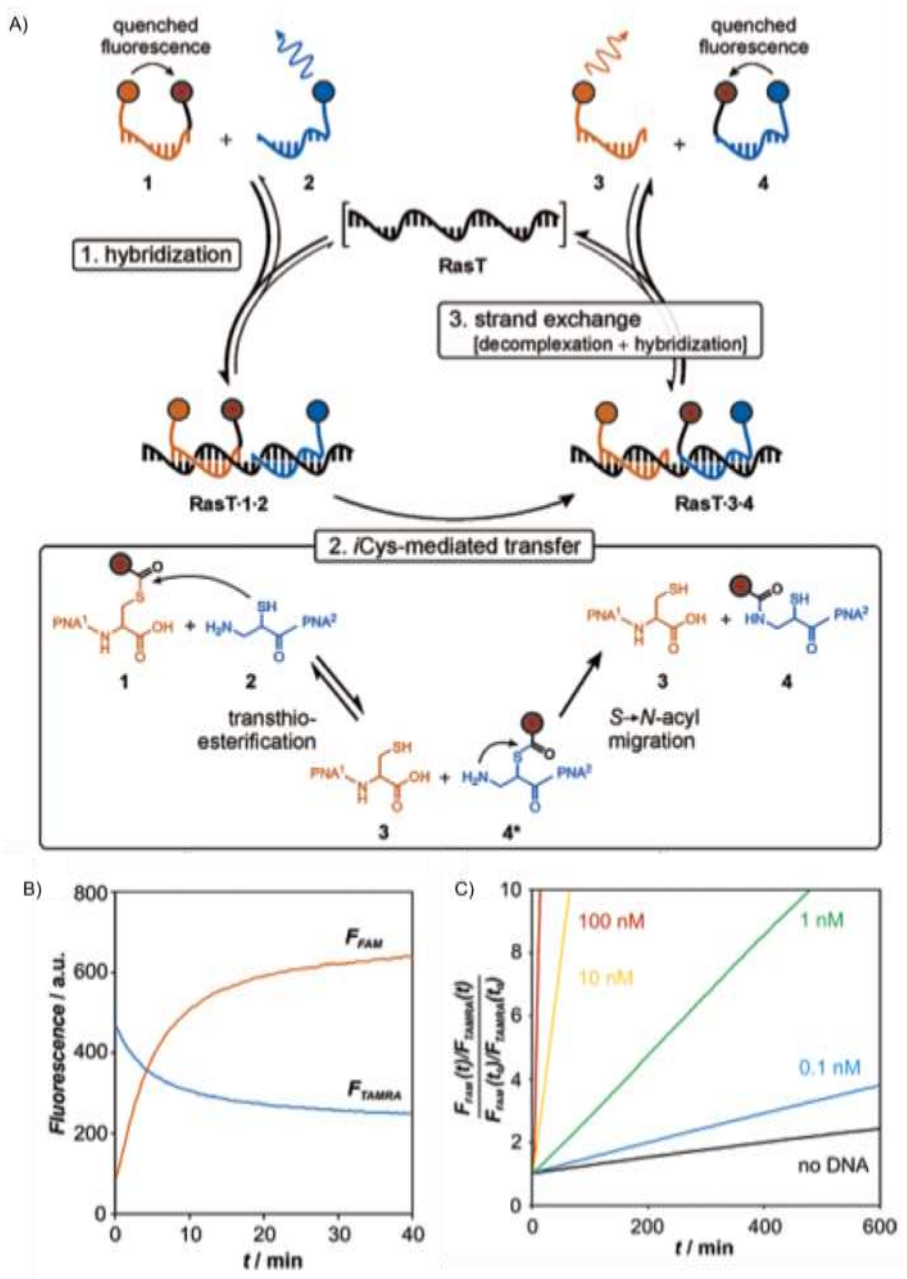

Figure 4-16 DNA-templated and Native Chemical Ligation-mediated small molecule transfer

A) Schematic for the catalytic cycle of DNA-catalyzed transfer of Dabcyl (top) and the *iso*-cysteine (*i*Cys)-mediated transfer reaction (bottom). When PNA probes 1 and 2 hybridize to RasT DNA, *i*Cys attacks the thioester in a NCL-like manner, resulting in transfer of Dabcyl and unquenching of 6-carboxyfluorescein (FAM) and quenching of 5-carboxytetramethylrhodamine (TAMRA). The cycle then proceeds as unreacted probes 1 and 2 displace the product probes 3 and 4 from the template strand. B) FAM (ex/em = 465/525 nm) and TAMRA (ex/em = 558/593 nm)

fluorescence was measured over time in the presence of 1 equivalent of RasT DNA (200 nM). C) Time course of releative $F_{\mathbf{FAM}}$ / $F_{\mathbf{TAMRA}}$ ratio at varying concentrations of RasT and 100 nM of each probe. This figure was adapted with permission from *J. Am. Chem. Soc.* **2006**, *128*. 15596-15597. Copyright 2006 American Chemical Society.

In an alternative approach, the Liu lab investigated stereoselectivity in DNA-templated nucleophilic substitution reactions using (*S*)- or (*R*)-2-bromopropionamide- and thiol-modified oligonucleotides.[700] The (*S*)- or (*R*)-2-bromopropionamide modification was incorporated at the 5' terminus of a hairpin while the thiol was installed at the 3' terminus of a 'reagent oligonucleotide' complementary to the stem of the hairpin (Figure 4-17A). In order to differentiate thioether products arising from (*S*)- or (*R*)-bromides, templates were designed at two distinct lengths, enabling separation by denaturing gel electrophoresis. Interestingly, rates of product formation were ~4-fold higher for the (*S*)-bromide-linked templates even when the bromide and thiol were separated by 12 nt. Moreover, stereoselectivity was independent of whether the thiol or bromide were conjugated to the template. Circular dichroism experiments with high salt concentrations to induce a Z-form DNA helix or low salt concentrations to induce a B-form DNA helix demonstrated a preference for (*R*)- or (*S*)-bromides, respectively, suggesting the conformation of the template and reagent oligonucleotides determines stereoselectivity in this DNA-templated reaction. Similarly, Ito and co-workers developed an approach for oligonucleotide detection using nucleophilic aromatic substitution.[701] Their design consisted of two DNA probes that bind adjacently to a template DNA strand. One of the probes was modified at the 5' terminus with a dinitrobenzenesulfonyl (DNs)-protected 7-amino-4-methyl-3-coumarinyl-acdetic acid (AMCA) while the other was functionalize with a nucleophilic phosphorothioate moiety at the 3' terminus (Figure 4-17B). When the probes hybridize to the template strand, the DNs group attacks the

phosphorothioate moiety in an S_NAr reaction, generating the Meisenheimer complex intermediate. Subsequently, the Meisenheimer complex decomposes to yield the fluorescent AMCA and transfer of the DNs group to the phosphorothioate probe. After optimization, the probes were utilized to target various template DNA sequences and it was determined that 5- and 10-base gaps between the two functional groups were detrimental to the reaction rate with no significant fluorescence signal detected after 4 h. Furthermore, the probes were capable of detecting single-base mismatches as demonstrated by an up to 90-fold reduction in reaction rate.

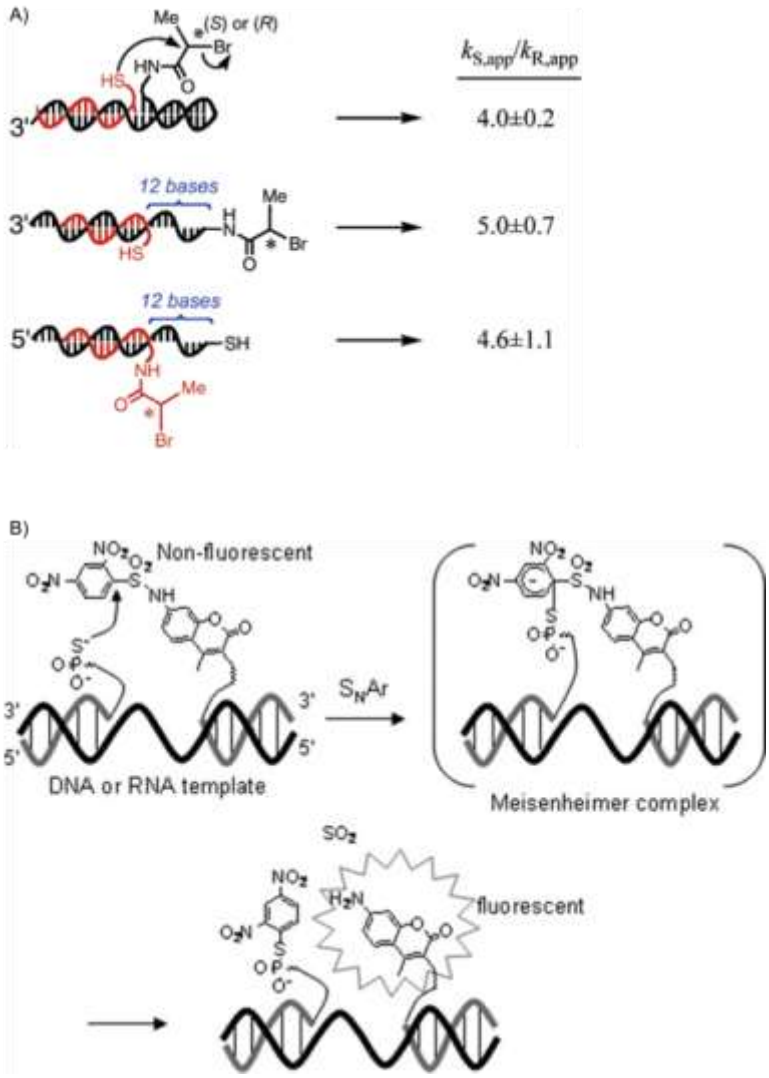

Figure 4-17 DNA-templated Reactions using S_N2/S_NAr

A) Schematic of stereoselective DNA-templated nucleophilic substitution reactions. Relative rates of product formation from (*S*)-bromides ($k_{S,app}$) / (*R*)-bromides ($k_{R,app}$) were determined by denaturing polyacrylamide gel electrophoresis followed by densitometry. B) Schematic of DNA-templated aromatic substitution reactions. The dinitrobenzenesulfonyl (DNs) protecting group attacks the phosphorothioate moeity triggering unmasking of the coumarin and production of a fluorescence signal. Adapted with permission from *J. Am. Chem. Soc.* **2003**, *125*, 10188 - 10189. Copyright 2003 American Chemical Society. Adapted with permission from *Chem. Commun.* **2009**, 6586 - 6588.

Analogously, templated Wittig olefination and aldol reactions can be utilized to afford fluorogenic small molecules via carbon-carbon bond formation. For example, Seitz and co-workers developed a DNA-templated Wittig reaction that resulted in de novo synthesis of a stilbene fluorophore.[702] The newly synthesized fluorophore was subsequently encapsulated by an α-cyclodextrin leading to a 100-fold enhancement in fluorescence in response to sub-stoichiometric amounts of the DNA template. An aldol condensation was employed by the Ladame laboratory for in situ synthesis of fluorescent probes for detecting G-quadruplexes.[703] Recently, Ladame and co-workers also developed a peptide nucleic acid (PNA)-templated Michael addition reaction to generate fluorogenic sensors for detection of miRNAs in prostate cancer as an isothermal, enzyme-free alternative to RT-qPCR.[704] In brief, 7 nt PNA probes were designed to target the 5' and 3' termini of miR-375 or -141 and bore a quenched coumarin 334 at the N-terminus or 4-butyl-thiol at the C-terminus, respectively. Hybridization of both probes to the target miRNA led to 1,4-addition of the thiol at the α,β-unsaturated ketone and subsequent restoration of fluorescence. As a proof-of-concept, the PNA probes were used to evaluate levels of miR-141 and miR-375—well-known to be upregulated in prostate cancer—in total RNA isolated from serum collected from prostate cancer patients. As expected, elevated levels of both miRNAs were detected by increases in fluorescence in patients with active cancers compared to those in remission, in good agreement with trends displayed via RT-qPCR experiments. Moreover, the probes were capable of detecting miR-141 and -375 in blood serum collected from prostate cancer patients without amplification or isolation—a distinct advantage over RT-qPCR.

Taken together, a variety of bioorthogonal reactions have been developed and utilized in the context of nucleic acid-templated systems. Low limit of detection, high biocompatibility, and enhanced chemoselectivity have enabled the design of oligonucleotide-based tools for evaluating

various biological systems. In light of these advances and in an effort to combine the precision of DNA computation devices with functional small molecule probes, we sought to develop DNA logic gates capable of responding to miRNA inputs by activating and releasing a small molecule.

4.4 Small Molecule Activation and Release via DNA Computation

As a proof-of-concept model, we functionalized synthetic DNA oligonucleotides with small molecule fluorophores which would remain inactive until triggered by a DNA computation reaction. miRNA sequences were selected as inputs for the DNA computation events. As discussed above, current DNA logic devices capable of recognizing RNA input patterns only release a fluorophore-bearing single-stranded oligonucleotide as the eventual output. The release and activation of a small molecule through DNA computation of miRNA inputs would enable the development of unique miRNA detection and visualization tools and miRNA-based therapeutics.

Our approach presented here utilizes a Staudinger reduction as a trigger for release of small molecules. The Staudinger reduction of an azide by a phosphine exhibits rapid kinetics and a high degree of bioorthogonality, as demonstrated by nucleic acid detection devices in test tubes,[705-709] bacterial,[710,711] and mammalian cells.[712-714] For example, Kool and co-workers developed quenched-Staudinger triggered α-azidoether release (Q-STAR) probes for detection of RNA expressed in *E. coli* and *S. enterica*.[715] The Q-STAR system consisted of two DNA probes: 1) A probe modified with a fluorophore at the 5' terminus and quencher covalently bound to the DNA via an α-azidoether linker; and 2) a triphenylphosphine (TPP)-DNA probe modified at the 3' terminus. Notably, while this approach was effective at reducing background fluorescence, it hindered sequence discrimination. In a recent alternative approach, the Kool laboratory coupled

the Q-STAR probes downstream of a pair of chemical autoligation (QUAL) probes in a two-step cascade.[716] The resultant chemical ligation product produced by the QUAL probes upon recognition of template RNA is destabilized due to the butyl linker, causing dissociation of the probes and recycling of the target. The ligated probes then serve as a template for the Q-STAR probes, leading to an increase in fluorescence with the release of the quencher. This design enabled detection of RNA down to 10 picomolar concentrations as well as detection of single point mutations in 16S ribosomal RNA (rRNA) in *H. pylori* lysate. Analogously, the Winssinger laboratory incorporated tris(2-carboxyethyl)phosphine (TCEP) and bis-azidorhodamine modifications onto the termini of guanidinium-modified PNAs (GPNAs) to enable miR-21-templated fluorescence unquenching in mammalian cells.[714]

This material was reprinted in its entirety with permission from Morihiro, K.; Ankenbruck, N.; Lukasak, B.; Deiters, A., *J. Am. Chem. Soc.* 2017, *139*, 13909.

In order to integrate this technology into DNA computation circuits, we designed gate complexes assembled from chemically-modified synthetic DNA oligonucleotides (Figure 4-18A). A free phosphine-modified DNA strand is generated as the result of an upstream DNA computation event that initiates a toehold-mediated strand displacement reaction to form a duplex with a small molecule-azido-modified oligonucleotide. The Staudinger reduction only occurs when a DNA hybridization events places the reaction partners into close proximity. The electron-donating amino group triggers fragmentation of the linker via 1,6-elimination and subsequent release and activation of the small molecule. This design was first validated with two fluorophores: 7-amino-4-methyl coumarin (AMC)[717-719] and 4-amino-N-butyl-1,8-naphthalimide (ABNI)[720-724] (Figure

4-18B). Their fluorescence is greatly reduced by converting their aromatic amino group into a carbamate moiety. The small molecule fluorophores are then activated upon release from the logic gate through carbamate fragmentation and regeneration of the amine. The excitation and emission wavelengths of the two AMC and ABNI fluorophores are sufficiently different to allow for the selective detection of independent small molecule activation.

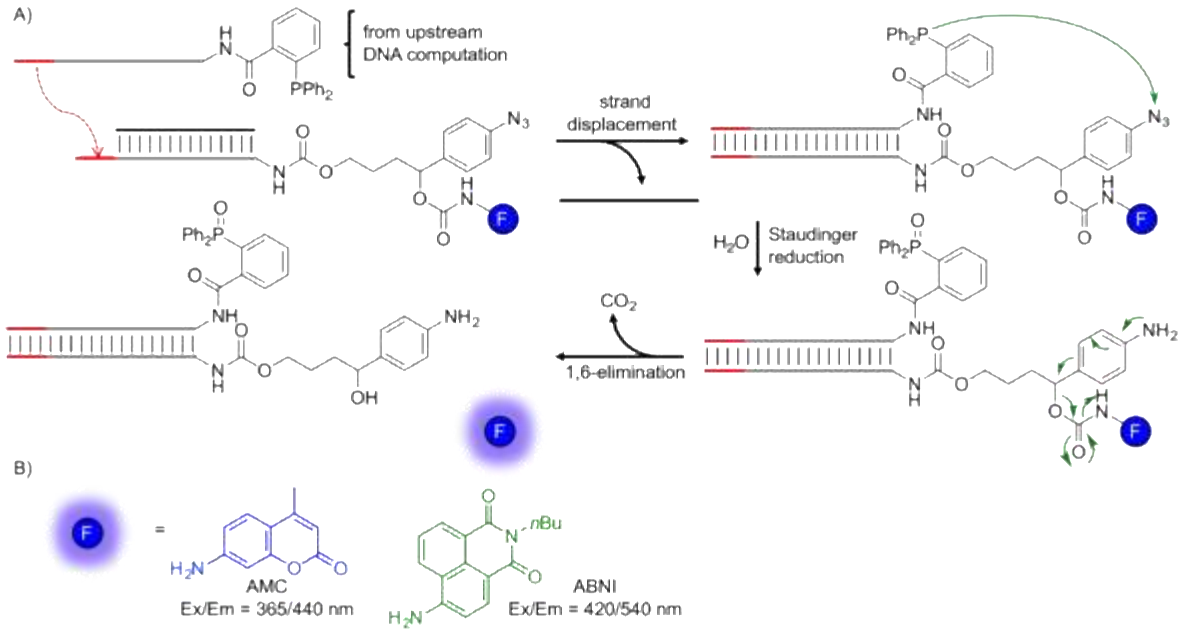

Figure 4-18 Staudinger reduction-mediated small molecule release gate design

A) The output from an upstream DNA computation event initiates a strand displacement reaction positioning the phosphine and azide moieties in close proximity. This results in release and activation of a small molecule through a Staudinger reduction and a concomitant 1,6-elimination. Toehold regions are shown in red. B) The structures and the excitation/emission wavelengths of the fluorophores F used in this study: AMC = 7-amino-4-methylcoumarin and ABNI = 4-amino-N-butyl-1,8-naphthalimide.

The fluorophore-azido- and phosphine-modified oligonucleotides were prepared via conjugation reactions between the corresponding NHS-ester and the 5'- or 3'-amino-modified DNA (Figure 4-19, Figure 4-20, Figure 4-21).

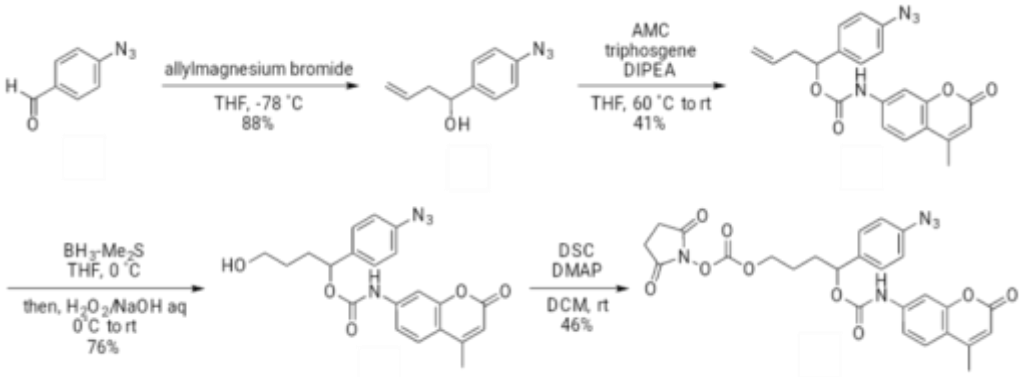

Figure 4-19 Chemical synthesis of AMC-azido-modified NHS-ester

Synthesis performed by Kunihiko Morihiro.

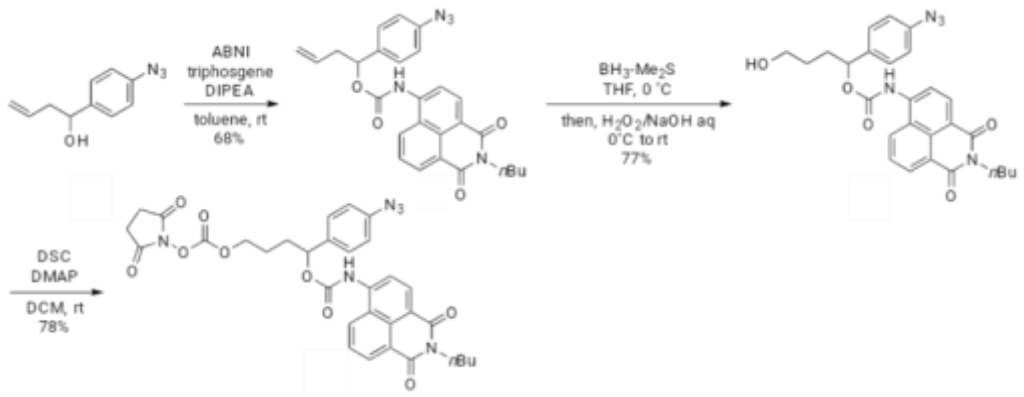

Figure 4-20 Chemical synthesis of ABNI-azido-modified NHS-ester

Synthesis performed by Kunihiko Morihiro.

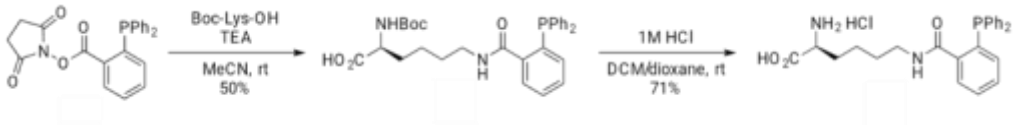

Figure 4-21 Chemical synthesis of 2DPBM-K

Synthesis performed by Kunihiko Morihiro.

To determine the requirement for full complementarity between the modified strands for release of a fluorophore, we tested 3-(diphenylphosphino)propanamido (3DPPM)-modified with complementary or non-complementary AMC-azido-modified DNA oligonucleotides in TE/Mg^{2+} buffer, which is commonly used for in vitro DNA computation experiments to enhance stability of DNA duplexes (Figure 4-22A).[725] One equivalent of 3DPPM-DNA combined with complementary AMC-azido-DNA led to small molecule fluorescence activation through Staudinger reduction within 1 h. However, when 3DPPM-modified DNA and scrambled AMC-azido-modified DNA were incubated at equimolar concentrations, significantly reduced reaction kinetics and lower fluorescence were observed. To further determine if the phosphine and azide moieties need to be in close proximity through DNA assembly in order to trigger small molecule release, we attempted to react AMC-azido-modified DNA with a small molecule, non-DNA-conjugated 2DPBM derivative (2DPBM-K, which has better water solubility than 2DPBM). Gratifyingly, we observed that a 100-fold excess of 2DPBM-K was required for the release of AMC from the fluorophore-azido-modified DNA (Figure 4-22B) compared to the DNA-conjugated phosphine, indicating the importance for DNA-hybridization enhanced local concentration of the reaction partners.[726,727] The reaction kinetics of the Staudinger reduction

strongly depend on the structure of the phosphine,[728,729] hence, we next optimized the structure of the phosphine-modified DNA. Among the phosphine-modified DNA strands investigated, 2-(diphenylphosphino)benzamido (2DPBM)-modified DNA demonstrated the fastest kinetics of AMC release (Figure 4-22C). We hypothesize that this is due to the *ortho*-amide group assisting hydrolysis of the intermediate aza-ylide through neighboring group participation.[728] Thus, 2DPBM-modified oligonucleotides were employed in all subsequent experiments.

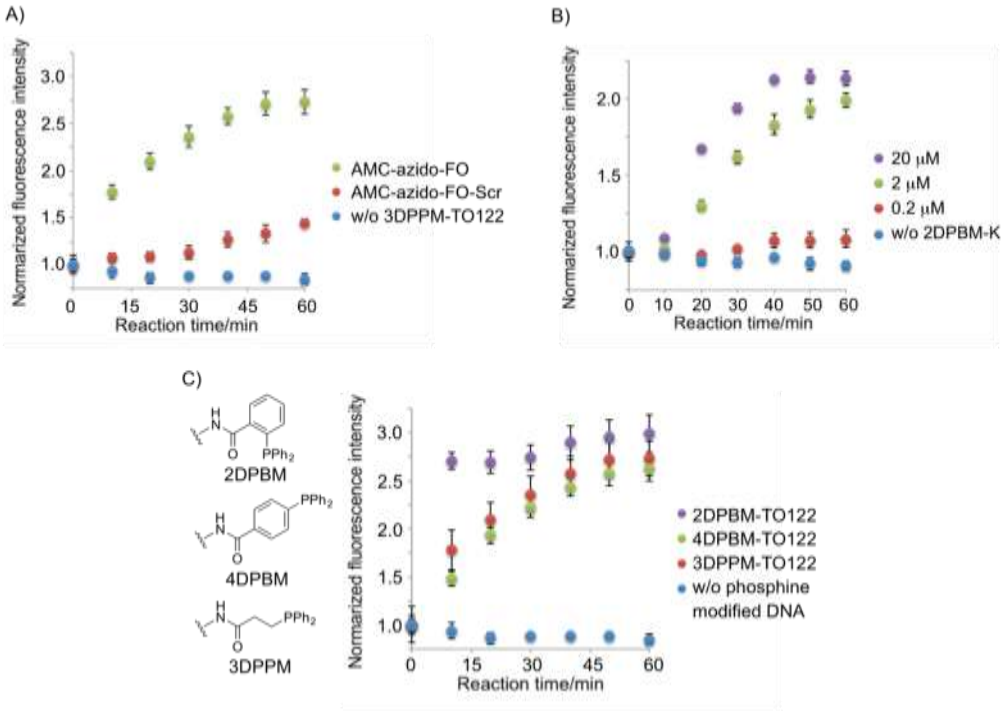

Figure 4-22 Evaluation of AMC activation and release

A) AMC release from the scrambled sequence. Conditions: AMC-azido-FO-Scr (0.2 μM) and 3DPPM-TO122 (0.2 μM) in TE/Mg^{2+} buffer. Reaction temperature = 37 ˚C. Ex/Em = 365/440 nm. B) AMC release from the AMC-azido-modified DNA by the addition of small molecule phosphine. Conditions: AMC-azido-modified FO (0.2 μM) in TE/Mg^{2+} buffer. Reaction temperature = 37 ˚C. Ex/Em = 365/440 nm. C) Screening of the phosphine-modified DNA.

Conditions: AMC-azido-modified FO (200 nM) and phosphine-modified TO122 (200 nM) in TE/Mg^{2+} buffer. Reaction temperature = 37 ˚C. Ex/Em = 365/440 nm. Data generated by Kunihiko Morihiro.

Following optimization of small molecule activation using single-stranded DNA, an AND gate that releases a small molecule after recognition of miR-122 and miR-21 input sequences (Figure 4-23A) was constructed based on design concepts reported by Winfree.[632] Both miRNAs have been implicated in several human diseases,[380,730] and targeted small molecule release may provide novel diagnostic and therapeutic opportunities. A translator gate (TG122) was used to convert the miR-122 input into a phosphine-modified strand. The miR-21 input removes the first gate strand from the AMC-azido-modified AND gate (AND-G21), exposing a new toehold, which is recognized by the 2DPBM-modified output from TG122. This results in the release of the final DNA strand and ultimately the activation and release of a small molecule fluorophore (Figure 4-23B). Staudinger reduction only occurs in response to hybridization of the 2DPBM-modified DNA and AMC-azido-modified DNA as a result of strand displacement reactions initiated by both inputs. DNA oligonucleotides with miRNA sequences were used as inputs, in line with previous studies.[632] Relative fluorophore output was calculated using standard curves of AMC- or ABNI-azido-modified DNA and free fluorophores as described in the Supporting Information. Measurements were normalized to the highest output signal in each DNA circuit. Maximal AMC release was observed only when both miR-21 and miR-122 sequences were added to the gate complex enabling unambiguous DNA logic gate outputs (Figure 4-23C). However, 0.4-fold background activation was observed with addition of only miR-21. We hypothesize that AT-rich regions within the second toehold sequence and at the end of the TG-122 duplex may partly dissociate (or fray), enabling background activation.[731] The current design may be improved by

the introduction of "clamps" to the toehold region,[634,732] single base mutations,[733,734] or additional GC pairs at the duplex termini.[735] Additionally, some background activation may have occurred because the gate duplexes were composed of unpurified DNA strands from Sigma Aldrich. This initial characterization revealed that the novel Staudinger reduction-based gate is functional and enables the selective release of a small molecule output.

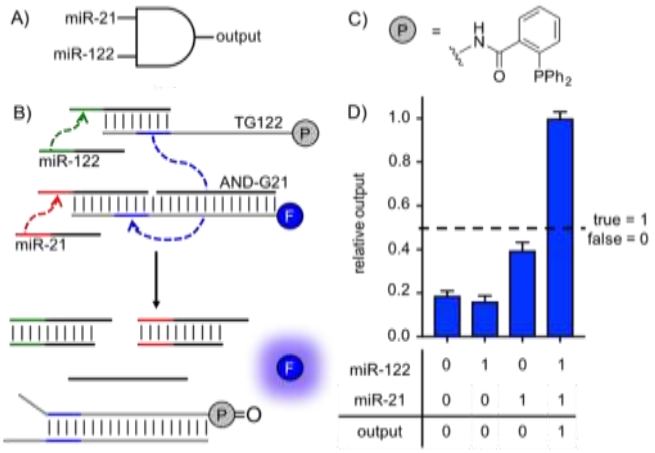

Figure 4-23 Small molecule activation and release from an AND logic gate

A) Electronic symbol for the miR-21 AND miR-122 gate. B) Simplified schematic of the small molecule release from the miR-21 AND miR-122 gate. Toehold regions are shown in green, red, and blue. C) The structure of the phosphine, 2DPBM, used in these experiments. D) AMC fluorescence is shown for addition of both miR-21 and miR-122 in different combinations to the gate complex. The mixture of TG122 and AND-G21 was incubated at 37 ˚C and the fluorescence intensity of AMC was measured after 1 h. Three independent experiments were averaged and the error bars represent standard deviations. Data generated by Kunihiko Morihiro.

The miR-21 AND miR-122 gate requires both miRNA inputs to generate the small molecule output. In order to further evaluate the applicability of the small molecule release gate,

we designed a DNA logic gate to respond to miR-122 OR miR-125b (Figure 4-24A). Unlike the AND gate, the miR-122 OR miR-125b gate provides an output in the presence of either or both of the two miRNA inputs. The gate design consists of two 2DPBM-modified translator gates (TG122 and TG125b) and an AMC-azido-modified reporter gate (FG) (Figure 4-24B). The output of TG122 and TG125b both have an identical toehold region capable of interacting with FG, which is blocked by a complementary DNA strand. When miR-122 or miR-125b is added to the gate circuit they can hybridize to their respective gate via an exposed toehold, releasing the 2DPBM-modified DNA from TG-122 or TG-125b, respectively. The 2DPBM-modified output strands then initiate the same subsequent strand displacement reaction with FG and release an AMC output via Staudinger reduction. As expected, AMC release was detected when either miR-122 or miR-125b was added; however, only 0.3-fold relative output of AMC was observed in the absence of any input miRNA, providing the expected OR response (Figure 4-24C).

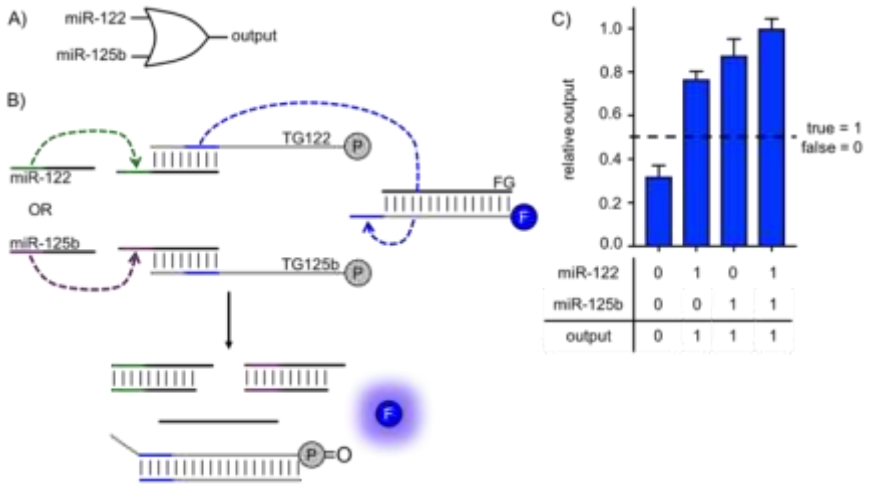

Figure 4-24 Small molecule activation and release from an OR logic gate

A) Electronic symbol for the miR-122 OR miR-125b gate. B) Simplified schematic of the small molecule release from the miR-122 OR miR-125b gate. Toehold regions are shown in green, purple, and blue. C) AMC fluorescence is

shown for addition of either miR-122 or miR-125b in different combinations to the gate complex. The mixture of TG122, TG125b and FG was incubated at 37 ˚C and the fluorescence intensities of AMC were measured after 1 h. Three independent experiments were averaged and the error bars represent standard deviations. Data generated by Kunihiko Morihiro.

The "wiring" of multiple DNA logic gates has enabled the construction of multilayer circuits that constitute more intricate devices.[736-738] To enable small molecule release in response to more complex miRNA input patterns, we designed a small DNA circuit in which an OR and AND gate were connected in series (Figure 4-25A). This circuit results in the release of a small molecule only when miR-21 and miR-122 or miR-125b are present. MiR-122 or miR-125b hybridize to the corresponding OR gate, converting the input strand into a 2DPBM-modified ssDNA oligonucleotide. Similar to the AND gate described above, the 2DPBM-modified strand can only hybridize to the AND gate after miR-21 displaces the top strand leading to exposure of a new toehold. The resultant strand displacement reaction triggers release and activation of the AMC output (Figure 4-25B). Consistent with the truth table for the circuit, high AMC release was observed only in the presence of both miR-122 and miR-21 or miR-125b and miR-21. As expected, addition of all three inputs led to an increase in AMC release and activation compared to combinations of miR-122 or miR-125b and miR-21 (Figure 4-25C). Additionally, only minor fluorescence was detected for other variations of the miRNA inputs.

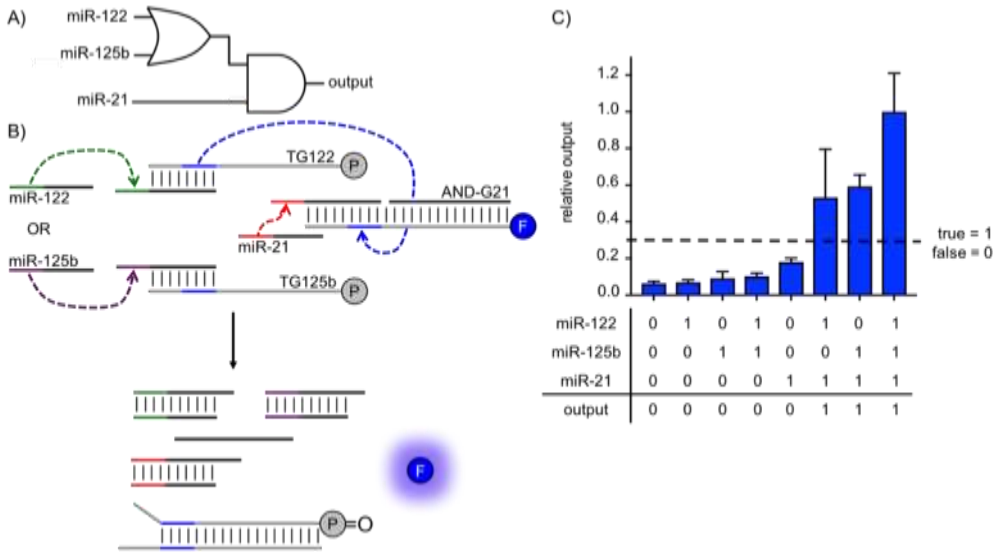

Figure 4-25 Small molecule acitvation and release from a multilayer circuit

A) Electronic circuit representing (miR-122 OR miR-125b) AND miR-21. A) Simplified schematic of the small molecule release from the (miR-122 OR miR-125b) AND miR-21 gate. Toehold regions are shown in green, purple, red, and blue. B) AMC fluorescence is shown for addition of both miR-122 and miR-21 or miR-125b and miR-21 in different combinations to the gate complex. The mixture of TG122, TG125b and AND-G21 was incubated at 37 ˚C and the fluorescence intensities of AMC were measured after 1 h. Three independent experiments were averaged and the error bars represent the standard deviations. Data generated by Kunihiko Morihiro.

In order to demonstrate the ability to orthogonally release two different small molecules in response to upstream DNA computation events, without any crosstalk between the two circuits, we designed a second logic gate circuit that could be activated independently of the initial gate design in order to provide a second unique small molecule output. We combined the miR-21 AND (miR-122 OR miR-125b) gate with a newly designed miR-10b AND (miR-15a OR miR-143) gate which would react independently to provide output 1 (AMC fluorophore) or output 2 (ABNI fluorophore) in response to a specific combination of miRNA inputs (Figure 4-26A).[739] We tested

fluorophore release from the gates through the addition of several permutations of the six miRNAs in the same test tube. As expected, AMC release was observed in the presence of both miR-122 or miR-125b and miR-21, while ABNI was released in the presence of both miR-15a or miR-143 and miR-10b (Figure 4-26B). Because the total concentration of phosphine-modified DNA contained in this multiplexed gate solution was 800 nM, we hypothesize that high background signal arises from the high phosphine-DNA concentration rather than non-specific interaction between azido-modified DNA and phosphine-modified DNA. This is consistent with elevated concentrations of small molecule phosphine being capable of activating AMC-azido-modified DNA in the absence of a DNA hybridization reaction (Figure 4-26B). This is a tradeoff that was made in demonstrating circuit multiplexing. More integrated circuit designs that do not utilize multiplexing and minimize the number of phosphine-DNA gates would most like show reduced background levels but would also require a more complicated sequence design. Using the circuits and thereby releasing small molecules at lower concentrations represents a separate solution. For example, IC_{50}s of cytotoxic drugs below 100 nM are quite common.[740-742]

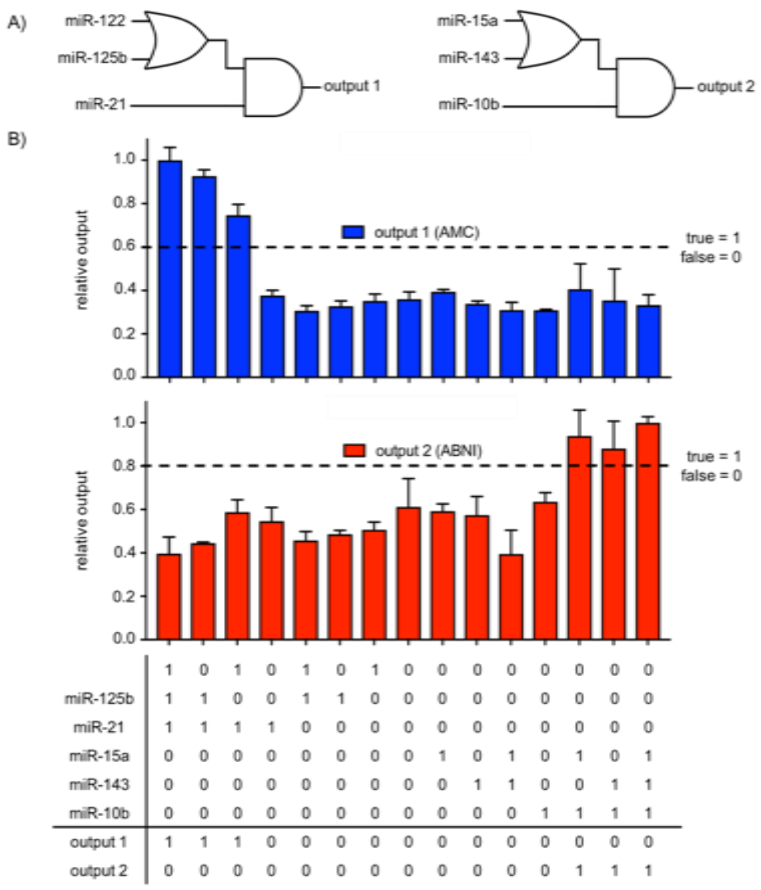

Figure 4-26 Independent small molecule release from two different logic gate circuits

A) Electronic circuits representing (miR-122 OR miR-125b) AND miR-21 and (miR-15a OR miR-143) AND miR-10b. B) AMC fluorescence is shown for addition of both miR-122 and miR-21 or both miR-125b and miR-21 in different combinations to the gate complex. ABNI fluorescence is shown for addition of both miR-15a and miR-10b or both miR143 and miR-10b in different combinations to the gate complex. The mixture of TG122, TG125b, AND-G21, TG15a, TG143 and AND-G10b was incubated at 37 ˚C and the fluorescence intensities of AMC and ABNI were measured after 1 h. Three independent experiments were averaged and the error bars represent standard deviations. Data generated by Kunihiko Morihiro.

Since the phosphine moiety introduced inherent limitations as a trigger molecule in biological systems—most notably through susceptibility to oxidation—we developed a second generation logic gate capable of activating and releasing a small molecule output. In this logic gate design, we employed an alternative bioorthogonal reaction for activation of the small molecule output utilizing a tetrazine and vinyl ether pair. Due to their versatility, robustness, bioorthogonality, and high reaction speed, tetrazines have been routinely used for conjugation of small molecules (e.g., fluorophores) to a variety of larger biomolecules such as DNA,[743] peptides,[744] and antibodies[745,746] through an inverse electron-demand Diels-Alder (IEDDA) reaction. Similarly, tetrazines have been employed as activators of strained alkene (e.g., *trans*-cyclooctene)-linked prodrugs.[747] However, reduced metabolic stability of strained alkenes in cells has prompted investigation into alternative tetrazine-reactive triggers.[748] For example, incorporation of a vinyl ether has been shown to sufficiently block fluorescence of fluorescein molecules[749] and self-immolative linkers bearing a vinyl ether have been demonstrated to release doxorubicin in response to a tetrazine trigger (Figure 4-27).[750]

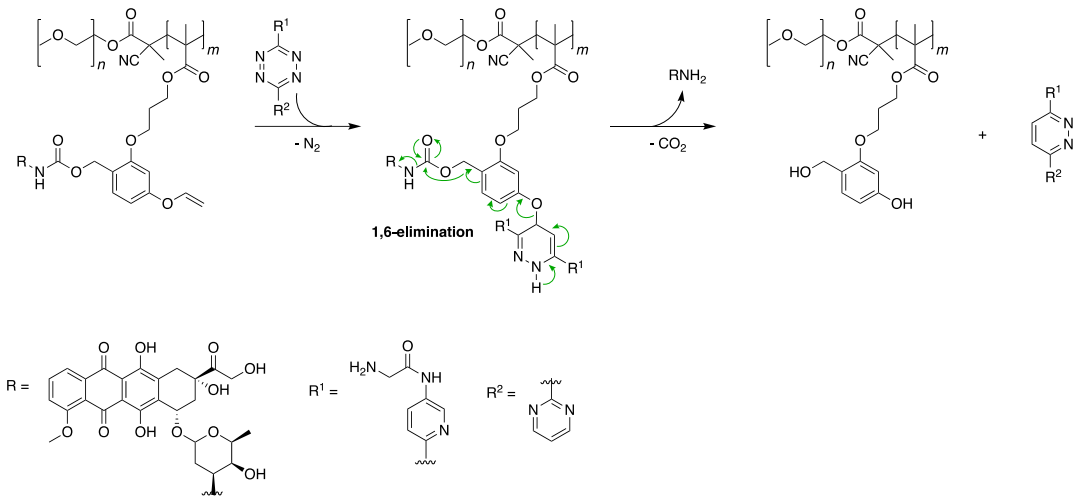

Figure 4-27 Scheme of tetrazine-mediated release of doxorubicin

Doxorubicin (R) was conjugated to nanoparticles via a PEG linker bearing a vinyl ether trigger. Addition of tetrazine leads to 1,6-elimination of the self-immolative linker and subsequent vinyl ether decaging followed by release of doxorubicin. n = 230; m = 4.

In order to evaluate the utility of IEDDA for templated activation of a small molecule through DNA computation, we first designed a reporter gate duplex functionalized with a tetrazine and vinyl ether-quenched fluorescein. One potential limitation to use of the vinyl ether is a significantly lower IEDDA reaction rate compared to strained alkenes.[748] As such, we decided to incorporate the vinyl ether-quenched fluorescein and the tetrazine trigger onto the same oligonucleotide (Figure 4-28A), hypothesizing that the enhanced kinetics of the intramolecular reaction would offset the entropic penalty incurred by not using a strained alkene.[751] In order to control hairpin formation and the corresponding reaction between the tetrazine and vinyl ether with an oligonucleotide input, the modified DNA oligomer was annealed to a complementary protecting strand bearing a 6 nt toehold. The output strand from an upstream DNA computation

circuit can then interacts with the DNA logic gate duplex, removing the protecting strand, thereby promoting formation of the reporter hairpin. Upon bringing the small molecule moieties in close proximity, the tetrazine uncages the vinyl either dienophile, unmasking the phenoxide and regenerating the fluorophore. As a proof-of-concept, we generated the non-modified reporter gate duplex (Figure 4-28B) and evaluated activation in response to a single input in a native PAGE experiment. Briefly, the gate duplex was annealed and purified via native PAGE gel, then incubated with or without input at a 4-fold excess for 3 h at room temperature. In the absence of input or presence of a negative control input, the hairpin did not form indicating the logic gate was not activated (Figure 4-28C). However, incubation with the appropriate input sequence led to complete formation of the hairpin output. Taken together, this suggests a small molecule release gate design wherein the reactive groups are contained in a single duplex, in contrast to our previous small molecule logic gates, may be an effective alternative strategy.

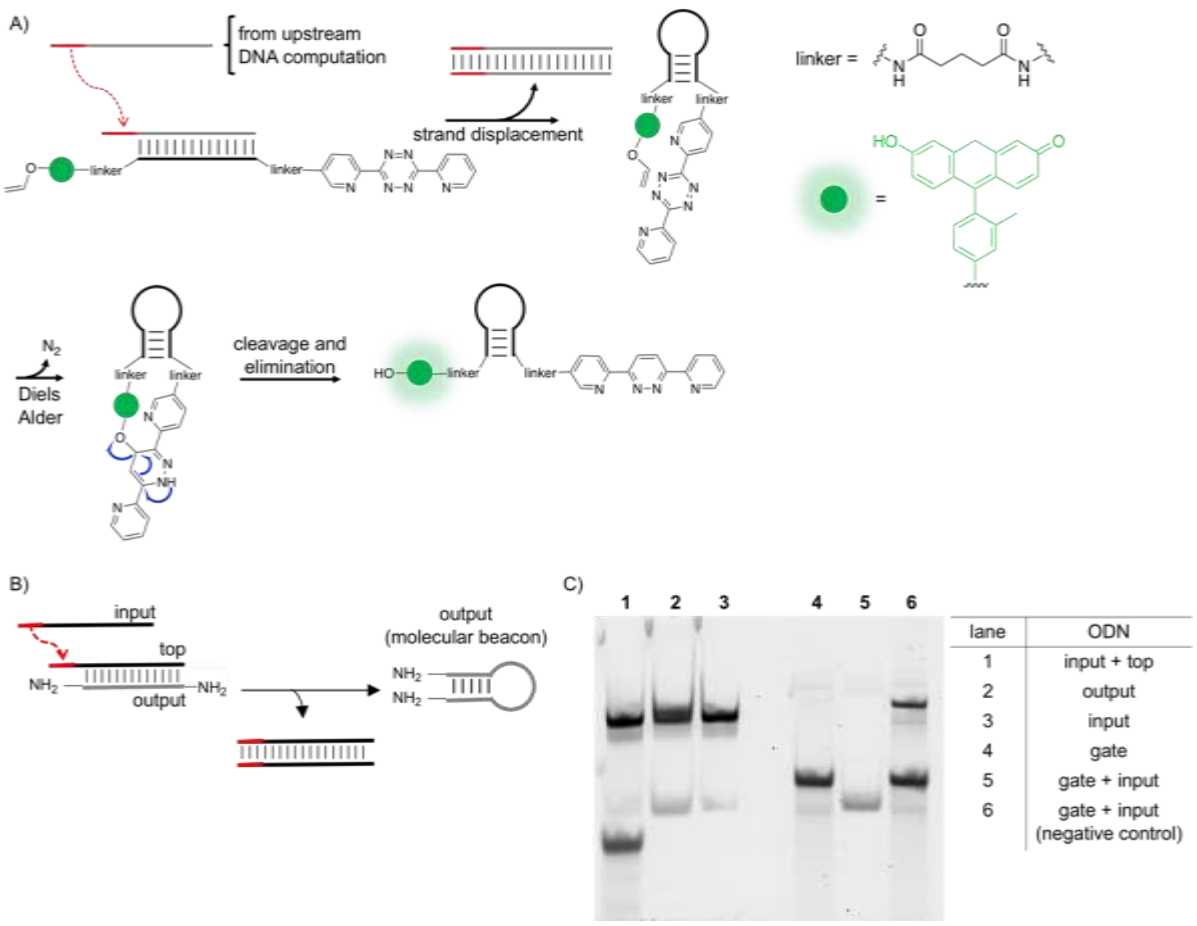

Figure 4-28 Second generation small molecule release gate

A) Schematic representation of the second generation small molecule release gate design. The output from an upstream DNA computation event initiates a strand displacement reaction, enabling hairpin formation and positioning the tetrazine and vinyl ether moieties in close proximity. This results in unmasking of the phenoxide and activation of the fluorophore. The fluorophore in the proof-of-concept design is fluorescein. Toehold regions are shown in red. B) Schematic representation of preliminary studies with the amine-modified duplex. Displacement of the top strand releases a hairpin output. C) Following incubation of the amine-modified gate duplex with the positive or negative control input for 4 h at 37 °C, gate reactions were analyzed via native PAGE, followed by SYBR gold stain.

4.4.1 Summary and Outlook

In conclusion, we demonstrated small molecule release through a variety of DNA logic gate circuits in response to synthetic oligonucleotide inputs. DNA computation has emerged as a highly versatile approach in the fields of synthetic biology and nanotechnology, however, translating single-stranded oligonucleotide outputs into triggers for biological and/or chemical events has been limited. We are addressing the restrictions that this imposes on the design and application of DNA computation through new AND and OR gates that generate small molecule outputs in response to miRNA input patterns. These systems are functional in the context of a small DNA-based circuit (3 inputs) and were quickly expanded into more complex systems through multiplexing (6 inputs). Due to the importance in understanding their regulation and function, several strategies have been previously been employed for the triggering of DNA nanodevices by miRNAs in cells and animals. For example, sequence-specific fluorescent peptide nucleic acid probes were utilized for imaging miRNAs in mammalian cells[714] and zebrafish embryos.[752] We and other groups previously employed DNA-based devices in the detection of miRNA expression in mammalian cells.[753,754] Signal amplification strategies utilizing DNA self-assembly allowed for detection of cellular miRNAs.[755-757] In addition to miRNAs, engineered DNA devices for detection of endogenous mRNAs in human cells have been reported.[648,758] However, current DNA logic devices capable of recognizing complex RNA input patterns beyond single sequences only release single-stranded oligonucleotides as the eventual outputs.[632,759-761] Compared with nucleic acids or proteins as outputs, small molecule outputs can be freely synthetized, expanding the utility of DNA computation approaches. Small molecules have been widely used as drugs, dyes, and research tools. Their broad biological function makes them important candidates for direct interfacing with DNA computation circuits. However, DNA logic

gates commonly release only an oligonucleotide output. Few oligonucleotide drugs are used in clinical practice, however, interfacing DNA circuits with hundreds of available FDA-approved small molecule drugs[762] would broaden the therapeutic potential of DNA computation. For example, the ability to release a functional small molecule following recognition of miRNA patterns could enable a therapeutic response to a distinct disease biomarker. Furthermore, this modular approach can be easily adapted to other DNA computation designs and miRNA expression patterns.

Future work will focus on conjugation of a dihydrotetrazine and vinyl ether-modified fluorescein molecule to the termini of the single-stranded dual amine-modified DNA oligonucleotide, followed by formation and purification of the gate duplex. Initial studies should be carried out to verify if 660 nm light is sufficient for conversion to the corresponding tetrazine or if an additional reactive oxygen species (ROS) generator (e.g. methylene blue) is required for oxidation. Following evaluation of the simple reporter gate complex, the duplex could easily be incorporated into more complex circuits. Furthermore, incorporation of chemical modifications as described above could enable small molecule activation as a probe for endogenous nucleic acids in mammalian cells. Finally, strategies to activate *and release* the small molecule at the completion of a strand displacement reaction should be employed toward the goal of enabling release of a drug in response to aberrant miRNA expression patterns in cells.

4.4.2 Materials and Methods

Modified DNA preparation. Modified DNAs were prepared by amide bond formation between the NHS-ester and the 5'- or 3'-amino-modified DNA (Table 23, Table 24, Table 25). Amino-modified DNAs were purchased with HPLC purification from IDT. For the preparation of the

fluorophore-azido-modified DNA, 10 nmol of the 3'-amino-modified DNA and 400 nmol of the corresponding NHS-ester in 100 mM sodium bicarbonate solution (H_2O:DMF = 3:2, 200 µl) were reacted for 4 h at room temperature. The reaction product was collected by ethanol precipitation and subsequently purified by reverse-phase HPLC (5-50% acetonitrile/100 mM triethylammonium acetate gradient). For the preparation of the phosphine-modified DNA, 6 nmol of the 5'-amino-modified DNA and 240 nmol of the corresponding NHS-ester in 100 mM sodium bicarbonate solution (H_2O:DMF = 7:3, 100 µl) were reacted for 4 h at room temperature. The reaction product was directly purified by reverse-phase HPLC (5-40% acetonitrile/10 mM triethylammonium acetate gradient). All DNA structures were confirmed by ESI-MS analysis.

Table 23 miR-21 AND miR-122 logic gate and input oligonucleotide sequences

name	**sequences (5' -> 3')**
miR-122	TGGAGTGTGACAATGGTGTTTG
miR-21	TAGCTTATCAGACTGATGTTGA
TC122	CAAACACCATTGTCACACTCCAATCATT
TO122	NH_2-GATGTTAGTTTCACGAAGACAATGATTGGAGTGTGA
AND-T21	AATGATTGGTCAACATCAGTCTGATAAGCTA
AND-OUT21	GATGTTAGTTTCACGAAGAC
AND-F21	CTGATGTTGACCAATCATTGTCTTCGTGAAACTAACATC-NH_2

Table 24 miR-122 OR miR-125b logic gate and input oligonucleotide sequences

name	**sequences (5' -> 3')**
miR-122	TGGAGTGTGACAATGGTGTTTG
miR-125b	TCCCTGAGACCCTAACTTGTGA
TC122	CAAACACCATTGTCACACTCCAATCATT
TO122	NH_2-GATGTTAGTTTCACGAAGACAATGATTGGAGTGTGA
TC125b	TCACAAGTTAGGGTCTCAGGGACCAATCATT
TO125b	NH_2-GATGTTAGTTTCACGAAGACAATGATTGGTCCCTGAGAC
FO	CCAATCATTGTCTTCGTGAAACTAACATC-NH_2
FC	GATGTTAGTTTCACGAAGAC

Table 25 (miR-15a OR miR-143) AND miR-10b logic gate and input oligonucleotide sequences

name	sequences (5' -> 3')
miR-15a	TAGCAGCACATAATGGTTTGTG
miR-143	TGAGATGAAGCACTGTAGCTCA
miR-10b	CCCTGTAGAACCGAATTTGTGT
TC15a	CACAAACCATTATGTGCTGCTAATCATT
TO15a	NH_2-GATGTTAGTTTCACGAAGACAATGATTAGCAGCACA
TC143	TGAGCTACAGTGCTTCATCTCACTAATCATT
TO143	NH_2-GATGTTAGTTTCACGAAGACAATGATTAGTGAGATGAAG
AND-T10b	AATGATTAGACACAAATTCGGTTATACAGGG
AND-OUT10b	GATGTTAGTTTCACGAAGAC
AND-F10b	GAATTTGTGTCTAATCATTGTCTTCGTGAAACTAACATC-NH_2

Logic gate preparation. Unmodified DNAs (Table 23, Table 24, Table 25) were purchased from Sigma. Gate complexes were formed by mixing final concentration of 2 μM of modified DNA and 4 μM of unmodified DNA in TE/Mg^{2+} buffer (Tris-HCl [0.01 M; pH 8.0], EDTA [100 mM], and $MgCl_2$ [12.5 mM]). The miR-21/miR-122 AND gate was generated by mixing 32 μl of AND-F21 (10 μM) with 32 μl of AND-T21 (20 μM) and 32 μl of AND-OUT21 (20 μM) in 16 μl of TE/Mg^{2+} buffer and 48 μl of nuclease-free water. The miR-122 translator gate was formed by mixing 44 μl of TO122 (10 μM) with 39 μl of TC122 (20 μM) in 13 μl of TE/Mg^{2+} buffer and 34 μl of nuclease-free water. The miR-122/miR-125b OR gate was generated by mixing 32 μl of FO (10 μM) with 64 μl of FC (10 μM) and 32 μl in 16 μl of TE/Mg^{2+} buffer and 48 μl nuclease-free water. The miR-125b translator gate was formed by mixing 44 μl of TO125b (10 μM) with 39 μl of TC125b (20 μM) in 13 μl of TE/Mg^{2+} buffer and 34 μl of nuclease-free water. For the multilayer (miR-122 OR miR-125b) AND miR-21 gate, the AND logic gate was generated by mixing 46 μl of AND-F21 (10 μM) with 46 μl of AND-T21 (20 μM) and 46 μl of AND-OUT21 (20 μM) in 23 μl of TE/Mg^{2+} buffer and 69 μl of nuclease-free water. miR-122 and miR-125b translator gates were generated by mixing 46 μl of TO122 or TO125b (10 μM) with 46 μl of TC122 or TC125b (20

µM), respectively, in 23 µl of TE/Mg^{2+} buffer and 115 µl of nuclease-free water. The (miR-15a OR miR-143) AND miR-10b gate components were prepared in the same way as the (miR-122 OR miR-125b) AND miR-21 gate. All individual gate mixes were incubated at room temperature on a bench top for 10 min prior to use. Gate formations were confirmed by 16% native polyacrylamide gel electrophoresis (PAGE) followed by SYBR gold staining as described in detail below (protocol 6.1.9 All gate complexes were directly used for following experiments without further purification.

For a detailed protocol of generation and purification of the second generation small molecule release gate for proof-of-concept experiments, see section 4.2.2 and general protocol 6.3.1 below using the sequences in Table 26.

Table 26 Oligonucleotide sequences for 2nd generation logic gate capable of small molecule activation and input

name	**sequences (5' -> 3')**
2ndGenSMGate-F	NH_2-GCGCGAAAAGAAGAAAAGGAAAAACGCGC-NH_2
2ndGenSMGate-T	GCGCGTTTTTCCTTTTCTTCTTTTCGCGCGGCCCG
2ndGenSMGate-In	CGGGCCGCGCGAAAAGAAGAAAAGGAAAAACGCGC
negative control In	GTACGGTGGGAGGTCCACACAAGAGTCGCAG

Functional examination of small molecule activation and release. Fluorescence was measured on a Tecan M1000 plate reader in black 96- (Greiner) or 384-well plates (Greiner). All gates were analyzed at 200 nM with 800 nM miRNA inputs in 100 or 50 µl of TE/Mg^{2+} buffer (Tris-HCl [0.01 M; pH 8.0], ethylenediaminetetraacetic acid [EDTA; 100 mM], and $MgCl_2$ [12.5 mM]) at 37 °C; for cost reasons, DNA oligonucleotides with the miRNA sequences were used as inputs. After gates were annealed, 10 µl of the fluorophore gate (AND or OR) was added to 10 µl of

TE/Mg^{2+} buffer, 10 µl of the translator gate(s), 8 µl of each input (where applicable), and nuclease-free water up to 100 µl for each well in a 96-well plate. For a 384-well plate, all volumes were reduced by half. Inputs were added last, immediately before the start of each experiment. To minimize variability between wells, master mixes containing the gates, buffer and water were prepared in larger volumes and then distributed into each well. After reaction mixes and inputs were added, the plate was placed in the plate reader and fluorescence intensity (ex/em = 365/440 nm for AMC, 420/540 nm for ABNI) was measured every 15 min for up to 4 h at a temperature of 37 ˚C. Relative concentrations of released fluorophores were calculated using standard curves of the AMC- or ABNI-azido-modified DNA and the fluorophore (Figure 4-29) and then normalized to the highest output signal. Triplicate experiments were performed for each condition.

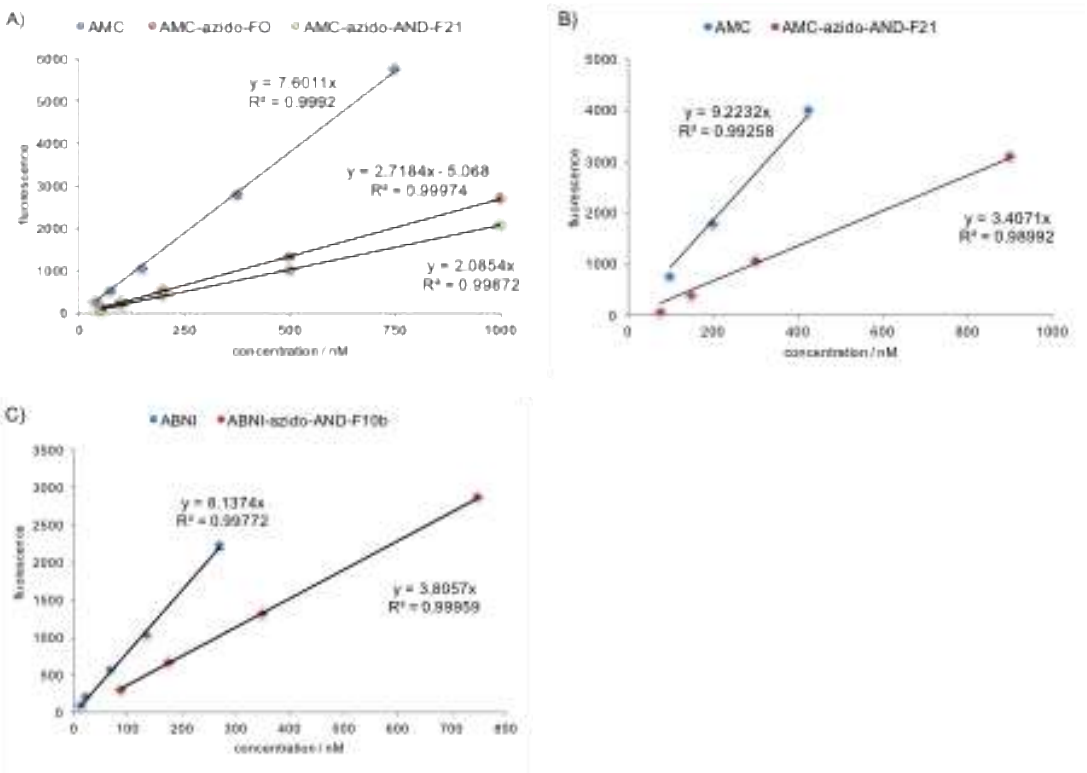

Figure 4-29 The standard curves for calculation of released fluorophore yields

Shown are the standard curves of the fluorescence intensities corresponding to A) AMC and AMC-azido-modified DNAs in 96 well plate; B) AMC and AMC-azido-modified AND-F21 in 384 well plate; C) ABNI and ABNI-azido-modified AND-F10b in 384 well plate. Conditions: TE/Mg^{2+} buffer (10 mM tris-HCl, 100 mM ethylenediaminetetraacetic acid (EDTA), and 12.5 mM $MgCl_2$). Temperature = 37 ˚C. Ex/Em = 365/440 nm for AMC, 420/540 nm for ABNI.

Determination of released fluorophore yields. Relative concentrations of released fluorophores were calculated using standard curves of the AMC- or ABNI-azido-modified DNA and the fluorophore (Figure 4-29). Briefly, we assumed that the total fluorescence signal was equivalent to the sum of fluorescence intensity of the AMC-azido or ABNI-azido modified gate and the released fluorophore. As such, we applied a linear fit to each standard curve: y=ax+b and y=cx'+d

for the free fluorophore and AMC-azido or ABNI-azido-modified gate respectively: where y is the total fluorescence in arbitrary fluorescence units (a.u.), a is the slope of the standard curve for the free small molecule fluorophore in a.u./nM, b is the y-intercept of the free small molecule fluorophore in a.u., c is the slope of the standard curve for the small molecule-modified DNA in a.u./nM, d is the y-intercept for the small molecule-modified DNA in a.u., and x and x' are the concentration of the released fluorophore and small molecule modified gate, respectively, in nM. The y-intercepts were set to 0 a.u. corresponding to no fluorescence intensity when x/x' = 0 nM. Summation of the two standard curves yields the equation $y = ax + cx'$. Because the initial gate concentration was 200 nM, the maximum concentration of the released fluorophore is 200 nM as well. As such, we assumed $x' = 200\ nM - x$. Substitution and distribution of this term into the sum of the standard curve gives: $y = (a-c)x + 200c$. Concentrations of released fluorophore for each experiment were calculated by substituting the fluorescence intensity of three separate gate experiments into this equation, followed by averaging and normalization to the highest output signal.

Yields of released fluorophore were calculated as below:

Calculation formulas were obtained from Figure 4-29;

Fluorophore fluorescence = $ax + b$

Gate fluorescence = $cx' + d$

Total fluorescence = Fluorophore fluorescence + Gate fluorescence

Total fluorescence = $ax + cx'$

Total fluorescence = $ax + c(200 - x)$

Total fluorescence = (a − c)x + 200c

x = (Total fluorescence − 200c) / (a − c) [nM]

x = concentration of released fluorophore [nM]

x’ = concentration of fluorophore-modified gate [nM]

x + x’ = 200 [nM]

Functional examination of 2nd generation small molecule activation gate. Proof-of-concept gate reactions were assembled similarly to the first generation small molecule activation and release gates. Briefly, 7.3 µl of the gate duplex (5.4 µM; [final] = 200 nM) was mixed with 5 µl of 10x TE/Mg^{2+} buffer and up to 50 µl of nuclease-free water. The inputs (10 µM) were added at a volume of 16 µl ([final] = 800 nM). After mixing all components, the gate was allowed to react for 4 h at 37 °C. Subsequently, the gate reactions, input, and product hairpin were separated on a 16% (v/v) native PAGE gel and analyzed via staining with SYBR gold as described below (see protocol 6.1.9

5.0 Caged Oligonucleotides

5.1 Introduction to Caged Oligonucleotides

This material was reprinted in its entirety with permission from Ankenbruck, N.; Courtney, T.; Naro, Y.; Deiters, A., *Angew. Chem. Int. Ed. Engl.* **2018**, *57*, 2768.

Nucleic acids have been extensively used as biological probes with additional developments into therapeutics already underway.[247,763,764] Oligonucleotides are ideal for studying biological pathways because they can impact processes at the DNA, RNA, and protein level in a sequence-specific and fully programmable fashion. Optical control of nucleic acid function has allowed for spatiotemporal control of RNAi, transcription, translation, gene-editing, and nucleic acid detection.[765-767] In contrast to proteins and small molecules, caged nucleic acids can be developed without genetic engineering and are sequence-specific, minimizing off-target effects.

Photocleavable groups have been synthetically incorporated into oligonucleotides in a variety of different ways to allow for precise activation or deactivation of nucleic acid function with spatiotemporal resolution (Figure 5-1). A straightforward approach consists of utilizing a photocleavable linker in, e.g., an antisense agent,[768-770] enabling optical activation of gene expression (Figure 5-1A). Photocleavable linkers have also been utilized in tethering of antagomirs,[771,772] peptide nucleic acids,[773] and morpholino oligonucleotides[774,775] directly to short inhibitor strands which block activity through hairpin formation. The inhibitory strand is removed with light, leading to activation of the antisense strand (Figure 5-1B). Recently, this approach was further advanced by synthesizing circular nucleic acids through the linking of both termini via a

photocleavable moiety. The resulting cyclic structure cannot efficiently hybridize to its target due to the induced curvature, until it is linearized through photochemical cleavage of the linker (Figure 5-1C).[171,776-779] Other optical control approaches include the introduction of chemical modifications such as caged phosphate backbones,[780-782] caged 2'-hydroxy groups,[783,784] and caged nucleobases.[785] Caged nucleobases have demonstrated particularly broad applicability since they block Watson-Crick hydrogen bonding, rendering the oligonucleotide inactive until irradiation. This has been employed in the light-regulation of antisense agents,[786,787] antagomirs,[788-790] splice-switching oligonucleotides,[791] PCR primers,[792,793] and many other oligonucleotides (Figure 5-1D).[794-797] The same approach can also be used for the optical deactivation of oligonucleotide function through light-triggered hairpin formation thereby sequestering the active nucleic acid sequence (Figure 5-1E), as demonstrated for antisense agents,[798] DNAzymes,[798] and triplex-forming oligonucleotides.[796]

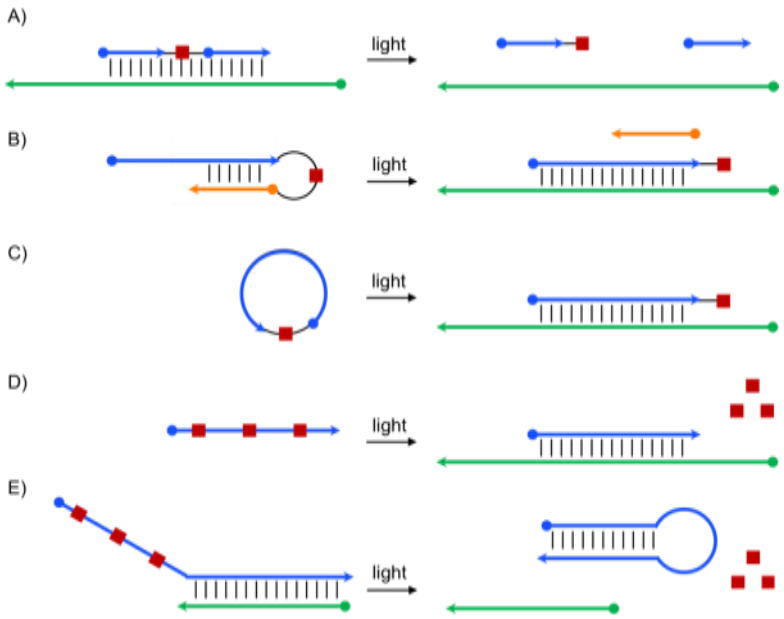

Figure 5-1 Approaches to the regulation of oligonucleotide hybridization using light-cleavable groups

A) An oligonucleotide sequence containing a photocleavable linker is able to bind its target sequence, inhibiting activity, until light-induced cleavage. B) Hairpin formation of a short inhibitory strand through a photocleavable linker blocks oligonucleotide function until irradiation. C) Formation of a cyclic oligonucleotide via a photocleavable linker inhibits function due to induced curvature until irradiated with light. D) Caged nucleobases inhibit oligonucleotide function until photo-deprotection. E) Deprotection of caged nucleobases results in hairpin formation, inhibiting oligonucleotide activity. Adapted with permission from Liu *et al.*, *Acc. Chem. Res.*, *47*, 45-55. Copyright 2013 American Chemical Society.

In a nucleobase-caging approach, Heckel first incorporated guanidine and thymidine deoxynucleotides carrying nitrobenzyl groups at the O6 and O4 positions into a siRNA reagent, specifically into nucleotides in close proximity to the mRNA cleavage site.[799] The disruption of hydrogen bonding and introduction of steric hindrance resulted in up to 90% inactivation of a caged siRNA targeting EGFP, however, after 28 hours fluorescence began to decrease in the

absence of light, possibly due to instability of the caging groups. Subsequently, a series of siRNA reagents were synthesized in which nitrobenzyl-caged uridine or guanosine residues were incorporated into the mRNA cleavage site or seed region of an siRNA duplex.[800] The photolabile groups were installed at the N1 or N3 position of guanosine or uridine, enhancing stability of the caged siRNAs for at least 48 hours and resulting in excellent off-to-on photoswitching. Moreover, optical control of siRNAs via installation of caged nucleobases within the seed region directly translates to the optical activation of miRNA function.

In a complementary fashion, miRNAs have commonly been silenced using antagomirs, synthetic phosphorothioate- and 2'OCH_3-modified oligonucleotides,[247,764,801,802] which have also been placed under optical control through a nucleobase-caging approach (Figure 5-1D).[789] This enabled the spatiotemporal investigation of miR-22 and miR-124 function in migrating neurons.[803] Alternatively, inhibition of antagomir function through temporary hairpin formation via a photocleavable linkers (Figure 5-1E) has also been utilized for optical activation of miRNA function.[771]

In addition to regulating gene expression, several nucleic acid-based detection tools have been designed to be controlled with light. Molecular beacons are short oligonucleotide hairpins which maintain an "off" state until a complementary DNA or RNA molecule hybridizes to the loop, separates the stem, and turns fluorescence "on".[804] Two approaches to achieve optical control over molecular beacons have been reported: (1) installation of caging groups into the stem region preventing formation of the hairpin[805] and (2) installation of caging groups into the loop region preventing target hybridization,[806] with the latter showing reduced background. In a system using a cell surface protein for uptake of the molecular beacon, the Tan lab developed optical control of a molecular beacon in breast cancer cells.[807] Because biological processes occur at specific times

and locations, this technology could easily be applied to the investigation of transcriptional events with enhanced precision relative to previous methods.

DNAzymes (deoxyribozymes) catalyze RNA cleavage.[808] They have been used as gene regulatory tools and as cellular sensors, but issues remain due to activity during cellular delivery and uptake. To circumvent this concern and achieve spatiotemporal control over activity, several strategies have been developed to optochemically regulate DNAzymes.[783,798,809-811] Caged adenosine bases were incorporated into the scissile position of the substrate strand for DNAzymes selective for Zn^{2+} or Pb^{2+} ions, demonstrating a modular approach for sensing metal ions in mammalian cells.[812] Recently, Xiang reported the development of a DNAzyme which was caged post-synthetically in order to circumvent the addition of caged phosphoramidites during solid-phase synthesis.[813] Following optimization in *in vitro* experiments, the fluorescently-labeled DNAzyme was delivered into HeLa cells along with the substrate and Zn^{2+} cofactor. After brief UV irradiation, the DNAzyme was activated, resulting in substrate cleavage and subsequent enhancement of the fluorescence signal, demonstrating temporal control of DNAzyme function.

In addition to the two-photon activation of morpholino oligonucleotides described below,[775] Heckel utilized coumarin (DEACM) and nitrobiphenyl (ANBP) caging groups,[814] which can be removed through orthogonal two-photon activation, to nucleobase-protect deoxythymidine and deoxyguanosine bases in two oligonucleotides, DNA 1 and DNA 2.[815] Decaging of DNA 1 and DNA 2, embedded in a hydrogel to prevent diffusion, initiated sequence-specific hybridizations of complement strands labeled with fluorophores, ATTO 565 and ATTO Rho14 respectively, as part of a light-triggered toehold mediated strand exchange. Irradiation with 980 nm light resulted in exclusive decaging of DNA 2, while irradiation with 840 nm light (at reduced laser power) selectively decaged DNA 1. However, upon irradiation with 840 nm light at increased

laser power, it was possible to decage both DNA 1 and DNA 2 resulting in the detection of both fluorophores. The strand exchange reaction triggered by DNA 1 was also demonstrated in hippocampal neurons. Because two-photon imaging has been routinely used in live tissues,[816-818] this approach provides an additional level of precision for probing biological pathways in model organisms with complex three-dimensional structures. Two-photon activation of oligonucleotide sensors provides an approach to oligonucleotide detection with three-dimensional resolution and spatiotemporal precision.

5.2 Optical Control of Transcription

This material was reprinted in its entirety with permission from Ankenbruck, N.; Courtney, T.; Naro, Y.; Deiters, A., *Angew. Chem. Int. Ed. Engl.* 2018, *57*, 2768.

Several approaches to optically control gene expression at the transcriptional level have been developed, including the light-activation of triplex forming oligonucleotides (TFOs).[819] TFOs are single-stranded oligonucleotides that bind to the major groove of DNA promoter regions via Hoogsteen hydrogen-bonding (Figure 5-2A), preventing transcription factor association.[820] Contrary to antisense agents which regulate gene translation by targeting mRNAs for which thousands of copies may be present in cells, TFOs target genomic DNA.[821] Optical control of transcription via photo-activation of a TFO containing caged thymidine bases was demonstrated (Figure 5-2B).[796]

Besides TFOs, DNA decoys have also been employed for transcriptional control. DNA decoys inhibit gene expression by sequestering transcription factors rather than relying on the binding to and blocking of promoter sequences.[822] Three caged thymidine bases were incorporated into a DNA decoy targeting NF-kB (Figure 5-2C) to optically regulate transcription factor binding by initially preventing formation of the DNA decoy dumbbell structure.[797] Following UV irradiation, the decoy was formed resulting in sequestration of the transcription factor and deactivation of gene expression. Complementary optochemical transcriptional activation was demonstrated using NF-kB DNA decoys[823] containing up to three 7-nitroindole moieties, a nucleobase mimic known to undergo elimination upon irradiation with UV light. Here, the decoy/transcription factor complex inhibiting gene expression, until exposure to UV light depurinates the photoresponsive nucleotides, resulting in release of the transcription factor and an activation of gene expression.

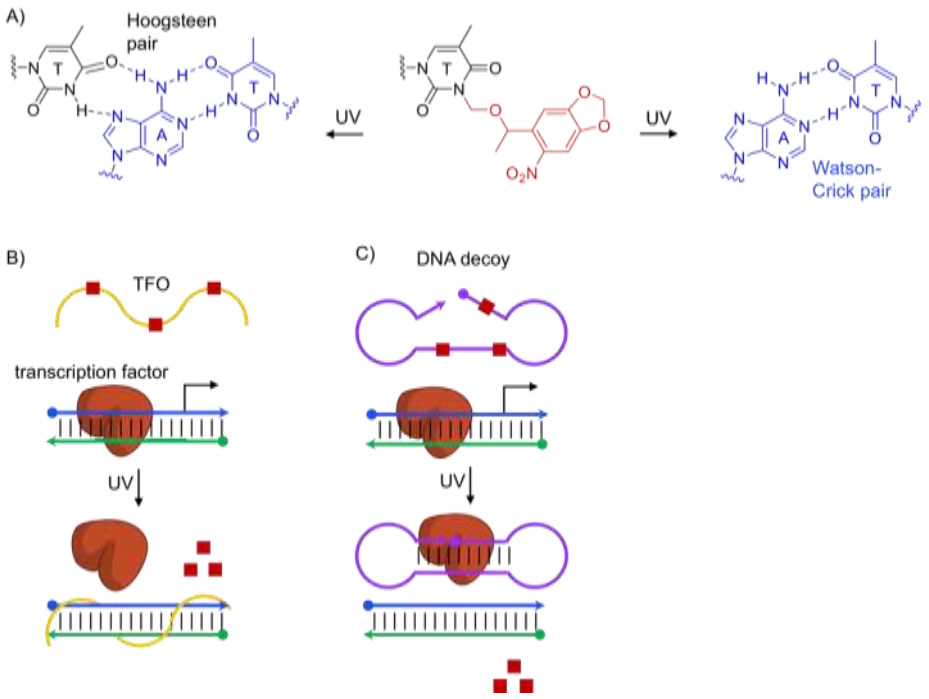

Figure 5-2 Optical tools for controlling transcription

A) Control of both Watson-Crick base pairing and Hoogsteen base pairing through photolysis of nucleobase-caged thymidines. B) Optical activation of a triplex-forming oligonucleotide (TFO; yellow) through nucleobase decaging and resulting DNA triplex formation via Hoogsteen base pairing. The TFO blocks binding of the transcription factor (brown) to the promoter region (blue/green), inhibiting gene expression. C) Optical activation of a DNA decoy through light-induced dumbbell formation, leading to sequestration of the transcription factor targeting the decoy promoter region, inhibiting gene expression.

Plasmids containing a cytomegalovirus (CMV) promoter-driven gene of interest are one of the most common expression platforms in mammalian cells.[824] Transcription is initiated when the TATA box binding protein binds to the TATA box sequence within the CMV promoter and recruits additional transcriptional machinery.[825] In order to achieve spatial and temporal activation of gene expression, caged thymidine nucleobases were site-specifically introduced into the TATA

box (Figure 5-3A).[826] The caged plasmid was inactive until a brief UV exposure removed the caging groups, forming the wild-type CMV promoter, and completely restoring gene expression, as demonstrated for EGFP and polo-like kinase 3. In order to apply this methodology in an animal model, the caged TATA box plasmid was injected into zebrafish embryos (Figure 5-3B). Following microinjection at the 1-cell stage, only embryos exposed to UV irradiation expressed EGFP. The ability to activate transcription using a caged expression plasmid at defined time points and locations in cells and animals has broad implications for investigating many biological pathways, including those involved in development, and it complements the previously discussed light-triggered inhibition of transcription and translation using light-activated nucleic acids. With recent advances in caging groups with different spectral properties, the activation and deactivation of multiple genes using light of different wavelengths will enable the study of increasingly complex genetic systems. Also, the caged plasmid system is assembled in a very modular fashion and will allow for optical control of any gene of interest.

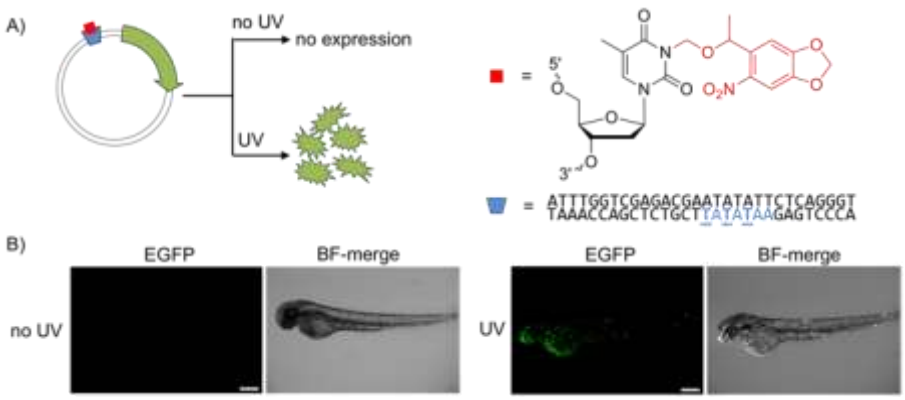

Figure 5-3 Optical control of transcription using a caged TATA box

A) Optical control of transcription using a caged promoter. EGFP is only expressed following removal of the nitrobenzyl caging group (red) via irradiation with UV light. Three caged thymidine residues (underlined) were incorporated into the TATA box sequence (blue). B) Optical activation of EGFP expression in zebrafish embryos. Following injection of the caged plasmid at the one-cell stage, embryos were either irradiated with 365 nm light or left in the dark. EGFP fluorescence and brightfield (BF)-merge micrographs are shown. Adapted with permission from Hemphill *et al., J. Am. Chem. Soc., 136,* 7152-7158. Copyright 2014 American Chemical Society.

5.2.1 Wavelength-Selective Optical Control of Transcription

As described above, application of different caging groups to separate plasmids could enable optical control of various stages of a genetic circuit as well as spatial and temporal control of multiple steps in a biological pathway. In order to demonstrate the utility of wavelength-selective control of transcription with light, we developed a second plasmid expressing mCherry that could be decaged independently of the previously reported caged EGFP construct. Because the 6-nitropiperonyloxymethyl (NPOM)-caged thymidine residues were decaged with UV light, we sought to incorporate a red-shifted caging group to enable orthogonal uncaging. Initially,

Anirban Bardhan, a synthetic chemist in our group, synthesized a 4-amino-4'-nitrobiphenyl (ANBP)-caged[827] thymidine. In order to evaluate the decaging efficiency of the ANBP-caged thymidine, Anirban irradiated the compound (100 μM in methanol) with a 405 nm or 447 nm LED. Subsequently, he monitored disappearance of the caged-thymidine peak via HPLC (260 and 280 nm; 5-95% acetonitrile/water). Unfortunately, while 90% decaging was observed following 405 nm irradiation of the ANBP-caged thymidine, only 30% of the compound was decaged after 10 min irradiation with 447 nm light. Due to inefficient decaging of ANBP at 447 nm and our hypothesis that 405 nm irradiation of the NPOM-caged thymidine would lead to background uncaging, we decided to pursue alternative red-shifted caging groups.[828-830]

Recently the Ellis-Davies group reported a bisstyrylthiophene (BIST) caging group that enabled photolysis with irradiation at 400-500 nm.[831] The symmetric BIST moiety was conjugated to a Ca^{2+} chelator, ethylene glycoltetraacetic acid (EGTA) to enable optical control of calcium release in mouse cardiac myocytes. In order to adapt the symmetric BIST group for caged oligonucleotides, Anirban Bardhan designed and synthesized a series of asymmetric BIST-caged thymidine analogs (Figure 5-4A). The nitro (**208**), methoxy (**209**), amino (**210**), and dimethylamino (**211**) analogs exhibited absorption maxima (λ_{max}) of 434, 422, 444, and 452 nm, respectively (Figure 5-4B). Unfortunately, even though **211** exhibited the most red-shifted spectral properties, it could not be incorporated into a full-length oligonucleotide via DNA synthesis. Because the next closest red-shifted analog, **210**, also caused synthetic difficulties, we proceeded with the nitro-BIST analog, **208**. Decaging studies via HPLC showed that 20 minute irradiation with 447 nm light led to almost 90% disappearance of the nitro-BIST-caged thymidine while 470 nm irradiation led to only 40% loss of the caged compound suggesting 447 nm light led to more efficient decaging (Figure 5-4C). Moreover, irradiation of the NPOM-caged thymidine with both

wavelengths led to <10% disappearance of the caged thymidine indicating it would be amenable to selective irradiation (Figure 5-4D).

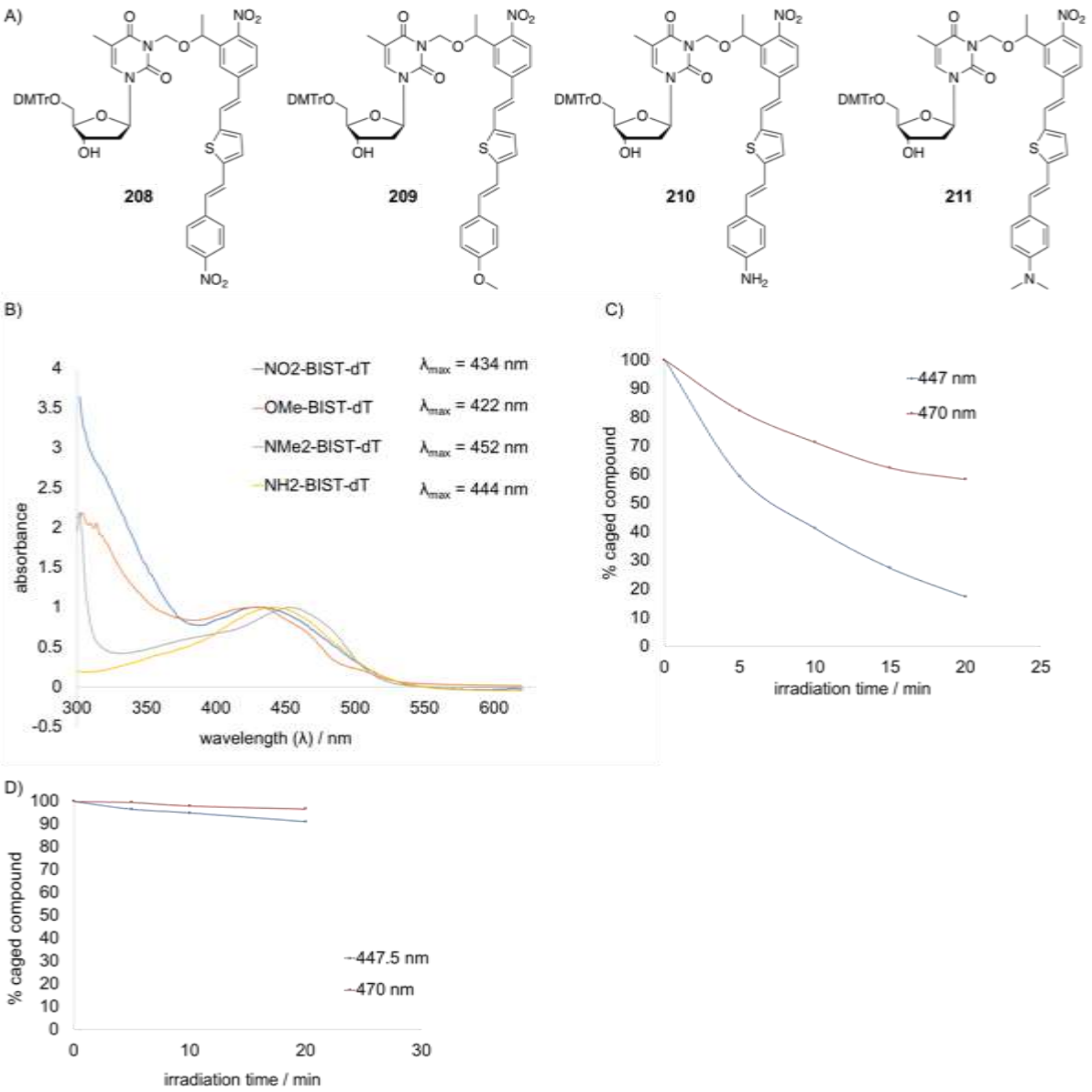

Figure 5-4 Evaluation of BIST analogs

A) Chemical structures of BIST-modified thymidine nucleobases. B) Absorbance spectra of the BIST-dT analogues. The absorbance vaues correspond to 50 µl of sample in MeOH in each case. C) Decaging plot of the nitro-BIST caged

dT analogue **208**. D) Decaging plot of the NPOM caged dT. Caged compounds (100 μM) were irradiated with LED lamp (447.5 nm or 470 nm) and the disappearance of the caged compounds was analyzed by HPLC. Data generated by Anirban Bardhan.

The BIST-caged reporter plasmid was generated following a similar approach to the previously developed NPOM-caged EGFP reporter.[826] Briefly, restriction sites for Nt.BstNBI restriction sites were cloned 15 bases upstream and immediately after the TATA box region in the pmCherry-N1 plasmid using site-directed mutagenesis (pmCherry-Bst). We also generated the corresponding pEGFP-Bst plasmid such that both constructs would utilize the same insert sequences (Figure 5-6A). Prior to generating the caged plasmids, we attempted to ligate a single-stranded DNA positive or negative control (Table 28) into the pmCherry-Bst or pEGFP-Bst constructs as a proof-of-concept and monitor construction via agarose gel electrophoresis (Figure 5-5B). The positive control was identical to the bold sequence in Figure 5-5A, while the negative control insert bore three T → C base substitutions (i.e., TATATAA → CACACAA). Briefly, the pmCherry-Bst plasmid was first digested with Nt.BstNBI for 2 h at 55 °C, followed by annealing to a complementary DNA oligonucleotide (Table 28; 2.5 nmol) to remove the input sequence. Then, following agarose gel purification, we phosphorylated the 5' terminus of the single-stranded DNA positive control or negative control and ligated them into the nicked backbone. Both the pEGFP- and pmCherry-Bst constructs displayed the expected band shift (super-coiled to nicked DNA) when analyzed via 0.8% (w/v) agarose gel electrophoresis (Figure 5-5C).

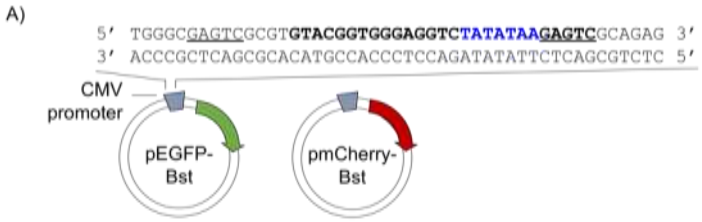

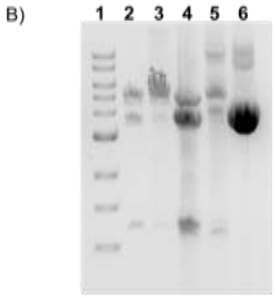

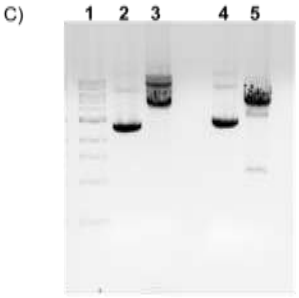

lane	condition
1	1 kb Tridye ladder
2	pmCherry-Bst
3	pmCherry-Bst (nicked)
4	pmCherry-Bst (nicked + annealed)
5	pmCherry-Bst (purified gap)
6	pmCherry-Bst (positive ligation)

lane	condition
1	1 kb Tridye ladder
2	pmEGFP-Bst
3	pmEGFP-Bst (purified gap)
4	pmCherry-Bst
5	pmCherry-Bst (purified gap)

Figure 5-5 Schematic and agarose gel analysis of pEGFP- and pmCherry-Bst plasmids

A) The NtBstNBI nicking enzyme sequences (underlined) were cloned into the pEGFP-N1 and pmCherry-N1 plasmids up and downstream of the TATA box (blue) generating the pEGFP- and pmCherry-Bst constructs. NtBstNBI nicked the plasmid at the termini of the bold sequence which was subsequently removed with a complementary DNA oligonucleotide. B) Agarose gel evaluation of the nicked pmCherry-Bst plasmid before (lane 3) and after (lane 4) annealing the complementary insert sequence, followed by agarose gel purification (lane 5) and ligation to the positive control insert (lane 6). C) The pEGFP-Bst and pmCherry-Bst constructs were evaluated via agarose gel electrophoresis (0.8% [w/v]) before and after the nicking reaction and subsequent purification. 1 kb Tridye ladder was included in lane 1 of both gels.

The resultant ligated plasmids were transfected into HEK293T cells and fluorescence was evaluated via widefield microscopy after 48 h. Cells transfected with the positive control plasmid were fluorescent, suggesting EGFP and mCherry were expressed from the ligated constructs (Figure 5-6A, B). Unfortunately, while the pmCherry negative control plasmid displayed no background fluorescence, several cells transfected with the EGFP negative control construct were fluorescent (Figure 5-6A, B). Similar observations of minor background signal for the EGFP negative control construct have been made previously.[826] Furthermore, there were much fewer cells expressing mCherry in the positive control ligation compared to the parent plasmid (Figure 5-6B). Taken together with the observation that the mCherry-Bst parent plasmid elicits fewer fluorescent cells, this may suggest that background is reduced for the mCherry-Bst negative control due to lower overall fluorescent protein expression.

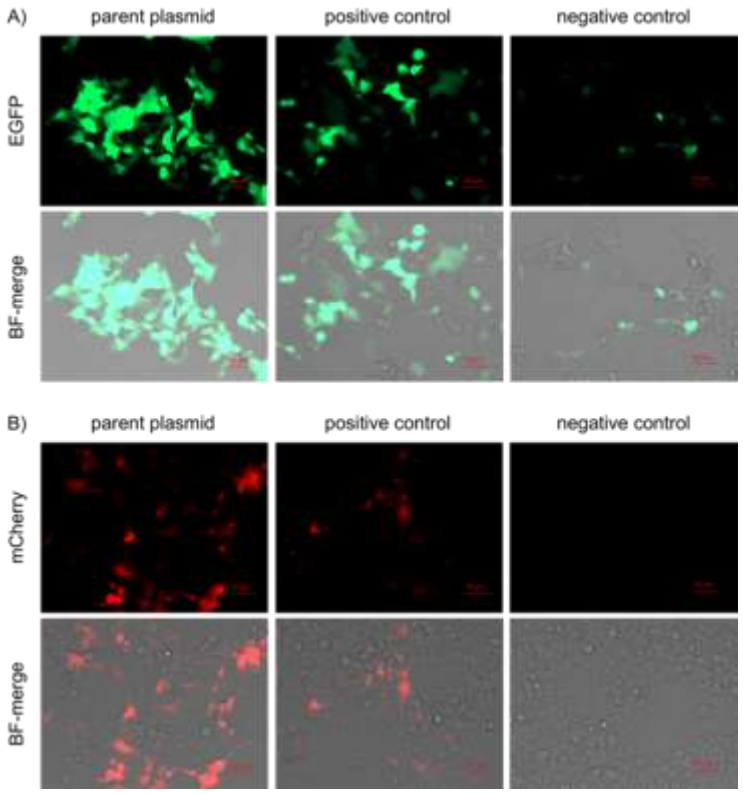

Figure 5-6 Ligation control experiments

A) The pEGFP-Bst plasmid was nicked with NtBstNBI and incubated with the reverse complement of the nicked sequence. Following purification, the T4 polynucleotide kinase (PNK)-treated positive or negative control insert were ligated into the nicked backbone. The resulting constructs were transfected into HEK293T cells. B) The nicked pmCherry-Bst plasmid was generated in an identical fashion and transfected into HEK293T cells following ligation. 20x magnification. EGFP (38HE filter; ex/em. = 470/525 nm), mCherry (43HE filter; ex/em. = 550/605 nm), and brightfield-merged images are shown. Scale bars indicate 200 µm.

To determine if we could still quantitatively discriminate between the positive and negative control plasmids, we attempted to analyze fluorescence via flow cytometry. Briefly, HEK293T cells were transfected with the pmCherry or pEGFP expressing positive and negative control

plasmids as well as their respective parent constructs then the number of fluorescent cells was quantified after 48 h on a Cytoflex S flow cytometer. In contrast to the fluorescence microscopy images, the pmCherry positive and negative controls were not discernable from each other (Figure 5-7A). A modest shift in the number of cells expressing EGFP was observed for parent and positive control constructs relative to the negative control plasmid (Figure 5-7B) suggesting this method would be amenable to quantifying EGFP fluorescence. Unfortunately, since both fluorophores could not be quantified via flow cytometry, we decided to continue analyzing transfection of the caged plasmids using microscopy.

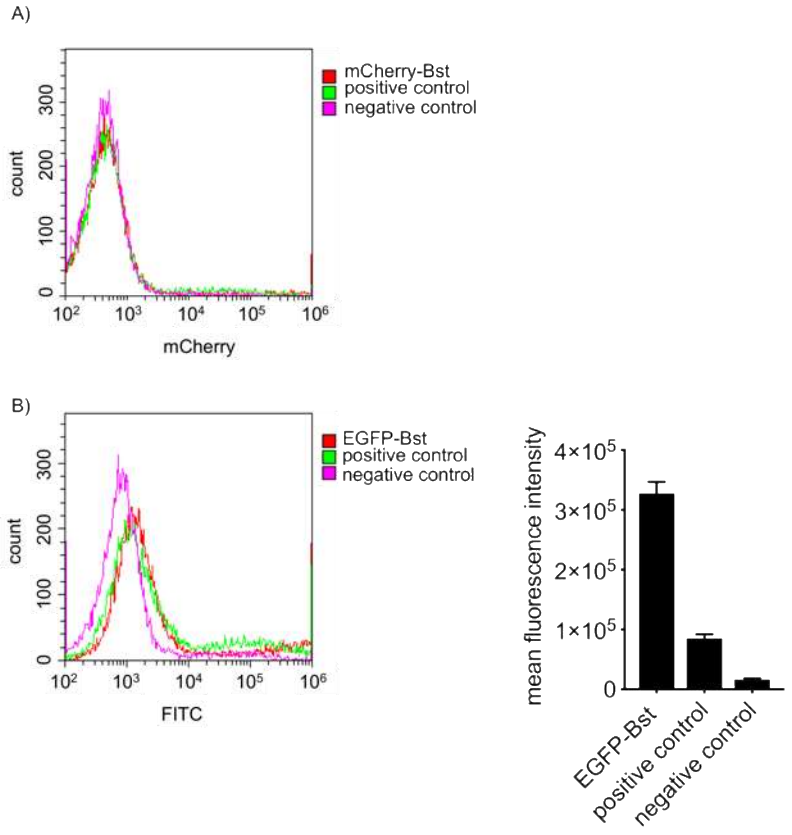

Figure 5-7 Flow cytometry analysis of mCherry and EGFP ligation control transfections

A) HEK293T cells transfected with mCherry-Bst, mCherry-Bst-positive control, or mCherry-Bst-negative control were analyzed using 561 nm laser and the mCherry filter (610 nm). B) HEK293T cells transfected with EGFP-Bst, EGFP-Bst-positive control, or EGFP-Bst-negative control were analyzed using 488 nm laser and the mCherry filter (525 nm). Mean fluorescence intensity ± standard deviation is normalized to number of cells per condition.

We hypothesized that the background fluorescence might be attributed to incomplete nicking of the parent plasmid and poor purification conditions leading to self-ligation and regeneration of the parent construct in the absence of the positive control insert. In order to overcome this potential limitation, we cloned SpeI and PvuI restriction sites into the pEGFP-N1

construct flanking the TATA box using site-directed mutagenesis. We expected that this design would be beneficial because restriction digest would result in linearization of the parent backbone which should overcome the ambiguity of the nicking reactions. After confirming insertion of the two new restriction sites did not impact EGFP expression (Figure 5-8A), we sequentially digested the resultant pEGFP-SpeI-PvuI plasmid with PvuI and SpeI. Because the enzymes are not active in the same buffer conditions, the linearized plasmid was purified using an E.Z.N.A Cycle Pure kit between digests. Following the digest with SpeI, the linear backbone was dephosphorylated using Antarctic Phosphatase (NEB), separated on a 0.8% (w/v) agarose gel, and purified using the E.Z.N.A. Gel Extraction kit. Subsequently, the positive control sense strand, negative control sense strand, and complementary antisense strand (Sigma-Aldrich; 30) were phosphorylated at the 5' terminus using T4 PNK. Then, the positive and negative control DNA duplex inserts were generated by annealing the positive or negative control sense strand to the antisense sequence in TE/Mg^{2+} buffer by heading the inserts to 95 °C and cooling to 12 °C over 10 min in a thermal cycler. The annealed inserts were then ligated into the linear backbone using T4 DNA ligase. The following day, ligation reactions were purified using the E.Z.N.A. Cycle Pure kit. After purification, the positive and negative control constructs were transfected into HEK293T cells for 48 h. Unfortunately, while background fluorescence for the negative control was greatly reduced, the positive control construct also expressed low levels of EGFP (Figure 5-8B). We hypothesized that the parent construct may not have been sufficiently digested by one of the restriction enzymes and thus explored if the order of restriction digests (i.e., SpeI first vs. PvuI first) had an effect on generation of the correct linearized backbone. After performing both sequential digests for 2 h at 37 °C and the subsequent ligation of the insert duplexes, PvuI was determined to be less efficient via agarose gel analysis (Figure 5-8C). As such, we decided to perform the PvuI digest overnight

first, then after gel purification, continue with SpeI digestion of the linearized backbone. The linearized plasmid and ligation products were analyzed by agarose gel electrophoresis (Figure 5-8D) prior to delivery into HEK293T cells to evaluate EGFP expression. Regrettably, while there was no background fluorescence from the negative control plasmid, the positive control construct still elicited low expression of EGFP relative to the non-digested parent construct (data not shown).

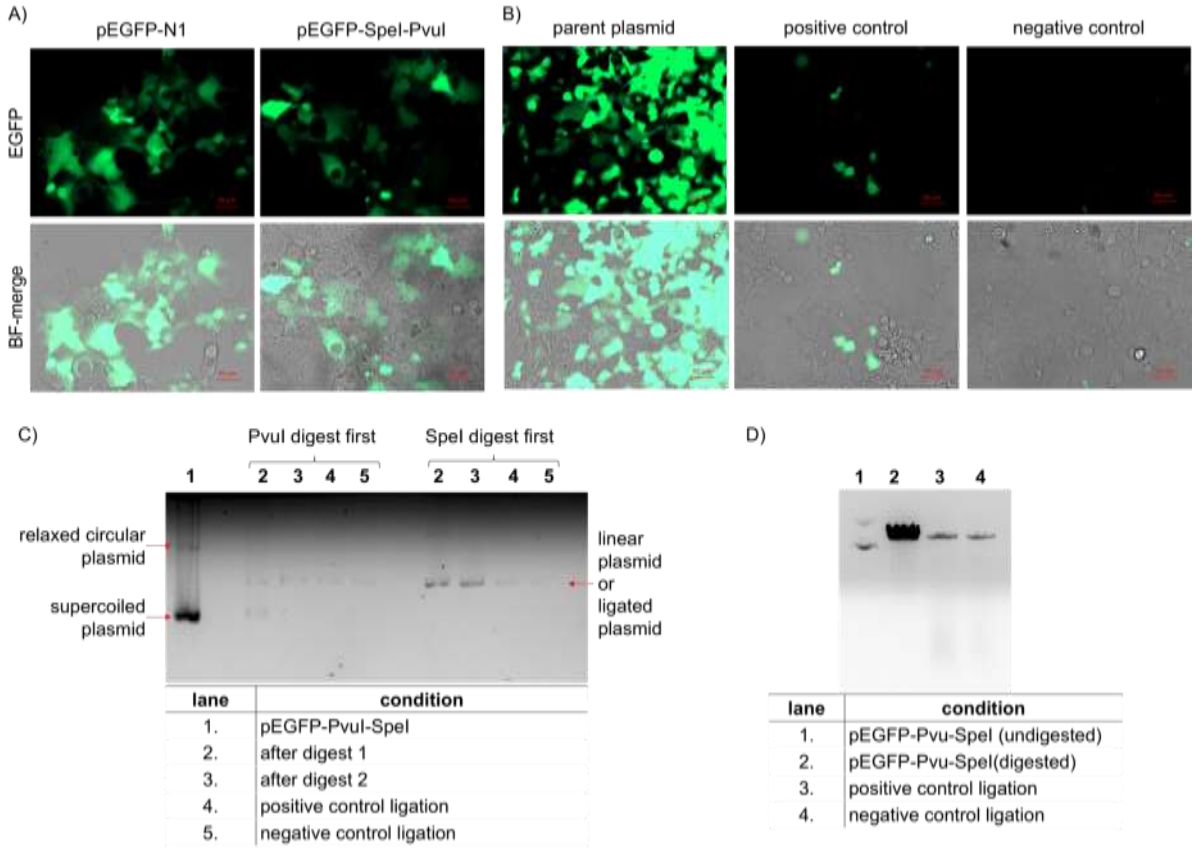

Figure 5-8 Evaluation of the pEGFP-SpeI-PvuI construct in cells

A) After mutating the pEGFP-N1 plasmid with SpeI and PvuI restriction sites, the resulting mutant construct was transfected into HEK293T cells to ensure minimal loss in EGFP expression. B) After digesting the pEGFP-SpeI-PvuI plasmid with PvuI followed by SpeI, and treating the plasmid with antarctic phosphatase, the T4 polynucleotide kinase (PNK)-treated and pre-annealed positive and negative control insert duplexes were ligated into the linear backbone.

After purification, the plasmids were transfected into HEK293T cells. 20x magnification. EGFP (38HE filter; ex/em. = 470/525 nm) and brightfield-merged images are shown. Scale bars indicate 200 µm. C) To analyze the efficiency of the digests, the order of restriction enzyme digest was varied with either PvuI or SpeI added first, followed by adding the other enzyme. The digests were analyzed via agarose gel electrophoresis. D) Agarose gel analysis of the pEGFP-SpeI-PvuI plasmid digest and ligations. Parent plasmid (lane 1) was digested with PvuI (overnight; 37 °C) followed by separation by agarose gel electrophoresis (0.8% [w/v]), gel extraction, and SpeI digest (lane 2). Annealed positive (lane 3) and negative (lane 4) control insert duplexes were ligated into the linear parent backbone.

In light of our inability to reduce background fluorescence of the negative control while maintaining expression with the positive control construct, we decided to return to the approach using the nicked plasmid. We hypothesized that while the negative control insert may not be sufficient for completely abrogating fluorescence, the caging groups may provide greater inhibition of duplex formation and thus reduce background expression. After nicking both the pmCherry-Bst and pEGFP-Bst plasmids, single-stranded positive or negative control DNA inserts were ligated into both constructs. Additionally, insert sequences bearing three NPOM- or BIST-caged thymidine residues within the TATA box synthesized by Anirban Bardhan were ligated into the nicked pEGFP-Bst and mCherry-Bst plasmids, respectively. Similar to the control plasmids described above, construction of the caged pEGFP and mCherry constructs was analyzed via 0.8% (w/v) agarose gel electrophoresis (Figure 5-9).

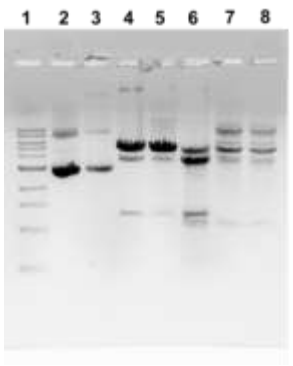

lane	condition
1	1 kb Tridye ladder
2	pmCherry-Bst
3	pEGFP-Bst
4	pEGFP-Bst (nicked)
5	pEGFP-Bst (nicked + annealed)
6	pEGFP-Bst (purified gap)
7	pmCherry-Bst-BIST
8	pEGFP-Bst-NPOM

Figure 5-9 Construction of the caged pEGFP and mCherry plasmids

Agarose gel evaluation of the nicked pEGFP-Bst plasmid before (lane 4) and after (lane 5) annealing the complementary insert sequence, followed by agarose gel purification (lane 6) and ligation to the NPOM-caged insert (lane 8). The pmCherry-Bst plasmid before (lane 2) and after (lane 7) ligation to the BIST-caged insert.

After purification, the ligated plasmids were transfected into HEK293T cells for 48 h, then evaluated via fluorescence microscopy. The EGFP positive control plasmid displayed modest fluorescence while the negative control and NPOM-caged plasmid showed little to no expression of EGFP (Figure 5-10A). Unfortunately, the BIST-caged mCherry construct induced similar levels of fluorescence to the positive control plasmid, suggesting the BIST caging group was degraded (Figure 5-10B).

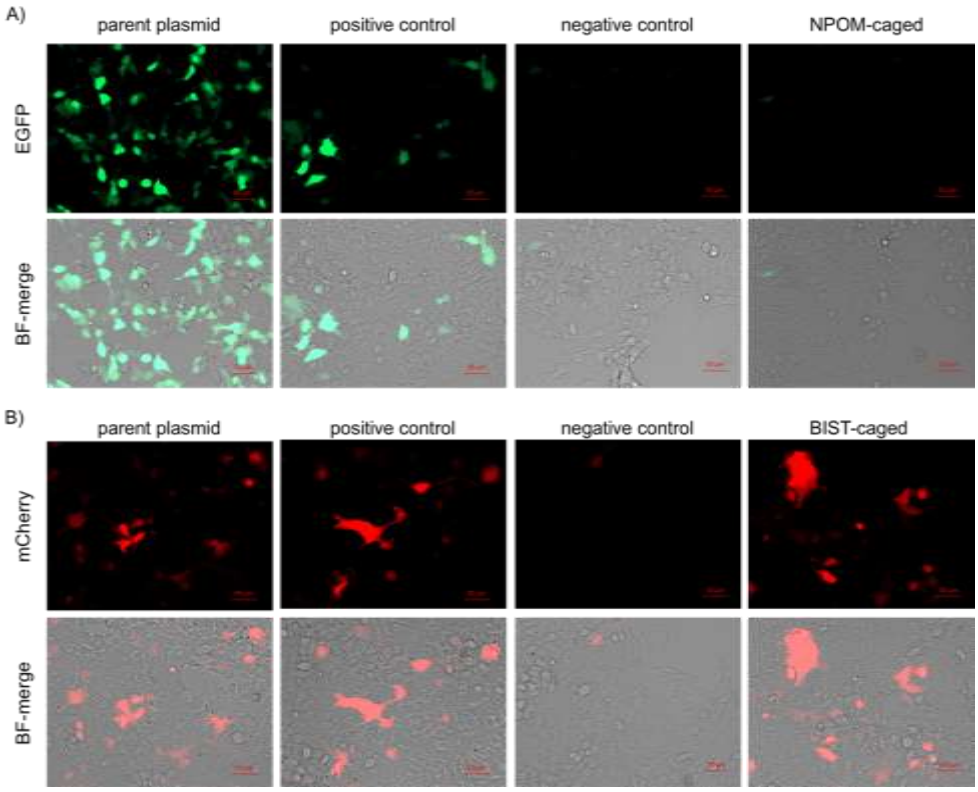

Figure 5-10 Evaluation of caged promoter constructs in HEK293T cells

A) The pEGFP-Bst plasmid was nicked with NtBstNBI, then the single-stranded positive control, negative control, and NPOM-caged inserts were ligated. B) The pmCherry-Bst plasmid was nicked with NtBstNBI, then the single-stranded positive control, negative control, and BIST-caged inserts were ligated. Following overnight ligations of all plasmids and subsequent purification, the resultant constructs were transfected into HEK293T cells and evaluated via fluorescence microscopy after 24 h. 20x magnification. EGFP (38HE filter; ex/em. = 470/525 nm), mCherry (43HE filter; ex/em. = 550/605 nm), and brightfield-merged images are shown. Scale bars indicate 200 µm.

In order to further investigate the BIST caging group, we attempted to ligate it into the nicked pEGFP-Bst plasmid and evaluated fluorescence in HEK293T cells via microscopy. The BIST-caged pEGFP and pmCherry constructs both elicited fluorescence corresponding to

respective protein of interest (Figure 5-11A, B), providing further support for the hypothesis that the caged insert had been compromised. Anirban Bardhan submitted the BIST-caged insert for mass spectrometry analysis, however the results were inconclusive.

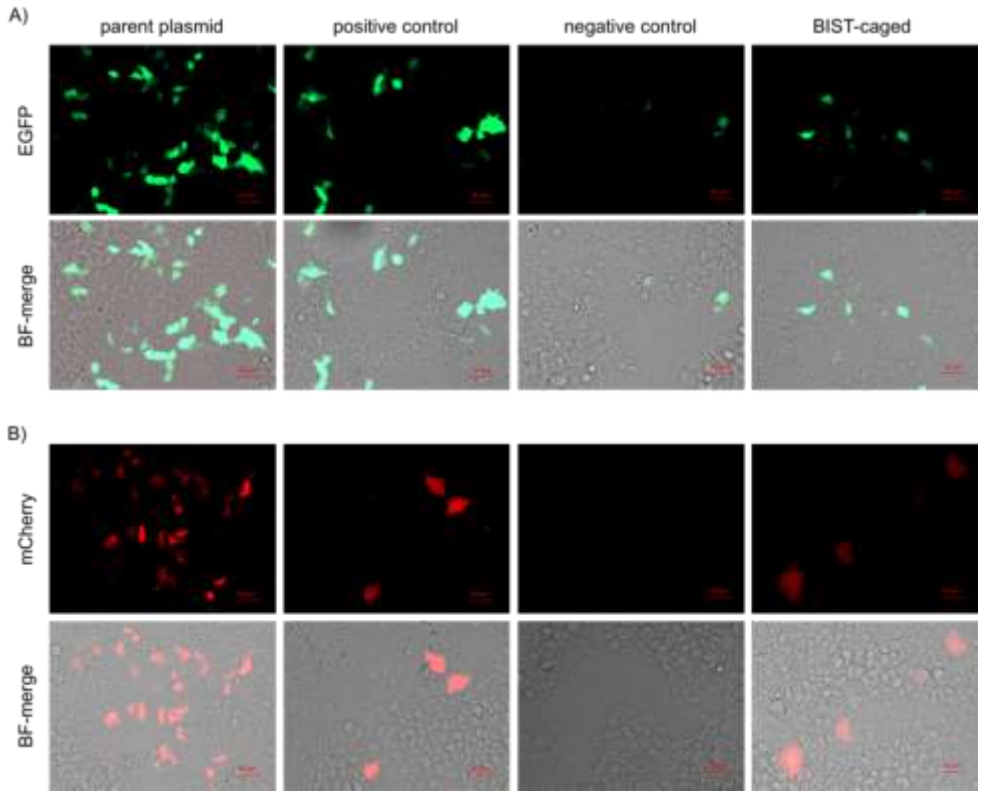

Figure 5-11 Evaluation of BIST-caged promoter constructs in HEK293T cells

A) The BIST-caged insert was ligated into the nicked pEGFP-Bst plasmid. B) Ligation of the BIST-caged insert into the nicked pmCherry-Bst backbone was repeated. Following overnight ligations of all plasmids and subsequent purification, the resultant constructs were transfected into HEK293T cells and evaluated via fluorescence microscopy after 24 h. 20x magnification. EGFP (38HE filter; ex/em. = 470/525 nm), mCherry (43HE filter; ex/em. = 550/605 nm), and brightfield-merged images are shown. Scale bars indicate 200 µm.

5.2.2 Summary and Outlook

In summary, we designed a second generation caged plasmid to enable orthogonal optical control of a second gene of interest in parallel with our previously developed NPOM-caged expression plasmid.[826] To allow for wavelength-selective activation of the caged plasmids, we attempted to incorporate the recently developed BIST caging group. As a proof-of-concept, we attempted to ligate a single-stranded DNA insert bearing three BIST-caged thymidine residues into a nicked plasmid encoding pmCherry. Unfortunately, our preliminary studies suggest that the BIST caging group may not be sufficient for inhibiting expression of the fluorescent protein.

Future work should include re-synthesis of the BIST-caged insert. Because the mass spectrometry analysis was inconclusive, it's possible that the DNA insert had degraded resulting in background fluorescence. If the newly synthesized BIST-caged insert still exhibits background activation, an alternative caging group should be pursued (e.g., ANBP). Furthermore, after optimizing the caged plasmids utilizing genes encoding fluorescent proteins as a proof-of-concept, the design should be applied to more biologically relevant proteins. For example, these tools could be utilized to explore multilayer genetic networks in which each caged plasmid encodes a protein within the network required to produce a measurable phenotype. Alternatively, the system could be utilized as a genetic switch wherein one plasmid encodes a protein of interest while the other encodes an siRNA for the same protein.

5.2.3 Materials and Methods

Cell culture. Experiments performed using HEK293T cell line cultured in Dulbecco's Modified Eagle Medium (DMEM; Gibco). Media was supplemented with 10% (v/v) Fetal Bovine Serum

(FBS; Sigma-Aldrich) and 1% (v/v) penicillin/streptomycin (VWR) and maintained at 37 °C in a 5% CO_2 atmosphere. Penicillin/streptomycin-free media was used for experiments. Cell line was used within passages 1-35 and was tested for mycoplasma contamination every three months.

Evaluation of BIST-caged thymidine residues. Experiments were performed by Anirban Bardhan. Analogs were diluted to 100 µM in 50 µl of methanol in a ½ dram vial and irradiated from the side using a custom LED source built by the University of Pittsburgh Machine Shop from LEDs (447.5 or 470 nm) purchased from LuxeonStar. In order to maintain consistent irradiation, the LED was held at ~2 cm from the vial at a power of 440 mW for the 447 nm LED and 115 mW for the 470 nm LED. Irradiations were performed in a dark room. After the specified irradiation time, compounds were analyzed on a Shimadzu LC-20ad using an ACE C18-AR column. Samples were evaluated using a gradient of 5-95% acetonitrile/water over 30 min and disappearance of the caged thymidine peak was monitored at 260 and 280 nm.

Construction of plasmids. See section 6.1 for detailed protocols of molecular biology techniques. The Nt.BstNBI restriction sites were cloned into pEGFP-N1 and pmCherry-N1 15 bases upstream and immediately after the TATA box region using site-directed mutagenesis and sequence-specific primers (Table 27) following protocol 6.1.2 Briefly, TATA SDM Fwd1 and TATA SDM Rev1 were used to introduce the Nt.BstNBI restriction site upstream of the TATA box, while TATA SDM Fwd2 and TATA SDM Rev2 were used to introduce the restriction site downstream of the TATA box. After confirming the sequence of each construct by Sanger sequencing (Genewiz), each plasmid was digested (40 µg) with Nt. BstNBI (NEB) at 55 °C for 2 h (500 µl) following protocol 6.1.3 Heat inactivation was performed at 80 °C for 20 min. Subsequently, the reverse

primer to the 31 bp DNA insert (Caged-TATA-complement) was added to the reaction (25 µl of a 100 µM stock) and annealed in TE/Mg^{2+} buffer (Tris-HCl [0.01 M; pH 8.0], EDTA [1 mM], $MgCl_2$ [12.5 mM]) by heating the solution to 95 °C and cooling to 12 °C on a thermal cycler (Bio-Rad). Next, the reaction was separated via agarose gel electrophoresis (see protocol 6.1.8 The reaction separated into two bands. The top band corresponded to the nicked plasmid and the bottom band corresponded to the plasmid in which the single-stranded sequence had been removed, leaving a gap. The bottom band was subsequently excised using and purified using the E.Z.N.A. Gel Extraction kit (Omega Bio-tek). The non-caged positive (Caged-TATA-positive) and negative control (Caged-TATA-negative) inserts as well as caged TATA box (Caged-TATA-insert) sequences (Table 28) were 5' phosphorylated with T4 polynucleotide kinase (PNK) at 50 µM (50 µl) and were subsequently ligated (10 µl of insert, 60 µl reaction) into the purified nicked parent plasmid following protocol 6.1.4 The ligation product was then purified using the E.Z.N.A. Cycle Pure kit (Omega Bio-tek) and quantified (ng/µl) by measuring UV absorbance at 260 nm on a Nanodrop ND-1000 spectrophotometer.

Table 27 Primer sequences used in cloning of the pEGFP- and pmCherry-Bst plasmids

Restriction sites are underlined

name	sequence (5' -> 3')
TATA SDM Fwd1	AGGTCTATATAAGAGTCGCAGAGCTGGTTTAGTGAAC
TATA SDM Rev1	GACTCTTATATAGACCTCCCACCGTACACGCCTA
TATA SDM Fwd2	AATGGGCGGTAGGAGTCGCGTGTACGGTGGGA
TATA SDM Rev2	GACTCCTACCGCCCATTTGCGTCAATGGGGCGGAGTT
Caged-TATA-complement	CTGCGACTCTTATATAGACCTCCCACCGTAC

Table 28 Sequences of the synthetic caged TATA box insert oligonucleotides

Sequences were designed for insertion into the TATA promoter region of the pEGFP- and pmCherry-Bst plasmids. NPOM- and BIST-caged thumidine residues are bolded and underlined.

name	**sequence (5' -> 3')**
Caged-TATA-positive	GTACGGTGGGAGGTCTATATAAGAGTCGCAG
Caged-TATA-negative	GTACGGTGGGAGGTCCACACAAGAGTCGCAG
Caged-TATA-insert	GTACGGTGGGAGGTC**T**A**T**A**T**AAGAGTCGCAG

Similarly, the SpeI and PvuI restriction sites were cloned into pEGFP-N1 15 bases upstream and immediately after the TATA box region using site-directed mutagenesis and sequence-specific primers (Table 29) following protocol 6.1.2 Briefly, pEGFP-TATA-fwd-SDM-1 and pEGFP-TATA-rev-SDM-1 were used to introduce the SpeI restriction site while pEGFP-TATA-fwd-SDM-2 and pEGFP-TATA-rev-SDM-2 were used to introduce the PvuI site. After confirming the sequence of each construct by Sanger sequencing (Genewiz), each plasmid was digested (40 µg) with SpeI or PvuI (NEB) for 2 h (500 µl) following protocol 6.1.3 Heat inactivation was performed at 80 °C for 20 min. The digest was purified using the E.Z.N.A. Cycle Pure kit (Omega Bio-tek) and used directly for the second digest. Next, the reaction was separated via agarose gel electrophoresis (see protocol 6.1.8 followed by purification using the E.Z.N.A. Gel Extraction kit (Omega Bio-tek). The non-caged positive (positiveTATAInS) and negative (negativeTATAInS) control inserts as well as the reverse complement (TATAInAS; Table 30) were 5' phosphorylated with T4 polynucleotide kinase (PNK) at 50 µM (50 µl) and annealed in TE/Mg^{2+} buffer (Tris-HCl [0.01 M; pH 8.0], EDTA [1 mM], $MgCl_2$ [12.5 mM]) by heating the solution to 95 °C and cooling to 12 °C on a thermal cycler (Bio-Rad). The duplexes were

subsequently ligated (10 µl of insert, 60 µl reaction) into the linear parent plasmid following protocol 6.1.4 The ligation product was then purified using the E.Z.N.A. Cycle Pure kit (Omega Bio-tek) and quantified (ng/µl) by measuring UV absorbance at 260 nm on a Nanodrop ND-1000 spectrophotometer.

Table 29 Primer sequences used in cloning of the pEGFP-SpeI-PvuI plasmid

Restriction sites are underlined.

name	sequence (5' -> 3')
pEGFP-TATA-fwd-SDM-1	CGGTAGACTAGTACGGTGGGAGGTCTATATAAGCAGAGCTCGTTTAGTG
pEGFP-TATA-rev-SDM-1	CACCGTACTAGTCTACCGCCCATTTGCGTCAATGGGG
pEGFP-TATA-fwd-SDM-2	ATATAACGATCGCTCGTTTAGTGAACCGTCAGATCCGCTA
pEGFP-TATA-rev-SDM-2	AACGAGCGATCGTTATATAGACCTCCCACCGTACTAGT

Table 30 Sequences of the synthetic TATA box insert oligonucleotides

Sequences were designed for insertion into the TATA promoter region of the pEGFP-SpeI-PvuI plasmid.

name	sequence (5' -> 3')
positiveTATAInS	CTAGTACGGTGGGAGGTCTATATAACGAT
negative TATAInS	CTAGTACGGTGGGAGGTCCACACAACGAT
TATAInAS	CGTTATATAGACCTCCCACCGTA

Transfection of plasmid constructs. HEK293T cells were seeded in a poly-D lysine-treated black 96-well plate (Greiner; see protocol 6.2.2 at 20,000 cells/well in DMEM growth media (Hyclone) supplemented with 10% FBS (Sigma-Aldrich). The following day, cells were transfected with 200 ng plasmid using LPEI (see protocol 6.2.3.3). After 48 h, media was removed, and cells were washed with sterile filtered 1x phosphate buffered saline (PBS). Media was then replaced with phenol red-free DMEM and imaged using the 20x LD Plan-Apochromat objective and the mCherry or EGFP filter set (38 HE) following protocol 6.2.5 on the Axio Observer Z1 microscope (Zeiss) using Zen 2.0 software.

Flow cytometry. HEK293T cells were seeded in a poly-D lysine treated 6-well plate (Corning; see protocol 6.2.2 at 125,000 cells/well in DMEM growth media (Hyclone) supplemented with 10% (v/v) FBS (Sigma-Aldrich). The following day, cells were transfected with 200 ng of pEGFP-Bst, pEGFP-positive control, pEGFP-negative control, pmCherry-Bst, pmCherry-positive control, or pmCherry-negative control using LPEI (see protocol 6.2.3.3). After 48 h, media was removed, and cells were washed with 500 µl of sterile filtered 1x phosphate buffered saline (PBS). Cells were then incubated in 200 µl of TrypLE Express reagent (Gibco) at 37 °C for 2 min. Once cells were lifted, 300 µl of 1x PBS was added to each well and cell suspensions were transferred to 1.7 ml Eppendorf tubes. Subsequently, cells were pelleted by centrifugation at 1000 g for 10 min at 4 °C. Supernatant was removed and cell pellet was resuspended in 500 µl of fluorescence activated cell sorting (FACS) buffer (1x PBS; pH 7.4, 0.5% [w/v] bovine serum albumin [BSA], 0.1% [w/v] sodium azide). The cell suspension was centrifuged a second time at 1000 g for 10 min at 4 °C. The supernatant was removed again, and cells were resuspended in 500 µl of FACS buffer then stored on ice until flow cytometry was performed.

Samples were analyzed on a Cytoflex S (Beckman-Coulter) using the 488 nm laser and FITC filter (525 nm) for EGFP constructs and 561 nm laser and the mCherry filter (610 nm) for mCherry constructs. Cells were selected using forward scatter (FSC) and side scatter (SSC) gained to 10 and 20, respectively and were thresholded at 1000. In total, 10,000 events were collected flowing at a rate of 10 µl per minute with an abort rate of less than 2%. Raw data were exported and analyzed in GraphPad (Prism). Histograms were generated by plotting average, standard deviation, and number of cells quantified (N).

5.3 Light-Activatable Cyclic Morpholino Oligomers

This material was reprinted in its entirety with permission from Ankenbruck, N.; Courtney, T.; Naro, Y.; Deiters, A., *Angew. Chem. Int. Ed. Engl.* **2018**, *57*, 2768.

While DNA/RNA-based oligonucleotides have been extensively used as antisense agents, other synthetic oligomers, such as morpholinos (MOs),[832-834] have advantages in specific applications – in particular, experiments in aquatic embryos. MOs are modified nucleic acids containing morpholine rings and phosphorodiamidate backbones instead of sugars and phosphodiesters, respectively, rendering them nuclease-resistant, less likely to interact non-specifically with cellular proteins, and still capable of binding to complementary sequences via Watson-Crick base pairing.[835] As such, MOs have been utilized as antisense agents for the inhibition of miRNA function, mRNA translation, and mRNA splicing.[836] Caged morpholinos (cMOs) have been developed as molecular probes of gene function in cells and animals because they provide precise spatiotemporal control of gene expression.[770,774,775,787,837,838] In early

developments, the Chen lab used the light-cleavable hairpin approach,[774] including the two-photon activation of cMOs containing a bromohydroxyquinoline-based linker (Figure 5-1B).[775]

However, this approach required careful inhibitor sequence design to minimize background activity, while still retaining rapid photoactivation. Additionally, release of the inhibitory oligonucleotide may create potential for off-target effects. Similarly, Washbourne utilized a MO inhibitor that contained a photocleavable linker (Figure 5-1B).[770] In contrast, optical control of MO function in cells and animals has also been demonstrated by incorporating caged thymidine nucleobases.[787] This approach avoided the necessity of an inhibitory oligonucleotide, however, multiple caging groups are needed to fully block MO:mRNA hybridization.

Recently, conformationally gated MOs[778,828,839,840] and DNA oligomers[171,841] were developed, where the introduction of curvature reduces antisense oligonucleotide:mRNA interaction thereby inhibiting gene silencing until photochemical cleavage of a linker linearizes the nucleic acid and fully restores mRNA hybridization. This nicely addresses both limitations discussed above, since only a single photolysis step is needed for activation and no inhibitory oligonucleotide is released.[840] Moreover, the ability to insert a wide range of chromophores into the circular MO enabled wavelength-specific gene silencing by sequentially irradiating zebrafish embryos with 405-470 nm (cleaving a diethylaminocoumarin, DEACM, group) and 365 nm (cleaving a 2-nitrobenzyl, NB, group) (Figure 5-12A).[828] The cyclic MOs were designed to target the T-box transcription factor spadetail (*spt/tbx16*) and the homeobox-containing repressor *flh*. *Spt* controls cell differentiation during embryogenesis and its transcription within the embryo midline is inhibited by *flh*. Mutation of *spt* also corresponds with the absence of myogenic differentiation 1 (*myod1*) while *flh* silencing leads to aberrant *myod1* expression in early stages of development.[842,843] Upon irradiation with 365 nm light, zebrafish injected with the NB cyclic *spt*

cMO displayed a drastic loss in *myod1* expression, but showed minimal response to irradiation with 405 or 470 nm light, whereas embryos injected with the DEACM cyclic *flh* cMO exhibited abnormal *myod1* expression when irradiated with either 470, 405, or 365 nm light, as expected (Figure 5-12B,C). Co-injection of both cMOs led to zebrafish embryos that displayed the *spt* mutant phenotype only after irradiation at 405/470 nm followed by 365 nm light exposure. Sequential irradiation at defined time points during embryonic development demonstrated that *spt* acts during gastrulation in embryos bearing *flh* mutations to direct muscle cell precursors toward muscle cell fates, showcasing the utility of orthogonally activated cMOs for the investigation of gene interactions in with precise temporal control.

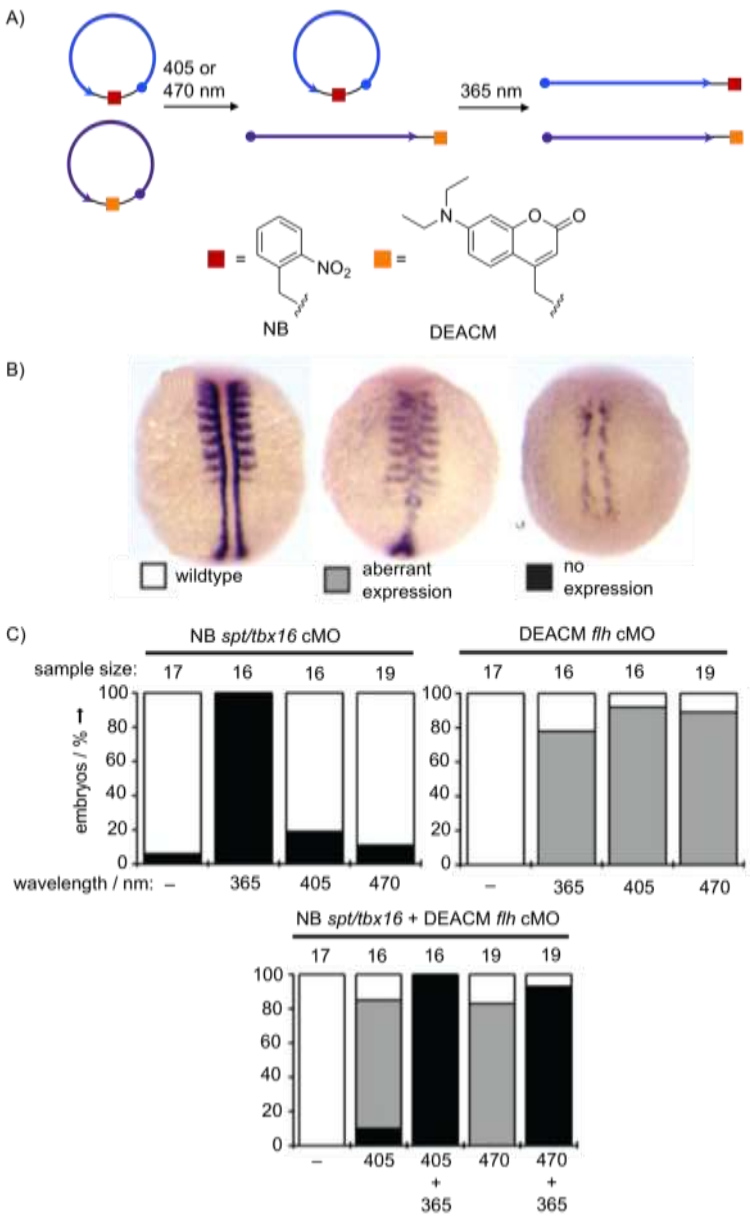

Figure 5-12 Wavelength-selective decaging of circular morpholinos

A) Sequential activation of cMOs targeting the genes *flh* (purple) or *spt* (blue). Structures of the NB (red) and DEACM (orange) caging groups. B) Representative images of *myod1* expression patterns from control (wildtype), *flh* knockdown (aberrant expression), and *spt* knockdown (no expression) phenotypes after irradiation. C) Quantification of phenotypes is displayed for embryos injected with the cMOs and irradiation conditions denoted in the graphs. Adapted with permission from Yamazoe *et al.*, *Angew. Chem, Int. Ed., 53*, 10114-10118. Copyright 2014 Wiley-VCH.

Several caged oligonucleotides have been established for optical control of gene function via blocking translation, including circular MOs. The development of circular MOs capable of orthogonal photoactivation by using wavelength-specific chromophores allows for investigation of more complex genetic networks via sequential knockdown of different gene targets. However, while nuclease-resistant MOs are attractive antisense agents, delivery into mammalian cells requires additional modifications.[844]

5.3.1 Optical Control of miRNA Function using Cyclic Morpholinos

While light-activatable circular MOs have afforded precise control over biological processes in zebrafish, they still suffer from a number of limitations. Notably, depending on the mRNA target sequence, background antisense activity of the circular MO can be observed.[845] It has been shown that as few as 11 complementary bases between a linear MO and its target were sufficient for splicing correction.[846] Furthermore, a study by Chen and co-workers demonstrated that cyclic MOs displayed a similar melting temperature (T*m*) to their linear counterparts in binding assays, especially as the length of the MO increased from 21 to 25 bases.[840] However, longer MO sequences are routinely selected in the design of cyclic cMOs because they demonstrate greater efficacy upon decaging. We hypothesized that while short 21-nucleotide MOs were less effective against mRNA targets after light irradiation, they may be able to inhibit miRNA function with greater success due to the shorter target sequence and limited secondary structure.

As a proof-of-concept, we chose to target miR-125b with a fully complementary cyclic caged morpholino. In humans, miR-125b has been identified as an oncogene in endometrium, breast, and prostate cancers.[847] Furthermore, miR-125b has been linked to drug resistance in several cancer phenotypes.[848] Alternatively in zebrafish, miR-125b has been implicated in

developmental processes[849] as well as fat metabolism,[850] but its role still remains poorly understood.

In order to evaluate function of the anti-miR-125b MO, we utilized a luciferase reporter plasmid (psiCHECK-miR125b) similar to the construct developed to identify small molecule modulators of miR-122 function as described above. As an initial approach to deliver the MO into cells, we attempted to use complementary DNA oligonucleotides in conjunction with commercial transfection reagents.[851,852] We hypothesized that the negatively charged DNA would enable a facile and cost-effective method of MO delivery with minimal disruption of MO function. As such, we designed a series of DNA delivery probes with complementary to 14 nucleotides of the anti-miR-125b MO. Analogous to the approach employed by Morcos,[852] we also appended a 10- or 15-base poly(A) tail to the 3'-terminus of the delivery probes (Figure 5-13A). Prior to delivery, the miR-125b MO or miR-125b antagomir were annealed to the complementary DNA sequences in PBS in a thermal cycler. Luis Vazquez-Máldonado, a chemist in our laboratory, verified that annealing of the two oligonucleotides formed the expected duplexes in a native PAGE gel experiment (Figure 5-13A). We first attempted to transfect the annealed oligonucleotides using cationic-lipid-based transfection reagents, Lipofectamine 2000 or XtremeGENE, in PC3 cells which are known to overexpress miR-125b.[489] The nucleic acid duplexes were delivered simultaneously with the psiCHECK-miR125b reporter plasmid for 4 h, then media was replaced with regular growth media. After 48 h, luciferase activity was measured using a dual luciferase assay. While initial results seemed promising (Figure 5-13B) with XtremeGENE-mediated delivery of the MO/DNA duplex eliciting up to ~15-fold increase in relative luciferase activity, the results were not reproducible (Figure 5-13C). We hypothesized that the duplex had not been properly formed in PBS which contributed to poor delivery through inadequate annealing. In light

of this, we annealed the duplexes in TE/Mg^{2+} buffer, then attempted to deliver the duplexes in conjunction with the psiCHECK-miR125b reporter using XtremeGENE. Unfortunately, delivery of the MO still did not elicit an increase in luminescence (Figure 5-13D).

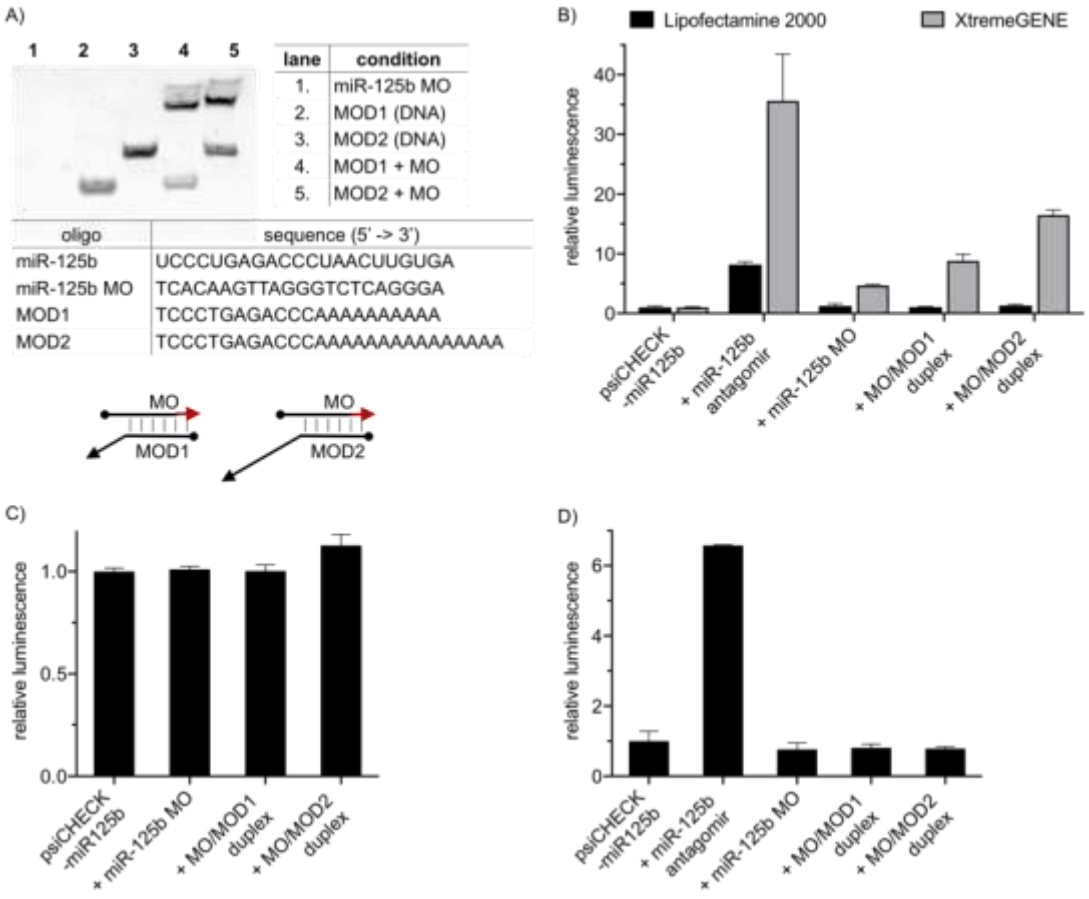

Figure 5-13 Morpholino-DNA duplex-mediated delivery with Lipofectamine 2000 or XtremeGENE

A) Complementary DNA oligonucleotides (MOD1 or MOD2) were annealed to the anti-miR-125b MO (10 pmol each), then analyzed via native PAGE followed by SYBR Gold stain. The red region in the cartoon denotes the sequence complementary to the seed region of miR-125b. Data were collected by Luis Vazquez-Máldonado. B) Following annealing of the MO/DNA duplexes in 1x PBS, transfection was performed in conjunction with the psiCHECK-miR125b reporter using Lipofectamine 2000 or XtremeGENE siRNA transfection reagents to facilitate delivery into PC3 cells. C) Transfection of the MO/DNA duplexes with the miR-125b reporter with XtremeGENE

was repeated to verify the delivery method. D) Anti-miR-125b MO and complementary DNA duplexes were annealed in TE/Mg^{2+}, then transfected using XtremeGENE. After 48 h, a dual luciferase assay was performed. Data are normalized to psiCHECK-miR125b for each transfection reagen represent the average ± standard deviation for three independent experiments.

Next, we designed a series of four MO delivery probes with 12 or 14-base complementarity to miR-125b to determine if length or sequence (e.g., blocking the seed region) of the duplex would affect activity of the MO upon delivery into cells (Figure 5-14A). Additionally, the probes bore either a 10- or 20-nucleotide poly(A) sequence on the 5'-terminus. After annealing the MO to the DNA probes in TE/Mg^{2+} buffer, we attempted to transfect the duplexes using XtremeGENE transfection reagent. Unfortunately, regardless of placement or length of the probes, none of the MOs inhibited miR-125b in the reporter assay (Figure 5-14B). We hypothesized that lack of activity may be attributed to the type of reagent employed for transfection. As such, we attempted to deliver the MO/DNA duplexes using the partially ionized, weakly basic ethoxylated polyethylenimine (EPEI)[852] ionic liposome-based delivery agent, Endo-Porter.[853] Both have been previously utilized to deliver MOs into cells. While both reagents led to a modest increase in luminescence upon delivery of the anti-miR-125b MO/DNA duplexes relative to the plasmid alone, the control MO/DNA duplexes also showed an increase suggesting the improvements in activity are likely artifacts (Figure 5-14C).

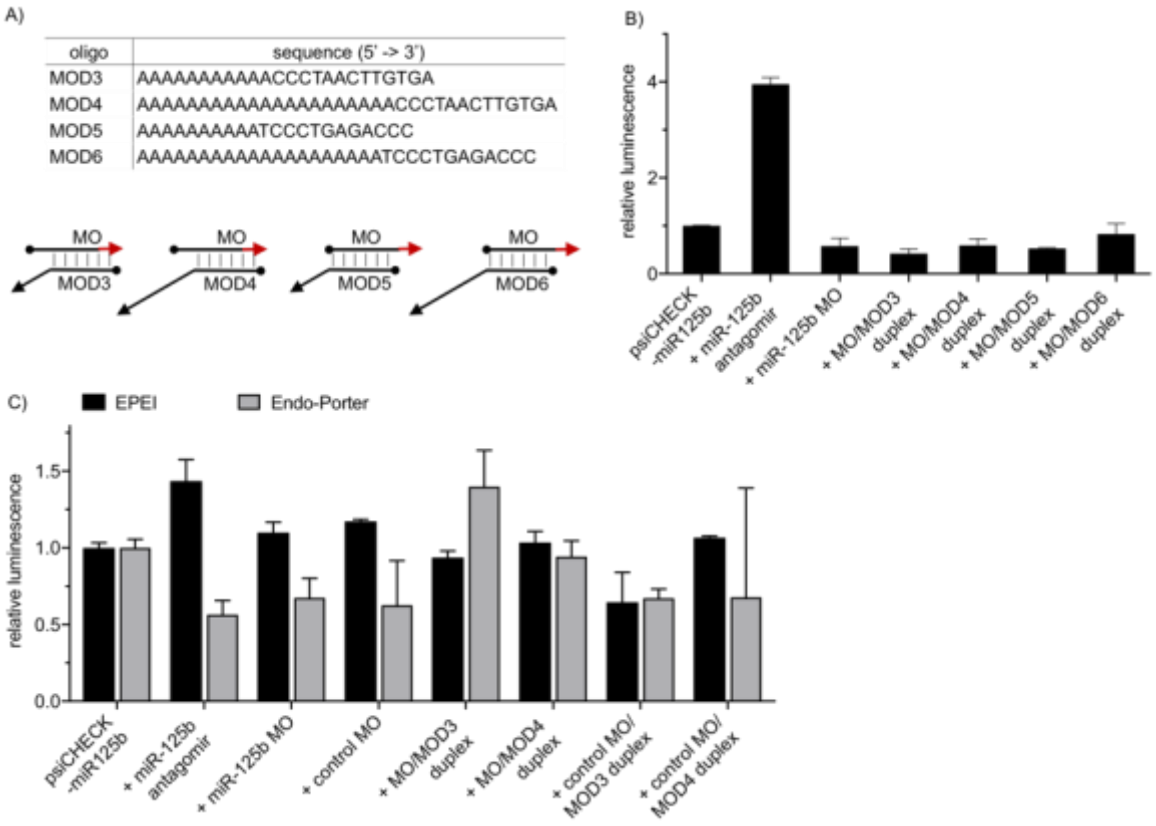

Figure 5-14 Delivery of morpholinos with EPEI and Endo-Porter

A) Schematic and sequences of alternative complementary DNA delivery strategy. The red region in the cartoon denotes the sequence complementary to the seed region of miR-125b. B) Anti-miR-125b MO and complementary DNA duplexes were annealed in TE/Mg^{2+} buffer, then transfected into PC3 cells in conjunction with the psiCHECK-miR125b reporter using XtremeGENE. C) The psiCHECK-miR125b reporter and all oligonucleotides were delivered using Endo-Porter or ethoxylated polyethylenimine (EPEI) transfection reagents. After 48 h, a dual luciferase assay was performed. An anti-no tail (*ntla*) MO was used as a contol. Data are normalized to psiCHECK-miR125b for each transfection reagent and represent the average ± standard deviation for three independent experiments.

To further evaluate why there was no observable inhibition of miR-125b in the luciferase assay, we attempted to deliver a fluorescein isothiocyanate (FITC)-modified DNA or MO into PC3 cells using XtremeGENE, EPEI or Endo-Porter. After 24 h, the FITC-labeled DNA was efficiently delivered using XtremeGENE, but no fluorescence was observed in conjunction with the EPEI or Endo-Porter reagent (Figure 5-15). Moreover, no fluorescence was observed for any of the conditions employed for the MO suggesting the lack of activity in the luciferase assay can be attributed to the failed delivery.

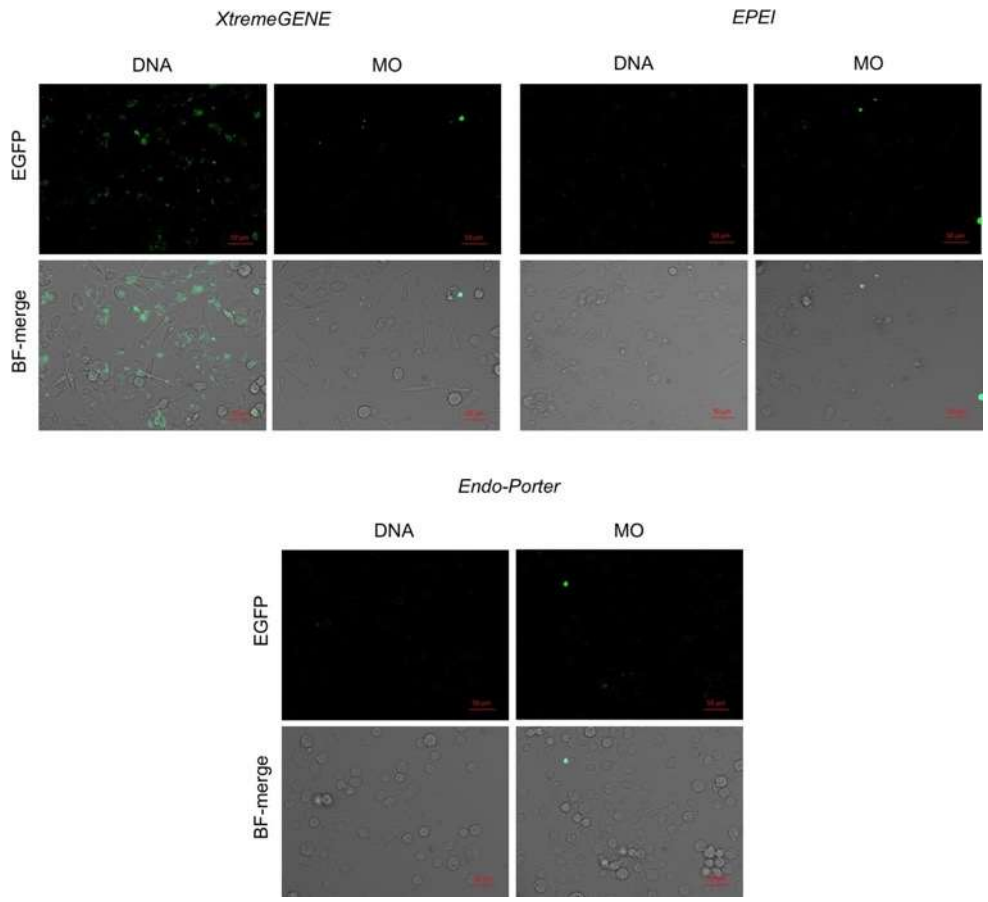

Figure 5-15 Delivery optimization of FITC-modified oligomers

Fluorescein isothiocyanate (FITC)-modified DNA or MO oligomers were delivered into PC3 cells using XtremeGENE siRNA transfection reagent, ethoxylated ethylenimine (EPEI), or Endo-Porter. 20x magnification. EGFP (38HE filter; ex/em. = 470/525 nm) and brightfield-merged images are shown. Scale bars indicate 200 µm.

In addition to inability to deliver the anti-miR-125b MO into mammalian cells, Luis Vazquez-Máldonado, a chemist in our laboratory, experienced difficulty in generating the cyclic cMO at concentrations amenable for zebrafish studies. We hypothesized that the high G content of the ant-miR-125b might give rise to undesirable secondary structures (e.g., G quadruplexes)

leading to insolubility of the MO. In order to circumvent this limitation, we selected another miRNA, miR-30e, as an alternative target. Similar to miR-125b, miR-30e has been implicated in mediating tumor growth and chemoresistance.[854-856] Additionally, the miR-30 family has roles in organ and tissue development in humans.[857] Moreover, miR-30 family members have been shown to regulate early muscle development in zebrafish,[858] and miR-30 family miRNAs are functionally conserved across multiple species.[47]

Similar to the miRNA reporters described previously, the miR-30e target sequence was inserted downstream of the *Renilla* luciferase gene in the 3' UTR using a multi-cloning site in the psiCHECK-2 plasmid. When HeLa or MCF7 cells were co-transfected with the resultant psiCHECK-miR30e reporter, a ~6-fold increase was observed relative to negative control antagomir (Figure 5-16A), confirming the reporter could be utilized to investigate changes in miR-30e activity. In light of the limitations observed with uptake of the MO/DNA duplexes, we decided to pursue alternative delivery methods. In an initial experiment, the miR-30e MO was conjugated to the HIV Tat cell-penetrating peptide (CPP). HeLa or MCF7 cells were transfected with the psiCHECK-miR30e reporter plasmid, then media was changed to normal growth media and cells were treated with the miR-30e-HIV Tat conjugate (2.5 μM). Cells were also treated with the CPP or MO and transfected with miR-30e antagomir or scrambled antagomir as controls. After 24 h, a dual luciferase assay was performed in order to evaluate activity. Unfortunately, while the miR-30e antagomir was capable of eliciting an increase in luminescence in both cell lines (Figure 5-16B), neither HeLa nor MCF7 cells responded to treatment with the MO suggesting either the MO was no efficiently delivered or did not inhibit function of miR-30e. To further elucidate the lack of activity, we conjugated the miR-30e MO to a FITC-labeled HIV Tat CPP to monitor uptake. After 48 h, weak fluorescence was observed for the CPP and the MO-CPP conjugate (Figure

5-16C). Unexpectedly, the miR-30e MO-CPP conjugate elicited a modest increase in luminescence relative to the MO or HIV Tat peptide alone as well as the miR-30e antagomir (Figure 5-16D), suggesting it was efficiently delivered and capable of inhibiting miRNA function.

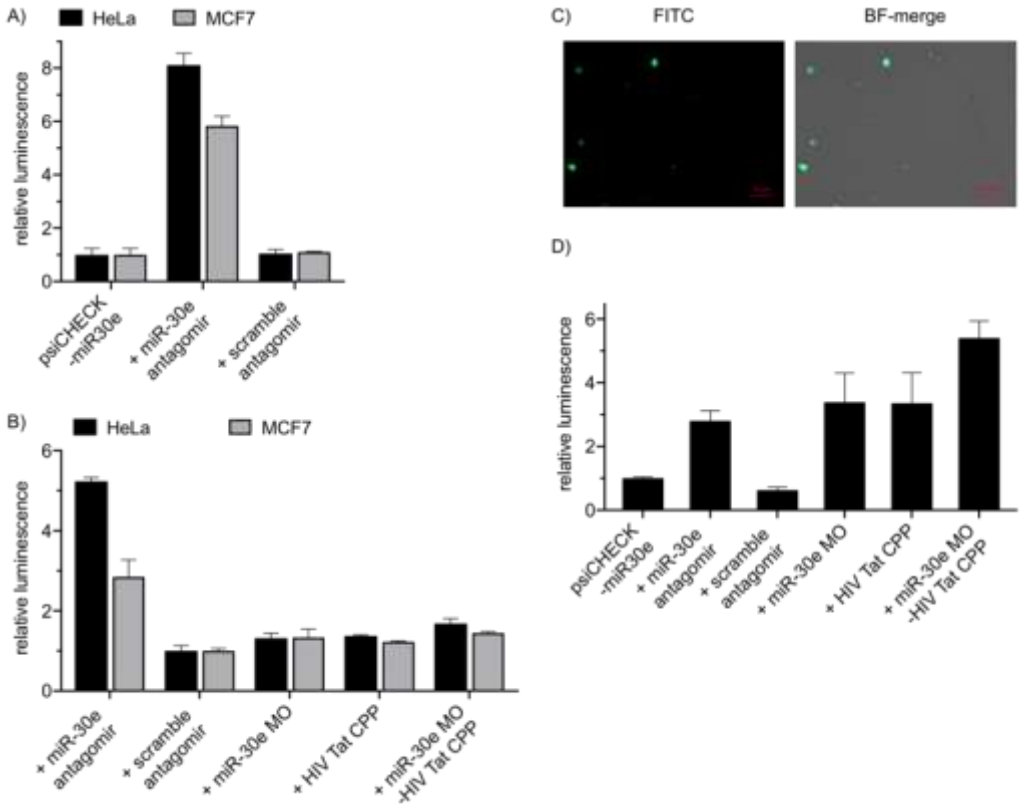

Figure 5-16 Evaluation of the miR-30e luciferase reporter

A) Activity of the psiCHECK-miR30e reporter was validated by transfecting the construct into HeLa or MCF7 cells with an anti-miR-30e or scramble antagomir using XtremeGENE. After 48 h, a dual luciferase assay was performed. Data are normalized to psiCHECK-miR30e for each cell line and represent the average ± standard deviation for three independent experiments. B) The anti-miR-30e MO was conjugated to an HIV Tat peptide by Luis Vazquez-Máldonado which was subsequently incubated with HeLa or MCF7 cells 24 h post-transfection with the psiCHECK-miR30e reporter construct. Transfection of the reporter construct and anti-miR-30e or scramble antagomir were

carried out using XtremeGENE. After 24 h, a dual luciferase assay was performed. Data are normalized to psiCHECK-miR30e + scramble antagomir for each cell line and represent the average ± standard deviation for three independent experiments. C) The psiCHECK-miR30e reporter construct was transfected into HeLa cells, then a fluorescein isothiocyanate (FITC)-modified HIV Tat CPP conjugated to the anti-miR-30e MO was added in fresh growth media to the cells. Cell uptake was evaluated after delivery for 48 h via fluorescence microscopy. 20x magnification. EGFP (38HE filter; ex/em. = 470/525 nm) and brightfield-merged images are shown. Scale bars indicate 200 µm. D) A dual luciferase assay was performed on HeLa cells transfected with the psiCHECK-miR30e reporter and incubated with the FITC-labeled MO-CPP conjugate. Data are normalized to psiCHECK-miR30e and represent the average ± standard deviation for two independent experiments.

In order to improve consistency and delivery of the MO-CPP conjugates, we attempted to optimize delivery of the FITC-modified HIV Tat peptide. First, HeLa cells were incubated with fluorescent CPP at 2.5, 5, 10, or 25 µM in normal growth media supplemented with FBS for up to 24 h, then imaged on a widefield microscope. Unfortunately, minimal FITC fluorescence was observed at concentrations below 25 µM, even after a 2 h incubation (Figure 5-17). Moreover, no fluorescence was observed at any concentration after 24 h incubation (data not shown). Importantly, presence of serum has been previously shown to inhibit uptake of CPPs.[859]

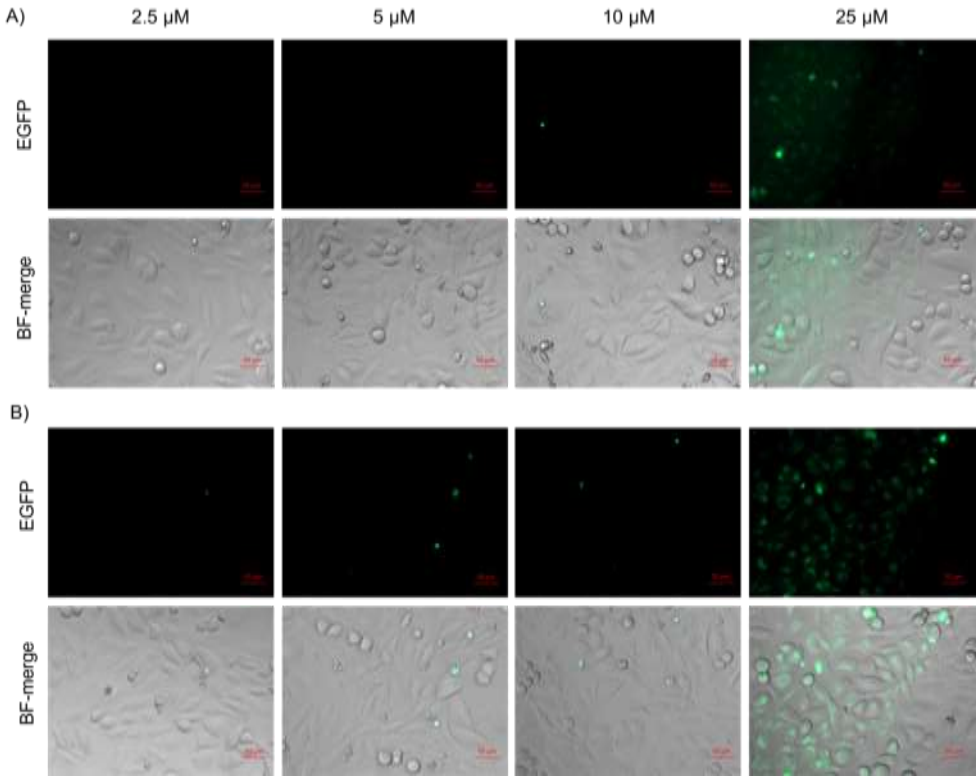

Figure 5-17 FITC-labeled HIV Tat CPP uptake studies in DMEM

Fluorescein isothiocyanate (FITC)-modified HIV Tat synthesized by Yuta Naro was incubated for A) 1 h in DMEM containing 10% FBS or B) 2 h in DMEM containing 10% FBS. Uptake was evaluated via fluorescence microscopy at 24 h post delivery. 20x magnification. EGFP (38HE filter; ex/em. = 470/525 nm) and brightfield-merged images are shown. Scale bars indicate 200 µm.

As such, we attempted to deliver the HIV Tat CPP in serum-free OptiMEM for up to 24 h. A dose-dependent increase in fluorescence was observed in cells following 1 or 2 h incubation with serum-free media (Figure 5-18). Furthermore, FITC fluorescence was observable at 10 µM of the CPP and the fluorescence intensity following 2 h delivery at 25 µM was greater compared to delivery studies in DMEM, providing further support for the hypothesis that serum inhibits

delivery of the CPP. Similar to the delivery studies in DMEM, no fluorescence was observed after 24 h, suggesting the peptide may have been exported from the cell. Due to the high concentration (25 µM) required to achieve near complete delivery of the HIV Tat peptide into cells, we decided to evaluate alternative CPPs.

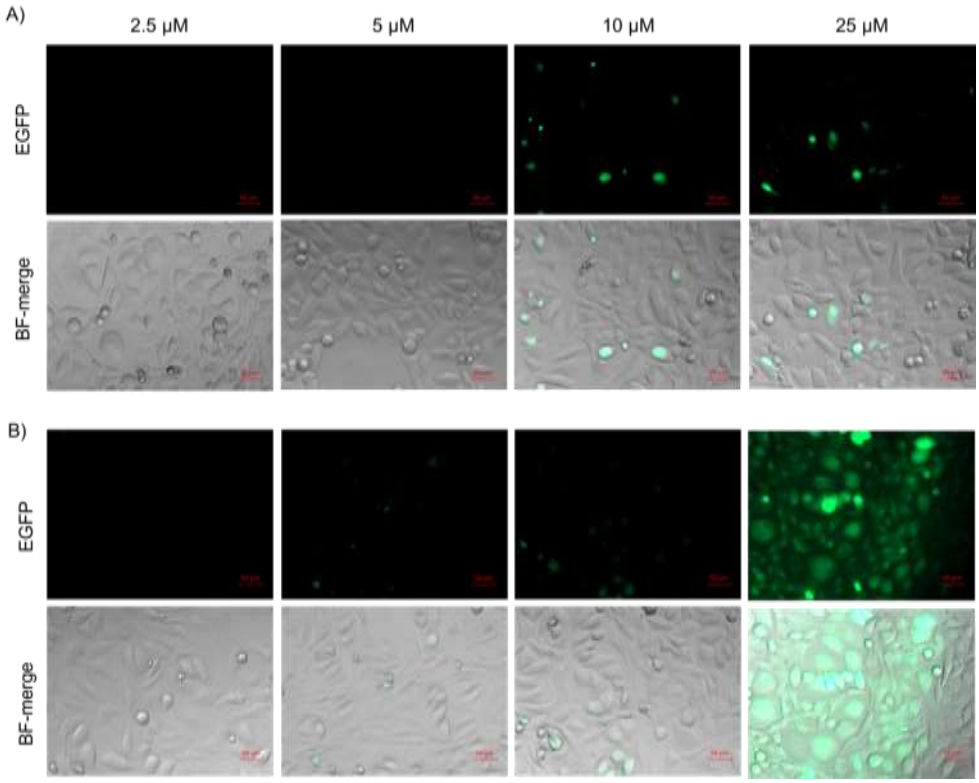

Figure 5-18 FITC-labeled HIV Tat CPP uptake studies in OptiMEM

Fluorescein isothiocyanate (FITC)-modified HIV Tat synthesized by Yuta Naro was incubated for A) 1 h in serum-free OptiMEM or B) 2 h in serum-free OptiMEM. Uptake was evaluated via fluorescence microscopy at 24 h post delivery. 20x magnification. EGFP (38HE filter; ex/em. = 470/525 nm) and brightfield-merged images are shown. Scale bars indicate 200 µm.

A poly-arginine peptide (R9) has been demonstrated to elicit more efficient uptake across multiple cell lines[860] and has been successfully utilized for delivery of non-charged oligonucleotides.[861-863] In light of these reports, we evaluated uptake of a FITC-labeled R9 peptide at 2.5, 5, or 10 μM in HeLa cells. Cells were incubated with the CPP for 4 h, then media was replaced to normal growth media. After 4 h delivery, fluorescence was observed for all four concentrations supporting the hypothesis that R9 displays enhanced uptake properties compared to HIV Tat (Figure 5-19A). At 24 h post-delivery, FITC was still visible at all concentrations, however, a decrease in fluorescence was observed, potentially due to exocytosis of the peptide from cells[864] (Figure 5-19B). After confirming the R9 peptide could be efficiently delivered into HeLa cells, the CPP was conjugated to the anti-miR-30e MO. Subsequently, HeLa cells were transfected with psiCHECK-miR30e then media was replaced, and cells were allowed to recover overnight. The next day, the anti-miR-30e MO-R9 CPP conjugate was delivered into cells for 4 h. At 48 h post-delivery, a dual luciferase assay was performed to assess miR-30e function. While the miR-30e antagomir control elicited a 3-fold increase in relative luminescence, the anti-miR-30e MO-R9 conjugate induced a modest 1.5-fold response relative to the psiCHECK-miR30e reporter (Figure 5-19C). The negative control antagomir and non-modified anti-miR-30e MO did not elicit an increase in luminescence. More concerningly, when we tried to repeat the assay with the inclusion of a conjugate consisting of an anti-'no tail' (*ntla*) MO and the same R9 CPP, the control MO conjugate elicited a similar response to the anti-miR-30e MO-R9 conjugate suggesting the increase in luminescence was non-specific (Figure 5-19D).

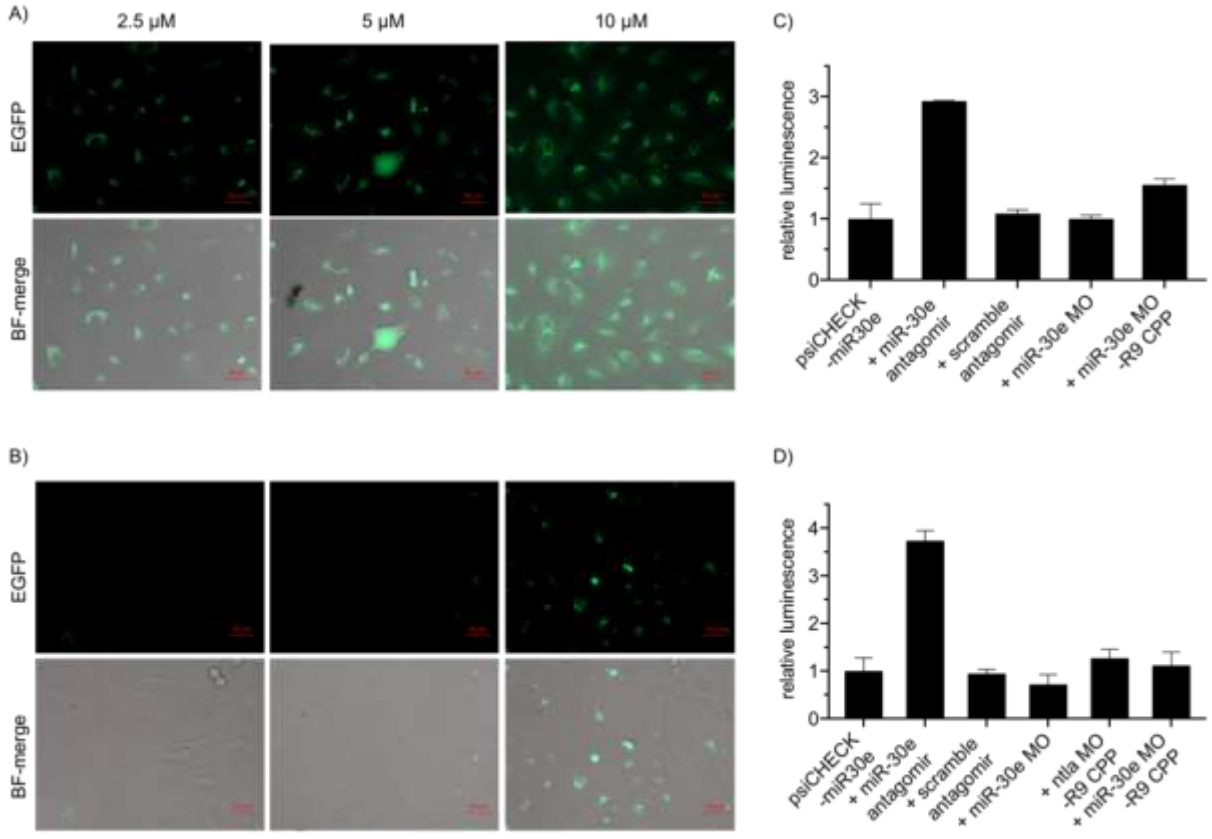

Figure 5-19 Delivery of miR-30e MO using the R9 CPP

HeLa cells were incubated with a fluorescein isothiocyanate (FITC)-labled R9 peptide synthesized by Yuta Naro at 2.5, 5, or 10 µM for 4 h. Cells were then imaged A) immediately after media was changed or B) after 24 h. 20x magnification. EGFP (38HE filter; ex/em. = 470/525 nm) and brightfield-merged images are shown. Scale bars indicate 200 µm. C) HeLa cells were transfected with the psiCHECK-miR30e reporter as well as anti-miR-30e or scramble antagomir controls using XtremeGENE. Following transfection of the reporter, media was changed and cells were incubated with a miR-30e-R9 peptide conjugate generated by Luis Vazquez-Máldonado (miR-30e-R9 CPP; 10 µM) for 4 h. A dual luciferase assay was performed at 48 h post-delivery. D) HeLa cells were transfected with the psiCHECK-miR30e reporter, then incubated with the miR-30e-R9 conjugate. An anti-no tail (*ntla*)-R9 conjugate was also delivered as a negative control. A dual luciferase assay was performed at 48 h post-delivery. Data are normalized to psiCHECK-miR30e and represent the average ± standard deviation for two independent experiments.

In order to improve the dynamic range upon MO-mediated inhibition of miR-30e, we compared delivery of the anti-miR-30e MO-R9 CPP conjugate into HeLa cells at 10 and 25 µM. Interestingly, treatment with the anti-miR-30e MO-R9 CPP conjugate at 10 µM induced a ~3-fold increase in luminescence (half the response observed for the miR-30e antagomir), incubation with 25 µM of the conjugate did not elicit a response (Figure 5-20A), likely due to toxicity at this concentration (Figure 5-20B). Due to the difficulty in attempting to deliver the MO into mammalian cells, we decided to move forward with evaluating miR-30e function with the luciferase reporter in zebrafish.

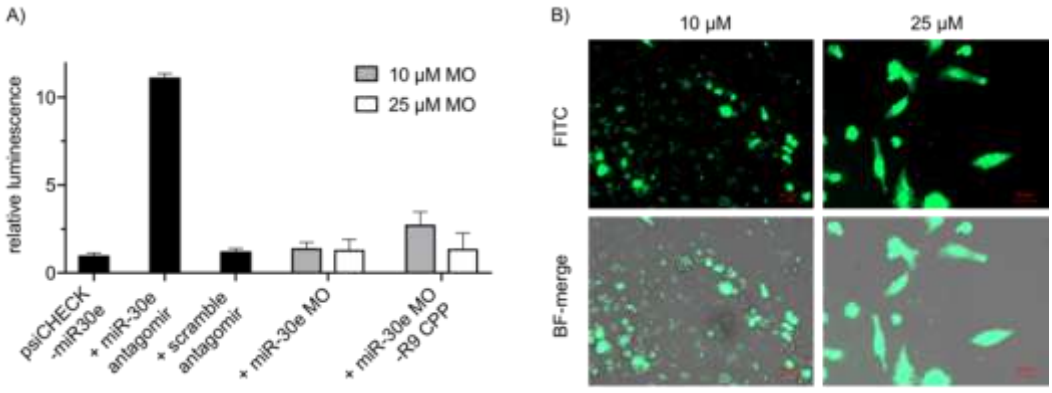

Figure 5-20 Delivery optimization of miR-30e MO-R9 CPP

A) HeLa cells were transfected with psiCHECK-miR30e using XtremeGENE. After 24 h, cells were incubated with anti-miR-30e MO-R9 CPP conjugate at 10 or 25 µM in fresh media for 4 h. A dual luciferase assay was performed at 48 h post-delivery. Data are normalized to psiCHECK-miR30e and represent the average ± standard deviation for two independent experiments. B) Fluorescence images of cells were captured immediately after 4 h delivery of MO-CPP conjugates to verify uptake. 20x magnification. EGFP (38HE filter; ex/em. = 470/525 nm) and brightfield-merged images are shown. Scale bars indicate 200 µm.

First, the miR-30e reporter was cloned into a pCS2+ expression plasmid to enable generation of the corresponding mRNA transcript. Briefly, the *Renilla* luciferase gene and miR-30e target sequence were PCR amplified from the psiCHECK-miR30e plasmid. The pCS2+ plasmid was digested with BamHI and EcoRI restriction enzymes, and subsequently the PCR-amplified insert was ligated using T4 DNA ligase. The resultant pCS2-Rluc-miR30e reporter plasmid was verified by sequencing. In order to verify the plasmid was capable of detecting changes in miR-30e function, it was transfected into HeLa cells along with an antagomir. The miR-30e antagomir (100 nM) elicited a 4-fold increase in luminescence confirming the reporter was responsive to miR-30e inhibition (Figure 5-21A). Next, the pCS2-Rluc-miR30e reporter was linearized using the NotI restriction enzyme and gel purified. The linearized plasmid was then used as a template for *in vitro* transcription using the mMessage mMachine SP6 kit and the corresponding transcript was purified via phenol/chloroform extraction. Simultaneously, we linearized and transcribed a pCS2+ reporter plasmid encoding *Renilla* luciferase with no miRNA target sequence as a control. Both transcripts elicited the expected bands via agarose gel electrophoresis (Figure 5-21B) and were given to Luis Vazquez-Máldonado for zebrafish studies. Subsequently, Luis injected 2 nl of miR-30e-Rluc mRNA (100 pg) with or without the anti-miR-30e MO (10 µM) into zebrafish zygotes at the 1- to 2-cell stage. Zebrafish zygotes were incubated in E3 water (NaCl [5 mM], KCl [0.17 mM], $CaCl_2$ [0.33 mM], $MgSO_4$ [0.33 mM], 10^{-5}% [w/v] of Methylene Blue) at 29 °C overnight. At 24 hpf, 10 embryos from each group were lysed and a *Renilla* Luciferase assay was performed. Unfortunately, no substantial increase in luminescence was observed upon incubation with the anti-miR-30e MO (Figure 5-21C) suggesting additional optimization was needed for zebrafish studies.

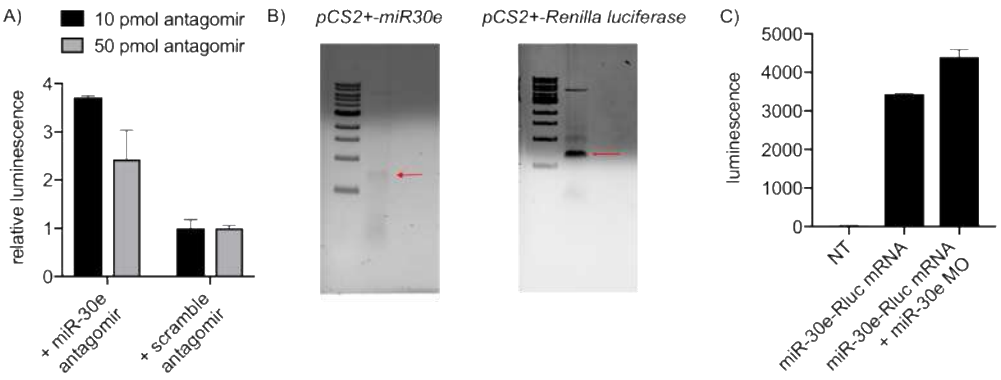

Figure 5-21 Preparation of miR-30e reporter mRNA for zebrafish injections

A) After cloning the *Renilla* luciferase-miR-30e target site fragment into the pCS2+ backbone, the resultant pCS2+-miR30e reporter was transfected into HeLa cells with 10 or 50 pmol of antagomir to verify activity. Data are normalized to pCS2+-miR30e and represent the average ± standard deviation for three independent experiments. B) The pCS2+-miR30e reporter or pCS2+-*Renilla* luciferase control plasmids were linearized and used as templates for SP6-mediated *in vitro* transcription. Resultant mRNA transcripts were analyzed via agarose gel electrophoresis. C) 100 pg of miR-30e-Rluc mRNA was injected into zebrafish zygotes at the 1- or 2-cell stage in addition to the miR-30e MO (10 µM). *Renilla* luciferase activity was evaluated at 24 hpf. Data represent the average ± standard deviation for two independent experiments and the experiment was performed by Luis Vazquez-Máldonado.

5.3.2 Summary and Outlook

In summary, we attempted to utilize two luciferase reporter constructs to evaluate MO mediated inhibition of miR-125b and miR-30e in mammalian cells. We determined that the anti-miR-125b exhibited poor solubility, likely due to secondary structure formation, and led to synthetic difficulties in cyclization. Because MOs are non-charged, we evaluated a variety of delivery methods including annealing to complementary DNA and attempting to transfect the

resultant duplexes using multiple different transfection reagents as well as conjugation to two different cell penetrating peptides. Unfortunately, after multiple attempts to optimize delivery of the MOs we were unsuccessful and thus decided to continue evaluation of the anti-miR-30e MO in zebrafish.

Future work should focus on confirming the MO is capable of inhibiting miR-30e using the pCS2-miR30e reporter construct as well as phenotypic assays in zebrafish. Once the linear MO has been shown to successfully inhibit miR-30e, the cyclized version should be generated. Subsequently, the cyclized MO should be evaluated in light irradiation experiments to enable spatial and temporal control of gene function in zebrafish. Additionally, it may be useful to perform *in vitro* translation experiments in lysate from mammalian cells known to overexpress miR-30e such as HeLa or MCF7 cells in order to evaluate activity of the anti-miR-30e MO.

5.3.3 Materials and Methods

Cell culture. Experiments performed using HeLa or MCF7 cell lines cultured in Dulbecco's Modified Eagle Medium (DMEM; Gibco). Experiments performed using PC3 cells were cultured in F-12K media. Media was supplemented with 10% (v/v) Fetal Bovine Serum (FBS; Sigma-Aldrich) and 1% (v/v) penicillin/streptomycin (VWR) and maintained at 37 °C in a 5% CO_2 atmosphere. Penicillin/streptomycin-free media was used for experiments. Cell line was used within passages 1-35 and was tested for mycoplasma contamination every three months.

Preparation of DNA/morpholino duplexes. Complementary DNA was purchased from IDT or synthesized by Luis Vazquez-Máldonado. Morpholino oligomers were obtained from Gene-Tools. When a complementary DNA oligonucleotide was used for delivery of morpholino oligomers, 10

pmol of each (for delivery into a single well) was combined in 1x phosphate-buffered saline or TE/Mg^{2+} buffer (Tris-HCl [0.01 M; pH 8.0], EDTA [1 mM], $MgCl_2$ [12.5 mM]) and annealed by heating the solution to 95 °C and cooling to 12 °C over 10 min in a thermal cycler. The reaction was scaled depending on the number of wells analyzed. After annealing, duplexes were added directly to 100 µl of media. After the time specified above, media was replaced with 200 µl of fresh P/S-free DMEM supplemented with 10% (v/v) FBS. The following day, media was removed, and cells were washed with 200 µl of sterile filtered 1x phosphate buffered saline (PBS). Media was then replaced with 100 µl of phenol red-free DMEM and imaged using the 20x LD Plan-Apochromat objective and the EGFP filter set (38 HE) following protocol 6.2.5 on the Axio Observer Z1 microscope (Zeiss) using Zen 2.0 software.

Construction of plasmids. See section 6.1 for detailed protocols of molecular biology techniques. The psiCHECK-miR30e reporter plasmid was generated by first digesting the psiCHECK-2 plasmid (5 µg; Promega) with NotI-HF (20 U; NEB) and XhoI (20 U; NEB) in a 100 µl reaction in CutSmart Buffer at 37 °C for 2 h, followed by Antarctic phosphatase (NEB) treatment at 37 °C for 1 h. The linear backbone was then separated via agarose gel electrophoresis (see protocol 6.1.8 and purified using the E.Z.N.A. Gel Extraction kit (Omega Bio-tek). Insert DNA containing the miR-30e binding sites (miR-30e S and miR-30e AS) were purchased from Sigma-Aldrich (Table 31) and 5' phosphorylated with T4 polynucleotide kinase (PNK) at 50 µM (10 µl) followed by annealing in TE/Mg^{2+} buffer (Tris-HCl [0.01 M; pH 8.0], EDTA [1 mM], $MgCl_2$ [12.5 mM]) by heating the solution to 95 °C and cooling to 12 °C on a thermal cycler (Bio-Rad). The inserts were subsequently ligated (0.5 µl of insert; 10 µl reaction) into the purified parent plasmid following protocol 6.1.4 The ligation product was then purified using the E.Z.N.A. Cycle Pure kit (Omega

Bio-tek) and transformed into chemically competent Top10 cells following protocol 6.1.5 The resultant construct was confirmed by Sanger Sequencing (Genewiz) using psiCHECK-fwd-seq (Table 31).

Table 31 Sequences of primers used to generate the psiCHECK-miR30e reporter plasmid

The miR-30e target site is underlined.

name	**sequence (5' -> 3')**
miR-30e S	TCGACCTTCCAGTCAAGGATGTTTACACTCGAGTAGC
miR-30e AS	GGCCGCTACTCGAGTGTAAACATCCTTGACTGGAAGG
psiCHECK-fwd-seq	GAGGGCGAGAAAATGGTGCTTGAG

To generate the pCS2+-miR30e construct, the *Renilla* luciferase gene and miR-30e target site were first PCR amplified from the psiCHECK-miR30e construct using synthetic DNA primers (JHL_pCS2-Rluc-F and miR-30e AS) purchased from Sigma-Aldrich (Table 32) following protocol 6.1.1 The pCS2+ reporter plasmid was digested with BamHI-HF (20 U; NEB) and XhoI (20 U; NEB) in a 100 µl reaction in CutSmart Buffer at 37 °C for 2 h, followed by Antarctic phosphatase (NEB) treatment at 37 °C for 1 h. The linear backbone was then separated via agarose gel electrophoresis (see protocol 6.1.8 and purified using the E.Z.N.A. Gel Extraction kit (Omega Bio-tek). The PCR-amplified insert was purified using the E.Z.N.A. Cycle Pure kit (Omega Bio-tek) and was used directly in the identical restriction digest to the parent plasmid. The digested insert was purified using the E.Z.N.A Cycle Pure kit and subsequently ligated (1 µl of insert; 10 µl reaction) into the linear parent plasmid following protocol 6.1.4 The ligation product was then

transformed directly into Top10 cells following protocol 6.1.5 The sequence of the plasmid was confirmed by Sanger Sequencing (Genewiz) using the using psiCHECK-fwd-seq (Table 31).

Table 32 Synthetic DNA primers for amplification of the *Renilla* luciferase-miR30e insert

name	**sequence (5' -> 3')**
JHL_pCS2-Rluc-F	TCTTTTTGCAGGATCCATGGCTTCCAAGGTGTACGACC
miR-30e AS	GGCCGCTACTCGAGTGTAAACATCCTTGACTGGAAGG

Luciferase assays. Cells were seeded into white 96-well plates (Greiner) and transfected with the respective transfection reagent as described above. The cells were incubated for 48 h, then analyzed for *Renilla* and firefly luciferase expression with a Dual Luciferase Assay Kit (Promega, see protocol 6.2.13 if transfected with the psiCHECK-miR125b or -miR30e reporter. For the pCS2-miR30e reporter, cells were seeded into two plates such that a *Renilla* luciferase assay (Promega) was performed on one of the plates and an XTT cell viability assay was performed on the other plate. For the *Renilla* luciferase assay, growth media was removed from the cells and 20 µl of 1x passive lysis buffer (1 ml of passive lysis buffer [supplied with the kit] in 4 ml of water). Subsequently, the cells were incubated with shaking at room temperature for 20 min. Then, the *Renilla* luciferase assay substrate (100x) was diluted to 1x in *Renilla* luciferase assay buffer (both supplied with the kit) generating the *Renilla* luciferase assay reagent. The *Renilla* luciferase assay reagent was prepared to a volume to enable addition of 100 µl of reagent per well. Luminescence for both the Dual luciferase assay and *Renilla* luciferase assay was measured on a microplate reader (Tecan M1000) with an integration time of 1 s and delay time of 5 s.

Luciferase assay analysis. Dual Luciferase Assays were analyzed as described below (see protocol 6.2.13 Briefly, *Renilla* luciferase values were divided by firefly luciferase values for each well. Then, averages and standard deviations for each treatment condition were calculated. Finally, averages and standard deviations were divided by the average relative luminescence for reporter plasmid alone.

Renilla luciferase assay data were analyzed similarly to Bright-Glo assays described in protocol 6.2.14 Briefly, the average relative change in absorbance values from the XTT assay were calculated as described below. Then, the *Renilla* luciferase values for each well in a single treatment condition were divided by the average relative change in absorbance value corresponding to that treatment condition from the XTT assay generating 'relative luminescence' values. Once all luciferase data had been divided by the respective XTT assay data, the average and standard deviation of the relative luminescence values were calculated then divided by the average relative luminescence of the pCS2-miR30e reporter.

Cell viability assays. HeLa cells were seeded at 10,000 cells/well (total media volume of 200 µl/well) in a white, clear-bottom, 96-well plate (Greiner). Following an overnight incubation, cells were transfected as described above in triplicate. After 48 h, an XTT assay was performed (GoldBio or Roche, see XTT assay protocol 6.2.16 .[522,523] Briefly, activated XTT reagent was added to each well. Absorbance was measured at 450 nm and 630 nm (background) after initial addition (Abs-t_{inital}) of the reagent, then incubated at 37 °C in a 5% CO_2 atmosphere for 4 hours, followed by measurement of end-point absorbance (Abs-t_{final}) on a Tecan M1000 plate reader.

Following background subtraction of the absorbance measurements at 630 nm, the difference in the Abs-t_{inital} and Abs-t_{final} at 450 nm absorbance measurements was calculated.

***In vitro* transcription**. *In vitro* transcription of the *Renilla* luciferase-miR30e reporter mRNA was performed using the mMessage mMachine SP6 Transcription kit (Thermo-Fisher Scientific) following the manufacturer's protocol. Briefly, 2 µg of the pCS2+-miR30e were digested with NotI-HF (2 U; NEB) in a 100 µl reaction (see protocol 6.1.3 After heat inactivation, the linear backbone was purified using the E.Z.N.A. Cycle Pure kit (Omega Bio-tek). Then, 1 µg of the template was added to a reaction mix consisting of 10 µl of NTP/CAP (2x), 2 µl of reaction buffer (10x), 2 µl of enzyme mix and up to 20 µl of nuclease-free water. The reaction was incubated at 37 °C for 6 h, then purified via phenol:chloroform extraction followed by ethanol precipitation. Briefly, 115 µl of nuclease-free water and 15 µl of ammonium acetate stop solution (supplied with the mMessage mMachine kit) were added to the reaction and mixed. Subsequently, 100 µl of QIAzol lysis reagent (QIAGEN) and 50 µl of chloroform was added and the solution was mixed by inversion. Two layers formed (organic and water) and the solution was centrifuged at 4 °C and 12,000 g for 15 min. The top water layer was removed and the organic layer was discarded. To the water layer was added 2 µl of glycogen (20 mg/ml), 10 µl of sodium acetate (3 M), 10 µl of magnesium chloride (0.1 M), 10 µl of lithium chloride (8 M), and 300 µl of pre-cooled ethanol. The resultant solution was incubated at -80 °C for 1 h, then centrifuged at 4 °C and 16,110 g for 30 min. Subsequently, the supernatant was removed and the RNA pellet was washed with 500 µl of ethanol (70% [v/v] in water), followed by centrifugation at 4 °C and 16,110 g for 30 min. The supernatant was again removed and the pellet was allowed to dry before resuspension in 50 µl of

autoclaved nuclease-free Milli-Q water. To verify the product, 5 µl of the RNA was analyzed via 0.8 % (w/v) agarose gel electrophoresis following protocol 6.1.8

5.4 Cellular Delivery of Oligonucleotides

While nucleic acids have garnered increasing attention in the way of clinical applications as well as for their utility in studying biological processes,[185,865,866] maximizing stability and cellular delivery remains a challenge. Additionally, distribution of oligonucleotides within the appropriate tissues and intracellular compartments to achieve high efficacy and limit exposure to other tissues and off-target effects need to be considered.[867] In general, all nucleic acids whether 'free', conjugated, or encapsulated in nanocarriers are internalized via endocytosis and subsequently trafficked through membrane-bound intracellular compartments.[868] Thus, improving efficacy of oligonucleotides relies on enhancing their uptake, lifetime (the half-life of single-stranded RNA in plasma is ~5 min),[869] and endosomal release. As such, several delivery systems have been developed in order to attempt to optimize these parameters.[867]

For example, among the most widely used oligonucleotide delivery system for negatively charged nucleic acids are cationic liposomes for encapsulation.[870] The cationic lipid consists of a hydrophobic chain and a cationic head that interacts with anionic oligonucleotides. Additionally, liposomes can be comprised of monovalent or multivalent lipids, where multivalent lipids are generally considered more ideal for high transfection efficiency.[871] While the cationic head is necessary for electrostatic interaction, the alkyl chain is important for cellular uptake and endosomal escape of the liposomes.[872] Furthermore, many cationic liposomes have been modified with polyethylene glycol (PEG) in order to improve lifetime of the liposomes in serum and reduce

cytotoxicity and adsorption of serum proteins.[873] Neutral liposomes have also been developed, however they are more frequently utilized as an adjuvant phospholipid in cationic liposomes because while they exhibit good biocompatibility and pharmacokinetic properties, they are less efficient at encapsulation of nucleic acids.[872] pH-sensitive ionizable liposomes capable of protonation or deprotonation depending on environment acidity have also been employed for oligonucleotide delivery. Ionizable liposomes are comprised of amino lipids with ionizable amine head groups and are ideal nanocarriers because they exhibit a positive charge for loading of the nucleic acid molecule, lose their charge after administration, and regain their positive charge once inside endosomes to facilitate release.[870] The key limitations to utilizing nanoparticles as delivery vessels include: 1) potential toxicity due to accumulation of carrier material and 2) limited biodistribution due to their large size (diameter ~100 nm).[867]

In contrast to lipid nanoparticle delivery systems that function by encapsulation of nucleic acids, several approaches in which the carrier is directly conjugated to the oligonucleotide have also been developed. Direct conjugation methods are advantageous for a number of reasons. For example, while nanoparticles are heterogeneous in size and composition, molecular conjugates often have a defined identity and structure. Additionally, smaller molecular conjugates are capable of improving biodistribution compared to lipid nanoparticles. Furthermore, direct conjugation of a ligand to a nucleic acid molecule may enable greater specificity. For example, a variety of targeted ligands capable of delivering oligonucleotides to a particular cell type or intracellular compartment including aptamers,[874-877] antibodies,[878-880] and glycoconjugates.[229,881-883] Despite their advantages, it's worth noting that there are a few limitations to the direct conjugation approach including: 1) rapid renal clearance; 2) limited copies of the oligonucleotide 'payload'; and 3) lack of protection from nucleases.[867] Moreover, direct conjugation requires a covalent bond

between the delivery agent and the nucleic acid which can impede activity, though several strategies have also been employed to disrupt the interaction once the conjugates are internalized.[884-886] In spite of these limitations, conjugation of cell-penetrating peptides (CPPs) remains among the most common methodologies for delivering oligonucleotides into cells in addition to drugs, peptides, and proteins.[867] CPPs consist of polycationic sequences—in some cases including amphipathic sequences to promote endosomal escape—and can vary in length. Additionally, CPPs can be incorporated into an oligonucleotide during synthesis or post-synthetically conjugated using a maleimide, disulfide, or amide linkage or via click chemistry.[887]

Taken together, several strategies have been developed in order to optimize delivery of oligonucleotides. Combined with chemical modifications to improve nuclease-resistance and thermostability of nucleic acids, these methods have enabled improved therapeutics and tools for investigation of biological processes. Among the more promising recent advancements in the field of modified oligonucleotides has been the development of γ-(peptide nucleic acids) PNAs. However, delivery of these novel biological tools has proved to be troublesome due to their non-charged backbone and as such, we sought to develop a methodology to overcome this limitation.

5.4.1 Delivery of γ-Peptide Nucleic Acids (PNAs) into Mammalian Cells

As described above (Section 1.2.2 γPNAs are non-charged nucleic acid analogs and promising alternatives to current oligonucleotide-based approaches to perturbing nucleic acid function in biological systems because they are resistant to nuclease cleavage and possess a high binding affinity to their complementary RNA sequence.[888,889] However, γPNAs are limited by poor cell permeability and, due to a lack of negative charge, an inability to transfect them into mammalian cells. Previous work has demonstrated that poly(lactic-co-glycolic acid) (PLGA

nanoparticles are capable of efficiently cellular delivery of γPNAs.[888,890] For example, injection of a 22-mer γPNA encapsulated in PLGA nanoparticles in a human tumor xenograft in mice led reduced cell proliferation and induction of necrosis and fibrosis.[214] In light of these successes, we sought to establish a system for delivery of γPNAs into mammalian cells based on methods established in the literature for the delivery of PNAs and other non-charged oligonucleotides.[851,853,891] Furthermore, we hypothesized that like the 'tiny LNAs' described above, [193] we could inhibit function of an oligonucleotide using a minimal sequence. Because of their increased binding affinity, shorter γPNAs could be utilized to target mRNA splice sites and miRNAs. We employed an anti-miR-122 and splice switching oligonucleotide (SSO) γPNA sequence as proofs-of-concept.

5.4.1.1 Amphiphilic Peptide Reagent

Amphiphilic peptides are characterized as having a hydrophobic tail and hydrophilic head and have been routinely utilized as nanocarriers and nanostructures for a variety of applications.[892] They are advantageous for use in biological systems for a number of reasons including: 1) prone to self-assembly due to hydrophobic interactions; 2) simplistic design; and 3) biocompatibility. Importantly, amphiphilic peptides have been used to successfully delivery PNAs across a cell membrane.[893] As such, we hypothesized that Endo-Porter,[853] a commercially available amphiphilic peptide reagent used to deliver non-ionic oligomers (specifically morpholinos), could be employed to deliver γPNAs into cells via endocytosis.

In order to test this hypothesis, we utilized the previously developed Huh7 cell line stably expressing a luciferase-based reporter for monitoring changes in miR-122 function in cells (Huh7-miR122).[413] Because of the successes of targeting miRNA seed regions with an 8-mer tiny LNA[894] and due to the enhanced binding affinity of γPNAs,[895] we hypothesized that an 8-mer γPNA

complementary to the seed region of miR-122 will be capable of inhibiting binding of the miRNA to its mRNA target with significant potency. As such, we designed 'anti-miR2' as an 8 nucleotide miniPEG γPNA (Figure 5-22; Table 33) to target the seed region of miR-122 and evaluated its function upon Endo-Porter-mediated delivery into Huh7-miR122 cells using a luciferase assay. Briefly, increasing concentrations of the γPNA were combined with Endo-Porter (6 μM final concentration) in growth media and added to cells. A full length anti-miR-122 or scramble antagomir (Table 33) were transfected as controls using XtremeGENE transfection reagent. Luciferase expression was analyzed via a Dual Luciferase assay after 48 h. A 4-fold increase in luminescence was observed following transfection of the anti-miR-122 antagomir, but no increase was observed with the scramble antagomir, confirming the reporter is adequate for detecting miR-122-specific inhibition (Figure 5-22). Unfortunately, no inhibition was observed upon delivery of the γPNA. We hypothesized that lack of function could be attributed to two reasons: 1) the short γPNA is not being efficiently delivered into cells; and 2) the shortened γPNA sequence is not sufficient for blocking miRNA function. In light of these results, we decided to pursue alternative delivery strategies.

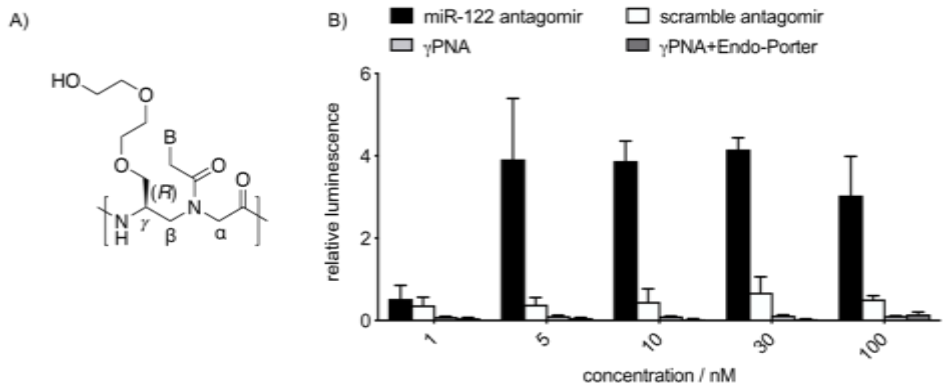

Figure 5-22 Evaluation of miniPEG γPNA delivery into a miR-122 reporter cell line

A) Chemical structure of a γPNA subunit wherein a mini-polyethylene glycol (PEG) linkage is functionalized to the γ-carbon. B) Huh7-miR122 stable cells were transfected with miR-122 antagomir or scramble antagomir using XtremeGENE siRNA transfection reagent. Cells were also incubated with an 8-mer γPNA alone or in the presence of Endo-Porter amphipathic peptide-based delivery reagent. After 48 h, a Dual Luciferase assay was performed. Data are normalized to Huh7-miR122 plus scramble antagomir and represent the average ± standard deviation for three independent experiments.

Table 33 Sequences for antimiR2 γPNA and antagomirs and structure of a miniPEG γPNA subunit

γPNAs were synthesized by PNA Innovations.

name	description	sequence (5’ -> 3’)
anti-miR2	miniPEG γPNA	CACACTCC
miR-122 antagomir	2’OMe/PS RNA	CAAACACCAUUGUCACACUCCA
scramble antagomir	2’OMe/PS RNA	AGUACUGCUUACGAUACGGUU

5.4.1.2 Cyclic CPP-γPNA Chimeras

Protein splicing is an important cellular process, as alternative splicing pathways enhance protein diversity[896] which in turn affects binding properties, intracellular localization, enzymatic activity, and posttranslational modifications of proteins.[897] It has been estimated that ~95% of genes in humans undergo alternative splicing.[898] As such, dysregulation of alternative splicing has been implicated in disease development.[899] Splice-switching oligonucleotides (SSOs) hybridize to the pre-mRNA in a sequence-specific manner, preventing interaction with the spliceosome and ultimately altering the splicing pathway. Our laboratory previously reported the use of caged SSOs in mammalian cells to optically trigger an OFF/ON fluorescent response due to splice-correction of an EGFP gene.[791] We hypothesized that γPNAs could be used to direct alternative splicing and, analogous to the anti-miR-122 oligonucleotide, shorter oligonucleotide sequences could be utilized and still achieve biological function. As in these previous studies, we employed the β-globin intron 1 as a proof-of-principle target, because it contains an aberrant splice site that can be corrected with SSOs. An enhanced green fluorescent protein (EGFP) gene interrupted by the mutant β-globin intron is stably expressed in a previously developed HeLa cell line (HeLa:EGFP654).[900] As an alternative to covalently attaching a CPP to an oligonucleotide, Armitage and co-workers recently demonstrated the use of a transactivator of transcription (TAT) CPP hairpin bearing a 6 nucleotide γPNA overhang to deliver proteins and DNA nanostructures into cells.[901] Use of the hairpin CPP afforded enhanced transduction efficiency compared to the linear CPP as well as a modular approach to delivery of nucleic acids without the need for potentially cumbersome chemical conjugation methods. We decided to utilize the TAT hairpin CPP to attempt to deliver SSO γPNAs into cells.

Similar to the anti-miR2 γPNA experiment described above, a 2'-*O*-methyl- and phosphorothioate-modified RNA SSO was used as a positive control (Table 34). A FITC-labeled γPNA was employed as a control for cellular uptake. In addition to the FITC-labeled γPNA, a 2'-*O*-Me- and PS-modified RNA SSO bearing a 6-nucleotide toehold sequence (SSO-toehold) was designed such that it could be hybridized to the cyclic TAT CPP (Figure 5-23A). The hairpin CPP was annealed to FITC-labeled γPNA or SSO toehold at 1:1 ratio in PBS buffer then diluted to a final concentration of 200 nM in growth media then added directly to HeLa:EGFP654 cells. After 4 or 12 h, media was replaced with fresh growth media. Cells treated with the FITC-labeled γPNA were imaged via fluorescence microscopy immediately after the media change, but unfortunately, no FITC fluorescence was observed suggesting the γPNA was not adequately delivered (Figure 5-23A). All cells were imaged the following day for EGFP fluorescence. Consistent with the lack of FITC fluorescence, minimal EGFP fluorescence was observed following attempted delivery of SSO-toehold (Figure 5-23B). We hypothesized that poor delivery could either be attributed to incomplete hybridization of the hairpin CPP to the oligonucleotides or inefficient delivery mediated by the CPP. In order to further elucidate the lack of EGFP fluorescence, SSO-toehold as well as an SSO not bearing the toehold were transiently transfected into HeLa:EGFP654 cells using XtremeGENE. Transfection of the SSO-toehold led to fewer fluorescent cells compared to the SSO control sequence (Figure 5-23B), suggesting the toehold inhibits splice switching activity of the SSO.

Table 34 Sequences for RNA splice-switching oligonucleotides (SSOs)

Toehold sequence is underlined

name	description	sequence (5’ -> 3’)
SSO	2’OMe, PS-modified EGFP654 SSO RNA	GUUAUUCUUUAGAAUGGUGC
SSO (toehold)	2’OMe RNA with 6 nt toehold for binding to hairpin CPP	AUUGGGGUUAUUCUUUAGAAUGGUGC

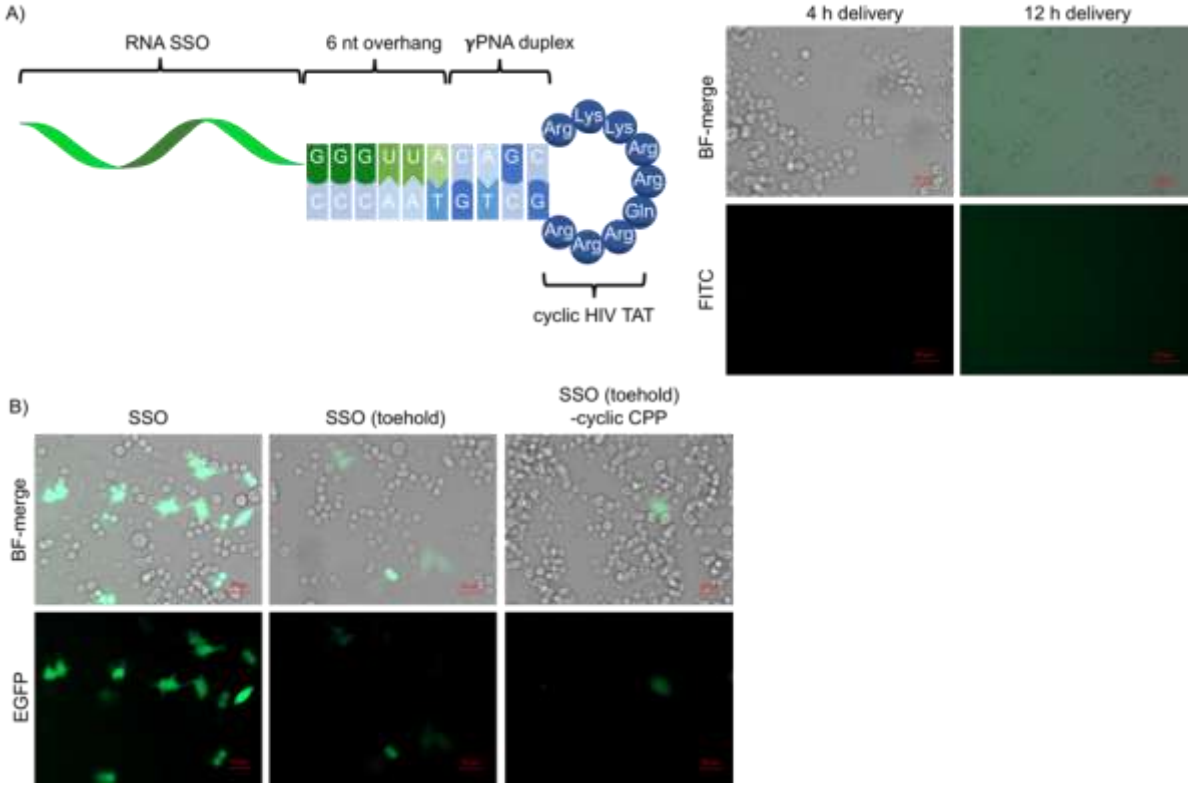

Figure 5-23 Delivery of SSO mediated by cyclic HIV TAT CPP chimera

A) Design of the RNA splice-switching oligonucleotide (SSO) with 6 nucleotide overhang for annealing to the complementary γPNA overhang of the cyclic HIV TAT cell-penetrating peptide (CPP) chimera. The cyclic CPP was annealed to a FITC-labeled control γPNA and delivered into HeLa:EGFP654 cells for 4 or 12 h, then imaged via microscopy immediately after. B) The SSO (toehold) was annnealed to the cyclic CPP and incubated with

HeLa:EGFP654 cells for 4 h, then imaged the following day. The SSO and SSO (toehold) were transfected using XtremeGENE siRNA transfection reagent as a control and visualized via microscopy the following day. 20x magnification. EGFP (38HE filter; ex/em. = 470/525 nm) and brightfield-merged images are shown. Scale bars indicate 200 μm.

5.4.1.3 Linear CPP-mediated Delivery of γPNA

As an alternative to the hairpin CPP described above, arginine-rich peptides such as R/W(9)[902] can be conjugated to PNAs and have been shown to effectively deliver uncharged nucleic acids into cells due to their positive charge. Because an TAMRA and azide-modified SSO γPNA can be readily synthesized, an N-terminal alkyne-modified R/W(9) peptide was synthesized for conjugation via click reaction. Utilizing the full length SSO sequence (SSO1) or truncated SSO sequences flanking the splice site (SSO2 and SSO3), γPNAs (Table 35) were coupled to the corresponding R/W(9) peptide overnight using a 10-fold excess of the CPP in 50:50 triethylammonium acetate (TEAA) buffer/DMSO with the addition of copper sulfate pentahydrate and tris(1-benzyl-4-triazolyl)methylamine (TBTA) (Figure 5-24).[141] After the conjugation, reactions were purified via acetone precipitation, then purity and identity were confirmed by reverse phase HPLC and MALDI, respectively. All of the SSO γPNAs were conjugated to the CPP and were obtained in ~50% yield.

Table 35 Sequences of SSO γPNAs

name	description	Sequence (N -> C)
SSO1	full-length EGFP654 SSO	TAMRA-PEG2Lys(N3)GTTATTCTTTAGAATGGTGC
SSO2	truncated EGFP654 SSO	TAMRA-PEG2Lys(N3)TATTCTTTAGAATGG
SSO3	truncated EGFP654 SSO	TAMRA-PEG2Lys(N3)TCTTTAGAAT

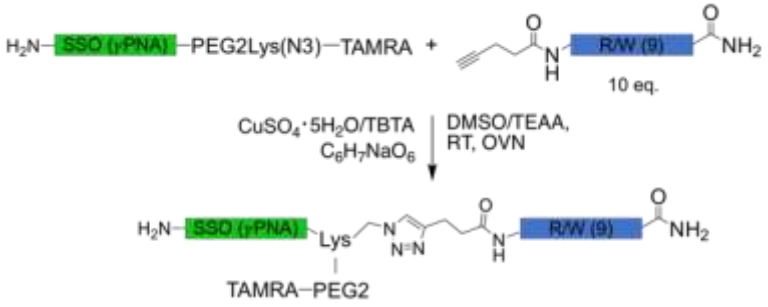

Figure 5-24 Click reaction with azido-modified γPNAs and alkyne-modified HIV TAT CPP

In order to evaluate delivery of the γPNAs, we attempted to deliver the SSO1, SSO2, and SSO3 γPNA-R/W(9) conjugates into HeLa:EGFP654. Briefly, 500 nM or 2 μM non-conjugated γPNA or γPNA-CPP conjugates were added to HeLa:EGFP654 cells in serum-free media for 4 h.[903] After the initial incubation, cells were supplemented with additional growth media for 48 h. Then, cells were washed with PBS to remove excess fluorescent γPNA and fixed with formaldehyde. EGFP expression was monitored via fluorescence microscopy post-delivery. The 2'-*O*-methyl- and PS-modified SSO was transfected as a control.[791] As expected, transfection of the RNA SSO resulted in alternative splicing and subsequent EGFP expression, though at

moderate levels (Figure 5-25A). TAMRA fluorescence was observed for the conjugates at 500 nM (Figure 5-25B) and 2 μM (Figure 5-25C) as expected, indicating efficient delivery into cells. Unfortunately, no EGFP fluorescence was observed upon treatment with the γPNA. Because transfection of the RNA SSO led to reduced EGFP expression compared to previous reports,[901,904-906] the lack of EGFP fluorescence observed upon delivery of the γPNA may be a result of reduced overall expression of the reporter.

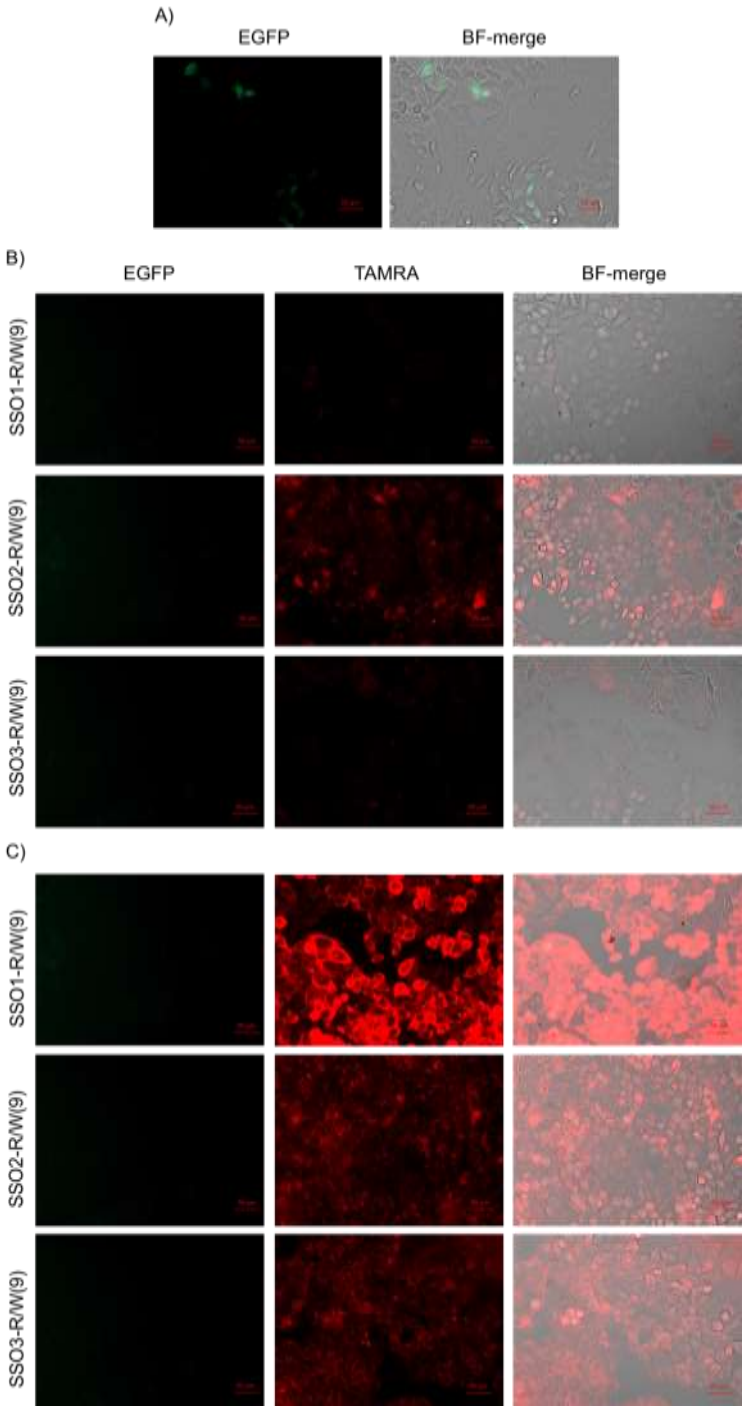

Figure 5-25 Delivery of γPNA SSO-R/W(9) CPP conjugates into HeLa:EGFP654 cells

A) RNA SSO was transfected into cells using XtremeGENE siRNA transfection reagent. HeLa:EGFP654 cells were incubated with γPNA SSO-R/W(9) CPP conjugates in serum-free OptiMEM at B) 500 nM or C) 2 µM for 4 h. Cells

were imaged in the TAMRA channel to monitor uptake and EGFP channel to monitor splice switching after 48 h via fluorescence microscopy. 20x magnification. EGFP (38HE filter; ex/em. = 470/525 nm), mCherry (43HE filter; ex/em. = 550/605 nm), and brightfield-merged images are shown. Scale bars indicate 200 μm.

The Juliano laboratory[907] and others have reported the use of small molecule enhancers of oligonucleotide function that allow efficient delivery of oligonucleotides into cells in the absence of transfection reagent and also release them from late stage endosomes in order to interact with their target. We hypothesized that a similar approach could be employed to overcome poor activity of the γPNA-CPP conjugate. In order to test this hypothesis, we simultaneously delivered the conjugate and treated cells with a common small molecule enhancer of oligonucleotide function, chloroquine,[908] at 10 μM. Following transfection of the RNA SSO control and subsequent treatment with chloroquine, more EGFP fluorescence was observed than in the absence of chloroquine (Figure 5-26A), suggesting the small molecule was capable of improving SSO function by inducing endosomal escape. Addition of chloroquine also improved delivery of the γPNA-CPP conjugates at 500 nM to a minor extent as shown by increased TAMRA fluorescence (Figure 5-26B); however, EGFP fluorescence was still not observed. Similar results were observed upon delivery of the γPNA-CPP conjugates at 2 μM accompanied by an increase in TAMRA fluorescence relative to conjugate delivery at 500 nM (Figure 5-26C). Moreover, incubation of the R/W(9) peptide followed by treatment with chloroquine led to an increase in toxicity of the HeLa:EGFP654 cells (Figure 5-26D). In spite of chloroquine addition, the γPNA-CPP conjugates appear to be unable to access the target mRNA transcript. Because alternative splicing occurs within the nucleus,[909] we hypothesize that cytoplasmic localization of the conjugates may be one factor in preventing splice-switching via the γPNA-CPP.

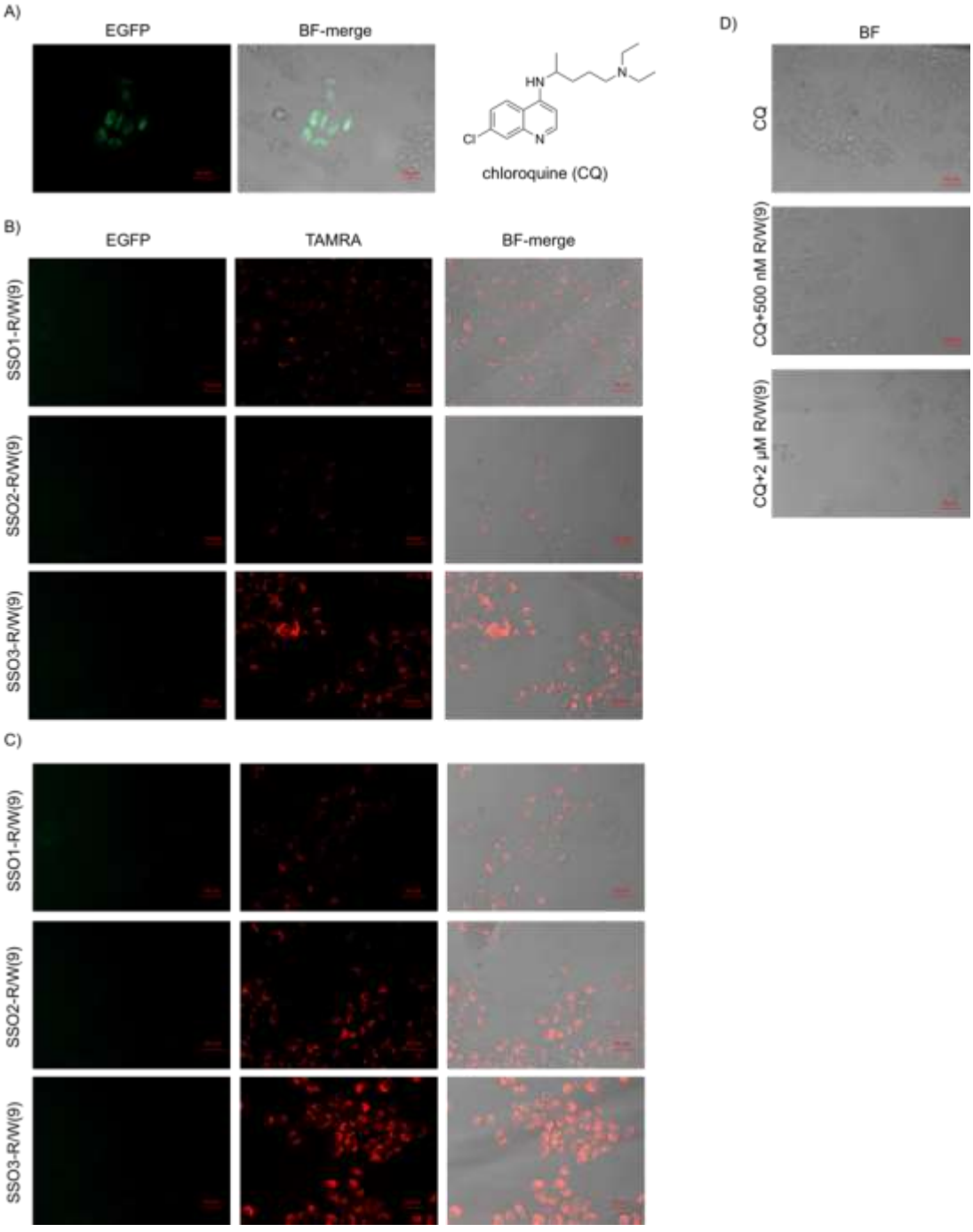

Figure 5-26 Delivery of γPNA SSO-R/W(9) CPP conjugates with chloroquine into HeLa:EGFP654 cells

A) RNA SSO was transfected into cells using XtremeGENE siRNA transfection reagent or HeLa:EGFP654 cells were incubated with γPNA SSO-R/W(9) CPP conjugates in serum-free OptiMEM at B) 500 nM or C) 2 µM for 4 h. Cells

were imaged in the TAMRA channel to monitor uptake of the γPNA and EGFP channel to monitor splice switching after 48 h via fluorescence microscopy. D) HeLa:EGFP654 cells were incubated with CPP alone at 500 nM or 2 μM for 4 h as a control to assess toxicity. In all conditions, chloroquine (10 μM) was added immediately after 4 h transfection or incubation with oligonucleotide or peptide. 20x magnification. EGFP (38HE filter; ex/em. = 470/525 nm), mCherry (43HE filter; ex/em. = 550/605 nm), and brightfield-merged images are shown. Scale bars indicate 200 μm.

5.4.2 Summary and Outlook

Taken together, γPNAs are novel oligonucleotide tools for probing biological systems, but their efficacy in cells and animals is hindered by poor uptake properties. Establishment of generalizable methods for adapting γPNAs to existing nucleic acid devices will greatly expand their utility. While formulation of cationic nanoparticles has seen some success in literature, attempts to employ an amphipathic peptide-based delivery reagent was not sufficient to improve cell uptake of γPNAs. Additionally, a strategy to deliver the γPNAs through attachment to a short hairpin CPP was also unsuccessful. Finally, direct conjugation to an R/W(9) peptide was the most promising in terms of cell uptake, however, once inside the cells the γPNAs failed to induce the expected activity suggesting further optimization is required.

In order to overcome the pitfalls encountered thus far in delivery of the γPNAs, future work should focus on trying to determine the source of functional inhibition of the SSOs as well as adapting alternative strategies for delivery of the nucleic acids into cells. For example, the RNA SSO should be conjugated to the R/W(9) CPP. We hypothesize that another reason we didn't observe splice switching upon delivery of the γPNA is that the CPP is inhibiting hybridization to the mRNA transcript. Conjugation of the CPP to the established RNA SSO, known to direct

alternative splicing, will serve as an adequate control experiment. Alternatively, it's possible that γPNAs are incapable of directing alternative splicing. Since tiny LNAs have been shown to effectively inhibit miRNA function by targeting the 8-mer seed region,[910] it may be more promising to try to optimize delivery of 'tiny γPNAs' that target miRNAs. Delivery of the anti-miR-122 γPNAs into the Huh7-miR122 stable cell line would also enable a more quantitative readout as opposed to the more qualitative fluorescence microscopy experiment. In order to re-evaluate anti-miR-122 γPNAs, the full length (22-mer) anti-miR-122 and seed-targeting (8-mer) anti-miR-122 γPNAs should be synthesized with an azido-lysine and TAMRA incorporated at the N-terminus. This will enable us to conjugate the anti-miR-122 γPNAs to a CPP if required for delivery and monitor uptake using fluorescence microscopy. Finally, guanidinium γPNAs have been shown to be readily taken up by cells with similar uptake efficiency to PNA-CPP conjugates[911] in the absence of a delivery peptide or alternative delivery reagent. Furthermore, guanidinium γPNAs display enhanced binding affinity to complementary DNA similar to miniPEG γPNAs suggesting they may exhibit potent biological function.

5.4.3 Materials and Methods

Cell culture. Experiments performed using HeLa:EGFP654 cell line cultured in Dulbecco's Modified Eagle Medium (DMEM; Gibco). Huh7-miR122 cells were cultured in DMEM supplemented with 500 µg/ml G418. Media was supplemented with 10% (v/v) Fetal Bovine Serum (FBS; Sigma-Aldrich) and 1% (v/v) penicillin/streptomycin (VWR) and maintained at 37 °C in a 5% CO_2 atmosphere. Penicillin/streptomycin-free media was used for experiments. Cell lines were used within passages 1-35 and was tested for mycoplasma contamination every three months.

Endo-Porter delivery. For Endo-Porter-mediated delivery of anti-miR2, Huh7-miR122 cells were seeded at 15,000 cells per well in a white 96-well plate (Greiner). The following day, the γPNA was added at a final concentration of 10, 50, 100, 300, or 1000 nM to 50 µl of P/S-free DMEM growth media supplemented with 10% (v/v) FBS. For conditions in which Endo-Porter was utilized, the delivery reagent (Gene-Tools; 1 mM) was added to 50 µl of P/S-free DMEM growth media supplemented with 10% (v/v) FBS to a final concentration of 12 µM. Media was removed from cells. Then, the Endo-Porter and γPNA solutions were mixed to a final volume of 100 µl and added directly to cells without additional incubation. In parallel, anti-miR-122 or scramble antagomir were transfected at the same concentrations using XtremeGENE siRNA transfection reagent (Roche) following protocol 6.2.3.2 below. Briefly, RNA and 0.8 µl per well of XtremeGENE siRNA transfection reagent were incubated in OptiMEM for 20 min, then added directly for cells. After a 4 h transfection, transfection media was removed and replaced with P/S-free DMEM supplemented with 10% (v/v) FBS. In both cases, cells were treated with oligonucleotide in triplicate. After 48 h, media was removed, cells were lysed in passive lysis buffer, and the Dual Luciferase assay (Promega; see protocol 6.2.13 was used to quantify luciferase activity. *Renilla* luciferase data were normalized to firefly luciferase data and set relative to DMSO control.

Cyclic CPP-γPNA chimera-mediated delivery. For cyclic CPP-γPNA chimera-mediated delivery of the FITC-labeled γPNA control or RNA SSO, HeLa:EGFP654 cells were seeded at 10,000 cells per well in a black 96-well plate (Greiner). The following day, γPNA and cyclic CPP were hybridized at 1:1 ratio (300 nM each) in 1x phosphate-buffered saline (PBS) buffer and annealed by heating to 95 °C and cooling to 12 °C over 10 minutes in a thermal cycler (Bio-Rad).

After annealing, the reaction mix was diluted to a final concentration of 20 nM in 200 µl of P/S-free DMEM growth media supplemented with 10% (v/v) FBS. Subsequently, delivery mix was added directly to cells and cells were treated in triplicate. Cells were incubated for 4 h or 16 h at 37 °C and then media was replaced. In both cases, cells were imaged 16 h after initial addition of the delivery mix on an Axio Observer Z1 microscope (Zeiss) using the EGFP filter cube and 20x Plan-Apochromat objective as described below (see protocol 6.2.5 Prior to imaging, cells were washed with 1x PBS and media was replaced with phenol-red free DMEM.

Click conjugation of R/W(9) peptide and SSO γPNAs. The R/W(9) CPP (H-XRRRRRRRRRW-$CONH_2$; X = 4-pentynoic acid) was synthesized by Yuta Naro. The TAMRA- and azido-modified γPNA SSOs 1, 2, and 3 (Table 35) were obtained from PNA Innovations, Inc. (Pittsburgh, PA). The γPNAs (1 mM; 4 µl) were combined with 10 µl of triethylammonium acetate buffer (TEAA; 2 M; 2.78 ml of triethylamine, 1.14 ml of acetic acid, water to 10 ml; pH 7.0) in 50 µl of DMSO and 13 µl of water in a 6 dram glass vial and vortexed. Subsequently, the R/W(9) CPP (5 mM; 8 µl) and 10 µl of ascorbic acid (5 mM; 18 mg of ascorbic acid dissolved in 20 ml of distilled water; prepared fresh) was added to the solution and vortexed briefly. A septum was placed on the top of the vial and nitrogen gas was bubbled into the solution for 30 s from a balloon to degas. Subsequently, 5 µl of 10 mM copper (II)-tris(benzyltriazolylmethyl)amine (TBTA) (50 mg of copper (II) sulfate pentahydrate in 10 ml of distilled water added to 116 mg of TBTA in 11 ml of DMSO) was added to the mixture. The vial was again degassed for 30 s with a nitrogen balloon, then the septum was replaced. The reaction was left on a benchtop at room temperature overnight. After the conjugation, reactions were purified via acetone precipitation. Briefly, 4 volumes of acetone (100 µl) was added to the reaction, then incubated at -20 °C for 20 min. The

reaction was transferred to a clean 1.7 ml Eppendorf tube and centrifuged at 16,110 g for 10 min. The supernatant was discarded and the pellet was washed with 2 ml of acetone, followed by centrifugation at 16,110 g for 10 min. The supernatant was discarded and the pellet was allowed to air dry for ~1 h before being resuspended in 50 µl of nuclease-free water and stored at room temperature. Conjugates were obtained in ~90-95% yield. Purity and identity were confirmed by reverse phase HPLC (Figure 5-27) and MALDI (Figure 5-28), respectively. HPLC was performed on an Agilent 1200 series HPLC system using an ACE Equivalence C18 column (part# EQV-3C18-1046). Samples were injected at a flow rate of 1 ml/min using a gradient of 5 – 95% acetonitrile/0.1% TFA over 30 min. γPNA SSO-CPP conjugates were observed at 545 nm with a retention time of ~12 min.

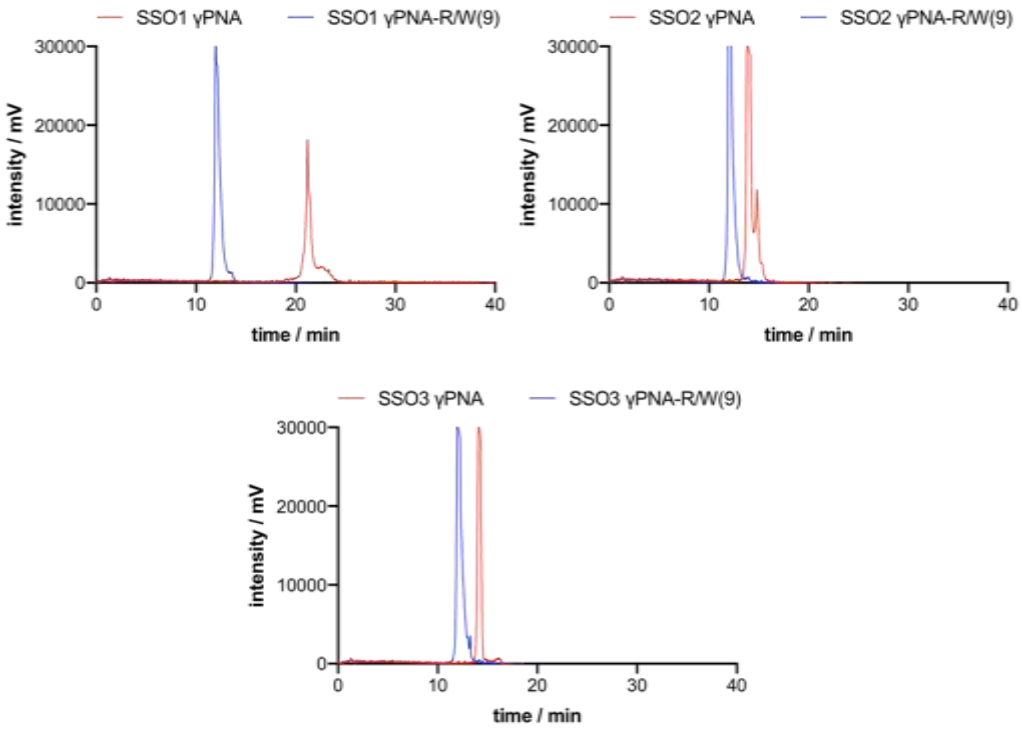

Figure 5-27 HPLC analysis of γPNA-CPP conjugates.

Conjugates were evaluated at 1 µM in in water on a Shimadzu LC-20AD monitored at 545 nm.

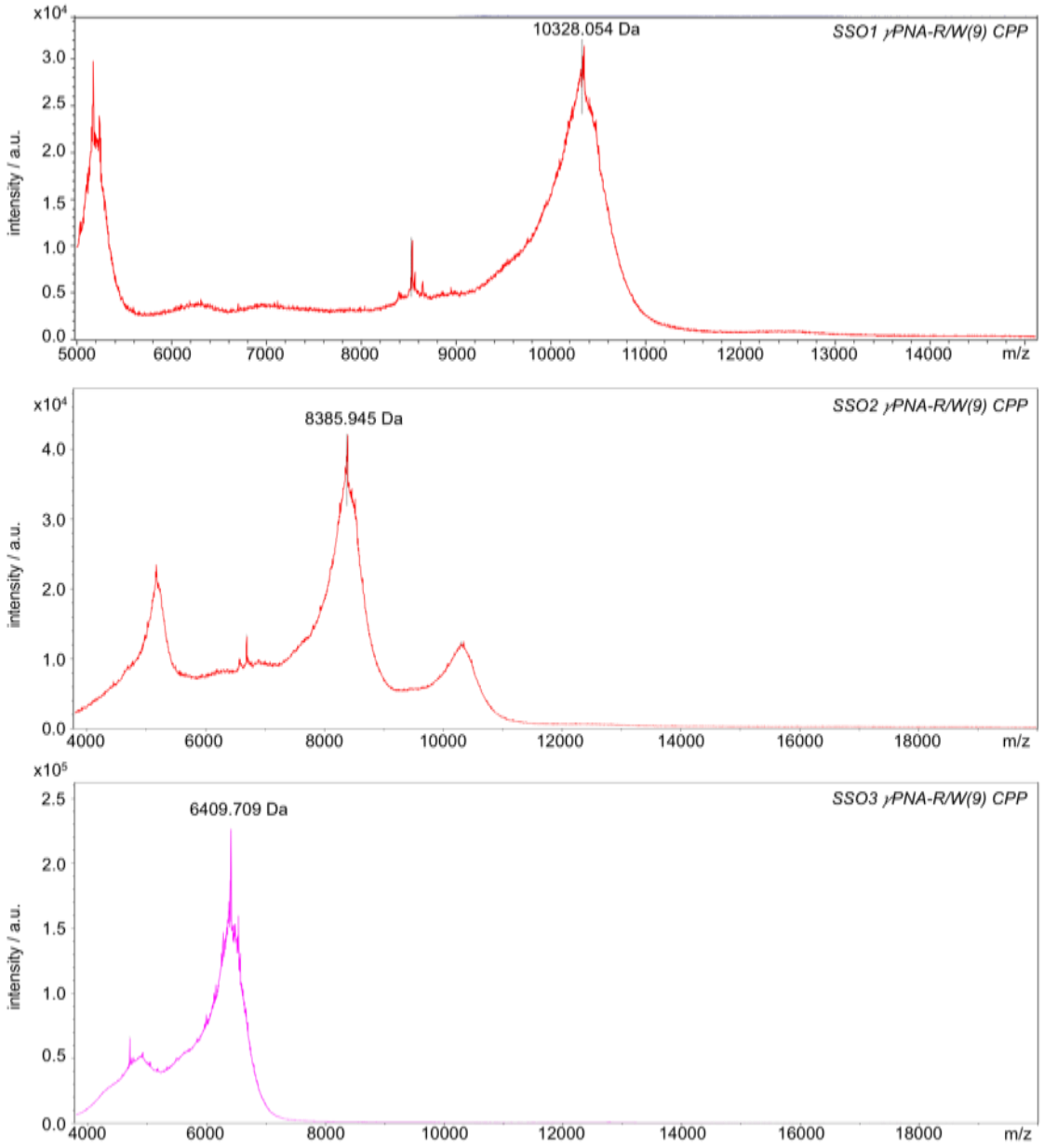

Figure 5-28 MALDI analysis of γPNA-CPP conjugates.

Conjugates were evaluated at 1 µM in α-cyano-4-hydroxycinnamic acid matrix on a Bruker Daltonics UltrafleXtreme MALDI TOF-TOF.

Delivery of linear R/W(9) peptide-SSO γPNA conjugates. After confirming purity and identify of the conjugates, delivery and function of the SSO γPNA-CPPs was evaluated in the HeLa:EGFP654 cell line. Cells were seeded at 10,000 cells per well in a black 96-well plate (Greiner). The following day, γPNA and γPNA-CPP conjugates were diluted in 200 µl of P/S-free DMEM growth media supplemented with 10% FBS of serum-free OptiMEM at the appropriate concentration as described above. Subsequently, delivery mix was added directly to cells. Experiments were performed in duplicate in two individual wells. Cells were incubated in the presence of delivery mix for the designated time at 37 °C and then media was replaced. Cells were imaged up to 48 h post-delivery on an Axio Observer Z1 microscope (Zeiss) using the EGFP filter cube or mCherry filter cube and 20x Plan-Apochromat objective as described below (see protocol 6.2.5 Prior to imaging, cells were washed with 1x PBS and media was replaced with phenol-red free DMEM.

6.0 Expanded Materials and Methods

6.1 General Molecular Biology Techniques

6.1.1 Polymerase chain reaction (PCR)

PCRs were carried out using commercial kits from Thermo-Fisher Scientific. For general PCRs, where low mutation rate was not essential, a *Taq* DNA polymerase kit (catalog# EP0402) was used. *Taq* DNA polymerase reaction was performed in a final volume of 50 µl with the following components:

- 5 µl of *Taq* buffer (10x)
- 1 µl of dNTP mix (10 mM)
- 2.5 µl of forward primer (10 µM)
- 2.5 µl of reverse primer (10 µM)
- 2.0 µl of $MgCl_2$ (25 mM)
- 50 ng of template DNA
- 1 µl of *Taq* DNA polymerase enzyme
- bring to 50 µl volume with nuclease-free water

Taq DNA polymerase PCR was performed as follows:

- initial denaturation: 95 °C, 60 s, 1 cycle
- PCR (30 cycles)
    - denaturation: 95 °C, 30 s
    - annealing: lower primer T_m minus 5 °C, 30 s

    - extension: 72 °C, 60 s per kilobase (product length)
- final extension
    - 72 °C, 10 min
    - 12 °C, hold

For larger amplifications, including large inserts (>500 bp) and site-directed mutagenesis (SDM) of plasmid DNA, high-fidelity Phusion DNA polymerase kit (catalog#: F530S) was used. Phusion DNA polymerase reaction was performed in a final volume of 50 µl with the following components:

- 10 µl of Phusion high fidelity (HF) buffer (5x)
- 1 µl of dNTP mix (10 mM)
- 2.5 µl of forward primer (10 µM)
- 2.5 µl of reverse primer (10 µM)
- 50 ng of template DNA
- 0.5 µl of Phusion DNA polymerase enzyme
- bring to 50 µl volume with nuclease-free water

Phusion DNA polymerase PCR was performed as follows:

- initial denaturation: 95 °C, 60 s, 1 cycle
- PCR (30 cycles)
    - denaturation: 95 °C, 10 s
    - annealing: lower primer T_m minus 5 °C, 15 s
    - extension: 72 °C, 30 s per kilobase (product length)
- final extension
    - 72 °C, 10 min

- 12 °C, hold

The reaction scale was modified depending on the application but was generally categorized into 1) analytical scale (25 µl; PCR screening, test PCR, SDM); or 2) preparatory scale (100 – 200 µl; gene amplification). PCR products were purified via agarose gel electrophoresis followed by a E.Z.N.A. Gel Extraction spin column purification kit (Omega Bio-Tek) or by E.Z.N.A. Cycle Pure spin column purification kit (Omega Bio-Tek) per manufacturer's protocol. Products were eluted in nuclease-free autoclaved Milli-Q purified water. For analytical verification of PCR product, agarose gel electrophoresis with ethidium bromide stain was employed (see general protocol for agarose gel electrophoresis 6.1.8 and the gel was subsequently imaged on a ChemiDoc XRS+ (Bio-Rad).

6.1.2 Site-directed mutagenesis (SDM)

SDM was performed following the previously reported overlap extension method.[912,913] Briefly, forward and reverse DNA primers were designed with partial overlapping (~10 – 15 bases) and partially non-overlapping (~20 bases) regions. The mutation site was included within the overlapping region while the non-overlapping region was designed to have a T_m of 5 – 10 °C greater than the overlapping region. Ideally, primers ended with a G/C base at the 3' terminus to ensure high thermostability during the annealing step of the PCR reaction.

SDM PCRs were performed as described for the Phusion High-Fidelity DNA polymerase protocol detailed above (Section 6.1.1 Briefly, reactions were performed in a total volume of 25 µl using 1 µM of each primer and 10 ng of template DNA. A negative control with no polymerase was included as a negative control. The annealing temperature was typically 50 – 60 °C but was dependent on primer design. Extension time was determined by the length (bp) of the gene product.

Following SDM, 3 µl of CutSmart buffer (10x; NEB) and 0.3 µl of *DpnI* restriction enzyme (NEB) were added to the reaction mixture to digest methylated parent plasmid and eliminate background. *DpnI* digest was carried out by incubation at 37 °C for 1 h, followed by heat inactivation at 80 °C for 20 min. Immediately following heat inactivation, 2 µl of the samples were transformed into chemically competent *E. coli* following protocol 6.1.5 and colonies were sequenced to confirm the correct mutation.

6.1.3 Restriction enzyme digest

Restriction enzymes were purchased from New England Biolabs (NEB) and restriction digest reactions were carried out in the optimized buffers supplied by the manufacturer. Restriction digest were typically carried out in 100 µl (2 µg of DNA) or 200 µl (4 µg of DNA) volumes and were incubated at 37 °C for 2 h, followed by heat inactivation at 80 °C for 20 min. Prior to purification, 5 µl of digest was analyzed by agarose gel electrophoresis (see general protocol for agarose gel electrophoresis 6.1.8 to confirm complete digestion. Digest products were purified by either agarose gel electrophoresis followed by gel extraction using the E.Z.N.A. Gel Extraction kit (Omega Bio-Tek) or the E.Z.N.A. Cycle Pure spin column purification kit (Omega Bio-Tek) following the manufacturer's protocol. Purified product concentrations (ng/µl) were determined using a NanoDrop ND-1000 spectrophotometer.

6.1.4 Plasmid ligation

The insert gene products were typically produced via PCR, followed by restriction enzyme digest and purification as described above (see general protocols 6.1.1 and 6.1.3 When synthetic oligonucleotides were used as an insert without digestion by a restriction enzyme, an intermediate step to add a 5' phosphate with T4 polynucleotide kinase (PNK; NEB) was performed. Briefly, single-stranded DNA (10 µM) was incubated with 1 µl of T4-PNK and 1 µl of T4 DNA ligase buffer (10x) containing ATP ([stock] = 10 mM; [final] = 1 mM) in a 20 µl reaction for 30 min at 37 °C followed by 80 °C for 20 min to heat inactivate the enzyme. Subsequently, both single-stranded oligonucleotides were combined (1 µM in 40 µl) and annealed (95 °C to 12 °C over 10 min in a thermal cycler [Bio-Rad]) in TE/Mg^{2+} buffer (Tris-HCl [0.01 M; pH 8.0], ethylenediaminetetraacetic acid [EDTA; 10 mM], magnesium chloride [12.5 mM]). Ligations were then performed in a 10 µl reaction, typically with a 1:6 backbone:insert molar ratio using 100 pg of backbone and T4 DNA ligase (NEB) following the manufacturer's protocol. A negative control reaction was performed with nuclease-free water instead of insert. Ligations were performed overnight at 4 °C and subsequently transformed into chemically competent bacterial cells (protocol 6.1.5

6.1.5 Plasmid *E. coli* transformation

Chemically competent bacteria cells for plasmid transformation were either included in commercial kits or were generated separately. For all cloning in this thesis, *E. coli* strains Top10 and Mach1 were used. The generation of chemically competent cells is performed by first streaking cell stocks on a Luria-Bertani (LB)-agar containing petri dish (~5 ml) with no antibiotics and

incubating overnight at 37 °C. The next day, a single colony was used to inoculate 5 ml of LB-broth which was then incubated overnight at 37 °C with shaking. Subsequently, 1 ml of the overnight culture was transferred into 50 ml of LB-broth and incubated with shaking at 37 °C until OD_{600} of 0.3 – 0.5 was reached, usually within 2 – 3 h. OD_{600} was measured on a Nanodrop ND-1000. The culture was then chilled on wet ice for 20 min and cells were pelleted by centrifugation (16,000 g, 5 min, 4 °C). The pellet was resuspended in ice-cold autoclaved transformation and storage solution (TSS; LB-broth [85% (v/v)], polyethylene glycol [PEG; 10% (w/v)], DMSO [5% (v/v)], $MgCl_2$ [50 mM]; pH 6.5) with a calculated volume of OD_{600} (determined of the 50 ml of culture above) x 10 ml. The suspension was then aliquoted into 1.5 ml Eppendorf tubes (pre-cooled at -80 °C) at 50 – 100 µl per tube and placed in a dry ice/isopropanol bath before long-term storage at -80 °C. Cell competency was then calculated by transformation of a pUC19 control plasmid (colony count x [transformation volume in µl / plating volume in µl]/ µg of plasmid DNA) and should be greater than 10^6 colonies per µg of DNA.

Transformations were typically performed in 50 µl of competent cell stocks. Cell stocks were briefly thawed on wet ice prior to transformation. Plasmid DNA (100 ng; 1-5 µl) or specific volume as defined by protocol (typically 1 – 10 µl; see protocols in 6.1) was added to chemically competent cells. Cells were incubated on ice for 30 min. Subsequently, cells were heat shocked in a 42 °C water bath for 30 s, then placed back on ice. Next, 250 µl of Super Optimal Broth with Catabolite Repression (S.O.C.) media was added and cells were grown with shaking at 37 °C for 1 h. Cultures were then plated (100 µl and 200 µl) onto LB-agar plates prepared with antibiotic as designated by the plasmid of interest. To prepare culture plates, autoclaved LB-agar was heated in the microwave for approximately 2 min or until melted. Once cooled to just above room temperature, antibiotics were diluted in the appropriate volume (5-10 ml of a LB-agar/plate).

Common antibiotics include: ampicillin (100 mg/ml stock; final conc. of 100 µg/ml) and kanamycin ([stock] = 50 mg/ml; [final] = 50 µg/ml). LB-agar/antibiotic mixture was poured into 10 cm petri dishes and cooled on the bench until solidified (~20 min). Preparation of LB-agar/antibiotic mixture and pouring plates should be done on a bench pre-wiped with ethanol and in close proximity to a Bunsen burner to prevent contamination. SOC cultures were spread, typically with a glass rod dipped in ethanol and flame sterilized, while spinning the plate. Once the SOC culture was plated, plates were left in the 37 °C incubator overnight, remove the next day, and stored for up to 1-2 months at 4 °C. Following overnight incubation, individual colonies were picked and inoculated into 5 ml of LB cultures in the presence of the appropriate antibiotic. Glycerol stocks of transformed cells for all plasmid bacteria were produced by mixing a saturated LB-broth culture with glycerol (1:1 in a final volume of 1 ml) and stored at -80 °C.

6.1.6 Plasmid purification

Plasmids were purified from bacterial cultures grown to saturation in LB-broth containing the appropriate antibiotics in either 5 ml or 100 ml cultures. Smaller cultures were purified using E.Z.N.A. Plasmid Mini Kit I (Q-spin; Omega Bio-Tek) following the manufacturer's protocol. Purifications were typically eluted in 50 µl of 65 °C nuclease-free autoclaved Milli-Q purified water. Larger cultures were purified using the PureYield Plasmid Midiprep System (Promega) following the manufacturer's protocol and eluted with 500 µl of 65 °C nuclease-free autoclaved Milli-Q purified water. Plasmid concentrations (ng/µl) were determined using a NanoDrop ND-1000 spectrophotometer. Typical concentrations ranges were 50 – 100 ng/µl for plasmids purified via Plasmid Mini Kit I and 500 – 1000 ng/µl for plasmids purified via the Plasmid Midiprep System.

6.1.7 Plasmid analysis and sequencing

DNA plasmids were analyzed via PCR screen (in-house) and Sanger sequencing analysis (Genewiz). For PCR screens, primers were designed such that one primer hybridizes within the gene of interest and the other hybridizes to the parent backbone and were used for analytical scale PCRs. Generally, colonies were picked following bacterial transformation using an inoculation loop, streaked on a petri dish containing LB-agar with the appropriate antibiotic for propagation, then dipped directly into the PCR mix. The PCR products (5 µl) were then separated via agarose gel electrophoresis (see agarose gel electrophoresis protocol 6.1.8 and imaged on a ChemiDoc XRS+ (Bio-Rad). Colonies expressing plasmids with the expected gene product should produce a distinct band on the gel at the expected size (bp) based on the primers. Positive hits were then further validated by Sanger sequencing to ensure the correct sequence. Sanger sequencing was performed by Genewiz using 1500 ng template DNA and sequencing primer (10 µM; premixed or with one of Genewiz's available primers). Sequence analysis and alignments were carried out using A plasmid Editor (ApE) software.

6.1.8 Agarose gel electrophoresis

Agarose gel electrophoresis was carried out by weighing out the desired agarose amount into a 125 ml Erlenmeyer flask. For a standard 0.8% (w/v) gel, 0.4 g of agarose was dissolved in 50 ml of 1x Tris-borate-EDTA (TBE) buffer (Tris-HCl [1 M; pH 8.0], boric acid [1 M], EDTA [0.02 M]) and the mixture was heated at maximum power in a microwave for a total of 1 min with pause and gentle shaking every 30 s. After the agarose was completely dissolved, the solution was allowed to stand at room temperature, or the flask was run under cool tap water to reduce the

temperature. Once the solution was just warm enough to touch, add ~1 µl of ethidium bromide stock solution (10 mg/ml in water; protected from light) and mix well. The liquid gel was poured into the gel caster (making sure no bubbles form) and appropriate well comb was added. The gel was then allowed to cool and solidify at room temperature for ~30 min. Once solidified, the gel was transferred to a Sub-Cell GT Cell (Bio-Rad) electrophoresis unit containing fresh 1x TBE buffer. Wells were then carefully loaded with the desired amount of DNA (up to 15 µl for a 15-well comb, up to 20 µl for a 10-well comb, up to 100 µl for a preparative comb) in 1x DNA loading dye (NEB; prepared from 4x stock) and run at 80 V for 45 – 60 min. DNA bands were visualized on the ChemiDoc XRS+ (Bio-Rad) or excised on the UV transilluminator (365 nm).

6.1.9 Native polyacrylamide gel electrophoresis (PAGE)

Native PAGE gels were used for analysis and purification of shorter nucleic acids, generally from 1 – 2000 bp. All native PAGE gels were cast in-house using the Mini-PROTEAN Tetra Cell system (Bio-Rad). Amounts of acrylamide were varied to adjust the percentage of the gel. General guidelines for nucleic acid separation based on gel percentage:

- 8% (w/v) gel: 60 – 400 bp
- 12% (w/v) gel: 50 – 200 bp
- 15% (w/v) gel: 25 – 150 bp
- 20% (w/v) gel: 5 – 100 bp

To cast a single 15% (w/v) gel, the following contents were mixed in a 15 ml conical tube to a total volume of 10 ml:

- 3.75 ml of acrylamide solution in water (40% [w/v])
- 6.25 ml of TBE buffer (1x)

- 100 µl of ammonium persulfate (APS; 10% [w/v])
- 15 µl of tetramethylethylenediamine (TEMED)

The percentage of the gel was adjusted by varying the acrylamide and TBE buffer volumes while maintaining a total volume of 10 ml for a single gel. The gel contents were mixed well and poured between the glass plates of the desired thickness (typically 1.5 mm) affixed in the caster, then a well comb was inserted into the gel and the gel was allowed to polymerize for ~20 min. Once solidified, the gel was placed into the Mini-PROTEAN Tetra Vertical Electrophoresis cell with fresh 1x TBE buffer. Voltage and time of electrophoresis was varied depending on the experiment and is described above. Once separated, the gel can be removed from the caster and stained or used for excision of the desired oligonucleotide for purification.

6.2 General Cell Culture Techniques

6.2.1 Cell growth and maintenance

All cell lines were maintained at 37 °C and 5% CO_2 in 10 cm plates, and all manipulations were performed in a biosafety cabinet certified on an annual basis. The majority of cell lines (e.g., Huh7, HeLa, HEK293T, HeLa:EGFP654, MCF7, HCT-116, MIA-PaCa-2, A172, and U-87) were cultured in Dulbecco's Modified Eagle Medium (DMEM; Hyclone) supplemented with fetal bovine serum (FBS; Sigma Aldrich; 10% [v/v]) and penicillin/streptomycin (P/S; VWR; 1% [v/v]). DMEM was made by dissolving 6.7 g of DMEM powder, 1.85 g of sodium bicarbonate, and 0.05 g of sodium pyruvate in 445 ml of Milli-Q purified water (EDM Millipore). The pH was then adjusted to 7.4 with hydrochloric acid (65% [v/v]). Subsequently, 50 ml of FBS and 5 ml of P/S

(100x) were added to the DMEM solution and the media was sterilized with a 0.2 µm filter unit (Thermo-Fisher Scientific). PC-3 cells were cultured in Kaighn's Modification of Ham's F-12 Medium (F-12K; Sigma Aldrich) which was prepared from a commercial reagent following the manufacturer's specifications. Briefly, 5.55 g of F-12K powder, 1.25 g of sodium bicarbonate, 0.05 g of sodium pyruvate, and 146.1 mg of L-glutamine were dissolved in 445 ml of Milli-Q purified water and pH was adjusted to 7.4 as described above. Finally, media was supplemented with 50 ml of FBS and 5 ml of P/S (100x) and filter sterilized. A498 cells were cultured in Roswell Park Memorial Institute (RPMI) 1640 medium (Invitrogen). RPMI 1640 medium was prepared from a commercial reagent following the manufacturer's protocol.

All cell lines were evaluated every three months for mycoplasma contamination using a commercially available MycoScope PCR Detection kit from Genlantis. Media (10 ml) was exchanged every 2 – 3 days for all cell lines (10 cm plate). Cells were passaged when they reached >90% confluence by removing media, gently rinsing the plate with 1 ml of TrypLE Express reagent (Invitrogen), followed by incubation in 1 ml of TrypLE Express reagent in the 37 °C incubator for ~2 min. To aid in lifting cells, the plate was gently rotated by hand. Cells were lifted from the plate using a 1 ml pipette and were resuspended in 9 ml growth media. The cells were passaged at a 1:10 dilution by adding 1 ml of cell suspension to 9 ml of growth media in a new 10 cm plate. Passages of cell stocks were tracked by date, cell line, and passage number. Cells stocks were discarded when they reached passage 30 or above, and new cells were thawed.

To thaw cells, the frozen cell vial was placed in a 37 °C water bath for no more than 2 min, then added directly to 10 cm plates containing growth media. Media was exchanged the following day to remove residual dimethyl sulfoxide (DMSO). Frozen stocks of cell lines were generated by passaging ~ 5 ml of cell suspension into 20 ml of growth media in a 15 cm plate. Cells were grown

to confluence, then lifted with TrypLE Express reagent (2 ml). The cells were then pelleted by centrifugation at 1,000 g for 10 min, then resuspended in an appropriate volume of growth medium such that cells can be stored at ~10^6 cells/ml in cryogenic preservation tubes (cryotubes). Cell suspension was then supplemented with 5% DMSO before pipetting 1 ml each into cryotubes. The cell vials were placed in the -20 °C freezer for 1 h, then into a -80 °C freezer overnight, followed transfer into a liquid nitrogen dewar.

For experiments, cells were counted on a hemocytometer (Fisher Scientific). Briefly, 10 µl of cell suspension was mixed with 30 µl of Trypan Blue Solution (Gibco) to selectively stain dead cells. After ~2 min incubation at room temperature, 10 µl of the stained cell suspension were added to each well of the hemocytometer. Live cells were summed in the four quadrants of each side of the hemocytometer and averaged between the two sides, then multiplied by 10,000 to calculate number of cells per ml. Based on this concentration, cells were then seeded at an appropriate number for the designated assay and plate type.

6.2.2 Poly-D lysine treatment

For experiments using HEK293T cells, all plates were treated with poly-D lysine (Fisher-Scientific). A stock of poly-D lysine (10 mg/ml) was prepared by dissolving 10 mg of poly-D lysine solid in 1 ml of nuclease-free water. This stock was stored at 4 °C for up to 1 year and was further diluted to 0.1 mg/ml in nuclease-free water prior to use. Volumes of poly-D lysine used to treat common plate formats include:

- 96-well plate = 40 µl/well
- 6-well plate = 400 µl/well
- 10 cm plate = 4 ml/plate

After diluting the stock to 0.1 mg/ml in the appropriate volume of water, the poly-D lysine solution was added directly to each well or plate and incubated with shaking at room temperature for ~10 min to ensure the bottom was completely coated. Then, the remaining poly-D lysine solution was removed from the plate and the plate was allowed to dry in the biosafety cabinet (usually 1 – 2 h). It was critical that the plate was completely dry prior to seeding cells, because excess poly-D lysine solution can be toxic to cells.

6.2.3 Mammalian cell transfection

Transient transfections were used to deliver foreign RNA and DNA into mammalian cells including plasmid DNA, siRNA, antagomirs, and logic gates (as described below 6.3.3 General amounts of materials transfected were optimized starting with the following conditions:

- Plasmid DNA
    - 96-well plate (Greiner) = 100 – 200 ng/well
    - 12-well plate = 750 – 1500 ng/well
    - 6-well plate = 1500 – 2500 ng/well
    - 10 cm plate = 10 µg/plate
- siRNAs and antagomirs
    - 96-well plate = 2– 20 pmol/well
    - 12-well plate = 15 – 150 pmol/well
    - 6-well plate = 1.5 – 2.5 nmol/well

All transfections were carried out as specified below using Lipofectamine 2000 (Invitrogen), XtremeGENE siRNA Transfection Reagent (Roche), or linear polyethylenimine

(LPEI).[914] White plates were used for luminescence experiments and XTT cell viability assays, while black plates were used for fluorescence experiments.

6.2.3.1 Lipofectamine 2000 transfection

Lipofectamine 2000 transfections were carried out following the manufacturer's protocol. Volumes of Lipofectamine 2000 reagent required were determined empirically using the formula: µg of oligonucleotide x 3 = volume (µl) of Lipofectamine 2000 reagent. To perform the transfection, OptiMEM serum-free media (Gibco) was added to 1.7 ml Eppendorf or 15 ml conical tubes according to the following standard volumes:

- 384-well plate (Greiner) = 50 µl
- 96-well plate = 100 µl
- 12-well plate = 1 ml
- 6-well plate = 2 ml
- 10 cm plate = 5 ml

The transfection mixture was prepared by adding DNA or RNA in the amounts described above directly to the appropriate volume of OptiMEM and was mixed by pipetting up and down. Subsequently, the appropriate volume of Lipofectamine 2000 reagent was added to the tubes and was pipetted up and down to mix. The transfection mix was then incubated at room temperature for 20 min. Finally, media was removed from cells plated and replaced with the transfection mix in the volume noted above. To remove media, the plate was tilted at a ~45° angle relative to the surface of the hood. Subsequently, a single- or multi-channel pipette was inserted into each well just above the interface of the side and bottom of the well. Media was then slowly aspirated from the cells. After changing tips, transfection mixes were taken up using the pipette and slowly added

to the well with the tips placed in the same location as they were in for media removal to minimize disruption to the cells. The same procedure was followed when exchanging transfection media for regular growth media. Cells were incubated with the transfection mix for 2 – 4 h, depending on experimental conditions. Following incubation, the transfection mix was removed from cells and replaced with the appropriate growth media.

6.2.3.2 XtremeGENE siRNA transfection

XtremeGENE siRNA Transfection Reagent (Roche) transfections were carried out following the manufacturer's protocol. Volumes of XtremeGENE reagent required were determined empirically using the formula: µg of oligonucleotide x 3 = volume (µl) of transfection reagent. To perform the transfection, OptiMEM serum-free media (Gibco) was added to 1.7 ml Eppendorf or 15 ml conical tubes according to the standard volumes described above. The transfection mixture was prepared by adding DNA or RNA in the amounts described above directly to the appropriate volume of OptiMEM and mixed by pipetting up and down. Subsequently, the appropriate volume of XtremeGENE reagent was added to the tubes and pipetted up and down to mix. The transfection mix was then incubated at room temperature for 20 min. Finally, media was removed from cells and replaced with the transfection mix in the volume noted above following the procedure outlined in 6.2.3.1 for removal and addition of media. Cells were incubated with the transfection mix for 4 h. Following incubation, the transfection mix was removed from cells and replaced with the appropriate growth media.

6.2.3.3 LPEI transfection

LPEI (Fisher Scientific; [stock] = 1 mg/ml) transfections were carried out following previous literature reports.[915-917] Volumes of LPEI reagent required were determined empirically using the formula: µg of oligonucleotide x 3 = volume (µl) of transfection reagent. To perform the transfection, growth media was added to 1.7 ml Eppendorf tubes according to the following volumes:

- 96-well plate = 230 µl
- 12-well plate = 800 µl
- 6-well plate = 1800 µl

OptiMEM serum-free media (Gibco) was added to 1.7 ml Eppendorf tubes according to the following standard volumes:

- 96-well plate = 20 µl
- 12-well plate = 100 µl
- 6-well plate = 200 µl

The transfection mixture was prepared by adding DNA or RNA in the amounts described above directly to the appropriate volume of OptiMEM and growth media and mixed by pipetting up and down. Subsequently, the appropriate volume of LPEI reagent (0.323 mg/ml stock solution in water) was added to the tubes and pipetted up and down to mix as described below:

- 96-well plate = 2 µl
- 12-well plate = 10 µl
- 6-well plate = 20 µl

The transfection mix was then incubated at room temperature for 20 min. Media was removed from plated cells and replaced a with the transfection mix in the volume noted above. Cells were incubated with the transfection mix for the desired time (typically 24 – 48 h) depending on experimental conditions.

6.2.4 Cell fixing

Cells were grown to 95 – 100% confluence in a 4-well (Fisher; catalog#: PEZGS0816) or 8-well (Fisher; catalog#: PEZGS0416) chamber slide with a glass bottom. Media was removed and cells were washed twice with 500 µl of PBS (pH 7.4, 4 °C). Cells were fixed on ice in 500 µl of 3.75% (v/v) formaldehyde (1 ml of 37.5% formaldehyde, 9 ml of PBS) for 15 min. Then, cells were washed three times with 500 µl of PBS at 4 °C. Cells were permeabilized with 200 µl of 0.5% (v/v) Triton X-100 (10 µl of Triton X-100 per 200 µl of PBS) at room temperature for 30 s. Next, cells were washed three times with 500 µl of 1x PBS at 4 °C. Staining was then performed as desired. Some common staining procedures included:

- Rhodamine Phalloidin for actin (Ex/Em: 540/565 nm; Thermo-Fisher Scientific; catalog# R415):
    - 7 µl (200 U/ml) per ml of PBS
    - 1% (w/v) of bovine serum albumin (BSA)
    - A volume of 200 µl per well in an 8-well chamber slide or 400 µl per well in a 4-well chamber slide was added and incubated at room temperature for 20 min
    - Cells were washed three times with 500 µl PBS at 4 °C
- Hoechst 33342 stain for nuclei (14.3 mM; Ex/Em: 365/460 nm; Fisher Scientific; catalog# H1399):

- 15 µl per ml of PBS
- A volume of 200 µl per well in an 8-well chamber slide or 400 µl per well in a 4-well chamber slide was added and incubated at room temperature for 20 min
- Cells were washed three times with 500 µl of PBS at 4 °C

When staining was complete, the chamber slide top was removed (if required) and the slide was allowed to air dry (~30 – 60 min). Finally, 1 drop (~10 – 20 µl) of ProLong Gold Antifade Mountant (Thermo-Fisher Scientific) was added into each well and a 0.17 mm coverslip (#1.5) was placed on top. All bubbles in the mountant were gently pushed out, then the slide was left in a dark drawer overnight to allow the mountant to cure.

6.2.5 Cell imaging

For live cell imaging, growth media was removed, and cells were washed twice with PBS. Media was then replaced with PBS or phenol red-free growth media to remove potential sources of background signal. All images in this thesis were captured on a Zeiss Axio Observer Z1 microscope using the following objectives:

- N-Achroplan 5x/0.13
- Plan-Apochromat 10x/0.4
- LD Plan-Apochromat 20x/0.4
- Plan-Apochromat 63x/1.4 (oil immersion)

And using the following filter sets:

- GFP (filter set 38 HE; Zeiss item# 489038-9901-000)
  - Ex. BP 470/40; Em. BP 525/50
- DsRed (filter set 43 HE; Zeiss item# 489043-9901-000)

    - Ex. BP 550/25; Em. BP 605/70
- DAPI (filter set 49; Zeiss item# 488049-9901-000)
    - Ex. G 365; Em. BP 445/50

Image processing was completed in Zen 2.0 software (Zeiss), ImageJ software (National Institutes of Health), or Slidebook 4.0 software (3i). For all cases, image intensity was adjusted by modifying histogram settings. To maintain consistency within each experiment, exposure times and histogram settings for each channel were copied to all images to be compared. Images were represented as a single channel or stacked images generated from overlaying multiple images. Images were exported as full resolution tif images (.tif extension) to ensure no loss of quality.

6.2.6 RNA isolation

Cells were passaged such that they reached 80% confluence on the day of treatment or transfection in a 6-well plate (Corning). Cells were treated or transfected as desired and grown for 48 h. Media was removed and cells were washed once with 700 µl of PBS (sterilized by passing through a 0.2 µm filter). Next, 700 µl of QIAzol lysis reagent (QIAGEN) was added and the plate was incubated with shaking for 5-10 min at room temperature to homogenize samples. Lysate was removed and added to labeled 1.7 ml Eppendorf tubes. Then, 140 µl of chloroform was added and tubes were inverted for ~15 s, followed by incubation on the benchtop at room temperature for 2-3 min. Subsequently, tubes were centrifuged at 12,000 g, 4 °C, for 15-20 min. The solution separated into a colorless aqueous phase on top (containing RNA), white interphase (containing DNA), and red phenol/chloroform containing organic phase on the bottom. Next, 200 – 300 µl of the aqueous phase was carefully collected, as not to disturb the interphase layer, and pipetted into a clean, labeled Eppendorf tube. Then, 1.5 volumes (typically 300 – 450 µl) of ethanol was added

and mixed by pipetting. The ethanol/RNA solution was added to a fresh filter tube (included in the miRNeasy kit from QIAGEN) and centrifuged at 16,110 g for 1 min. The flow-through was discarded and 700 µl of RWT buffer (supplied with the miRNeasy kit) was added, followed by centrifugation at 4 °C and 16,100 g for 15 s. The flow-through was discarded and 500 µl of RPE buffer (supplied with the miRNeasy kit) was added, followed by centrifugation at 4 °C and 16,110 g for 15 s. The flow-through was discarded and another 500 µl of RPE buffer was added, followed by centrifugation again. The filters were removed and placed into a new collection tube. The filters were spun in the centrifuge at 16,110 g for 10 min to completely dry the filter. Total RNA was eluted into a clean Eppendorf tube with 30 µl of nuclease-free water. Each sample was quantified using the Nanodrop ND-1000 spectrophotometer. The concentration was measured twice for each sample and two values were averaged. If high variability between the two measurements was observed, the concentration of the sample was measured a third time. Finally, the samples were diluted to 3 ng/µl in 15 µl of nuclease-free water in separate tubes and the remaining RNA was stored at -80 °C.

6.2.7 Mature miRNA analysis by quantitative real-time PCR (RT-qPCR)

Following total RNA isolation, samples were reverse-transcribed using the TaqMan microRNA Reverse Transcription Kit (Life Technologies) in conjunction with either the mature miRNA or RNU19 (control) TaqMan reverse transcription (RT) primer. The primers (5x), RNA template, dNTPs (supplied with the kit), and 10x RT buffer (supplied with the kit) were thawed on ice prior to assembly of reaction mixes. For each 15 µl RT reaction, a master mix was prepared containing 0.15 µl of dNTPs, 1.5 µl of reaction buffer (10x), 4.16 µl of nuclease-free water, 3 µl of primer (5x), with 1 µl of reverse transcriptase and 0.19 µl of RNA inhibitor (both added last).

The master mix was prepared in quantities such that 10 µl of mix could be added per RNA sample. Once the master mix was prepared, 5 µl of RNA (15 ng) was combined with 10 µl of master mix in a PCR tube. The reaction was gently mixed by flicking the tube, then the samples were incubated in the thermal cycler (Bio-Rad) using the following program: 16 °C, 30 min; 42 °C, 30 min; 85 °C, 5 min, hold at 12 °C.

Quantitative Real Time PCR was conducted with a TaqMan Universal PCR Master Mix without AmpErase UNG (Applied Biosystems; 2x) and the appropriate TaqMan miRNA assay (Life Technologies). Briefly, a master mix was made for each probe consisting of 10 µl of TaqMan Universal PCR Master Mix (2x), 7.7 µl of nuclease-free water, and 1 µl of TaqMan probe (20x). Master mixes were prepared to a final volume such that each sample could be analyzed in quadruplicate. The samples were only analyzed in triplicate, but the extra volume in the master mix was added to ensure all wells received the correct/sufficient amount. Next, 18.7 µl of the master mix was added to a well in a black 96-well thin-wall PCR plate (Bio-Rad) such that each sample could be analyzed in triplicate. Then, 1.3 µl of cDNA from the RT reaction was added to each well. The plate was sealed with a qPCR microseal membrane (Bio-Rad) and briefly centrifuged at 1000 g and 4 °C for 1 min to make sure all liquid was at the bottom of the well. qPCR was performed on a Bio-Rad CFX96 RT-PCR thermocycler using the following program: 95 °C, 10 min; followed by 40 cycles of 95 °C, 15 s; 60 °C, 60 s. The triplicate threshold cycles (CT) obtained for each small molecule treatment were used to determine the relative levels of miRNA in small molecule treated cells relative to the DMSO control using the $2^{-\Delta\Delta Ct}$ method.[427]

6.2.8 Primary miRNA analysis by quantitative real-time PCR (RT-qPCR)

When total RNA samples were analyzed by RT-qPCR to measure the expression levels of pri-miRNA, 1 µg of each RNA sample were reverse transcribed using the iScript cDNA synthesis kit (Bio-Rad). The RNA was diluted in a final volume of 15 µl of nuclease-free water. To each RNA sample, 4 µl of iScript Reverse Transcription Supermix (Bio-Rad) and 1 µl of Reverse Transcriptase (from the iScript kit) was added. RT was performed in a thermal cycler (Bio-Rad) using the following program: 25 °C, 5 min; 42 °C, 30 min; 85 °C, 5 min. Quantitative Real Time PCR was conducted with TaqMan Universal PCR Master Mix without AmpErase UNG (2x) and the appropriate TaqMan primers for hsa-pri-miRNA and GAPDH (Life Technologies) on a Bio-Rad CFX96 RT-PCR thermocycler (2 µl of RT PCR product; 95 °C, 10 min; followed by 40 cycles of 95 °C, 15 s; 60 °C, 60 s) as described above. To adjust for the extra volume from the RT reaction, the volume of water in the qPCR master mix was reduced from 7.7 µl to 7 µl. The triplicate threshold cycles (Ct) obtained for each small molecule treatment were used to determine the relative levels of pri-miRNA in small molecule-treated cells relative to the DMSO control and normalized to the GAPDH endogenous control using the $2^{-\Delta\Delta Ct}$ method.

6.2.9 Messenger RNA analysis by quantitative real-time PCR (RT-qPCR)

When total RNA samples were analyzed by RT-qPCR to measure the expression levels of mRNA, 1 µg of each RNA sample were reverse transcribed using the iScript cDNA synthesis kit (Bio-Rad) as described above (section 6.2.8 Quantitative Real Time PCR was conducted with iTaq Universal SYBR Green qPCR Master Mix (Bio-Rad; 2x) on a Bio-Rad CFX96 RT-PCR thermocycler (2 µl of RT PCR product; 95 °C, 10 min; followed by 40 cycles of 95 °C, 15 s; 60

°C, 60 s) as described above. Primers for mRNA and GAPDH (Table 36) were purchased non-modified from Sigma Aldrich. A master reaction mix was prepared by mixing the following: 10 µl of iTaq Universal SYBR Green qPCR Master Mix (Bio-Rad; 2x), 0.5 µl of forward primer (10 µM), 0.5 µl of reverse primer (10 µM), and 6 µl of nuclease-free water to a final volume of 18 µl per well. The master mix (18 µl) was subsequently added to a well, followed by 2 µl of RT product in triplicate wells and qPCR was performed. The triplicate threshold cycles (Ct) obtained for each small molecule treatment were used to determine the relative levels of mRNA in small molecule-treated cells relative to the DMSO control and normalized to the GAPDH endogenous control using the $2^{-\Delta\Delta Ct}$ method.

Table 36 RT-qPCR primer sequences for GAPDH mRNA.

name	sequence (5' -> 3')
GAPDH Fwd	AACGGGAAGCTTGTCATCAATGGAAA
GAPDH Rev	GCATCAGCAGAGGGGGCAGAG

6.2.10 Data analysis of qPCR experiments

At the completion of qPCR, a sigmoidal amplification curve was displayed for each individual well. If the amplification curves did not display the expected sigmoidal curve (e.g., the curve did not reach a maximum and plateau at the completion of the experiment), the experiment was repeated. While the 'Quantification' tab was displayed, 'settings' was selected, and Cq determination mode was set to 'Regression' to apply a multivariable, nonlinear regression model

to individual well traces and adapt the model toward computing an optimal Cq value. The 'Gene Expression – Bar Chart' tab then displayed a histogram of the relative expression for each sample. To the right of the bar chart, 'Normalized expression (ΔΔCq)' was selected under the 'Mode' drop-down menu. Under the 'Graph Data' drop-down menu, 'Relative to zero' was selected. The 'Control sample' was set to DMSO. Next, under 'Experiment Settings', the 'Reference' box corresponding to RNU19 or GAPDH (depending on the experiment) was checked, and all boxes were checked under 'Display on Chart' in order to normalize expression of the experimental samples to the internal control. Finally, 'Export All Data Sheets to Excel' was selected under the 'Export' tab. This generated a file folder containing an individual Excel file for each data tab.

For statistical analysis, the file ending in 'Gene Expression Results – Bar Chart.xlsx' was opened and the 'Expression' (average) and 'Expression SEM' (error) values were copied into a GraphPad (Prism) file. Subsequently, P values were calculated by performing an unpaired t test in the software using the Holm-Sidak method[918,919] with alpha = 0.01.

6.2.11 Protein isolation from mammalian cells for SDS-PAGE

Prior to protein isolation, cells were grown to 95 – 100% confluence in a 6-well plate (Corning). Prepare 1x stock of radioimmunoprecipitation assay (RIPA) lysis buffer (50 mM Tris-HCl, pH 8.0, 150 mM NaCl, 0.1% Triton X-100, 0.1% SDS). Dilute Halt Protease Inhibitor Cocktail (Thermo-Fisher Scientific) to 1x in a sufficient volume of RIPA buffer to add 150 µl/well to each well. Remove media from cells and wash with 500 µl PBS. Add 150 µl lysis buffer with protease inhibitor and shake on ice for ~20 min. Remove lysate and collect in 1.5 ml Eppendorf tubes. Spin the lysate at 4 °C and 16,110 g for 10 – 20 min. The supernatant was carefully transferred to a new Eppendorf tube and the cell debris pellet was discarded. The supernatant was

then aliquoted into PCR tubes (75 µl) and boiled in 25 µl of Laemmli buffer (SDS [2% (w/v)], glycerol[10% (w/v)], bromophenol blue [0.002% (w/v)], Tris-HCl [0.0625 M], and 2-mercaptoethanol [5% (v/v)] added fresh each time) by heating the sample to 95 °C in a heat block for 20 min, then allowing the sample to return to room temperature on the bench top. Boiled protein samples were stored for up to 1 week at 4 °C prior to analysis by SDS-PAGE but should be analyzed as soon as possible.

6.2.12 Protein analysis

6.2.12.1 Sodium dodecyl sulfate polyacrylamide gel electrophoresis (SDS-PAGE)

SDS-PAGE gels were utilized for characterization of proteins. All SDS-PAGE gels were poured from scratch using the Mini-PROTEAN Tetra Cell system (Bio-Rad). Polyacrylamide (40% [w/v] stock; Fisher Scientific) percentage was adjusted based on molecular weight of proteins analyzed:

- 15% (w/v) gel: 10 – 50 kDa
- 12% (w/v) gel: 20 – 70 kDa
- 8% (w/v) gel: 50 – 200 kDa
- 4 – 6% (w/v) gel: >200 kDa

To cast a 15% (w/v) running gel, mix the following contents in a 15 ml conical tube to a final volume of 8 ml:

- 3 ml of acrylamide (40% [w/v])
- 2.8 ml of distilled water
- 2 ml of Tris-HCl (1.5 M; pH 8.8)

- 80 µl of SDS (10% [w/v])
- 80 µl of ammonium persulfate (APS; 10% [w/v])
- 8 µl of tetramethylethylenediamine (TEMED)

Water and acrylamide volumes were varied to adjust the percentage of the gel. The components were mixed by inversion, then poured into a caster between glass faceplates of the desired gel thickness (typically 1.5 mm). To ensure the top of the gel was flat, 1 ml of saturated butanol-water was carefully pipetted onto the top of the gel. The gel was allowed to polymerize for 20 – 30 min, followed by rinsing the top of the gel 2 – 3 times with distilled water to remove saturated butanol. Subsequently, a 4% (w/v) stacking gel was added to the top of the running gel. To cast a stacking gel, mix the following in a 15 ml conical tube to a final volume of 5 ml:

- 0.5 ml of acrylamide (40% [w/v])
- 3.1 ml of distilled water
- 1.25 ml of Tris-HCl (0.5 M; pH 6.8)
- 50 µl of SDS (10% [w/v])
- 50 µl of APS (10% [w/v])
- 5 µl of TEMED

The components were mixed by inversion before pouring on top of the running gel. A well comb matching the gel thickness was added and the gel was allowed to polymerize for 20 – 30 min. Once solidified, the gel was removed from the casters and the comb was carefully removed. The gel was then placed in a Mini-PROTEAN Tetra Electrode Assembly (Bio-Rad) in a buffer tank. If only one gel was to be analyzed, a Mini-PROTEAN spacer plate was placed in the electrode assembly opposite the gel. Fresh 1x SDS running buffer (Tris-HCl [25 mM], glycine [200 mM], SDS [0.1% (w/v)]) was used to fill the inner chamber (between the gel and spacer plate)

while previously used 1x SDS running buffer can be used to fill the rest of the gel tank. Do not reuse running buffer more than 3-times. Boiled protein samples (up to 40 µl) were pipetted into the wells in addition to one well with 10 µl of PageRuler pre-stained molecular weight ladder (Thermo-Fisher Scientific). Electrophoresis was performed in two phases:

- Phase 1 – stacking: run gel at 60 V for 20 min
- Phase 2 – separation: run gel at 150 V for 75 min

Following electrophoresis, additional analysis techniques were utilized to visualized the gel on a Chemi-Doc Gel Imaging System (Bio-Rad) such as Coomassie protein stain (general Coomassie protein stain 6.2.12.2) or western blot (general western blot protocol 6.2.12.3)

6.2.12.2 Coomassie protein staining of SDS-PAGE gels

Coomassie staining solution (15 mg of Brilliant Blue G dye [Sigma Aldrich], 35 ml of distilled water, 20 ml of methanol, and 10 ml of acetic acid) was added to an SDS-PAGE gel in a plastic box with a lid. The box was heated for 30 s in a microwave and then allowed to cool down to room temperature over 30 min. This was repeated once. To destain the gel, remove the Coomassie staining solution and add fresh destaining solution (10% [v/v] acetic acid, 20% [v/v] methanol, 70% [v/v] distilled water) to the gel. The box was incubated with shaking at room temperature overnight. After destaining, the gel was imaged on the ChemiDoc XRS+ (Bio-Rad) using the Coomassie filter and automatic exposure time settings for intense bands.

6.2.12.3 Western blot protocol

After SDS-PAGE separation of proteins, the gel was removed from the glass faceplates and placed in a box containing 4 °C transfer buffer (Tris-HCl [25 mM], glycine [192 mM]; pH 8.3). Separately, a glass baking dish was filled with ~1 L of transfer buffer at 4 °C. Next, a transfer

cassette (Bio-Rad) was placed into the buffer with the black negative plate on the bottom. Then, a sponge was placed onto the negative plate, followed by blotting filter paper cut to the size of the gel, and finally the gel. Make sure there were no bubbles between the gel and the filter paper by gently smoothing the gel by hand. Next, add the polyvinylidene difluoride (PVDF; GE) membrane, cut to the size of the gel and pre-activated by soaking in methanol for 1 – 5 min and also make sure there were no bubbles between the membrane and the gel. Finally, add a second piece of blotting filter paper and the second sponge and close the cassette by folding the clear plastic place on top of the resultant transfer sandwich and locking it with the attached clip. The transfer cassette was then transferred to a Mini Trans-Blot Cell (Bio-Rad) with the black plate of the cassette facing the negative black part of the cell. The buffer tank was filled with 1 L of transfer buffer from the glass baking dish and an ice pack was placed inside of the tank to maintain the temperature at 4 °C throughout the transfer. The tank was placed inside a Nalgene pan filled with 50:50 ice and water. The transfer was run at 80 V for 1.5 h. Following transfer, the cassette was disassembled, the membrane was removed and placed in a clear plastic blotting box. Next, the membrane was rinsed once with Tris-buffered saline plus Tween 20 (TBST; Tris-HCl [10 mM; pH 7.5], NaCl [15 mM], Tween 20 [0.01% (v/v)]) and blocking solution (either 5% [w/v] bovine serum albumin [BSA] or 5% [w/v] non-fat dry milk in TBST) was added. The membrane was incubated at room temperature with rocking for 1 h. Then, the blocking solution was removed, and the primary antibody was diluted in fresh blocking solution (according to the manufacturer's specifications) and added to the membrane. The membrane was incubated with the primary antibody overnight at 4 °C in the cold room. The following day, the membrane was washed 3 times (~5 ml of TBST with rocking at room temperature for 5 min each) and secondary antibody in TBST was added (according to the manufacturer's specifications). After a 1 h incubation with rocking at room

temperature, the membrane was washed again 3 times (~5 ml of TBST with rocking at room temperature for 5 min each). Finally, for secondary antibodies conjugated to horseradish peroxidase (HRP), 3 ml of the SuperSignal West Pico PLUS Luminol/Enhancer Solution (Thermo-Fisher Scientific) was added to 3 ml of SuperSignal West Pico PLUS Stable Peroxide Solution (Thermo-Fisher Scientific) in a 15 ml conical tube and inverted to mix. The resulting solution was added directly to the membrane and incubated with rocking for 2 – 5 min at room temperature. After incubation, the reagent was poured off and the membrane was placed inside of a clear plastic sheet protector. The membrane was then imaged on a ChemiDoc XRS+ using the 'Chemi' method and either autodetection or manual exposure time. Typically, exposure times below 300 s were optimal.

6.2.13 Dual-Luciferase Assay System

For cells expressing both the *Renilla* luciferase enzyme and firefly luciferase enzyme, media was first removed from wells and passive cell lysis buffer (provided in Dual-Luciferase Assay kit from Promega) was added at $1/5^{th}$ of the original media volume. The plate was incubated with shaking for 20 min to allow for complete cell lysis. While the cells were being lysing, the automatic liquid handling injectors on the Tecan M1000 microplate reader were prepared. The inlet for injector 1 was placed in the Luciferase Assay Reagent (LAR, provided in Dual-Luciferase Assay kit from Promega) and the inlet for injector 2 was placed in the Stop & Glo Reagent (S&G, provided in Dual-Luciferase Assay kit from Promega). Both injectors were primed with 1 mL of the respective reagent using the ‘prime’ function in the injection settings. After priming, the injection shaft was placed into the hole at the top of the microplate reader. Next, the multiwell plate containing lysed cells was placed inside the instrument and the Dual-Luciferase assay

template protocol within the Tecan software was opened. The plate type and manufacturer were selected, and the wells of interest were highlighted. Injection volumes were set to 50% (e.g., 50 – 100 µl for a 96-well plate or 25 µl for a 384-well plate) and all other settings were kept default per the template protocol (200 µl/s injection speed, 100 µl/s refill speed, 2 s wait time). Firefly luciferase values were recorded first followed by *Renilla* luciferase values. Once the assay was complete, the injection shaft was replaced and the multiwell plate was removed. The injector settings were opened again and the 'backflush' function was selected to reclaim unused reagent to their respective tubes for future use. Reagents were stored at -80 °C long-term. The inlets for injectors 1 and 2 were then removed and placed into ethanol (70% [v/v] in water). Under the injector settings, the 'wash' function was selected and washing was performed twice, followed by replacement of the injector inlets and storage in their respective stands.

6.2.14 Bright-Glo Assay System

To cells expressing firefly luciferase enzyme, add ½ of the total media volume Bright-Glo reagent (Promega; prepared by dissolving Bright-Glo substrate in Bright-Glo buffer). For example, 25 µl of Bright-Glo reagent was added to 50 µl of media for cells grown in a 384-well plate and 100 µl of Bright-Glo reagent was added to 100 µl of media for cells grown in a 96-well plate using a multichannel pipette. When the Bright-Glo assay was performed on cells grown in a 96-well plate format, 100 µl of media was removed prior to addition of the Bright-Glo reagent. In some cases where plasmid expression resulted in raw luciferase values >100,000 the volume was further reduced to conserve Bright-Glo reagent. For example, 50 µl of Bright-Glo reagent was added to 100 µl cells in a 96-well plate format. Because the lysis reagent was included in the Bright-Glo buffer, so there was no need for an additional lysis step prior to addition of the Bright-Glo reagent.

The plate was incubated with shaking for 10 min at room temperature to allow for cell lysis and stabilization of luminescence signal. Luminescence signal was monitored on a Tecan M1000 microplate reader using the luminescence read-out with attenuation OFF and integration time between 100 – 1000 ms. While a 1000 ms integration time was standard for most assays, the integration time was determined based on intensity of the luminescence signal. For example, for high signals (detector indicates: OVER), an integration time of 100 ms was required to prevent saturation.

6.2.15 Data analysis of luciferase assays

For dual luciferase assays in which the changes in *Renilla* luciferase activity were monitored (e.g., the miRNA target sequence was downstream of the *Renilla* luciferase gene in the reporter construct), luminescence values for *Renilla* luciferase activity were divided by luminescence values corresponding to firefly luciferase activity for each individual well. In contrast, for dual luciferase assays in which changes in firefly luciferase activity were monitored, luminescence values for firefly luciferase activity were divided by luminescence values for *Renilla* luciferase. Then, the average and standard deviation of three wells was calculated for resultant 'relative luminescence' values for each treatment condition. Finally, the average ± standard deviation relative luminescence value for each condition was divided by the average relative luminescence value for the DMSO control. In experiments where the data were reported as a percentage, the resultant average ± standard deviation values were multiplied by 100.

The Bright-Glo assay was typically paired with an XTT assay (see protocol 6.2.16 to monitor cell viability. When these experiments were performed, cells were plated at the same time in two separate plates such that one assay (Bright-Glo or XTT) was performed on each plate. After

obtaining the average changes in absorbance from the XTT assay as described below, the raw luminescence values from the Bright-Glo assay for each well were divided by the corresponding change in absorbance for each treatment condition. Subsequently, the average and standard deviation of three wells was calculated for the 'relative luminescence' values for each treatment condition. Finally, the relative luminescence data for each treatment condition were divided by the relative luminescence for the DMSO control.

6.2.16 XTT assay

Cells were typically seeded at 500 or 1000 cells per well in white, clear-bottom, 384-well plates (Greiner) such that cells were at ~50% confluence on the day of treatment. Following an overnight incubation, cells were treated in triplicate for the desired amount of time followed by analysis with an XTT assay (Roche).[522] When cell proliferation was monitored (GI_{50}), cells were plated in the same way and the XTT assay was plated the following day immediately before treating the cells. XTT reagent (2,3-bis-(2-methoxy-4-nitro-5-sulfophenyl)-2*H*-tetrazolium-5-barboxanilide was dissolved in 500 ml of PBS buffer to a concentration of 1 mg/ml. The reagent was stirred and warmed in a 37 °C water bath for no more than 10 min to ensure complete dissolution of the solid. Next, the reagent was sterile filtered through a 0.2 µm filter via vacuum filtration[920] and aliquoted (10 ml) into 15 ml conical tubes which were stored at -80 °C until use. The activation reagent, menadione, was prepared by dissolving the solid in acetone to a final concentration of 1.7 mg/ml and was stirred until completely dissolved. To prepare the activated XTT reagent, menadione was added to an appropriate volume of XTT to enable addition of 40% media volume for the assay (8 µl of menadione per 1 ml of XTT) and mixed. The activated XTT reagent was added to each well. Absorbance was measured at 450 nm and 630 nm (background)

on a Tecan M1000 microplate reader after initial addition (Abs-t_{inital}) of the reagent, then the plate was incubated at 37 °C in a 5% CO_2 atmosphere for 4 h. Following the incubation end-point absorbance (Abs-t_{final}) was measured on a Tecan M1000 plate reader. After background subtraction of the absorbance measurements at 630 nm, the difference in the Abs-t_{inital} and Abs-t_{final} 450 nm absorbance measurements was calculated. The difference in absorbance for each well was normalized to the DMSO control, then averaged and multiplied by 100 to determine the percent cell viability relative to DMSO. [920,921] IC_{50} values were calculated by fitting the data with a variable slope sigmoidal dose response curve using GraphPad (Prism) software.

To calculate the GI_{50}, the difference between Abs-t_{inital} and Abs-t_{final} at 450 nm was calculated for each well from the XTT assay performed on the day of treatment (RAbs-t_0) and the XTT assay performed after treatment for 72 h (RAbs-t_{72}). Additionally, the average RAbs-t_0 and average RAbs-t_{72} for DMSO (RAbs-t_{72} [DMSO]) treated cells were calculated. Subsequently, the following equation was used: [(RAbs-t_0 – RAbs-t_{72} [compound treatment]) / (RAbs-t_{72} [DMSO] – RAbs-t_{72} [compound treatment])] x 100 = percent growth inhibition, where RAbs-t_{72} [compound treatment] corresponded to the relative absorbance following compound treatment for each individual well. Finally, the average percent growth inhibition ± standard deviation was calculated for each treatment concentration, plotted in GraphPad prism, and a GI_{50} was calculated using the protocol described above. On the GI_{50} sigmoidal curve, values <0 (i.e., negative values) corresponded to cell death, values = 0 corresponded to no growth, and values >0 (i.e., positive values) indicated cells were proliferating.

6.2.17 CellTiter-Glo cell viability assay

Cells were treated with a serial dilution of small molecule (in 0.1% [v/v] DMSO) or 0.1% (v/v) DMSO in triplicate for 72 h in a 384-well plate. The CellTiter-Glo reagent (Promega) was prepared by combining the CellTiter-Glo Substrate and CellTiter-Glo Buffer, then aliquoting it (10 ml) into 15 ml conical tubes. Following treatment, 12.5 µl of the CellTiter-Glo reagent was added directly to 50 µl of media in each well. There was no requirement to remove media for an additional lysis step because the lysis reagent was included in the CellTiter-Glo Buffer. After addition of the CellTiter-Glo reagent, the plate was incubated with shaking for 10 – 15 min at room temperature to allow for cell lysis and stabilization of luminescence signal production. Luminescence was monitored on a Tecan M1000 microplate reader using the luminescence read-out, attenuation set to OFF, and an integration time of 1000 ms. Finally, average luminescence values ± standard deviation were calculated and average values for compound treatment were normalized to DMSO, then multiplied by 100 and reported in % cell viability.

6.2.18 Clonogenic assay

The clonogenic assays were performed as described previously.[524] Briefly, a base layer solution was prepared by heating a solution of 1.4% (w/v) agarose in sterile MilliQ purified water to melt and mixing it in equal volumes with 2x growth media (2x growth media powder, fetal bovine serum [FBS; 20% (v/v)], penicillin-streptomycin [2% (v/v)]). The agarose was allowed to cool to a temperature such that it was warm enough to be melted and to handle comfortably, but not too hot. To add to a 12-well plate (Corning), the P1000 pipet (VWR) was set to 700 µl, then the plunger was pushed all the way down (past the first stop) and the agarose/media solution was

slowly drawn up. The tip of the pipet tip was placed at the bottom of the well and the solution was gently dispensed until the first stop was reached. Continuing past the first stop was found to result in bubbles. After the base layer was added to all wells, the 12-well plates were placed in the 4 °C fridge for 20 – 30 min to solidify.

To generate the cell/treatment layer, 0.9% (w/v) low melt agarose was first heated in a microwave briefly and mixed with an equal volume of 2x growth media in a 15 ml conical tube. Volumes were calculated to enable addition of 300 µl of low melt agarose and 300 µl of 2x growth media per well in triplicate (i.e., 900 µl of each). Then, cells were trypsinized, resuspended in 1x growth media, and counted using the hemocytometer. Compounds at a concentration 1000-fold higher than the final concentration (e.g., 10 mM for a 10 µM [final]) were diluted in the low melt agarose/2x growth media solution. DMSO was also included as a vehicle control. Then cells were diluted in 1x growth media in a separate 15 ml conical tube such that the final cell density was 10,000 cells in 150 µl per well. Finally, 750 µl of the cell solution was added to the agarose layer in each well of the 12-well plate as described for the base layer. After two weeks, cells were stained with 0.1% (w/v) crystal violet in PBS. Images of each well were captured using an MRm camera (Axiocam) and N-Achroplan 5x/0.13 M27 objective on an Axio Observer Z1 microscope (Zeiss) using the 'tiling' and 'z-stack' modules. In order to capture images of the whole well, a z-stack of 17 slices over 800 µm was obtained. Each slice contained 192 tiles (12 x 16) which were stitched together immediately following image capture using Zen 2.0 software. Z-stacks were exported as .tif files and focus stacking was used to convert the individual slices to generate an extended depth of field image using Helicon Focus software (https://www.heliconsoft.com). Extended depth of field images were analyzed using ImageJ.[525] Briefly, identical contrast settings were applied to each image by adjusting the maximum and minimum pixel values to match the histogram. The

threshold for each image was then set to 1.03%. Colonies were counted using the "Colony Counter" plugin using a particle size of 500-infinity. Total colonies per well were averaged and normalized to DMSO control. IC_{50} values were calculated by fitting the data with a variable slope sigmoidal dose response curve using GraphPad (Prism) software.

6.3 General DNA Computation Techniques

6.3.1 Gate duplex purification

Non-modified (IDT or Sigma-Aldrich), 5' TAMRA- and 3' BHQ2- (Alpha DNA), or 5' Iowa Black RQ- and 3' TAMRA-modified (IDT) oligonucleotides were purchased from commercial vendors. The oligonucleotides were received as lyophilized samples and were diluted in autoclaved nuclease-free Milli-Q purified water to a stock concentration of 100 µM, calculated based on the amount of DNA (nmol) received. Concentrations of stock solutions were validated by measured absorbance at 260 nm on a Nanodrop ND-1000 spectrophotometer. Gate duplexes were assembled at ~20 µM in 200 µl of 1x TE/Mg^{2+} buffer (Tris-HCl [0.01 M; pH 8.0], ethylenediaminetetraacetic acid [EDTA; 10 mM], $MgCl_2$ [12.5 mM]). These concentrations were achieved by pipetting 20 µl of each ssDNA into a PCR tube in addition to 20 µl of 10x TE/Mg^{2+} solution and up to 200 µl total volume with nuclease-free water. The ssDNA oligonucleotides were subsequently annealed in a thermal cycler (Bio-Rad) by heating the solution to 95 °C, then cooling it to 12 °C over 10 min. Gate duplexes were then purified on 1.5 mm 20% (v/v) native TBE-PAGE gels (200 V, 40 min; see protocol 6.1.9 The full-size gate duplex was excised from the gel using UV back shadowing on a TLC plate to visualize the DNA. Briefly, the gel was removed from the

glass plates and carefully transferred to a TLC plate pre-wet with distilled water. Then, a handheld UV lamp was held at a ~45° angle to the benchtop and shined on the gel. The DNA duplex will then be visible as a dark band in the gel and the edges of the band can be marked with a razor blade. The amount of time the DNA was illuminated by the UV lamp was limited to prevent photodamage. The DNA band was then completely excised from the gel and cut into smaller pieces of ~1 mm^3. The gel pieces were transferred to a 1.7 ml Eppendorf tube and incubated with shaking at room temperature overnight in 500 µl of TE/Mg^{2+} buffer to elute the gate duplex. The following day, elutions were transferred to a new 1.7 mL Eppendorf tube and centrifuged at 3000 g for 5 min to remove residual gel debris from the solution. The supernatant was transferred to a clean 1.7 ml Eppendorf tube and gate concentrations (typically 5 – 10 µM) were determined by measuring absorbance at 260 nm on a Nanodrop ND-1000 spectrophotometer and calculated with the duplex extinction coefficient as determined by the IDT OligoAnalyzer 3.1.

6.3.2 Fluorescence analysis

Gate reactions were set up in 50 µl (384-well plate; black) or 100 µl (96-well plate; black) of TE/Mg^{2+} buffer in three separate wells and incubated at 37 °C or room temperature as described in each individual gate experiment. Unless otherwise specified, for *in vitro* gate activation experiments, AND gates were used at 200 nM with 200 nM translator gates and 800 nM input strands. TAMRA fluorescence was monitored on a Tecan M1000 microplate reader (ex. 545 nm; em. 585 nm; reading from the bottom). Reactions were normalized as described in each individual experiment, but typically to the positive control.

6.3.3 Gate transfections

Logic gate transfections were performed in black 96-well plates using 0.8 µl of XtremeGENE siRNA transfection reagent (Roche) per well in 100 µl of serum-free OptiMEM. The gates were transfected at 50 nM with 50 or 200 nM translator gate where applicable. Gates were complexed with XtremeGENE siRNA transfection reagent as described in the general protocol 6.2.3.2. After 4 h incubation, transfection mixes were removed and replaced with phenol red-free growth media for imaging as described above (see protocol 6.2.5 TAMRA signal was normalized to a standard fluorescence intensity setting for all samples in a given experiment in Zen 2.0. Images were shown with fluorescence and brightfield (BF) channels merged.

7.0 Plasmid Maps

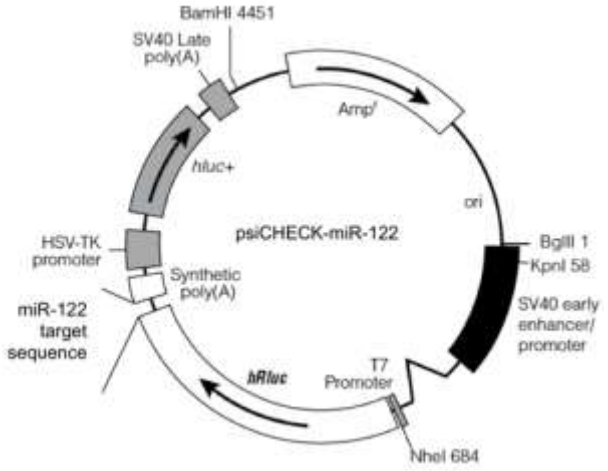

Figure 7-1 psiCHECK-miR122 plasmid map

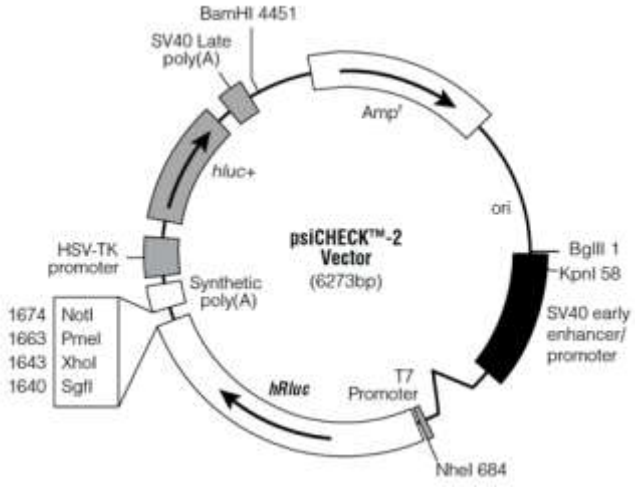

Figure 7-2 psiCHECK-empty plasmid map

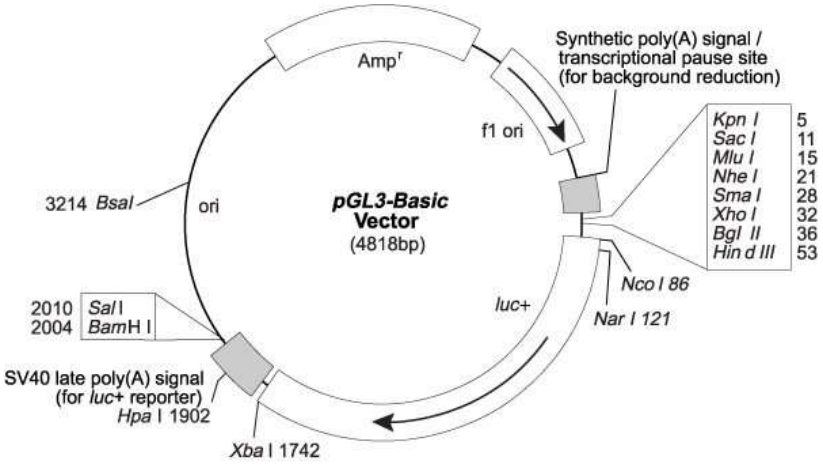

Figure 7-3 pGL3-basic plasmid map

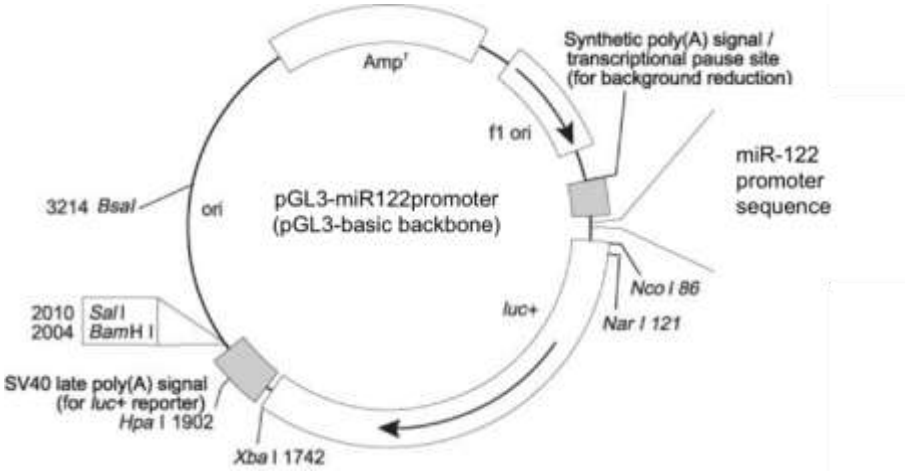

Figure 7-4 pGL3-miR122 promoter plasmid map

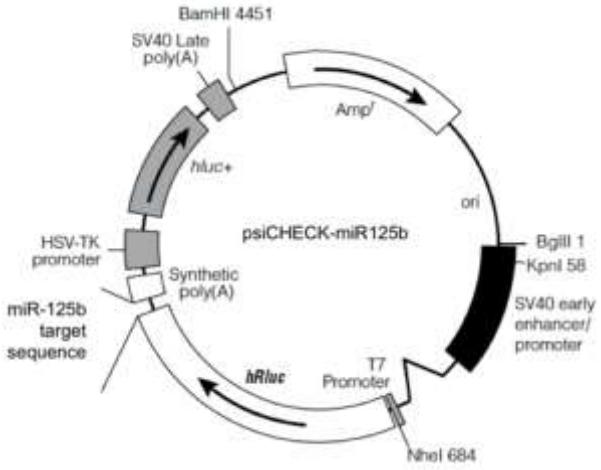

Figure 7-5 psiCHECK-miR125b plasmid map

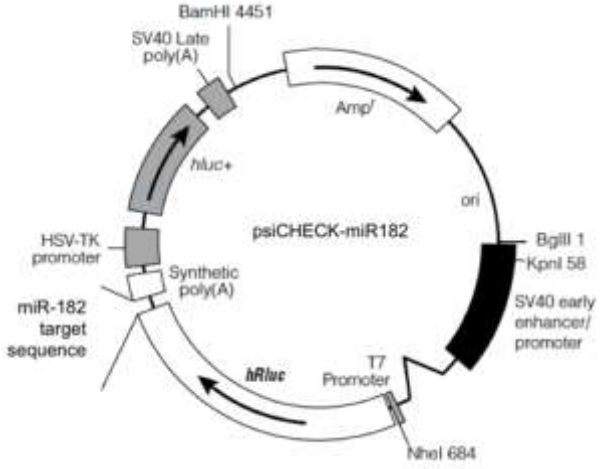

Figure 7-6 psiCHECK-miR182 plasmid map

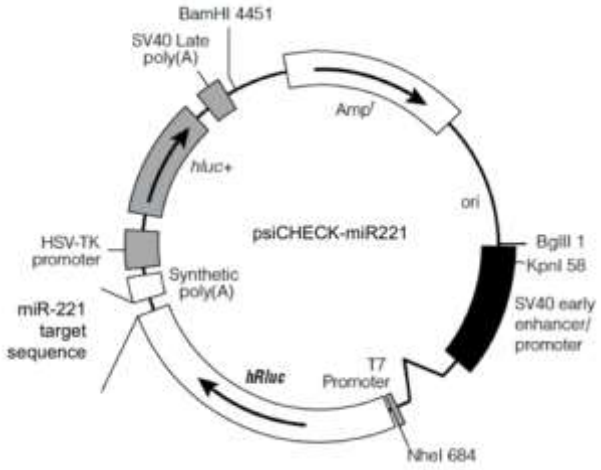

Figure 7-7 psiCHECK-miR221 plasmid map

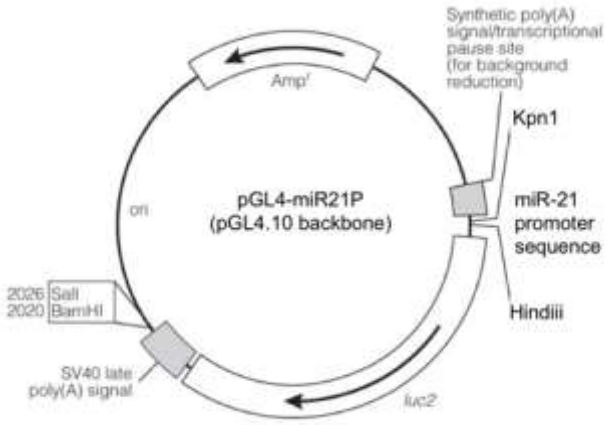

Figure 7-8 pGL4-miR21promoter plasmid map

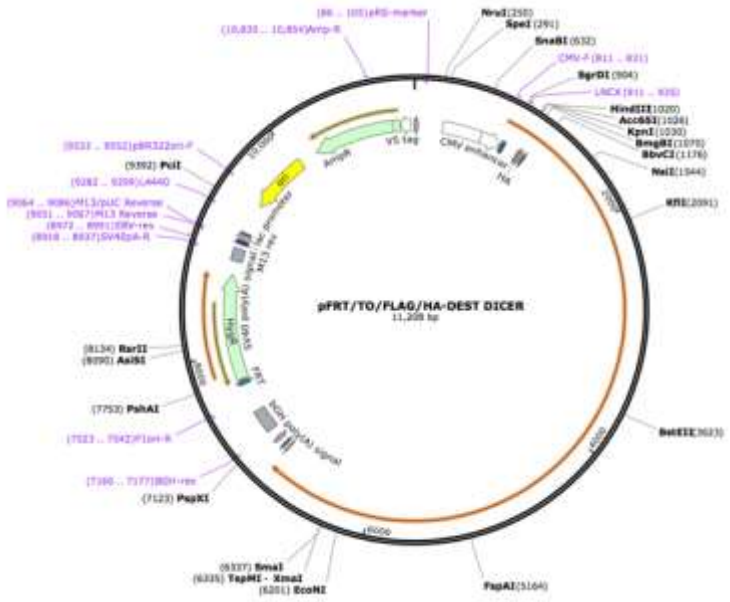

Figure 7-9 pFRT/TO/FLAG/HA-DEST/DICER plasmid map

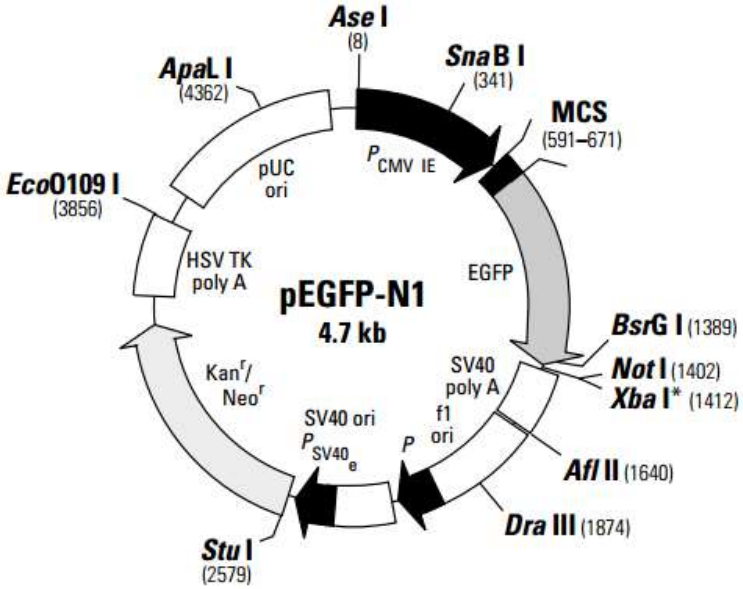

Figure 7-10 pEGFP-N1 plasmid map

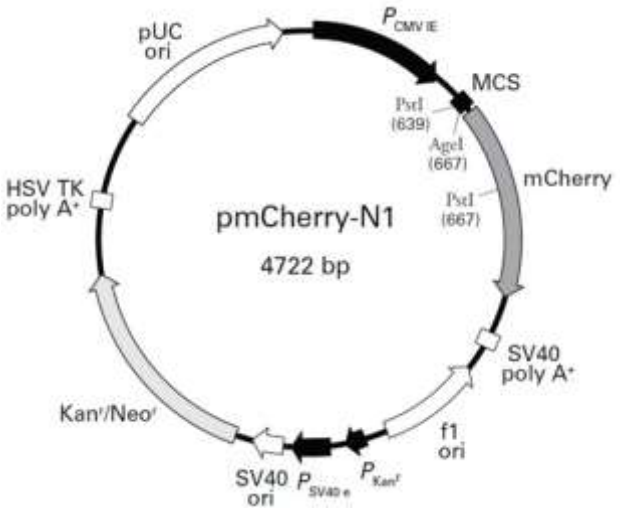

Figure 7-11 pmCherry-N1 plasmid map

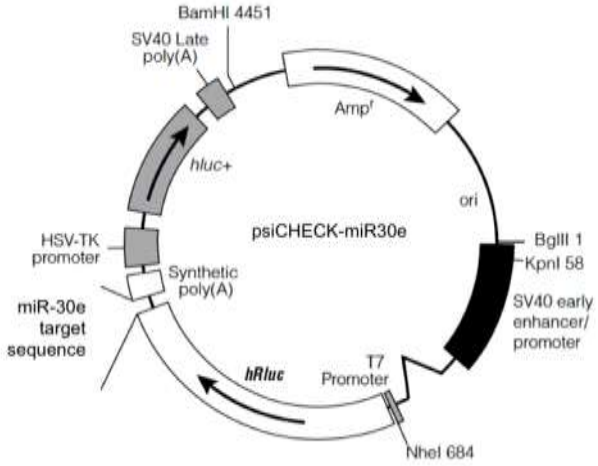

Figure 7-12 psiCHECK-miR30e plasmid map

Appendix A List of Buffer Recipes

10x Phosphate buffered saline (PBS; 500 ml):

- 40 g of sodium chloride
- 1 g of potassium chloride
- 7.2 g of sodium phosphate (dibasic)
- 1.2 g of potassium phosphate (monobasic)

All solids were combined in a 500 ml glass bottle and 500 ml of MilliQ purified water was added. The pH was adjusted to 7.4 ± 0.2 and the solution was autoclaved to sterilize. The buffer was stored at room temperature and diluted to 1x in MilliQ purified water prior to use.

10x Tris-buffered saline (TBS; 1 L):

- 87.6 g of sodium chloride
- 12.1 g of Tris-HCl

All solids were combined in a 1 L glass bottle and 1 L of MilliQ purified water was added. The pH was adjusted to 7.6 ± 0.2. The buffer was stored at room temperature.

Tris-buffered saline with Tween-20 (TBST; 1 L):

- 100 ml of TBS (10x)
- 1 ml of Tween-20

Solutions were combined in a 1 L glass bottle and 900 ml of MilliQ purified water was added. The buffer was stored at room temperature.

10x Western blot transfer buffer (1 L):

- 30.3 g of Tris-HCl
- 144 g of glycine

The solids were combined in a 1 L glass bottle and 1 L of MilliQ purified water was added. The buffer was stored at 4 °C.

Western blot transfer buffer (1 L):

- 100 ml of western blot transfer buffer (10x)
- 200 ml of methanol
- 0.5 g of sodium dodecyl sulfate (SDS)

Solutions were combined with SDS in a 1 L glass bottle and 700 ml of MilliQ purified water was added. The buffer was mixed by gentle inversion and sonication to avoid producing bubbles and was stored at 4 °C.

10x SDS-PAGE running buffer (500 ml):

- 15 g of Tris-HCl
- 72 g of glycine
- 10 g of sodium dodecyl sulfate

All solids were combined in a 500 ml glass bottle and 500 ml of MilliQ purified water was added. The buffer was mixed by gentle inversion and sonication to avoid producing bubbles and was stored at room temperature. SDS-PAGE running buffer was diluted to 1x in MilliQ purified water prior to use and was reused up to 5 times.

4x SDS-PAGE loading dye (Laemmli buffer; 10 ml):

- 2 ml of Tris-HCl (1 M; pH 6.8)
- 0.8 g of sodium dodecyl sulfate
- 4 ml of glycerol
- 8 mg of bromophenol blue

All solids were combined in a 15 ml conical tube and 10 ml of MilliQ purified water was added. The buffer was mixed by gentle inversion and sonication to avoid producing bubbles and was stored at room temperature. Prior to use, 900 µl of SDS-PAGE loading dye was combined with 100 µl of β-mercaptoethanol, then diluted to 1x in cell lysate.

1x Radioimmunoprecipitation assay buffer (RIPA; 50 ml):

- 0.303 g of Tris-HCl (pH 8.0)
- 0.438 g of sodium chloride
- 50 µl of Triton X-100
- 0.05 g of sodium dodecyl sulfate

All solids were combined in a 50 ml conical tube and 50 ml of MilliQ purified water was added. The solution was mixed by inversion to prevent bubbles and stored at room temperature. The buffer was combined with 100x Halt protease inhibitor cocktail (Thermo-Fisher Scientific; 1x [final]) prior to use.

10x Tris-ethylenediaminetetraacetic acid magnesium chloride buffer (TE/Mg^{2+}; 50 ml):

- 0.605 g of Tris-HCl (pH 8.0)
- 1.46 g of (ethylenediaminetetraacetic acid) EDTA

- 0.595 g of magnesium chloride

All solids were combined in a 50 ml conical tube and 50 ml of MilliQ purified water was added. The solution was mixed by inversion and stored at room temperature. The buffer was diluted to 1x in MilliQ purified water prior to use.

10x Tris-boric acid EDTA buffer (TBE; 500 ml):

- 54 g of Tris-HCl
- 27.5 g of boric acid
- 4.65 g of EDTA

All solids were combined in a 500 ml glass bottle and 50 ml of MilliQ purified water was added. The solution was mixed by inversion and the pH was adjusted to 8.3 ± 0.2. The buffer was stored at room temperature stored. The buffer was diluted to 1x in MilliQ purified water prior to use.

Appendix B List of Antibodies and Dilutions

anti-Flag (mouse monoclonal)	Proteintech (catalog# 66008-3lg; 1:1000 dilution)
anti-HA (rabbit monoclonal)	Cell Signaling Technology (catalog# 3724S; 1:1000 dilution)
anti-E-cadherin (rabbit monoclonal)	Cell Signaling Technology (catalog# 3195S; 1:5000 dilution)
anti-GAPDH (rabbit monoclonal)	Cell Signaling Technology (catalog# 2118S; 1:5000 dilution)
anti-CAT1 (rabbit polyclonal)	Abcam (catalog# ab37588; 1:1000 dilution)
anti-β tubulin (mouse (monoclonal)	Santa Cruz (catalog# sc-5274; 1:5000 dilution)

Bibliography

(1) The, E. P. C.; Dunham, I.; Kundaje, A.; Aldred, S. F.; Collins, P. J.; Davis, C. A.; Doyle, F.; Epstein, C. B.; Frietze, S.; Harrow, J.; et al.; An integrated encyclopedia of DNA elements in the human genome. *Nature* **2012,** *489*, 57.

(2) Djebali, S.; Davis, C. A.; Merkel, A.; Dobin, A.; Lassmann, T.; Mortazavi, A.; Tanzer, A.; Lagarde, J.; Lin, W.; Schlesinger, F.; et al.; Landscape of transcription in human cells. *Nature* **2012,** *489*, 101.

(3) Cheng, J.; Kapranov, P.; Drenkow, J.; Dike, S.; Brubaker, S.; Patel, S.; Long, J.; Stern, D.; Tammana, H.; Helt, G.; et al.; Transcriptional Maps of 10 Human Chromosomes at 5-Nucleotide Resolution. *Science* **2005,** *308* (5725), 1149-1154.

(4) Boland, C. R. Non-coding RNA: It's Not Junk. *Dig. Dis. Sci.* **2017,** *62* (11), 3260-3260.

(5) Anastasiadou, E.; Jacob, L. S.; Slack, F. J. Non-coding RNA networks in cancer. *Nat. Rev. Cancer* **2017,** *18*, 5.

(6) Carthew, R. W. Gene regulation by microRNAs. *Curr. Opin. Genet. Dev.* **2006,** *16* (2), 203-208.

(7) Lee, R. C.; Feinbaum, R. L.; Ambros, V. The C. elegans heterochronic gene lin-4 encodes small RNAs with antisense complementarity to lin-14. *Cell* **1993,** *75* (5), 843-854.

(8) Wightman, B.; Ha, I.; Ruvkun, G. Posttranscriptional regulation of the heterochronic gene lin-14 by lin-4 mediates temporal pattern formation in C. elegans. *Cell* **1993,** *75* (5), 855-862.

(9) Pasquinelli, A. E.; Reinhart, B. J.; Slack, F.; Martindale, M. Q.; Kuroda, M. I.; Maller, B.; Hayward, D. C.; Ball, E. E.; Degnan, B.; Muller, P.; et al.; Conservation of the sequence and temporal expression of let-7 heterochronic regulatory RNA. *Nature* **2000,** *408* (6808), 86-89.

(10) Almeida, M. I.; Reis, R. M.; Calin, G. A. MicroRNA history: Discovery, recent applications, and next frontiers. *Mutat. Res.* **2011,** *717* (1), 1-8.

(11) Kozomara, A.; Griffiths-Jones, S. miRBase: annotating high confidence microRNAs using deep sequencing data. *Nucleic Acids Res.* **2014,** *42* (Database issue), D68-D73.

(12) Hafner, M.; Landthaler, M.; Burger, L.; Khorshid, M.; Hausser, J.; Berninger, P.; Rothballer, A.; Ascano, M.; Jungkamp, A.-C.; Munschauer, M.; et al.; Transcriptome-wide Identification of RNA-Binding Protein and MicroRNA Target Sites by PAR-CLIP. *Cell* **2010,** *141* (1), 129-141.

(13) Paul, P.; Chakraborty, A.; Sarkar, D.; Langthasa, M.; Rahman, M.; Bari, M.; Singha, R. S.; Malakar, A. K.; Chakraborty, S. Interplay between miRNAs and human diseases. *J. Cell Physiol.* **2018,** *233* (3), 2007-2018.

(14) Pritchard, C. C.; Cheng, H. H.; Tewari, M. MicroRNA profiling: approaches and considerations. *Nat. Rev. Genet.* **2012,** *13* (5), 358-369.

(15) O'Brien, J.; Hayder, H.; Zayed, Y.; Peng, C. Overview of MicroRNA Biogenesis, Mechanisms of Actions, and Circulation. *Front. Endocrinol.* **2018,** *9*, 402-402.

(16) Alarcón, C. R.; Lee, H.; Goodarzi, H.; Halberg, N.; Tavazoie, S. F. N6-methyladenosine marks primary microRNAs for processing. *Nature* **2015,** *519* (7544), 482-485.

(17) Krol, J.; Sobczak, K.; Wilczynska, U.; Drath, M.; Jasinska, A.; Kaczynska, D.; Krzyzosiak, W. J. J. J. o. B. C. Structural features of microRNA (miRNA) precursors and their relevance to miRNA biogenesis and small interfering RNA/short hairpin RNA design. *J. Biol. Chem.* **2004,** *279* (40), 42230-42239.

(18) Park, J.-E.; Heo, I.; Tian, Y.; Simanshu, D. K.; Chang, H.; Jee, D.; Patel, D. J.; Kim, V. N. Dicer recognizes the 5' end of RNA for efficient and accurate processing. *Nature* **2011,** *475* (7355), 201-205.

(19) Okada, C.; Yamashita, E.; Lee, S. J.; Shibata, S.; Katahira, J.; Nakagawa, A.; Yoneda, Y.; Tsukihara, T. A High-Resolution Structure of the Pre-microRNA Nuclear Export Machinery. *Science* **2009,** *326* (5957), 1275-1279.

(20) Fareh, M.; Yeom, K.-H.; Haagsma, A. C.; Chauhan, S.; Heo, I.; Joo, C. TRBP ensures efficient Dicer processing of precursor microRNA in RNA-crowded environments. *Nat. Commun.* **2016,** *7*, 13694-13694.

(21) Wilson, R. C.; Tambe, A.; Kidwell, M. A.; Noland, C. L.; Schneider, C. P.; Doudna, J. A. Dicer-TRBP complex formation ensures accurate mammalian microRNA biogenesis. *Mol. Cell* **2015,** *57* (3), 397-407.

(22) Chendrimada, T. P.; Gregory, R. I.; Kumaraswamy, E.; Norman, J.; Cooch, N.; Nishikura, K.; Shiekhattar, R. TRBP recruits the Dicer complex to Ago2 for microRNA processing and gene silencing. *Nature* **2005,** *436* (7051), 740-744.

(23) MacRae, I. J.; Ma, E.; Zhou, M.; Robinson, C. V.; Doudna, J. In vitro reconstitution of the human RISC-loading complex. *Proc. Natl. Acad. Sci. U.S.A.* **2008,** *105* (2), 512-517.

(24) Herrera-Carrillo, E.; Berkhout, B. Dicer-independent processing of small RNA duplexes: mechanistic insights and applications. *Nucleic Acids Res.* **2017,** *45* (18), 10369-10379.

(25) Nakanishi, K. Anatomy of RISC: how do small RNAs and chaperones activate Argonaute proteins? *Wiley Interdiscip. Rev. RNA* **2016,** *7* (5), 637-660.

(26) Pratt, A. J.; MacRae, I. The RNA-induced silencing complex: a versatile gene-silencing machine. *J. Biol. Chem.* **2009,** *284* (27), 17897-17901.

(27) Chi, S. W.; Hannon, G. J.; Darnell, R. B. An alternative mode of microRNA target recognition. *Nat. Struct. Mol. Biol.* **2012,** *19*, 321.

(28) Seok, H.; Ham, J.; Jang, E.-S.; Chi, S. W. MicroRNA Target Recognition: Insights from Transcriptome-Wide Non-Canonical Interactions. *Mol. Cells* **2016,** *39* (5), 375-381.

(29) Gu, W.; Xu, Y.; Xie, X.; Wang, T.; Ko, J.-H.; Zhou, T. The role of RNA structure at 5' untranslated region in microRNA-mediated gene regulation. *RNA* **2014,** *20* (9), 1369-1375.

(30) Brümmer, A.; Hausser, J. MicroRNA binding sites in the coding region of mRNAs: Extending the repertoire of post-transcriptional gene regulation. **2014,** *36* (6), 617-626.

(31) Fabian, M. R.; Sonenberg, N. The mechanics of miRNA-mediated gene silencing: a look under the hood of miRISC. *Nat. Struct. Mol. Biol.* **2012,** *19*, 586.

(32) Meijer, H. A.; Kong, Y. W.; Lu, W. T.; Wilczynska, A.; Spriggs, R. V.; Robinson, S. W.; Godfrey, J. D.; Willis, A. E.; Bushell, M. Translational Repression and eIF4A2 Activity Are Critical for MicroRNA-Mediated Gene Regulation. *Science* **2013,** *340* (6128), 82-85.

(33) Höck, J.; Weinmann, L.; Ender, C.; Rüdel, S.; Kremmer, E.; Raabe, M.; Urlaub, H.; Meister, G. Proteomic and functional analysis of Argonaute-containing mRNA-protein complexes in human cells. *EMBO Rep.* **2007,** *8* (11), 1052-1060.

(34) Liu, J.; Carmell, M. A.; Rivas, F. V.; Marsden, C. G.; Thomson, J. M.; Song, J.-J.; Hammond, S. M.; Joshua-Tor, L.; Hannon, G. J. Argonaute2 Is the Catalytic Engine of Mammalian RNAi. *Science* **2004,** *305* (5689), 1437-1441.

(35) van den Berg, A.; Mols, J.; Han, J. RISC-target interaction: cleavage and translational suppression. *Biochim. Biophys. Acta.* **2008,** *1779* (11), 668-677.

(36) Valencia-Sanchez, M. A.; Liu, J.; Hannon, G. J.; Parker, R. Control of translation and mRNA degradation by miRNAs and siRNAs. *Genes Dev.* **2006,** *20* (5), 515-524.

(37) Djuranovic, S.; Nahvi, A.; Green, R. miRNA-mediated gene silencing by translational repression followed by mRNA deadenylation and decay. *Science* **2012,** *336* (6078), 237-240.

(38) Bazzini, A. A.; Lee, M. T.; Giraldez, A. J. Ribosome profiling shows that miR-430 reduces translation before causing mRNA decay in zebrafish. *Science* **2012,** *336* (6078), 233-237.

(39) Ingolia, N. T.; Ghaemmaghami, S.; Newman, J. R. S.; Weissman, J. S. Genome-wide analysis in vivo of translation with nucleotide resolution using ribosome profiling. *Science* **2009,** *324* (5924), 218-223.

(40) Kim, D. H.; Saetrom, P.; Snøve, O., Jr.; Rossi, J. J. MicroRNA-directed transcriptional gene silencing in mammalian cells. *Proc. Natl. Acad. Sci. U.S.A.* **2008,** *105* (42), 16230-16235.

(41) Tan, Y.; Zhang, B.; Wu, T.; Skogerbø, G.; Zhu, X.; Guo, X.; He, S.; Chen, R. Transcriptional inhibiton of Hoxd4 expression by miRNA-10a in human breast cancer cells. *BMC Mol. Biol.* **2009,** *10*, 12-12.

(42) Huang, V.; Place, R. F.; Portnoy, V.; Wang, J.; Qi, Z.; Jia, Z.; Yu, A.; Shuman, M.; Yu, J.; Li, L.-C. Upregulation of Cyclin B1 by miRNA and its implications in cancer. *Nucleic Acids Res.* **2012,** *40* (4), 1695-1707.

(43) Matsui, M.; Chu, Y.; Zhang, H.; Gagnon, K. T.; Shaikh, S.; Kuchimanchi, S.; Manoharan, M.; Corey, D. R.; Janowski, B. A. Promoter RNA links transcriptional regulation of inflammatory pathway genes. *Nucleic Acids Res.* **2013,** *41* (22), 10086-10109.

(44) Modarresi, F.; Faghihi, M. A.; Lopez-Toledano, M. A.; Fatemi, R. P.; Magistri, M.; Brothers, S. P.; van der Brug, M. P.; Wahlestedt, C. Inhibition of natural antisense transcripts in vivo results in gene-specific transcriptional upregulation. *Nat. Biotechnol.* **2012,** *30* (5), 453-459.

(45) Morris, K. V.; Santoso, S.; Turner, A.-M.; Pastori, C.; Hawkins, P. G. Bidirectional transcription directs both transcriptional gene activation and suppression in human cells. *PLoS Genet.* **2008,** *4* (11), e1000258-e1000258.

(46) Ha, M.; Kim, V. N. Regulation of microRNA biogenesis. *Nat. Rev. Mol. Cell Biol.* **2014,** *15*, 509.

(47) Guess, M. G.; Barthel, K. K. B.; Harrison, B. C.; Leinwand, L. A. miR-30 Family microRNAs Regulate Myogenic Differentiation and Provide Negative Feedback on the microRNA Pathway. *PLoS One* **2015,** *10* (2), e0118229.

(48) Zhang, Y.; Yun, Z.; Gong, L.; Qu, H.; Duan, X.; Jiang, Y.; Zhu, H. Comparison of miRNA Evolution and Function in Plants and Animals. *Microrna* **2018,** *7* (1), 4-10.

(49) Ludwig, N.; Leidinger, P.; Becker, K.; Backes, C.; Fehlmann, T.; Pallasch, C.; Rheinheimer, S.; Meder, B.; Stähler, C.; Meese, E.; et al.; Distribution of miRNA expression across human tissues. *Nucleic Acids Res.* **2016,** *44* (8), 3865-3877.

(50) Ninova, M.; Ronshaugen, M.; Griffiths-Jones, S. Conserved temporal patterns of microRNA expression in Drosophila support a developmental hourglass model. *Genome Biol. Evol.* **2014,** *6* (9), 2459-2467.

(51) Miska, E. A.; Alvarez-Saavedra, E.; Townsend, M.; Yoshii, A.; Šestan, N.; Rakic, P.; Constantine-Paton, M.; Horvitz, H. R. Microarray analysis of microRNA expression in the developing mammalian brain. *Genome Biol.* **2004,** *5* (9), R68.

(52) Wienholds, E.; Kloosterman, W. P.; Miska, E.; Alvarez-Saavedra, E.; Berezikov, E.; de Bruijn, E.; Horvitz, H. R.; Kauppinen, S.; Plasterk, R. H. A. MicroRNA Expression in Zebrafish Embryonic Development. *Science* **2005,** *309* (5732), 310-311.

(53) Rupaimoole, R.; Slack, F. J. MicroRNA therapeutics: towards a new era for the management of cancer and other diseases. *Nat. Rev. Drug Discov.* **2017,** *16*, 203.

(54) Eulalio, A.; Huntzinger, E.; Izaurralde, E. Getting to the Root of miRNA-Mediated Gene Silencing. *Cell* **2008,** *132* (1), 9-14.

(55) Calin, G. A.; Dumitru, C. D.; Shimizu, M.; Bichi, R.; Zupo, S.; Noch, E.; Aldler, H.; Rattan, S.; Keating, M.; Rai, K.; et al.; Frequent deletions and down-regulation of micro- RNA genes miR15 and miR16 at 13q14 in chronic lymphocytic leukemia. *Proc. Natl. Acad. Sci. U.S.A.* **2002,** *99* (24), 15524-15529.

(56) Cimmino, A.; Calin, G. A.; Fabbri, M.; Iorio, M. V.; Ferracin, M.; Shimizu, M.; Wojcik, S. E.; Aqeilan, R. I.; Zupo, S.; Dono, M.; et al.; miR-15 and miR-16 induce apoptosis by targeting BCL2. *Proc. Natl. Acad. Sci. U.S.A.* **2005,** *102* (39), 13944-13949.

(57) He, L.; Thomson, J. M.; Hemann, M. T.; Hernando-Monge, E.; Mu, D.; Goodson, S.; Powers, S.; Cordon-Cardo, C.; Lowe, S. W.; Hannon, G. J.; et al.; A microRNA polycistron as a potential human oncogene. *Nature* **2005,** *435*, 828.

(58) O'Donnell, K. A.; Wentzel, E. A.; Zeller, K. I.; Dang, C. V.; Mendell, J. T. c-Myc-regulated microRNAs modulate E2F1 expression. *Nature* **2005,** *435*, 839.

(59) Calin, G. A.; Sevignani, C.; Dumitru, C. D.; Hyslop, T.; Noch, E.; Yendamuri, S.; Shimizu, M.; Rattan, S.; Bullrich, F.; Negrini, M.; et al.; Human microRNA genes are frequently located at fragile sites and genomic regions involved in cancers. *Proc. Natl. Acad. Sci. U.S.A.* **2004,** *101* (9), 2999-3004.

(60) Chen, X.; Ba, Y.; Ma, L.; Cai, X.; Yin, Y.; Wang, K.; Guo, J.; Zhang, Y.; Chen, J.; Guo, X.; et al.; Characterization of microRNAs in serum: a novel class of biomarkers for diagnosis of cancer and other diseases. *Cell Res.* **2008,** *18*, 997.

(61) Mitchell, P. S.; Parkin, R. K.; Kroh, E. M.; Fritz, B. R.; Wyman, S. K.; Pogosova-Agadjanyan, E. L.; Peterson, A.; Noteboom, J.; O'Briant, K. C.; Allen, A.; et al.; Circulating microRNAs as stable blood-based markers for cancer detection. *Proc. Natl. Acad. Sci. U.S.A.* **2008,** *105* (30), 10513-10518.

(62) Chim, S. S. C.; Shing, T. K. F.; Hung, E. C. W.; Leung, T.-y.; Lau, T.-k.; Chiu, R. W. K.; Dennis Lo, Y. M. Detection and Characterization of Placental MicroRNAs in Maternal Plasma. *Clin. Chem.* **2008,** *54* (3), 482-490.

(63) Lawrie, C. H.; Gal, S.; Dunlop, H. M.; Pushkaran, B.; Liggins, A. P.; Pulford, K.; Banham, A. H.; Pezzella, F.; Boultwood, J.; Wainscoat, J. S.; et al.; Detection of elevated levels of tumour-associated microRNAs in serum of patients with diffuse large B-cell lymphoma. *Br. J. Haematol.* **2008,** *141* (5), 672-675.

(64) Park, N. J.; Zhou, H.; Elashoff, D.; Henson, B. S.; Kastratovic, D. A.; Abemayor, E.; Wong, D. T. Salivary microRNA: Discovery, Characterization, and Clinical Utility for Oral Cancer Detection. *Clin. Cancer Res.* **2009,** *15* (17), 5473-5477.

(65) Hanke, M.; Hoefig, K.; Merz, H.; Feller, A. C.; Kausch, I.; Jocham, D.; Warnecke, J. M.; Sczakiel, G. A robust methodology to study urine microRNA as tumor marker: microRNA-126 and microRNA-182 are related to urinary bladder cancer. *Urol. Oncol.* **2010,** *28* (6), 655-661.

(66) Kosaka, N.; Izumi, H.; Sekine, K.; Ochiya, T. microRNA as a new immune-regulatory agent in breast milk. *Silence* **2010,** *1* (1), 7.

(67) Weber, J. A.; Baxter, D. H.; Zhang, S.; Huang, D. Y.; How Huang, K.; Jen Lee, M.; Galas, D. J.; Wang, K. The MicroRNA Spectrum in 12 Body Fluids. *Clin. Chem.* **2010,** *56* (11), 1733-1741.

(68) Iftikhar, H.; Carney, G. E. Evidence and potential in vivo functions for biofluid miRNAs: From expression profiling to functional testing. *Bioessays* **2016,** *38* (4), 367-378.

(69) Gallo, A.; Tandon, M.; Alevizos, I.; Illei, G. G. The majority of microRNAs detectable in serum and saliva is concentrated in exosomes. *PloS One* **2012,** *7* (3), e30679-e30679.

(70) Turchinovich, A.; Weiz, L.; Langheinz, A.; Burwinkel, B. Characterization of extracellular circulating microRNA. *Nucleic Acids Res.* **2011,** *39* (16), 7223-7233.

(71) Arroyo, J. D.; Chevillet, J. R.; Kroh, E. M.; Ruf, I. K.; Pritchard, C. C.; Gibson, D. F.; Mitchell, P. S.; Bennett, C. F.; Pogosova-Agadjanyan, E. L.; Stirewalt, D. L.; et al.; Argonaute2 complexes carry a population of circulating microRNAs independent of vesicles in human plasma. *Proc. Natl. Acad. Sci. U.S.A.* **2011,** *108* (12), 5003-5008.

(72) Valadi, H.; Ekström, K.; Bossios, A.; Sjöstrand, M.; Lee, J. J.; Lötvall, J. O. Exosome-mediated transfer of mRNAs and microRNAs is a novel mechanism of genetic exchange between cells. *Nat. Cell. Biol.* **2007,** *9*, 654.

(73) Skog, J.; Würdinger, T.; van Rijn, S.; Meijer, D. H.; Gainche, L.; Sena-Esteves, M.; Curry, W. T., Jr.; Carter, B. S.; Krichevsky, A. M.; Breakefield, X. O. Glioblastoma microvesicles transport RNA and proteins that promote tumour growth and provide diagnostic biomarkers. *Nat. Cell. Biol.* **2008,** *10* (12), 1470-1476.

(74) Collino, F.; Deregibus, M. C.; Bruno, S.; Sterpone, L.; Aghemo, G.; Viltono, L.; Tetta, C.; Camussi, G. Microvesicles derived from adult human bone marrow and tissue specific mesenchymal stem cells shuttle selected pattern of miRNAs. *PloS One* **2010,** *5* (7), e11803-e11803.

(75) Pigati, L.; Yaddanapudi, S. C. S.; Iyengar, R.; Kim, D.-J.; Hearn, S. A.; Danforth, D.; Hastings, M. L.; Duelli, D. M. Selective release of microRNA species from normal and malignant mammary epithelial cells. *PloS One* **2010,** *5* (10), e13515-e13515.

(76) Mittelbrunn, M.; Gutiérrez-Vázquez, C.; Villarroya-Beltri, C.; González, S.; Sánchez-Cabo, F.; González, M. Á.; Bernad, A.; Sánchez-Madrid, F. Unidirectional transfer of microRNA-loaded exosomes from T cells to antigen-presenting cells. *Nature Commun.* **2011,** *2*, 282-282.

(77) Turchinovich, A.; Samatov, T. R.; Tonevitsky, A. G.; Burwinkel, B. Circulating miRNAs: cell-cell communication function? *Front. Genet.* **2013,** *4*, 119-119.

(78) Cheng, G. Circulating miRNAs: Roles in cancer diagnosis, prognosis and therapy. *Adv. Drug Deliv. Rev.* **2015,** *81*, 75-93.

(79) Joglekar, M. V.; Parekh, V. S.; Mehta, S.; Bhonde, R. R.; Hardikar, A. A. MicroRNA profiling of developing and regenerating pancreas reveal post-transcriptional regulation of neurogenin3. *Dev. Biol.* **2007,** *311* (2), 603-612.

(80) Baroukh, N.; Ravier, M. A.; Loder, M. K.; Hill, E. V.; Bounacer, A.; Scharfmann, R.; Rutter, G. A.; Van Obberghen, E. MicroRNA-124a regulates Foxa2 expression and intracellular signaling in pancreatic β-cells lines. *J. Biol. Chem.* **2007**.

(81) Kloosterman, W. P.; Lagendijk, A. K.; Ketting, R. F.; Moulton, J. D.; Plasterk, R. H. A. Targeted Inhibition of miRNA Maturation with Morpholinos Reveals a Role for miR-375 in Pancreatic Islet Development. *PLoS Biol.* **2007,** *5* (8), e203.

(82) Poy, M. N.; Hausser, J.; Trajkovski, M.; Braun, M.; Collins, S.; Rorsman, P.; Zavolan, M.; Stoffel, M. miR-375 maintains normal pancreatic α- and β-cell mass. *Proc. Natl. Acad. Sci. U.S.A.* **2009,** *106* (14), 5813-5818.

(83) Hennessy, E.; Clynes, M.; Jeppesen, P. B.; O'Driscoll, L. Identification of microRNAs with a role in glucose stimulated insulin secretion by expression profiling of MIN6 cells. *Biochem. Biophys. Res. Commun.* **2010,** *396* (2), 457-462.

(84) Rayner, K. J.; Moore, K. J. MicroRNA control of high-density lipoprotein metabolism and function. *Circ. Res.* **2014,** *114* (1), 183-192.

(85) Wilkins, J. T.; Ning, H.; Stone, N. J.; Criqui, M. H.; Zhao, L.; Greenland, P.; Lloyd-Jones, D. M. Coronary heart disease risks associated with high levels of HDL cholesterol. *J. Am. Heart Assoc.* **2014,** *3* (2), e000519-e000519.

(86) Barwari, T.; Joshi, A.; Mayr, M. MicroRNAs in Cardiovascular Disease. *J. Am. Coll. Cardiol.* **2016,** *68* (23), 2577-2584.

(87) Femminella, G. D.; Ferrara, N.; Rengo, G. The emerging role of microRNAs in Alzheimer's disease. *Front. Physiol.* **2015,** *6* (40).

(88) Dehghani, R.; Rahmani, F.; Rezaei, N. MicroRNA in Alzheimer's disease revisited: implications for major neuropathological mechanisms. *Rev. Neurosci.* **2018,** *29* (2), 161-182.

(89) Šimić, G.; Babić Leko, M.; Wray, S.; Harrington, C.; Delalle, I.; Jovanov-Milošević, N.; Bažadona, D.; Buée, L.; de Silva, R.; Di Giovanni, G.; et al.; Tau Protein Hyperphosphorylation and Aggregation in Alzheimer's Disease and Other Tauopathies, and Possible Neuroprotective Strategies. *Biomolecules* **2016,** *6* (1), 6-6.

(90) Paladini, L.; Fabris, L.; Bottai, G.; Raschioni, C.; Calin, G. A.; Santarpia, L. Targeting microRNAs as key modulators of tumor immune response. *J. Exp. Clin. Cancer Res.* **2016,** *35*, 103-103.

(91) Takeuchi, O.; Akira, S. Pattern Recognition Receptors and Inflammation. *Cell* **2010,** *140* (6), 805-820.

(92) Yin, Y.; Cai, X.; Chen, X.; Liang, H.; Zhang, Y.; Li, J.; Wang, Z.; Chen, X.; Zhang, W.; Yokoyama, S.; et al.; Tumor-secreted miR-214 induces regulatory T cells: a major link between immune evasion and tumor growth. *Cell Res.* **2014,** *24* (10), 1164-1180.

(93) Ward-Hartstonge, K. A.; Kemp, R. A. Regulatory T-cell heterogeneity and the cancer immune response. *Clin. Transl. Immunology.* **2017,** *6* (9), e154-e154.

(94) Zhou, X.; Li, X.; Wu, M. miRNAs reshape immunity and inflammatory responses in bacterial infection. *Signal Transduct. Target. Ther.* **2018,** *3* (1), 14.

(95) Watanabe, Y.; Kishi, A.; Yachie, N.; Kanai, A.; Tomita, M. Computational analysis of microRNA-mediated antiviral defense in humans. *FEBS Lett.* **2007,** *581* (24), 4603-4610.

(96) Kitab, B.; Alj, H. S.; Ezzikouri, S.; Benjelloun, S. MicroRNAs as Important Players in Host-hepatitis B Virus Interactions. *J. Clin. Transl. Hepatol.* **2015,** *3* (2), 149-161.

(97) Zhang, G.-l.; Li, Y.-x.; Zheng, S.-q.; Liu, M.; Li, X.; Tang, H. Suppression of hepatitis B virus replication by microRNA-199a-3p and microRNA-210. *Antiviral Res.* **2010,** *88* (2), 169-175.

(98) Venkatakrishnan, B.; Zlotnick, A. The Structural Biology of Hepatitis B Virus: Form and Function. *Annu. Rev. Virol.* **2016,** *3* (1), 429-451.

(99) Cornberg, M.; Wong, V. W.-S.; Locarnini, S.; Brunetto, M.; Janssen, H. L. A.; Chan, H. L.-Y. The role of quantitative hepatitis B surface antigen revisited. *J. Hepatol.* **2017,** *66* (2), 398-411.

(100) Zeng, F.-R.; Tang, L.-J.; He, Y.; Garcia, R. C. An update on the role of miRNA-155 in pathogenic microbial infections. *Microbes Infect.* **2015,** *17* (9), 613-621.

(101) Lu, F.; Weidmer, A.; Liu, C.-G.; Volinia, S.; Croce, C. M.; Lieberman, P. M. Epstein-Barr virus-induced miR-155 attenuates NF-kappaB signaling and stabilizes latent virus persistence. *J. Virol.* **2008,** *82* (21), 10436-10443.

(102) Pichlmair, A.; Reis e Sousa, C. Innate Recognition of Viruses. *Immunity* **2007,** *27* (3), 370-383.

(103) Pedersen, I. M.; Cheng, G.; Wieland, S.; Volinia, S.; Croce, C. M.; Chisari, F. V.; David, M. Interferon modulation of cellular microRNAs as an antiviral mechanism. *Nature* **2007,** *449* (7164), 919-922.

(104) Wang, J.; Chen, J.; Sen, S. MicroRNA as Biomarkers and Diagnostics. *J. Cell Physiol.* **2016,** *231* (1), 25-30.

(105) Peng, Y.; Croce, C. M. The role of MicroRNAs in human cancer. *Signal Transduction Targeted Ther.* **2016,** *1*, 15004.

(106) Sondka, Z.; Bamford, S.; Cole, C. G.; Ward, S. A.; Dunham, I.; Forbes, S. A. The COSMIC Cancer Gene Census: describing genetic dysfunction across all human cancers. *Nat. Rev. Cancer* **2018,** *18* (11), 696-705.

(107) Yang, Z.; Wu, L.; Wang, A.; Tang, W.; Zhao, Y.; Zhao, H.; Teschendorff, A. E. dbDEMC 2.0: updated database of differentially expressed miRNAs in human cancers. *Nucleic Acids Res.* **2017,** *45* (D1), D812-D818.

(108) Bobbili, M. R.; Mader, R. M.; Grillari, J.; Dellago, H. OncomiR-17-5p: alarm signal in cancer? *Oncotarget* **2017,** *8* (41), 71206-71222.

(109) Svoronos, A. A.; Engelman, D. M.; Slack, F. J. OncomiR or Tumor Suppressor? The Duplicity of MicroRNAs in Cancer. *Cancer Res.* **2016,** *76* (13), 3666-3670.

(110) Gebert, L. F.; MacRae, I. J. Regulation of microRNA function in animals. *Nat. Rev. Mol. Cell Biol.* **2018,** *10*.

(111) Gulyaeva, L. F.; Kushlinskiy, N. E. Regulatory mechanisms of microRNA expression. *J. Transl. Med.* **2016,** *14* (1), 143-143.

(112) Morales, S.; Monzo, M.; Navarro, A. Epigenetic regulation mechanisms of microRNA expression. *Biomol. Concepts* **2017,** *8* (5-6), 203-212.

(113) Bueno, M. J.; Pérez de Castro, I.; Gómez de Cedrón, M.; Santos, J.; Calin, G. A.; Cigudosa, Juan C.; Croce, C. M.; Fernández-Piqueras, J.; Malumbres, M. Genetic and Epigenetic Silencing of MicroRNA-203 Enhances ABL1 and BCR-ABL1 Oncogene Expression. *Cancer Cell* **2008,** *13* (6), 496-506.

(114) Baer, C.; Claus, R.; Plass, C. Genome-Wide Epigenetic Regulation of miRNAs in Cancer. *Cancer Res.* **2013,** *73* (2), 473-477.

(115) Pan, Z.; Zhang, M.; Ma, T.; Xue, Z.-Y.; Li, G.-F.; Hao, L.-Y.; Zhu, L.-J.; Li, Y.-Q.; Ding, H.-L.; Cao, J.-L. Hydroxymethylation of microRNA-365-3p Regulates Nociceptive Behaviors via Kcnh2. *J. Neurosci.* **2016,** *36* (9), 2769-2781.

(116) Haffner, M. C.; Chaux, A.; Meeker, A. K.; Esopi, D. M.; Gerber, J.; Pellakuru, L. G.; Toubaji, A.; Argani, P.; Iacobuzio-Donahue, C.; Nelson, W. G.; et al.; Global 5-hydroxymethylcytosine content is significantly reduced in tissue stem/progenitor cell compartments and in human cancers. *Oncotarget* **2011,** *2* (8), 627-637.

(117) Kudo, Y.; Tateishi, K.; Yamamoto, K.; Yamamoto, S.; Asaoka, Y.; Ijichi, H.; Nagae, G.; Yoshida, H.; Aburatani, H.; Koike, K. Loss of 5-hydroxymethylcytosine is accompanied with malignant cellular transformation. *Cancer Sci.* **2012,** *103* (4), 670-676.

(118) Li, C.-H.; Xiao, Z.; Tong, J. H. M.; To, K.-F.; Fang, X.; Cheng, A. S.; Chen, Y. EZH2 coupled with HOTAIR to silence MicroRNA-34a by the induction of heterochromatin formation in human pancreatic ductal adenocarcinoma. *Int. J. Cancer* **2017,** *140* (1), 120-129.

(119) Chang, T.-C.; Yu, D.; Lee, Y.-S.; Wentzel, E. A.; Arking, D. E.; West, K. M.; Dang, C. V.; Thomas-Tikhonenko, A.; Mendell, J. T. Widespread microRNA repression by Myc contributes to tumorigenesis. *Nat. Genet.* **2008,** *40* (1), 43-50.

(120) Baugh, E. H.; Ke, H.; Levine, A. J.; Bonneau, R. A.; Chan, C. S. Why are there hotspot mutations in the TP53 gene in human cancers? *Cell Death Differ.* **2017,** *25*, 154.

(121) Raver-Shapira, N.; Marciano, E.; Meiri, E.; Spector, Y.; Rosenfeld, N.; Moskovits, N.; Bentwich, Z.; Oren, M. Transcriptional Activation of miR-34a Contributes to p53-Mediated Apoptosis. *Mol. Cell* **2007,** *26* (5), 731-743.

(122) Chang, T.-C.; Wentzel, E. A.; Kent, O. A.; Ramachandran, K.; Mullendore, M.; Lee, K. H.; Feldmann, G.; Yamakuchi, M.; Ferlito, M.; Lowenstein, C. J.; et al.; Transactivation of miR-34a by p53 broadly influences gene expression and promotes apoptosis. *Mol. Cell* **2007,** *26* (5), 745-752.

(123) Yamakuchi, M.; Lowenstein, C. J. MiR-34, SIRT1, and p53: The feedback loop. *Cell Cycle* **2009,** *8* (5), 712-715.

(124) Creugny, A.; Fender, A.; Pfeffer, S. Regulation of primary microRNA processing. *FEBS Lett.* **2018,** *592* (12), 1980-1996.

(125) Yeom, K.-H.; Lee, Y.; Han, J.; Suh, M. R.; Kim, V. N. Characterization of DGCR8/Pasha, the essential cofactor for Drosha in primary miRNA processing. *Nucleic Acids Res.* **2006,** *34* (16), 4622-4629.

(126) Zhang, X.; Li, P.; Lin, J.; Huang, H.; Yin, B.; Zeng, Y. The insertion in the double-stranded RNA binding domain of human Drosha is important for its function. *Biochim. Biophys. Acta. Gene Regul. Mech.* **2017,** *1860* (12), 1179-1188.

(127) Kranick, J. C.; Chadalavada, D. M.; Sahu, D.; Showalter, S. A. Engineering double-stranded RNA binding activity into the Drosha double-stranded RNA binding domain results in a loss of microRNA processing function. *PLoS One* **2017,** *12* (8), e0182445.

(128) Han, J.; Pedersen, J. S.; Kwon, S. C.; Belair, C. D.; Kim, Y.-K.; Yeom, K.-H.; Yang, W.-Y.; Haussler, D.; Blelloch, R.; Kim, V. N. Posttranscriptional crossregulation between Drosha and DGCR8. *Cell* **2009,** *136* (1), 75-84.

(129) Partin, A. C.; Ngo, T. D.; Herrell, E.; Jeong, B.-C.; Hon, G.; Nam, Y. Heme enables proper positioning of Drosha and DGCR8 on primary microRNAs. *Nat. Commun.* **2017,** *8* (1), 1737.

(130) Nguyen, Tuan A.; Jo, Myung H.; Choi, Y.-G.; Park, J.; Kwon, S. C.; Hohng, S.; Kim, V. N.; Woo, J.-S. Functional Anatomy of the Human Microprocessor. *Cell* **2015,** *161* (6), 1374-1387.

(131) Szychot, E.; Apps, J.; Pritchard-Jones, K. Wilms' tumor: biology, diagnosis and treatment. *Transl. Pediatr.* **2014,** *3* (1), 12-24.

(132) Walz, A. L.; Ooms, A.; Gadd, S.; Gerhard, D. S.; Smith, M. A.; Guidry Auvil, J. M.; Meerzaman, D.; Chen, Q.-R.; Hsu, C. H.; Yan, C.; et al.; Recurrent DGCR8, DROSHA, and SIX homeodomain mutations in favorable histology Wilms tumors. *Cancer Cell* **2015,** *27* (2), 286-297.

(133) Liu, H.; Liang, C.; Kollipara, Rahul K.; Matsui, M.; Ke, X.; Jeong, B.-C.; Wang, Z.; Yoo, Kyoung S.; Yadav, Gaya P.; Kinch, Lisa N.; et al.; HP1BP3, a Chromatin Retention Factor for Co-transcriptional MicroRNA Processing. *Mol. Cell* **2016,** *63* (3), 420-432.

(134) Suzuki, H. I.; Young, R. A.; Sharp, P. A. Super-Enhancer-Mediated RNA Processing Revealed by Integrative MicroRNA Network Analysis. *Cell* **2017,** *168* (6), 1000-1014.e15.

(135) Pawlicki, J. M.; Steitz, J. A. Primary microRNA transcript retention at sites of transcription leads to enhanced microRNA production. *J. Cell. Biol.* **2008,** *182* (1), 61-76.

(136) Gromak, N. Intronic microRNAs: a crossroad in gene regulation. *Biochem. Soc. Trans.* **2012,** *40* (4), 759-761.

(137) Janas, M. M.; Khaled, M.; Schubert, S.; Bernstein, J. G.; Golan, D.; Veguilla, R. A.; Fisher, D. E.; Shomron, N.; Levy, C.; Novina, C. D. Feed-Forward Microprocessing and Splicing Activities at a MicroRNA–Containing Intron. *PLoS Genet.* **2011,** *7* (10), e1002330.

(138) Sakamoto, S.; Aoki, K.; Higuchi, T.; Todaka, H.; Morisawa, K.; Tamaki, N.; Hatano, E.; Fukushima, A.; Taniguchi, T.; Agata, Y. The NF90-NF45 complex functions as a negative regulator in the microRNA processing pathway. *Mol. Cell Biol.* **2009,** *29* (13), 3754-3769.

(139) Michlewski, G.; Guil, S.; Semple, C. A.; Cáceres, J. F. Posttranscriptional regulation of miRNAs harboring conserved terminal loops. *Mol. Cell* **2008,** *32* (3), 383-393.

(140) Thomson, J. M.; Newman, M.; Parker, J. S.; Morin-Kensicki, E. M.; Wright, T.; Hammond, S. M. Extensive post-transcriptional regulation of microRNAs and its implications for cancer. *Genes Dev.* **2006,** *20* (16), 2202-2207.

(141) Lau, P.-W.; Guiley, K. Z.; De, N.; Potter, C. S.; Carragher, B.; MacRae, I. J. The molecular architecture of human Dicer. *Nat. Struct. Mol. Biol.* **2012,** *19* (4), 436-440.

(142) Flemr, M.; Malik, R.; Franke, V.; Nejepinska, J.; Sedlacek, R.; Vlahovicek, K.; Svoboda, P. A Retrotransposon-Driven Dicer Isoform Directs Endogenous Small Interfering RNA Production in Mouse Oocytes. *Cell* **2013,** *155* (4), 807-816.

(143) Kurzynska-Kokorniak, A.; Pokornowska, M.; Koralewska, N.; Hoffmann, W.; Bienkowska-Szewczyk, K.; Figlerowicz, M. Revealing a new activity of the human Dicer DUF283 domain in vitro. *Sci. Rep.* **2016,** *6*, 23989-23989.

(144) Song, M.-S.; Rossi, J. J. Molecular mechanisms of Dicer: endonuclease and enzymatic activity. *Biochem. J.* **2017,** *474* (10), 1603-1618.

(145) Paroo, Z.; Ye, X.; Chen, S.; Liu, Q. Phosphorylation of the human microRNA-generating complex mediates MAPK/Erk signaling. *Cell* **2009,** *139* (1), 112-122.

(146) Tokumaru, S.; Suzuki, M.; Yamada, H.; Nagino, M.; Takahashi, T. let-7 regulates Dicer expression and constitutes a negative feedback loop. *Carcinogenesis* **2008,** *29* (11), 2073-2077.

(147) Martello, G.; Rosato, A.; Ferrari, F.; Manfrin, A.; Cordenonsi, M.; Dupont, S.; Enzo, E.; Guzzardo, V.; Rondina, M.; Spruce, T.; et al.; A MicroRNA Targeting Dicer for Metastasis Control. *Cell* **2010,** *141* (7), 1195-1207.

(148) Karube, Y.; Tanaka, H.; Osada, H.; Tomida, S.; Tatematsu, Y.; Yanagisawa, K.; Yatabe, Y.; Takamizawa, J.; Miyoshi, S.; Mitsudomi, T.; et al.; Reduced expression of Dicer associated with poor prognosis in lung cancer patients. *Cancer Sci.* **2005,** *96* (2), 111-115.

(149) Dedes, K. J.; Natrajan, R.; Lambros, M. B.; Geyer, F. C.; Lopez-Garcia, M. A.; Savage, K.; Jones, R. L.; Reis-Filho, J. S. Down-regulation of the miRNA master regulators Drosha and Dicer is associated with specific subgroups of breast cancer. *Eur. J. Cancer* **2011,** *47* (1), 138-150.

(150) Sand, M.; Gambichler, T.; Skrygan, M.; Sand, D.; Scola, N.; Altmeyer, P.; Bechara, F. G. Expression Levels of the microRNA Processing Enzymes Drosha and Dicer in Epithelial Skin Cancer. *Cancer Invest.* **2010,** *28* (6), 649-653.

(151) Merritt, W. M.; Lin, Y. G.; Han, L. Y.; Kamat, A. A.; Spannuth, W. A.; Schmandt, R.; Urbauer, D.; Pennacchio, L. A.; Cheng, J.-F.; Nick, A. M.; et al.; Dicer, Drosha, and outcomes in patients with ovarian cancer. *N. Engl. J. Med.* **2008,** *359* (25), 2641-2650.

(152) Pampalakis, G.; Diamandis, E. P.; Katsaros, D.; Sotiropoulou, G. Down-regulation of dicer expression in ovarian cancer tissues. *Clin. Biochem.* **2010,** *43* (3), 324-327.

(153) Chiosea, S.; Jelezcova, E.; Chandran, U.; Acquafondata, M.; McHale, T.; Sobol, R. W.; Dhir, R. Up-regulation of dicer, a component of the MicroRNA machinery, in prostate adenocarcinoma. *Am. J. Pathol.* **2006,** *169* (5), 1812-1820.

(154) Kaul, D.; Sikand, K. Defective RNA-mediated c-myc gene silencing pathway in Burkitt's lymphoma. *Biochem. Biophys. Res. Commun.* **2004,** *313* (3), 552-554.

(155) Foulkes, W. D.; Priest, J. R.; Duchaine, T. F. DICER1: mutations, microRNAs and mechanisms. *Nat. Rev. Cancer* **2014,** *14*, 662.

(156) Balzeau, J.; Menezes, M. R.; Cao, S.; Hagan, J. P. The LIN28/let-7 Pathway in Cancer. *Front. Genet.* **2017,** *8*, 31-31.

(157) Kawahara, Y.; Mieda-Sato, A. TDP-43 promotes microRNA biogenesis as a component of the Drosha and Dicer complexes. *Proc. Natl. Acad. Sci. U. S. A.* **2012,** *109* (9), 3347-3352.

(158) Treiber, T.; Treiber, N.; Plessmann, U.; Harlander, S.; Daiß, J.-L.; Eichner, N.; Lehmann, G.; Schall, K.; Urlaub, H.; Meister, G. A Compendium of RNA-Binding Proteins that Regulate MicroRNA Biogenesis. *Mol. Cell* **2017,** *66* (2), 270-284.e13.

(159) Melo, S. A.; Moutinho, C.; Ropero, S.; Calin, G. A.; Rossi, S.; Spizzo, R.; Fernandez, A. F.; Davalos, V.; Villanueva, A.; Montoya, G.; et al.; A Genetic Defect in Exportin-5 Traps Precursor MicroRNAs in the Nucleus of Cancer Cells. *Cancer Cell* **2010,** *18* (4), 303-315.

(160) The Cancer Genome Atlas Research, N.; Bell, D.; Berchuck, A.; Birrer, M.; Chien, J.; Cramer, D. W.; Dao, F.; Dhir, R.; DiSaia, P.; Gabra, H.; et al.; Integrated genomic analyses of ovarian carcinoma. *Nature* **2011,** *474*, 609.

(161) The Cancer Genome Atlas Research, N.; McLendon, R.; Friedman, A.; Bigner, D.; Van Meir, E. G.; Brat, D. J.; M. Mastrogianakis, G.; Olson, J. J.; Mikkelsen, T.; Lehman, N.; et al.; Comprehensive genomic characterization defines human glioblastoma genes and core pathways. *Nature* **2008,** *455*, 1061.

(162) Khan, M.; Khan, Z.; Uddin, Y.; Mustafa, S.; Shaukat, I.; Pan, J.; Höti, N. Evaluating the Oncogenic and Tumor Suppressor Role of XPO5 in Different Tissue Tumor Types. *Asian Pac. J. Cancer Prev.* **2018,** *19* (4), 1119-1125.

(163) Shen, J.; Hung, M.-C. Signaling-Mediated Regulation of MicroRNA Processing. *Cancer Res.* **2015,** *75* (5), 783-791.

(164) Qi, H. H.; Ongusaha, P. P.; Myllyharju, J.; Cheng, D.; Pakkanen, O.; Shi, Y.; Lee, S. W.; Peng, J.; Shi, Y. Prolyl 4-hydroxylation regulates Argonaute 2 stability. *Nature* **2008,** *455*, 421.

(165) Wu, C.; So, J.; Davis-Dusenbery, B. N.; Qi, H. H.; Bloch, D. B.; Shi, Y.; Lagna, G.; Hata, A. Hypoxia potentiates microRNA-mediated gene silencing through posttranslational modification of Argonaute2. *Mol. Cell Biol.* **2011,** *31* (23), 4760-4774.

(166) Rybak, A.; Fuchs, H.; Hadian, K.; Smirnova, L.; Wulczyn, E. A.; Michel, G.; Nitsch, R.; Krappmann, D.; Wulczyn, F. G. The let-7 target gene mouse lin-41 is a stem cell specific E3 ubiquitin ligase for the miRNA pathway protein Ago2. *Nat. Cell. Biol.* **2009,** *11*, 1411.

(167) Chang, H.-M.; Martinez, N. J.; Thornton, J. E.; Hagan, J. P.; Nguyen, K. D.; Gregory, R. I. Trim71 cooperates with microRNAs to repress Cdkn1a expression and promote embryonic stem cell proliferation. *Nat. Commun.* **2012,** *3*, 923-923.

(168) Chen, J.; Lai, F.; Niswander, L. The ubiquitin ligase mLin41 temporally promotes neural progenitor cell maintenance through FGF signaling. *Genes Dev.* **2012,** *26* (8), 803-815.

(169) Leung, A. K. L.; Vyas, S.; Rood, J. E.; Bhutkar, A.; Sharp, P. A.; Chang, P. Poly(ADP-ribose) regulates stress responses and microRNA activity in the cytoplasm. *Mol. Cell* **2011,** *42* (4), 489-499.

(170) Rüdel, S.; Wang, Y.; Lenobel, R.; Körner, R.; Hsiao, H.-H.; Urlaub, H.; Patel, D.; Meister, G. Phosphorylation of human Argonaute proteins affects small RNA binding. *Nucleic Acids Res.* **2011,** *39* (6), 2330-2343.

(171) Shen, J.; Xia, W.; Khotskaya, Y. B.; Huo, L.; Nakanishi, K.; Lim, S.-O.; Du, Y.; Wang, Y.; Chang, W.-C.; Chen, C.-H.; et al.; EGFR modulates microRNA maturation in response to hypoxia through phosphorylation of AGO2. *Nature* **2013,** *497* (7449), 383-387.

(172) Huang, J.-T.; Wang, J.; Srivastava, V.; Sen, S.; Liu, S.-M. MicroRNA Machinery Genes as Novel Biomarkers for Cancer. *Front. Oncol.* **2014,** *4* (113).

(173) Yang, W.; Chendrimada, T. P.; Wang, Q.; Higuchi, M.; Seeburg, P. H.; Shiekhattar, R.; Nishikura, K. Modulation of microRNA processing and expression through RNA editing by ADAR deaminases. *Nat. Struct. Mol. Biol.* **2006,** *13* (1), 13-21.

(174) Kawahara, Y.; Zinshteyn, B.; Chendrimada, T. P.; Shiekhattar, R.; Nishikura, K. RNA editing of the microRNA-151 precursor blocks cleavage by the Dicer-TRBP complex. *EMBO Rep.* **2007,** *8* (8), 763-769.

(175) Iizasa, H.; Wulff, B.-E.; Alla, N. R.; Maragkakis, M.; Megraw, M.; Hatzigeorgiou, A.; Iwakiri, D.; Takada, K.; Wiedmer, A.; Showe, L.; et al.; Editing of Epstein-Barr virus-encoded BART6 microRNAs controls their dicer targeting and consequently affects viral latency. *J. Biol. Chem.* **2010,** *285* (43), 33358-33370.

(176) Kawahara, Y.; Zinshteyn, B.; Sethupathy, P.; Iizasa, H.; Hatzigeorgiou, A. G.; Nishikura, K. Redirection of silencing targets by adenosine-to-inosine editing of miRNAs. *Science* **2007,** *315* (5815), 1137-1140.

(177) Nigita, G.; Acunzo, M.; Romano, G.; Veneziano, D.; Laganà, A.; Vitiello, M.; Wernicke, D.; Ferro, A.; Croce, C. M. microRNA editing in seed region aligns with cellular changes in hypoxic conditions. *Nucleic acids research* **2016,** *44* (13), 6298-6308.

(178) Katoh, T.; Sakaguchi, Y.; Miyauchi, K.; Suzuki, T.; Kashiwabara, S.-I.; Baba, T.; Suzuki, T. Selective stabilization of mammalian microRNAs by 3' adenylation mediated by the cytoplasmic poly(A) polymerase GLD-2. *Genes Dev.* **2009,** *23* (4), 433-438.

(179) Burns, D. M.; D'Ambrogio, A.; Nottrott, S.; Richter, J. D. CPEB and two poly(A) polymerases control miR-122 stability and p53 mRNA translation. *Nature* **2011,** *473* (7345), 105-108.

(180) Wyman, S. K.; Knouf, E. C.; Parkin, R. K.; Fritz, B. R.; Lin, D. W.; Dennis, L. M.; Krouse, M. A.; Webster, P. J.; Tewari, M. Post-transcriptional generation of miRNA variants by multiple nucleotidyl transferases contributes to miRNA transcriptome complexity. *Genome Res.* **2011,** *21* (9), 1450-1461.

(181) Krol, J.; Busskamp, V.; Markiewicz, I.; Stadler, M. B.; Ribi, S.; Richter, J.; Duebel, J.; Bicker, S.; Fehling, H. J.; Schübeler, D.; et al.; Characterizing Light-Regulated Retinal MicroRNAs Reveals Rapid Turnover as a Common Property of Neuronal MicroRNAs. *Cell* **2010,** *141* (4), 618-631.

(182) Rüegger, S.; Großhans, H. MicroRNA turnover: when, how, and why. *Trends Biochem. Sci.* **2012,** *37* (10), 436-446.

(183) Shah, M. Y.; Ferrajoli, A.; Sood, A. K.; Lopez-Berestein, G.; Calin, G. A. microRNA Therapeutics in Cancer - An Emerging Concept. *EBioMedicine* **2016,** *12*, 34-42.

(184) Deleavey, Glen F.; Damha, Masad J. Designing Chemically Modified Oligonucleotides for Targeted Gene Silencing. *Chem. Biol.* **2012,** *19* (8), 937-954.

(185) Shen, X.; Corey, D. R. Chemistry, mechanism and clinical status of antisense oligonucleotides and duplex RNAs. *Nucleic Acids Res.* **2018,** *46* (4), 1584-1600.

(186) Hutvágner, G.; Simard, M. J.; Mello, C. C.; Zamore, P. D. Sequence-specific inhibition of small RNA function. *PLoS Biol.* **2004,** *2* (4), E98-E98.

(187) Krützfeldt, J.; Rajewsky, N.; Braich, R.; Rajeev, K. G.; Tuschl, T.; Manoharan, M.; Stoffel, M. Silencing of microRNAs in vivo with 'antagomirs'. *Nature* **2005,** *438*, 685.

(188) Soutschek, J.; Akinc, A.; Bramlage, B.; Charisse, K.; Constien, R.; Donoghue, M.; Elbashir, S.; Geick, A.; Hadwiger, P.; Harborth, J.; et al.; Therapeutic silencing of an endogenous gene by systemic administration of modified siRNAs. *Nature* **2004,** *432*, 173.

(189) Jaroszewski, J. W.; Clausen, V.; Cohen, J. S.; Dahl, O. NMR investigations of duplex stability of phosphorothioate and phosphorodithioate DNA analogues modified in both strands. *Nucleic Acids Res.* **1996,** *24* (5), 829-834.

(190) Iwamoto, N.; Butler, D. C. D.; Svrzikapa, N.; Mohapatra, S.; Zlatev, I.; Sah, D. W. Y.; Meena; Standley, S. M.; Lu, G.; Apponi, L. H.; et al.; Control of phosphorothioate stereochemistry substantially increases the efficacy of antisense oligonucleotides. *Nat. Biotechnol.* **2017,** *35*, 845.

(191) Davis, S.; Lollo, B.; Freier, S.; Esau, C. Improved targeting of miRNA with antisense oligonucleotides. *Nucleic Acids Res.* **2006,** *34* (8), 2294-2304.

(192) Fabani, M. M.; Gait, M. J. miR-122 targeting with LNA/2'-O-methyl oligonucleotide mixmers, peptide nucleic acids (PNA), and PNA-peptide conjugates. *RNA* **2008,** *14* (2), 336-346.

(193) Obad, S.; dos Santos, C. O.; Petri, A.; Heidenblad, M.; Broom, O.; Ruse, C.; Fu, C.; Lindow, M.; Stenvang, J.; Straarup, E. M.; et al.; Silencing of microRNA families by seed-targeting tiny LNAs. *Nat. Genet.* **2011,** *43* (4), 371-378.

(194) Ebert, M. S.; Neilson, J. R.; Sharp, P. A. MicroRNA sponges: competitive inhibitors of small RNAs in mammalian cells. *Nat. Methods* **2007,** *4* (9), 721.

(195) Thomson, D. W.; Dinger, M. E. Endogenous microRNA sponges: evidence and controversy. *Nat. Rev. Genet.* **2016,** *17*, 272.

(196) Wang, Z. The Principles of MiRNA-Masking Antisense Oligonucleotides Technology. In *MicroRNA and Cancer: Methods and Protocols*, Wu, W., Ed. Humana Press: Totowa, NJ, 2011; pp 43-49.

(197) Trang, P.; Wiggins, J. F.; Patrawala, L.; Cheng, A.; Ford, L.; Weidhaas, J. B.; Brown, D.; Bader, A. G.; Slack, F. J. The let-7 microRNA reduces tumor growth in mouse models of lung cancer *Cell Cycle* **2008,** *7* (6), 759-764.

(198) Bonci, D.; Coppola, V.; Musumeci, M.; Addario, A.; Giuffrida, R.; Memeo, L.; D'urso, L.; Pagliuca, A.; Biffoni, M.; Labbaye, C. The miR-15a–miR-16-1 cluster controls prostate cancer by targeting multiple oncogenic activities. *Nat. Med.* **2008,** *14* (11), 1271.

(199) Trang, P.; Medina, P. P.; Wiggins, J. F.; Ruffino, L.; Kelnar, K.; Omotola, M.; Homer, R.; Brown, D.; Bader, A. G.; Weidhaas, J. B. Regression of murine lung tumors by the let-7 microRNA. *Oncogene* **2010,** *29* (11), 1580.

(200) Hosseinahli, N.; Aghapour, M.; Duijf, P. H. G.; Baradaran, B. Treating cancer with microRNA replacement therapy: A literature review. *J. Cell Physiol.* **2018,** *233* (8), 5574-5588.

(201) Geary, R. S.; Norris, D.; Yu, R.; Bennett, C. F. Pharmacokinetics, biodistribution and cell uptake of antisense oligonucleotides. *Adv. Drug Deliv. Rev.* **2015,** *87*, 46-51.

(202) Blum, J. S.; Saltzman, W. M. High loading efficiency and tunable release of plasmid DNA encapsulated in submicron particles fabricated from PLGA conjugated with poly-L-lysine. *J. Control Release* **2008,** *129* (1), 66-72.

(203) Trang, P.; Wiggins, J. F.; Daige, C. L.; Cho, C.; Omotola, M.; Brown, D.; Weidhaas, J. B.; Bader, A. G.; Slack, F. J. Systemic delivery of tumor suppressor microRNA mimics using a neutral lipid emulsion inhibits lung tumors in mice. *Mol. Ther.* **2011,** *19* (6), 1116-1122.

(204) Aigner, A. Delivery systems for the direct application of siRNAs to induce RNA interference (RNAi) in vivo. *J. Biomed. Biotechnol.* **2006,** *2006* (4), 71659-71659.

(205) Duncan, R.; Izzo, L. Dendrimer biocompatibility and toxicity. *Adv. Drug Deliv. Rev.* **2005,** *57* (15), 2215-2237.

(206) Dias, N.; Stein, C. A. Antisense Oligonucleotides: Basic Concepts and Mechanisms. *Mol. Cancer Ther.* **2002,** *1* (5), 347-355.

(207) Li, Z.; Rana, T. M. Therapeutic targeting of microRNAs: current status and future challenges. *Nat. Rev. Drug Discov.* **2014,** *13*, 622.

(208) Watts, J. K.; Corey, D. R. Silencing disease genes in the laboratory and the clinic. *J. Pathol.* **2012,** *226* (2), 365-379.

(209) Fröhlich, E. The role of surface charge in cellular uptake and cytotoxicity of medical nanoparticles. *Int. J. Nanomedicine* **2012,** *7*, 5577-5591.

(210) Egholm, M.; Buchardt, O.; Nielsen, P. E.; Berg, R. H. Peptide nucleic acids (PNA). Oligonucleotide analogs with an achiral peptide backbone. *J. Am. Chem. Soc.* **1992,** *114* (5), 1895-1897.

(211) Montazersaheb, S.; Hejazi, M. S.; Nozad Charoudeh, H. Potential of Peptide Nucleic Acids in Future Therapeutic Applications. *Adv. Pharm. Bull.* **2018,** *8* (4), 551-563.

(212) Fabani, M. M.; Abreu-Goodger, C.; Williams, D.; Lyons, P. A.; Torres, A. G.; Smith, K. G. C.; Enright, A. J.; Gait, M. J.; Vigorito, E. Efficient inhibition of miR-155 function in vivo by peptide nucleic acids. *Nucleic Acids Res.* **2010,** *38* (13), 4466-4475.

(213) Cheng, C. J.; Bahal, R.; Babar, I. A.; Pincus, Z.; Barrera, F.; Liu, C.; Svoronos, A.; Braddock, D. T.; Glazer, P. M.; Engelman, D. M.; et al.; MicroRNA silencing for cancer therapy targeted to the tumour microenvironment. *Nature* **2015,** *518* (7537), 107-110.

(214) Gupta, A.; Quijano, E.; Liu, Y.; Bahal, R.; Scanlon, S. E.; Song, E.; Hsieh, W.-C.; Braddock, D. E.; Ly, D. H.; Saltzman, W. M.; et al.; Anti-tumor Activity of miniPEG-γ-Modified PNAs to Inhibit MicroRNA-210 for Cancer Therapy. *Mol. Ther. Nucleic Acids* **2017,** *9*, 111-119.

(215) Paul, S.; Caruthers, M. H. Synthesis of Phosphorodiamidate Morpholino Oligonucleotides and Their Chimeras Using Phosphoramidite Chemistry. *J. Am. Chem. Soc.* **2016,** *138* (48), 15663-15672.

(216) Martello, G.; Zacchigna, L.; Inui, M.; Montagner, M.; Adorno, M.; Mamidi, A.; Morsut, L.; Soligo, S.; Tran, U.; Dupont, S.; et al.; MicroRNA control of Nodal signalling. *Nature* **2007,** *449*, 183.

(217) Flynt, A. S.; Li, N.; Thatcher, E. J.; Solnica-Krezel, L.; Patton, J. G. Zebrafish miR-214 modulates Hedgehog signaling to specify muscle cell fate. *Nat. Genet.* **2007,** *39* (2), 259-263.

(218) Kloosterman, W. P.; Lagendijk, A. K.; Ketting, R. F.; Moulton, J. D.; Plasterk, R. H. A. Targeted inhibition of miRNA maturation with morpholinos reveals a role for miR-375 in pancreatic islet development. *PLoS Biol.* **2007,** *5* (8), e203-e203.

(219) Stenvang, J.; Petri, A.; Lindow, M.; Obad, S.; Kauppinen, S. Inhibition of microRNA function by antimiR oligonucleotides. *Silence* **2012,** *3* (1), 1-1.

(220) Tufro, A. Morpholino-mediated gene knockdown in mammalian organ culture. *Methods Mol. Biol.* **2012,** *886*, 305-309.

(221) Chakraborty, C.; Sharma, A. R.; Sharma, G.; Doss, C. G. P.; Lee, S.-S. Therapeutic miRNA and siRNA: Moving from Bench to Clinic as Next Generation Medicine. *Mol. Ther. Nucleic Acids* **2017,** *8*, 132-143.

(222) Elmén, J.; Lindow, M.; Silahtaroglu, A.; Bak, M.; Christensen, M.; Lind-Thomsen, A.; Hedtjärn, M.; Hansen, J. B.; Hansen, H. F.; Straarup, E. M.; et al.; Antagonism of microRNA-122 in mice by systemically administered LNA-antimiR leads to up-regulation of a large set of predicted target mRNAs in the liver. *Nucleic Acids Res.* **2008,** *36* (4), 1153-1162.

(223) Elmén, J.; Lindow, M.; Schütz, S.; Lawrence, M.; Petri, A.; Obad, S.; Lindholm, M.; Hedtjärn, M.; Hansen, H. F.; Berger, U.; et al.; LNA-mediated microRNA silencing in non-human primates. *Nature* **2008,** *452*, 896.

(224) Jopling, C. L.; Yi, M.; Lancaster, A. M.; Lemon, S. M.; Sarnow, P. Modulation of Hepatitis C Virus RNA Abundance by a Liver-Specific MicroRNA. *Science* **2005,** *309* (5740), 1577-1581.

(225) Janssen, H. L.; Reesink, H. W.; Lawitz, E. J.; Zeuzem, S.; Rodriguez-Torres, M.; Patel, K.; van der Meer, A. J.; Patick, A. K.; Chen, A.; Zhou, Y. Treatment of HCV infection by targeting microRNA. *N. Engl. J. Med.* **2013,** *368* (18), 1685-1694.

(226) Tsai, W.-C.; Hsu, S.-D.; Hsu, C.-S.; Lai, T.-C.; Chen, S.-J.; Shen, R.; Huang, Y.; Chen, H.-C.; Lee, C.-H.; Tsai, T.-F.; et al.; MicroRNA-122 plays a critical role in liver homeostasis and hepatocarcinogenesis. *J. Clin. Invest.* **2012,** *122* (8), 2884-2897.

(227) Hsu, S.-H.; Wang, B.; Kota, J.; Yu, J.; Costinean, S.; Kutay, H.; Yu, L.; Bai, S.; La Perle, K.; Chivukula, R. R.; et al.; Essential metabolic, anti-inflammatory, and anti-tumorigenic functions of miR-122 in liver. *J. Clin. Invest.* **2012,** *122* (8), 2871-2883.

(228) van der Ree, M. H.; de Vree, J. M.; Stelma, F.; Willemse, S.; van der Valk, M.; Rietdijk, S.; Molenkamp, R.; Schinkel, J.; van Nuenen, A. C.; Beuers, U.; et al.; Safety, tolerability,

and antiviral effect of RG-101 in patients with chronic hepatitis C: a phase 1B, double-blind, randomised controlled trial. *Lancet* **2017,** *389* (10070), 709-717.

(229) Prakash, T. P.; Graham, M. J.; Yu, J.; Carty, R.; Low, A.; Chappell, A.; Schmidt, K.; Zhao, C.; Aghajan, M.; Murray, H. F. Targeted delivery of antisense oligonucleotides to hepatocytes using triantennary N-acetyl galactosamine improves potency 10-fold in mice. *Nucleic Acids Res.* **2014,** *42* (13), 8796-8807.

(230) Keown, A. SoCal's Regulus Sinks After AstraZeneca PLC Bails on Lead NASH Drug.

(231) Levy, A., miRagen Announces New Clinical Data in Patients With Three Different Types of Blood Cancers Treated With Cobomarsen. https://globalnewswire.com: online, 2019.

(232) Querfeld, C.; Foss, F. M.; Pinter-Brown, L. C.; Porcu, P.; William, B. M.; Pacheco, T.; Haverkos, B. M.; Kim, Y. H.; Guitart, J.; Halwani, A. S.; et al.; Phase 1 Study of the Safety and Efficacy of MRG-106, a Synthetic Inhibitor of microRNA-155, in CTCL Patients. *Blood* **2017,** *130* (Suppl 1), 820-820.

(233) Gallant-Behm, C. L.; Piper, J.; Dickinson, B. A.; Dalby, C. M.; Pestano, L. A.; Jackson, A. L. A synthetic microRNA-92a inhibitor (MRG-110) accelerates angiogenesis and wound healing in diabetic and nondiabetic wounds. *Wound Repair Regen.* **2018,** *26* (4), 311-323.

(234) Levy, A., miRagen Therapeutics Announces Initiation of Second Phase 1 Clinical Trial of MRG-110. https://globenewswire.com: onilne, 2018.

(235) Bader, A. G. miR-34 - a microRNA replacement therapy is headed to the clinic. *Front. Genet.* **2012,** *3*, 120-120.

(236) Cortez, M. A.; Valdecanas, D.; Zhang, X.; Zhan, Y.; Bhardwaj, V.; Calin, G. A.; Komaki, R.; Giri, D. K.; Quini, C. C.; Wolfe, T.; et al.; Therapeutic delivery of miR-200c enhances radiosensitivity in lung cancer. *Mol. Ther.* **2014,** *22* (8), 1494-1503.

(237) Beg, M. S.; Brenner, A. J.; Sachdev, J.; Borad, M.; Kang, Y.-K.; Stoudemire, J.; Smith, S.; Bader, A. G.; Kim, S.; Hong, D. S. Phase I study of MRX34, a liposomal miR-34a mimic, administered twice weekly in patients with advanced solid tumors. *Invest. New Drugs* **2017,** *35* (2), 180-188.

(238) Hong, D. S.; Kang, Y.-K.; Brenner, A. J.; Sachdev, J. C.; Ejadi, S.; Borad, M. J.; Kim, T.-Y.; Lim, H. Y.; Park, K.; Becerra, C. MRX34, a liposomal miR-34 mimic, in patients with advanced solid tumors: Final dose-escalation results from a first-in-human phase I trial of microRNA therapy. *J. Clin. Oncol.* **2016**.

(239) Beg, M. S.; Brenner, A.; Sachdev, J.; Ejadi, S.; Borad, M.; Kang, Y.-K.; Lim, H.; Kim, T.; Bader, A.; Stoudemire, J. Abstract C43: Safety, tolerability, and clinical activity of MRX34, the first-in-class liposomal miR-34 mimic, in patients with advanced solid tumors. *Mol. Cancer Ther.* **2015**.

(240) Anderson, W., Austin cancer fighters halt drug development after deaths. Anderson, W., Ed. Austin Business Journal: online, 2016.

(241) Reid, G.; Williams, M.; Kirschner, M. B.; Mugridge, N.; Weiss, J.; Brahmbhatt, H.; MacDiarmid, J.; van Zandwijk, N. Targeted delivery of a synthetic microRNA-based mimic as an approach to cancer therapy. *Mol. Cell Biol.* **2015**.

(242) van Zandwijk, N.; Pavlakis, N.; Kao, S. C.; Linton, A.; Boyer, M. J.; Clarke, S.; Huynh, Y.; Chrzanowska, A.; Fulham, M. J.; Bailey, D. L.; et al.; Safety and activity of microRNA-loaded minicells in patients with recurrent malignant pleural mesothelioma: a first-in-man, phase 1, open-label, dose-escalation study. *Lancet Oncol.* **2017,** *18* (10), 1386-1396.

(243) Levy, A., miRagen Therapeutics Announces Initiation of Phase 2 Clinical Trial of MRG-201. https://globenewswire.com: online, 2018.

(244) Gallant-Behm, C. L.; Piper, J.; Lynch, J. M.; Seto, A. G.; Hong, S. J.; Mustoe, T. A.; Maari, C.; Pestano, L. A.; Dalby, C. M.; Jackson, A. L.; et al.; A MicroRNA-29 Mimic (Remlarsen) Represses Extracellular Matrix Expression and Fibroplasia in the Skin. *J. Invest. Dermatol.* **2018**.

(245) Gallant-Behm, C.; Maari, C.; Jackson, A.; Seto, A.; Lynch, J.; Ruckman, J.; Landry, M.; Pestano, L.; Dickinson, B.; Dalby, C. LB948 Pharmacodynamic activity of a microRNA-29b mimic (MRG-201) in human skin incisions. *J. Invest. Dermatol.* **2017,** *137* (10), B4.

(246) Li, Z.; Yang, C.-S.; Nakashima, K.; Rana, T. M. Small RNA-mediated regulation of iPS cell generation. *EMBO J.* **2011,** *30* (5), 823-834.

(247) Bennett, C. F.; Swayze, E. E. RNA Targeting Therapeutics: Molecular Mechanisms of Antisense Oligonucleotides as a Therapeutic Platform. *Annu. Rev. Pharmacol. Toxicol.* **2010,** *50* (1), 259-293.

(248) Connelly, C. M.; Moon, M. H.; Schneekloth Jr, J. S. The emerging role of RNA as a therapeutic target for small molecules. *Cell Chem. Biol.* **2016,** *23* (9), 1077-1090.

(249) Velagapudi, S. P.; Gallo, S. M.; Disney, M. D. Sequence-based design of bioactive small molecules that target precursor microRNAs. *Nat. Chem. Biol.* **2014,** *10* (4), 291.

(250) Guan, L.; Disney, M. D. Recent advances in developing small molecules targeting RNA. *ACS Chem. Biol.* **2012,** *7* (1), 73-86.

(251) Thomas, J. R.; Hergenrother, P. J. Targeting RNA with small molecules. *Chem. Rev.* **2008,** *108* (4), 1171-1224.

(252) Stelzer, A. C.; Frank, A. T.; Kratz, J. D.; Swanson, M. D.; Gonzalez-Hernandez, M. J.; Lee, J.; Andricioaei, I.; Markovitz, D. M.; Al-Hashimi, H. M. Discovery of selective bioactive small molecules by targeting an RNA dynamic ensemble. *Nat. Chem. Biol.* **2011,** *7* (8), 553.

(253) Parsons, J.; Castaldi, M. P.; Dutta, S.; Dibrov, S. M.; Wyles, D. L.; Hermann, T. Conformational inhibition of the hepatitis C virus internal ribosome entry site RNA. *Nat. Chem. Biol.* **2009,** *5* (11), 823.

(254) Davidson, A.; Leeper, T. C.; Athanassiou, Z.; Patora-Komisarska, K.; Karn, J.; Robinson, J. A.; Varani, G. Simultaneous recognition of HIV-1 TAR RNA bulge and loop sequences by cyclic peptide mimics of Tat protein. *Proc. Natl. Acad. Sci. U. S. A.* **2009,** *106* (29), 11931-11936.

(255) Arambula, J. F.; Ramisetty, S. R.; Baranger, A. M.; Zimmerman, S. C. A simple ligand that selectively targets CUG trinucleotide repeats and inhibits MBNL protein binding. *Proc. Natl. Acad. Sci. U. S. A.* **2009,** *106* (38), 16068-16073.

(256) Childs-Disney, J. L.; Hoskins, J.; Rzuczek, S. G.; Thornton, C. A.; Disney, M. D. Rationally designed small molecules targeting the RNA that causes myotonic dystrophy type 1 are potently bioactive. *ACS Chem. Biol.* **2012,** *7* (5), 856-862.

(257) Ofori, L. O.; Hoskins, J.; Nakamori, M.; Thornton, C. A.; Miller, B. L. From dynamic combinatorial 'hit'to lead: in vitro and in vivo activity of compounds targeting the pathogenic RNAs that cause myotonic dystrophy. *Nucleic Acids Res.* **2012,** *40* (13), 6380-6390.

(258) Kumar, A.; Parkesh, R.; Sznajder, L. J.; Childs-Disney, J. L.; Sobczak, K.; Disney, M. D. Chemical correction of pre-mRNA splicing defects associated with sequestration of muscleblind-like 1 protein by expanded r (CAG)-containing transcripts. *ACS Chem. Biol.* **2012,** *7* (3), 496-505.

(259) Barros, S. A.; Yoon, I.; Chenoweth, D. M. Modulation of the E. coli rpoH Temperature Sensor with Triptycene- Based Small Molecules. *Angew. Chem. Int. Ed. Engl.* **2016,** *128* (29), 8398-8401.

(260) Spring, D. R. Chemical genetics to chemical genomics: small molecules offer big insights. *Chem. Soc. Rev.* **2005,** *34* (6), 472-482.

(261) Zhang, S.; Chen, L.; Jung, E. J.; Calin, G. A. Targeting microRNAs with small molecules: from dream to reality. *Clin. Pharmacol. Ther.* **2010,** *87* (6), 754-758.

(262) Connelly, C. M.; Abulwerdi, F. A.; Schneekloth, J. S. Discovery of RNA Binding Small Molecules Using Small Molecule Microarrays. In *Small Molecule Microarrays: Methods and Protocols*, Uttamchandani, M.; Yao, S. Q., Eds. Springer New York: New York, NY, 2017; pp 157-175.

(263) Chirayil, S.; Chirayil, R.; Luebke, K. J. Discovering ligands for a microRNA precursor with peptoid microarrays. *Nucleic Acids Res.* **2009,** *37* (16), 5486-5497.

(264) Pai, J.; Hyun, S.; Hyun, J. Y.; Park, S.-H.; Kim, W.-J.; Bae, S.-H.; Kim, N.-K.; Yu, J.; Shin, I. Screening of Pre-miRNA-155 Binding Peptides for Apoptosis Inducing Activity Using Peptide Microarrays. *J. Am. Chem. Soc.* **2016,** *138* (3), 857-867.

(265) Connelly, C. M.; Boer, R. E.; Moon, M. H.; Gareiss, P.; Schneekloth, J. S. Discovery of Inhibitors of MicroRNA-21 Processing Using Small Molecule Microarrays. *ACS Chem. Biol.* **2017,** *12* (2), 435-443.

(266) Maiti, M.; Nauwelaerts, K.; Herdewijn, P. Pre-microRNA binding aminoglycosides and antitumor drugs as inhibitors of Dicer catalyzed microRNA processing. *Bioorg. Med. Chem. Lett.* **2012,** *22* (4), 1709-1711.

(267) Disney, M. D.; Labuda, L. P.; Paul, D. J.; Poplawski, S. G.; Pushechnikov, A.; Tran, T.; Velagapudi, S. P.; Wu, M.; Childs-Disney, J. L. Two-dimensional combinatorial screening identifies specific aminoglycoside− RNA internal loop partners. *J. Am. Chem. Soc.* **2008,** *130* (33), 11185-11194.

(268) Disney, M. D.; Angelbello, A. J. Rational Design of Small Molecules Targeting Oncogenic Noncoding RNAs from Sequence. *Acc. Chem. Res.* **2016,** *49* (12), 2698-2704.

(269) Velagapudi, S. P.; Costales, M. G.; Vummidi, B. R.; Nakai, Y.; Angelbello, A. J.; Tran, T.; Haniff, H. S.; Matsumoto, Y.; Wang, Z. F.; Chatterjee, A. K.; et al.; Approved Anti-cancer Drugs Target Oncogenic Non-coding RNAs. *Cell Chem. Biol.* **2018**.

(270) Sunters, A.; Springer, C. J.; Bagshawe, K. D.; Souhami, R. L.; Hartley, J. A. The cytotoxicity, DNA crosslinking ability and DNA sequence selectivity of the aniline mustards melphalan, chlorambucil and 4-[bis (2-chloroethyl) amino] benzoic acid. *Biochem. Pharmacol.* **1992,** *44* (1), 59-64.

(271) Davies, B. P.; Arenz, C. A fluorescence probe for assaying micro RNA maturation. *Bioorg. Med. Chem.* **2008,** *16* (1), 49-55.

(272) Davies Brian, P.; Arenz, C. A Homogenous Assay for Micro RNA Maturation. *Angew. Chem. Int. Ed. Engl.* **2006,** *45* (33), 5550-5552.

(273) Vo, D. D.; Staedel, C.; Zehnacker, L.; Benhida, R.; Darfeuille, F.; Duca, M. Targeting the Production of Oncogenic MicroRNAs with Multimodal Synthetic Small Molecules. *ACS Chem. Biol.* **2014,** *9* (3), 711-721.

(274) Bose, D.; Jayaraj, G. G.; Kumar, S.; Maiti, S. A Molecular-Beacon-Based Screen for Small Molecule Inhibitors of miRNA Maturation. *ACS Chem. Biol.* **2013,** *8* (5), 930-938.

(275) Klemm Claudine, M.; Berthelmann, A.; Neubacher, S.; Arenz, C. Short and Efficient Synthesis of Alkyne- Modified Amino Glycoside Building Blocks. *Eur. J. Org. Chem.* **2009,** *2009* (17), 2788-2794.

(276) Vo Duc, D.; Tran Thi Phuong, A.; Staedel, C.; Benhida, R.; Darfeuille, F.; Di Giorgio, A.; Duca, M. Oncogenic MicroRNAs Biogenesis as a Drug Target: Structure–Activity Relationship Studies on New Aminoglycoside Conjugates. *Chem. Eur. J.* **2016,** *22* (15), 5350-5362.

(277) Chittapragada, M.; Roberts, S.; Ham, Y. W. Aminoglycosides: Molecular Insights on the Recognition of RNA and Aminoglycoside Mimics. *Perspect. Med. Chem.* **2009,** *3*, 21-37.

(278) Tran, T. P. A.; Vo, D. D.; Di Giorgio, A.; Duca, M. Ribosome-targeting antibiotics as inhibitors of oncogenic microRNAs biogenesis: Old scaffolds for new perspectives in RNA targeting. *Bioorg. Med. Chem.* **2015,** *23* (17), 5334-5344.

(279) Roos, M.; Pradère, U.; Ngondo, R. P.; Behera, A.; Allegrini, S.; Civenni, G.; Zagalak, J. A.; Marchand, J.-R.; Menzi, M.; Towbin, H.; et al.; A Small-Molecule Inhibitor of Lin28. *ACS Chem. Biol.* **2016,** *11* (10), 2773-2781.

(280) Nam, Y.; Chen, C.; Gregory, Richard I.; Chou, James J.; Sliz, P. Molecular Basis for Interaction of let-7 MicroRNAs with Lin28. *Cell* **2011,** *147* (5), 1080-1091.

(281) Lim, D.; Byun, W. G.; Koo, J. Y.; Park, H.; Park, S. B. Discovery of a Small-Molecule Inhibitor of Protein–MicroRNA Interaction Using Binding Assay with a Site-Specifically Labeled Lin28. *J. Am. Chem. Soc.* **2016,** *138* (41), 13630-13638.

(282) Lightfoot, H. L.; Miska, E. A.; Balasubramanian, S. Identification of small molecule inhibitors of the Lin28-mediated blockage of pre-let-7g processing. *Org. Biomol. Chem.* **2016,** *14* (43), 10208-10216.

(283) Tan, G. S.; Chiu, C.-H.; Garchow, B. G.; Metzler, D.; Diamond, S. L.; Kiriakidou, M. Small Molecule Inhibition of RISC Loading. *ACS Chem. Biol.* **2012,** *7* (2), 403-410.

(284) Gonzalez, R. G.; Haxo, R. S.; Schleich, T. Mechanism of action of polymeric aurintricarboxylic acid, a potent inhibitor of protein-nucleic acid interactions. *Biochem.* **1980,** *19* (18), 4299-4303.

(285) Lorenz, D. A.; Song, J. M.; Garner, A. L. High-Throughput Platform Assay Technology for the Discovery of pre-microRNA-Selective Small Molecule Probes. *Bioconjug. Chem.* **2015,** *26* (1), 19-23.

(286) Lorenz, D. A.; Vander Roest, S.; Larsen, M. J.; Garner, A. L. Development and Implementation of an HTS-Compatible Assay for the Discovery of Selective Small-Molecule Ligands for Pre-microRNAs. *SLAS Discov.* **2017,** *23* (1), 47-54.

(287) Lorenz, D.; Kaur, T.; Kerk, S. A.; Gallagher, E.; Sandoval, J.; Garner, A. L. Expansion of cat-ELCCA for the Discovery of Small Molecule Inhibitors of the pre-let-7-Lin28 RNA-Protein Interaction. *ACS Med. Chem. Lett.* **2018**.

(288) Baell, J. B.; Holloway, G. A. New Substructure Filters for Removal of Pan Assay Interference Compounds (PAINS) from Screening Libraries and for Their Exclusion in Bioassays. *J. Med. Chem.* **2010,** *53* (7), 2719-2740.

(289) Thorne, N.; Inglese, J.; Auld, D. S. Illuminating insights into firefly luciferase and other bioluminescent reporters used in chemical biology. *Chem. Biol.* **2010,** *17* (6), 646-657.

(290) Thorne, N.; Auld, D. S.; Inglese, J. Apparent Activity in High-Throughput Screening: Origins of Compound-Dependent Assay Interference. *Curr. Opin. Chem. Biol.* **2010,** *14* (3), 315-324.

(291) Auld, D. S.; Thorne, N.; Nguyen, D.-T.; Inglese, J. A Specific Mechanism for Nonspecific Activation in Reporter-Gene Assays. *ACS Chem. Biol.* **2008,** *3* (8), 463-470.

(292) Shan, G.; Li, Y.; Zhang, J.; Li, W.; Szulwach, K. E.; Duan, R.; Faghihi, M. A.; Khalil, A. M.; Lu, L.; Paroo, Z.; et al.; A small molecule enhances RNA interference and promotes microRNA processing. *Nat. Biotechnol.* **2008,** *26*, 933.

(293) Daniels, S. M.; Melendez-Peña, C. E.; Scarborough, R. J.; Daher, A.; Christensen, H. S.; El Far, M.; Purcell, D. F. J.; Lainé, S.; Gatignol, A. Characterization of the TRBP domain required for Dicer interaction and function in RNA interference. *BMC Mol. Biol.* **2009,** *10*, 38-38.

(294) Melo, S.; Villanueva, A.; Moutinho, C.; Davalos, V.; Spizzo, R.; Ivan, C.; Rossi, S.; Setien, F.; Casanovas, O.; Simo-Riudalbas, L.; et al.; Small molecule enoxacin is a cancer-specific growth inhibitor that acts by enhancing TAR RNA-binding protein 2-mediated microRNA processing. *Proc. Natl. Acad. Sci. U. S. A.* **2011,** *108* (11), 4394-4399.

(295) Sousa, E. J.; Graça, I.; Baptista, T.; Vieira, F. Q.; Palmeira, C.; Henrique, R.; Jerónimo, C. Enoxacin inhibits growth of prostate cancer cells and effectively restores microRNA processing. *Epigenetics* **2013,** *8* (5), 548-558.

(296) Abell, N. S.; Mercado, M.; Cañeque, T.; Rodriguez, R.; Xhemalce, B. Click Quantitative Mass Spectrometry Identifies PIWIL3 as a Mechanistic Target of RNA Interference Activator Enoxacin in Cancer Cells. *J. Am. Chem. Soc.* **2017,** *139* (4), 1400-1403.

(297) Frankel, L. B.; Christoffersen, N. R.; Jacobsen, A.; Lindow, M.; Krogh, A.; Lund, A. H. Programmed cell death 4 (PDCD4) is an important functional target of the microRNA miR-21 in breast cancer cells. *J. Biol. Chem.* **2008,** *283* (2), 1026-1033.

(298) Debojit, B.; Gopal, J.; Hemant, S.; Prachi, A.; Kumar, P. S.; Rajkumar, B.; Souvik, M. The Tuberculosis Drug Streptomycin as a Potential Cancer Therapeutic: Inhibition of miR- 21 Function by Directly Targeting Its Precursor. *Angew. Chem. Int. Ed. Engl.* **2012,** *51* (4), 1019-1023.

(299) Carter, A. P.; Clemons, W. M.; Brodersen, D. E.; Morgan-Warren, R. J.; Wimberly, B. T.; Ramakrishnan, V. Functional insights from the structure of the 30S ribosomal subunit and its interactions with antibiotics. *Nature* **2000,** *407*, 340.

(300) Xiao, Z.; Li, C. H.; Chan, S. L.; Xu, F.; Feng, L.; Wang, Y.; Jiang, J.-D.; Sung, J. J. Y.; Cheng, C. H. K.; Chen, Y. A Small-Molecule Modulator of the Tumor-Suppressor miR34a Inhibits the Growth of Hepatocellular Carcinoma. *Cancer Res.* **2014,** *74* (21), 6236.

(301) Slabáková, E.; Culig, Z.; Remšík, J.; Souček, K. Alternative mechanisms of miR-34a regulation in cancer. *Cell Death Dis.* **2017,** *8*, e3100.

(302) Velagapudi, S. P.; Costales, M. G.; Vummidi, B. R.; Nakai, Y.; Angelbello, A. J.; Tran, T.; Haniff, H. S.; Matsumoto, Y.; Wang, Z. F.; Chatterjee, A. K.; et al.; Approved Anti-cancer Drugs Target Oncogenic Non-coding RNAs. *Cell Chem. Biol.*

(303) Zhu, T.; Cao, S.; Su, P.-C.; Patel, R.; Shah, D.; Chokshi, H. B.; Szukala, R.; Johnson, M. E.; Hevener, K. E. Hit Identification and Optimization in Virtual Screening: Practical Recommendations Based Upon a Critical Literature Analysis. *J. Med. Chem.* **2013,** *56* (17), 6560-6572.

(304) Chen, X.; Huang, C.; Zhang, W.; Wu, Y.; Chen, X.; Zhang, C.-y.; Zhang, Y. A universal activator of microRNAs identified from photoreaction products. *Chem. Commun.* **2012,** *48* (51), 6432-6434.

(305) Tan, S.-B.; Huang, C.; Chen, X.; Wu, Y.; Zhou, M.; Zhang, C.; Zhang, Y. Small molecular inhibitors of miR-1 identified from photocycloadducts of acetylenes with 2-methoxy-1,4-naphthalenequinone. *Bioorg. Med. Chem.* **2013,** *21* (20), 6124-6131.

(306) Ai, J.; Zhang, R.; Gao, X.; Niu, H.-F.; Wang, N.; Xu, Y.; Li, Y.; Ma, N.; Sun, L.-H.; Pan, Z.-W.; et al.; Overexpression of microRNA-1 impairs cardiac contractile function by damaging sarcomere assembly. *Cardiovasc. Res.* **2012,** *95* (3), 385-393.

(307) Petrocca, F.; Vecchione, A.; Croce, C. M. Emerging Role of miR-106b-25/miR-17-92 Clusters in the Control of Transforming Growth Factor β Signaling. *Cancer Res.* **2008,** *68* (20), 8191.

(308) Yang, H.; Kong, W.; He, L.; Zhao, J.-J.; O'Donnell, J. D.; Wang, J.; Wenham, R. M.; Coppola, D.; Kruk, P. A.; Nicosia, S. V. MicroRNA expression profiling in human ovarian cancer: miR-214 induces cell survival and cisplatin resistance by targeting PTEN. *Cancer Res.* **2008,** *68* (2), 425-433.

(309) Contreras, J.; Rao, D. S. MicroRNAs in inflammation and immune responses. *Leukemia* **2011,** *26*, 404.

(310) Callis, T. E.; Chen, J.-F.; Wang, D.-Z. MicroRNAs in Skeletal and Cardiac Muscle Development. *DNA Cell Biol.* **2007,** *26* (4), 219-225.

(311) Tan, S.-B.; Li, J.; Chen, X.; Zhang, W.; Zhang, D.; Zhang, C.; Li, D.; Zhang, Y. Small Molecule Inhibitor of Myogenic microRNAs Leads to a Discovery of miR-221/222-myoD-myomiRs Regulatory Pathway. *Chem. Biol.* **2014,** *21* (10), 1265-1270.

(312) Rao, P. K.; Kumar, R. M.; Farkhondeh, M.; Baskerville, S.; Lodish, H. F. Myogenic factors that regulate expression of muscle-specific microRNAs. *Proc. Natl. Acad. Sci. U. S. A.* **2006,** *103* (23), 8721.

(313) Berkes, C. A.; Tapscott, S. J. MyoD and the transcriptional control of myogenesis. *Semin. Cell Dev. Biol.* **2005,** *16* (4), 585-595.

(314) Mayr, C.; Hemann, M. T.; Bartel, D. P. Disrupting the Pairing Between let-7 and Hmga2 Enhances Oncogenic Transformation. *Science* **2007,** *315* (5818), 1576.

(315) Johnson, S. M.; Grosshans, H.; Shingara, J.; Byrom, M.; Jarvis, R.; Cheng, A.; Labourier, E.; Reinert, K. L.; Brown, D.; Slack, F. J. RAS Is Regulated by the let-7 MicroRNA Family. *Cell* **2005,** *120* (5), 635-647.

(316) Guo, R.; Abdelmohsen, K.; Morin, P. J.; Gorospe, M. Novel MicroRNA Reporter Uncovers Repression of Let-7 by GSK-3β. *PLoS One* **2013,** *8* (6), e66330.

(317) Ghosh, J. C.; Altieri, D. C. Activation of p53-Dependent Apoptosis by Acute Ablation of Glycogen Synthase Kinase-3β in Colorectal Cancer Cells. *Clin. Cancer Res.* **2005,** *11* (12), 4580.

(318) Saleh, A. D.; Savage, J. E.; Cao, L.; Soule, B. P.; Ly, D.; DeGraff, W.; Harris, C. C.; Mitchell, J. B.; Simone, N. L. Cellular Stress Induced Alterations in MicroRNA let-7a and let-7b Expression Are Dependent on p53. *PLoS One* **2011,** *6* (10), e24429.

(319) Cinkornpumin, J.; Roos, M.; Nguyen, L.; Liu, X.; Gaeta, X.; Lin, S.; Chan, D. N.; Liu, A.; Gregory, R. I.; Jung, M.; et al.; A small molecule screen to identify regulators of let-7 targets. *Sci. Rep.* **2017,** *7* (1), 15973.

(320) Keiser, M. J.; Roth, B. L.; Armbruster, B. N.; Ernsberger, P.; Irwin, J. J.; Shoichet, B. K. Relating protein pharmacology by ligand chemistry. *Nat. Biotechnol.* **2007,** *25*, 197.

(321) Im, K.; Song, J.; Han, Y. T.; Lee, S.; Kang, S.; Hwang, K. W.; Min, H.; Min, K. H. Identification of aminosulfonylarylisoxazole as microRNA-31 regulators. *PLoS One* **2017,** *12* (8), e0182331.

(322) Lee, S.-Y.; Lee, S.; Choi, E.; Ham, O.; Lee, C. Y.; Lee, J.; Seo, H.-H.; Cha, M.-J.; Mun, B.; Lee, Y.; et al.; Small molecule-mediated up-regulation of microRNA targeting a key cell death modulator BNIP3 improves cardiac function following ischemic injury. *Sci. Rep.* **2016,** *6*, 23472.

(323) Kubasiak, L. A.; Hernandez, O. M.; Bishopric, N. H.; Webster, K. A. Hypoxia and acidosis activate cardiac myocyte death through the Bcl-2 family protein BNIP3. *Proc. Natl. Acad. Sci. U. S. A.* **2002,** *99* (20), 12825-12830.

(324) Liu, C.; Li, Y.; Semenov, M.; Han, C.; Baeg, G.-H.; Tan, Y.; Zhang, Z.; Lin, X.; He, X. Control of β-Catenin Phosphorylation/Degradation by a Dual-Kinase Mechanism. *Cell* **2002,** *108* (6), 837-847.

(325) Hara, H.; Takeda, N.; Komuro, I. Pathophysiology and therapeutic potential of cardiac fibrosis. *Inflammation Regener.* **2017,** *37* (1), 13.

(326) Todd, A.; Anderson, R.; Groundwater, P. W. Rational drug design-identifying and characterising a target. *Pharm. J.* **2009,** *283* (7559), 19-20.

(327) Mathews, D. H.; Disney, M. D.; Childs, J. L.; Schroeder, S. J.; Zuker, M.; Turner, D. H. Incorporating chemical modification constraints into a dynamic programming algorithm for prediction of RNA secondary structure. *Proc. Natl. Acad. Sci. U. S. A.* **2004,** *101* (19), 7287-7292.

(328) Breaker, R. R.; Gesteland, R.; Cech, T.; Atkins, J., The RNA world. Cold Spring Harbor Laboratory Press: New York: 2006.

(329) Velagapudi, S. P.; Seedhouse, S. J.; Disney, M. D. Structure–activity relationships through sequencing (StARTS) defines optimal and suboptimal RNA motif targets for small molecules. *Angew. Chem. Int. Ed. Engl.* **2010,** *49* (22), 3816-3818.

(330) Paul, D. J.; Seedhouse, S. J.; Disney, M. D. Two-dimensional combinatorial screening and the RNA Privileged Space Predictor program efficiently identify aminoglycoside–RNA hairpin loop interactions. *Nucleic Acids Res.* **2009,** *37* (17), 5894-5907.

(331) Disney, M. D.; Barrett, O. J. An aminoglycoside microarray platform for directly monitoring and studying antibiotic resistance. *Biochem.* **2007,** *46* (40), 11223-11230.

(332) Velagapudi, S. P.; Seedhouse, S. J.; French, J.; Disney, M. D. Defining the RNA internal loops preferred by benzimidazole derivatives via 2D combinatorial screening and computational analysis. *J. Am. Chem. Soc.* **2011,** *133* (26), 10111-10118.

(333) Xu, S.; Witmer, P. D.; Lumayag, S.; Kovacs, B.; Valle, D. MicroRNA (miRNA) transcriptome of mouse retina and identification of a sensory organ-specific miRNA cluster. *J. Biol. Chem.* **2007,** *282* (34), 25053-25066.

(334) Lu, H.; Huang, H. FOXO1: a potential target for human diseases. *Curr. Drug Targets* **2011,** *12* (9), 1235-1244.

(335) Xie, L.; Ushmorov, A.; Leithäuser, F.; Guan, H.; Steidl, C.; Färbinger, J.; Pelzer, C.; Vogel, M. J.; Maier, H. J.; Gascoyne, R. D. FOXO1 is a tumor suppressor in classical Hodgkin lymphoma. *Blood* **2012**, blood-2011-09-381905.

(336) Guttilla, I. K.; White, B. A. Coordinate regulation of FOXO1 by miR-27a, miR-96, and miR-182 in breast cancer cells. *J. Biol. Chem.* **2009**, jbc. M109. 031427.

(337) Velagapudi, S. P.; Cameron, M. D.; Haga, C. L.; Rosenberg, L. H.; Lafitte, M.; Duckett, D. R.; Phinney, D. G.; Disney, M. D. Design of a small molecule against an oncogenic noncoding RNA. *Proc. Natl. Acad. Sci. U. S. A.* **2016,** *113* (21), 5898-5903.

(338) Costales, M. G.; Haga, C. L.; Velagapudi, S. P.; Childs-Disney, J. L.; Phinney, D. G.; Disney, M. D. Small molecule inhibition of microRNA-210 reprograms an oncogenic hypoxic circuit. *J. Am. Chem. Soc.* **2017,** *139* (9), 3446-3455.

(339) Kelly, T. J.; Souza, A. L.; Clish, C. B.; Puigserver, P. A hypoxia-induced positive feedback loop promotes hypoxia-inducible factor 1α stability through miR-210 suppression of glycerol-3-phosphate dehydrogenase 1-like. *Mol. Cell Biol.* **2011,** *31* (13), 2696-2706.

(340) Maxwell, P. H.; Wiesener, M. S.; Chang, G.-W.; Clifford, S. C.; Vaux, E. C.; Cockman, M. E.; Wykoff, C. C.; Pugh, C. W.; Maher, E. R.; Ratcliffe, P. J. The tumour suppressor protein VHL targets hypoxia-inducible factors for oxygen-dependent proteolysis. *Nature* **1999,** *399* (6733), 271.

(341) Haga, C. L.; Velagapudi, S. P.; Strivelli, J. R.; Yang, W.-Y.; Disney, M. D.; Phinney, D. G. Small molecule inhibition of miR-544 biogenesis disrupts adaptive responses to hypoxia by modulating ATM-mTOR signaling. *ACS Chem. Biol.* **2015,** *10* (10), 2267-2276.

(342) Haga, C.; Phinney, D. MicroRNAs in the imprinted DLKI-DIO3 region repress the Epithelial-to-Mesenchymal transition by targeting the TWIST1 signaling network. *J. Biol. Chem.* **2012,** *287* (51), 42695-707.

(343) Cam, H.; Easton, J. B.; High, A.; Houghton, P. J. mTORC1 signaling under hypoxic conditions is controlled by ATM-dependent phosphorylation of HIF-1α. *Mol. Cell* **2010,** *40* (4), 509-520.

(344) Childs-Disney, J. L.; Disney, M. D. Small molecule targeting of a microRNA associated with hepatocellular carcinoma. *ACS Chem. Biol.* **2015,** *11* (2), 375-380.

(345) Pang, F.; Zha, R.; Zhao, Y.; Wang, Q.; Chen, D.; Zhang, Z.; Chen, T.; Yao, M.; Gu, J.; He, X. MiR-525-3p enhances the migration and invasion of liver cancer cells by downregulating ZNF395. *PLoS One* **2014,** *9* (3), e90867.

(346) Nakatani, K.; Sando, S.; Saito, I. Recognition of a single guanine bulge by 2-acylamino-1, 8-naphthyridine. *J. Am. Chem. Soc.* **2000,** *122* (10), 2172-2177.

(347) Suda, H.; Kobori, A.; Zhang, J.; Hayashi, G.; Nakatani, K. N, N′-Bis (3-aminopropyl)-2, 7-diamino-1, 8-naphthyridine stabilized a single pyrimidine bulge in duplex DNA. *Bioorg. Med. Chem.* **2005,** *13* (14), 4507-4512.

(348) Zhang, J.; Takei, F.; Nakatani, K. Emission of characteristic fluorescence from the ligand–cytosine complex in U_A/ACU bulged RNA duplex. *Bioorg. Med. Chem.* **2007,** *15* (14), 4813-4817.

(349) Murata, A.; Otabe, T.; Zhang, J.; Nakatani, K. BZDANP, a small-molecule modulator of pre-miR-29a maturation by Dicer. *ACS Chem. Biol.* **2016,** *11* (10), 2790-2796.

(350) Qiu, F.; Sun, R.; Deng, N.; Guo, T.; Cao, Y.; Yu, Y.; Wang, X.; Zou, B.; Zhang, S.; Jing, T. miR-29a/b enhances cell migration and invasion in nasopharyngeal carcinoma progression by regulating SPARC and COL3A1 gene expression. *PloS One* **2015,** *10* (3), e0120969.

(351) Cho, W. J.; Shin, J. M.; Kim, J. S.; Lee, M. R.; Hong, K. S.; Lee, J.-H.; Koo, K. H.; Park, J. W.; Kim, K.-S. miR-372 regulates cell cycle and apoptosis of ags human gastric cancer cell line through direct regulation of LATS2. *Mol. Cells* **2009,** *28* (6), 521-527.

(352) Voorhoeve, P. M.; Le Sage, C.; Schrier, M.; Gillis, A. J.; Stoop, H.; Nagel, R.; Liu, Y.-P.; Van Duijse, J.; Drost, J.; Griekspoor, A. A genetic screen implicates miRNA-372 and miRNA-373 as oncogenes in testicular germ cell tumors. *Cell* **2006,** *124* (6), 1169-1181.

(353) Lee, K.-H.; Goan, Y.-G.; Hsiao, M.; Lee, C.-H.; Jian, S.-H.; Lin, J.-T.; Chen, Y.-L.; Lu, P.-J. MicroRNA-373 (miR-373) post-transcriptionally regulates large tumor suppressor, homolog 2 (LATS2) and stimulates proliferation in human esophageal cancer. *Exp. Cell Res.* **2009,** *315* (15), 2529-2538.

(354) Rippe, V.; Dittberner, L.; Lorenz, V. N.; Drieschner, N.; Nimzyk, R.; Sendt, W.; Junker, K.; Belge, G.; Bullerdiek, J. The two stem cell microRNA gene clusters C19MC and miR-371-3 are activated by specific chromosomal rearrangements in a subgroup of thyroid adenomas. *PloS One* **2010,** *5* (3), e9485.

(355) Duca, M.; Malnuit, V.; Barbault, F.; Benhida, R. Design of novel RNA ligands that bind stem–bulge HIV-1 TAR RNA. *Chem. Commun.* **2010,** *46* (33), 6162-6164.

(356) Mei, H.-Y.; Mack, D. P.; Galan, A. A.; Halim, N. S.; Heldsinger, A.; Loo, J. A.; Moreland, D. W.; Sannes-Lowery, K. A.; Sharmeen, L.; Truong, H. N. Discovery of selective, small-molecule inhibitors of RNA complexes—1. The tat protein/TAR RNA complexes required for HIV-1 transcription. *Bioorg. Med. Chem.* **1997,** *5* (6), 1173-1184.

(357) Zapp, M. L.; Stern, S.; Green, M. R. Small molecules that selectively block RNA binding of HIV-1 Rev protein inhibit Rev function and viral production. *Cell* **1993,** *74* (6), 969-978.

(358) Kumar, S.; Kellish, P.; Robinson Jr, W. E.; Wang, D.; Appella, D. H.; Arya, D. P. Click dimers to target HIV TAR RNA conformation. *Biochem.* **2012,** *51* (11), 2331-2347.

(359) Duca, M.; Vekhoff, P.; Oussedik, K.; Halby, L.; Arimondo, P. B. The triple helix: 50 years later, the outcome. *Nucleic Acids Res.* **2008,** *36* (16), 5123.

(360) Malnuit, V.; Duca, M.; Benhida, R. Targeting DNA base pair mismatch with artificial nucleobases. Advances and perspectives in triple helix strategy. *Org. Biomol. Chem.* **2011,** *9* (2), 326-336.

(361) Guianvarc'h, D.; Benhida, R.; Fourrey, J.-L.; Maurisse, R.; Sun, J.-S. Incorporation of a novel nucleobase allows stable oligonucleotide-directed triple helix formation at the target sequence containing a purine· pyrimidine interruption. *Chem. Commun.* **2001,** (18), 1814-1815.

(362) Guianvarc'h, D.; Fourrey, J.-L.; Maurisse, R.; Sun, J.-S.; Benhida, R. Design of artificial nucleobases for the recognition of the AT inversion by triple-helix forming oligonucleotides: A structure–stability relationship study and neighbour bases effect. *Bioorg. Med. Chem.* **2003,** *11* (13), 2751-2759.

(363) Belair, C.; Baud, J.; Chabas, S.; Sharma, C. M.; Vogel, J.; Staedel, C.; Darfeuille, F. Helicobacter pylori interferes with an embryonic stem cell micro RNA cluster to block cell cycle progression. *Silence* **2011,** *2* (1), 7.

(364) Bartel, D. P. MicroRNAs: target recognition and regulatory functions. *Cell* **2009,** *136* (2), 215-233.

(365) Schmidt, M. F.; Korb, O.; Abell, C. MicroRNA-specific argonaute 2 protein inhibitors. *ACS Chem. Biol.* **2013,** *8* (10), 2122-2126.

(366) Irwin, J. J.; Sterling, T.; Mysinger, M. M.; Bolstad, E. S.; Coleman, R. G. ZINC: a free tool to discover chemistry for biology. *J. Chem. Inf. Model.* **2012,** *52* (7), 1757-1768.

(367) Jones, G.; Willett, P.; Glen, R. C.; Leach, A. R.; Taylor, R. Development and validation of a genetic algorithm for flexible docking11Edited by F. E. Cohen. *J. Mol. Biol.* **1997,** *267* (3), 727-748.

(368) Korb, O.; Stutzle, T.; Exner, T. E. Empirical scoring functions for advanced protein− ligand docking with PLANTS. *J. Chem. Inf. Model.* **2009,** *49* (1), 84-96.

(369) Jones, G.; Willett, P.; Glen, R. C. Molecular recognition of receptor sites using a genetic algorithm with a description of desolvation. *J. Cell Biol. Mol. Sci.* **1995,** *245* (1), 43-53.

(370) Schmidt, M. F.; Korb, O.; Howard, N. I.; Dias, M. V.; Blundell, T. L.; Abell, C. Discovery of Schaeffer's Acid Analogues as Lead Structures of Mycobacterium tuberculosis Type II Dehydroquinase Using a Rational Drug Design Approach. *ChemMedChem* **2013,** *8* (1), 54-58.

(371) Shi, Z.; Zhang, J.; Qian, X.; Han, L.; Zhang, K.; Chen, L.; Liu, J.; Ren, Y.; Yang, M.; Zhang, A. AC1MMYR2, an inhibitor of dicer-mediated biogenesis of oncomir miR-21, reverses epithelial–mesenchymal transition and suppresses tumor growth and progression. *Cancer res.* **2013,** *73* (17), 5519-5531.

(372) Parisien, M.; Major, F. The MC-Fold and MC-Sym pipeline infers RNA structure from sequence data. *Nature* **2008,** *452* (7183), 51.

(373) Ponder, J. W. TINKER: Software tools for molecular design. *Washington University School of Medicine, Saint Louis, MO* **2004,** *3*.

(374) Chang, J.; Nicolas, E.; Marks, D.; Sander, C.; Lerro, A.; Buendia, M. A.; Xu, C.; Mason, W. S.; Moloshok, T.; Bort, R. miR-122, a mammalian liver-specific microRNA, is processed from hcr mRNA and maydownregulate the high affinity cationic amino acid transporter CAT-1. *RNA Biol.* **2004,** *1* (2), 106-113.

(375) Lagos-Quintana, M.; Rauhut, R.; Yalcin, A.; Meyer, J.; Lendeckel, W.; Tuschl, T. Identification of Tissue-Specific MicroRNAs from Mouse. *Curr. Biol.* **2002,** *12* (9), 735-739.

(376) Landgraf, P.; Rusu, M.; Sheridan, R.; Sewer, A.; Iovino, N.; Aravin, A.; Pfeffer, S.; Rice, A.; Kamphorst, A. O.; Landthaler, M.; et al.; A mammalian microRNA expression atlas based on small RNA library sequencing. *Cell* **2007,** *129* (7), 1401-1414.

(377) Denzler, R.; Agarwal, V.; Stefano, J.; Bartel, D. P.; Stoffel, M. Assessing the ceRNA hypothesis with quantitative measurements of miRNA and target abundance. *Mol. Cell* **2014,** *54* (5), 766-776.

(378) Thakral, S.; Ghoshal, K. miR-122 is a unique molecule with great potential in diagnosis, prognosis of liver disease, and therapy both as miRNA mimic and antimir. *Curr. Gene Ther.* **2015,** *15* (2), 142-150.

(379) Bandiera, S.; Pfeffer, S.; Baumert, T. F.; Zeisel, M. B. miR-122 – A key factor and therapeutic target in liver disease. *J. Hepatol.* **2015,** *62* (2), 448-457.

(380) Coulouarn, C.; Factor, V. M.; Andersen, J. B.; Durkin, M. E.; Thorgeirsson, S. S. Loss of miR-122 expression in liver cancer correlates with suppression of the hepatic phenotype and gain of metastatic properties. *Oncogene* **2009,** *28* (40), 3526-3536.

(381) Xu, H.; He, J.-H.; Xiao, Z.-D.; Zhang, Q.-Q.; Chen, Y.-Q.; Zhou, H.; Qu, L.-H. Liver-enriched transcription factors regulate MicroRNA-122 that targets CUTL1 during liver development. *Hepatology* **2010,** *52* (4), 1431-1442.

(382) Laudadio, I.; Manfroid, I.; Achouri, Y.; Schmidt, D.; Wilson, M. D.; Cordi, S.; Thorrez, L.; Knoops, L.; Jacquemin, P.; Schuit, F.; et al.; A Feedback Loop Between the Liver-Enriched Transcription Factor Network and Mir-122 Controls Hepatocyte Differentiation. *Gastroenterology* **2012,** *142* (1), 119-129.

(383) Gatfield, D.; Le Martelot, G.; Vejnar, C. E.; Gerlach, D.; Schaad, O.; Fleury-Olela, F.; Ruskeepää, A.-L.; Oresic, M.; Esau, C. C.; Zdobnov, E. M.; et al.; Integration of microRNA miR-122 in hepatic circadian gene expression. *Genes Dev.* **2009,** *23* (11), 1313-1326.

(384) Esau, C.; Davis, S.; Murray, S. F.; Yu, X. X.; Pandey, S. K.; Pear, M.; Watts, L.; Booten, S. L.; Graham, M.; McKay, R.; et al.; miR-122 regulation of lipid metabolism revealed by in vivo antisense targeting. *Cell Metab.* **2006,** *3* (2), 87-98.

(385) Cheung, O.; Puri, P.; Eicken, C.; Contos, M. J.; Mirshahi, F.; Maher, J. W.; Kellum, J. M.; Min, H.; Luketic, V. A.; Sanyal, A. J. Nonalcoholic steatohepatitis is associated with altered hepatic MicroRNA expression. *Hepatology* **2008,** *48* (6), 1810-1820.

(386) Hebbard, L.; George, J. Animal models of nonalcoholic fatty liver disease. *Nat. Rev. Gastroenterol. Hepatol.* **2010,** *8*, 35.

(387) Hsu, S.-H.; Wang, B.; Kutay, H.; Bid, H.; Shreve, J.; Zhang, X.; Costinean, S.; Bratasz, A.; Houghton, P.; Ghoshal, K. Hepatic loss of miR-122 predisposes mice to hepatobiliary cyst and hepatocellular carcinoma upon diethylnitrosamine exposure. *Am. J. Pathol.* **2013,** *183* (6), 1719-1730.

(388) Nakao, K.; Miyaaki, H.; Ichikawa, T. Antitumor function of microRNA-122 against hepatocellular carcinoma. *J. Gastroenterol.* **2014,** *49* (4), 589-593.

(389) Schult, P.; Roth, H.; Adams, R. L.; Mas, C.; Imbert, L.; Orlik, C.; Ruggieri, A.; Pyle, A. M.; Lohmann, V. microRNA-122 amplifies hepatitis C virus translation by shaping the structure of the internal ribosomal entry site. *Nat. Commun.* **2018,** *9*, 2613.

(390) Jopling, C. L.; Yi, M.; Lancaster, A. M.; Lemon, S. M.; Sarnow, P. Modulation of Hepatitis C Virus RNA Abundance by a Liver-Specific MicroRNA. *Science.* **2005,** *309* (5740), 1577-1581.

(391) Ahmed, C. S.; Winlow, P. L.; Parsons, A. L.; Jopling, C. L. Eukaryotic translation initiation factor 4AII contributes to microRNA-122 regulation of hepatitis C virus replication. *Nucleic Acids Res.* **2018,** *46* (12), 6330-6343.

(392) Thibault, P. A.; Huys, A.; Amador-Cañizares, Y.; Gailius, J. E.; Pinel, D. E.; Wilson, J. A. Regulation of Hepatitis C Virus Genome Replication by Xrn1 and MicroRNA-122 Binding to Individual Sites in the 5' Untranslated Region. *J. Virol.* **2015,** *89* (12), 6294-6311.

(393) Yamane, D.; Selitsky, S. R.; Shimakami, T.; Li, Y.; Zhou, M.; Honda, M.; Sethupathy, P.; Lemon, S. M. Differential hepatitis C virus RNA target site selection and host factor activities of naturally occurring miR-122 3′ variants. *Nucleic Acids Res.* **2017,** *45* (8), 4743-4755.

(394) Ono, C.; Fukuhara, T.; Motooka, D.; Nakamura, S.; Okuzaki, D.; Yamamoto, S.; Tamura, T.; Mori, H.; Sato, A.; Uemura, K.; et al.; Characterization of miR-122-independent propagation of HCV. *PLoS Pathog.* **2017,** *13* (5), e1006374-e1006374.

(395) Mitchell, J.; Lemon, S. M.; McGivern, D. R. How do persistent infections with hepatitis C virus cause liver cancer? *Curr. Opin. Virol.* **2015,** *14*, 101-108.

(396) New Hepatitis C Infections Nearly Tripled over Five Years. In *Deadly virus concentrated among baby boomers and increasing rapidly among new generations of Americans*, CDC: Online, 2017.

(397) WHO *Global hepatitis report 2017*; 2017; p 83.

(398) Sagan, S. M.; Chahal, J.; Sarnow, P. cis-Acting RNA elements in the hepatitis C virus RNA genome. *Virus Res.* **2015,** *206*, 90-98.

(399) Wang, L.; Jeng, K.-S.; Lai, M. M. C. Poly(C)-binding protein 2 interacts with sequences required for viral replication in the hepatitis C virus (HCV) 5' untranslated region and directs HCV RNA replication through circularizing the viral genome. *J. Virol.* **2011,** *85* (16), 7954-7964.

(400) Friebe, P.; Bartenschlager, R. Role of RNA structures in genome terminal sequences of the hepatitis C virus for replication and assembly. *J. Virol.* **2009,** *83* (22), 11989-11995.

(401) Henke, J. I.; Goergen, D.; Zheng, J.; Song, Y.; Schüttler, C. G.; Fehr, C.; Jünemann, C.; Niepmann, M. microRNA-122 stimulates translation of hepatitis C virus RNA. *EMBO J.* **2008,** *27* (24), 3300-3310.

(402) Shimakami, T.; Yamane, D.; Jangra, R. K.; Kempf, B. J.; Spaniel, C.; Barton, D. J.; Lemon, S. M. Stabilization of hepatitis C virus RNA by an Ago2-miR-122 complex. *Proc. Natl. Acad. Sci. U. S. A.* **2012,** *109* (3), 941-946.

(403) Masaki, T.; Arend, Kyle C.; Li, Y.; Yamane, D.; McGivern, David R.; Kato, T.; Wakita, T.; Moorman, Nathaniel J.; Lemon, Stanley M. miR-122 Stimulates Hepatitis C Virus

RNA Synthesis by Altering the Balance of Viral RNAs Engaged in Replication versus Translation. *Cell Host Microbe.* **2015,** *17* (2), 217-228.

(404) Qian, X.-J.; Zhu, Y.-Z.; Zhao, P.; Qi, Z.-T. Entry inhibitors: New advances in HCV treatment. *Emerg. Microbes Infect.* **2016,** *5* (1), e3-e3.

(405) Schinazi, R.; Halfon, P.; Marcellin, P.; Asselah, T. HCV direct-acting antiviral agents: the best interferon-free combinations. *Liver Int.* **2014,** *34* (s1), 69-78.

(406) Keating, G. M.; Vaidya, A. Sofosbuvir: First Global Approval. *Drugs.* **2014,** *74* (2), 273-282.

(407) Scott, L. J. Ledipasvir/Sofosbuvir: A Review in Chronic Hepatitis C. *Drugs.* **2018,** *78* (2), 245-256.

(408) Gandhi, Y.; Eley, T.; Fura, A.; Li, W.; Bertz, R. J.; Garimella, T. Daclatasvir: A Review of Preclinical and Clinical Pharmacokinetics. *Clin. Pharmacokinet.* **2018,** *57* (8), 911-928.

(409) Horsley-Silva, J. L.; Vargas, H. E. New Therapies for Hepatitis C Virus Infection. *Gastroenterol. Hepatol. (N.Y.)* **2017,** *13* (1), 22-31.

(410) Young, D. D.; Connelly, C. M.; Grohmann, C.; Deiters, A. Small molecule modifiers of microRNA miR-122 function for the treatment of hepatitis C virus infection and hepatocellular carcinoma. *J. Am. Chem. Soc.* **2010,** *132* (23), 7976-7981.

(411) Gumireddy, K.; Young, D. D.; Xiong, X.; Hogenesch, J. B.; Huang, Q.; Deiters, A. Small Molecule Inhibitors of MicroRNA miR-21 Function. *Angew. Chem. Int. Ed. Engl.* **2008,** *47* (39), 7482-7484.

(412) Cheng, A. M.; Byrom, M. W.; Shelton, J.; Ford, L. P. Antisense inhibition of human miRNAs and indications for an involvement of miRNA in cell growth and apoptosis. *Nucleic Acids Res.* **2005,** *33* (4), 1290-1297.

(413) Connelly, C. M.; Thomas, M.; Deiters, A. High-Throughput Luciferase Reporter Assay for Small-Molecule Inhibitors of MicroRNA Function. *J. Biomol. Screen.* **2012,** *17* (6), 822-828.

(414) Wilson, J. A.; Sagan, S. M. Hepatitis C virus and human miR-122: insights from the bench to the clinic. *Curr. Opin. Virol.* **2014,** *7*, 11-18.

(415) Lin, C. J.-F.; Gong, H.-Y.; Tseng, H.-C.; Wang, W.-L.; Wu, J.-L. miR-122 targets an anti-apoptotic gene, Bcl-w, in human hepatocellular carcinoma cell lines. *Biochem. Biophys. Res. Commun.* **2008,** *375* (3), 315-320.

(416) Hsiang, Y.-H.; Jiang, J. B.; Liu, L. F. Topoisomerase II-mediated DNA cleavage by amonafide and its structural analogs. *Mol. Pharmacol.* **1989,** *36* (3), 371-376.

(417) Stone, R. M.; Mazzola, E.; Neuberg, D.; Allen, S. L.; Pigneux, A.; Stuart, R. K.; Wetzler, M.; Rizzieri, D.; Erba, H. P.; Damon, L. Phase III open-label randomized study of cytarabine in combination with amonafide L-malate or daunorubicin as induction therapy for patients with secondary acute myeloid leukemia. *J. Clin. Oncol.* **2015,** *33* (11), 1252-1257.

(418) Hummel, R.; Wang, T.; Watson, D. I.; Michael, M. Z.; Van der Hoek, M.; Haier, J.; Hussey, D. J. Chemotherapy-induced modification of microRNA expression in esophageal cancer. *Oncol. Rep.* **2011,** *26* (4), 1011-1017.

(419) Roccaro, A. M.; Sacco, A.; Chen, C.; Runnels, J.; Leleu, X.; Azab, F.; Azab, A. K.; Jia, X.; Ngo, H. T.; Melhem, M. R.; et al.; microRNA expression in the biology, prognosis, and therapy of Waldenström macroglobulinemia. *Blood* **2009,** *113* (18), 4391-4402.

(420) Garzon, R.; Pichiorri, F.; Palumbo, T.; Visentini, M.; Aqeilan, R.; Cimmino, A.; Wang, H.; Sun, H.; Volinia, S.; Alder, H.; et al.; MicroRNA gene expression during retinoic acid-induced differentiation of human acute promyelocytic leukemia. *Oncogene* **2007,** *26*, 4148.

(421) Saito, Y.; Liang, G.; Egger, G.; Friedman, J. M.; Chuang, J. C.; Coetzee, G. A.; Jones, P. A. Specific activation of microRNA-127 with downregulation of the proto-oncogene BCL6 by chromatin-modifying drugs in human cancer cells. *Cancer Cell* **2006,** *9* (6), 435-443.

(422) Lujambio, A.; Ropero, S.; Ballestar, E.; Fraga, M. F.; Cerrato, C.; Setién, F.; Casado, S.; Suarez-Gauthier, A.; Sanchez-Cespedes, M.; Gitt, A.; et al.; Genetic Unmasking of an Epigenetically Silenced microRNA in Human Cancer Cells. *Cancer Res.* **2007,** *67* (4), 1424.

(423) Changmin, Y.; Linghui, Q.; Mahesh, U.; Lin, L.; Q., Y. S. Single-Vehicular Delivery of Antagomir and Small Molecules to Inhibit miR-122 Function in Hepatocellular Carcinoma Cells by using "Smart" Mesoporous Silica Nanoparticles. *Angew. Chem. Int. Ed. Engl.* **2015,** *127* (36), 10720-10724.

(424) Auld, D. S.; Thorne, N.; Maguire, W. F.; Inglese, J.; Collins, F. A. Mechanism of PTC124 Activity in Cell-Based Luciferase Assays of Nonsense Codon Suppression. *Proc. Natl. Acad. Sci. U.S.A.* **2009,** *106* (9), 3585-3590.

(425) Auld, D. S.; Inglese, J. Eli Lilly & Company and the National Center for Advancing Translational Sciences: 2016.

(426) Lassalas, P.; Gay, B.; Lasfargeas, C.; James, M. J.; Tran, V.; Vijayendran, K. G.; Brunden, K. R.; Kozlowski, M. C.; Thomas, C. J.; Smith, A. B.; et al.; Structure Property Relationships of Carboxylic Acid Isosteres. *J. Med. Chem.* **2016,** *59* (7), 3183-3203.

(427) Livak, K. J.; Schmittgen, T. D. Analysis of Relative Gene Expression Data Using Real-Time Quantitative PCR and the 2−ΔΔCT Method. *Methods* **2001,** *25* (4), 402-408.

(428) Gumireddy, K.; Young, D. D.; Xiong, X.; Hogenesch, J. B.; Huang, Q.; Deiters, A. Small Molecule Inhibitors of MicroRNA miR-21 Function. *Angew. Chem., Int. Ed. Engl.* **2008,** *47* (39), 7482-7484.

(429) Wang, N.; Wang, Q.; Shen, D.; Sun, X.; Cao, X.; Wu, D. Downregulation of microRNA-122 promotes proliferation, migration, and invasion of human hepatocellular carcinoma cells by activating epithelial–mesenchymal transition. *OncoTargets Ther.* **2016,** *9*, 2035-2047.

(430) Li, Z.-Y.; Xi, Y.; Zhu, W.-N.; Zeng, C.; Zhang, Z.-Q.; Guo, Z.-C.; Hao, D.-L.; Liu, G.; Feng, L.; Chen, H.-Z.; et al.; Positive regulation of hepatic miR-122 expression by HNF4α. *J. Hepatol.* **2011,** *55* (3), 602-611.

(431) Farré, D.; Roset, R.; Huerta, M.; Adsuara, J. E.; Roselló, L.; Albà, M. M.; Messeguer, X. Identification of patterns in biological sequences at the ALGGEN server: PROMO and MALGEN. *Nucleic Acids Res.* **2003,** *31* (13), 3651-3653.

(432) Messeguer, X.; Escudero, R.; Farré, D.; Núñez, O.; Martínez, J.; Albà, M. M. PROMO: Detection of known transcription regulatory elements using species-tailored searches. *Bioinformatics* **2002,** *18* (2), 333-334.

(433) Kiselyuk, A.; Lee, S.-H.; Farber-Katz, S.; Zhang, M.; Athavankar, S.; Cohen, T.; Pinkerton, Anthony B.; Ye, M.; Bushway, P.; Richardson, Adam D.; et al.; HNF4α Antagonists Discovered by a High-Throughput Screen for Modulators of the Human Insulin Promoter. *Chem. Biol.* **2012,** *19* (7), 806-818.

(434) Levy, G.; Habib, N.; Guzzardi, M. A.; Kitsberg, D.; Bomze, D.; Ezra, E.; Uygun, B. E.; Uygun, K.; Trippler, M.; Schlaak, J. F.; et al.; Nuclear receptors control pro-viral and antiviral metabolic responses to hepatitis C virus infection. *Nat. Chem. Biol.* **2016,** *12*, 1037.

(435) Janssen, H. L. A.; Reesink, H. W.; Lawitz, E. J.; Zeuzem, S.; Rodriguez-Torres, M.; Patel, K.; van der Meer, A. J.; Patick, A. K.; Chen, A.; Zhou, Y.; et al.; Treatment of HCV Infection by Targeting MicroRNA. *N. Engl. J. Med.* **2013,** *368* (18), 1685-1694.

(436) van der Ree, M. H.; van der Meer, A. J.; van Nuenen, A. C.; de Bruijne, J.; Ottosen, S.; Janssen, H. L.; Kootstra, N. A.; Reesink, H. W. Miravirsen dosing in chronic hepatitis C patients results in decreased microRNA-122 levels without affecting other microRNAs in plasma. *Aliment. Pharmacol. Ther.* **2016,** *43* (1), 102-113.

(437) Ottosen, S.; Parsley, T. B.; Yang, L.; Zeh, K.; van Doorn, L.-J.; van der Veer, E.; Raney, A. K.; Hodges, M. R.; Patick, A. K. In vitro antiviral activity and preclinical and clinical resistance profile of miravirsen, a novel anti-hepatitis C virus therapeutic targeting the human factor miR-122. *Antimicrob. Agents and Chemotherapy* **2015,** *59* (1), 599-608.

(438) Li, Y.; Masaki, T.; Yamane, D.; McGivern, D. R.; Lemon, S. M. Competing and noncompeting activities of miR-122 and the 5′ exonuclease Xrn1 in regulation of hepatitis C virus replication. *Proc. Natl. Acad. Sci. U.S.A.* **2013,** *110* (5), 1881-1886.

(439) Mortimer, S. A.; Doudna, J. A. Unconventional miR-122 binding stabilizes the HCV genome by forming a trimolecular RNA structure. *Nucleic Acids Res.* **2013,** *41* (7), 4230-4240.

(440) Roberts, A. P.; Lewis, A. P.; Jopling, C. L. miR-122 activates hepatitis C virus translation by a specialized mechanism requiring particular RNA components. *Nucleic Acids Res.* **2011,** *39* (17), 7716-7729.

(441) Bernier, A.; Sagan, S. M. Beyond sites 1 and 2, miR-122 target sites in the HCV genome have negligible contributions to HCV RNA accumulation in cell culture. *J. Gen. Virol.* **2019,** *100* (2), 217-226.

(442) Li, Y.; Yamane, D.; Masaki, T.; Lemon, S. M. The yin and yang of hepatitis C: synthesis and decay of hepatitis C virus RNA. *Nat. Rev. Microbiol.* **2015,** *13* (9), 544-558.

(443) Berezhna, S. Y.; Supekova, L.; Sever, M. J.; Schultz, P. G.; Deniz, A. A. Dual regulation of hepatitis C viral RNA by cellular RNAi requires partitioning of Ago2 to lipid droplets and P-bodies. *RNA.* **2011,** *17* (10), 1831-1845.

(444) Connelly, C. M.; Thomas, M.; Deiters, A. High-Throughput Luciferase Reporter Assay for Small-Molecule Inhibitors of MicroRNA Function. *J. Biomol. Screening* **2012,** *17* (6), 822-828.

(445) Kozikowski, B. A.; Burt, T. M.; Tirey, D. A.; Williams, L. E.; Kuzmak, B. R.; Stanton, D. T.; Morand, K. L.; Nelson, S. L. The Effect of Freeze/Thaw Cycles on the Stability of Compounds in DMSO. *J. Biomol. Screen.* **2003,** *8* (2), 210-215.

(446) Auld, D. S.; Thorne, N.; Maguire, W. F.; Inglese, J. Mechanism of PTC124 activity in cell-based luciferase assays of nonsense codon suppression. *Proc. Natl. Acad. Sci. U.S.A.* **2009,** *106* (9), 3585-3590.

(447) Livak, K. J.; Schmittgen, T. D. Analysis of Relative Gene Expression Data Using Real-Time Quantitative PCR and the 2−ΔΔCT Method. *Methods.* **2001,** *25* (4), 402-408.

(448) Schmittgen, T. D.; Jiang, J.; Liu, Q.; Yang, L. A high-throughput method to monitor the expression of microRNA precursors. *Nucleic Acids Res.* **2004,** *32* (4), e43-e43.

(449) Ho, S. N.; Hunt, H. D.; Horton, R. M.; Pullen, J. K.; Pease, L. R. Site-directed mutagenesis by overlap extension using the polymerase chain reaction. *Gene* **1989,** *77* (1), 51-59.

(450) Cai, X.; Hagedorn, C. H.; Cullen, B. R. Human microRNAs are processed from capped, polyadenylated transcripts that can also function as mRNAs. *RNA* **2004,** *10* (12), 1957-1966.

(451) Chan, J. A.; Krichevsky, A. M.; Kosik, K. S. MicroRNA-21 Is an Antiapoptotic Factor in Human Glioblastoma Cells. *Cancer Res.* **2005,** *65* (14), 6029.

(452) Roldo, C.; Missiaglia, E.; Hagan, J. P.; Falconi, M.; Capelli, P.; Bersani, S.; Calin, G. A.; Volinia, S.; Liu, C.-G.; Scarpa, A.; et al.; MicroRNA Expression Abnormalities in Pancreatic Endocrine and Acinar Tumors Are Associated With Distinctive Pathologic Features and Clinical Behavior. *J. Clin. Oncol.* **2006,** *24* (29), 4677-4684.

(453) Ji, R.; Cheng, Y.; Yue, J.; Yang, J.; Liu, X.; Chen, H.; Dean, D. B.; Zhang, C. MicroRNA Expression Signature and Antisense-Mediated Depletion Reveal an Essential Role of MicroRNA in Vascular Neointimal Lesion Formation. *Circ. Res.* **2007,** *100* (11), 1579-1588.

(454) Tatsuguchi, M.; Seok, H. Y.; Callis, T. E.; Thomson, J. M.; Chen, J.-F.; Newman, M.; Rojas, M.; Hammond, S. M.; Wang, D.-Z. Expression of microRNAs is dynamically regulated during cardiomyocyte hypertrophy. *J. Mol. Cell Cardiol.* **2007,** *42* (6), 1137-1141.

(455) Volinia, S.; Calin, G. A.; Liu, C.-G.; Ambs, S.; Cimmino, A.; Petrocca, F.; Visone, R.; Iorio, M.; Roldo, C.; Ferracin, M.; et al.; A microRNA expression signature of human solid tumors defines cancer gene targets. *Proc. Natl. Acad. Sci. U. S. A.* **2006,** *103* (7), 2257-2261.

(456) Kutay, H.; Bai, S.; Datta, J.; Motiwala, T.; Pogribny, I.; Frankel, W.; Jacob, S. T.; Ghoshal, K. Downregulation of miR-122 in the Rodent and Human Hepatocellular Carcinomas. *J. Cell. Biochem.* **2006,** *99* (3), 671-678.

(457) Zhang, Z.; Li, Z.; Gao, C.; Chen, P.; Chen, J.; Liu, W.; Xiao, S.; Lu, H. miR-21 plays a pivotal role in gastric cancer pathogenesis and progression. *Lab. Invest.* **2008,** *88* (12), 1358-1366.

(458) Iorio, M. V.; Visone, R.; Di Leva, G.; Donati, V.; Petrocca, F.; Casalini, P.; Taccioli, C.; Volinia, S.; Liu, C.-G.; Alder, H.; et al.; MicroRNA Signatures in Human Ovarian Cancer. *cancer Res.* **2007,** *67* (18), 8699-8707.

(459) Lui, W.-O.; Pourmand, N.; Patterson, B. K.; Fire, A. Patterns of Known and Novel Small RNAs in Human Cervical Cancer. *Cancer Res.* **2007,** *67* (13), 6031-6043.

(460) Tran, N.; McLean, T.; Zhang, X.; Zhao, C. J.; Thomson, J. M.; O'Brien, C.; Rose, B. MicroRNA expression profiles in head and neck cancer cell lines. *Biochem. Biophys. Res. Commun.* **2007,** *358* (1), 12-17.

(461) Tetzlaff, M.; Liu, A.; Xu, X.; Master, S.; Baldwin, D.; Tobias, J.; Livolsi, V.; Baloch, Z. Differential Expression of miRNAs in Papillary Thyroid Carcinoma Compared to Multinodular Goiter Using Formalin Fixed Paraffin Embedded Tissues. *Endocr Pathol* **2007,** *18* (3), 163-173.

(462) Fujita, S.; Ito, T.; Mizutani, T.; Minoguchi, S.; Yamamichi, N.; Sakurai, K.; Iba, H. miR-21 Gene Expression Triggered by AP-1 Is Sustained through a Double-Negative Feedback Mechanism. *J. Mol. Biol.* **2008,** *378* (3), 492-504.

(463) Frankel, L. B.; Christoffersen, N. R.; Jacobsen, A.; Lindow, M.; Krogh, A.; Lund, A. H. Programmed Cell Death 4 (PDCD4) Is an Important Functional Target of the MicroRNA miR-21 in Breast Cancer Cells. *J. Biol. Chem.* **2008,** *283* (2), 1026-1033.

(464) Asangani, I. A.; Rasheed, S. A. K.; Nikolova, D. A.; Leupold, J. H.; Colburn, N. H.; Post, S.; Allgayer, H. MicroRNA-21 (miR-21) post-transcriptionally downregulates tumor suppressor Pdcd4 and stimulates invasion, intravasation and metastasis in colorectal cancer. *Oncogene* **2007,** *27* (15), 2128-2136.

(465) Gabriely, G.; Wurdinger, T.; Kesari, S.; Esau, C. C.; Burchard, J.; Linsley, P. S.; Krichevsky, A. M. MicroRNA 21 Promotes Glioma Invasion by Targeting Matrix Metalloproteinase Regulators. *Mol. Cell. Biol.* **2008,** *28* (17), 5369-5380.

(466) Cmarik, J. L.; Min, H.; Hegamyer, G.; Zhan, S.; Kulesz-Martin, M.; Yoshinaga, H.; Matsuhashi, S.; Colburn, N. H. Differentially expressed protein Pdcd4 inhibits tumor promoter-induced neoplastic transformation. *Proceedings of the National Academy of Sciences* **1999,** *96* (24), 14037-14042.

(467) Jansen, A. P.; Camalier, C. E.; Colburn, N. H. Epidermal Expression of the Translation Inhibitor Programmed Cell Death 4 Suppresses Tumorigenesis. *Cancer Research* **2005,** *65* (14), 6034-6041.

(468) Leupold, J. H.; Yang, H. S.; Colburn, N. H.; Asangani, I.; Post, S.; Allgayer, H. Tumor suppressor Pdcd4 inhibits invasion//intravasation and regulates urokinase receptor (u-PAR) gene expression via Sp-transcription factors. *Oncogene* **2007,** *26* (31), 4550-4562.

(469) Talotta, F.; Cimmino, A.; Matarazzo, M. R.; Casalino, L.; De Vita, G.; D'Esposito, M.; Di Lauro, R.; Verde, P. An autoregulatory loop mediated by miR-21 and PDCD4 controls the AP-1 activity in RAS transformation. *Oncogene* **2008,** *28* (1), 73-84.

(470) Yang, H.-S.; Knies, J. L.; Stark, C.; Colburn, N. H. Pdcd4 suppresses tumor phenotype in JB6 cells by inhibiting AP-1 transactivation. *Oncogene* **2003,** *22*, 3712.

(471) Clark, J. M.; Thomas, D.; Choong, P. M.; Dass, C. RECK—a newly discovered inhibitor of metastasis with prognostic significance in multiple forms of cancer. *Cancer Metastasis Rev* **2007,** *26* (3-4), 675-683.

(472) Song, M. S.; Salmena, L.; Pandolfi, P. P. The functions and regulation of the PTEN tumour suppressor. *Nat Rev Mol Cell Biol* **2012,** *13* (5), 283-296.

(473) Blower, P. E.; Chung, J.-H.; Verducci, J. S.; Lin, S.; Park, J.-K.; Dai, Z.; Liu, C.-G.; Schmittgen, T. D.; Reinhold, W. C.; Croce, C. M.; et al.; MicroRNAs modulate the chemosensitivity of tumor cells. *Mol. Cancer Ther.* **2008,** *7* (1), 1-9.

(474) Hong, L.; Han, Y.; Zhang, Y.; Zhang, H.; Zhao, Q.; Wu, K.; Fan, D. MicroRNA-21: a therapeutic target for reversing drug resistance in cancer. *Expert Opin. Ther. Targets.* **2013,** *17* (9), 1073-1080.

(475) J.A. Chan, A. M. K., and K.S. Kosik MicroRNA-21 Is an Antiapoptotic Factor in Human Glioblastoma Cells. *Cancer Res* **2005,** *65* (14), 6029-6033.

(476) Chen, Z.; Yuan, Y.-C.; Wang, Y.; Liu, Z.; Chan, H. J.; Chen, S. Down-regulation of programmed cell death 4 (PDCD4) is associated with aromatase inhibitor resistance and a poor prognosis in estrogen receptor-positive breast cancer. *Breast Cancer Res. Treat.* **2015,** *152* (1), 29-39.

(477) Dong, J.; Zhao, Y.-P.; Zhou, L.; Zhang, T.-P.; Chen, G. Bcl-2 Upregulation Induced by miR-21 Via a Direct Interaction Is Associated with Apoptosis and Chemoresistance in MIA PaCa-2 Pancreatic Cancer Cells. *Arch. Med. Res.* **2011,** *42* (1), 8-14.

(478) Meng, F.; Henson, R.; Wehbe-Janek, H.; Ghoshal, K.; Jacob, S. T.; Patel, T. MicroRNA-21 regulates expression of the PTEN tumor suppressor gene in human hepatocellular cancer. *Gastroenterology* **2007,** *133* (2), 647-658.

(479) Yang, S.-m.; Huang, C.; Li, X.-f.; Yu, M.-z.; He, Y.; Li, J. miR-21 confers cisplatin resistance in gastric cancer cells by regulating PTEN. *Toxicology* **2013,** *306*, 162-168.

(480) Li, F.; Lv, J.-H.; Liang, L.; Wang, J.-c.; Li, C.-R.; Sun, L.; Li, T. Downregulation of microRNA-21 inhibited radiation-resistance of esophageal squamous cell carcinoma. *Cancer Cell Int.* **2018,** *18* (1), 39.

(481) Ma, Y.; Xia, H.; Liu, Y.; Li, M. Silencing miR-21 sensitizes non-small cell lung cancer A549 cells to ionizing radiation through inhibition of PI3K/Akt. *Biomed Res. Int.* **2014,** *2014*, 617868-617868.

(482) Liu, S.; Song, L.; Zhang, L.; Zeng, S.; Gao, F. miR-21 modulates resistance of HR-HPV positive cervical cancer cells to radiation through targeting LATS1. *Biochem. Biophys. Res. Commun.* **2015,** *459* (4), 679-685.

(483) Feng, Y.-H.; Tsao, C.-J. Emerging role of microRNA-21 in cancer. *Biomed. Rep.* **2016,** *5* (4), 395-402.

(484) Schmittgen, T. D.; Jiang, J.; Liu, Q.; Yang, L. A high- throughput method to monitor the expression of microRNA precursors. *Nucleic Acids Res.* **2004,** *32* (4), e43-e43.

(485) Changmin, Y.; Linghui, Q.; Jingyan, G.; Jiaqi, F.; Peiyan, Y.; L., Y. S. C.; Q., Y. S. Cell-Penetrating Poly(disulfide) Assisted Intracellular Delivery of Mesoporous Silica Nanoparticles for Inhibition of miR-21 Function and Detection of Subsequent Therapeutic Effects. *Angew. Chem. Int. Ed. Engl.* **2016,** *55* (32), 9272-9276.

(486) Jiang, C.-S.; Wang, X.-M.; Zhang, S.-Q.; Meng, L.-S.; Zhu, W.-H.; Xu, J.; Lu, S.-M. Discovery of 4-benzoylamino-N-(prop-2-yn-1-yl)benzamides as novel microRNA-21 inhibitors. *Bioorg. Med. Chem.* **2015,** *23* (19), 6510-6519.

(487) Naro, Y.; Thomas, M.; Stephens, M. D.; Connelly, C. M.; Deiters, A. Aryl amide small-molecule inhibitors of microRNA miR-21 function. *Bioorg. Med. Chem. Lett.* **2015,** *25* (21), 4793-4796.

(488) Guha, R. On exploring structure activity relationships. *Methods Mol. Biol.* **2013,** *993*, 81-94.

(489) Lee, Y. S.; Kim, H. K.; Chung, S.; Kim, K.-S.; Dutta, A. Depletion of Human Micro-RNA miR-125b Reveals That It Is Critical for the Proliferation of Differentiated Cells but Not

for the Down-regulation of Putative Targets during Differentiation. *J. Biol. Chem.* **2005,** *280* (17), 16635-16641.

(490) Amir, S.; Ma, A.-H.; Shi, X.-B.; Xue, L.; Kung, H.-J.; deVere White, R. W. Oncomir miR-125b suppresses p14ARF to modulate p53-dependent and p53-independent apoptosis in prostate cancer. *PloS One* **2013,** *8* (4), e61064.

(491) Tang, T.; Wong, H. K.; Gu, W.; Yu, M.-y.; To, K.-F.; Wang, C. C.; Wong, Y. F.; Cheung, T. H.; Chung, T. K. H.; Choy, K. W. MicroRNA-182 plays an onco-miRNA role in cervical cancer. *Gynecol. Oncol.* **2013,** *129* (1), 199-208.

(492) Mercatelli, N.; Coppola, V.; Bonci, D.; Miele, F.; Costantini, A.; Guadagnoli, M.; Bonanno, E.; Muto, G.; Frajese, G. V.; De Maria, R. The inhibition of the highly expressed miR-221 and miR-222 impairs the growth of prostate carcinoma xenografts in mice. *PloS One* **2008,** *3* (12), e4029.

(493) Naro, Y.; Thomas, M.; Stephens, M. D.; Connelly, C. M.; Deiters, A. Aryl amide small-molecule inhibitors of microRNA miR-21 function. *Bioorganic Med. Chem. Lett.* **2015,** *25* (21), 4793-4796.

(494) Maiti, M.; Nauwelaerts, K.; Herdewijn, P. Pre-microRNA binding aminoglycosides and antitumor drugs as inhibitors of Dicer catalyzed microRNA processing. *Bioorganic Med. Chem. Lett.* **2012,** *22* (4), 1709-1711.

(495) Velagapudi, S. P.; Gallo, S. M.; Disney, M. D. Sequence-based design of bioactive small molecules that target precursor microRNAs. *Nat. Chem. Biol.* **2014,** *10* (4), 291-297.

(496) Connelly, C. M.; Boer, R. E.; Moon, M. H.; Gareiss, P.; Schneekloth, J. S. Discovery of inhibitors of microRNA-21 processing using small molecule microarrays. *ACS Chem. Bio.* **2017,** *12* (2), 435-443.

(497) Jin, E.; Katritch, V.; Olson, W. K.; Kharatisvili, M.; Abagyan, R.; Pilch, D. S. Aminoglycoside binding in the major groove of duplex RNA: the thermodynamic and electrostatic forces that govern recognition1. *J. Mol. Biol.* **2000,** *298* (1), 95-110.

(498) Krol, J.; Loedige, I.; Filipowicz, W. The widespread regulation of microRNA biogenesis, function and decay. *Nature Rev. Genet.* **2010,** *11*, 597.

(499) Loedige, I.; Filipowicz, W. TRIM-NHL proteins take on miRNA regulation. *Cell* **2009,** *136* (5), 818-820.

(500) Wulczyn, F. G.; Cuevas, E.; Franzoni, E.; Rybak, A. miRNAs need a trim. In *Regulation of microRNAs*, Grobhans, H., Ed. Springer US: New York, NY, 2010; pp 85-105.

(501) Bai, B.; Liu, H.; Laiho, M. Small RNA expression and deep sequencing analyses of the nucleolus reveal the presence of nucleolus-associated microRNAs. *FEBS Open Bio* **2014,** *4*, 441-449.

(502) Leung, A. K. L. The whereabouts of miRNA actions: cytoplasm and beyond. *Trends Cell Biol.* **2015,** *25* (10), 601-610.

(503) Poria, D. K.; Guha, A.; Nandi, I.; Ray, P. S. RNA-binding protein HuR sequesters microRNA-21 to prevent translation repression of proinflammatory tumor suppressor gene programmed cell death 4. *Oncogene* **2016,** *35* (13), 1703-1715.

(504) Xia, M.; Huang, R.; Witt, K. L.; Southall, N.; Fostel, J.; Cho, M.-H.; Jadhav, A.; Smith, C. S.; Inglese, J.; Portier, C. J.; et al.; Compound cytotoxicity profiling using quantitative high-throughput screening. *Environ. Health Perspect.* **2008,** *116* (3), 284-291.

(505) Gaudelot, K.; Gibier, J.-B.; Pottier, N.; Hémon, B.; Van Seuningen, I.; Glowacki, F.; Leroy, X.; Cauffiez, C.; Gnemmi, V.; Aubert, S.; et al.; Targeting miR-21 decreases expression of multi-drug resistant genes and promotes chemosensitivity of renal carcinoma. *Tumor Biol.* **2017,** *39* (7), 1010428317707372.

(506) Ren, Y.; Zhou, X.; Mei, M.; Yuan, X.-B.; Han, L.; Wang, G.-X.; Jia, Z.-F.; Xu, P.; Pu, P.-Y.; Kang, C.-S. MicroRNA-21 inhibitor sensitizes human glioblastoma cells U251 (PTEN-mutant) and LN229 (PTEN-wild type) to taxol. *BMC Cancer* **2010,** *10* (1), 27.

(507) Li, Y.; Zhu, X.; Gu, J.; Hu, H.; Dong, D.; Yao, J.; Lin, C.; Fei, J. Anti-miR-21 oligonucleotide enhances chemosensitivity of leukemic HL60 cells to arabinosylcytosine by inducing apoptosis. *Hematology* **2010,** *15* (4), 215-221.

(508) Zhang, S.; Wan, Y.; Pan, T.; Gu, X.; Qian, C.; Sun, G.; Sun, L.; Xiang, Y.; Wang, Z.; Shi, L. MicroRNA-21 inhibitor sensitizes human glioblastoma U251 stem cells to chemotherapeutic drug temozolomide. *J. Mol. Neurosci.* **2012,** *47* (2), 346-356.

(509) Park, J.-K.; Lee, E. J.; Esau, C.; Schmittgen, T. D. Antisense inhibition of microRNA-21 or-221 arrests cell cycle, induces apoptosis, and sensitizes the effects of gemcitabine in pancreatic adenocarcinoma. *Pancreas* **2009,** *38* (7), e190-e199.

(510) ten Bokkel Huinink, W.; Lane, S. R.; Ross, G. A. Long-term survival in a phase III, randomised study of topotecan versus paclitaxel in advanced epithelial ovarian carcinoma. *Ann. Oncol.* **2004,** *15* (1), 100-103.

(511) Brave, M.; Dagher, R.; Farrell, A.; Abraham, S.; Ramchandani, R.; Gobburu, J.; Booth, B.; Jiang, X.; Sridhara, R.; Justice, R. Topotecan in combination with cisplatin for the

treatment of stage IVB, recurrent, or persistent cervical cancer. *Oncology* **2006,** *20* (11), 1401-4.

(512) Ardizzoni, A. Topotecan in the Treatment of Recurrent Small Cell Lung Cancer: An Update. *Oncologist* **2004,** *9* (suppl 6), 4-13.

(513) Law, T. M.; Ilson, D. H.; Motzer, R. J. Phase II trial of topotecan in patients with advanced renal cell carcinoma. *Invest. New Drugs* **1994,** *12* (2), 143-145.

(514) Gupta, D.; Bronstein, I. B.; Holden, J. A. Expression of DNA topoisomerase I in neoplasms of the kidney: Correlation with histological grade, proliferation, and patient survival. *Hum. Pathol.* **2000,** *31* (2), 214-219.

(515) Chen, J. U. N.; Zhu, H. E.; Zhang, Y. A. N.; Cui, M.-H.; Han, L.-Y.; Jia, Z.-H.; Wang, L.; Teng, H.; Miao, L.-N. Low expression of phosphatase and tensin homolog in clear-cell renal cell carcinoma contributes to chemoresistance through activating the Akt/HDM2 signaling pathway. *Mol. Med. Rep.* **2015,** *12* (2), 2622-2628.

(516) Yuan, H.; Xin, S.; Huang, Y.; Bao, Y.; Jiang, H.; Zhou, L.; Ren, X.; Li, L.; Wang, Q.; Zhang, J. Downregulation of PDCD4 by miR-21 suppresses tumor transformation and proliferation in a nude mouse renal cancer model. *Oncol. Lett.* **2017,** *14* (3), 3371-3378.

(517) Shen, H.; Zhu, F.; Liu, J.; Xu, T.; Pei, D.; Wang, R.; Qian, Y.; Li, Q.; Wang, L.; Shi, Z.; et al.; Alteration in miR-21/PTEN expression modulates gefitinib resistance in non-small cell lung cancer. *PLoS One* **2014,** *9* (7), e103305.

(518) Ren, W.; Wang, X.; Gao, L.; Li, S.; Yan, X.; Zhang, J.; Huang, C.; Zhang, Y.; Zhi, K. miR-21 modulates chemosensitivity of tongue squamous cell carcinoma cells to cisplatin by targeting PDCD4. *Mol. Cell. Biochem.* **2014,** *390* (1), 253-262.

(519) Shi, G.-h.; Ye, D.-w.; Yao, X.-d.; Zhang, S.-l.; Dai, B.; Zhang, H.-l.; Shen, Y.-j.; Zhu, Y.; Zhu, Y.-p.; Xiao, W.-j.; et al.; Involvement of microRNA-21 in mediating chemo-resistance to docetaxel in androgen-independent prostate cancer PC3 cells. *Acta Pharmacol. Sin.* **2010,** *31*, 867.

(520) Gumireddy, K.; Young, D. D.; Xiong, X.; Hogenesch, J. B.; Huang, Q.; Deiters, A. Small-molecule inhibitors of microRNA miR-21 function. *Angew. Chem. Int. Ed.* **2008,** *47* (39), 7482-7484.

(521) Schmittgen, T. D.; Lee, E. J.; Jiang, J.; Sarkar, A.; Yang, L.; Elton, T. S.; Chen, C. Real-time PCR quantification of precursor and mature microRNA. *Methods* **2008,** *44* (1), 31-38.

(522) Scudiero, D. A.; Shoemaker, R. H.; Paull, K. D.; Monks, A.; Tierney, S.; Nofziger, T. H.; Currens, M. J.; Seniff, D.; Boyd, M. R. Evaluation of a Soluble Tetrazolium/Formazan Assay for Cell Growth and Drug Sensitivity in Culture Using Human and Other Tumor Cell Lines. *Cancer Res.* **1988,** *48* (17), 4827-4833.

(523) Sittampalam, G. S.; Coussens, N. P.; Brimacombe, K.; Grossman, A.; Arkin, M.; Auld, D.; Austin, C.; Baell, J.; Bejcek, B.; Chung, T. D. Y. Assay guidance manual. **2004**.

(524) Zhou, Y.; Zhou, Y.; Shingu, T.; Feng, L.; Chen, Z.; Ogasawara, M.; Keating, M. J.; Kondo, S.; Huang, P. Metabolic Alterations in Highly Tumorigenic Glioblastoma Cells: Preference for hypoxia and high dependency on glycolysis. *J. Biol. Chem.* **2011,** *286* (37), 32843-32853.

(525) Schneider, C. A.; Rasband, W. S.; Eliceiri, K. W. NIH Image to ImageJ: 25 years of Image Analysis. *Nature methods* **2012,** *9* (7), 671-675.

(526) Thorne, N.; Shen, M.; Lea, Wendy A.; Simeonov, A.; Lovell, S.; Auld, Douglas S.; Inglese, J. Firefly Luciferase in Chemical Biology: A Compendium of Inhibitors, Mechanistic Evaluation of Chemotypes, and Suggested Use As a Reporter. *Chem. Biol.* **2012,** *19* (8), 1060-1072.

(527) Du, G.; Cao, D.; Meng, L. miR-21 inhibitor suppresses cell proliferation and colony formation through regulating the PTEN/AKT pathway and improves paclitaxel sensitivity in cervical cancer cells. *Mol. Med. Rep.* **2017,** *15* (5), 2713-2719.

(528) Gu, J.-B.; Bao, X.-B.; Ma, Z. Effects of miR-21 on proliferation and apoptosis in human gastric adenocarcinoma cells. *Oncol. Lett.* **2018,** *15* (1), 618-622.

(529) Zhou, B.; Wang, D.; Sun, G.; Mei, F.; Cui, Y.; Xu, H. Effect of miR-21 on Apoptosis in Lung Cancer Cell Through Inhibiting the PI3K/ Akt/NF-κB Signaling Pathway *Cellular Physiol. Biochem.* **2018,** *46* (3), 999-1008.

(530) Najafi, Z.; Sharifi, M.; Javadi, G. Degradation of miR-21 induces apoptosis and inhibits cell proliferation in human hepatocellular carcinoma. *Cancer Gene Ther.* **2015,** *22* (11), 530.

(531) Wagenaar, T. R.; Zabludoff, S.; Ahn, S.-M.; Allerson, C.; Arlt, H.; Baffa, R.; Cao, H.; Davis, S.; Garcia-Echeverria, C.; Gaur, R.; et al.; Anti–miR-21 Suppresses Hepatocellular Carcinoma Growth via Broad Transcriptional Network Deregulation. *Mol. Cancer Res.* **2015,** *13* (6), 1009-1021.

(532) Lam, H. C.; Liu, H.-J.; Baglini, C. V.; Filippakis, H.; Alesi, N.; Nijmeh, J.; Du, H.; Lope, A. L.; Cottrill, K. A.; Handen, A. Rapamycin-induced miR-21 promotes mitochondrial homeostasis and adaptation in mTORC1 activated cells. *Oncotarget* **2017,** *8* (39), 64714.

(533) Wang, P.; Guan, Q.; Zhou, D.; Yu, Z.; Song, Y.; Qiu, W. miR-21 Inhibitors Modulate Biological Functions of Gastric Cancer Cells via PTEN/PI3K/mTOR Pathway. *DNA Cell Biol.* **2018,** *37* (1), 38-45.

(534) Yao, Q.; Xu, H.; Zhang, Q.-Q.; Zhou, H.; Qu, L.-H. MicroRNA-21 promotes cell proliferation and down-regulates the expression of programmed cell death 4 (PDCD4) in HeLa cervical carcinoma cells. *Biochem. Biophys. Res. Commun.* **2009,** *388* (3), 539-542.

(535) Bose, D.; Jayaraj, G.; Suryawanshi, H.; Agarwala, P.; Pore, S. K.; Banerjee, R.; Maiti, S. The Tuberculosis Drug Streptomycin as a Potential Cancer Therapeutic: Inhibition of miR-21 Function by Directly Targeting Its Precursor. *Angew. Chem. Int. Ed. Engl.* **2012,** *51* (4), 1019-1023.

(536) Velagapudi, S. P.; Costales, M. G.; Vummidi, B. R.; Nakai, Y.; Angelbello, A. J.; Tran, T.; Haniff, H. S.; Matsumoto, Y.; Wang, Z. F.; Chatterjee, A. K.; et al.; Approved Anti-cancer Drugs Target Oncogenic Non-coding RNAs. *Cell Chem. Biol.* **2018,** *25* (9), 1086-1094.e7.

(537) Naro, Y.; Ankenbruck, N.; Thomas, M.; Tivon, Y.; Connelly, C. M.; Gardner, L.; Deiters, A. Small Molecule Inhibition of MicroRNA miR-21 Rescues Chemosensitivity of Renal-Cell Carcinoma to Topotecan. *J. Med. Chem.* **2018,** *61* (14), 5900-5909.

(538) Gumireddy, K.; Young, D. D.; Xiong, X.; Hogenesch, J. B.; Huang, Q.; Deiters, A. Small-molecule inhibitors of microrna miR-21 function. *Angew. Chem. Int. Ed. Engl.* **2008,** *47* (39), 7482-7484.

(539) Kölmel, D. K.; Kool, E. T. Oximes and Hydrazones in Bioconjugation: Mechanism and Catalysis. *Chem. Rev.* **2017,** *117* (15), 10358-10376.

(540) Abu Ajaj, K.; El-Abadla, N.; Welker, P.; Azab, S.; Zeisig, R.; Fichtner, I.; Kratz, F. Comparative evaluation of the biological properties of reducible and acid-sensitive folate prodrugs of a highly potent doxorubicin derivative. *Eur. J. Cancer.* **2012,** *48* (13), 2054-2065.

(541) Huan, M.; Zhang, B.; Teng, Z.; Cui, H.; Wang, J.; Liu, X.; Xia, H.; Zhou, S.; Mei, Q. In Vitro and In Vivo Antitumor Activity of a Novel pH-Activated Polymeric Drug Delivery System for Doxorubicin. *PLoS One.* **2012,** *7* (9), e44116.

(542) Thorne, N. I., J.; Auld, D. Illuminating Insights into Firefly Luciferase and Other Bioluminescent Reporters Used in Chemical Biology. *Chem. Biol.* **2010,** *17* (6), 646-657.

(543) Clamp, M.; Fry, B.; Kamal, M.; Xie, X.; Cuff, J.; Lin, M. F.; Kellis, M.; Lindblad-Toh, K.; Lander, E. S. Distinguishing protein-coding and noncoding genes in the human genome. *Proc. Natl. Acad. Sci. U. S. A.* **2007,** *104* (49), 19428-19433.

(544) Ezkurdia, I.; Juan, D.; Rodriguez, J. M.; Frankish, A.; Diekhans, M.; Harrow, J.; Vazquez, J.; Valencia, A.; Tress, M. L. Multiple evidence strands suggest that there may be as few as 19,000 human protein-coding genes. *Hum. Mol. Genet.* **2014,** *23* (22), 5866-5878.

(545) Hopkins, A. L.; Groom, C. R. The druggable genome. *Nat. Rev. Drug Discov.* **2002,** *1*, 727.

(546) Overington, J. P.; Al-Lazikani, B.; Hopkins, A. L. How many drug targets are there? *Nat. Rev. Drug Discov.* **2006,** *5*, 993.

(547) Dixon, S. J.; Stockwell, B. R. Identifying druggable disease-modifying gene products. *Curr. Opin. Chem. Biol.* **2009,** *13* (5-6), 549-555.

(548) Santos, R.; Ursu, O.; Gaulton, A.; Bento, A. P.; Donadi, R. S.; Bologa, C. G.; Karlsson, A.; Al-Lazikani, B.; Hersey, A.; Oprea, T. I.; et al.; A comprehensive map of molecular drug targets. *Nat. Rev. Drug Discov.* **2017,** *16* (1), 19-34.

(549) Matsui, M.; Corey, D. R. Non-coding RNAs as drug targets. *Nat. Rev. Drug Discov.* **2017,** *16* (3), 167-179.

(550) Adams, B. D.; Parsons, C.; Walker, L.; Zhang, W. C.; Slack, F. J. Targeting noncoding RNAs in disease. *J. Clin. Invest.* **2017,** *127* (3), 761-771.

(551) Ganser, L. R.; Lee, J.; Rangadurai, A.; Merriman, D. K.; Kelly, M. L.; Kansal, A. D.; Sathyamoorthy, B.; Al-Hashimi, H. M. High-performance virtual screening by targeting a high-resolution RNA dynamic ensemble. *Nat. Struct. Mol. Biol.* **2018,** *25* (5), 425-434.

(552) Barril, X.; Morley, S. D. Unveiling the Full Potential of Flexible Receptor Docking Using Multiple Crystallographic Structures. *J. Med. Chem.* **2005,** *48* (13), 4432-4443.

(553) Tian, S.; Sun, H.; Pan, P.; Li, D.; Zhen, X.; Li, Y.; Hou, T. Assessing an Ensemble Docking-Based Virtual Screening Strategy for Kinase Targets by Considering Protein Flexibility. *J. Chem. Inf. Model.* **2014,** *54* (10), 2664-2679.

(554) Tolman, J. R.; Flanagan, J. M.; Kennedy, M. A.; Prestegard, J. H. Nuclear magnetic dipole interactions in field-oriented proteins: information for structure determination in solution. *Proc. Natl. Acad. Sci. U. S. A.* **1995,** *92* (20), 9279-9283.

(555) Tjandra, N.; Bax, A. Direct Measurement of Distances and Angles in Biomolecules by NMR in a Dilute Liquid Crystalline Medium. *Science* **1997,** *278* (5340), 1111.

(556) Bender, A.; Glen, R. C. A Discussion of Measures of Enrichment in Virtual Screening: Comparing the Information Content of Descriptors with Increasing Levels of Sophistication. *J. Chem. Inf. Model.* **2005,** *45* (5), 1369-1375.

(557) DiMasi, J. A.; Grabowski, H. G.; Hansen, R. W. Innovation in the pharmaceutical industry: New estimates of R&D costs. *J. Health Econ.* **2016,** *47*, 20-33.

(558) Arun, G.; Diermeier, S. D.; Spector, D. L. Therapeutic Targeting of Long Non-Coding RNAs in Cancer. *Trends Mol. Med.* **2018,** *24* (3), 257-277.

(559) Liu, Y.; Wang, J. Therapeutic Potentials of Noncoding RNAs: Targeted Delivery of ncRNAs in Cancer Cells. In *The Long and Short Non-coding RNAs in Cancer Biology*, Song, E., Ed. Springer Singapore: Singapore, 2016; pp 429-458.

(560) Dai, Z.; Chu, H.; Ma, J.; Yan, Y.; Zhang, X.; Liang, Y. The Regulatory Mechanisms and Therapeutic Potential of MicroRNAs: From Chronic Pain to Morphine Tolerance. *Front. Mol. Neurosci.* **2018,** *11*, 80.

(561) Luck, M. E.; Muljo, S. A.; Collins, C. B. Prospects for Therapeutic Targeting of MicroRNAs in Human Immunological Diseases. *J. Immunol.* **2015,** *194* (11), 5047.

(562) Cole, J.; Morris, P.; Dickman, M. J.; Dockrell, D. H. The therapeutic potential of epigenetic manipulation during infectious diseases. *Pharmacol. Ther.* **2016,** *167*, 85-99.

(563) Wood, I. C. The Contribution and Therapeutic Potential of Epigenetic Modifications in Alzheimer's Disease. *Front. Neurosci.* **2018,** *12*, 649-649.

(564) Gillet, L. C.; Leitner, A.; Aebersold, R. Mass Spectrometry Applied to Bottom-Up Proteomics: Entering the High-Throughput Era for Hypothesis Testing. *Annu. Rev. Anal. Chem. (Palo Alto Calif.).* **2016,** *9* (1), 449-472.

(565) Rohman, M.; Wingfield, J. High-Throughput Screening Using Mass Spectrometry within Drug Discovery. In *Methods Mol. Biol.*, Janzen, W. P., Ed. Springer New York: New York, NY, 2016; pp 47-63.

(566) Sajic, T.; Liu, Y.; Aebersold, R. Using data-independent, high-resolution mass spectrometry in protein biomarker research: Perspectives and clinical applications. *Proteomics Clin. Appl.* **2015,** *9* (3-4), 307-321.

(567) Cleland, T. P.; DeHart, C. J.; Fellers, R. T.; VanNispen, A. J.; Greer, J. B.; LeDuc, R. D.; Parker, W. R.; Thomas, P. M.; Kelleher, N. L.; Brodbelt, J. S. High-Throughput Analysis of Intact Human Proteins Using UVPD and HCD on an Orbitrap Mass Spectrometer. *J. Proteome Res.* **2017,** *16* (5), 2072-2079.

(568) Horváth, I. T.; Rábai, J. Facile Catalyst Separation Without Water: Fluorous Biphase Hydroformylation of Olefins. *Science* **1994,** *266* (5182), 72.

(569) Spargo, P. L. Handbook of Fluorous Chemistry Edited by John A. Gladysz, Dennis P. Curran, and Istvan T. Horvath. Wiley-VCH: Weinheim. 2004. 595 pp. £125. ISBN 3-527-30617-x. *Org. Process Res. Dev.* **2005,** *9* (6), 1019-1020.

(570) Song, Z.; Zhang, Q. Fluorous Aryldiazirine Photoaffinity Labeling Reagents. *Org. Lett.* **2009,** *11* (21), 4882-4885.

(571) Miriyala, B. Fluorous Methods for the Synthesis of Peptides and Oligonucleotides. In *Top Curr. Chem.*, Horváth, I. T., Ed. Springer Berlin Heidelberg: Berlin, Heidelberg, 2012; pp 105-133.

(572) Miller, M. A.; Sletten, E. M. A General Approach to Biocompatible Branched Fluorous Tags for Increased Solubility in Perfluorocarbon Solvents. *Org. Lett.* **2018,** *20* (21), 6850-6854.

(573) Pearson, W. H.; Berry, D. A.; Stoy, P.; Jung, K.-Y.; Sercel, A. D. Fluorous Affinity Purification of Oligonucleotides. *J. Org. Chem.* **2005,** *70* (18), 7114-7122.

(574) Porel, M.; Thornlow, D. N.; Phan, N. N.; Alabi, C. A. Sequence-defined bioactive macrocycles via an acid-catalysed cascade reaction. *Nat. Chem.* **2016,** *8*, 590.

(575) Zhao, M.; Deng, C. Designed synthesis of fluorous-functionalized magnetic mesoporous microspheres for specific enrichment of phosphopeptides with fluorous derivatization. *Proteomics* **2016,** *16* (7), 1051-1058.

(576) Huang, H.; Haar Petersen, M.; Ibañez-Vea, M.; Lassen, P. S.; Larsen, M. R.; Palmisano, G. Simultaneous Enrichment of Cysteine-containing Peptides and Phosphopeptides Using a Cysteine-specific Phosphonate Adaptable Tag (CysPAT) in Combination with titanium dioxide (TiO2) Chromatography. *Mol. Cell Proteomics.* **2016,** *15* (10), 3282-3296.

(577) Li, B.-Y.; Juang, D. S.; Adak, A. K.; Hwang, K.-C.; Lin, C.-C. Fabrication of a protein microarray by fluorous-fluorous interactions. *Sci. Rep.* **2017,** *7* (1), 7053.

(578) Vegas, A. J.; Bradner, J. E.; Tang, W.; McPherson, O. M.; Greenberg, E. F.; Koehler, A. N.; Schreiber, S. L. Fluorous-based small-molecule microarrays for the discovery of histone deacetylase inhibitors. *Angew. Chem. Int. Ed. Engl.* **2007,** *46* (42), 7960-7964.

(579) Flynn, G. E.; Withers, J. M.; Macias, G.; Sperling, J. R.; Henry, S. L.; Cooper, J. M.; Burley, G. A.; Clark, A. W. Reversible DNA micro-patterning using the fluorous effect. *Chem. Commun.* **2017,** *53* (21), 3094-3097.

(580) Yates III, J. R. Mass spectrometry and the age of the proteome. *J. Mass Spectrom.* **1998,** *33* (1), 1-19.

(581) Singhal, N.; Kumar, M.; Kanaujia, P. K.; Virdi, J. S. MALDI-TOF mass spectrometry: an emerging technology for microbial identification and diagnosis. *Front. Microbiol.* **2015,** *6* (791).

(582) Yalcin, E. B.; de la Monte, S. M. Review of Matrix-Assisted Laser Desorption Ionization-Imaging Mass Spectrometry for Lipid Biochemical Histopathology. *J. Histochem. Cytochem.* **2015,** *63* (10), 762-771.

(583) Steuer, A. E.; Poetzsch, M.; Kraemer, T. MALDI-MS drug analysis in biological samples: opportunities and challenges. *Bioanalysis* **2016,** *8* (17), 1859-1878.

(584) Chou, C.-W.; Limbach, P. A.; Cole, R. B. Fragmentation pathway studies of oligonucleotides in matrix-assisted laser desorption/ionization mass. *J. Am. Soc. Mass Spectrom.* **2002,** *13* (12), 1407-1417.

(585) Chen, W.-Y.; Chen, Y.-C. MALDI MS Analysis of Oligonucleotides: Desalting by Functional Magnetite Beads Using Microwave-Assisted Extraction. *Anal. Chem.* **2007,** *79* (21), 8061-8066.

(586) Weng, M.-F.; Chen, Y.-C. Using sol–gel/crown ether hybrid materials as desalting substrates for matrix-assisted laser desorption/ionization analysis of oligonucleotides. *Rapid Commun. Mass Spectrom.* **2004,** *18* (13), 1421-1428.

(587) Jiang, Y.; Hofstadler, S. A. A highly efficient and automated method of purifying and desalting PCR products for analysis by electrospray ionization mass spectrometry. *Anal. Biochem.* **2003,** *316* (1), 50-57.

(588) Fountain, K. J.; Gilar, M.; Gebler, J. C. Electrospray ionization mass spectrometric analysis of nucleic acids using high-throughput on-line desalting. *Rapid Commun. Mass Spectrom.* **2004,** *18* (12), 1295-1302.

(589) Fu, Y.; Xu, S.; Pan, C.; Ye, M.; Zou, H.; Guo, B. A matrix of 3,4-diaminobenzophenone for the analysis of oligonucleotides by matrix-assisted laser desorption/ionization time-of-flight mass spectrometry. *Nucleic Acids Res.* **2006,** *34* (13), e94-e94.

(590) Zagorevskii, D. V.; Aldersley, M. F.; Ferris, J. P. MALDI Analysis of Oligonucleotides Directly from Montmorillonite. *J. Am. Soc. Mass Spectrom.* **2006,** *17* (9), 1265-1270.

(591) Tang, K.; Garcia, B. A.; Shahgholi, M.; Chiu, N. H. L.; Heaney, P. J. Sugar additives for MALDI matrices improve signal allowing the smallest nucleotide change (A:T) in a DNA sequence to be resolved. *Nucleic Acids Res.* **2001,** *29* (19), e91-e91.

(592) Lecchi, P.; Le, H. M.; Pannell, L. K. 6-Aza-2-thiothymine: a matrix for MALDI spectra of oligonucleotides. *Nucleic Acids Res.* **1995,** *23* (7), 1276-1277.

(593) Asara, J. M.; Allison, J. Enhanced Detection of Oligonucleotides in UV MALDI MS Using the Tetraamine Spermine as a Matrix Additive. *Anal. Chem.* **1999,** *71* (14), 2866-2870.

(594) Tsubery, H.; Mrksich, M. Biochemical Assays of Immobilized Oligonucleotides with Mass Spectrometry. *Langmuir* **2008,** *24* (10), 5433-5438.

(595) Kim, J.; Mrksich, M. Profiling the selectivity of DNA ligases in an array format with mass spectrometry. *Nucleic Acids Res.* **2010,** *38* (1), e2-e2.

(596) Shumaker-Parry, J. S.; Zareie, M. H.; Aebersold, R.; Campbell, C. T. Microspotting Streptavidin and Double-Stranded DNA Arrays on Gold for High-Throughput Studies of Protein−DNA Interactions by Surface Plasmon Resonance Microscopy. *Anal. Chem.* **2004,** *76* (4), 918-929.

(597) Chivers, C. E.; Crozat, E.; Chu, C.; Moy, V. T.; Sherratt, D. J.; Howarth, M. A streptavidin variant with slower biotin dissociation and increased mechanostability. *Nat. Methods* **2010,** *7*, 391.

(598) Gurard-Levin, Z. A.; Scholle, M. D.; Eisenberg, A. H.; Mrksich, M. High-throughput screening of small molecule libraries using SAMDI mass spectrometry. *ACS Comb. Sci.* **2011,** *13* (4), 347-350.

(599) Ahmed, R.; Spikings, E.; Zhou, S.; Thompsett, A.; Zhang, T. Pre-hybridisation: An efficient way of suppressing endogenous biotin-binding activity inherent to biotin–streptavidin detection system. *J. Immunol. Methods.* **2014,** *406*, 143-147.

(600) Norton, R.; Heuzenroeder, M.; Manning, P. A. Non-Specific Serum Binding to Streptavidin in a Biotinylated Peptide Based Enzyme Immunoassay. *J. Immunoassay.* **1996,** *17* (3), 195-204.

(601) Morris, P. D.; Byrd, A. K.; Tackett, A. J.; Cameron, C. E.; Tanega, P.; Ott, R.; Fanning, E.; Raney, K. D. Hepatitis C Virus NS3 and Simian Virus 40 T Antigen Helicases Displace Streptavidin from 5‘-Biotinylated Oligonucleotides but Not from 3‘-Biotinylated Oligonucleotides: Evidence for Directional Bias in Translocation on Single-Stranded DNA. *Biochemistry* **2002,** *41* (7), 2372-2378.

(602) Schwartz, A.; Margeat, E.; Rahmouni, A. R.; Boudvillain, M. Transcription Termination Factor Rho Can Displace Streptavidin from Biotinylated RNA. *J. Biol. Chem.* **2007,** *282* (43), 31469-31476.

(603) Beloqui, A.; Calvo, J.; Serna, S.; Yan, S.; Wilson, I. B. H.; Martin-Lomas, M.; Reichardt, N. C. Analysis of Microarrays by MALDI-TOF MS. *Angew. Chem. Int. Ed. Engl.* **2013,** *52* (29), 7477-7481.

(604) López de Laorden, C.; Beloqui, A.; Yate, L.; Calvo, J.; Puigivila, M.; Llop, J.; Reichardt, N.-C. Nanostructured Indium Tin Oxide Slides for Small-Molecule Profiling and Imaging Mass Spectrometry of Metabolites by Surface-Assisted Laser Desorption Ionization MS. *Anal. Chem.* **2015,** *87* (1), 431-440.

(605) Telonis, A. G.; Loher, P.; Jing, Y.; Londin, E.; Rigoutsos, I. Beyond the one-locus-one-miRNA paradigm: microRNA isoforms enable deeper insights into breast cancer heterogeneity. *Nucleic Acids Res.* **2015,** *43* (19), 9158-9175.

(606) Fukunaga, R.; Han, B. W.; Hung, J.-H.; Xu, J.; Weng, Z.; Zamore, P. D. Dicer partner proteins tune the length of mature miRNAs in flies and mammals. *Cell.* **2012,** *151* (3), 533-546.

(607) Yan, H.; Bhattarai, U.; Guo, Z.-F.; Liang, F.-S. Regulating miRNA-21 Biogenesis By Bifunctional Small Molecules. *J. Am. Chem. Soc.* **2017,** *139* (14), 4987-4990.

(608) De, N.; Macrae, I. J. Purification and assembly of human Argonaute, Dicer, and TRBP complexes. *Methods Mol. Biol.* **2011,** *725*, 107-119.

(609) Martinez, N. J.; Gregory, R. I. Argonaute2 expression is post-transcriptionally coupled to microRNA abundance. *RNA* **2013,** *19* (5), 605-612.

(610) Bouvette, J.; Korkut, D. N.; Fouillen, A.; Amellah, S.; Nanci, A.; Durocher, Y.; Omichinski, J. G.; Legault, P. High-yield production of human Dicer by transfection of human HEK293-EBNA1 cells grown in suspension. *BMC Biotechnol.* **2018,** *18* (1), 76.

(611) Saito, K.; Ishizuka, A.; Siomi, H.; Siomi, M. C. Processing of Pre-microRNAs by the Dicer-1–Loquacious Complex in Drosophila Cells. *PLoS Biol.* **2005,** *3* (7), e235.

(612) Elbashir, S. M.; Lendeckel, W.; Tuschl, T. RNA interference is mediated by 21- and 22-nucleotide RNAs. *Genes Dev.* **2001,** *15* (2), 188-200.

(613) Zhang, H.; Kolb, F. A.; Brondani, V.; Billy, E.; Filipowicz, W. Human Dicer preferentially cleaves dsRNAs at their termini without a requirement for ATP. *EMBO J.* **2002,** *21* (21), 5875-5885.

(614) Yan, H.; Bhattarai, U.; Song, Y.; Liang, F.-S. Design, synthesis and activity of light deactivatable microRNA inhibitor. *Bioorg. Chem.* **2018,** *80*, 492-497.

(615) Meng, Z.; Limbach, P. A. Mass spectrometry of RNA: linking the genome to the proteome. *Brief. Funct. Genomic. Proteomic.* **2006,** *5* (1), 87-95.

(616) Pan, C.; Xu, S.; Zhou, H.; Fu, Y.; Ye, M.; Zou, H. Recent developments in methods and technology for analysis of biological samples by MALDI-TOF-MS. *Anal. Bioanal. Chem.* **2007,** *387* (1), 193-204.

(617) Yang, W. Y.; Chiu, N. H. L. Comparison of Accuracy on DNA Quantitation Determined by MALDI-TOF Mass Spectrometry and UV Spectrometry. *Spectrosc. Lett.* **2010,** *43* (7-8), 602-608.

(618) Distler, A. M.; Allison, J. 5-methoxysalicylic acid and spermine: a new matrix for the matrix-assisted laser desorption/ionization mass spectrometry analysis of oligonucleotides. *J. Am. Soc. Mass Spectrom.* **2001,** *12* (4), 456-462.

(619) Adleman, L. M. Molecular Computation of Solutions to Combinatorial Problems. *Science* **1994,** *266* (5187), 1021-1024.

(620) Benenson, Y. Biomolecular computing systems: principles, progress and potential. *Nat. Rev. Genet.* **2012,** *13*, 455-468.

(621) Yoshida, W.; Yokobayashi, Y. Photonic boolean logic gates based on DNA aptamers. *Chemical Communications* **2007,** (2), 195-197.

(622) Lederman, H.; Macdonald, J.; Stefanovic, D.; Stojanovic, M. N. Deoxyribozyme-Based Three-Input Logic Gates and Construction of a Molecular Full Adder†. *Biochemistry* **2006,** *45* (4), 1194-1199.

(623) Zhu, J.; Zhang, L.; Li, T.; Dong, S.; Wang, E. Enzyme-Free Unlabeled DNA Logic Circuits Based on Toehold-Mediated Strand Displacement and Split G-Quadruplex Enhanced Fluorescence. *Advanced Materials* **2013,** *25* (17), 2440-2444.

(624) Lake, A.; Shang, S.; Kolpashchikov, D. M. Molecular Logic Gates Connected through DNA Four-Way Junctions. *Angew. Chem. Int. Ed. Engl.* **2010,** *49* (26), 4459-4462.

(625) Benenson, Y. Biocomputers: from test tubes to live cells. *Molecular BioSystems* **2009,** *5* (7), 675-685.

(626) De Silva, P. Y.; Ganegoda, G. U. New Trends of Digital Data Storage in DNA. *BioMed Res. Int.* **2016**, 8072463-8072463.

(627) Parker, J. Computing with DNA. *EMBO Rep.* **2003,** *4* (1), 7-10.

(628) Appuswamy, R.; Lebrigand, K.; Barbry, P.; Antonini, M.; Madderson, O.; Freemont, P.; McDonald, J.; Heinis, T., OligoArchive: Using DNA in the DBMS storage hierarchy. In *Biennal Conference on Innovative Data Systems Research*, Eurecom: Asilomar, California, 2019.

(629) Zhang, D. Y.; Winfree, E. Control of DNA Strand Displacement Kinetics Using Toehold Exchange. *J. Am. Chem. Soc.* **2009,** *131* (47), 17303-17314.

(630) Srinivas, N.; Ouldridge, T. E.; Sulc, P.; Schaeffer, J. M.; Yurke, B.; Louis, A. A.; Doye, J. P. K.; Winfree, E. On the biophysics and kinetics of toehold-mediated DNA strand displacement. *Nucleic Acids Res.* **2013,** *41* (22), 10641-10658.

(631) Yin, P.; Choi, H. M. T.; Calvert, C. R.; Pierce, N. A. Programming biomolecular self-assembly pathways. *Nature* **2008,** *451*, 318.

(632) Seelig, G.; Soloveichik, D.; Zhang, D. Y.; Winfree, E. Enzyme-Free Nucleic Acid Logic Circuits. *Science* **2006,** *314* (5805), 1585-1588.

(633) Zhang, D. Y.; Turberfield, A. J.; Yurke, B.; Winfree, E. Engineering Entropy-Driven Reactions and Networks Catalyzed by DNA. *Science* **2007,** *318* (5853), 1121-1125.

(634) Qian, L.; Winfree, E. Scaling Up Digital Circuit Computation with DNA Strand Displacement Cascades. *Science* **2011,** *332* (6034), 1196-1201.

(635) Li, W.; Zhang, F.; Yan, H.; Liu, Y. DNA based arithmetic function: a half adder based on DNA strand displacement. *Nanoscale* **2016,** *8* (6), 3775-3784.

(636) Han, W.; Zhou, C. 8-Bit Adder and Subtractor with Domain Label Based on DNA Strand Displacement. *Molecules* **2018,** *23* (11), 2989.

(637) Qian, L.; Winfree, E.; Bruck, J. Neural network computation with DNA strand displacement cascades. *Nature* **2011,** *475*, 368.

(638) Chen, Y.; Song, Y.; Wu, F.; Liu, W.; Fu, B.; Feng, B.; Zhou, X. A DNA logic gate based on strand displacement reaction and rolling circle amplification, responding to multiple low-abundance DNA fragment input signals, and its application in detecting miRNAs. *Chem. Commun.* **2015,** *51* (32), 6980-6983.

(639) Douglas, S. M.; Bachelet, I.; Church, G. M. A Logic-Gated Nanorobot for Targeted Transport of Molecular Payloads. *Science* **2012,** *335* (6070), 831-834.

(640) You, M.; Zhu, G.; Chen, T.; Donovan, M. J.; Tan, W. Programmable and Multiparameter DNA-Based Logic Platform For Cancer Recognition and Targeted Therapy. *J. Am. Chem. Soc.* **2015,** *137* (2), 667-674.

(641) Wu, C.; Cansiz, S.; Zhang, L.; Teng, I. T.; Qiu, L.; Li, J.; Liu, Y.; Zhou, C.; Hu, R.; Zhang, T.; et al.; A Nonenzymatic Hairpin DNA Cascade Reaction Provides High Signal Gain of mRNA Imaging inside Live Cells. *J. Am. Chem. Soc.* **2015,** *137* (15), 4900-4903.

(642) Kahan-Hanum, M.; Douek, Y.; Adar, R.; Shapiro, E. A library of programmable DNAzymes that operate in a cellular environment. *Sci. Rep.* **2013,** *3*, 1535.

(643) Chatterjee, G.; Chen, Y.-J.; Seelig, G. Nucleic Acid Strand Displacement with Synthetic mRNA Inputs in Living Mammalian Cells. *ACS Syn. Biol.* **2018,** *7* (12), 2737-2741.

(644) Li, D.; Zhou, W.; Yuan, R.; Xiang, Y. A DNA-Fueled and Catalytic Molecule Machine Lights Up Trace Under-Expressed MicroRNAs in Living Cells. *Anal. Chem.* **2017,** *89* (18), 9934-9940.

(645) Hemphill, J.; Deiters, A. DNA Computation in Mammalian Cells: MicroRNA Logic Operations. *J. Am. Chem. Soc.* **2013,** *135* (28), 10512-10518.

(646) Tian, W.; Dong, X.; Liu, X.; Wang, G.; Dong, Z.; Shen, W.; Zheng, G.; Lu, J.; Chen, J.; Wang, Y.; et al.; High-throughput functional microRNAs profiling by recombinant AAV-based microRNA sensor arrays. *PLoS One* **2012,** *7* (1), e29551.

(647) Esau, C.; Davis, S.; Murray, S. F.; Yu, X. X.; Pandey, S. K.; Pear, M.; Watts, L.; Booten, S. L.; Graham, M.; McKay, R.; et al.; miR-122 regulation of lipid metabolism revealed by in vivo antisense targeting. *Cell Metabolism* **2006,** *3* (2), 87-98.

(648) Groves, B.; Chen, Y.-J.; Zurla, C.; Pochekailov, S.; Kirschman, J. L.; Santangelo, P. J.; Seelig, G. Computing in mammalian cells with nucleic acid strand exchange. *Nat Nanotechnol* **2016,** *11* (3), 287-294.

(649) Cheglakov, Z.; Cronin, T. M.; He, C.; Weizmann, Y. Live Cell MicroRNA Imaging Using Cascade Hybridization Reaction. *J. Am. Chem. Soc.* **2015,** *137* (19), 6116-6119.

(650) Bi, S.; Yue, S.; Zhang, S. Hybridization chain reaction: a versatile molecular tool for biosensing, bioimaging, and biomedicine. *Chem. Soc. Rev.* **2017,** *46* (14), 4281-4298.

(651) Li, L.; Feng, J.; Liu, H.; Li, Q.; Tong, L.; Tang, B. Two-color imaging of microRNA with enzyme-free signal amplification via hybridization chain reactions in living cells. *Chem. Sci.* **2016,** *7* (3), 1940-1945.

(652) Ren, K.; Xu, Y.; Liu, Y.; Yang, M.; Ju, H. A Responsive "Nano String Light" for Highly Efficient mRNA Imaging in Living Cells via Accelerated DNA Cascade Reaction. *ACS Nano.* **2018,** *12* (1), 263-271.

(653) Shen, Y.; Li, Z.; Wang, G.; Ma, N. Photocaged Nanoparticle Sensor for Sensitive MicroRNA Imaging in Living Cancer Cells with Temporal Control. *ACS Sens.* **2018,** *3* (2), 494-503.

(654) Yue, R.; Li, Z.; Wang, G.; Li, J.; Ma, N. Logic Sensing of MicroRNA in Living Cells Using DNA-Programmed Nanoparticle Network with High Signal Gain. *ACS Sens.* **2019,** *4* (1), 250-256.

(655) Wu, Z.; Liu, G.-Q.; Yang, X.-L.; Jiang, J.-H. Electrostatic Nucleic Acid Nanoassembly Enables Hybridization Chain Reaction in Living Cells for Ultrasensitive mRNA Imaging. *J. Am. Chem. Soc.* **2015,** *137* (21), 6829-6836.

(656) Yasuga, H.; Kawano, R.; Takinoue, M.; Tsuji, Y.; Osaki, T.; Kamiya, K.; Miki, N.; Takeuchi, S. Logic Gate Operation by DNA Translocation through Biological Nanopores. *PloS One* **2016,** *11* (2), e0149667-e0149667.

(657) Hiratani, M.; Kawano, R. DNA Logic Operation with Nanopore Decoding To Recognize MicroRNA Patterns in Small Cell Lung Cancer. *Anal. Chem.* **2018,** *90* (14), 8531-8537.

(658) Amir, Y.; Ben-Ishay, E.; Levner, D.; Ittah, S.; Abu-Horowitz, A.; Bachelet, I. Universal computing by DNA origami robots in a living animal. *Nat. Nanotechnol.* **2014,** *9*, 353.

(659) Surana, S.; Bhat, J. M.; Koushika, S. P.; Krishnan, Y. An autonomous DNA nanomachine maps spatiotemporal pH changes in a multicellular living organism. *Nat. Commun.* **2011,** *2*, 340.

(660) Li, S.; Jiang, Q.; Liu, S.; Zhang, Y.; Tian, Y.; Song, C.; Wang, J.; Zou, Y.; Anderson, G. J.; Han, J.-Y.; et al.; A DNA nanorobot functions as a cancer therapeutic in response to a molecular trigger in vivo. *Nat. Biotechnol.* **2018,** *36*, 258.

(661) Chen, Y.-J.; Groves, B.; Muscat, R. A.; Seelig, G. DNA nanotechnology from the test tube to the cell. *Nat. Nanotechnol.* **2015,** *10*, 748.

(662) Lu, J.; Getz, G.; Miska, E. A.; Alvarez-Saavedra, E.; Lamb, J.; Peck, D.; Sweet-Cordero, A.; Ebert, B. L.; Mak, R. H.; Ferrando, A. A.; et al.; MicroRNA expression profiles classify human cancers. *Nature* **2005,** *435* (7043), 834-838.

(663) Singh, P. K.; Preus, L.; Hu, Q.; Yan, L.; Long, M. D.; Morrison, C. D.; Nesline, M.; Johnson, C. S.; Koochekpour, S.; Kohli, M.; et al.; Serum microRNA expression patterns that predict early treatment failure in prostate cancer patients. *Oncotarget* **2014,** *5* (3), 824-840.

(664) Leichter, A. L.; Sullivan, M. J.; Eccles, M. R.; Chatterjee, A. MicroRNA expression patterns and signalling pathways in the development and progression of childhood solid tumours. *Mol. Cancer.* **2017,** *16* (1), 15-15.

(665) Scida, K.; Li, B.; Ellington, A. D.; Crooks, R. M. DNA Detection Using Origami Paper Analytical Devices. *Anal. Chem.* **2013,** *85* (20), 9713-9720.

(666) Feliciano, A.; Castellvi, J.; Artero-Castro, A.; Leal, J. A.; Romagosa, C.; Hernández-Losa, J.; Peg, V.; Fabra, A.; Vidal, F.; Kondoh, H.; et al.; miR-125b Acts as a Tumor Suppressor in Breast Tumorigenesis via Its Novel Direct Targets ENPEP, CK2-α, CCNJ, and MEGF9. *PLoS One* **2013,** *8* (10), e76247.

(667) Tian, W.; Dong, X.; Liu, X.; Wang, G.; Dong, Z.; Shen, W.; Zheng, G.; Lu, J.; Chen, J.; Wang, Y.; et al.; High-throughput functional microRNAs profiling by recombinant AAV-based microRNA sensor arrays. *PloS One* **2012,** *7* (1), e29551-e29551.

(668) Shi, G.-h.; Ye, D.-w.; Yao, X.-d.; Zhang, S.-l.; Dai, B.; Zhang, H.-l.; Shen, Y.-j.; Zhu, Y.; Zhu, Y.-p.; Xiao, W.-j.; et al.; Involvement of microRNA-21 in mediating chemo-resistance to docetaxel in androgen-independent prostate cancer PC3 cells. *Acta Pharmacol. Sin.* **2010,** *31* (7), 867-873.

(669) Xu, G.; Zhang, Y.; Wei, J.; Jia, W.; Ge, Z.; Zhang, Z.; Liu, X. MicroRNA-21 promotes hepatocellular carcinoma HepG2 cell proliferation through repression of mitogen-activated protein kinase-kinase 3. *BMC Cancer.* **2013,** *13*, 469-469.

(670) Li, J.; Fang, L.; Yu, W.; Wang, Y. MicroRNA-125b suppresses the migration and invasion of hepatocellular carcinoma cells by targeting transcriptional coactivator with PDZ-binding motif. *Oncol. Lett.* **2015,** *9* (4), 1971-1975.

(671) Fukuhara, T.; Kambara, H.; Shiokawa, M.; Ono, C.; Katoh, H.; Morita, E.; Okuzaki, D.; Maehara, Y.; Koike, K.; Matsuura, Y. Expression of microRNA miR-122 facilitates an efficient replication in nonhepatic cells upon infection with hepatitis C virus. *J. Virol.* **2012,** *86* (15), 7918-7933.

(672) Hamad, I. A. Y.; Fei, Y.; Kalea, A. Z.; Yin, D.; Smith, A. J. P.; Palmen, J.; Humphries, S. E.; Talmud, P. J.; Walker, A. P. Demonstration of the presence of the "deleted" MIR122 gene in HepG2 cells. *PloS One* **2015,** *10* (3), e0122471-e0122471.

(673) Dagle, J. M.; Weeks, D. L.; Walder, J. A. Pathways of Degradation and Mechanism of Action of Antisense Oligonucleotides in Xenopus laevis Embryos. *Antisense Res. Dev.* **1991,** *1* (1), 11-20.

(674) Fisher, T. L.; Terhorst, T.; Cao, X.; Wagner, R. W. Intracellular disposition and metabolism of fluorescently-labeled unmodified and modified oligonucleotides microinjected into mammalian cells. *Nucleic Acids Res.* **1993,** *21* (16), 3857-3865.

(675) Monia, B. P.; Johnston, J. F.; Sasmor, H.; Cummins, L. L. Nuclease Resistance and Antisense Activity of Modified Oligonucleotides Targeted to Ha-ras. *J. Biol. Chem.* **1996,** *271* (24), 14533-14540.

(676) Fern, J.; Schulman, R. Design and Characterization of DNA Strand-Displacement Circuits in Serum-Supplemented Cell Medium. *ACS Syn. Biol.* **2017,** *6* (9), 1774-1783.

(677) Abdelgany, A.; Wood, M.; Beeson, D. Hairpin DNAzymes: a new tool for efficient cellular gene silencing. *J. Gene Med.* **2007,** *9* (8), 727-738.

(678) Young, D. D.; Lively, M. O.; Deiters, A. Activation and deactivation of DNAzyme and antisense function with light for the photochemical regulation of gene expression in mammalian cells. *J. Am. Chem. Soc.* **2010,** *132* (17), 6183-6193.

(679) Yoshizawa, S.; Ueda, T.; Ishido, Y.; Miura, K.; Watanabe, K.; Hirao, I. Nuclease resistance of an extraordinarily thermostable mini-hairpin DNA fragment, d(GCGAAGC) and its application to in vitro protein synthesis. *Nucleic Acids Res.* **1994,** *22* (12), 2217-2221.

(680) Zadeh, J. N.; Steenberg, C. D.; Bois, J. S.; Wolfe, B. R.; Pierce, M. B.; Khan, A. R.; Dirks, R. M.; Pierce, N. A. NUPACK: Analysis and design of nucleic acid systems. *J. Comput. Chem.* **2011,** *32* (1), 170-173.

(681) Keum, J.-W.; Bermudez, H. Enhanced resistance of DNAnanostructures to enzymatic digestion. *Chem. Commun.* **2009,** (45), 7036-7038.

(682) Peterlin, B. M.; Okamoto, H.; Fontes, J. D.; Jabrane-Ferrat, N.; Garovoy, M. R.; Anthony Hunt, C.; Lim, C. S. Sequence-Independent Inhibition of RNA Transcription by DNA Dumbbells and Other Decoys. *Nucleic Acids Res.* **1997,** *25* (3), 575-581.

(683) Campbell, J. M.; Bacon, T. A.; Wickstrom, E. Oligodeoxynucleoside phosphorothioate stability in subcellular extracts, culture media, sera and cerebrospinal fluid. *J. Biochem. Biophys. Meth.* **1990,** *20* (3), 259-267.

(684) Kibler-Herzog, L.; Zon, G.; Uznanski, B.; Whittier, G.; Wilson, W. D. Duplex stabilities of phosphorothioate, methylphosphonate, and RNA analogs of two DNA 14-mers. *Nucleic Acids Res.* **1991,** *19* (11), 2979-2986.

(685) Piao, X.; Wang, H.; Binzel, D. W.; Guo, P. Assessment and comparison of thermal stability of phosphorothioate-DNA, DNA, RNA, 2'-F RNA, and LNA in the context of Phi29 pRNA 3WJ. *RNA.* **2018,** *24* (1), 67-76.

(686) Wang, B.; Thachuk, C.; Ellington, A. D.; Winfree, E.; Soloveichik, D. Effective design principles for leakless strand displacement systems. *Proc. Natl. Acad. Sci. U.S.A.* **2018,** *115* (52), E12182.

(687) Thompson, L. A.; Ellman, J. A. Synthesis and Applications of Small Molecule Libraries. *Chem Rev* **1996,** *96* (1), 555-600.

(688) Lavis, L. D.; Raines, R. T. Bright ideas for chemical biology. *ACS Chem Biol* **2008,** *3* (3), 142-55.

(689) Wienken, C. J.; Baaske, P.; Rothbauer, U.; Braun, D.; Duhr, S. Protein-binding assays in biological liquids using microscale thermophoresis. *Nat. Commun.* **2010,** *1*, 100.

(690) Di Pisa, M.; Seitz, O. Nucleic Acid Templated Reactions for Chemical Biology. *ChemMedChem* **2017,** *12* (12), 872-882.

(691) Sletten, E. M.; Bertozzi, C. R. Bioorthogonal chemistry: fishing for selectivity in a sea of functionality. *Angew. Chem. Int. Ed. Engl.* **2009,** *48* (38), 6974-6998.

(692) Ma, Z.; Taylor, J.-S. Nucleic acid-triggered catalytic drug release. *Proc. Natl. Acad. Sci. U. S. A.* **2000,** *97* (21), 11159.

(693) Battle, C.; Chu, X.; Jayawickramarajah, J. Oligonucleotide-based systems for input-controlled and non-covalently regulated protein binding. *Supramol. Chem.* **2013,** *25* (12), 848-862.

(694) Diezmann, F.; Seitz, O. DNA-guided display of proteins and protein ligands for the interrogation of biology. *Chem. Soc. Rev.* **2011,** *40* (12), 5789-5801.

(695) Li, X.; Liu, D. R. DNA-Templated Organic Synthesis: Nature's Strategy for Controlling Chemical Reactivity Applied to Synthetic Molecules. *Angew. Chem. Int. Ed. Engl.* **2004,** *43* (37), 4848-4870.

(696) Jacobsen, M. F.; Cló, E.; Mokhir, A.; Gothelf, K. V. Model Systems for Activation of Nucleic Acid Encoded Prodrugs. *ChemMedChem* **2007,** *2* (6), 793-799.

(697) Gorska, K.; Winssinger, N. Reactions Templated by Nucleic Acids: More Ways to Translate Oligonucleotide-Based Instructions into Emerging Function. *Angew. Chem. Int. Ed. Engl.* **2013,** *52* (27), 6820-6843.

(698) Shibata, A.; Abe, H.; Ito, Y. Oligonucleotide-templated reactions for sensing nucleic acids. *Molecules.* **2012,** *17* (3), 2446-2463.

(699) Grossmann, T. N.; Seitz, O. DNA-Catalyzed Transfer of a Reporter Group. *J. Am. Chem. Soc.* **2006,** *128* (49), 15596-15597.

(700) Li, X.; Liu, D. R. Stereoselectivity in DNA-Templated Organic Synthesis and Its Origins. *J. Am. Chem. Soc.* **2003,** *125* (34), 10188-10189.

(701) Shibata, A.; Abe, H.; Ito, M.; Kondo, Y.; Shimizu, S.; Aikawa, K.; Ito, Y. DNA templated nucleophilicaromatic substitution reactions for fluorogenic sensing of oligonucleotides. *Chem. Commun.* **2009,** (43), 6586-6588.

(702) Chen, X.-H.; Roloff, A.; Seitz, O. Consecutive Signal Amplification for DNA Detection Based on De Novo Fluorophore Synthesis and Host–Guest Chemistry. *Angew. Chem. Int. Ed. Engl.* **2012,** *51* (18), 4479-4483.

(703) Meguellati, K.; Koripelly, G.; Ladame, S. DNA-Templated Synthesis of Trimethine Cyanine Dyes: A Versatile Fluorogenic Reaction for Sensing G-Quadruplex Formation. *Angew. Chem. Int. Ed. Engl.* **2010,** *49* (15), 2738-2742.

(704) Metcalf, G. A. D.; Shibakawa, A.; Patel, H.; Sita-Lumsden, A.; Zivi, A.; Rama, N.; Bevan, C. L.; Ladame, S. Amplification-Free Detection of Circulating microRNA Biomarkers from Body Fluids Based on Fluorogenic Oligonucleotide-Templated Reaction between Engineered Peptide Nucleic Acid Probes: Application to Prostate Cancer Diagnosis. *Anal. Chem.* **2016,** *88* (16), 8091-8098.

(705) Pianowski, Z. L.; Winssinger, N. Fluorescence-based detection of single nucleotide permutation in DNA via catalytically templated reaction. *Chem Commun (Camb)* **2007,** (37), 3820-2.

(706) Franzini, R. M.; Kool, E. T. 7-Azidomethoxy-coumarins as profluorophores for templated nucleic acid detection. *Chembiochem.* **2008,** *9* (18), 2981-8.

(707) Furukawa, K.; Abe, H.; Wang, J.; Uda, M.; Koshino, H.; Tsuneda, S.; Ito, Y. Reduction-triggered red fluorescent probes for dual-color detection of oligonucleotide sequences. *Org Biomol Chem* **2009,** *7* (4), 671-7.

(708) Furukawa, K.; Abe, H.; Tamura, Y.; Yoshimoto, R.; Yoshida, M.; Tsuneda, S.; Ito, Y. Fluorescence detection of intron lariat RNA with reduction-triggered fluorescent probes. *Angew Chem Int Ed Engl* **2011,** *50* (50), 12020-3.

(709) Tamura, Y.; Furukawa, K.; Yoshimoto, R.; Kawai, Y.; Yoshida, M.; Tsuneda, S.; Ito, Y.; Abe, H. Detection of pre-mRNA splicing in vitro by an RNA-templated fluorogenic reaction. *Bioorg Med Chem Lett* **2012,** *22* (23), 7248-51.

(710) Abe, H.; Wang, J.; Furukawa, K.; Oki, K.; Uda, M.; Tsuneda, S.; Ito, Y. A reduction-triggered fluorescence probe for sensing nucleic acids. *Bioconjug Chem* **2008,** *19* (6), 1219-26.

(711) Franzini, R. M.; Kool, E. T. Efficient nucleic acid detection by templated reductive quencher release. *J Am Chem Soc* **2009,** *131* (44), 16021-3.

(712) Furukawa, K.; Abe, H.; Hibino, K.; Sako, Y.; Tsuneda, S.; Ito, Y. Reduction-triggered fluorescent amplification probe for the detection of endogenous RNAs in living human cells. *Bioconjug Chem* **2009,** *20* (5), 1026-36.

(713) Pianowski, Z.; Gorska, K.; Oswald, L.; Merten, C. A.; Winssinger, N. Imaging of mRNA in live cells using nucleic acid-templated reduction of azidorhodamine probes. *J. Am. Chem. Soc.* **2009,** *131* (18), 6492-7.

(714) Gorska, K.; Keklikoglou, I.; Tschulena, U.; Winssinger, N. Rapid fluorescence imaging of miRNAs in human cells using templated Staudinger reaction. *Chemical Science* **2011,** *2* (10), 1969-1975.

(715) Franzini, R. M.; Kool, E. T. Efficient nucleic acid detection by templated reductive quencher release. *J. Am. Chem. Soc.* **2009,** *131* (44), 16021-16023.

(716) Velema, W. A.; Kool, E. T. Fluorogenic Templated Reaction Cascades for RNA Detection. *J. Am. Chem. Soc.* **2017,** *139* (15), 5405-5411.

(717) Lo, L. C.; Chu, C. Y. Development of highly selective and sensitive probes for hydrogen. *Chem Commun (Camb)* **2003,** (21), 2728-9.

(718) Matikonda, S. S.; Orsi, D. L.; Staudacher, V.; Jenkins, I. A.; Fiedler, F.; Chen, J. Y.; Gamble, A. B. Bioorthogonal prodrug activation driven by a strain-promoted 1,3-dipolar cycloaddition. *Chemical Science* **2015,** *6* (2), 1212-1218.

(719) Fan, X.; Ge, Y.; Lin, F.; Yang, Y.; Zhang, G.; Ngai, W. S.; Lin, Z.; Zheng, S.; Wang, J.; Zhao, J.; et al.; Optimized Tetrazine Derivatives for Rapid Bioorthogonal Decaging in Living Cells. *Angew Chem Int Ed Engl* **2016,** *55* (45), 14046-14050.

(720) Zhu, B.; Zhang, X.; Jia, H.; Li, Y.; Liu, H.; Tan, W. A highly selective ratiometric fluorescent probe for 1,4-dithiothreitol (DTT) detection. *Org. Biomol. Chem.* **2010,** *8* (7), 1650-4.

(721) Zhu, B.; Zhang, X.; Li, Y.; Wang, P.; Zhang, H.; Zhuang, X. A colorimetric and ratiometric fluorescent probe for thiols and its bioimaging applications. *Chem. Commun.* **2010,** *46* (31), 5710-2.

(722) Jiang, J.; Jiang, H.; Liu, W.; Tang, X.; Zhou, X.; Liu, W.; Liu, R. A colorimetric and ratiometric fluorescent probe for palladium. *Org Lett* **2011,** *13* (18), 4922-5.

(723) Hettiarachchi, S. U.; Prasai, B.; McCarley, R. L. Detection and cellular imaging of human cancer enzyme using a turn-on, wavelength-shiftable, self-immolative profluorophore. *J. Am. Chem. Soc.* **2014,** *136* (21), 7575-8.

(724) Zhang, L.; Li, S.; Hong, M.; Xu, Y.; Wang, S.; Liu, Y.; Qian, Y.; Zhao, J. A colorimetric and ratiometric fluorescent probe for the imaging of endogenous hydrogen sulphide in living cells and sulphide determination in mouse hippocampus. *Org. Biomol. Chem.* **2014,** *12* (28), 5115-25.

(725) Owczarzy, R.; Moreira, B. G.; You, Y.; Behlke, M. A.; Walder, J. A. Predicting stability of DNA duplexes in solutions containing magnesium and monovalent cations. *Biochemistry* **2008,** *47* (19), 5336-5353.

(726) Li, X.; Liu, D. R. DNA-Templated Organic Synthesis: Nature's Strategy for Controlling Chemical Reactivity Applied to Synthetic Molecules. *Angew Chem Int Ed* **2004,** *43* (37), 4848-4870.

(727) Meng, W.; Muscat, R. A.; McKee, M. L.; Milnes, P. J.; El-Sagheer, A. H.; Bath, J.; Davis, B. G.; Brown, T.; O'Reilly, R. K.; Turberfield, A. J. An autonomous molecular assembler for programmable chemical synthesis. *Nat Chem* **2016,** *8* (6), 542-548.

(728) Saneyoshi, H.; Ochikubo, T.; Mashimo, T.; Hatano, K.; Ito, Y.; Abe, H. Triphenylphosphinecarboxamide: an effective reagent for the reduction of azides and its application to nucleic acid detection. *Org Lett* **2014,** *16* (1), 30-3.

(729) Luo, J.; Liu, Q.; Morihiro, K.; Deiters, A. Small-molecule control of protein function through Staudinger reduction. *Nat Chem* **2016,** *8* (11), 1027-1034.

(730) Medina, P. P.; Nolde, M.; Slack, F. J. OncomiR addiction in an in vivo model of microRNA-21-induced pre-B-cell lymphoma. *Nature* **2010,** *467* (7311), 86-90.

(731) Srinivas, N.; Ouldridge, T. E.; Šulc, P.; Schaeffer, J. M.; Yurke, B.; Louis, A. A.; Doye, J. P. K.; Winfree, E. On the biophysics and kinetics of toehold-mediated DNA strand displacement. *Nucleic Acids Res* **2013,** *41* (22), 10641-10658.

(732) Thubagere, A. J.; Thachuk, C.; Berleant, J.; Johnson, R. F.; Ardelean, D. A.; Cherry, K. M.; Qian, L. Compiler-aided systematic construction of large-scale DNA strand displacement circuits using unpurified components. *Nat Commun* **2017,** *8*, 14373.

(733) Olson, X.; Kotani, S.; Padilla, J. E.; Hallstrom, N.; Goltry, S.; Lee, J.; Yurke, B.; Hughes, W. L.; Graugnard, E. Availability: A Metric for Nucleic Acid Strand Displacement Systems. *ACS Synth. Biol.* **2017,** *6* (1), 84-93.

(734) Jiang, Y. S.; Bhadra, S.; Li, B.; Ellington, A. D. Mismatches Improve the Performance of Strand-Displacement Nucleic Acid Circuits. *Angew Chemie Int Ed* **2014,** *126* (7), 1876-1879.

(735) Zgarbová, M.; Otyepka, M.; Šponer, J.; Lankaš, F.; Jurečka, P. Base Pair Fraying in Molecular Dynamics Simulations of DNA and RNA. *J. Chem. Theory Comput.* **2014,** *10* (8), 3177-3189.

(736) Stojanovic, M. N.; Stefanovic, D. Deoxyribozyme-based half-adder. *J. Am. Chem. Soc.* **2003,** *125* (22), 6673-6.

(737) Frezza, B. M.; Cockroft, S. L.; Ghadiri, M. R. Modular multi-level circuits from immobilized DNA-based logic gates. *J. Am. Chem. Soc.* **2007,** *129* (48), 14875-9.

(738) Qian, L.; Winfree, E. Scaling up digital circuit computation with DNA strand displacement cascades. *Science* **2011,** *332* (6034), 1196-201.

(739) Seelig, G.; Soloveichik, D.; Zhang, D. Y.; Winfree, E. Enzyme-free nucleic acid logic circuits. *Science* **2006,** *314* (5805), 1585-8.

(740) Pulido, J.; Sobczak, A. J.; Balzarini, J.; Wnuk, S. F. Synthesis and Cytostatic Evaluation of 4-N-Alkanoyl and 4-N-Alkyl Gemcitabine Analogues. *J. Med. Chem.* **2014,** *57* (1), 191-203.

(741) Haba, K.; Popkov, M.; Shamis, M.; Lerner, R. A.; Barbas, C. F.; Shabat, D. Single-Triggered Trimeric Prodrugs. *Angew Chem Int Ed* **2005,** *44* (5), 716-720.

(742) Shamis, M.; Lode, H. N.; Shabat, D. Bioactivation of Self-Immolative Dendritic Prodrugs by Catalytic Antibody 38C2. *J. Am. Chem. Soc.* **2004,** *126* (6), 1726-1731.

(743) Bußkamp, H.; Batroff, E.; Niederwieser, A.; Abdel-Rahman, O. S.; Winter, R. F.; Wittmann, V.; Marx, A. Efficient labelling of enzymatically synthesized vinyl-modified DNA by an inverse-electron-demand Diels–Alder reaction. *Chem. Commun.* **2014,** *50* (74), 10827-10829.

(744) Selvaraj, R.; Giglio, B.; Liu, S.; Wang, H.; Wang, M.; Yuan, H.; Chintala, S. R.; Yap, L.-P.; Conti, P. S.; Fox, J. M.; et al.; Improved Metabolic Stability for 18F PET Probes Rapidly Constructed via Tetrazine trans-Cyclooctene Ligation. *Bioconjug. Chem.* **2015,** *26* (3), 435-442.

(745) Devaraj, N. K.; Weissleder, R. Biomedical Applications of Tetrazine Cycloadditions. *Acc. Chem. Res.* **2011,** *44* (9), 816-827.

(746) Lang, K.; Davis, L.; Torres-Kolbus, J.; Chou, C.; Deiters, A.; Chin, J. W. Genetically encoded norbornene directs site-specific cellular protein labelling via a rapid bioorthogonal reaction. *Nat. Chem.* **2012,** *4*, 298.

(747) Neumann, K.; Gambardella, A.; Bradley, M. The Emerging Role of Tetrazines in Drug-Activation Chemistries. *Chembiochem.* **2019,** *20* (7), 872-876.

(748) Jiménez-Moreno, E.; Guo, Z.; Oliveira, B. L.; Albuquerque, I. S.; Kitowski, A.; Guerreiro, A.; Boutureira, O.; Rodrigues, T.; Jiménez-Osés, G.; Bernardes, G. J. L. Vinyl Ether/Tetrazine Pair for the Traceless Release of Alcohols in Cells. *Angew. Chem. Int. Ed. Engl.* **2017,** *56* (1), 243-247.

(749) Wu, H.; Alexander, S. C.; Jin, S.; Devaraj, N. K. A Bioorthogonal Near-Infrared Fluorogenic Probe for mRNA Detection. *J. Am. Chem. Soc.* **2016,** *138* (36), 11429-11432.

(750) Neumann, K.; Jain, S.; Gambardella, A.; Walker, S. E.; Valero, E.; Lilienkampf, A.; Bradley, M. Tetrazine-Responsive Self-immolative Linkers. *Chembiochem.* **2017,** *18* (1), 91-95.

(751) Armstrong, A. A.; Amzel, L. M. Role of Entropy in Increased Rates of Intramolecular Reactions. *J. Am. Chem. Soc.* **2003,** *125* (47), 14596-14602.

(752) Holtzer, L.; Oleinich, I.; Anzola, M.; Lindberg, E.; Sadhu, K. K.; Gonzalez-Gaitan, M.; Winssinger, N. Nucleic Acid Templated Chemical Reaction in a Live Vertebrate. *Acs Central Sci* **2016,** *2* (6), 394-400.

(753) Hemphill, J.; Deiters, A. DNA Computation in Mammalian Cells: MicroRNA Logic Operations. *J Am Chem Soc* **2013,** *135* (28), 10512-10518.

(754) Zhang, P.; He, Z.; Wang, C.; Chen, J.; Zhao, J.; Zhu, X.; Li, C.-Z.; Min, Q.; Zhu, J.-J. In Situ Amplification of Intracellular MicroRNA with MNAzyme Nanodevices for Multiplexed Imaging, Logic Operation, and Controlled Drug Release. *ACS Nano.* **2015,** *9* (1), 789-798.

(755) Cheglakov, Z.; Cronin, T. M.; He, C.; Weizmann, Y. Live Cell MicroRNA Imaging Using Cascade Hybridization Reaction. *J Am Chem Soc* **2015,** *137* (19), 6116-6119.

(756) Deng, R.; Tang, L.; Tian, Q.; Wang, Y.; Lin, L.; Li, J. Toehold-initiated Rolling Circle Amplification for Visualizing Individual MicroRNAs In Situ in Single Cells. *Angew Chem Int Ed* **2014,** *53* (9), 2389-2393.

(757) Wu, H.; Cisneros, B. T.; Cole, C. M.; Devaraj, N. K. Bioorthogonal Tetrazine-Mediated Transfer Reactions Facilitate Reaction Turnover in Nucleic Acid-Templated Detection of MicroRNA. *J. Am. Chem. Soc.* **2014,** *136* (52), 17942-17945.

(758) Wu, H.; Alexander, S. C.; Jin, S.; Devaraj, N. K. A Bioorthogonal Near-Infrared Fluorogenic Probe for mRNA Detection. *J Am Chem Soc* **2016,** *138* (36), 11429-11432.

(759) Chen, Y.; Song, Y.; Wu, F.; Liu, W.; Fu, B.; Feng, B.; Zhou, X. A DNA logic gate based on strand displacement reaction and rolling circle amplification, responding to multiple low-abundance DNA fragment input signals, and its application in detecting miRNAs. *Chem Commun* **2015,** *51* (32), 6980-6983.

(760) Wang, D.; Fu, Y.; Yan, J.; Zhao, B.; Dai, B.; Chao, J.; Liu, H.; He, D.; Zhang, Y.; Fan, C.; et al.; Molecular Logic Gates on DNA Origami Nanostructures for MicroRNA Diagnostics. *Anal. Chem.* **2014,** *86* (4), 1932-1936.

(761) Kahan-Hanum, M.; Douek, Y.; Adar, R.; Shapiro, E. A library of programmable DNAzymes that operate in a cellular environment. *Sci Rep* **2013,** *3*, 1535.

(762) Santos, R.; Ursu, O.; Gaulton, A.; Bento, A. P.; Donadi, R. S.; Bologa, C. G.; Karlsson, A.; Al-Lazikani, B.; Hersey, A.; Oprea, T. I.; et al.; A comprehensive map of molecular drug targets. *Nat Rev Drug Discov* **2017,** *16* (1), 19-34.

(763) Sharma, V. K.; Rungta, P.; Prasad, A. K. Nucleic acid therapeutics: basic concepts and recent developments. *RSC Advances* **2014,** *4* (32), 16618-16631.

(764) Reautschnig, P.; Vogel, P.; Stafforst, T. The notorious R.N.A. in the spotlight - drug or target for the treatment of disease. *RNA Biology* **2016**, 1-18.

(765) Liu, Q.; Deiters, A. Optochemical control of deoxyoligonucleotide function via a nucleobase-caging approach. *Acc. Chem. Res.* **2014,** *47* (1), 45.

(766) Lubbe, A. S.; Szymanski, W.; Feringa, B. L. Recent developments in reversible photoregulation of oligonucleotide structure and function. *Chem. Soc. Rev.* **2017,** *46* (4), 1052-1079.

(767) Ruble, B. K.; Yeldell, S. B.; Dmochowski, I. J. Caged oligonucleotides for studying biological systems. *J. Inorg. Biochem.* **2015,** *150*, 182-188.

(768) Richards, J. L.; Tang, X.; Turetsky, A.; Dmochowski, I. J. RNA bandages for photoregulating in vitro protein synthesis. *Bioorg. Med. Chem. Lett.* **2008,** *18* (23), 6255-6258.

(769) Tomasini, A. J.; Schuler, A. D.; Zebala, J. A.; Mayer, A. N. PhotoMorphs™: A novel light-activated reagent for controlling gene expression in zebrafish. *genesis* **2009,** *47* (11), 736-743.

(770) Tallafuss, A.; Gibson, D.; Morcos, P.; Li, Y.; Seredick, S.; Eisen, J.; Washbourne, P. Turning gene function ON and OFF using sense and antisense photo-morpholinos in zebrafish. *Development (Cambridge, England)* **2012,** *139* (9), 1691-1699.

(771) Zheng, G.; Cochella, L.; Liu, J.; Hobert, O.; Li, W.-h. Temporal and spatial regulation of microRNA activity with photo-activatable cantimirs. *ACS Chem. Biol.* **2011,** *6* (12), 1332-1338.

(772) Griepenburg, J. C.; Ruble, B. K.; Dmochowski, I. J. Caged oligonucleotides for bidirectional photomodulation of let-7 miRNA in zebrafish embryos. *Bioorg. Med. Chem.* **2013,** *21* (20), 6198-6204.

(773) Tang, X.; Swaminathan, J.; Gewirtz, A. M.; Dmochowski, I. J. Regulating gene expression in human leukemia cells using light-activated oligodeoxynucleotides. *Nucleic Acids Res.* **2008,** *36* (2), 559-569.

(774) Shestopalov, I. A.; Sinha, S.; Chen, J. K. Light-controlled gene silencing in zebrafish embryos. *Nat. Chem. Biol.* **2007,** *3* (10), 650-651.

(775) Ouyang, X.; Shestopalov, I. A.; Sinha, S.; Zheng, G.; Pitt, C. L. W.; Li, W.-H.; Olson, A. J.; Chen, J. K. Versatile Synthesis and Rational Design of Caged Morpholinos. *J. Am. Chem. Soc.* **2009,** *131* (37), 13255-13269.

(776) Griepenburg, J. C.; Rapp, T. L.; Carroll, P. J.; Eberwine, J.; Dmochowski, I. J. Ruthenium-Caged Antisense Morpholinos for Regulating Gene Expression in Zebrafish Embryos. *Chem. Sci. (RSC)* **2015,** *6* (4), 2342-2346.

(777) Wang, Y.; Wu, L.; Wang, P.; Lv, C.; Yang, Z.; Tang, X. Manipulation of gene expression in zebrafish using caged circular morpholino oligomers. *Nucleic Acids Research* **2012,** *40* (21), 11155-11162.

(778) Yamazoe, S.; Shestopalov, I. A.; Provost, E.; Leach, S. D.; Chen, J. K. Cyclic Caged Morpholinos: Conformationally Gated Probes of Embryonic Gene Function. *Angewandte Chemie* **2012,** *124* (28), 7014-7017.

(779) Seyfried, P.; Eiden, L.; Grebenovsky, N.; Mayer, G.; Heckel, A. Photo-Tethers for the (Multi-)Cyclic, Conformational Caging of Long Oligonucleotides. *Angew. Chem. Int. Ed. Engl.* **2017,** *129* (1), 365-369.

(780) Monroe, W. T.; McQuain, M. M.; Chang, M. S.; Alexander, J. S.; Haselton, F. R. Targeting Expression with Light Using Caged DNA. *J. Biol. Chem.* **1999,** *274* (30), 20895-20900.

(781) Ando, H.; Furuta, T.; Tsien, R. Y.; Okamoto, H. Photo-mediated gene activation using caged RNA/DNA in zebrafish embryos. *Nat Genet* **2001,** *28* (4), 317-325.

(782) Shah, S.; Rangarajan, S.; Friedman, S. H. Light-Activated RNA Interference. *Angew. Chem. Int. Ed. Engl.* **2005,** *44* (9), 1328-1332.

(783) Chaulk, S. G.; MacMillan, A. M. Caged RNA: photo-control of a ribozyme reaction. *Nucleic Acids Res.* **1998,** *26* (13), 3173-3178.

(784) Chaulk, S. G.; MacMillan, A. M. Separation of Spliceosome Assembly from Catalysis with Caged pre-mRNA Substrates. *Angew. Chem. Int. Ed. Engl.* **2001,** *40* (11), 2149-2152.

(785) Usui, K.; Aso, M.; Fukuda, M.; Suemune, H. Photochemical Generation of Oligodeoxynucleotide Containing a C4‘-Oxidized Abasic Site and Its Efficient Amine Modification: Dependence on Structure and Microenvironment. *J. Org. Chem.* **2008,** *73* (1), 241-248.

(786) Young, D. D.; Lusic, H.; Lively, M. O.; Yoder, J. A.; Deiters, A. Gene Silencing in Mammalian Cells with Light-Activated Antisense Agents. *Chembiochem.* **2008,** *9* (18), 2937-2940.

(787) Deiters, A.; Garner, R. A.; Lusic, H.; Govan, J. M.; Dush, M.; Nascone-Yoder, N. M.; Yoder, J. A. Photocaged Morpholino Oligomers for the Light-Regulation of Gene Function in Zebrafish and Xenopus Embryos. *J. Am. Chem. Soc.* **2010,** *132* (44), 15644-15650.

(788) Schäfer, F.; Wagner, J.; Knau, A.; Dimmeler, S.; Heckel, A. Regulating Angiogenesis with Light-Inducible AntimiRs. *Angew. Chem. Int. Ed. Engl.* **2013,** *52* (51), 13558-13561.

(789) Connelly, C. M.; Deiters, A. Control of Oncogenic miRNA Function by Light-Activated miRNA Antagomirs. In *Cancer Cell Signaling: Methods and Protocols*, Robles-Flores, M., Ed. Springer New York: New York, NY, 2014; pp 99-114.

(790) Connelly, C. M.; Uprety, R.; Hemphill, J.; Deiters, A. Spatiotemporal control of microRNA function using light-activated antagomirs. *Mol. BioSystems* **2012,** *8* (11), 2987-2993.

(791) Hemphill, J.; Liu, Q.; Uprety, R.; Samanta, S.; Tsang, M.; Juliano, R. L.; Deiters, A. Conditional Control of Alternative Splicing through Light-Triggered Splice-Switching Oligonucleotides. *J. Am. Chem. Soc.* **2015,** *137* (10), 3656-3662.

(792) Young, D. D.; Edwards, W. F.; Lusic, H.; Lively, M. O.; Deiters, A. Light-triggered polymerase chain reaction. *Chem. Commun.* **2008,** (4), 462-464.

(793) Tanaka, K.; Katada, H.; Shigi, N.; Kuzuya, A.; Komiyama, M. Site-Selective Blocking of PCR by a Caged Nucleotide Leading to Direct Creation of Desired Sticky Ends in The Products. *Chembiochem.* **2008,** *9* (13), 2120-2126.

(794) Prokup, A.; Hemphill, J.; Deiters, A. DNA Computation: A Photochemically Controlled AND Gate. *J. Am. Chem. Soc.* **2012,** *134* (8), 3810-3815.

(795) Govan, J. M.; Young, D. D.; Lively, M. O.; Deiters, A. Optically Triggered Immune Response through Photocaged Oligonucleotides. *Tetrahedron Lett.* **2015,** *56* (23), 3639-3642.

(796) Govan, J. M.; Uprety, R.; Hemphill, J.; Lively, M. O.; Deiters, A. Regulation of Transcription through Light-Activation and Light-Deactivation of Triplex-Forming Oligonucleotides in Mammalian Cells. *ACS Chem. Biol.* **2012,** *7* (7), 1247-1256.

(797) Govan, J. M.; Lively, M. O.; Deiters, A. Photochemical Control of DNA Decoy Function Enables Precise Regulation of Nuclear Factor κB Activity. *J. Am. Chem. Soc.* **2011,** *133* (33), 13176-13182.

(798) Young, D. D.; Lively, M. O.; Deiters, A. Activation and Deactivation of DNAzyme and Antisense Function with Light for the Photochemical Regulation of Gene Expression in Mammalian Cells. *Journal of the American Chemical Society* **2010,** *132* (17), 6183-6193.

(799) Mikat, V.; Heckel, A. Light-dependent RNA interference with nucleobase-caged siRNAs. *RNA* **2007,** *13* (12), 2341-2347.

(800) Govan, J. M.; Young, D. D.; Lusic, H.; Liu, Q.; Lively, M. O.; Deiters, A. Optochemical control of RNA interference in mammalian cells. *Nucleic Acids Res.* **2013,** *41* (22), 10518-10528.

(801) Krutzfeldt, J.; Rajewsky, N.; Braich, R.; Rajeev, K. G.; Tuschl, T.; Manoharan, M.; Stoffel, M. Silencing of microRNAs in vivo with 'antagomirs'. *Nature* **2005,** *438* (7068), 685-689.

(802) Bennett, C. F.; Swayze, E. E. RNA targeting therapeutics: molecular mechanisms of antisense oligonucleotides as a therapeutic platform. *Annual review of pharmacology and toxicology* **2010,** *50*, 259-293.

(803) Volvert, M.-L.; Prévot, P.-P.; Close, P.; Laguesse, S.; Pirotte, S.; Hemphill, J.; Rogister, F.; Kruzy, N.; Sacheli, R.; Moonen, G.; et al.; MicroRNA Targeting of CoREST Controls Polarization of Migrating Cortical Neurons. *Cell Rep.* **2014,** *7* (4), 1168-1183.

(804) Tan, W.; Wang, K.; Drake, T. J. Molecular beacons. *Curr. Opin. Chem. Biol.* **2004,** *8* (5), 547-553.

(805) Wang, C.; Zhu, Z.; Song, Y.; Lin, H.; Yang, C. J.; Tan, W. Caged molecular beacons: controlling nucleic acid hybridization with light. *Chem. Commun.* **2011,** *47* (20), 5708-5710.

(806) Joshi, K. B.; Vlachos, A.; Mikat, V.; Deller, T.; Heckel, A. Light-activatable molecular beacons with a caged loop sequence. *Chem. Commun.* **2012,** *48* (22), 2746-2748.

(807) Qiu, L.; Wu, C.; You, M.; Han, D.; Chen, T.; Zhu, G.; Jiang, J.; Yu, R.; Tan, W. A Targeted, Self-Delivered, and Photocontrolled Molecular Beacon for mRNA Detection in Living Cells. *J. Am. Chem. Soc.* **2013,** *135* (35), 12952-12955.

(808) Fokina, A. A.; Stetsenko, D. A.; François, J.-C. DNA enzymes as potential therapeutics: towards clinical application of 10-23 DNAzymes. *Expert Opin. Biol. Ther.* **2015,** *15* (5), 689-711.

(809) Richards, J. L.; Seward, G. K.; Wang, Y.-H.; Dmochowski, I. J. Turning the 10–23 DNAzyme On and Off with Light. *Chembiochem.* **2010,** *11* (3), 320-324.

(810) Lusic, H.; Young, D. D.; Lively, M. O.; Deiters, A. Photochemical DNA Activation. *Org. Lett.* **2007,** *9* (10), 1903-1906.

(811) Richards, J. L.; Seward, G. K.; Wang, Y.-H.; Dmochowski, I. J. Turning the 10-23 DNAzyme On and Off with light. *Chembiochem.* **2010,** *11* (3), 320-324.

(812) Hwang, K.; Wu, P.; Kim, T.; Lei, L.; Tian, S.; Wang, Y.; Lu, Y. Photocaged DNAzymes as a General Method for Sensing Metal Ions in Living Cells. *Angew. Chem. Int. Ed. Engl.* **2014,** *53* (50), 13798-13802.

(813) Wang, X.; Feng, M.; Xiao, L.; Tong, A.; Xiang, Y. Postsynthetic Modification of DNA Phosphodiester Backbone for Photocaged DNAzyme. *ACS Chem. Biol.* **2016,** *11* (2), 444-451.

(814) Donato, L.; Mourot, A.; Davenport, C. M.; Herbivo, C.; Warther, D.; Léonard, J.; Bolze, F.; Nicoud, J.-F.; Kramer, R. H.; Goeldner, M.; et al.; Water-Soluble, Donor–Acceptor Biphenyl Derivatives in the 2-(o-Nitrophenyl)propyl Series: Highly Efficient Two-Photon Uncaging of the Neurotransmitter γ-Aminobutyric Acid at λ = 800 nm(). *Angew. Chem. Int. Ed. Engl.* **2012,** *51* (8), 1840-1843.

(815) Fichte, M. A. H.; Weyel, X. M. M.; Junek, S.; Schäfer, F.; Herbivo, C.; Goeldner, M.; Specht, A.; Wachtveitl, J.; Heckel, A. Three-Dimensional Control of DNA Hybridization by Orthogonal Two-Color Two-Photon Uncaging. *Angew. Chem. Int. Ed. Engl.* **2016,** *55* (31), 8948-8952.

(816) Benninger, R. K. P.; Piston, D. W. Two-Photon Excitation Microscopy for the Study of Living Cells and Tissues. *Current protocols in cell biology / editorial board, Juan S. Bonifacino ... [et al.]* **2013,** *0 4*, Unit-4.1124.

(817) Miller, M. J.; Wei, S. H.; Parker, I.; Cahalan, M. D. Two-Photon Imaging of Lymphocyte Motility and Antigen Response in Intact Lymph Node. *Science* **2002,** *296* (5574), 1869.

(818) Belluscio, L. Two-Photon Imaging in Live Rodents. In *Current Protocols in Neuroscience*, John Wiley & Sons, Inc.: 2001.

(819) Jain, A.; Magistri, M.; Napoli, S.; Carbone, G. M.; Catapano, C. V. Mechanisms of triplex DNA-mediated inhibition of transcription initiation in cells. *Biochimie* **2010,** *92* (3), 317-320.

(820) Schleifman, E. B.; Chin, J. Y.; Glazer, P. M. Triplex-Mediated Gene Modification. In *Chromosomal Mutagenesis*, Davis, G. D.; Kayser, K. J., Eds. Humana Press: Totowa, NJ, 2008; pp 175-190.

(821) Yang, N.; Singh, S.; Mahato, R. I. Targeted TFO Delivery to Hepatic Stellate Cells. *J. Control. Release.* **2011,** *155* (2), 326-330.

(822) Kemme, C. A.; Nguyen, D.; Chattopadhyay, A.; Iwahara, J. Regulation of transcription factors via natural decoys in genomic DNA. *Transcription* **2016,** *7* (4), 115-120.

(823) Struntz, N. B.; Harki, D. A. Catch and Release DNA Decoys: Capture and Photochemical Dissociation of NF-κB Transcription Factors. *ACS Chem. Biol.* **2016,** *11* (6), 1631-1638.

(824) Kamensek, U.; Sersa, G.; Vidic, S.; Tevz, G.; Kranjc, S.; Cemazar, M. Irradiation, Cisplatin, and 5-Azacytidine Upregulate Cytomegalovirus Promoter in Tumors and Muscles: Implementation of Non-invasive Fluorescence Imaging. *Mol. Imaging Biol.* **2011,** *13* (1), 43-52.

(825) Alberini, C. M. Transcription Factors in Long-Term Memory and Synaptic Plasticity. *Physiol. Rev.* **2009,** *89* (1), 10.1152/physrev.00017.2008.

(826) Hemphill, J.; Govan, J.; Uprety, R.; Tsang, M.; Deiters, A. Site-Specific Promoter Caging Enables Optochemical Gene Activation in Cells and Animals. *J. Am. Chem. Soc.* **2014,** *136* (19), 7152-7158.

(827) Donato, L.; Mourot, A.; Davenport, C. M.; Herbivo, C.; Warther, D.; Léonard, J.; Bolze, F.; Nicoud, J.-F.; Kramer, R. H.; Goeldner, M.; et al.; Water-soluble, donor-acceptor biphenyl derivatives in the 2-(o-nitrophenyl)propyl series: highly efficient two-photon uncaging of the neurotransmitter γ-aminobutyric acid at λ = 800 nm. *Angew. Chem. Int. Ed. Engl.* **2012,** *51* (8), 1840-1843.

(828) Yamazoe, S.; Liu, Q.; McQuade, L. E.; Deiters, A.; Chen, J. K. Sequential Gene Silencing Using Wavelength-Selective Caged Morpholino Oligonucleotides. *Angew. Chem. Int. Ed. Engl.* **2014,** *53* (38), 10114-10118.

(829) Liaunardy-Jopeace, A.; Murton, B. L.; Mahesh, M.; Chin, J. W.; James, J. R. Encoding optical control in LCK kinase to quantitatively investigate its activity in live cells. *Nat. Struct. Mol. Biol.* **2017,** *24* (12), 1155-1163.

(830) Veetil, A. T.; Chakraborty, K.; Xiao, K.; Minter, M. R.; Sisodia, S. S.; Krishnan, Y. Cell-targetable DNA nanocapsules for spatiotemporal release of caged bioactive small molecules. *Nat. Nanotechnol.* **2017,** *12*, 1183.

(831) Agarwal, H. K.; Janicek, R.; Chi, S.-H.; Perry, J. W.; Niggli, E.; Ellis-Davies, G. C. R. Calcium Uncaging with Visible Light. *J. Am. Chem. Soc.* **2016,** *138* (11), 3687-3693.

(832) Watanabe, T.; Hoshida, T.; Sakyo, J.; Kishi, M.; Tanabe, S.; Matsuura, J.; Akiyama, S.; Nakata, M.; Tanabe, Y.; Suzuki, A. Z.; et al.; Synthesis of nucleobase-caged peptide nucleic acids having improved photochemical properties. *Org. Biomol. Chem.* **2014,** *12* (28), 5089-5093.

(833) Guha, S.; Graf, J.; Göricke, B.; Diederichsen, U. Nucleobase-caged peptide nucleic acids: PNA/PNA duplex destabilization and light-triggered PNA/PNA recognition. *J. Pept. Sci.* **2013,** *19* (7), 415-422.

(834) Stafforst, T.; Hilvert, D. Modulating PNA/DNA Hybridization by Light. *Angew. Chem. Int. Ed. Engl.* **2010,** *49* (51), 9998-10001.

(835) Summerton, J.; Weller, D. Morpholino Antisense Oligomers: Design, Preparation, and Properties. *Antisense Nucleic Acid Drug Dev.* **1997,** *7* (3), 187-195.

(836) Eisen, J. S.; Smith, J. C. Controlling morpholino experiments: don't stop making antisense. *Development* **2008,** *135* (10), 1735-1743.

(837) Shestopalov, I. A.; Chen, J. K. Spatiotemporal Control of Embryonic Gene Expression Using Caged Morpholinos. *Methods Cell Biol.* **2011,** *104*, 151-172.

(838) Payumo, A. Y.; McQuade, L. E.; Walker, W. J.; Yamazoe, S.; Chen, J. K. Tbx16 regulates hox gene activation in mesodermal progenitor cells. *Nat Chem Biol* **2016,** *12* (9), 694-701.

(839) Yamazoe, S.; McQuade, L. E.; Chen, J. K. Nitroreductase-Activatable Morpholino Oligonucleotides for in Vivo Gene Silencing. *ACS Chem. Biol.* **2014,** *9* (9), 1985-1990.

(840) Yamazoe, S.; Shestopalov, I. A.; Provost, E.; Leach, S. D.; Chen, J. K. Cyclic caged morpholinos: conformationally gated probes of embryonic gene function. *Angew. Chem. Int. Ed. Engl.* **2012,** *51* (28), 6908-6911.

(841) Tang, X.; Su, M.; Yu, L.; Lv, C.; Wang, J.; Li, Z. Photomodulating RNA cleavage using photolabile circular antisense oligodeoxynucleotides. *Nucleic Acids Res.* **2010**.

(842) Weinberg, E. S.; Allende, M. L.; Kelly, C. S.; Abdelhamid, A.; Murakami, T.; Andermann, P.; Doerre, O. G.; Grunwald, D. J.; Riggleman, B. Developmental regulation of zebrafish MyoD in wild-type, no tail and spadetail embryos. *Development* **1996,** *122* (1), 271.

(843) Amacher, S. L.; Kimmel, C. B. Promoting notochord fate and repressing muscle development in zebrafish axial mesoderm. *Development* **1998,** *125* (8), 1397.

(844) Ferguson, D. P.; Schmitt, E. E.; Lightfoot, J. T. Vivo-morpholinos induced transient knockdown of physical activity related proteins. *PLoS One* **2013,** *8* (4), e61472.

(845) Bedell, V. M.; Westcot, S. E.; Ekker, S. C. Lessons from morpholino-based screening in zebrafish. *Brief. Funct. Genomics.* **2011,** *10* (4), 181-188.

(846) Joris, M.; Schloesser, M.; Baurain, D.; Hanikenne, M.; Muller, M.; Motte, P. Number of inadvertent RNA targets for morpholino knockdown in Danio rerio is largely underestimated: evidence from the study of Ser/Arg-rich splicing factors. *Nucleic Acids Res.* **2017,** *45* (16), 9547-9557.

(847) Sun, Y.-M.; Lin, K.-Y.; Chen, Y.-Q. Diverse functions of miR-125 family in different cell contexts. *J. Hematol. Oncol.* **2013,** *6*, 6-6.

(848) Corrà, F.; Agnoletto, C.; Minotti, L.; Baldassari, F.; Volinia, S. The Network of Non-coding RNAs in Cancer Drug Resistance. *Front. Oncol.* **2018,** *8*, 327.

(849) Le, M. T. N.; Teh, C.; Shyh-Chang, N.; Xie, H.; Zhou, B.; Korzh, V.; Lodish, H. F.; Lim, B. MicroRNA-125b is a novel negative regulator of p53. *Genes Dev.* **2009,** *23* (7), 862-876.

(850) Wang, X.; Zheng, Y.; Ma, Y.; Du, L.; Chu, F.; Gu, H.; Dahlgren, R. A.; Li, Y.; Wang, H. Lipid metabolism disorder induced by up-regulation of miR-125b and miR-144 following β-diketone antibiotic exposure to F0-zebrafish (Danio rerio). *Ecotoxicol. Environ. Saf.* **2018,** *164*, 243-252.

(851) Doyle, D. F.; Braasch, D. A.; Janowski, B. A.; Corey, D. R. Inhibition of Gene Expression Inside Cells by Peptide Nucleic Acids: Effect of mRNA Target Sequence, Mismatched Bases, and PNA Length. *Biochemistry* **2001,** *40* (1), 53-64.

(852) Morcos, P. A. Achieving efficient delivery of morpholino oligos in cultured cells. *Genesis.* **2001,** *30* (3), 94-102.

(853) Summerton, J. E. Endo-Porter: A Novel Reagent for Safe, Effective Delivery of Substances into Cells. *Annals of the New York Academy of Sciences* **2005,** *1058* (1), 62-75.

(854) Liu, M.-m.; Li, Z.; Han, X.-d.; Shi, J.-h.; Tu, D.-y.; Song, W.; Zhang, J.; Qiu, X.-l.; Ren, Y.; Zhen, L.-l. MiR-30e inhibits tumor growth and chemoresistance via targeting IRS1 in Breast Cancer. *Sci. Rep.* **2017,** *7* (1), 15929.

(855) Mao, J.; Hu, X.; Pang, P.; Zhou, B.; Li, D.; Shan, H. miR-30e acts as a tumor suppressor in hepatocellular carcinoma partly via JAK1/STAT3 pathway. *Oncol. Rep.* **2017,** *38* (1), 393-401.

(856) Neri, P.; Gratton, K.; Ren, L.; Johnson, J.; Slaby, J.; Duggan, P.; Stewart, D. A.; Bahlis, N. J. Role of Mir-30e in Multiple Myeloma Cells Resistance to Lenalidomide and Bortezomib. *Blood* **2012,** *120* (21), 323.

(857) Mao, L.; Liu, S.; Hu, L.; Jia, L.; Wang, H.; Guo, M.; Chen, C.; Liu, Y.; Xu, L. miR-30 Family: A Promising Regulator in Development and Disease. *Biomed. Res. Int.* **2018,** *2018*, 9623412-9623412.

(858) Ketley, A.; Warren, A.; Holmes, E.; Gering, M.; Aboobaker, A. A.; Brook, J. D. The miR-30 MicroRNA Family Targets smoothened to Regulate Hedgehog Signalling in Zebrafish Early Muscle Development. *PLoS One* **2013,** *8* (6), e65170.

(859) Bendifallah, N.; Rasmussen, F. W.; Zachar, V.; Ebbesen, P.; Nielsen, P. E.; Koppelhus, U. Evaluation of Cell-Penetrating Peptides (CPPs) as Vehicles for Intracellular Delivery of Antisense Peptide Nucleic Acid (PNA). *Bioconjug. Chem.* **2006,** *17* (3), 750-758.

(860) Sarko, D.; Beijer, B.; Garcia Boy, R.; Nothelfer, E.-M.; Leotta, K.; Eisenhut, M.; Altmann, A.; Haberkorn, U.; Mier, W. The Pharmacokinetics of Cell-Penetrating Peptides. *Mol. Pharm.* **2010,** *7* (6), 2224-2231.

(861) Ndeboko, B.; Ramamurthy, N.; Lemamy, G. J.; Jamard, C.; Nielsen, P. E.; Cova, L. Role of Cell-Penetrating Peptides in Intracellular Delivery of Peptide Nucleic Acids Targeting Hepadnaviral Replication. *Mol. Ther. Nucleic Acids* **2017,** *9*, 162-169.

(862) Wu, R. P.; Youngblood, D. S.; Hassinger, J. N.; Lovejoy, C. E.; Nelson, M. H.; Iversen, P. L.; Moulton, H. M. Cell-penetrating peptides as transporters for morpholino oligomers: effects of amino acid composition on intracellular delivery and cytotoxicity. *Nucleic Acids Res.* **2007,** *35* (15), 5182-5191.

(863) Margus, H.; Padari, K.; Pooga, M. Cell-penetrating Peptides as Versatile Vehicles for Oligonucleotide Delivery. *Mol. Ther.* **2012,** *20* (3), 525-533.

(864) Dalal, C.; Jana, N. R. Multivalency Effect of TAT-Peptide-Functionalized Nanoparticle in Cellular Endocytosis and Subcellular Trafficking. *J. Phys. Chem. B.* **2017,** *121* (14), 2942-2951.

(865) Khvorova, A.; Watts, J. K. The chemical evolution of oligonucleotide therapies of clinical utility. *Nat. Biotechnol.* **2017,** *35*, 238.

(866) McClorey, G.; Wood, M. J. An overview of the clinical application of antisense oligonucleotides for RNA-targeting therapies. *Curr. Opin. Pharmacol.* **2015,** *24*, 52-58.

(867) Juliano, R. L. The delivery of therapeutic oligonucleotides. *Nucleic Acids Res.* **2016,** *44* (14), 6518-6548.

(868) Juliano, R. L.; Carver, K. Cellular uptake and intracellular trafficking of oligonucleotides. *Adv. Drug Deliv. Rev.* **2015,** *87*, 35-45.

(869) Agrawal, S.; Temsamani, J.; Galbraith, W.; Tang, J. Pharmacokinetics of antisense oligonucleotides. *Clin. Pharmacokinet.* **1995,** *28* (1), 7-16.

(870) Wang, Y.; Miao, L.; Satterlee, A.; Huang, L. Delivery of oligonucleotides with lipid nanoparticles. *Adv. Drug Deliv. Rev.* **2015,** *87*, 68-80.

(871) Lam, J. K. W.; Chow, M. Y. T.; Zhang, Y.; Leung, S. W. S. siRNA Versus miRNA as Therapeutics for Gene Silencing. *Mol. Ther. Nucleic Acids.* **2015,** *4* (9), e252-e252.

(872) Yuba, E.; Nakajima, Y.; Tsukamoto, K.; Iwashita, S.; Kojima, C.; Harada, A.; Kono, K. Effect of unsaturated alkyl chains on transfection activity of poly(amidoamine) dendron-bearing lipids. *J. Control Release.* **2012,** *160* (3), 552-560.

(873) Meissner, J. M.; Toporkiewicz, M.; Czogalla, A.; Matusewicz, L.; Kuliczkowski, K.; Sikorski, A. F. Novel antisense therapeutics delivery systems: In vitro and in vivo studies of liposomes targeted with anti-CD20 antibody. *J. Control Release* **2015,** *220*, 515-528.

(874) Wullner, U.; Neef, I.; Eller, A.; Kleines, M.; Tur, M. K.; Barth, S. Cell-specific induction of apoptosis by rationally designed bivalent aptamer-siRNA transcripts silencing eukaryotic elongation factor 2. *Curr. Cancer Drug Targets.* **2008,** *8* (7), 554-565.

(875) Zhou, J.; Tiemann, K.; Chomchan, P.; Alluin, J.; Swiderski, P.; Burnett, J.; Zhang, X.; Forman, S.; Chen, R.; Rossi, J. Dual functional BAFF receptor aptamers inhibit ligand-induced proliferation and deliver siRNAs to NHL cells. *Nucleic Acids Res.* **2013,** *41* (7), 4266-4283.

(876) Catuogno, S.; Rienzo, A.; Di Vito, A.; Esposito, C. L.; de Franciscis, V. Selective delivery of therapeutic single strand antimiRs by aptamer-based conjugates. *J. Control Release.* **2015,** *210*, 147-159.

(877) Esposito, C. L.; Cerchia, L.; Catuogno, S.; De Vita, G.; Dassie, J. P.; Santamaria, G.; Swiderski, P.; Condorelli, G.; Giangrande, P. H.; de Franciscis, V. Multifunctional aptamer-miRNA conjugates for targeted cancer therapy. *Mol. Ther.* **2014,** *22* (6), 1151-1163.

(878) Song, E.; Zhu, P.; Lee, S.-K.; Chowdhury, D.; Kussman, S.; Dykxhoorn, D. M.; Feng, Y.; Palliser, D.; Weiner, D. B.; Shankar, P.; et al.; Antibody mediated in vivo delivery of small interfering RNAs via cell-surface receptors. *Nat. Biotechnol.* **2005,** *23*, 709.

(879) Yao, Y.-d.; Sun, T.-m.; Huang, S.-y.; Dou, S.; Lin, L.; Chen, J.-n.; Ruan, J.-b.; Mao, C.-q.; Yu, F.-y.; Zeng, M.-s.; et al.; Targeted Delivery of PLK1-siRNA by ScFv Suppresses Her2+ Breast Cancer Growth and Metastasis. *Sci. Transl. Med.* **2012,** *4* (130), 130ra48.

(880) Cuellar, T. L.; Barnes, D.; Nelson, C.; Tanguay, J.; Yu, S.-F.; Wen, X.; Scales, S. J.; Gesch, J.; Davis, D.; van Brabant Smith, A.; et al.; Systematic evaluation of antibody-mediated siRNA delivery using an industrial platform of THIOMAB-siRNA conjugates. *Nucleic Acids Res.* **2015,** *43* (2), 1189-1203.

(881) Spinelli, N.; Defrancq, E.; Morvan, F. Glycoclusters on oligonucleotide and PNA scaffolds: synthesis and applications. *Chem. Soc. Rev.* **2013,** *42* (11), 4557-4573.

(882) Nair, J. K.; Willoughby, J. L. S.; Chan, A.; Charisse, K.; Alam, M. R.; Wang, Q.; Hoekstra, M.; Kandasamy, P.; Kel'in, A. V.; Milstein, S.; et al.; Multivalent N-Acetylgalactosamine-Conjugated siRNA Localizes in Hepatocytes and Elicits Robust RNAi-Mediated Gene Silencing. *J. Am. Chem. Soc.* **2014,** *136* (49), 16958-16961.

(883) Matsuda, S.; Keiser, K.; Nair, J. K.; Charisse, K.; Manoharan, R. M.; Kretschmer, P.; Peng, C. G.; V. Kel'in, A.; Kandasamy, P.; Willoughby, J. L. S.; et al.; siRNA Conjugates Carrying Sequentially Assembled Trivalent N-Acetylgalactosamine Linked Through Nucleosides Elicit Robust Gene Silencing In Vivo in Hepatocytes. *ACS Chem. Biol.* **2015,** *10* (5), 1181-1187.

(884) Govan, J. M.; Uprety, R.; Thomas, M.; Lusic, H.; Lively, M. O.; Deiters, A. Cellular delivery and photochemical activation of antisense agents through a nucleobase caging strategy. *ACS Chem. Biol.* **2013,** *8* (10), 2272-2282.

(885) Santiana, J. J.; Sui, B.; Gomez, N.; Rouge, J. L. Programmable Peptide-Cross-Linked Nucleic Acid Nanocapsules as a Modular Platform for Enzyme Specific Cargo Release. *Bioconjug. Chem.* **2017,** *28* (12), 2910-2914.

(886) Turner, J. J.; Williams, D.; Owen, D.; Gait, M. J. Disulfide Conjugation of Peptides to Oligonucleotides and Their Analogs. *Curr. Protoc. Nucleic Acid Chem.* **2006,** *24* (1), 4.28.1-4.28.21.

(887) Boisguérin, P.; Deshayes, S.; Gait, M. J.; O'Donovan, L.; Godfrey, C.; Betts, C. A.; Wood, M. J. A.; Lebleu, B. Delivery of therapeutic oligonucleotides with cell penetrating peptides. *Adv. Drug Deliv. Rev.* **2015,** *87*, 52-67.

(888) Bahal, R.; McNeer, N. A.; Ly, D. H.; Saltzman, W. M.; Glazer, P. M. Nanoparticle for delivery of antisense γPNA oligomers targeting CCR5. *Artificial DNA, PNA & XNA* **2013,** *4* (2), 49-57.

(889) Demidov, V. V.; Potaman, V. N.; Frank-Kamenetskil, M.; Egholm, M.; Buchard, O.; Sönnichsen, S. H.; Nlelsen, P. E. Stability of peptide nucleic acids in human serum and cellular extracts. *Biochem. Pharmacol.* **1994,** *48* (6), 1310-1313.

(890) Bahal, R.; Quijano, E.; McNeer, N. A.; Liu, Y.; Bhunia, D. C.; Lopez-Giraldez, F.; Fields, R. J.; Saltzman, W. M.; Ly, D. H.; Glazer, P. M. Single-stranded γPNAs for in vivo site-specific genome editing via Watson-Crick recognition. *Curr. Gene Ther.* **2014,** *14* (5), 331-342.

(891) Koppelhus, U.; Nielsen, P. E. Cellular delivery of peptide nucleic acid (PNA). *Adv. Drug Deliv. Rev.* **2003,** *55* (2), 267-280.

(892) Qiu, F.; Chen, Y.; Tang, C.; Zhao, X. Amphiphilic peptides as novel nanomaterials: design, self-assembly and application. *Int. J. Nanomedicine.* **2018,** *13*, 5003-5022.

(893) Maier, M. A.; Esau, C. C.; Siwkowski, A. M.; Wancewicz, E. V.; Albertshofer, K.; Kinberger, G. A.; Kadaba, N. S.; Watanabe, T.; Manoharan, M.; Bennett, C. F.; et al.; Evaluation of basic amphipathic peptides for cellular delivery of antisense peptide nucleic acids. *J. Med. Chem.* **2006,** *49* (8), 2534-2542.

(894) Obad, S.; dos Santos, C. O.; Petri, A.; Heidenblad, M.; Broom, O.; Ruse, C.; Fu, C.; Lindow, M.; Stenvang, J.; Straarup, E. M.; et al.; Silencing of microRNA families by seed-targeting tiny LNAs. *Nat. Genet.* **2011,** *43* (4), 371-378.

(895) Manicardi, A.; Corradini, R. Effect of chirality in gamma-PNA: PNA interaction, another piece in the picture. *Artif. DNA PNA XNA* **2014,** *5* (3), e1131801.

(896) Graveley, B. R. Alternative splicing: increasing diversity in the proteomic world. *Trends in Genetics* **2001,** *17* (2), 100-107.

(897) Stamm, S.; Ben-Ari, S.; Rafalska, I.; Tang, Y.; Zhang, Z.; Toiber, D.; Thanaraj, T. A.; Soreq, H. Function of alternative splicing. *Gene* **2005,** *344*, 1-20.

(898) Lee, L. J.; Frey, B. J.; Blencowe, B. J.; Shai, O.; Pan, Q. Deep surveying of alternative splicing complexity in the human transcriptome by high-throughput sequencing. *Nat. Genet.* **2008,** *40* (12), 1413-1415.

(899) Cieply, B.; Carstens, R. P. Functional roles of alternative splicing factors in human disease. *Wiley Interdiscip. Rev. RNA* **2015,** *6* (3), 311-326.

(900) Sazani, P.; Kang, S. H.; Maier, M. A.; Wei, C.; Dillman, J.; Summerton, J.; Manoharan, M.; Kole, R. Nuclear antisense effects of neutral, anionic and cationic oligonucleotide analogs. *Nucleic acids research* **2001,** *29* (19), 3965-3974.

(901) Sazani, P.; Kang, S. H.; Maier, M. A.; Wei, C.; Dillman, J.; Summerton, J.; Manoharan, M.; Kole, R. Nuclear antisense effects of neutral, anionic and cationic oligonucleotide analogs. *Nucleic Acids Res.* **2001,** *29* (19), 3965-3974.

(902) Cordier, C.; Boutimah, F.; Bourdeloux, M.; Dupuy, F.; Met, E.; Alberti, P.; Loll, F.; Chassaing, G.; Burlina, F.; Saison-Behmoaras, T. E. Delivery of Antisense Peptide Nucleic Acids to Cells by Conjugation with Small Arginine-Rich Cell-Penetrating Peptide (R/W)9. *PLoS One* **2014,** *9* (8), e104999.

(903) Zhao, X.-L.; Chen, B.-C.; Han, J.-C.; Wei, L.; Pan, X.-B. Delivery of cell-penetrating peptide-peptide nucleic acid conjugates by assembly on an oligonucleotide scaffold. *Sci. Rep.* **2015,** *5*, 17640.

(904) Sazani, P.; Gemignani, F.; Kang, S.-H.; Maier, M. A.; Manoharan, M.; Persmark, M.; Bortner, D.; Kole, R. Systemically delivered antisense oligomers upregulate gene expression in mouse tissues. *Nat. Biotechnol.* **2002,** *20* (12), 1228-1233.

(905) Zhang, X.; Castanotto, D.; Nam, S.; Horne, D.; Stein, C. 6BIO Enhances Oligonucleotide Activity in Cells: A Potential Combinatorial Anti-androgen Receptor Therapy in Prostate Cancer Cells. *Mol. Ther.* **2017,** *25* (1), 79-91.

(906) Zhang, X.; Castanotto, D.; Liu, X.; Shemi, A.; Stein, C. A. Ammonium and arsenic trioxide are potent facilitators of oligonucleotide function when delivered by gymnosis. *Nucleic Acids Res.* **2018,** *46* (7), 3612-3624.

(907) Yang, B.; Ming, X.; Cao, C.; Laing, B.; Yuan, A.; Porter, M. A.; Hull-Ryde, E. A.; Maddry, J.; Suto, M.; Janzen, W. P.; et al.; High-throughput screening identifies small molecules that enhance the pharmacological effects of oligonucleotides. *Nucleic Acids Res.* **2015,** *43* (4), 1987-1996.

(908) Lönn, P.; Kacsinta, A. D.; Cui, X.-S.; Hamil, A. S.; Kaulich, M.; Gogoi, K.; Dowdy, S. F. Enhancing Endosomal Escape for Intracellular Delivery of Macromolecular Biologic Therapeutics. *Sci. Rep.* **2016,** *6*, 32301.

(909) Han, J.; Xiong, J.; Wang, D.; Fu, X.-D. Pre-mRNA splicing: where and when in the nucleus. *Trends in Cell Biology* **2011,** *21* (6), 336-343.

(910) Obad, S.; dos Santos, C. O.; Petri, A.; Heidenblad, M.; Broom, O.; Ruse, C.; Fu, C.; Lindow, M.; Stenvang, J.; Straarup, E. M.; et al.; Silencing of microRNA families by seed-targeting tiny LNAs. *Nature Genetics* **2011,** *43*, 371.

(911) Sahu, B.; Chenna, V.; Lathrop, K. L.; Thomas, S. M.; Zon, G.; Livak, K. J.; Ly, D. H. Synthesis of Conformationally Preorganized and Cell-Permeable Guanidine-Based γ-Peptide Nucleic Acids (γGPNAs). *J. Org. Chem.* **2009,** *74* (4), 1509-1516.

(912) Liu, H.; Naismith, J. H. An efficient one-step site-directed deletion, insertion, single and multiple-site plasmid mutagenesis protocol. *BMC Biotechnol.* **2008,** *8* (1), 91.

(913) Zheng, L.; Baumann, U.; Reymond, J.-L. An efficient one-step site-directed and site-saturation mutagenesis protocol. *Nucleic Acids Res.* **2004,** *32* (14), e115-e115.

(914) Ogris, M.; Wagner, E. Synthesis of Linear Polyethylenimine and Use in Transfection. *Cold Spring Harb. Protoc.* **2012,** *2012* (2), pdb.prot067868.

(915) Boussif, O.; Lezoualc'h, F.; Zanta, M. A.; Mergny, M. D.; Scherman, D.; Demeneix, B.; Behr, J. P. A versatile vector for gene and oligonucleotide transfer into cells in culture and in vivo: polyethylenimine. *Proc. Natl. Acad. Sci. U. S. A.* **1995,** *92* (16), 7297-7301.

(916) Longo, P. A.; Kavran, J. M.; Kim, M.-S.; Leahy, D. J. Transient mammalian cell transfection with polyethylenimine (PEI). *Methods Enzymol.* **2013,** *529*, 227-240.

(917) Hsu, C. Y. M.; Uludağ, H. A simple and rapid nonviral approach to efficiently transfect primary tissue–derived cells using polyethylenimine. *Nat. Protoc.* **2012,** *7*, 935.

(918) Abdi, H. Bonferroni and Šidák corrections for multiple comparisons. *Encyc. Meas. Stat.* **2007,** *3*, 103-107.

(919) Holm, S. A simple sequentially rejective multiple test procedure. *Scand. J. Stat.* **1979**, 65-70.

(920) Riss, T. L.; Moravec, R. A.; Niles, A. L.; Duellman, S.; Benink, H. A.; Worzella, T. J.; Minor, L. Cell Viability Assays. **2016**.

(921) Sittampalam, G.; Coussens, N.; Brimacombe, K.; Grossman, A.; Arkin, M.; Auld, D.; Austin, C.; Baell, J.; Bejcek, B.; Chung, T. Assay guidance manual. **2004**.